Scaling Laws for the Energy Transfer in Space Plasma Turbulence

Raffaele Marino, Luca Sorriso-Valvo

Scaling Laws for the Energy Transfer in Space Plasma Turbulence

Raffaele Marino[a,*], Luca Sorriso-Valvo[b,c,*]

[a] *Université de Lyon, CNRS, École Centrale de Lyon, INSA de Lyon, Université Claude Bernard Lyon 1, Laboratoire de Mécanique des Fluides et d'Acoustique, F-69134 Écully, France*

[b] *CNR/ISTP – Istituto per la Scienza e Tecnologia dei Plasmi, Via Amendola 122/D, 70126 Bari, Italy*

[c] *Swedish Institute of Space Physics (IRF), Ångström Laboratory, Lägerhyddsvägen 1, SE-751 21 Uppsala, Sweden*

Abstract

One major trait of space plasmas is the multi-scale dynamics resulting from non-linear transfers and conversions of various forms of energy. Routinely evidenced in a range from the large-scale solar structures down to the characteristic scales of ions and electrons, turbulence is a major cross-scale energy transfer mechanism in space plasmas. At intermediate scales, the fate of the energy in the outer space is mainly determined by the interplay of turbulent motions and propagating waves. More mechanisms are advocated to account for the transfer and conversion of energy, including magnetic reconnection, emission of radiation and particle energization, all contributing to make the dynamical state of solar and heliospheric plasmas difficult to predict. The characterization of the energy transfer in space plasmas benefited from numerous robotic missions. However, together with breakthrough technologies, novel theoretical developments and methodologies for the analysis of data played a crucial role in advancing our understanding of how energy is transferred across the scales in the space. In recent decades, several scaling laws were obtained providing effective ways to model the energy flux in turbulent plasmas. Under certain assumptions, these relations enabled to utilize reduced knowledge (in terms of degrees of freedom) of the fields from space-

*Corresponding Authors

Email addresses: raffaele.marino@cnrs.fr (Raffaele Marino), luca.sorrisovalvo@cnr.it (Luca Sorriso-Valvo)

craft observations to obtain direct estimates of the energy transfer rates (and not only) in the interplanetary space, also in the proximity of the Sun and planets. Starting from the first third-order exact law for the magnetohydrodynamics by Politano and Pouquet (1998), we present a detailed review of the main scaling laws for the energy transfer in plasma turbulence and their application, presenting theoretical and observational milestones of what has become one of the main approaches for the characterization of turbulent dynamics and energetics in space plasmas.

Keywords: Space Plasmas, Turbulence, Energy transfer, Magnetohydrodynamics, Scaling Laws, Solar Wind, Heliosphere, Sun, Waves

---

Contents

1. Introduction

Nature is pervaded by a multitude of flows whose dynamics is determined by the sources of the physical fields and by the interplay between mechanisms competing for the conversion and redistribution of energy over a wide range of modes and scales. The complexity of these frameworks stems from the large number of degrees of freedom and the existence of characteristic scales identifying ranges where different physical phenomena dominate, yet with structures from all the regimes interacting in a non-linear fashion. This is the typical phenomenological scenario for geophysical and astrophysical flows and in particular for the solar wind, a supersonic, weakly collisional plasma stream produced by the Sun that represents *de facto* the widest multi-scale natural flow accessible through *in situ* observations. The solar wind blows from the Sun's corona, filling the interplanetary space unhindered for hundreds of millions of kilometers, except at very few locations where it is shaped by the planetary magnetospheres.

Solar wind velocity and magnetic field are forced when they originate at the scales of the large dynamical structures developing over the solar surface and in the solar corona, where energy is injected into this unique plasma framework. The transfer of energy towards smaller scales, and sometimes back to the larger, entangles with small-scale field-particle interaction processes, resulting in continued conversion between kinetic and magnetic energy and, eventually, in particle energization and enhancement of collisions. Turbulence and plasma physics processes drive the complex, cross-scale and trans-regime dynamics of the interplanetary plasma, connecting solar-system macroscopic to wave-particle microscopic spatial and temporal scales. How these processes influence each other remains one major, fascinating puzzle in space and astrophysical plasma physics.

Because of today's computational limitations, numerical simulations are unable to resolve plasma dynamics from the magnetohydrodynamic (MHD) to the kinetic scales in three dimensions. Likewise, technology constraints do not presently permit to produce weakly collisional plasmas in laboratory with an extended dynamical range. On the other hand, the heliospheric missions that measured *in situ* the interplanetary plasma in the last decades, together with the great dynamism and creativity of the growing space plasma community, favoured huge steps forward in understanding the underlying dynamics of MHD and kinetic plasmas. Thanks to the unprecedented resolution reached by the most recent observers, the solar wind has therefore become

an indispensable framework to develop turbulence theories and verify fundamental plasma physics laws. This has been the case for the extension to the plasma case of classical fluid turbulence scaling laws, whose broad scientific relevance resides in their capability to capture universal features of many self-similar processes in multi-physics frameworks in nature, from superfluids to the interstellar space. A boost to research on space plasma turbulence and to the cross-scale plasma dynamics was given by the derivation of an exact law analogous of the Von-Kármán Howarth equation for homogeneous isotropic turbulent fluids, by H. Politano & A. Pouquet, known as P&P law (Politano and Pouquet, 1998; Politano and Pouquet, 1998). This scaling relation for the mixed third-order structure function of velocity and magnetic field represents a cornerstone for the investigation of the turbulent energy transfer in space plasmas. Its merit has been to provide the community with a tool immediately applicable to space observations, which is able to connect without ambiguity macro and micro scales in the weakly collisional solar wind plasma. The first observations of the P&P law in the solar wind (MacBride et al., 2005; Sorriso-Valvo et al., 2007) have made it possible to ascertain the turbulent nature of velocity and magnetic field fluctuations in space plasmas and to estimate for the first time the turbulent energy transfer rate in the solar wind, as well as the extent of its contribution to the local heating of the interplanetary medium (Marino et al., 2008). These findings contributed to advance the understanding of non-relativistic space plasmas at a very fundamental level, providing insights on both statistical properties and phenomenology. Indeed, the direct evidence of the turbulent heating as is inferred through the P&P law qualifies the solar wind as an out-of-equilibrium framework, where a time-irreversible energy conversion channel must be accomplished (together with its extraction from the system through other routes). Since it does, the small-scale transfer is likely to happen by wave-particle interaction mechanisms, among others, which might be as well the case for cosmic plasmas outside the heliosphere, thus making the solar wind a laboratory for the investigation of astrophysical plasmas and of low density, unconfined plasmas in general. These early works opened a whole research sub-field in the space community and the utilization of the P&P law and its later extensions to the compressible and/or anisotropic MHD, Hall-MHD, etc. cases has in the meantime evolved to that of a major tool for the investigation of dynamics and energetics in interplanetary plasmas. More than twenty years after the derivation of the original P&P law, with two of the most technologically advanced space plasma missions just being

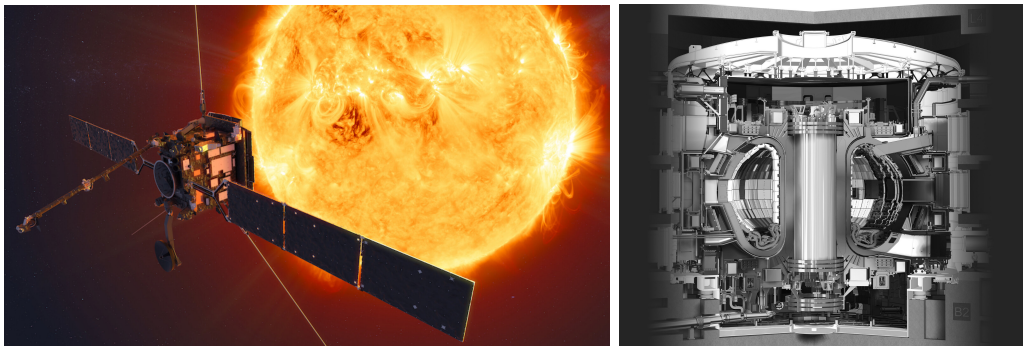

Figure 1: Left: artist's impression of the ESA Solar Orbiter spacecraft (from `www.esa.int`). Right: rendering of the ITER tokamak (from `www.iter.org`).

launched (Parker Solar Probe - Fox et al. (2016) and Solar Orbiter - Müller et al. (2020), see Figure 1) and the project of the most powerful plasma fusion machine (ITER, see Figure 1, Rebut, 1995) on the way, we propose a comprehensive review of hypotheses, range of validity and main observational evidences of the scaling laws for plasmas and the breakthrough they allowed in the space studies field, focusing on their application for the characterization of the global and local energy transfer and the resulting particle energization processes in the interplanetary plasma.

The availability of large data-set from cutting-edge missions is going to enable extensive implementations of the exact laws approach that will make it possible to connect scales in space plasmas, shedding new light on the mechanisms by which energy is converted into heat within the solar wind (such as the Landau damping), and to build a reference framework for interpretation of analogous mechanisms in different nonlinear physical frameworks. A focus of this review will be to highlight the aspects of plasma theory and phenomenology that can be inferred from exact scaling laws for plasmas, in particular the insights on diverse field alignments between the velocity, vorticity, magnetic field, magnetic potential and current. These geometrical features can be measured through various helicity functionals (kinetic-, magnetic- and cross- helicity) and are related to the strength of nonlinearities and of the energy fluxes in space plasma turbulence. The latter are of major importance not only from a fundamental point of view but also to advance the development of operational space weather models and to better understand the coupling of the heliospheric plasmas with the upper atmosphere and the Earth's climate system.

In this review we thus describe theoretical and observational results leading to an increasingly accurate description of features of the turbulent energy transfer in space plasmas. Starting from the seminal work by Politano and Pouquet (1998) and its firsts applications to the to ecliptic (MacBride et al., 2005; MacBride et al., 2008) and polar solar wind (Sorriso-Valvo et al., 2007; Marino et al., 2008), we shall present underlying hypothesis, theoretical derivations and observational evidences of a variety of scaling laws for the characterization of the energy flux in the interplanetary space. This will be done following logical steps, not necessarily analytical, starting from the original framework introduced in Politano and Pouquet (1998) to derive an exact law for the mixed third-order moment of the Elsasser fields in the incompressible, homogeneous and isotropic magnetohydrodynamic case, and then relaxing its hypotheses. In particular, extensions to the anisotropic and/or compressible plasmas, including the Hall effects, will be presented. Numerical results used to explore the validity and accuracy of the introduced scaling laws will be also covered, while the validation by means of spacecraft observations will be proposed to discuss the wide spectrum of conditions and physical processes determining the properties of turbulence and the energy transfer in space plasmas. In particular, we reviewed the validation of scaling laws for the energy transfer in the near-Earth solar wind, in the expanding solar wind from the coronal boundaries to the outer heliosphere, in the interstellar medium, in terrestrial and planetary magnetospheres, and in other specific solar system structures where spacecraft observations allowed to asses the turbulent dynamics. The role of turbulence in the outstanding problem of solar wind non-adiabatic heating is also discussed. Finally, a description of emerging local approaches to the energy transfer is presented, along with a discussion on their usefulness for the identification and the understanding of the kinetic dissipative processes occurring in weakly collisional plasmas. We then conclude with a description of open issues and potential perspectives to extend the reach of the scaling law approach and to provide further support to answer fundamental questions about how the solar system works. Major results that appeared in the literature are reviewed here, anticipated by a first chapter introducing interplanetary space plasmas, where a formal though succinct description of the main theoretical models for the description of plasmas is also presented. Equations and symbols throughout the text were made mostly consistent. Analogies as well as discrepancies among models and scaling laws presented have been thoroughly commented, though some familiarity with the vector formalism is assumed. To give the reader the

chance to identify the contents reported from referenced articles, we made the choice to keep original notations, providing sufficient clarifications in order to reconcile analogous mathematical developments and variables appearing in the different sections.

2. Interplanetary Space Plasmas

The solar system dynamics is largely driven by its most prominent actor: the Sun (Stix, 2002). This is not only true for the gravitational interactions resulting in the planetary dynamics, or for the solar radiation releasing energy to planetary atmospheres and surfaces and to the minor solar system's bodies, but also for the less popular, yet equally important, dynamics of the near-vacuum interplanetary space. Concerning this specific framework, the main solar drivers are the particles continuously flowing from the Sun's atmosphere (the solar corona) together with the solar magnetic field, stretching into the whole solar system as a high-speed plasma stream called the solar wind (Hundhausen, 1972). Within the solar wind, kinetic and magnetic energy are stored and constantly converted and transferred across a gigantic range of scales, spanning from solar to atomic scales, under the joint action of a variety of universal physical mechanisms, including turbulence, waves, magnetic reconnection and particles energization.

2.1. The Heliosphere and the Solar Wind

The existence of a flow of particles in the heliosphere was first suggested to account for the observed correlations between solar activity and geomagnetic activity. It was initially proposed, already in the mid 1800, that signatures of solar events could travel in the interplanetary space and interact with the Earth's magnetic field, generating perturbations measured by magnetometers and eventually producing polar auroras (Carrington, 1859; Loomis, 1860; Stewart, 1861; Loomis, 1862). Later observation of continuous, rather than sporadic, presence of auroral emission led scientists to think that a continuous flow of positive and negative charged particle of solar origin was reaching the Earth at all times (Birkeland, 1913, 1916). Decades later, this idea received support from the observation and modeling of the stretching of the gaseous comets tails as due to a constant particle flow from the Sun (Biermann, 1951). In contrast, a fundamental theoretical study used the first observation of the extremely high temperature in the solar corona to predict

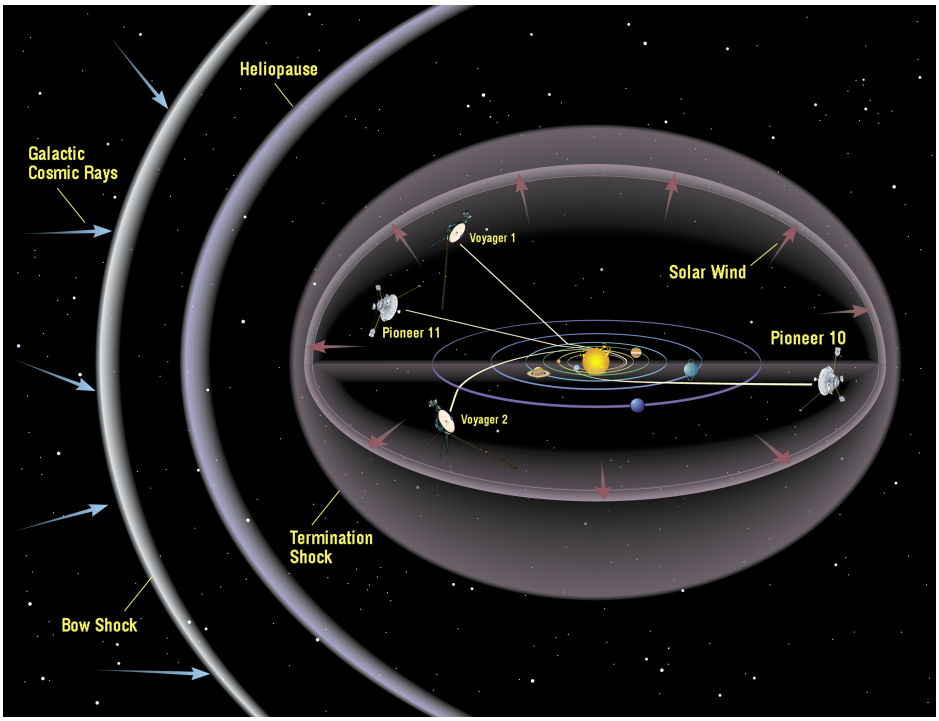

Figure 2: Schematic view of the heliosphere structure, also showing the Voyager and Pioneer missions. Credits: NASA/Ames, figure available at: `https://www.nasa.gov/centers/ames/images/content/72408main_ACD97-0036-1.jpg`.

a static solar atmosphere, that would extend beyond the Earth's orbit (Chapman and Zirin, 1957). Such contradiction was finally overcome by E. Parker, who realized that the hydrodynamic modeling also admitted the alternative solution of a solar corona rapidly accelerated to a supersonic flow, then named the solar wind (Parker, 1958). Although Parker's idea was heavily contrasted, the birth of space exploration soon resulted in a series of experimental evidences confirming the existence of solar wind particles, which were first provided by the spacecraft Lunik 2, Lunik 3 (Gringauz et al., 1960) and Mariner 2 (Neugebauer and Snyder, 1962).

Starting from the first satellite observations of the solar wind, huge efforts were put in the scientific investigation of the interplanetary medium, which entered the agenda of the space exploration programs of national and international agencies, worldwide. Spacecraft have been launched in various regions of the solar system, carrying instrumentation able to measure plasma distribution functions, energetic particles and electromagnetic fields in the interplanetary space. To this date, measurements have been obtained in the inner heliosphere by numerous satellites, among which Helios 1 and 2, Venus Express, Messenger, and more recently by Parker Solar Probe, Bepi-Colombo and Solar Orbiter, revealing the early-stage evolution of the solar wind dynamics. The outer heliosphere was largely explored by the Pioneer and Voyager probes, as well as by other robotic probes such as Ulysses, STEREO, MAVEN, and observatories launched in the frame of several other planetary missions, that confirmed and helped constraining parameters and models of the solar wind expansion. The near-Earth solar-wind and magnetospheric regions have been explored by a large number of space missions, including single-spacecraft (e.g. ISEE, ACE, Wind) and multi-spacecraft (e.g. Cluster, MMS, THEMIS, Swarm) configurations. All these missions altogether provided uninterrupted, detailed observations of the interplanetary medium for more than 50 years, generating an impressive database that is still under-exploited. Thanks to those missions, the knowledge of dynamics and processes of the solar and of other regions characterized by the presence of solar plasmas, has greatly advanced, although several major questions still remain open (see, for example, McComas et al., 2007; Viall and Borovsky, 2020).

It is now well established that the solar wind is a flow of quasi-neutral plasma of solar origin, mostly composed of protons (about 96% of the particle number density), α-particles (about 4%), minor populations of heavy ions, traces of neutral atoms, and electrons. Typical plasma parameters are listed

	n (cm^{-3})	T (keV)	B (nT)	ν_{ei} (Hz)
Local interstellar medium	1	10^{-5}	1	10^{8}
Solar wind (1 au)	10	10^{-2}	10	10^{-4}
Solar corona	10^{6}	10^{-1}	10^{5}	1
Earth's ionosphere	10^{6}	10^{-4}	10^{3}	10^{4}

Table 1: Typical plasma parameters for the solar wind and other heliospheric systems: plasma density n, ion temperature T, magnetic field magnitude B and ion-electron collisional frequency ν_{ei}.

in Table 1 for the solar wind and for some other heliospheric plasma systems.

The proton (n_p) and electron (n_e) densities are typically a few particles per cubic centimeter at the Earth orbit (1 au $\equiv 1.5{\times}10^8$ km), and decrease from the solar corona according to the spherical expansion of the solar wind. At the same distance, the typical proton and electron temperature is $T_p \simeq T_e \simeq 10$ eV ($\simeq 10^5$ K). The radial temperature profile shows a multiple power-law decrease which, however, is slower than for an adiabatic expansion. This will be discussed more in detail in Section 4.3. The solar wind departs from the solar corona with nearly radial speed V_{sw}, which reaches approximately values in the range 100—800 km/s, and is relatively steady after an initial acceleration occurring close to the Sun. The Parker's analytical solution predicting the accelerated, supersonic solar wind expansion is shown in the left panel of Figure 3 (Parker, 1958). During its expansion, the solar wind plasma carries out the frozen-in dipolar solar magnetic field. The combined effects of wind expansion, solar rotation and solar magnetic variability result in a complex large-scale structure of the interplanetary magnetic field. This includes the typical spiral-shaped field lines, known as the Parker spiral (see a schematic illustration in the right panel of Figure 3, Parker, 1958), as well as an undulated ecliptic neutral current sheath, due to the change of polarity of the Sun's magnetic field across the solar equator. The latter is reminiscent of a rotating ballerina skirt, marking the transition between north and south heliospheric magnetic polarities. While the solar wind expands predominantly with radial velocity, and the macroscopic interplanetary magnetic field is typically directed along the Parker spiral, three-dimensional fluctuations of both fields are present everywhere, thus in all directions, disregarding the reference frame. At large scales, the complex interactions between the plasma flow and the interplanetary magnetic field

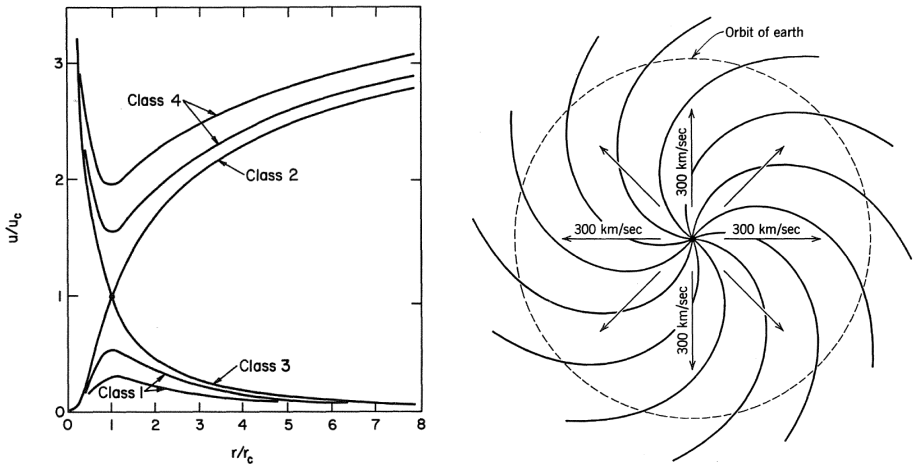

Figure 3: Parker's analytical solutions showing the solar wind velocity profile, u/u_c, versus the radial distance from the Sun, r/r_C (left panel, the subscript C indicating the coronal Alfvénic critical point, see Hundhausen, 1972), and a schematics of the interplanetary magnetic field spiral. Figure adapted from Hundhausen (1972).

result in a rich variety of magnetohydrodynamic phenomena. Given the typical plasma parameters, the large expansion velocity exceeds both the sound and the Alfvén speeds. In these conditions, the solar wind is mostly found in a state of highly developed turbulence (Tu and Marsch, 1995; Bruno and Carbone, 2013; Matthaeus, 2021), and at the same time it supports the propagation of various waves and instabilities (Alexandrova et al., 2013) that superpose and interact with the turbulence (Khotyaintsev et al., 2021; Carbone et al., 2021). Solar wind turbulence studies have been developed in depth for nearly 50 years, showing the ubiquitous presence of power-law trends in the power spectral density of velocity, density and magnetic field (Coleman, 1968; Alexandrova et al., 2008), with spectral exponents broadly compatible with the standard Kolmogorov phenomenology (Kolmogorov, 1941) or with the Iroshnikov-Kraichnan phenomenology (Iroshnikov, 1964; Kraichnan, 1965). Intermittency is also largely observed (Tu and Marsch, 1995; Sorriso-Valvo et al., 1999), and typically much stronger than in neutral fluids. Solar wind turbulence is also characterized by anisotropy (Bieber et al., 1996), and is further complicated by the unsteady energy input of solar and coronal origin, which are in turn turbulent processes themselves. Spherical expansion adds even more complexity, as do the weakly collisional nature of the plasma and

the interaction with pick-up ions from the interstellar medium. It is worth to mention that a large numbers of studies, based on observations and theoretical modeling of the heliospheric plasma, emphasized an evolution of the solar wind dynamics with both heliospheric distance and heliolatitude, as it will be addressed in this review. As we will discuss, the importance of turbulence in the global dynamics of the heliosphere is paramount, and this review addresses the current most advanced theoretical and experimental approach to its proper description (Matthaeus and Velli, 2011).

2.2. Description of space plasmas: from kinetic to magnetohydrodynamic equations

Weakly collisional space and astrophysical plasmas are often characterized by an extended dynamical range of spatial and temporal scales. These span from the typically solar corona scales ($\sim 10^8$ m, $\sim 10^6$ s), determining the large-scale input and synoptic behaviour of the heliospheric solar wind, to electron kinetic scales ($\sim 10^{-2}$ m, $\sim 10^{-4}$ s), where wave-particle interactions dominate the dynamics, ultimately leading to the dissipation of the energy. The most detailed and most general description of the space plasma dynamics is provided by the kinetic model, whose mathematical formulation is given in terms of a set of Boltzmann equations, one for each of the main plasma components (for example, at the most basic level, protons and electrons). These equations provide a description of the plasma particles at a microscopic level, controlling the phase-space dynamical evolution of their velocity distribution functions (VDF), $f_s(\mathbf{r}, \mathbf{v})$. The subscript s refers to either protons p or electrons e, but the kinetic model can also include fully ionized Helium (α particles) and heavier ions. The VDF evolution is determined by the advective action of the plasma flow, combined with the effects of electromagnetic Lorentz forces acting on the particles, and of particle collisions. The Boltzmann equations thus read as:

$$\frac{\partial f_s}{\partial t} + \mathbf{v}_s \cdot \boldsymbol{\nabla} f_s + \frac{q_s}{m_s}(\mathbf{E} + \mathbf{v}_s \times \mathbf{B}) \cdot \frac{\partial f_s}{\partial \mathbf{v}_s} = \left(\frac{\partial f_s}{\partial t}\right)_{\text{collisions}} \tag{1}$$

where $\mathbf{v}_s$ is the s-particle species average flow speed, namely the first-order moment of the s-particle distribution, $\mathbf{v}_s = n_s^{-1} \int \mathbf{v}_s f(\mathbf{r}, \mathbf{v}_s) d\mathbf{v}_s$ (the total number of particles of the s-particle being given by the zeroth-order moment, $n_s = \int f(\mathbf{r}, \mathbf{v}_s) d\mathbf{v}_s$). $\mathbf{E}$ and $\mathbf{B}$ are the electric and magnetic fields, and q_s and m_s are the charge and mass of the particle s, respectively. Equation (1)

includes terms accounting for modifications of the VDF due to inter- and intra-species collisions, generically indicated as $(\partial f_s/\partial t)_{\text{collisions}}$. Collisional terms have been modeled under various approximations, but are typically complex to handle (see, e.g., Pezzi et al., 2019, and references therein). It is important to point out that the different species interact both through the Lorentz force, and through the inter-species collisional terms. However, as stated previously, space plasmas are often described in the nearly-collisionless limit. The validity of such approach poses fundamental and still open issues (Landau, 1936; Rosenbluth et al., 1957; Pezzi et al., 2016), but is nevertheless an extremely useful approximation to describe the main kinetic plasma processes occurring when collisions are not dominating. In such a case, collisional terms can thus be neglected, resulting in the model described by the Vlasov equations:

$$\frac{\partial f_s}{\partial t} + \mathbf{v}_s \cdot \boldsymbol{\nabla} f_s + \frac{q_s}{m_s}(\mathbf{E} + \mathbf{v}_s \times \mathbf{B}) \cdot \frac{\partial f_s}{\partial \mathbf{v}_s} = 0\,. \tag{2}$$

Both sets of Boltzmann and Vlasov equations require closure through the Maxwell equations for the evolution of the electromagnetic fields. The computational requirements for the numerical integration of the equations of the Boltzmann or Vlasov models, in a broad range of time and space scales, are currently out of reach when it comes to the simulation of the plasma in a parameter space compatible with that of the heliospheric environment, in three dimensions. Therefore, the kinetic description of space plasmas is usually limited to the exploration of the small-scale dynamics, or to the use of approximated equations for the modelling of specific processes or geometries (see, e.g., Howes et al., 2011; Karimabadi et al., 2013; Palmroth et al., 2018). One important approximation that allows the study of an intermediate range of scales —accessible through modern observations and with state-of-the-art supercomputers— over which dynamics of turbulence develop in space plasmas is magnetohydrodynamics (MHD), which consists in considering the plasma as a multi-fluid flow, disregarding the details of the field-particle interactions (Alfvén, 1942). This can be done if the scales of interest are large enough for the plasma to be assumed in a local thermal equilibrium state, for which the limit distribution for the particle species is the Maxwellian (Kivelson and Russel, 1995). If this is the case, it is then possible to integrate the Boltzmann (or Vlasov) equations in the velocity space, for each species, in order to obtain corresponding equations of the so called fluid model. Upon plain velocity-space integration, equations (2) result in the evolution equa-

tions of the zeroth-order moment, the number density of each particle species (continuity equation for the species s). However, this includes the first-order moment (velocity). Similarly, integrating equations (2) after multiplication of each term by the velocity gives the evolution equations for the first-order moment, the fluid velocity (Navier-Stokes moment equation for the species s), which, again, include the second-order moment (the pressure tensor). In fact, the integration of the Vlasov equations to a given order systematically introduces the moment of the next higher order, namely a new variable, which makes the system not closed and, therefore, not immediately solvable. In order to close the system at some desired integration order, it is necessary to introduce a supplementary equation based on some model of the plasma. In most cases, and for the purpose of this review, the space plasmas considered are non-relativistic and quasi-neutrality of charge holds, provided their evolution is investigated over spatio-temporal scales larger than the largest characteristic separation time and length scale between positive and negative charges. The former is assumed to be the inverse of the plasma frequency $\Omega_P = \sqrt{\frac{4\pi n_e e^2}{m_e}}$ (n_e and m_e being electron density and mass, respectively, and e the elementary charge), whereas the latter is in general the Debye length λ_D. The order of magnitude of these characteristic scales in two reference frameworks such as the solar wind at 1 au and the solar corona are:

- Solar corona: $\Omega_P \sim 10^9$ Hz $\rightarrow \tau_{sep} = \frac{1}{\Omega_P} \sim 1$ nsec ; $\lambda_D \sim 1$ mm
- Solar wind (1 au): $\Omega_P \sim 10^5$ Hz $\rightarrow \tau_{sep} = \frac{1}{\Omega_P} \sim 10$ μsec ; $\lambda_D \sim 10$ m

These estimates can be used to identify the boundaries within which the magnetohydrodynamics can be considered as a valid model to describe the dynamics of turbulence and waves in space plasmas, and therefore to correctly interpret spacecraft observations. Under the assumption of quasi-neutrality, the mass density and bulk velocity of the plasma reduce to the mass density and the velocity of the protons. Indeed, if $n_p \approx n_e$, since $m_p \gg m_e$, then $\rho = \rho_p + \rho_e = m_p n_p + m_e n_e \simeq m_p n_p$ and $\mathbf{v} = (m_p v_p + m_e v_e)/(m_p + m_e) \simeq \mathbf{v_p}$ (subscripts e, p stand as usual for electrons and protons, respectively), allowing together to treat the plasma as a single-species proton fluid that carry an electron current. On the other hand, assuming a non-relativistic regime for the plasma enables to slightly modify the set of the Maxwell equations, so that the electromagnetic force appearing in the two-fluid model equations (not shown) reduces to the sole Laplace force ($f_{EM} = \cancel{\rho_c \mathbf{e}} + \frac{1}{c}\mathbf{J} \times \mathbf{B}$),

the net charge density ρ_c being very small if the plasma velocity is much smaller than the speed of light, c. Again from the Maxwell equations, in the non-relativistic approximation it is possible to derive an induction equation describing the evolution of the magnetic field $\mathbf{B}$. Eventually, all the assumptions above being made and additionally assuming incompressibility, $\partial\rho/\partial t + (\mathbf{v}\cdot\boldsymbol{\nabla})\rho = 0$, from the two-fluid model it is possible to extract the core set of equations representing the formal framework of the so called magnetohydrodynamic description of plasmas, or MHD (for detailed descriptions of the MHD framework, the reader can refer to Biskamp, 1993; Kivelson and Russel, 1995; Galtier, 2016):

$$\begin{aligned}
\boldsymbol{\nabla}\cdot\mathbf{v} &= 0 && (3)\\
\rho\left(\frac{\partial\mathbf{v}}{\partial t} + (\mathbf{v}\cdot\boldsymbol{\nabla})\mathbf{v}\right) &= -\boldsymbol{\nabla}P_{tot} + \frac{1}{4\pi}(\mathbf{B}\cdot\boldsymbol{\nabla})\mathbf{B} + \eta\nabla^2\mathbf{v} && (4)\\
\frac{\partial\mathbf{B}}{\partial t} &= \boldsymbol{\nabla}\times(\mathbf{v}\times\mathbf{B}) + \frac{c^2}{4\pi\sigma}\nabla^2\mathbf{B} && (5)\\
\boldsymbol{\nabla}^2 P_{tot} &= -\rho\boldsymbol{\nabla}\left[(\mathbf{v}\cdot\boldsymbol{\nabla})\mathbf{v} - \frac{1}{4\pi\rho}(\mathbf{B}\cdot\boldsymbol{\nabla})\mathbf{B}\right], && (6)
\end{aligned}$$

σ being the conductivity and η the absolute viscosity. The Poisson equation for the total pressure, $P_{tot} = (P + \frac{B^2}{8\pi})$, equation (6), is obtained taking the divergence of equation (4). Indeed, in many cases the initial density of the system can be assumed uniform ($\rho_0 = \rho(t)$), which for an incompressible plasma means that the density is uniform also at later times as the dynamics develop. This condition allows to eliminate the variable ρ together with one of the system equations, which is why one of the three equations for the velocity, equation (4), can be used to retrieve an equation for the pressure, equation (6). Finally, exploiting the incompressibility to modify the induction equation, the MHD analytical framework becomes:

$$\begin{aligned}
\boldsymbol{\nabla}\cdot\mathbf{v} &= 0 && (7)\\
\frac{\partial\mathbf{v}}{\partial t} + (\mathbf{v}\cdot\boldsymbol{\nabla})\mathbf{v} &= (\mathbf{b}\cdot\boldsymbol{\nabla})\mathbf{b} + \nu\boldsymbol{\nabla}^2\mathbf{v} - \frac{1}{\rho}\boldsymbol{\nabla}P_{tot} && (8)\\
\frac{\partial\mathbf{b}}{\partial t} + (\mathbf{v}\cdot\boldsymbol{\nabla})\mathbf{b} &= (\mathbf{b}\cdot\boldsymbol{\nabla})\mathbf{v} + \lambda\boldsymbol{\nabla}^2\mathbf{b} && (9)\\
\boldsymbol{\nabla}^2 P_{tot} &= -\rho\boldsymbol{\nabla}\left[(\mathbf{v}\cdot\boldsymbol{\nabla})\mathbf{v} - (\mathbf{b}\cdot\boldsymbol{\nabla})\mathbf{b}\right], && (10)
\end{aligned}$$

where $\nu = \eta/\rho$ is now the kinematic viscosity, λ the magnetic diffusivity, the magnetic field being written in velocity units through a change of variables:

$\mathbf{b} = \mathbf{B}(4\pi\rho_0)^{-1/2}$. The Maxwell equations, needed to close the system, under the assumptions of the incompressible MHD model read as:

$$\begin{aligned} \boldsymbol{\nabla} \cdot \mathbf{E} &= 4\pi\rho_c & (11)\\ \boldsymbol{\nabla} \cdot \mathbf{B} &= 0 & (12)\\ \frac{\partial \mathbf{B}}{dt} &= -c\,(\boldsymbol{\nabla} \times \mathbf{E}) & (13)\\ \boldsymbol{\nabla} \times \mathbf{B} &= \frac{4\pi}{c}\mathbf{J}\,. & (14) \end{aligned}$$

It is worth to mention that, in the incompressible case, the MHD equations can be re-arranged in a form that is more convenient for the investigation of the dynamics developing in space plasmas. This is done using the so called Elsasser variables (Elsasser, 1950), defined as $\mathbf{z}^{\pm}(\mathbf{x}, t) = \mathbf{v} \pm \mathbf{b}$, that allow to better characterize the evolution of correlations between velocity and magnetic field, the latter playing a very important role in the heliosphere. The MHD equations written in terms of these new variables obtain essentially by summing and subtracting equations 8 and 9, leading to:

$$\boldsymbol{\nabla} \cdot \mathbf{z}^{\pm} = 0 \qquad (15)$$

$$\frac{\partial}{\partial_t}\mathbf{z}^{\pm} + \left(\mathbf{z}^{\mp} \cdot \boldsymbol{\nabla}\right)\mathbf{z}^{\pm} = \left(\frac{\nu \pm \lambda}{2}\right)\boldsymbol{\nabla}^2\mathbf{z}^{\pm} + \left(\frac{\nu \mp \lambda}{2}\right)\boldsymbol{\nabla}^2\mathbf{z}^{\mp} - \frac{1}{\rho}\boldsymbol{\nabla}P_{tot}\,. \qquad (16)$$

It is very important to point out how the nonlinear terms in equations 16 do couple Elsasser fields with opposite signs. In this formulation of the incompressible MHD model, it appears therefore clear that nonlinear dynamics are suppressed when the plasma is in a purely Alfvénic state, meaning in a state where $\mathbf{v}$ and $\mathbf{b}$ are perfectly correlated or anti-correlated (thus $\mathbf{z}^{-} = 0$ or $\mathbf{z}^{+} = 0$). This is actually a condition that occurs quite often in space plasmas, at least approximately, as it will be discussed in the following sections. Finally, it is convenient to define some important physical quantities and their relation to the Elsasser fields. With the brackets indicating averages over time or space, after defining the pseudo energies $e^{\pm} = \langle(\mathbf{z}^{\pm})^2\rangle/2$, the total energy $e = (\langle\mathbf{v}^2\rangle + \langle\mathbf{b}^2\rangle)/2$, the residual energy $e_r = (\langle\mathbf{v}^2\rangle - \langle\mathbf{b}^2\rangle)/2$ and the cross-helicity $e_c = \langle\mathbf{v} \cdot \mathbf{b}\rangle/2$, one can also introduce the normalized cross-helicity, $\sigma_c = (e^{+} - e^{-})/(e^{+} + e^{-}) = 2e_c/e$, and normalized residual energy, $\sigma_r = 2e_r/(e^{+} + e^{-})$.

2.3. The injection of energy in space plasmas

The ubiquitous observations of power-law spectra of magnetic and velocity fluctuations, obtained through measurements from spacecraft, suggest that the solar wind is in a turbulent state (Marsch and Tu, 1997; Bruno and Carbone, 2013; Matthaeus and Velli, 2011; Alexandrova et al., 2013; Smith and Vasquez, 2021). Yet the mechanisms driving turbulence dynamics in the interplanetary space are still largely undetermined. It is however understood that the abundant presence of interacting Alfvén waves —propagating in opposite direction along a mean large-scale magnetic field— in the vicinity of the solar corona, the geometry of the solar wind expansion, its high speed, and the inhomogeneous and variable dynamics of the originating solar coronal regions, may all play a role in injecting energy into the large scales of the accelerating solar wind. At the solar wind source, these can span from the typical period and wavelength of the Alfvén waves (of the order of minutes and Mm), to the temporal and spatial scale of coronal structures, that can last up to days and reach the Gm scale (Sorriso-Valvo et al., 2010). A standard view of the origin of solar wind turbulence, still only partially supported by observational evidence, can be described as follows. Solar photospheric motions due to convection (Stix, 2002; Stein, 2012), coronal waves (Warmuth, 2015) and proper Sun's oscillating modes (Vecchio et al., 2005; Basu, 2016), continuously stir and shake the foot-point of the coronal magnetic field. This results in the excitation of Alfvénic fluctuations (McIntosh et al., 2011; Morton et al., 2015), which propagate in the expanding corona, where various instabilities may destabilize them, thus triggering the initial nonlinear interactions of kinetic and magnetic energy modes that seed coronal turbulence. The process is then continuously supported by several mechanisms during the coronal and solar wind expansion (see Section 6 for a brief account of the radial evolution of solar wind turbulence). For example, the radial expansion of the solar wind contributes by generating gradients in the transverse components of velocity and magnetic field, whose scale increases the larger the distance from the Sun. Additionally, and more specific to the solar wind magnetohydrodynamic scales, as the plasma expands, the parametric decay of outward Alfvén waves generates in turn the inward Alfvén modes needed to activate the nonlinear interactions leading to the turbulent cascade (Velli et al., 1990; Grappin et al., 1993; Malara et al., 2000; Malara et al., 2001; Matteini, 2012; Tenerani and Velli, 2017; Primavera et al., 2019). The continuous alternation and superposition of wind streams with different speed, depending on the originating coronal regions and on the acceleration mecha-

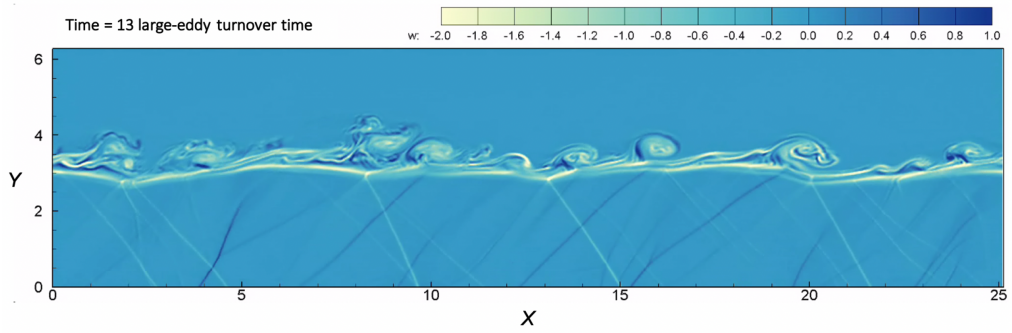

Figure 4: Snapshot of a two-dimensional compressible magnetohydrodynamic numerical simulation of the Kelvin Helmholtz instability, extracted after 13 large-eddy turnover times (Kieokaew, R. et al., 2021). The simulation is performed in a rectangular box of size $L_x \times L_y = 8\pi \times 4\pi$ with $n_x \times n_y = 1024 \times 512$ resolution. It uses empirical plasma and fields values measured in a Kelvin-Helmholtz boundary region crossed by the Solar Orbiter spacecraft (Müller et al., 2020, see Section 1) on 23 July 2020, between 20:10 UT and 21:50 UT. The color scale represents the out-of-plane vorticity, $\omega = \boldsymbol{\nabla} \times \mathbf{v}$, where $\mathbf{v}(x, y)$ is the flow velocity. Rolled-up and coalescing vortices are clearly visible in the central region. Figure from Kieokaew, R. et al. (2021).

nisms, act as well as an energy injection source for the large-scale structures (Bruno and Carbone, 2013; Shi et al., 2020). A broad variety of medium- to large-scale plasma structures, known as microstreams (Neugebauer et al., 1995) and switchbacks (Bale et al., 2019; Kasper et al., 2019), also recently observed in the corona (Telloni et al., 2022a), are present in fast or Alfvénic solar wind, representing a viable additional source of energy (Goldstein et al., 2003; Hernández et al., 2021). The heliospheric current sheet, marking the undulated and irregular separation between opposite magnetic polarities from the two solar hemispheres, introduces shear and boundary layers in the whole interplanetary space at ecliptic latitudes, which are most often explored by spacecraft (Smith, 2001). Other fluid or plasma instabilities are also known to develop occasionally injecting further energy at large scales at specific locations. For example, Kelvin-Helmholtz vortices are commonly observed in the heliosphere (e.g. Mishin and Tomozov, 2016, and references therein), and more specifically in the solar corona (Foullon et al., 2011; Ofman and Thompson, 2011), in the solar wind (Neugebauer et al., 1986; Sasunov et al., 2012; Telloni et al., 2020; Kieokaew, R. et al., 2021; Telloni et al., 2022a) and in the terrestrial magnetosheath (Hasegawa et al., 2004; Hwang et al., 2012; Eriksson et al., 2016; Di Mare et al., 2019). Interaction of the plasma with

magnetic reconnection exhausts (Manchester et al., 2005; Bandyopadhyay et al., 2021a) or with shocks propagating in the interplanetary medium, including coronal mass ejections (CMEs) (Shaikh et al., 2017; Fan et al., 2018; Kilpua et al., 2021; Sorriso-Valvo et al., 2021) and corotating interaction regions (CIRs) (Smith et al., 2011; Richardson, 2018), can also contribute to inject additional energy in the solar wind turbulence processes during the wind expansion.

All of the above phenomena, with the addition of a variety of impulsive solar events, can effectively provide energy inputs on a broad range of temporal and spatial scales, in a continuous, periodic or sporadic manner, in some cases also interacting with each other. This eventually results in a complex, mostly irregular, sometimes time-correlated, but certainly uninterrupted injection of energy in the system, supporting one of the most impressive cases of turbulence observed in nature. Indeed, given the solar wind high expansion speed and the interaction of counter-propagating waves, the energy from different sources will unavoidably undergo a nonlinear turbulent cascade and generate smaller scale structures, eventually resulting in a fully turbulent state with the superposition of the field fluctuations over a wide range of scales.

A simple modeling of the von Kármán decay rate (de Karman and Howarth, 1938) provides an approximate way to estimate from observations the amount of energy that is injected into a MHD turbulent cascade, irrespective of the specific injection mechanism. In the case of MHD flows, this provides a phenomenological relation between the mean energy injection rate, ε, and the root mean square fluctuation values of the standard Elsasser fields $\mathbf{z}^{\pm}$ (Hossain et al., 1995; Bandyopadhyay et al., 2019),

$$\varepsilon = \frac{1}{2}\frac{d}{dt}\left[(z^+)^2 + (z^-)^2\right] = \frac{\alpha_+(z^+)^2 z^-}{2L^+} + \frac{\alpha_-(z^-)^2 z^+}{2L^-}\,, \tag{17}$$

where $L_{\pm}$ are characteristic scales of the energy containing structures. The numerical coefficients $\alpha_{\pm} \simeq 0.03$ are related to the dimensionless dissipation rate of MHD turbulence, and are weakly depending on plasma parameters, such as, for example, the mean-magnetic-field strength, or the correlations between velocity and magnetic fluctuations (Matthaeus et al., 2004; Linkmann et al., 2015; Bandyopadhyay et al., 2018b). The energy injection rate has been estimated using solar wind data at different distances from the Sun, providing values ranging from 10^4 to 10^5 J kg^{-}1 s^{-1} (Bandyopadhyay et al., 2020; Wu et al., 2022a). An example is given in Figure 5, where the

outer-scale energy is estimated using data collected by the Parker Solar Probe in the inner heliosphere, during its first three perihelia (Wu et al., 2022a). In the same figure, the measurement is compared with modeled estimates of the ion heating rate, indicated by H (left), and of the energy source represented by the large-scale part of the spectrum. In the Alfvénic solar wind, such energy reservoir for the turbulent cascade is typically identified with a $1/f$ spectral range of magnetic fluctuations (Kiyani et al., 2015), commonly associated to the superposition of large-scale, Alfvénic fluctuations, which include the spatial structure and temporal variability of the coronal sources (see, e.g. Verdini et al., 2012; Bruno and Carbone, 2013; Chandran, 2018). Indeed, in space plasmas as well as in natural fluid frameworks, the energy is redistributed among frequencies and scales as a result of the competition of waves and turbulent motions (Dobrowolny et al., 1980; Marino et al., 2015b; Herbert et al., 2016). Such complex dynamics determines the correlation time of the fields involved, whose spectra are expected to be flat at frequencies lower than the reciprocal characteristic time scales of the system. The presence of a low-frequency $1/f$ range must thus be related to the existence of correlation times longer than the typical large scale turnover time and of energy injection and dissipation time scales. A range over which the low-frequency spectrum of physical quantities follows a power law trend close to -1 is observed in geophysical fluids (Fraedrich and Blender, 2003; Costa et al., 2014), quasi-2D turbulent flows in laboratory (Herault et al., 2015), numerical simulations of hydrodynamic and magnetohydrodynamic flows (Dmitruk and Matthaeus, 2007), and of course in the interplanetary space. Some studies suggest the possibility that the emergence of coherent structures and/or condensation of energy at large scales would be at the origin of the $1/f$ spectrum in turbulent flows. In particular, it was shown that in liquid metal experiments, at high Reynolds number, both three-dimensional shear flows and quasi-two dimensional flows exhibit a low-frequency $1/f$ range due to the increase of the power spectral density in the gravest modes, in turn caused by unstable shear layers (Pereira et al., 2019) and large-scale flow circulation (Herault et al., 2015) respectively. Evidences of the presence of long time fluctuations and the $1/f$ low-frequency spectrum were provided also in hydrodynamic and MHD frameworks characterized by condensation of invariants (or quasi-invariants). That happens in three-dimensional MHD plasmas, with or without a background magnetic field, as well as in rotating fluids (Dmitruk et al., 2011), where inverse cascades of helicity or energy are observed (Pouquet et al., 2019b). Ultimately, one can speculate that the

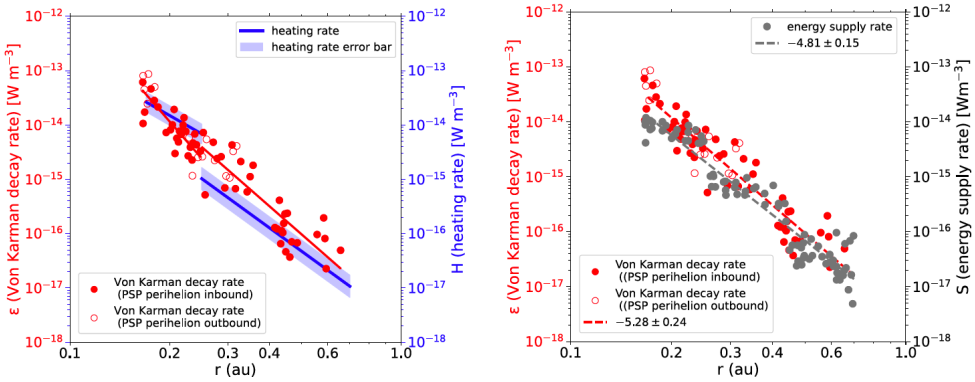

Figure 5: Radial profile of energy injection rate, ε, as measured by Parker Solar Probe during its first perihelion, compared with the estimated plasma heating rate, H (left panel), and with the estimated energy reservoir from the low-frequency fluctuations, S (right panel). Full and empty symbols refer to the inbound and outbound portion of the spacecraft orbit, respectively. Figure adapted from Wu et al. (2022a).

latter might be the underlying mechanism of the $1/f$ spectrum also in space plasmas, in which the existence of a low-frequency $1/f$ spectral scaling in the Alfvénic solar wind was recently related to the saturation of the magnetic field fluctuations at large scale (Matteini et al., 2018; Bruno et al., 2019).

The above estimate of the large-scale energy injection rate, equation (17), is based on the assumption of homogeneous turbulence, so that impulsive, sporadic energy injection mechanisms cannot be adequately included. Yet, it gives the order of magnitude of the solar wind large-scale turbulent energy that is feeding the turbulent cascade. In the following sections we will see how this estimate compares with the inertial range turbulent energy transfer rate evaluated through the exact third-order laws formulated to characterize space plasmas.

3. Third-order incompressible scaling laws in space plasmas

3.1. Magnetohydrodynamic turbulent cascade phenomenology

As it emerged in the previous sections, modeling turbulence in the outer space is a challenging endeavour still being pursued by the community. The most basic model, yet used as a reference to describe the MHD turbulent cascade in space plasmas, is the standard Kolmogorov phenomenology for neutral flows. Such model predicts the classical power-law scaling for the

kinetic energy spectrum, $E_v(k) \sim k^{-\alpha}$ (where $k = \ell^{-1}$ is a wavevector and ℓ the corresponding spatial scale), with $\alpha = 5/3$ (Kolmogorov, 1941), or with a slightly different spectral exponent when intermittency corrections are considered (Kolmogorov, 1962; Anselmet et al., 1984; Frisch, 1995). However, MHD specific features must be included to account for the presence of Alfvénic correlations between velocity and magnetic field. The phenomenology of turbulence in the case of magnetohydrodynamic plasmas dominated by a background magnetic field has indeed been addressed by Iroshnikov (1964); Kraichnan (1965) (IK). The IK framework takes into account the fact that the sweeping effect of counter-propagating Alfvén waves interferes with scale-to-scale interactions between structures, slowing down the turbulent cascade process. The IK phenomenology was later on extended by Dobrowolny et al. (1980) to explain the apparent paradox of Alfvénic turbulence in the solar wind, namely the simultaneous observation in the interplanetary plasma of well developed power laws in kinetic and magnetic energy spectra and the presence of strong correlations between the velocity and magnetic fields. The latter corresponds to the vanishing of one of the two Elsasser modes, $\mathbf{z}^{\pm}(\mathbf{x}, t)$ —solutions of the linearized incompressible MHD dynamics— resulting in the absence of either inward or outward propagating Alfvén waves. The fact that the nonlinear terms in equation (16) couple Alfvén modes with opposite polarities and those propagate in opposite direction along an underlying background magnetic field (the so called Alfvén effect), marks a major difference between hydrodynamic and MHD turbulence. Like in the classical Kolmogorov phenomenology, the statistical properties of MHD turbulence —in the incompressible ideal case— at scale ℓ depend essentially on the energy transfer rate, $\Pi^{\pm}$, in the inertial range, which is governed by two main phenomena: the propagation of Alfvén waves, characterized by a timescale $\tau_A^{\ell} \sim \ell/v_A$ (Alfvén time), and the nonlinear coupling between structures, acting on the nonlinear time scale $\tau_{NL}^{\pm} \sim \ell/z^{\pm}$. The Alfvén effect can be incorporated in the MHD phenomenology by introducing a small parameter accounting for the competition between the two time scales, $\tau_A^{\ell}/\tau_{NL}^{\ell}$, then used to define a new characteristic interaction time in the case of turbulent plasmas dominated by Alfvén waves, $\tau_I = \tau_{NL}^{\pm}/\tau_I = (\tau_{NL}^{\pm})^2/v_A$. Assuming the same pseudo-energy transfer for the two Alfvén modes, $\varepsilon \sim \Pi^+ \sim \Pi^-$, the hydrodynamic phenomenology translates into the IK phenomenology as follows: $\varepsilon \sim z^{\pm}/\tau_I = (z^{\pm})^4/v_A\ell$, leading to the so-called IK spectrum, $E_v(k) \sim (\varepsilon v_A)^{1/2} k^{-3/2}$. Also called the Kraichnan spectrum, this is the reference spectral energy distribution for the Alfvénic solar wind, and has been

long used, together with the Kolmogorov spectrum (Kolmogorov, 1941), to characterize the turbulent state of space plasmas. When considering the symmetry breaking introduced by the presence of a strong large-scale interplanetary mean magnetic field B_0, anisotropic models of turbulence need to be used (Biskamp, 1993). Indeed, Alfvénic fluctuations tend to travel along the mean field, so that the cascade inhibition should occur predominantly in such direction. In a standard view, solar wind turbulence is thus described by two different sets of scaling laws, one (Kraichnan-like) in the direction of the magnetic field, and a different one (Kolmogorov-like) in the plane perpendicular to this. In reality, there are various other sources of anisotropy, as for example the radial expansion of the plasma and the presence of a boundary layer in correspondence of the heliospheric current sheet, separating the north and south magnetic sectors. The anisotropic nature of solar wind turbulence is therefore a complex matter that is still being studied, and which is not completely captured by models yet (see, for example, Matthaeus et al., 1990; Bieber et al., 1996; Boldyrev, 2006; Zank et al., 2011; Horbury et al., 2012; Adhikari et al., 2015b,a; Oughton and Matthaeus, 2020, and references therein).

3.2. Intermittency in fully developed turbulence

Like in the case of ordinary fluids, plasma turbulence is also characterized by intermittency. Universally observed in turbulent flows, intermittency describes the inhomogeneous nature of the cascade, which favours the transfer of energy where gradients are larger. As a result, as the energy is transferred towards smaller scales it is also concentrated on increasingly sparse regions of space, generating highly energetic intermittent structures that stick out from the fluctuations' background (e.g., see Frisch, 1995, and references therein). Consequently, the statistics of the fields fluctuations is scale-dependent. This is usually described through the scale-dependent probability distribution functions of the two-point increments $\Delta v(\mathbf{x}, \boldsymbol{\ell}) = v(\mathbf{x}+\boldsymbol{\ell}) - v(\mathbf{x})$, where v is a generic turbulent field (either a scalar or a vector components), $\mathbf{x}$ the position, and $\boldsymbol{\ell}$ a scale. At large scales, fluctuations Δv are often uncorrelated, and their statistics is observed to be predominantly Gaussian. As the nonlinear interactions transfer the energy to smaller scales, the formation of small-scale structures produces raising tails of the fluctuations' probability distributions. The associated high-order moments $S_q(\ell) = \langle \Delta v^q \rangle \sim \ell^{\zeta_q}$, called structure functions, increase as power laws of the scale. For scale-dependent statistics, their scaling exponents, ζ_q, deviate from a linear func-

tion of the order q, as captured by several theoretical models (see, e.g., She and Leveque, 1994; Frisch, 1995, and references therein). Among these, the p-model (Meneveau and Sreenivasan, 1987) is occasionally used in this review to quantify intermittency. Based on a multifractal description of the turbulent cascade (Frisch et al., 1978), such simple model assumes that, at each step of the nonlinear energy cascade, a fraction of energy P or $1-P$ is randomly transferred to each of two "daughter" structures, where $0.5 \leq P \leq 1$ is a free parameter indicating the concentration of the energy on small-scale structures. For $P = 0.5$, the energy is equally redistributed in the volume, so that the cascade is homogeneous, volume-filling and non intermittent. Larger values of P therefore indicate stronger intermittency. According to the p-model, the scaling exponents of the structure functions are

$$\zeta_q = 1 - \log_2 \left[P^{qh} + (1-P)^{qh}\right], \tag{18}$$

where h is the similarity (Hurst) exponent of the field that can be approximately obtained from the spectrum as $2h = \alpha - 1$. An additional useful tool to quickly quantify intermittency is the flatness, namely the fourth-order structure function normalized to the second-order one, $F(\ell) = S_4(\ell)/S_2^2(\ell) \sim \ell^{-\kappa}$. For Gaussian fields $F = 3$, while larger values indicate leptokurtic statistics, with raising tails representing the emergence of energetic structures. Its values, scaling behaviour and scaling exponent κ can therefore be used to quantitatively account for intermittency. A relation can be easily established between the scaling exponent of the flatness and, for example, the intermittency parameter P of the p-model, $\kappa = 2\,\zeta_2 - \zeta_4 = 1 - 2log_2[P^{2h} + (1-P)^{2h}] + log_2[P^{4h} + (1-P)^{4h}]$, which for $0 < h < 1$ is a monotonically increasing function of P. For instance, for $h = 1/3$ (Kolmogorov scaling) and $P = 0.7$ (a standard value for fluid turbulence, see e.g. Anselmet et al., 1984; Meneveau and Sreenivasan, 1987), one obtains $\kappa = 0.29$. Spectral power density and structure functions analysis represent the standard approach for the fine description of turbulence. Routinely observed in MHD numerical simulations (Sorriso-Valvo et al., 2000), solar wind plasmas typically also show intense intermittency, whose characteristics are strongly modulated by the wind variability (Tu and Marsch, 1995; Sorriso-Valvo et al., 1999; Pagel and Balogh, 2003). Finally, it is worth pointing out that, in the presence of internal waves, intermittent phenomena can develop as well at large scales in turbulent flows. In stratified fluids, as for instance in the Earth's atmosphere and in the oceans, non-stationary energetic bursts are indeed observed at scales comparable to that of the mean flow (Klymak et al., 2008; van Haren et al.,

2015). Recent numerical and theoretical studies provided major insights on the dynamics underlying the sudden amplification of the temperature and of the vertical component of the velocity in stratified turbulent flows (Rorai et al., 2014; Feraco et al., 2018), also in the presence of rotation (Buaria et al., 2020), explaining how large-scale intermittency stems from the resonant interaction of gravity waves and turbulent motions. It has been also shown how large-scale intermittent events feed back on the dynamics of the small scales, modulating the classical (small-scale or internal) intermittency (Pouquet et al., 2019a; Feraco et al., 2021), enhancing turbulence and local dissipation (Marino et al., 2022).

3.3. The Politano & Pouquet law for Magnetohydrodynamics

Highly Alfvénic states correspond to dynamical regimes of the plasma characterized by weak non-linear couplings, resulting in the impossibility for a MHD turbulent cascade to fully develop in the limit of vanishing non-linear terms in equation (16). While the systematic observation of the IK spectrum in the solar wind (Bruno and Carbone, 2013) suggests that interplanetary space plasmas are indeed in a turbulent state, phenomenological predictions of the energy spectra and intermittency do not enable to draw definitive conclusions on the possibility that a condition corresponding to Alvénic turbulence may actually exists. Most importantly, assuming Alfvénic turbulence as existing, neither the K41 nor IK phenomenology do really permit to estimate the rate of the scale-to-scale of energy transfer in the turbulent inertial range. A known approach in fluid mechanics is to build structure functions of increasing order based on the velocity field increments, which provides quantitative assessment of properties of turbulence and intermittency. In particular, since the seminal work of Kolmogorov (Frisch, 1995) a lot of attention has focused on the mathematical manipulation of the third-order longitudinal structure function in fluid turbulence, known as the Kolmogorov 4/5 law, where longitudinal velocity fluctuations are those parallel to the lag direction. The 4/5 law is obtained analytically from the Navier-Stokes equations and is considered *"[...] one of the most important result in fully developed turbulence because it is both exact and non-trivial"* (Frisch, 1995). The end point of the Kolmogorov theorem can be summarized as follows: under the hypothesis of homogeneity, isotropy and incompressibility, in the limit of infinite Reynolds number, assuming finite energy dissipation, ε, the third-order longitudinal velocity structure function scales linearly with the

spatial increment, ℓ:

$$S_3(\ell) = \langle \Delta v(\ell)^3 \rangle = -\frac{4}{5}\varepsilon\ell\,. \tag{19}$$

An analogous exact law for magnetohydrodynamic plasmas was originally obtained by H. Politano and A. Pouquet (Politano and Pouquet, 1998; Politano and Pouquet, 1998), providing the space plasma community with an invaluable tool to characterize turbulence in the heliosphere and even further away from the Sun, beyond the heliopause, using observations from spacecraft with onboard plasma and magnetic field instruments. This exact relation, widely known as P&P law, is derived in the following from the MHD equations with an approach analogous to the one devised in Danaila et al. (2001a) to obtain the Kolmogorov 4/5 law of hydrodynamic turbulence. The latter approach will be carried out on the basis of the Elsasser fields in MHD and invokes several hypothesis such as the assumption of local homogeneity and isotropy (Carbone et al., 2009b). It must be stressed, however, that as far as the tensor calculus of these fields is concerned, this mixes the statistics of an axial vector, the magnetic field, which is unchanged under reflections, and a polar vector, the velocity, which changes sign (Robertson, 1940). We also refer the reader to the original work by Chandrasekhar who derives evolution equation for correlation functions in the original velocity and magnetic field variables (Chandrasekhar, 1951) as well as a recent derivation of a hierarchy of structure functions equations in MHD (Friedrich et al., 2016; Friedrich, 2020). Finally, we remark that we will present a thorough, step-by-step derivation of the incompressible, isotropic MHD version of the third-order moment scaling law, which should serve as a reference for the mathematical handling of this type of relations. However, the one presented here is not the only possible approach: different techniques exist in the literature that lead to equivalent relations.

We start from the MHD equations (15)-(16) written in terms of Elsasser variables,

$$\partial_t z_i^{\pm} + z_\alpha^{\mp}\partial_\alpha z_i^{\pm} = -\partial_i \Pi + \frac{\nu \pm \lambda}{2}\partial_\alpha^2 z_i^{+} - \frac{\nu \mp \lambda}{2}\partial_\alpha^2 z_i^{-}\,, \tag{20}$$

with $\tilde{P} = P_{tot}/\rho$, ν the kinematic viscosity, λ the magnetic diffusivity, $\partial_t \equiv \frac{\partial}{\partial t}$ and $\partial_\alpha \equiv \frac{\partial}{\partial x_\alpha}$. Summation over identical indices is assumed. Moreover, we make the additional assumption that $\nu = \lambda$ (which corresponds to a Prandtl number of one) so that the coupling between $\mathbf{z}^+$ and $\mathbf{z}^-$ occurs only in the

nonlinear term:

$$\partial_t z_i^{\pm} + z_\alpha^{\mp} \partial_\alpha z_i^{\pm} = -\partial_i \tilde{P} + \nu \partial_\alpha^2 z_i^{\pm} \,. \tag{21}$$

Let us introduce two independent points $\mathbf{x}$ and $\mathbf{x}' = \mathbf{x} + \mathbf{r}$. From this point on, "primed" variables are intended as calculated at the point $\mathbf{x}'$, for example $(\mathbf{z}^{\pm})' = \mathbf{z}^{\pm}(\mathbf{x} + \mathbf{r})$. Equation (21) can now be written for the variables $\mathbf{z}^{\pm}$ at the two points $\mathbf{x}$ and $\mathbf{x}'$:

$$\partial_t z_i^{\pm} + z_\alpha^{\mp} \partial_\alpha z_i^{\pm} = -\partial_i \tilde{P} + \nu \partial_\alpha^2 z_i^{\pm} \tag{22}$$

and

$$\partial_t z_i^{\pm\prime} + z_\alpha^{\mp\prime} \partial'_\alpha z_i^{\pm\prime} = -\partial'_i \tilde{P}' + \nu \partial_\alpha^{2\prime} z_i^{\pm\prime} \,. \tag{23}$$

Here, $\mathbf{z}^{\pm}(\mathbf{x}, t)$ and $\tilde{P}(\mathbf{x}, t)$ depend only on $\mathbf{x}$, so that

$$\begin{aligned} \frac{\partial}{\partial x'_\alpha} z_\alpha^{\pm} &= \partial'_\alpha z_\alpha^{\pm} = 0 \\ \frac{\partial}{\partial x'_\alpha} \tilde{P} &= \partial'_\alpha \tilde{P} = 0 \,. \end{aligned} \tag{24}$$

On the other hand, $\mathbf{z}^{\pm}(\mathbf{x}', t)$ and $\tilde{P}'(\mathbf{x}', t)$ depend only on $\mathbf{x}'$, therefore:

$$\begin{aligned} \frac{\partial}{\partial x_\alpha} z_\alpha^{\pm\prime} &= \partial_\alpha z_\alpha^{\pm\prime} = 0 \\ \frac{\partial}{\partial x_\alpha} \tilde{P}' &= \partial_\alpha \tilde{P}' = 0 \,. \end{aligned} \tag{25}$$

Subtracting equation (23) from equation (22) yields the equation for the increments $\Delta\mathbf{z}^{\pm} = (\mathbf{z}^{\pm})' - \mathbf{z}^{\pm}$:

$$\partial_t \left(z_i^{\pm} - z_i^{\pm\prime} \right) + z_\alpha^{\mp} \partial_\alpha z_\alpha^{\pm} - z_\alpha^{\mp\prime} \partial'_\alpha z_\alpha^{\pm\prime} = -\partial_i \tilde{P} + \partial'_i \tilde{P}' + \nu \left(\partial_\alpha^2 z_i^{\pm} - \partial_\alpha^{2\prime} z_i^{\pm\prime} \right) \,. \tag{26}$$

Exploiting the independence of x_i and x'_i we can write:

$$\begin{aligned} -\partial_i \tilde{P} &= -\partial_i \left(\tilde{P} - \tilde{P}' \right) \quad \text{since} \quad \partial_i \tilde{P}' = 0 \\ \partial'_i \tilde{P}' &= -\partial'_i \left(\tilde{P} - \tilde{P}' \right) \quad \text{since} \quad \partial'_i \tilde{P} = 0 \\ \partial_\alpha z_i^{\pm} &= \partial_\alpha \left(z_i^{\pm} - z_i^{\pm\prime} \right) \quad \text{since} \quad \partial_\alpha z_i^{\pm\prime} = 0 \\ -\partial'_\alpha z_i^{\pm\prime} &= \partial'_\alpha \left(z_i^{\pm} - z_i^{\pm\prime} \right) \quad \text{since} \quad \partial'_\alpha z_i^{\pm} = 0 \,. \end{aligned} \tag{27}$$

Equation (26) can thus be written as

$$\begin{aligned}\partial_t\left(z_i^{\pm}-z_i^{\pm\prime}\right)+z_\alpha^{\mp}\partial_\alpha\left(z_i^{\pm}-z_i^{\pm\prime}\right)+z_\alpha^{\mp\prime}\partial'_\alpha\left(z_i^{\pm}-z_i^{\pm\prime}\right)=\partial_i\left(\tilde{P}-\tilde{P}'\right)\\ -\partial'_i\left(\tilde{P}-\tilde{P}'\right)+\nu\left[\partial_\alpha^2\left(z_i^{\pm}-z_i^{\pm\prime}\right)-\partial_\alpha^{2\prime}\left(z_i^{\pm}-z_i^{\pm\prime}\right)\right]\end{aligned} \tag{28}$$

At this point, it is convenient to introduce the variables for the fluctuations of $z_i^{\pm}$ and $\tilde{P}$:

$$\Delta z_i^{\pm}=z_i^{\pm}-z_i^{\pm\prime}\quad\text{and}\quad\Delta P=\tilde{P}'-\tilde{P} \tag{29}$$

Equation (28) can now be written as

$$\partial_t\Delta z_i^{\pm}+z_\alpha^{\mp}\partial_\alpha\Delta z_i^{\pm}+z_\alpha^{\mp\prime}\partial'_\alpha\Delta z_i^{\pm}=-\partial_i\Delta P-\partial'_i\Delta P+\nu\left[\partial_\alpha^2\Delta z_i^{\pm}-\partial_\alpha^{2\prime}\Delta z_i^{\pm}\right]. \tag{30}$$

By adding and subtracting $z_\alpha^{\mp\prime}\partial_\alpha\Delta z_i^{\pm}$ one obtains:

$$\begin{aligned}\partial_t\Delta z_i^{\pm}+z_\alpha^{\mp}\partial_\alpha\Delta z_i^{\pm}+z_\alpha^{\mp\prime}\partial'_\alpha\Delta z_i^{\pm}+z_\alpha^{\mp\prime}\partial_\alpha\Delta z_i^{\pm}-z_\alpha^{\mp\prime}\partial_\alpha\Delta z_i^{\pm}=\\ -\partial_i\Delta P-\partial'_i\Delta P+\nu\left[\partial_\alpha^2\Delta z_i^{\pm}-\partial_\alpha^{2\prime}\Delta z_i^{\pm}\right],\end{aligned} \tag{31}$$

and thus:

$$\begin{aligned}\partial_t\Delta z_i^{\pm}+\Delta z_\alpha^{\mp}\partial_\alpha\Delta z_i^{\pm}+z_\alpha^{\mp\prime}\left(\partial_\alpha+\partial'_\alpha\right)\Delta z_i^{\pm}=\\ -\left(\partial_i+\partial'_i\right)\Delta P+\nu\left(\partial_\alpha^2+\partial_\alpha^{2\prime}\right)\Delta z_i^{\pm}.\end{aligned} \tag{32}$$

We are trying to derive an equation for the second-order correlation tensor $\langle\Delta z_i^{\pm}\Delta z_j^{\pm}\rangle$, which is linked to pseudo-energies. In a more general approach one should look at a mixed tensor $\langle\Delta z_i^{\pm}\Delta z_j^{\mp}\rangle$, thus considering not only pseudo-energies but also cross-helicity terms, $\langle z_i^{+}z_j^{-}\rangle$ and $\langle z_i^{-}z_j^{+}\rangle$. However, using the DIA closure (Kraichnan and Nagarajan, 1967), it is possible to demonstrate that these elements are in general poorly correlated. Being interested in the energy cascade, the most interesting is indeed an equation describing correlations of Alfvénic fluctuations of the same sign. To obtain the equations for pseudo-energies we multiply equation (32) by $\Delta z_j^{\pm}$:

$$\begin{aligned}\Delta z_j^{\pm}\partial_t\Delta z_i^{\pm}+\Delta z_j^{\pm}\Delta z_\alpha^{\mp}\partial_\alpha\Delta z_i^{\pm}+\Delta z_j^{\pm}z_\alpha^{\mp\prime}\left(\partial_\alpha+\partial'_\alpha\right)\Delta z_i^{\pm}=\\ -\Delta z_j^{\pm}\left(\partial_i+\partial'_i\right)\Delta P+\Delta z_j^{\pm}\nu\left(\partial_\alpha^2+\partial_\alpha^{2\prime}\right)\Delta z_i^{\pm}.\end{aligned} \tag{33}$$

After a permutation of the indices, equation (33) becomes:

$$\begin{aligned}\Delta z_i^{\pm}\partial_t\Delta z_j^{\pm}+\Delta z_i^{\pm}\Delta z_\alpha^{\mp}\partial_\alpha\Delta z_j^{\pm}+\Delta z_i^{\pm}z_\alpha^{\mp\prime}\left(\partial_\alpha+\partial'_\alpha\right)\Delta z_j^{\pm}=\\ -\Delta z_i^{\pm}\left(\partial_j+\partial'_j\right)\Delta P+\Delta z_i^{\pm}\nu\left(\partial_j^2+\partial_j^{2\prime}\right)\Delta z_j^{\pm}.\end{aligned} \tag{34}$$

Adding together equations (33) and (34), one obtains the following terms

$$
\begin{aligned}
&\bullet\ \Delta z_j^{\pm}\partial_t\Delta z_i^{\pm} + \Delta z_i^{\pm}\partial_t\Delta z_j^{\pm} = \partial_t\left(\Delta z_i^{\pm}\Delta z_j^{\pm}\right)\\
&\bullet\ \Delta z_j^{\pm}\Delta z_\alpha^{\mp}\partial_\alpha\Delta z_i^{\pm} + \Delta z_i^{\pm}\Delta z_\alpha^{\mp}\partial_\alpha\Delta z_j^{\pm} = \partial_\alpha\Delta z_\alpha^{\mp}\left(\Delta z_i^{\pm}\Delta z_j^{\pm}\right)\\
&\bullet\ \Delta z_j^{\pm} z_\alpha^{\mp\prime}\left(\partial_\alpha+\partial'_\alpha\right)\Delta z_i^{\pm} + \Delta z_i^{\pm} z_\alpha^{\mp\prime}\left(\partial_\alpha+\partial'_\alpha\right)\Delta z_j^{\pm} = \left(\partial_\alpha+\partial'_\alpha\right) z_\alpha^{\mp\prime}\left(\Delta z_i^{\pm}\Delta z_j^{\pm}\right)\\
&\bullet\ \left[-\Delta z_i^{\pm}\left(\partial_j+\partial'_j\right)\Delta P - \Delta z_j^{\pm}\left(\partial_i+\partial'_i\right)\Delta P\right]\\
&\bullet\ \nu\left[\Delta z_j^{\pm}\left(\partial_\alpha^2+\partial_\alpha^{2\prime}\right)\Delta z_i^{\pm} + \Delta z_i^{\pm}\left(\partial_\alpha^2+\partial_\alpha^{2\prime}\right)\Delta z_j^{\pm}\right].
\end{aligned}
\tag{35}
$$

Here, we made use of the incompressibility of the Elsasser fields, $\partial_\alpha z_\alpha^{\pm}=0$, in order to pull the divergence in front of the expressions.

Finally summing up the above terms and taking the ensemble average:

$$
\begin{aligned}
\partial_t\left\langle\Delta z_i^{\pm}\Delta z_j^{\pm}\right\rangle + \partial_\alpha\left\langle\Delta z_\alpha^{\mp}\left(\Delta z_i^{\pm}\Delta z_j^{\pm}\right)\right\rangle + \left(\partial_\alpha+\partial'_\alpha\right)\left\langle z_\alpha^{\mp\prime}\left(\Delta z_i^{\pm}\Delta z_j^{\pm}\right)\right\rangle = \\
-\left\langle\Delta z_i^{\pm}\left(\partial_j+\partial'_j\right)\Delta P\right\rangle - \left\langle\Delta z_j^{\pm}\left(\partial_i+\partial'_i\right)\Delta P\right\rangle \\
+\nu\left\langle\Delta z_i^{\pm}\left(\partial_\alpha^2+\partial_\alpha^{2\prime}\right)\Delta z_j^{\pm} + \Delta z_j^{\pm}\left(\partial_\alpha^2+\partial_\alpha^{2\prime}\right)\Delta z_i^{\pm}\right\rangle .
\end{aligned}
\tag{36}
$$

Making at this point a local homogeneity hypothesis, let us introduce the variables $\boldsymbol{\ell}=\mathbf{r}=\mathbf{x}-\mathbf{x}'$ and $\mathbf{X}=(\mathbf{x}+\mathbf{x}')/2$. If the plasma is locally homogeneous, its statistics must be varying more rapidly over a certain scale ℓ in comparison to a lager scale X. In other words, local homogeneity can be explained by saying that plasma fields are assumed to have almost no variations over X (implying small $\partial/\partial\mathbf{X}$ derivatives) while the variations over smaller distances ℓ are instead not negligible. At the level of the equations, this implies in turn that when derivatives in equation (36) ($\partial/\partial\mathbf{x}$ and $\partial/\partial\mathbf{x}'$) are replaced by $\partial/\partial\mathbf{X}$ and $\partial/\partial\boldsymbol{\ell}$, and the former acts on an averaged quantity $\partial/\partial\mathbf{X}\langle\ldots\rangle\simeq 0$, then the following holds:

$$
\begin{aligned}
\partial'_\alpha &= \frac{\partial}{\partial x'_\alpha} = -\frac{\partial}{\partial\ell_\alpha} + \frac{1}{2}\frac{\partial}{\partial X_\alpha} \simeq -\frac{\partial}{\partial\ell_\alpha}\\
\partial_\alpha &= \frac{\partial}{\partial x_\alpha} = \frac{\partial}{\partial\ell_\alpha} + \frac{1}{2}\frac{\partial}{\partial X_\alpha} \simeq \frac{\partial}{\partial\ell_\alpha}.
\end{aligned}
$$

Let us now examine the individual terms in equation (36).

- Nonlinear terms:

$$
\begin{aligned}
\partial_\alpha\langle\Delta z_\alpha^{\mp}\left(\Delta z_i^{\pm}\Delta z_j^{\pm}\right)\rangle + \underbrace{\left(\partial_\alpha+\partial'_\alpha\right)\left\langle z_\alpha^{\mp\prime}\left(\Delta z_i^{\pm}\Delta z_j^{\pm}\right)\right\rangle}_{=0} \\
= \frac{\partial}{\partial\ell_\alpha}\langle\Delta z_\alpha^{\mp}\left(\Delta z_i^{\pm}\Delta z_j^{\pm}\right)\rangle
\end{aligned}
\tag{37}
$$

- Pressure term:

$$T_{ij} = \left\langle \Delta z_i^{\pm} \left(\partial_j + \partial_j'\right) \Delta P \right\rangle + \left\langle \Delta z_j^{\pm} \left(\partial_i + \partial_i'\right) \Delta P \right\rangle . \tag{38}$$

We first write the term T_{ij} according to

$$T_{ij} = \left\langle (z_i^{\pm} - z_i^{\pm\prime}) \partial_j \Delta P \right\rangle + \left\langle (z_i^{\pm} - z_i^{\pm\prime}) \partial_j' \Delta P \right\rangle + (i \leftrightarrow j) , \tag{39}$$

where $(i \leftrightarrow j)$ stands for the first expression on the r.h.s. with interchanged indices. The first term now reads

$$\begin{aligned} &\left\langle (z_i^{\pm} - z_i^{\pm\prime}) \partial_j \Delta P \right\rangle = \partial_j \left\langle (z_i^{\pm} - z_i^{\pm\prime}) \Delta P \right\rangle - \left\langle \partial_j z_i^{\pm} \Delta P \right\rangle \\ &= [\underbrace{\partial_j + \partial_j'}_{=0} - \partial_j'] \left\langle (z_i^{\pm} - z_i^{\pm\prime}) \Delta P \right\rangle - \left\langle \partial_j z_i^{\pm} \Delta P \right\rangle \\ &= -\partial_j' \left\langle (z_i^{\pm} - z_i^{\pm\prime}) \Delta P \right\rangle - \left\langle \partial_j z_i^{\pm} \Delta P \right\rangle \\ &= -\left\langle (z_i^{\pm} - z_i^{\pm\prime}) \partial_j' \Delta P \right\rangle + \left\langle \partial_j' z_i^{\pm\prime} \Delta P \right\rangle - \left\langle \partial_j z_i^{\pm} \Delta P \right\rangle , \end{aligned} \tag{40}$$

where we used the assumption of local homogeneity. Substituting this result for the first term in equation (38) yields

$$T_{ij} = \left\langle (\partial_j' z_i^{\pm\prime} - \partial_j z_i^{\pm}) \Delta P \right\rangle + (i \leftrightarrow j) . \tag{41}$$

Hence, the diagonal terms of the tensor $\tilde{P}_{ij}$ vanishes, $(\partial_i' z_i^{\pm\prime} - \partial_i z_i^{\pm}) = 0$, due to the incompressibility of the Elsasser fields, $\partial_\alpha z_\alpha^{\pm} = 0$. We thus obtain $\tilde{P}_{ii} = 0$, which will be sufficient for the derivation of a budget equation for $i = j$. Nevertheless, it can be shown on the basis of local homogeneity and isotropy that the pressure term T_{ij} vanishes for $i \neq j$ as well (Hill, 1997).

- Viscous term

$$\nu \left\langle \Delta z_i^{\pm} \left(\partial_\alpha^2 + \partial_\alpha^{2\prime}\right) \Delta z_j^{\pm} + \Delta z_j^{\pm} \left(\partial_\alpha^2 + \partial_\alpha^{2\prime}\right) \Delta z_i^{\pm} \right\rangle \tag{42}$$

We consider the first term and obtain

$$\begin{aligned} &\nu \left\langle \Delta z_i^{\pm} \partial_\alpha^2 \Delta z_j^{\pm} \right\rangle = \nu \partial_\alpha \left\langle \Delta z_i^{\pm} \partial_\alpha \Delta z_j^{\pm} \right\rangle - \nu \left\langle (\partial_\alpha \Delta z_i^{\pm})(\partial_\alpha \Delta z_j^{\pm}) \right\rangle \\ &= \nu \partial_\alpha^2 \left\langle \Delta z_i^{\pm} \Delta z_j^{\pm} \right\rangle - \nu \partial_\alpha \left\langle (\partial_\alpha \Delta z_i^{\pm}) \Delta z_j^{\pm} \right\rangle - \nu \left\langle (\partial_\alpha \Delta z_i^{\pm})(\partial_\alpha \Delta z_j^{\pm}) \right\rangle \\ &= \nu \partial_\alpha^2 \left\langle \Delta z_i^{\pm} \Delta z_j^{\pm} \right\rangle - \nu \left\langle (\partial_\alpha^2 \Delta z_i^{\pm}) \Delta z_j^{\pm} \right\rangle - 2\nu \left\langle (\partial_\alpha \Delta z_i^{\pm})(\partial_\alpha \Delta z_j^{\pm}) \right\rangle . \end{aligned} \tag{43}$$

Here, we can bring the second term on the r.h.s. in equation (43) to the l.h.s. and obtain

$$\begin{aligned} &\nu \left\langle \Delta z_i^{\pm} \partial_\alpha^2 \Delta z_j^{\pm} \right\rangle + \nu \left\langle \Delta z_j^{\pm} \partial_\alpha^2 \Delta z_i^{\pm} \right\rangle \\ &= \nu \partial_\alpha^2 \left\langle \Delta z_i^{\pm} \Delta z_j^{\pm} \right\rangle - 2\nu \left\langle (\partial_\alpha z_i^{\pm})(\partial_\alpha z_j^{\pm}) \right\rangle , \end{aligned} \tag{44}$$

where we have written the last term in the original Elsasser fields in the last step. Similarly, we can treat the "primed" derivatives in equation (42) and obtain

$$\begin{aligned}&\nu \left\langle \Delta z_i^{\pm} \left(\partial_\alpha^2 + \partial_\alpha^{2\prime}\right) \Delta z_j^{\pm} + \Delta z_j^{\pm} \left(\partial_\alpha^2 + \partial_\alpha^{2\prime}\right) \Delta z_i^{\pm} \right\rangle \\ &= \nu(\partial_\alpha^2 + \partial_\alpha^{2\prime}) \left\langle \Delta z_i^{\pm} \Delta z_j^{\pm} \right\rangle - \varepsilon_{ij}^{\pm} = 2\nu \frac{\partial^2}{\partial \ell_\alpha^2} \left\langle \Delta z_i^{\pm} \Delta z_j^{\pm} \right\rangle - \varepsilon_{ij}^{\pm} \,,\end{aligned} \tag{45}$$

where we made use of the assumption of local homogeneity in the last step. Furthermore, we defined the local energy dissipation rate tensor as

$$\varepsilon_{ij}^{\pm} = 2\nu \left\langle (\partial_\alpha z_i^{\pm})(\partial_\alpha z_j^{\pm}) + (\partial'_\alpha z_i^{\pm\prime})(\partial'_\alpha z_j^{\pm\prime}) \right\rangle \,. \tag{46}$$

Assuming local isotropy, one can show (Hill, 1997) that this term is connected to the averaged local energy dissipation rates of the Elsasser fields, $\varepsilon^{\pm}$, according to

$$\varepsilon_{ij}^{\pm} = \frac{4}{3} \varepsilon^{\pm} \delta_{ij} \,, \tag{47}$$

where δ_{ij} denotes the Kronecker delta. Equation (36) thus simplifies to

$$\partial_t \left\langle \Delta z_i^{\pm} \Delta z_j^{\pm} \right\rangle + \frac{\partial}{\partial \ell_\alpha} \left\langle \Delta z_\alpha^{\mp} \left(\Delta z_i^{\pm} \Delta z_j^{\pm} \right) \right\rangle = 2\nu \frac{\partial^2}{\partial \ell_\alpha^2} \left\langle \Delta z_i^{\pm} \Delta z_j^{\pm} \right\rangle - \frac{4}{3} \varepsilon^{\pm} \delta_{ij} \,. \tag{48}$$

Summation over $i = j$ yields

$$\partial_t \left\langle \left(\Delta z_i^{\pm} \right)^2 \right\rangle + \frac{\partial}{\partial \ell_\alpha} \left\langle \Delta z_\alpha^{\mp} \left(\Delta z_i^{\pm} \right)^2 \right\rangle = 2\nu \frac{\partial^2}{\partial \ell_\alpha^2} \left\langle \left(\Delta z_i^{\pm} \right)^2 \right\rangle - 4\varepsilon^{\pm} \,. \tag{49}$$

In the stationary case, the first term vanishes, $\partial_t \langle \left(\Delta z_i^{\pm} \right)^2 \rangle = 0$, and we obtain

$$\frac{\partial}{\partial \ell_\alpha} \left\langle \Delta z_\alpha^{\mp} \left(\Delta z_i^{\pm} \right)^2 \right\rangle = 2\nu \frac{\partial^2}{\partial \ell_\alpha^2} \left\langle \left(\Delta z_i^{\pm} \right)^2 \right\rangle - 4\varepsilon^{\pm} \,. \tag{50}$$

If we assume that the flow is locally homogeneous and isotropic, the second- and third-order tensors can be obtained using the invariant theory of homogeneous and isotropic turbulence (Robertson, 1940; Monin and Yaglom, 1971), as explicitly derived in Appendix A) and B) at the end of this Section. We thus obtain:

$$\left(\frac{\partial}{\partial \ell} + \frac{2}{\ell} \right) \left\langle \Delta z_L^{\mp} (\Delta z_i^{\pm})^2 \right\rangle = 2\nu \left(\frac{\partial}{\partial \ell} + \frac{2}{\ell} \right) \frac{\partial}{\partial \ell} \left\langle (\Delta z_i^{\pm})^2 \right\rangle - 4\varepsilon^{\pm} \,, \tag{51}$$

where $\Delta z_L^{\mp}$ denotes the projection on the longitudinal direction $\Delta z_L^{\mp} = \frac{\ell_\alpha}{\ell}\Delta z_\alpha^{\mp}$. The latter equation can be cast as

$$\left(\frac{\partial}{\partial \ell} + \frac{2}{\ell}\right)\left[\left\langle \Delta z_L^{\mp}(\Delta z_i^{\pm})^2\right\rangle - 2\nu\frac{\partial}{\partial \ell}\left\langle(\Delta z_i^{\pm})^2\right\rangle + \frac{4}{3}\varepsilon^{\pm}\ell\right] = 0\,. \qquad (52)$$

Similarly to the original Von Kármán-Howarth equation of hydrodynamic turbulence (see Monin and Yaglom, 1971, Vol. 2, p. 122), the only solution of this equation that is non-singular at $\ell = 0$ is obtained if the square brackets vanish, i.e.,

$$\left\langle \Delta z_L^{\mp}(\Delta z_i^{\pm})^2\right\rangle = 2\nu\frac{\partial}{\partial \ell}\left\langle(\Delta z_i^{\pm})^2\right\rangle - \frac{4}{3}\varepsilon^{\pm}\ell\,. \qquad (53)$$

Furthermore, in the inertial range, the viscous term can be neglected for high Reynolds numbers, so that we finally obtain

$$Y^{\pm}(\ell) = \left\langle \Delta z_L^{\mp}(\Delta z_i^{\pm})^2\right\rangle = -\frac{4}{3}\varepsilon^{\pm}\ell\,, \qquad (54)$$

which is the original P&P law obtained in Politano and Pouquet (1998).

The P&P law can be alternatively written using velocity and magnetic field instead of the Elsasser fields, as can be obtained by simply averaging the two relations (for Δz^+ and Δz^-) in equation (54). In vector notation, this yields:

$$Y(\ell) = \left\langle \Delta v_L(|\Delta\mathbf{v}|^2 + |\Delta\mathbf{b}|^2) - 2\Delta b_L(\Delta\mathbf{v}\cdot\Delta\mathbf{b})\right\rangle = -\frac{4}{3}\varepsilon\ell\,, \qquad (55)$$

where the subscript L indicates again the longitudinal components of velocity and magnetic field, and the latter is expressed in velocity units (see sec. 2.2). The coefficient $\varepsilon = (\varepsilon^+ + \varepsilon^-)/2$ is now the mean turbulent energy transfer rate. In the left-hand term, two contributions can be separated: one associated to the kinetic and magnetic energies coupled to the velocity shears (the "energy" term), and one associated to the correlated velocity and magnetic field fluctuations, coupled with the longitudinal magnetic gradients (the "cross-helicity" term). It is evident that, if velocity and magnetic field fluctuations are perfectly correlated or anticorrelated, as for example in the case of Alfvén waves, the cross-helicity term and the energy term cancel out, resulting in the absence of a measurable energy cascade. This is consistent with the vanishing of the nonlinear terms in equation (16), occurring when magnetohydrodynamic plasmas are in purely Alfvénic states. Therefore, if

Alfvénic fluctuations are present, the cross-helicity term, associated with a negative sign, can reduce the cross-scale transport of energy, thus inhibiting, or reducing, the turbulent cascade. As we shall demonstrate in the following of this review, equations (54) and (55), as well as their subsequent extensions, represent invaluable tools for the study of turbulence in space plasmas. Indeed, their validation in observational samples provides a rigorous proof of the existence of turbulent cascade fully developing in the heliosphere. Being obtained analytically from the plasma governing equations, thus exact — within the bounds of the assumption made for their derivation—, the range of scales over which third-order laws linear scaling extends can be used as a more formal definition of the inertial range of turbulence. This is not the case for the power-law regimes observed in spectra of velocity and magnetic field in space plasmas, whose theoretical reference (the Kolmogorov or the Iroshnikov-Kraichnan spectra) only stems from phenomenology. Fitting the third-order moment laws within their linear scaling ranges provides in general an estimate of the mean energy transfer rate, a quantity otherwise difficult to estimate with a reduced knowledge (in terms of degrees of freedom) of the fields, as is the case for spacecraft observations, though fundamental for the description of the heliospheric dynamics. These and other reasons that will become clear in the following chapters make the P&P law one of the most important recent theoretical results for the study of space plasmas.

Appendix A): Second-order tensor

The second-order tensor, $D^{\pm\pm}_{i\,j}(\boldsymbol{\ell}) = \left\langle \Delta z^{\pm}_i \Delta z^{\pm}_j \right\rangle$, is symmetric in the components i and j. Under the assumption of isotropy, this tensor obeys the following relation (Monin and Yaglom, 1971):

$$D^{\pm\pm}_{i\,j}(\boldsymbol{\ell}) = (D^{\pm\pm}_{LL}(\ell) - D^{\pm\pm}_{TT}(\ell))\frac{\ell_i \ell_j}{\ell^2} + D^{\pm\pm}_{TT}(\ell)\delta_{ij}\,, \tag{56}$$

where $D^{\pm}_{LL}(\ell)$ and $D^{\pm}_{TT}(\ell)$ denote the longitudinal and transverse structure function, respectively, and $\ell = |\boldsymbol{\ell}|$. Summing over $i = j$ yields:

$$D^{\pm\pm}_{i\,i}(\boldsymbol{\ell}) = D^{\pm\pm}_{LL}(\ell) + 2D^{\pm\pm}_{TT}(\ell)\,. \tag{57}$$

Operating with the Laplacian on this quantity thus yields:

$$\begin{aligned}
&\frac{\partial^2}{\partial \ell_\alpha^2}\left(D_{LL}^{\pm\pm}(\ell)+2D_{TT}^{\pm\pm}(\ell)\right)=\frac{\partial}{\partial \ell_\alpha}\frac{\ell_\alpha}{\ell}\frac{\partial}{\partial \ell}(D_{LL}^{\pm\pm}(\ell)+2D_{TT}^{\pm\pm}(\ell))\\
&=\left(\frac{3}{\ell}-\frac{\ell_\alpha\ell_\alpha}{\ell^3}\right)\frac{\partial}{\partial \ell}(D_{LL}^{\pm\pm}(\ell)+2D_{TT}^{\pm\pm}(\ell))+\frac{\ell_\alpha\ell_\alpha}{\ell^2}\frac{\partial^2}{\partial \ell^2}(D_{LL}^{\pm\pm}(\ell)+2D_{TT}^{\pm\pm}(\ell))\\
&=\left(\frac{\partial}{\partial \ell}+\frac{2}{\ell}\right)\frac{\partial}{\partial l}\left(D_{LL}^{\pm\pm}(\ell)+2D_{TT}^{\pm\pm}(\ell)\right)=\left(\frac{\partial}{\partial \ell}+\frac{2}{\ell}\right)\frac{\partial}{\partial l}\left\langle \Delta z_i^{\pm}\Delta z_i^{\pm}\right\rangle ,
\end{aligned} \tag{58}$$

where we made use of $\ell_\alpha\ell_\alpha=\ell^2$

Appendix B): third-order tensor

The third-order tensor that enters equation (48) is $D_{\alpha,\,i\,j}^{\mp\pm\pm}(\boldsymbol{\ell})=\left\langle \Delta z_\alpha^{\mp}(\Delta z_i^{\pm}\Delta z_j^{\pm})\right\rangle$. This tensor is symmetric in i and j. In principle, to determine its tensor form, one would have to rewrite the tensor in the original fields, namely, velocity and magnetic fields and apply the tensor calculus devised by Chandrasekhar (1951) (for a recent application see also Friedrich et al., 2016). Here, we simply chose the isotropic form of the tensor which is symmetric in all three indices, namely:

$$\begin{aligned}
D_{\alpha,i\,j}^{\mp\pm\pm}(\boldsymbol{\ell})=&\left(D_{L,LL}^{\mp\pm\pm}(\ell)-D_{L,TT}^{\mp\pm\pm}(\ell)-2D_{T,LT}^{\mp\pm\pm}(\ell)\right)\frac{\ell_\alpha\ell_i\ell_j}{\ell^3}\\
&+D_{T,LT}^{\mp\pm\pm}(\ell)\left(\frac{\ell_j}{\ell}\delta_{i\alpha}+\frac{\ell_i}{\ell}\delta_{j\alpha}\right)+D_{L,TT}\frac{\ell_\alpha}{\ell}\delta_{ij}\,.
\end{aligned} \tag{59}$$

Summing over $i=j$ yields:

$$D_{\alpha,i\,i}^{\mp\pm\pm}(\boldsymbol{\ell})=(D_{L,LL}^{\mp\pm\pm}(\ell)+2D_{L,TT}^{\mp\pm\pm}(\ell))\frac{\ell_\alpha}{\ell}\,. \tag{60}$$

Furthermore, projection on the longitudinal direction yields:

$$\left\langle \Delta z_L^{\mp}(\Delta z_i^{\pm}\Delta z_i^{\pm})\right\rangle=\frac{\ell_\alpha}{\ell}D_{\alpha,i\,i}^{\mp\pm\pm}(\boldsymbol{\ell})=(D_{L,LL}^{\mp\pm\pm}(\ell)+2D_{L,TT}^{\mp\pm\pm}(\ell))\,. \tag{61}$$

For equation (49), we have to calculate the divergence with respect to $\frac{\partial}{\partial \ell_\alpha}$ which yields:

$$\begin{aligned}
&\frac{\partial}{\partial \ell_\alpha}(D^{\mp\pm\pm}_{L,LL}(\ell) + 2D^{\mp\pm\pm}_{L,TT}(\ell))\frac{\ell_\alpha}{\ell} \\
&= \frac{\ell_\alpha \ell_\alpha}{\ell^2}\frac{\partial}{\partial \ell}(D^{\mp\pm\pm}_{L,LL}(\ell) + 2D^{\mp\pm\pm}_{L,TT}(\ell)) + (D^{\mp\pm\pm}_{L,LL}(\ell) + 2D^{\mp\pm\pm}_{L,TT}(\ell))\left(\frac{3}{\ell} - \frac{\ell_\alpha \ell_\alpha}{\ell^3}\right) \\
&= \left(\frac{\partial}{\partial \ell} + \frac{2}{\ell}\right)(D^{\mp\pm\pm}_{L,LL}(\ell) + 2D^{\mp\pm\pm}_{L,TT}(\ell)) = \left(\frac{\partial}{\partial \ell} + \frac{2}{\ell}\right)\left\langle \Delta z^{\mp}_L (\Delta z^{\pm}_i \Delta z^{\pm}_i)\right\rangle ,
\end{aligned} \tag{62}$$

where we inserted equation (61).

3.4. Validation of the P&P law in numerical simulations of incompressible magnetohydrodynamic turbulence

The P&P law is an elegant, rigorous theoretical result that enables the characterization of turbulence in MHD plasmas. As it will emerge in the next chapters, space plasmas measurements are not always easy to handle, and the interplanetary space is an extremely complex framework where the P&P law observation is not obvious, unless some conditions are met. For this reason, it was very important to check the validity of the law, as well as its usability in MHD frameworks, by means of numerical experiments. To the best of our knowledge, the first numerical observation of the P&P law in MHD simulations was obtained a few years after the first derivation. The difficult statistical convergence of the signed third-order moment indeed requires a sufficiently resolved inertial range, thus a large integration domain. Massive cancellations between positive and negative fluctuations of the terms involved in the averaging of the third-order tensor, representative of the generally two-way cross-scale energy flux, indeed result in only a small fraction of the total energy exchanges. Using a relatively long two-dimensional direct numerical simulation of incompressible MHD turbulence, on a grid of 1024^2 points, Sorriso-Valvo et al. (2002) computed the third-order moments, equation (54). A snapshot of the out-of-plane current density, J_z, taken at the maximum of the turbulent activity, is shown in the left panel of Figure 6. In order to achieve statistical convergence, ten outputs were extracted during the statistically stationary state of the simulation, namely when the turbulence spectra and the mean current, $\langle J_z^2 \rangle$, are steady. Those snapshots were finally used to build an ensemble and estimate the P&P law. The right panel

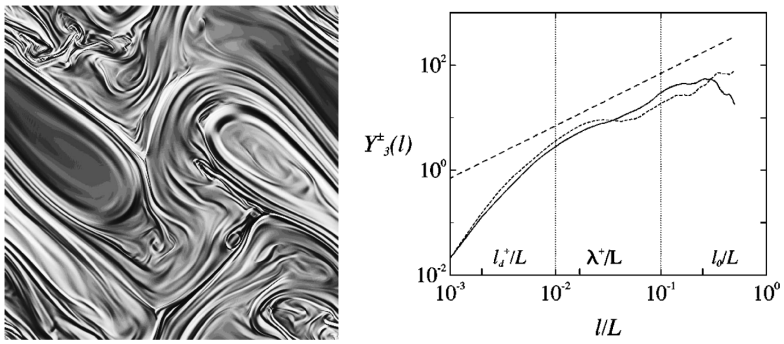

Figure 6: Validation of the P&P law in two-dimensional numerical simulations of the MHD equations. Left panel: a snapshot of the current J_z in the statistically steady state of the simulation, when the turbulence is fully developed. Right panel: time-averaged third-order correlators in equation (54), Y^+ (full line) and Y^- (dotted line), versus the scale (normalized to the simulation box size, L). A linear relation is also shown (dashed line). The two vertical lines identify the inertial range. For the $\mathbf{z}^+$ field, the dissipation scale, l_d^+, the Taylor microscale, λ^+, and the integral scale, l_0, are labeled on the x-axis. Figure adapted from Sorriso-Valvo et al. (2002).

of Figure 6 shows the time-averaged (over the ten outputs) linear dependence of the third-order moments $Y^{\pm}$ as a function of the scale. A range with clear linear scaling is present between 10^{-2} and 10^{-1} (in units of the simulation box size L) as marked by vertical lines in the figure, indicating the turbulence inertial range. The P&P law was then used to determine the energy transfer rates, $\varepsilon^+ = 550$ and $\varepsilon^- = 440$ (given in simulation units, see details in Sorriso-Valvo et al., 2002). The slightly different quality of the linear scaling law, clearer for the Y^+ case, and the difference in the energy transfer rate, were probably due to non-vanishing cross-helicity. These values were then used to estimate the typical scales of the turbulence in the framework of the IK phenomenology, namely the dissipative scale $l_d^{\pm} = (\nu^2 B_0/\varepsilon^{\pm})^{1/3}$ and the Taylor microscale, $\lambda^{\pm} = (2\nu E^{\pm}/\varepsilon^{\pm})^{1/2}$, where ν is the viscosity coefficient, $E^{\pm}$ the energy associated with the Elsasser fields, and B_0 the ambient magnetic field.

The first follow-up study in three-dimension was performed later on a much larger grid, thanks to booming evolution of high performance computing and the development of codes able to exploit parallel architectures (Mininni et al., 2011a; Rosenberg et al., 2020; Foldes et al., 2022). A 1536^3 grid points direct numerical simulation of incompressible, decaying MHD turbulence was used by Mininni and Pouquet (2009) to study, among other

turbulence properties, the linear P&P scaling law. The high-resolution simulation has been performed using the Geophysical High Order Suite for Turbulence (GHOST) code (Mininni et al., 2011a; Rosenberg et al., 2020), a pseudo-spectral framework designed to solve with high accuracy and efficiency a variety of partial differential equations, including the governing equations of MHD and Hall-MHD plasmas. Using one snapshot of the simulation at the peak of the turbulence (i.e, at the maximum of the mean current density, $\langle J^2 \rangle$), shown in the top panels of Figure 7, the two correlators, $Y^{\pm}$, were estimated. Results of the analysis are shown in the bottom panels of the same figure, where a linear scaling is also plotted for reference. Although the associated energy transfer rate was not determined through a linear fit, differences between the Y^+ and Y^- scaling appear evident from the figure. Like in the two-dimensional case, one of the two correlators (in this case Y^-) shows both a better linear scaling, including a more extended inertial range, and a larger energy transfer rate. Curiously, both of the articles described above did not focus on the validation of the third-order moment scaling law for the MHD but, rather, used it as a tool to determine other turbulence quantities: in Sorriso-Valvo et al. (2002) the typical scales of the turbulence have been identified in order to evaluate the sign-singularity and cancellation properties of the current density, while Mininni and Pouquet (2009) used the mixed third-order moments to perform intermittency analysis, and in particular to determine the anomalous scaling exponents of the structure functions via extended self similarity analysis (Benzi et al., 1993). Nevertheless, they both represent crucial first validations of the MHD third-order moment scaling law in direct numerical simulations of two and three dimensional plasma turbulence.

4. Evidence of the Politano & Pouquet law in the solar wind

The firsts attempt to verify the P&P law, equation (54), in space plasmas dates back to 2005. Although several approaches have been developed based on the original P&P law and its generalization (i.e., using different hypotheses and/or including extra terms, as we shall see in the following sections), the observational assessment of the mixed third-order structure functions in the heliosphere, as separate kinetic/magnetic energy and cross-helicity terms, or in terms of pseudo energies employing the Elsasser variables, relied so far on the analysis of time-series from single spacecraft observations. Data analysis techniques proposed in numerous scientific articles have therefore all

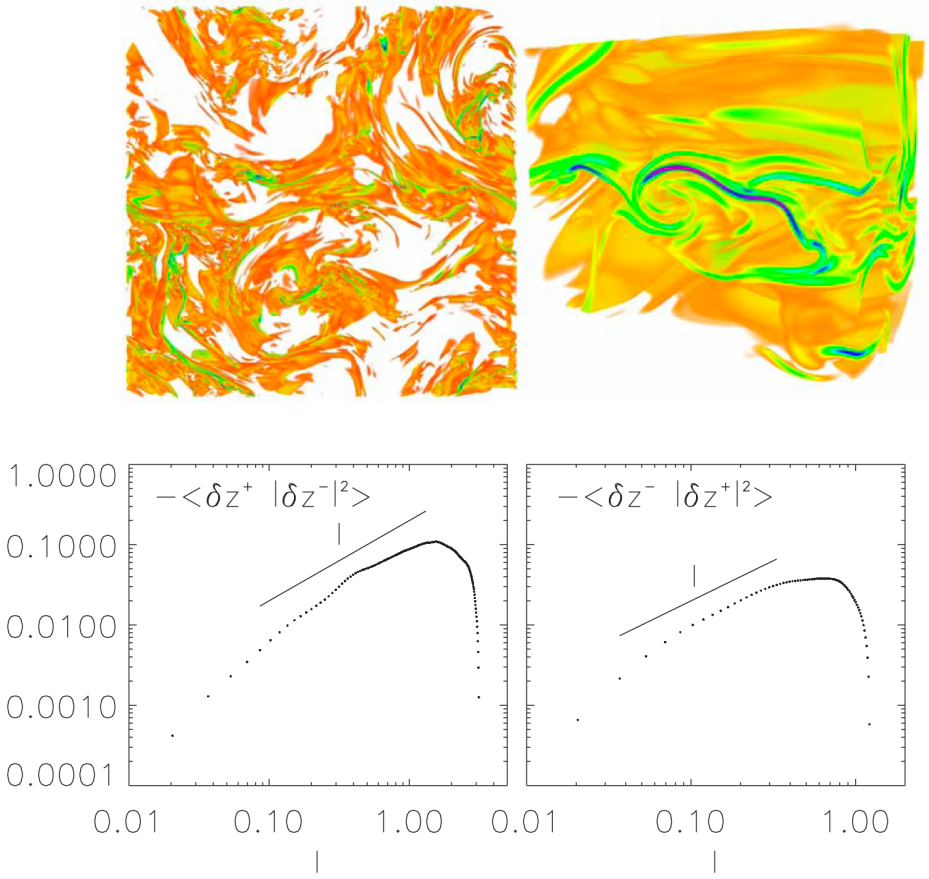

Figure 7: Validation of the P&P law in three-dimensional MHD numerical simulations. Top panels: a three-dimensional visualization of a snapshot of the current density (top-left) and a magnification showing the roll-up of the turbulent structures (top-right). Bottom panels: third-order correlators Y^+ (bottom-left) and Y^- (bottom-right) versus the scale. A linear relation is also shown as full line. Figure adapted from Mininni and Pouquet (2009).

resorted to the Taylor frozen-in hypotheses (Taylor, 1938) to set the equivalence between time and spatial lags. Disregarding the reference frame in which the space plasma is collected, once a longitudinal direction is identified (normally the sampling direction, i.e., the one aligned with the solar wind stream), assuming the average solar wind speed in the spacecraft frame over the investigated sample, $-\langle v_R \rangle$, to be much larger than the typical velocity fluctuations, time fluctuations can be replaced by spatial variations of the

fields. These are related through the Taylor hypothesis, so that $r = -\langle v_R \rangle \tau$, τ and r being time and space respectively. Note the opposite sign linking temporal and spatial directional increments, due to the vector nature of the transformation. Indeed, if the coordinate system has an axis oriented in the same direction of the flow, then a probe samples the plasma with larger coordinate first. If the axis of the probe is oriented opposite to the plasma flow, then both the sign of the mean velocity and of the spatial increment vector are inverted, resulting again in opposite sign for the two increments. In-depth discussions on the validity of the Taylor hypothesis in solar wind turbulence can be found in Perri et al. (2017); Perez et al. (2021a); Verma (2022). For the purposes of this review, the validity conditions are generally met to a large extent, so we will implicitly use it unless stated otherwise.

4.1. First observation of an interplanetary turbulent cascade in the ecliptic solar wind

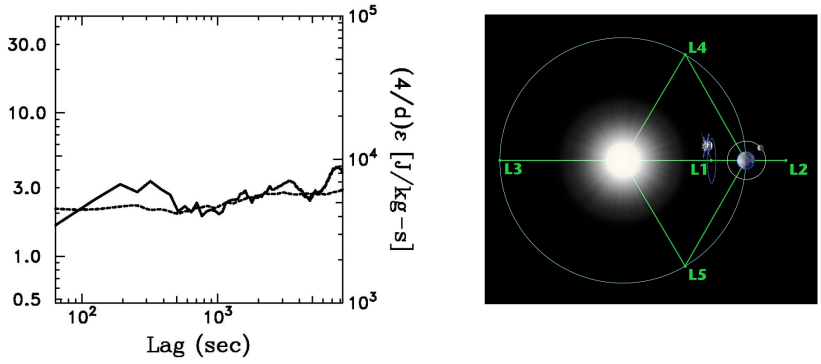

Figure 8: Left panel: compensated third-order moment of the Elsasser field fluctuations, computed on the ACE database spanning from 1998 through 2004. The solid line refers to the P&P law as in equation (54), though here the dimension of the problem d is considered unknown. Figure adapted from MacBride et al. (2005). Right panel: the NASA's Advanced Composition Explorer (ACE) orbits around the point between Earth and the Sun called a Lagrange point, labeled here as L1, indicated in the figure. Sitting well outside of Earth's magnetosphere, ACE observed the plasma streaming off the Sun before it enters near-Earth space. Credit: NASA/H. Zell, available at: `https://www.nasa.gov/mission_pages/sunearth/news/ace-15th.html`

.

In a seminal work proposing the implementation of the third-order exact law approach, MacBride et al. (2005) computed the mixed third-order tensor

in equation (54) using extensive samples of plasma and magnetic field observed by the ACE spacecraft from 1998 through 2004, each sample's length spanning from one month to several Carrington rotations. A linear scaling of the third-order structure function of the Elsasser variables computed on the solar wind fields was obtained by these authors, allowing the estimate of the pseudo-energy transfer rate. Assuming two-dimensional turbulence, thus a dimensionality parameter $d = 2$ in the left y-axis label of the left-hand panel of Figure 8, the pseudo-energy transfer rate was found of the order of $\varepsilon \simeq 10^4$ J kg^{-}1. The data utilized in this study were collected by the ACE spacecraft in the ecliptic plane, specifically, at the Lagrangian point L1 (McComas et al., 1998a), shown in Figure 8 (right), across a maximum of the solar activity. Given the very large temporal extension of the samples analyzed, these included both fast and slow solar wind streams, though no details concerning the solar wind speed were provided in MacBride et al. (2005). The sample also included large-scale structures and residual dynamics of solar energetic events occurring during solar maxima. Averages over many months required the use of low-order de-trending routines to guarantee some degree of the homogeneity required for the P&P law, assuming some degree of stationarity and no feedback of the large-scale structures filtered on the turbulent dynamics of the inertial range. A later work by the same authors proposed a refined analysis of the same ACE dataset, this time performed over shorter intervals (2-days), without de-trending the signals and separating fast and slow wind (MacBride et al., 2008, see Section 4.5).

4.2. First observation of an interplanetary turbulent cascade in the high latitude solar wind

The work by (MacBride et al., 2005) pioneered the use of the third order structure function analysis in the ecliptic heliospheric plasma, mixing fast and slow solar wind measurements collected over extended periods, with varying solar activity. First evidences of the existence of an inertial range turbulent cascade in the out-of-ecliptic solar wind and the possibility that MHD turbulence could act as a heating mechanism for the solar wind, were instead provided by Sorriso-Valvo et al. (2007); Marino et al. (2008). The analyses implemented by these authors, using the observations of the Ulysses spacecraft (Balogh et al., 1995), demonstrated the local character of the MHD turbulent cascade in the solar wind and how its features depend drastically on local —in time and space— parameters and conditions of the heliosphere, such as the location (heliolatitude and heliocentric distance) of the analyzed

plasma, solar activity and the type of solar wind (fast or slow). All that supported the need for a methodological approach in the implementation of the P&P in space plasmas different than in MacBride et al. (2005), based indeed on the selection of shorter time-series, corresponding to periods of consistent solar activity, stationarity (at least in a weak sense), and of one single type of solar wind, either fast or slow. This approach, later on also implemented in MacBride et al. (2008), was validated by several evidences, as is shown in the following and in Marino et al. (2011); Marino et al. (2012), and is now widely adopted.

A simple strategy for avoiding the inhomogeneity caused by the shearing between fast and slow solar wind streams, as well as by the alternation of magnetic sectors with different polarities, both commonly developing in the ecliptic plane (and likely producing sign switches of the P&P law tensor), is to use solar wind sampled at high heliolatitude. Since the Sun's poles are mostly covered by coronal holes and free of active regions, the wind originating at high latitude is essentially steady, and the magnetic polarity of high latitude sectors of the heliosphere is stable. Launched in 1995, the Ulysses spacecraft, depicted in the left panel of Figure 9, was designed to explore the high-latitude heliosphere (Smith et al., 1995b; Balogh et al., 1995). To this aim, it used planetary gravitational assists to reach its orbit out of the ecliptic plane. Measures from Ulysses confirmed that the polar solar wind is extremely steady during solar minima, while at maxima, when solar equatorial activity expands towards the poles, variability reaches higher latitudes. This is clearly visible in the famous latitudinal profile of velocity and magnetic field measurements collected by Ulysses during its first polar orbit, from 1995 to 1997, shown in the right panel of Figure 9. At high latitude (both north and south), the polar solar wind speed (blue and red lines) is convincingly stationary, while near the ecliptic stronger variability is observed. Similarly, the magnetic polarity, color-coded in red (outward field) and blue (inward field), is nearly always fixed in the polar wind, while at low latitude several polarity changes highlight the spacecraft crossings of the heliospheric current sheet.

In a series of works, (Sorriso-Valvo et al., 2007; Marino et al., 2008; Carbone et al., 2009a; Marino et al., 2011; Marino et al., 2012) used the steady polar solar wind observed by Ulysses at high heliolatitude to obtain large stationary intervals, suitable for the implementation of the third-order structure function analysis using the P&P law (equation 54). In particular, in Sorriso-Valvo et al. (2007), solar wind velocity, density and magnetic field were col-

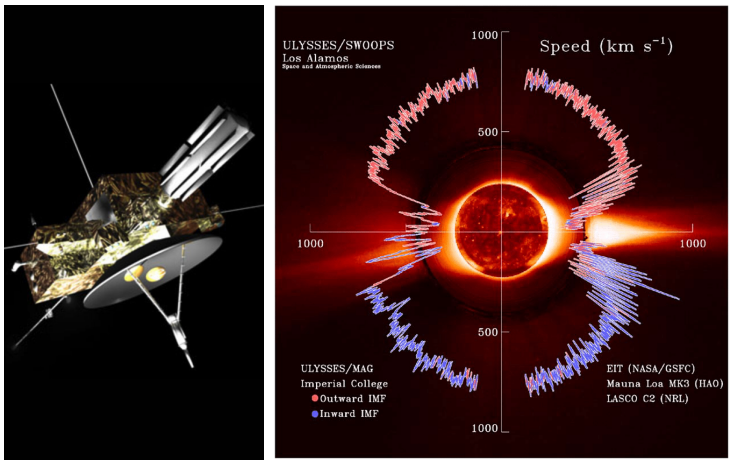

Figure 9: Left panel: rendering of the Ulysses spacecraft. Figure from `https://www.esa.int/Enabling_Support/Operations/Joint_ESA_NASA_Ulysses_mission_to_end`. Right panel: latitudinal plot of the solar wind speed (line) and magnetic field polarity (red and blue color of the velocity profile) measured by Ulysses during its first polar orbit (1995—1997). The combined solar corona images were taken by the Extreme ultraviolet Imaging Telescope (EIT) onboard the SOHO spacecraft, the Mauna Loa High Altitude Observatory (HAO) coronagraph, and by the C2 camera of the Large Angle and Spectrometric Coronagraph Experiment (LASCO) coronagraph. Figure adapted from McComas et al. (1998b)

.

lected during the first seven months of 1996, when the heliocentric distance of Ulysses slowly increased from 3 au to 4 au, and its heliolatitude decreased from about 55° to 30°. During that time frame, the solar activity was exploring a minimum of the solar cycle, allowing to collect long time series of nearly-stationary solar wind (see Figure 10). 8-minute averaged time series of the El-

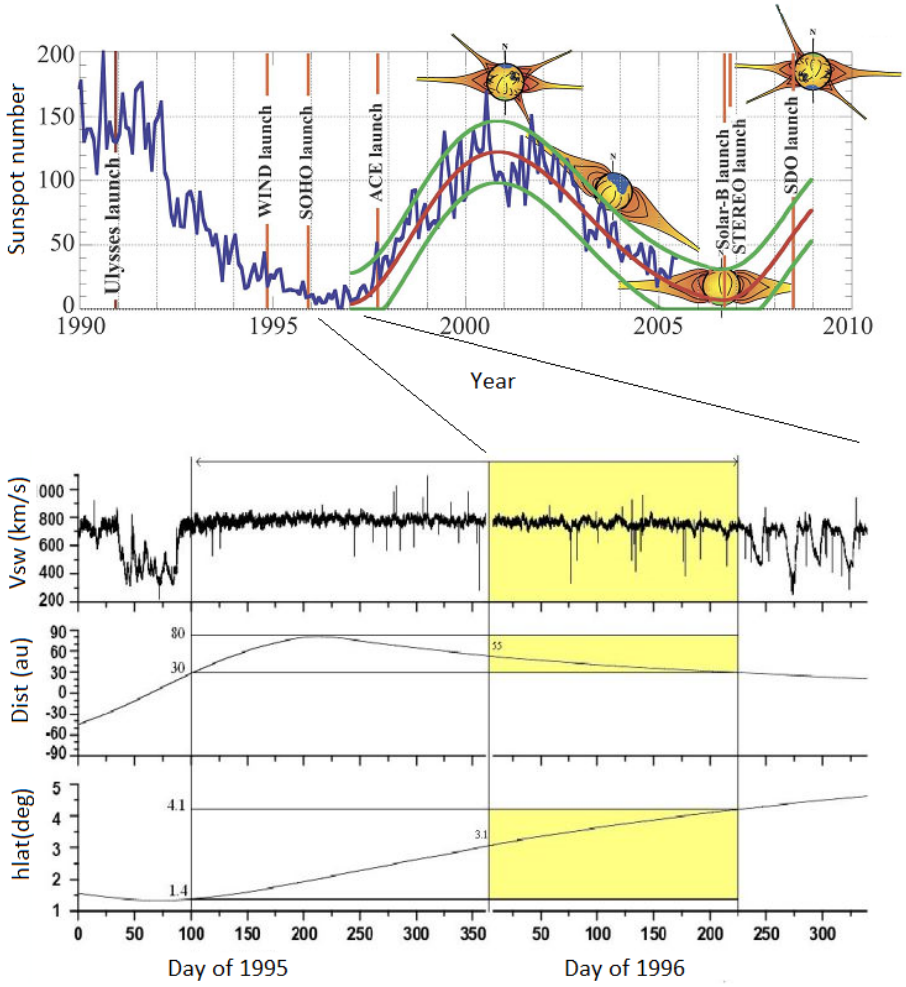

Figure 10: Top panel: varying solar cycle and various spacecraft launches, during Ulysses's lifetime. Credit: S. Suess (available at `https://sci.esa.int/web/ulysses/-/40378-solar-activity-and-mission-launches`). Bottom panel: solar wind velocity measured by Ulysses during the years 1995 and 1996. The highlighted period has been analysed in Sorriso-Valvo et al. (2007); Marino et al. (2008).

sasser fields ($\Delta z^{\pm}$) were used to compute the mixed third-order tensor of the P&P law over windows of $\simeq$ 11 days, $Y^{\pm}(\tau) = \left\langle \Delta z_L^{\mp} (\Delta z_i^{\pm})^2 \right\rangle = \frac{4}{3} \varepsilon^{\pm} \langle v_R \rangle_t \, \tau$. Here $\tau \equiv \Delta t$ is the time scale obtained, as usual, through the Taylor hypothesis, $\ell = -\langle v_R \rangle_t \, \tau$, with $\langle v_R \rangle_t$ being the solar wind speed averaged over each 11-day window. The window size was selected in order to be large enough as to include several correlation lengths (typically of the order of several hours up to a day in the steady polar wind), in order to ensure ergodicity, but short enough as to provide reasonable stationarity of the solar wind samples within each window, and to avoid remarkable distance or latitudinal variation (Sorriso-Valvo et al., 2007; Sorriso-Valvo et al., 2010). Figure 11 shows, for

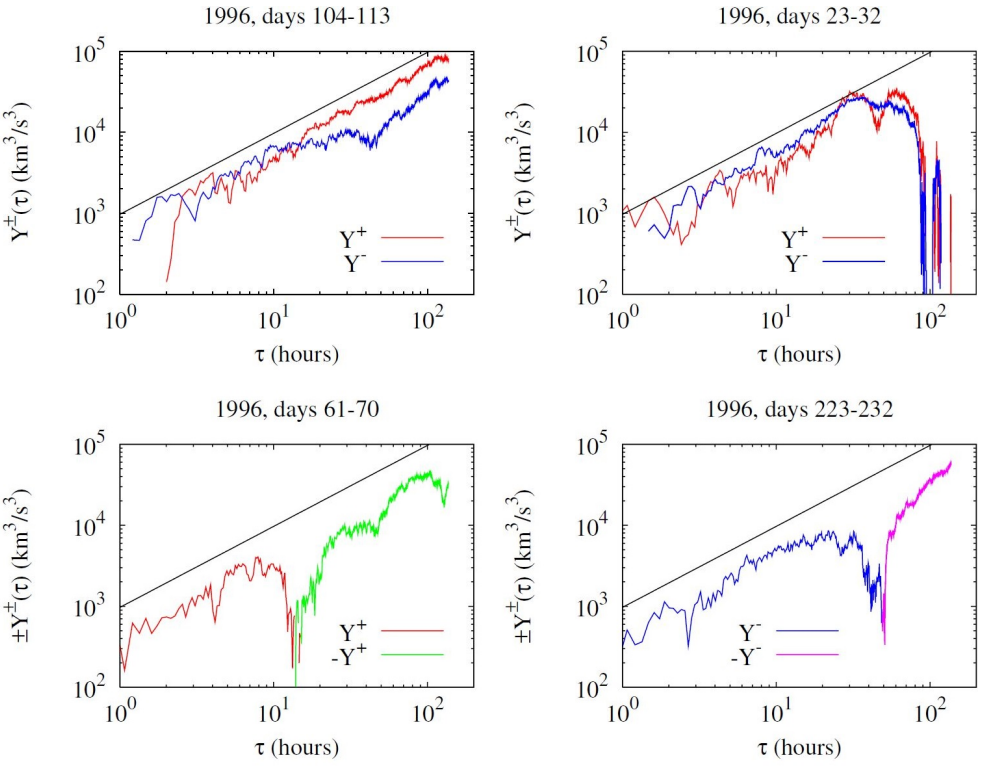

Figure 11: $Y^{\pm}(\tau)$ as a function of the time scale τ for four of the periods analyzed in Sorriso-Valvo et al. (2007). Different colours refer to positive and negative values of the mixed third-order structure function $Y^{\pm}(\tau)$, corresponding to either positive or negative $\varepsilon^{\pm}$. The solid black is a linear function, and is added as a reference. Figure adapted from Sorriso-Valvo et al. (2007).

four examples of periods where the P&P was observed, the tensor $Y^{\pm}(\tau)$ plot-

DOY 1996	$(\epsilon^- \pm \delta\epsilon^-)\ \frac{J}{kg\ s}$	$(\langle V \rangle \pm \delta\langle V \rangle)\ \frac{km}{s}$	Inertial range Y^-
$24 \div 35$	176 ± 13	709 ± 114	$3\ h \div 2\ d$
$74 \div 85$	154 ± 32	699 ± 102	$1\ h \div 4\ d$
$178 \div 189$	66 ± 24	678 ± 95	$5\ h \div 4\ d$
DOY 1996	$(\epsilon^+ \pm \delta\epsilon^+)\ \frac{J}{kg\ s}$	$(\langle V \rangle \pm \delta\langle V \rangle)\ \frac{km}{s}$	Inertial range Y^+
$11 \div 22$	-167 ± 13	701 ± 105	$1\ h \div 3\ d$
$21 \div 32$	436 ± 32	694 ± 112	$30\ m \div 2\ d$
$56 \div 67$	174 ± 24	707 ± 131	$1\ h \div 3\ d$
$68 \div 79$	115 ± 19	675 ± 96	$2\ h \div 4\ d$
$69 \div 80$	113 ± 12	674 ± 102	$2\ h \div 4\ d$
$81 \div 92$	185 ± 25	690 ± 90	$3\ h \div 4\ d$
$103 \div 114$	194 ± 22	690 ± 85	$5\ h \div 4\ d$
$117 \div 128$	-121 ± 13	696 ± 94	$2\ h \div 4\ d$
$135 \div 146$	218 ± 28	707 ± 110	$3\ h \div 2\ d$
$172 \div 183$	-126 ± 15	678 ± 103	$10\ h \div 4\ d$
$184 \div 195$	216 ± 25	696 ± 88	$30\ m \div 4\ d$
$192 \div 203$	-91 ± 11	690 ± 94	$4\ h \div 4\ d$

Table 2: 11-day interval given in terms of day of the year (DOY) 1996; pseudo-energy transfer rates $\varepsilon^{\pm}$ estimated through fits of the P&P law; average solar wind speed within the interval; extension of the detected inertial range.

ted against the time scale, τ. A clear linear scaling, visible in the examples in the figure, emerged in this study in a significant fraction of the intervals analyzed, with a detected inertial range spanning up to two decades of scales. Table 2 collects a selection of the 11-day periods among those analyzed in Sorriso-Valvo et al. (2007); Marino et al. (2008, 2012), for which a particularly extended inertial range in the fast solar wind was identified. These observations represented the first robust evidence of an interplanetary turbulent cascade in the polar solar wind plasma. Together with the identification of the inertial range of the solar wind turbulent cascade, Sorriso-Valvo et al. (2007) also provided the first estimate of the pseudo-energy transfer rate in the high-latitude solar wind, listed in Table 2 for the selected examples.

The analysis also revealed the possible presence of inverse energy transfer in the interplanetary space plasma, inferred through the sign of the estimated pseudo-energy transfer rate. In several of the 11-day windows analyzed, the

sign of $Y^{\pm}(\tau)$ within the linear range was observed to be consistently positive or negative. Since the pseudo-energy dissipation rates are positive definite, and considering the sign switch due to the Taylor hypothesis, positive $Y^{\pm}(\tau)$ indicates a forward transfer of the pseudo-energy, from the large to the small scales. Conversely, negative $Y^{\pm}(\tau)$ could be indicative of an inverse constant-flux pseudo-energy transfer, thus toward larger scales. On the other hand, for a significant number of samples analyzed in Sorriso-Valvo et al. (2007); Marino et al. (2008, 2012) $Y^{\pm}(\tau)$ exhibit sign switches from positive to negative linear scaling (see the bottom panels of Figure 11), suggesting a dual pseudo-energy transfer to both large and small scales in the space plasma analyzed. The existence of a dual-cascade paradigm in solar wind turbulence is still subject of numerical and observational investigations. However, dual constant-flux cascades are an established feature of hydrodynamic turbulence in the presence of anisotropy and internal waves, and have also been explored in the context of magnetohydrodynamic simulations with variable vector potential and aspect ratio (Alexakis and Biferale, 2018). In particular, rotating and stratified flows are known to develop a dual cascade of both kinetic and potential energy, resulting from the interplay of internal waves and turbulent motions, as observed in direct numerical simulations (Marino et al., 2013; Marino et al., 2014; Pouquet and Marino, 2013; Marino et al., 2015a). The detection of an inverse cascade of pseudo-energy in the solar wind might be linked to the bidimensionalization of the heliospheric plasma, due to the enhancement of the background magnetic field. Indeed, the dimensionality of the system is known to play a major role in the scale-by-scale transfer of quadratic invariants in both fluid and plasma turbulence (Alexakis and Biferale, 2018). However, there is still no consensus on the possible reason for observing negative scaling in space plasma turbulence. Numerical and experimental studies reported possible causes for observation of reversed sign, such as the dominance of outward or inward Elsasser modes in Alfvénic turbulence (Coburn et al., 2015), the presence of large-scale shears (Stawarz et al., 2011), or anisotropy (Verdini et al., 2015). We will describe some of these in the following sections, but we believe that more studies are still necessary to fully understand the actual meaning, or meanings, of the observed negative scaling.

4.2.1. Occurrence of the P&P law in the Solar Wind

In order to characterize the occurrence of the P&P scaling in the high-latitude solar wind, Marino et al. (2012) extracted three extended peri-

ods from the Ulysses spacecraft database, each nearly one year long (from day of year/DoY 209/1993 to DoY 253/1994; from DoY 212/1995 to DoY 224/1996; and from DoY 20/2006 to DoY 23/2007, as reported in figure 12), so that during each period —corresponding to roughly a semi-orbit of Ulysses— the spacecraft collected solar wind measurements with comparable variations of its orbital parameters: radial distance ($\sim$ 2—4.5 au) and heliolatitude ($\sim 30°$—$80°$, north or south). Semi-orbit I was taken during the solar activity decreasing phase, near a minimum; semi-orbit II at the solar minimum; semi-orbit III during the next decreasing phase, close to an anomalous minimum (Wang et al., 2009).
The P&P law, equation (54), has been evaluated throughout the three solar wind periods defined above using 11-day running windows. Figure 13 shows one of the 11-day windows where a clear P&P linear scaling was observed (Marino et al., 2012). The P&P scaling was observed in a relevant fraction of such relatively short sampling windows, likely whenever local conditions enabled a homogeneous, isotropic, incompressible MHD cascade contribution to turbulence. Lack of isotropy could be one of the main reason for the discontinuous identification of the turbulent cascade by means of the P&P law in the solar wind. Based on this consideration, modified versions of the Kármán-Howarth scaling law, taking into account anisotropy, have been derived for plasmas (Galtier, 2011), and simplified models assuming solar wind turbulence anisotropy have been broadly used (Smith et al., 2009; Wan et al., 2009; Stawarz et al., 2011), as will be presented further on in this review.

For the P&P scaling case illustrated in Figure 13, the inertial range extends from one hour to about 48 hours (Goldstein et al., 1995). The smaller scale is clearly limited by the data resolution (8 minutes), which for Ulysses is about one order of magnitude larger than the typical lower limit of the MHD inertial range (Leamon et al., 1998; Alexandrova et al., 2007; Alexandrova et al., 2008). On the other hand, the upper limit of the inertial range in the fast polar wind was found varying from a few hours to a few $(2-3)$ days for different intervals (see Table 2). These values reach significantly larger scales than the commonly adopted correlation lengths in the ecliptic wind, typically of a few hours (see e.g. Bruno and Carbone, 2013). On this note, it should be pointed out that polar wind might have different, much extended inertial range, not being affected by ecliptic modulations. Indeed, for the events showing extended inertial range, magnetic spectra also showed power-law scaling down to exceptionally low frequencies (Marino et al., 2012),

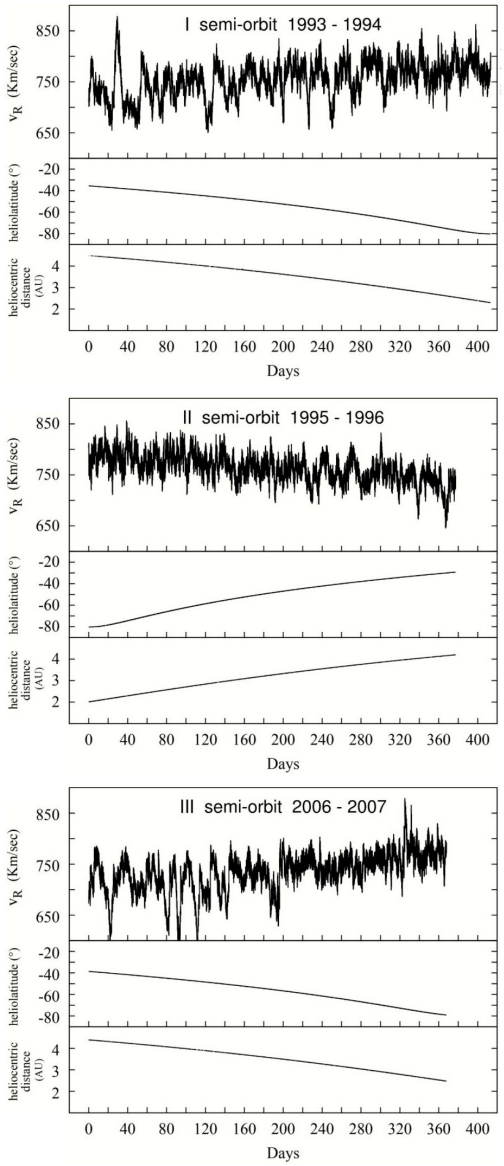

Figure 12: Radial solar wind velocity observed by the Ulysses, roughly corresponding to three semi-orbits of the spacecraft. For each panel, the top sub-panel shows the radial velocity v_r, the central sub-panel the heliolatitude θ, and the bottom sub-panel the heliocentric distance R. Figure adapted from Marino et al. (2012).

suggesting that the steady and homogeneous high-latitude wind from polar coronal holes might be associated to large-scale drivers of coronal origin (Sorriso-Valvo et al., 2010). Additionally, it should be noticed that the P&P law generally provides a more rigorous localization of the turbulence inertial range, with respect to the identification achieved through second order quantities such as the energy spectrum (Frisch, 1995).

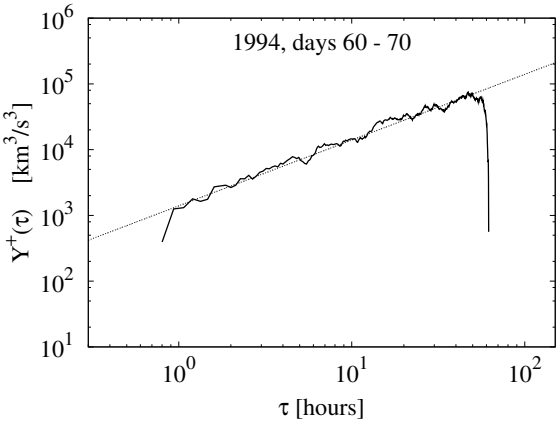

Figure 13: An example of clear P&P linear scaling Y^+ observed in an 11-day sample collected by the Ulysses spacecraft from $\sim$ day 60 to 70 of 1994. Figure adapted from Marino et al. (2012).

It is interesting to provide a quantitative estimate of how often the P&P scaling law is observed in polar solar wind, and to explore possible dependencies on various parameters. The bottom panels of Figure 14 show the fraction of 11-day intervals in which the liner scaling of equation (54) was observed (indicated as "scaling ratio"). In order to evaluate the variation with orbital parameters, the intervals were split in four groups of different heliolatitude and radial distance. The scaling ratio appears to be smaller at higher latitude and closer to the Sun (with values of $\sim$ 10%), whereas it increases remarkably in the solar wind measured towards the heliographic poles and far from the Sun (up to 30%). This indicates that, if we assume stationarity of the polar coronal source, the conditions for the observation of the P&P law —and therefore the local turbulence properties— do evolve along with the solar wind expansion in the outer heliosphere and with the heliolatitude.

As discussed more in detail in the following sections, the pseudo-energy transfer rate estimates were also found to anti-correlate with Alfvénicity in the ecliptic solar wind (Smith et al., 2009), as evaluated through the normalized cross-helicity (Goldstein et al., 1996):

$$\sigma_c \equiv \frac{(\Delta z^+)^2 - (\Delta z^-)^2}{(\Delta z^+)^2 + (\Delta z^-)^2} = 2\langle \Delta \mathbf{v} \cdot \Delta \mathbf{b} \rangle / (\langle \Delta \mathbf{v}^2 \rangle + \langle \Delta \mathbf{b}^2 \rangle) \,. \tag{63}$$

The possible role of cross-helicity was briefly introduced at the end of Section 3.3, where cross-helicity related terms were highlighted in the version of the P&P law in terms of velocity and magnetic field. It might be thus expected in general that large cross-helicity states should result in an observed reduced cascade rate, or even the absence of turbulent cascades.

Following the usual local approach, Marino et al. (2012) performed a systematic investigation of the correlations between the pseudo-energy transfer rates estimated through the P&P law, $\epsilon^{\pm}$, and the cross-helicity magnitude, $|\sigma_c|$, in the high latitude wind. The top panels of Figure 14 show the absolute value of the normalized cross-helicity, computed inside each 11-day window, then averaged over heliolatitude and radial distance bins, using the data relative to the three semi-orbits of Ulysses (Figure 12).
$\langle |\sigma_c| \rangle$ (brackets indicating here the average computed over the local 11-days samples) increases at higher latitudes, confirming the enhancement of outgoing Alfvénic fluctuations in the fast wind coming from polar coronal holes (Smith et al., 1995a), and decreases with the radial distance, in agreement with observations of radial decay of Alfvénic fluctuations (Bavassano et al., 2000; Sorriso-Valvo et al., 2022). Figure 14 shows a clear anti-correlation between the scaling ratio and $\langle |\sigma_c| \rangle$, suggesting that the smaller the imbalance between Elsasser modes, the higher the probability of observing linear scaling of the mixed third-order moment, consistently with what is expected in the MHD framework.

Values of the scaling ratio computed separately for each of the three Ulysses' semi-orbits analyzed (thus not binned in terms of the helicentric distance or the heliolatitude of the 11-day sub-samples) show as well good correlation with $\langle |\sigma_c| \rangle$ (see the discussion in Section 4.2.2 and the related Figure 16). Indeed, the first and third semi-orbits are characterized by a scaling ratio of about 50%, and rather small cross-helicity ($\langle |\sigma_c| \rangle \simeq 0.2$). However, the second semi-orbit shows a smaller occurrence of P&P scaling regions (about 10% of the whole signal), with a larger value of the mean cross-helicity ($\langle |\sigma_c| \rangle \simeq 0.5$). This emphasizes the substantial differences between

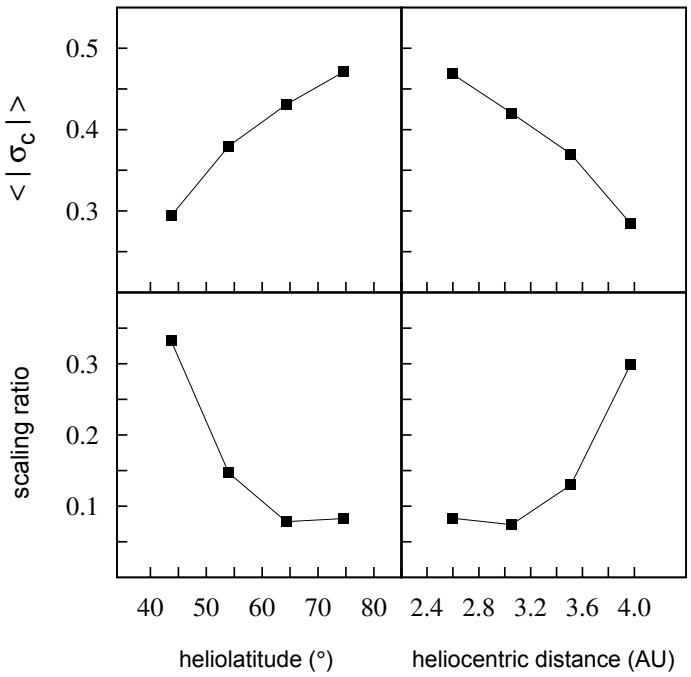

Figure 14: Variation of the mean cross-helicity (top panels) and of the fraction of 11 day intervals where the P&P linear scaling is observed (scaling ratio, bottom panels), versus the heliolatitude (left panels) and the heliocentric distance (right panels). Values of the normalized cross-helicity $|\sigma_c|$ and the scaling ratio have been computed in 11-day running windows, then averaged over four statistical bins. Figure adapted from Marino et al. (2012).

the output of P&P analysis conducted in periods with different solar activity, evidencing the need for separating solar wind measurements —relative to periods of high and low solar activities— in computing the third-order structure functions of the Elsasser fluctuations in heliospheric plasmas.

In order to investigate more quantitatively the irregular occurrence of the P&P scaling law in Alfvénic solar wind turbulence, a conditional statistical analysis was performed. The data was split into two classes, namely 11-day windows with (dataset 1) and without (dataset 2) P&P linear scaling, and the properties of turbulence were analysed separately for the two sets (Marino et al., 2012). The main features found for the samples satisfying the P&P law are: (i) kinetic and magnetic spectral indexes closer to the typical values of the classical turbulent phenomenology ($\alpha \simeq -1.5$); (ii) power-law spectral

ranges extending toward larger scales (larger than what is typically found in the samples not showing the P&P scaling). A very important remark, already mentioned before, is that in those specific samples of fast polar wind in which the P&P law is satisfied up to very large timescales, the inertial range estimated from kinetic and/or magnetic spectra also appears to be more extended to low frequencies, as shown in Figure 15. On the other hand, the spectra relative to regions where the P&P law is not observed are characterized by shallower exponents and/or reduced extension of the power law scaling range, classically associated with the turbulence inertial range. In other words, the observation of the P&P law in the polar solar wind seems to be associated to the presence of a spectrum closer to Kolmogorov-type and extending over wider ranges of scales, suggesting that the turbulence is better developed than in the cases without P&P scaling (Figure 15). This further confirms the validity of the scaling law approach for the identification of turbulent cascades in the solar wind.

4.2.2. Modulation of the MHD turbulent cascade by the solar activity

Among the possible causes for variability in the observed turbulence properties, solar activity appear immediately as a likely parameter. Indeed, it regulates the level of coronal fluctuations and the outflow wind speed, which may be in turn regulating the turbulent cascade through injection of velocity or magnetic shears in the early-stage solar wind.

Although the three semi-orbits analyzed in Marino et al. (2012) refer to periods close to minima of the solar cycle, some modulation of solar activity is still present, enabling a preliminary study of the dependency of features of the MHD turbulent cascade on the activity level. The top panel of Figure 16 shows the mean solar activity (in coronal units, i.e, millionths of intensity of the solar disk, Rybanský et al., 1994), integrated in the polar regions, namely between 40°—80° north or south, depending on the Ulysses' semi-orbit considered. The figure shows as well the scaling ratio (second panel from the top, see section 4.2.1); the cross-helicity $\langle|\sigma_c|\rangle$, computed by averaging the absolute value of the normalized cross-helicity obtained for all 11-day windows, over each semi-orbit, after separating regions with and without the P&P scaling (third panel from the top); the mean turbulent pseudo-energy transfer rates, $\varepsilon \simeq \varepsilon^{\pm}$, estimated from the the P&P law (fourth panel from the top); the mean value of $rms(|\tilde{\sigma_c}|)$ for each semi-orbit, where $\tilde{\sigma_c} = 2(\Delta\mathbf{v}\cdot\Delta\mathbf{b})/(\Delta\mathbf{v}^2+\Delta\mathbf{b}^2)$ is the "local cross-helicity", evaluated for every single point of the dataset, so that the rms of $(|\tilde{\sigma_c}|)$ computed over 11-day in-

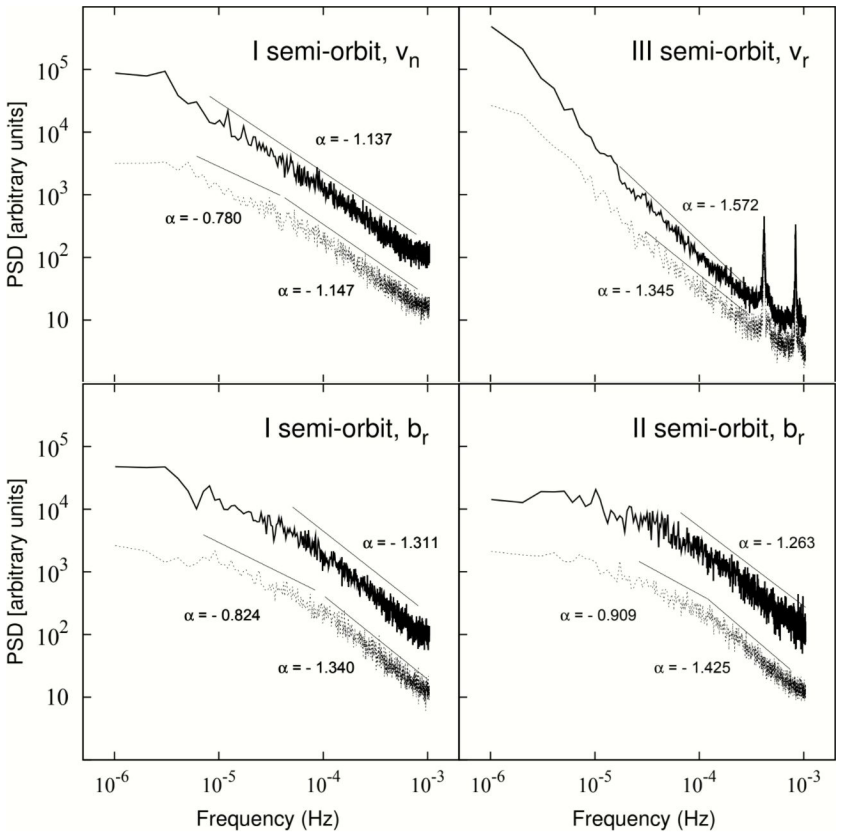

Figure 15: Velocity (top panels) and magnetic field (bottom panels) components power spectra, computed using 11-day high latitude (fast) solar wind samples collected by the Ulysses spacecraft. The spectra are computed (separately) in regions with (solid line) and without (dashed line) P&P scaling. For sake of clarity, the spectra are given in arbitrary units and have been vertically shifted. Spectral indices obtained from fits of the detected power-law ranges are indicated in the plot. Figure adapted from Marino et al. (2012).

tervals represents the degree of fluctuation of the alignment between velocity and magnetic field in each eleven-day window (bottom panel). The values of $\langle|\sigma_c|\rangle$ and $\langle rms(|\tilde{\sigma_c}|)\rangle$ are plotted separately for the regions with (squares, solid line) and without (circles, dashed line) P&P scaling. In figure 16, it appears very clearly that the scaling ratio and the averaged pseudo-energy transfer rate correlate with the solar activity: in the semi-orbit II, characterized by very low solar activity, the percentage of intervals in which the P&P law appears is $\sim$ 10%, while in semi-orbits I and III, characterized

by higher solar activity, the percentage goes up to above 50%. Figure 16 emphasizes as well the anti-correlation between the normalized cross-helicity and the solar activity, but only for averages computed over 11-day periods where P&P scaling is present, while $\langle|\sigma_c|\rangle$ is roughly constant when averaged over the remaining samples. While these observations suggest the importance of the solar input for solar wind turbulence, the local variability of $|\sigma_c|$ and of the level of fluctuation of the local alignment (between velocity and magnetic field) are certainly associated with the irregular occurrence of the MHD turbulent cascade as it is detected through the P&P law. Even though the causation between lower cross-helicity states and higher probability for the MHD turbulence cascade to develop in the solar wind is still not demonstrated, the work by Marino et al. (2012) does show that the two are correlated. This is also a reasonable correlation, since highly Alfvénic fluctuations should inhibit nonlinear interactions by sweeping away the interacting structures, and therefore reduce the cascade rate. The bottom panel of figure 16 indicates a higher degree of fluctuations of the local velocity and magnetic field alignment when the MHD cascade is observed, which further confirms that the correlation with solar activity and energy transfer rate exists for the P&P scaling regions only.

The phenomenological picture emerging from the investigation of solar wind turbulence properties through the P&P law is not in line with the dynamic alignment theory (Boldyrev, 2005). Indeed, the latter sees the solar wind plasma relaxing toward high cross-helicity states (Dobrowolny et al., 1980) as it expands from the Sun. The characterization of the occurrence of the third-order P&P law estimated in data samples of just a few days —thus locally— suggests however the description of the high-latitude outer heliosphere as a framework in which velocity and magnetic field in the expanding solar wind plasma are lesser correlated the larger the distance from the Sun. This results in a higher probability for the P&P law to be verified at larger heliocentric distances, as shown in Figure 14 (Marino et al., 2012). Such discrepancy, however, is consistent with the existence of a local mechanism that would act as trigger for MHD turbulence in solar wind, such as for instance, the velocity and density shears associated with the P&P law, as will be discussed in Section 4.2.3. Consistently, the correlation between solar activity variations and the occurrence of the P&P scaling in the fast polar wind, shown in Figure 14, can be related to the enhanced energy input (e.g. in form of velocity and density shears) during higher solar activity. Ultimately, the results presented in Marino et al. (2012) confirm the non-universal nature of

solar wind turbulence, underlining the importance of selecting homogeneous samples (in terms of solar wind type, fast/slow, and the solar activity level) when performing statistical analysis of velocity, density and magnetic field from heliospheric spacecraft.

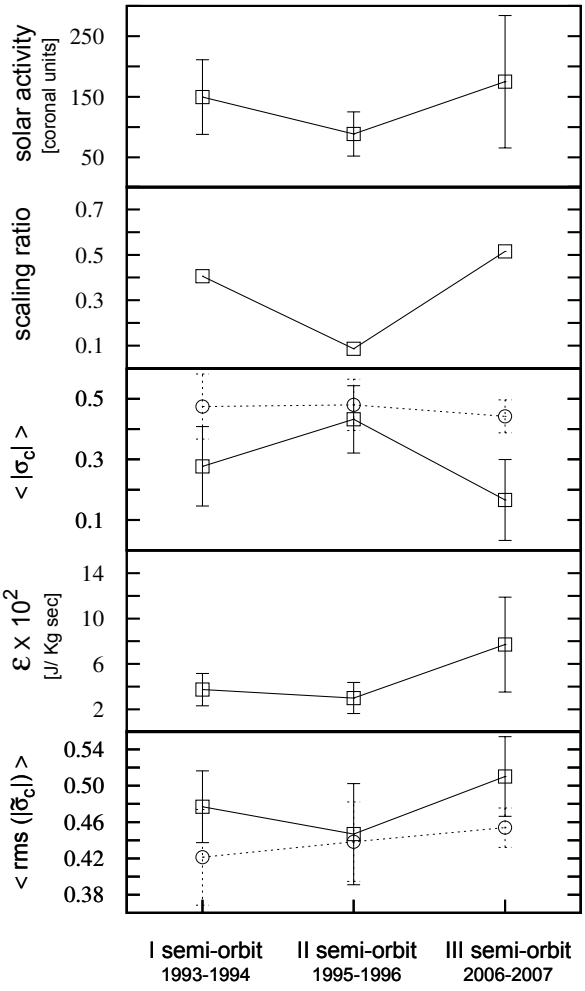

Figure 16: From top to bottom: average values of solar activity, fraction of 11 day intervals where the P&P linear scaling is observed (scaling ratio), mean cross-helicity, pseudo-energy transfer rate and rms local cross-helicity the three Ulysses' semi-orbits. For the cross-helicity panels, full lines represent values for 11-day samples exhibiting P&P scaling, while dotted lines refer to regions without scaling. Figure adapted from Marino et al. (2012).

4.2.3. Role of shears in triggering the turbulent cascade in the fast polar wind

In order to further characterize the role of the large-scale fields shears in the MHD turbulent cascade, Marino et al. (2012) examined the evolution and the features of the probability distribution functions (PDFs) of solar wind density, velocity and magnetic field components, at different scales $\tau \equiv \Delta t$, yet discriminating between plasma samples with and without the P&P scaling. The PDFs of the scale-dependent fluctuations of velocity (top panels), magnetic (central panels) and density (bottom panels) are shown in Figure 17. Left panels refer to increments at small-scale (8 minutes), central panels at medium-large scale (10 hours), and right panels at large scale (1 day). As already done previously, conditional statistics were computed to separate intervals with and without P&P scaling. In each panel, solid lines indicate PDFs computed over all the intervals with P&P linear scaling, while dashed lines are the PDFs referring to periods where no scaling was observed. In order to explore the role of large-scale shears the authors focused on the PDFs of the large-scale field increments. As highlighted by the high, non-Gaussian tails of the distributions of the radial velocity component (top-right panel of Figure 17), in the intervals with linear scaling velocity shears are present (solid line). In other words, the observed non-Gaussian behavior, thus the presence of large-scale shears, is more likely detected in those region of the outer heliosphere where also MHD turbulent cascades develop. This is clearly not the case for the intervals with no scaling (dashed line). Though unrelated to the plasma case, it is worth to mention that large-scale intermittency is observed also in fluid systems whose phenomenological framework is similar to that of incompressible MHD. This is the case of stratified geophysical flows, in which (as reported in Sec. 3.2) due to the interplay of gravity waves and turbulent motions, temperature and vertical velocity may exhibit an intermittent behavior in the large scales, and this is associated to enhanced turbulence and dissipation (Feraco et al., 2018, 2021; Marino et al., 2022). PDFs of the density are characterized by more symmetric tails yet highly leptokurtic for large-scale increments, when statistics are computed over the solar wind samples with P&P scaling, as shown in the middle panel of Figure 17. On the contrary, the statistics of the radial magnetic field component is unaffected by the presence or not of the P&P law. The conclusions drawn in Marino et al. (2012) are that the P&P law is observed essentially when large scale velocity and density shears are present in the flow, and that these may act as a driver for the MHD turbulent cascade, representing a

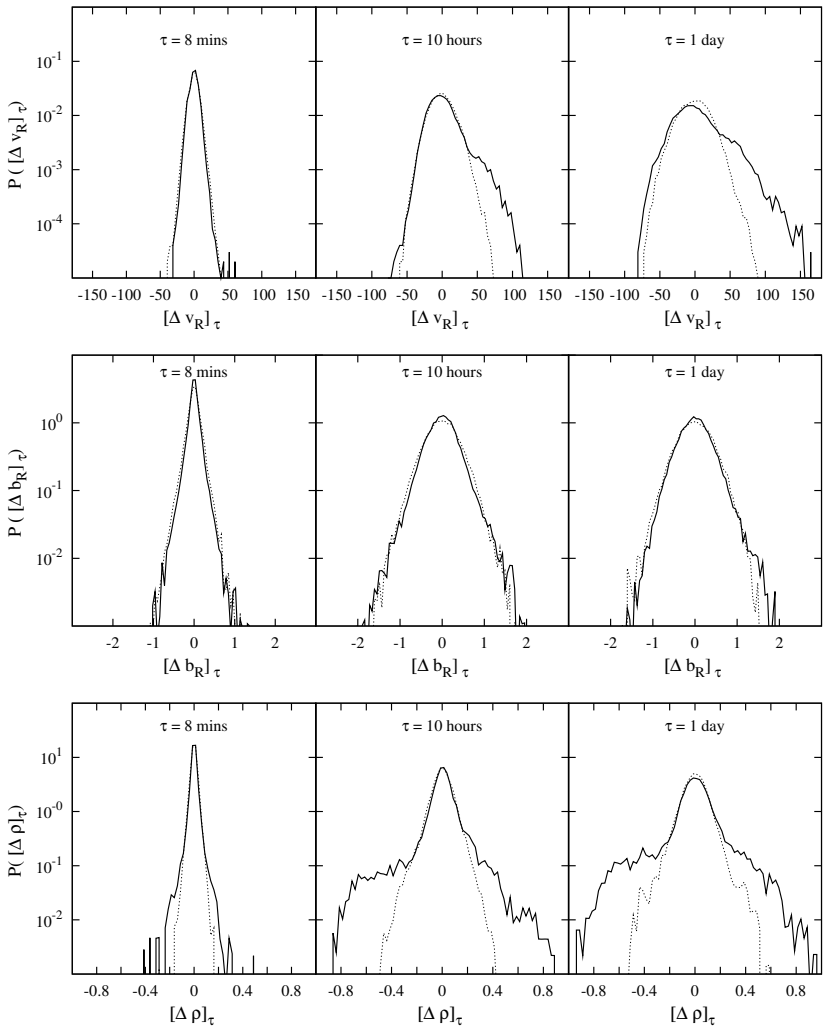

Figure 17: Probability distribution functions of field fluctuations for solar wind radial velocity (top), radial magnetic field (center), and density (bottom), at different time lags. PDFs are computed separately for set 1 (P&P scaling: full line) and for set 2 (absence of P&P scaling, dotted line). Figure adapted from Marino et al. (2012).

local energy source, as originally proposed by Coleman using Mariner 2 data (Coleman, 1968) and later supported by numerical results (Roberts et al., 1992).

4.3. Heating the solar wind by magnetohydrodynamic turbulence

Early observations of solar wind plasma measurements revealed that the expanding profile of proton temperature (as well as of electrons and α particles temperature) are not described by the expected decay for an adiabatic radial expansion, $T(r) = T_0(r/r_0)^{-4/3}$ (Hundhausen, 1972; Marsch et al., 1983; Richardson et al., 1995; Richardson and Smith, 2003), where r is the distance from the satellite to the Sun, and T_0 is the temperature at a reference distance r_0, typically taken near the solar corona. Spacecraft measurements have indeed shown that the radial decay of T was rather characterized by a decrease $T(r) \sim T_0(r_0/r)^{\xi}$ in the ecliptic plane, with fitted exponents $\xi \in [0.7 \div 1]$, thus considerably smaller than for the adiabatic case, 4/3 (Schwenn, 1983; Freeman et al., 1992; Goldstein et al., 1996). This is clearly visible for example in the top panel of Figure 18, where the radial proton temperature profile measured by the Voyager 2 spacecraft in the outer heliosphere is shown together with the adiabatic prediction (Smith et al., 2006). Moreover, the weakly collisional solar wind is filled with non-thermal, energized particles. For example, proton and electron beams, high tails, or temperature anisotropy are frequently observed in the particle velocity distribution functions, as shown for example in the bottom panels of Figure 18 (Marsch et al., 1982; Tang et al., 2019; Louarn et al., 2021). Particles are thus accelerated to non-thermal speeds and the plasma is pushed far from thermodynamic equilibrium by mechanisms that are not completely understood yet. In particular, such robust experimental evidences imply the existence of processes that provide energy necessary to heat the plasma and to accelerate particles while the solar wind expands. Several processes have been invoked to explain such heating, which include the interaction with pick-up ions from the interstellar medium (Isenberg, 1986; Fahr, 2002; Smith et al., 2006; Zank et al., 2018), wave damping and resonance mechanisms (Hollweg, 1973; Ofman, 2010; Perez et al., 2021b; Chen et al., 2019; Squire et al., 2020) and various forms of turbulent dissipation (Verma et al., 1995; Matthaeus et al., 1999; Vasquez et al., 2007; Hansteen and Velli, 2012; Sorriso-Valvo et al., 2019a; Carbone et al., 2022). The above mechanisms might all be contributing to solar wind heating and energization, though, in more recent years, it emerged that the energy release occurring at the end of a turbulent MHD cascade in the heliospheric plasma (Frisch, 1995; Dobrowolny et al., 1980) is one of the possible sources that support the heating of the expanding solar wind (Marino et al., 2008; Stawarz et al., 2009; Matthaeus and Velli, 2011). This possibility was explored for example in Verma et al. (1995);

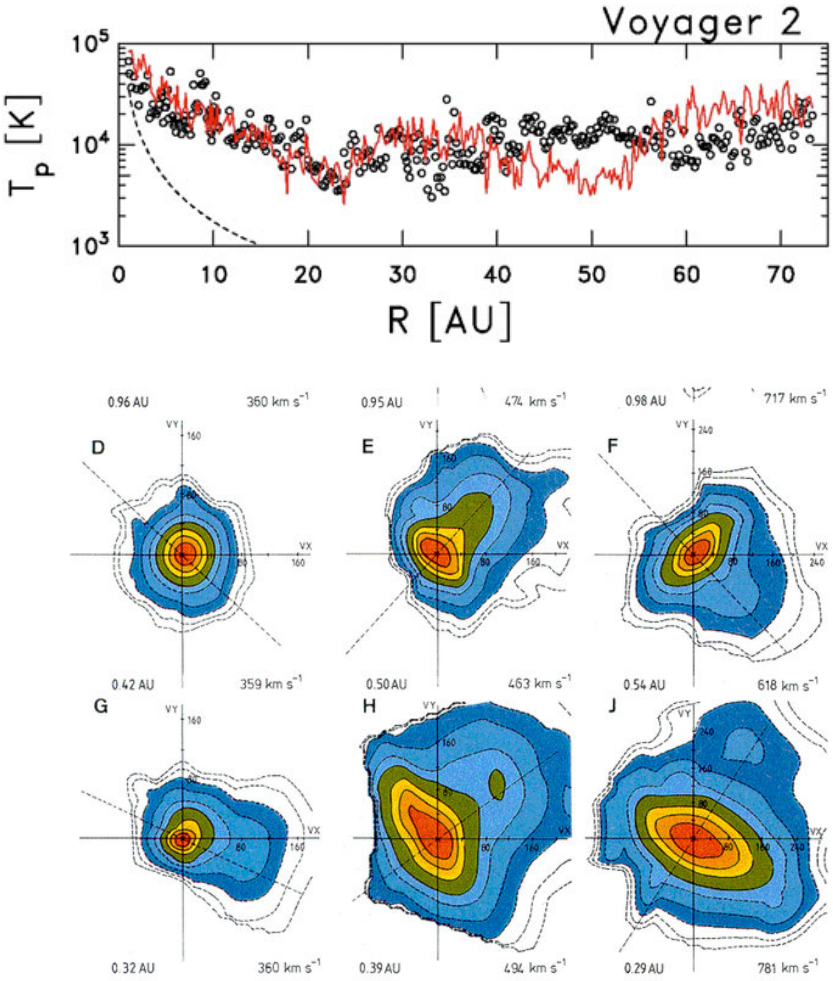

Figure 18: Top panel: radial proton temperature profile measured by Voyager 2 (black symbols) and predicted by a turbulent energy transport model (Matthaeus et al., 1999, red line), compared to predicted adiabatic profile (black dashed line). Figure from Smith and Vasquez (2021) (adapted from Smith et al., 2006). Bottom panel: two-dimensional equatorial plane cuts of solar wind proton velocity distribution functions as measured by the Helios spacecraft. Isocontours are normalized to the maximum of the distribution. Thee dashed line indicates the magnetic field projection. Non-Maxwellian features are evident in most cases. Figure adapted from Marsch et al. (1982).

Vasquez et al. (2007), where models aimed at explaining the observed proton temperature decay have been developed, assuming turbulence as the main mechanism involved in the heating of the plasma. The validation of the P&P law made it thus possible to compare direct estimates of the MHD turbulent energy transfer rate in solar wind with the heating obtained from solar wind heating rate models, necessary to reproduce the radial decrease of the proton temperature. To this aim, Marino et al. (2008) used estimates of the pseudo-energy flux rates, $\varepsilon^{\pm}$, in the fast polar wind measured by Ulysses during first six months of 1996. Results show that, at those distances from the Sun, the transfer rate is typically of the order of 10^2 J (kg s)$^{-1}$. Values for the intervals used in this study are listed in Table 3, and are shown in Figure 19 (bottom-left panel) as a function of the heliocentric distance, r.

r	V_{SW}	T_1	T_2	ε_1	ε_2	$\lvert\varepsilon^{\pm}\rvert$	$\lvert\varepsilon^{\pm}\rvert/\varepsilon_1$	$\lvert\varepsilon^{\pm}\rvert/\varepsilon_2$
3.22	765 ± 20	163 ± 18	90 ± 15	2696 ± 301	414 ± 68	436 ± 32	0.16	1.05
3.23	770 ± 19	164 ± 19	90 ± 15	2715 ± 314	412 ± 69	176 ± 13	0.07	0.43
3.42	764 ± 16	148 ± 20	81 ± 14	2308 ± 308	349 ± 62	174 ± 24	0.08	0.50
3.49	736 ± 18	136 ± 17	73 ± 12	2005 ± 256	298 ± 51	115 ± 19	0.06	0.39
3.49	734 ± 17	135 ± 17	73 ± 13	1983 ± 262	294 ± 53	113 ± 12	0.06	0.38
3.52	746 ± 24	145 ± 21	80 ± 16	2149 ± 320	326 ± 66	154 ± 32	0.07	0.47
3.56	769 ± 21	153 ± 19	82 ± 14	2304 ± 292	340 ± 60	185 ± 25	0.08	0.54
3.67	749 ± 20	147 ± 19	79 ± 15	2091 ± 271	309 ± 61	194 ± 22	0.09	0.63
3.83	760 ± 22	148 ± 27	81 ± 19	2044 ± 381	308 ± 75	218 ± 28	0.11	0.71
4.04	732 ± 25	146 ± 20	70 ± 18	1841 ± 259	245 ± 44	66 ± 24	0.04	0.27
4.06	743 ± 20	159 ± 18	82 ± 16	2031 ± 234	290 ± 58	216 ± 25	0.11	0.75

Table 3: Measured turbulent energy transfer rates $\varepsilon^{\pm}$ (in J kg^{-1} s^{-1}) at different distances from the sun r (au), along with the expected heating rates $\varepsilon_{1,2}$ (same units) as computed using the parameters V_{SW} (km s^{-1}), $\xi_{1,2}$, and the two temperature estimates T_1 and T_2 measured by the Ulysses spacecraft (in 10^3 K). All wind parameters were computed as mean over 11 days windows, along with their standard deviations. In the case of the distance r, the variation within each 11 days window is roughly 0.05 au. The heating rates $\varepsilon_{1,2}$ are estimated from the parameters in equation (64), using the two different values of the temperature. The first column indicates the initial time t_0 of the 11 days window in the time series (in day of the year 1996).

Each measured value of $\varepsilon^{\pm}$ was used in Marino et al. (2008) as a surrogate for the energy flux, ε. As mentioned, Verma et al. (1995) retrieved a relation for the evolution of the proton temperature with the heliocentric distance, including the corrections necessary to account for the turbulent heating that occur at the bottom of the MHD cascade. Assuming the observed power-law proton temperature decrease, $T \sim T_0(r_0/r)^{\xi}$, a model for the radial evolution

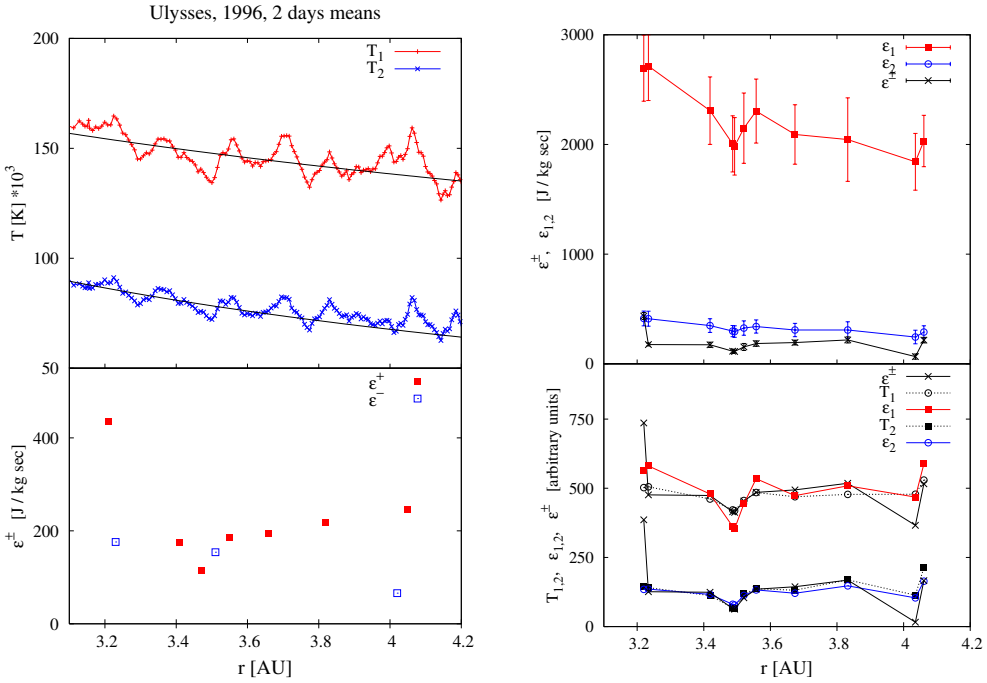

Figure 19: Top-left panel: radial decrease of the solar wind temperature provided by Ulysess (2 days averages), T_1 and T_2 are known to overestimate and underestimate the actual temperature of the plasma, respectively. Superimposed are the power law fits $T(r) \propto r^{-\xi}$, with $\xi_1 = 0.49 \pm 0.06$ and $\xi_2 = 1.10 \pm 0.08$. Bottom-left panel: values of the turbulent pseudo-energy transfer rates, $\varepsilon^{\pm}$, as obtained from the fit of the P&P scaling law (54), in $\mathrm{J\,kg^{-1}\,s^{-1}}$. $\varepsilon_{1,2} \equiv \varepsilon_{heat}$ are instead the heating rates obtained through the model equation (64) using the two temperature estimates $T_{1,2}$. Top-right panel: the values of $\varepsilon^{\pm}$ and $\varepsilon_{1,2}$. Bottom-right panel: comparison of the behaviour of the measured $\varepsilon^{\pm}$ with the estimated $\varepsilon_{1,2}$, after removing the $r^{-1-\xi}$ trend and adding an arbitrary offset. The same is done for the temperature $T_{1,2}$, where the $r^{-\xi}$ trend has been removed and arbitrary rescaling and offset have been applied. Units are arbitrary and offsets have been added to separate the two plots, to better show the high correlation between the signals. Figure adapted from Marino et al. (2008).

of the heating rate $\varepsilon_{heat}(r)$ necessary to obtain the observed radial proton temperature profile can be obtained (Verma et al., 1995; Vasquez et al., 2007):

$$\varepsilon_{heat}(r) = \frac{3}{2}\left(\frac{4}{3} - \xi\right)\frac{V_{SW}(r)\, k_B\, T(r)}{r\, m_p}\ , \tag{64}$$

where $V_{SW}(r)$ is the radial profile of the bulk solar wind speed, k_B is the

Boltzmann constant and m_p the proton mass. The above model is obtained considering a polytropic index $\gamma = 5/3$ for the solar wind adiabatic expansion, and assumes protons as the only particles heated in the process. It should be kept in mind that the latter is a severe approximation, since electrons are also expected to play a major role in the heat exchange.

The Ulysses database provides two different estimates for the temperature, T_1 and T_2, known to overestimate and underestimate the true temperature, respectively. From these data, Marino et al. (2008) used Equation (64) and averaged speed, temperature and distance to estimate the heating rate in the same 11-day intervals where the energy cascade was identified through the P&P law (see Table 3). The scaling exponents of the temperature profiles, ξ, were then evaluated through power-law fits of the data, from 1995 April 10 to 1996 August 10. Figure 19 (top left panel) shows the proton radial temperature profile for both T_1 and T_2 and the relative fits, the measured exponents being $\xi_1 = 0.49 \pm 0.06$ and $\xi_2 = 1.10 \pm 0.08$ respectively. The values of ε_1 and ε_2 are estimates of ε_{heat} obtained from the model (64) using $T_{1,2}$, and are plotted in Figure 19, and again reported in Table 3, together with the associated turbulent transfer rates estimated from fits of the P&P law, equation (54). Comparing the heating rate with the energy transfer rate shows that the MHD turbulent cascade contributes to the *in situ* solar wind heating from 8 % (T_1) to 50 % (T_2) on average, and up to 100 % in some of the intervals. This evidence indicates that turbulent energy flux might indeed be responsible for a significant amount of the expected heating. The bottom panel of the same figure shows again normalized profiles of the observed turbulent energy transfer rate, along with temperature and estimated heating obtained for the same locations. The variations in these signals show clear correlations. It is precisely the correlation between solar wind temperature and estimated energy transfer that permits to speculate on the leading role of the MHD turbulent cascade in the heating of the solar wind (Marino et al., 2008). Though the causation between these phenomena still needs to be proven, the indication that turbulent heating is present in the solar wind, and well correlated with the wind temperature, is a result of major importance.

4.4. Incompressible exact law in the ecliptic solar wind

The pioneering contribution by MacBride et al. (2005) was based on the assessment of the P&P law in the ecliptic solar wind performing averages over several years of data, thus mixing both fast and slow wind, as well as periods

with variable (high and low) solar activity. The work by Sorriso-Valvo et al. (2007) and Marino et al. (2008) emphasized instead the local character of the MHD turbulent cascade in the out-of-ecliptic heliospheric plasma, showing that the occurrence of the P&P linear scaling and the strength of the pseudo-energy transfer rate are modulated by the solar activity. In order to shed light on the possibility that the MHD turbulent cascade may indeed have significantly different features in fast and slow solar wind streams at low latitudes, Marino et al. (2011) implemented a local analysis of the P&P law using 11-day intervals of ecliptic solar wind measured by the Ulysses spacecraft from day 220 of 1996 for about 6 months. Figure 20 shows the P&P

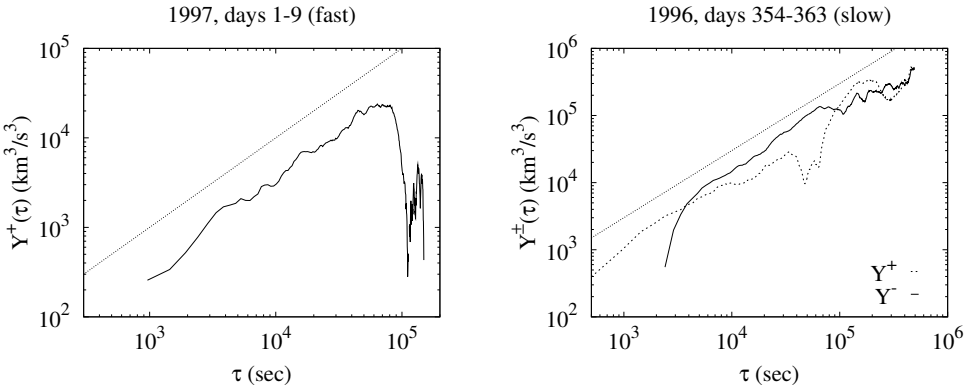

Figure 20: Mixed third order pseudo-energy flux $Y^+(\tau)$ in fast (left) and $Y^{\pm}(\tau)$ slow (right) streams of the ecliptic wind, as computed from the Ulysses data. The values of the pseudo-energies are $\varepsilon_f^+ = 403\,\mathrm{J\,kg^{-1}\,s^{-1}}$, $\varepsilon_s^+ = 1702 \pm 45\,\mathrm{J\,kg^{-1}\,s^{-1}}$, $\varepsilon_s^- = 2591 \pm 120\,\mathrm{J\,kg^{-1}\,s^{-1}}$. In the slow wind case, it is also possible to estimate the total energy $\varepsilon_{tot}^{(s)} = 2147 \pm 83\,\mathrm{J\,kg^{-1}\,s^{-1}}$. Figure adapted from Marino et al. (2011).

scaling emerging in fast and slow ecliptic solar wind streams. The left panel shows the mixed third order moment computed from a fast solar wind stream measured at heliolatitude $\sim 18°$ and heliocentric distance ~ 4.7 au. The right panel shows the simultaneous Y^+ and Y^- P&P scaling in a slow solar wind ecliptic stream, at heliolatitude $\sim 19°$ and heliocentric distance ~ 4.7 au. The top panel of Figure 21 indicates instead the times of the intervals in the alternating fast and slow ecliptic solar wind streams where a clear P&P scaling was found. The corresponding values of the pseudo-energy transfer rates are plotted in the bottom panel of the same figure. It is possible to appreciate a clear difference between fast and slow wind. The pseudo-energy

transfers relative to the fast wind streams (cyan and magenta markers) are of the order of $\varepsilon_f^{\pm} \simeq 100$ J (kg s)$^{-1}$, comparable with the estimates in the fast polar wind obtained in Sorriso-Valvo et al. (2007); Marino et al. (2008). The slow solar wind streams (blue and red markers) show larger values, $\varepsilon_s^{\pm} \simeq 1000$ J (kg s)$^{-1}$, with a clear separation between the populations corresponding to fast and slow solar wind streams, appearing in Figure 21 as distinct groups of points, separated by the dashed line. It is worth pointing out that, in general, in the fast streams only one type of tensor (either Y^+ or Y^-) is observed to satisfy the P&P law, at any given location. On the other hand, in the slow streams the two tensors show simultaneous scaling, allowing for estimates of the total energy, $\varepsilon_{tot} \sim (\varepsilon^+ + \varepsilon^-)/2$ (black asterisks). This difference suggests that enhanced Alfvénic correlations (characteristic of the fast solar wind) may inhibit the onset of the turbulent cascade of one of the Elsasser ($z^{\pm}$) modes in the fast ecliptic wind. In slow streams, the scaling samples are found in correspondence with the fast-slow stream interfaces (figure 21), suggesting that the MHD turbulent cascade detected through the P&P law could be triggered by local energy injection due to the shears of velocity and magnetic field, characterizing the interface regions, analogously to what was found in the out-of-ecliptic fast solar wind (Marino et al., 2012), as reported in section 4.2.1. The results presented in Marino et al. (2011) suggest that while the fast streams in the ecliptic have properties similar to those of the fast polar wind, slow streams are instead characterized by a much higher energy transfer, further supporting the need to separate the analysis of the two types of wind.

4.5. Observation of anisotropic scaling in the ecliptic solar wind

Zhou and Matthaeus (1990) first, then Zank et al. (1996) and Matthaeus et al. (1999) developed a turbulent transport model able to provide the right amount of energy to account for the observed solar wind heating, assuming dissipation would occur at a rate such to equal the turbulent energy cascade rate. The model is based on the assumption that fluctuation vectors and wavevectors are confined in 2D planes perpendicular to the background magnetic field, with the heliospheric plasma developing a forward cascade towards the scales where dissipation is accomplished. The outcome of the observations of Matthaeus et al. (1990) and subsequent analyses by Bieber et al. (1996) emphasized as well that large-scale 2D energy containing fluctuations are indeed embedded in the solar wind. That motivated investigations based on a modified implementation of the third-order exact law approach,

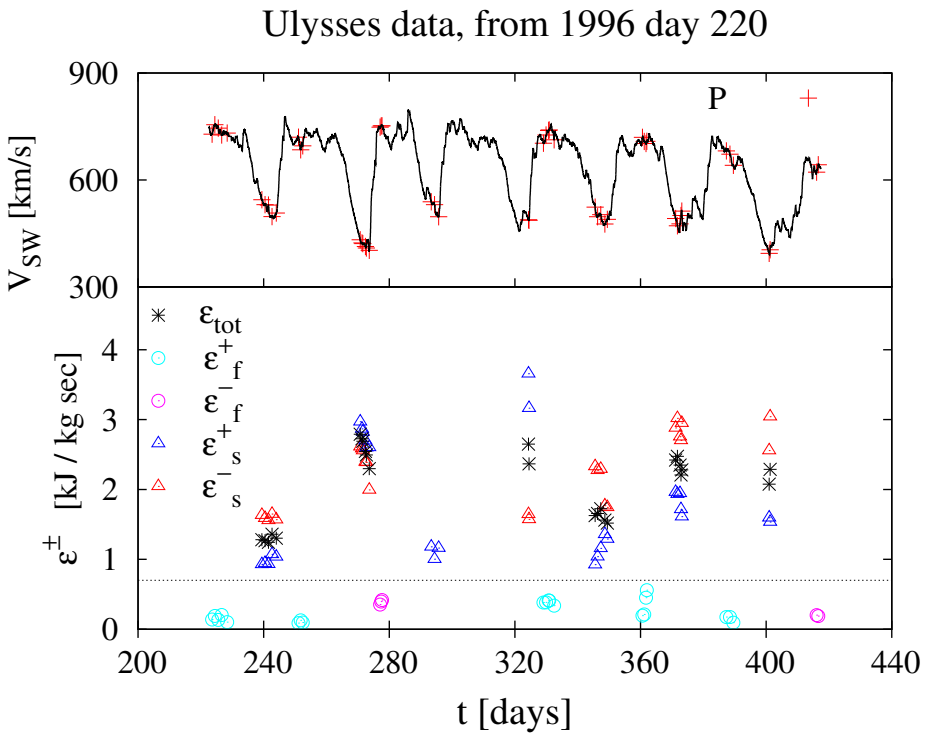

Figure 21: Top panel: starting points of the 11 days windows where the P&P scaling was observed (crosses), indicated on top of the solar wind bulk speed, V_{SW} (solid line). Bottom panel: estimated pseudo-energy transfer rates $\varepsilon^{\pm}$ in the ecliptic wind measured by Ulysses starting from day 220 of 1996 (in J (kg s)$^{-1}$), for fast (circles) and slow (triangles) wind. The values of the total energy, $\varepsilon_{tot} \sim (\varepsilon^+ + \varepsilon^-)/2$, are as well shown (stars) whenever both pseudo-energy fluxes ($\varepsilon^{\pm}$) are available. Figure adapted from Marino et al. (2011).

taking into account the possibility that the turbulent energy transfer in the solar wind could be strongly anisotropic. This scenario has been explored by several authors, through the analysis of a variety of spacecraft observations. MacBride et al. (2008) tested a slightly modified version of the P&P law, obtained after rotating magnetic field and velocity fluctuations into the mean field coordinates, where the z-direction is taken along the mean magnetic

field:

$$ {}^{2D}D_3^{\pm} = \langle \Delta z_y^{\mp} \left| \Delta z_i^{\pm} \right|^2 \rangle = 2\varepsilon^{\pm} \langle v_R \rangle_t \tau \sin\theta_{BR} \tag{65} $$

$$ {}^{1D}D_3^{\pm} = \langle \Delta z_z^{\mp} \left| \Delta z_i^{\pm} \right|^2 \rangle = 2\varepsilon^{\pm} \langle v_R \rangle_t \tau \cos\theta_{BR} \,. \tag{66} $$

Equation (65) is used when the third-order moment vector field, here indicated by $\mathbf{D_3^{\pm}}(\boldsymbol{\ell})$, is perpendicular to the mean magnetic field (or varies only with the component of $\boldsymbol{\ell}$ that is perpendicular to the mean field, and has cylindrical symmetry), $\langle v_R \rangle_t$ being the mean solar wind speed, $\Delta z_y^{\mp}$ the Elsasser fluctuation measured along the direction $\hat{\mathbf{e}}_{\mathbf{y}}$, and θ_{BR} the angle between the mean field direction and the flow velocity (approximately radial). This formalism is considered by the authors analogous to the 2.5-dimensional MHD geometry, in which magnetic and velocity fluctuations have all the three components, and the wavevectors are confined to the 2D plane perpendicular to the mean magnetic field (Montgomery and Turner, 1982). Equation (66) is instead obtained if the $\mathbf{D_3^{\pm}}(\boldsymbol{\ell})$ is parallel to the mean magnetic field (or varies only with the component of $\boldsymbol{\ell}$ that is parallel to the mean field). MacBride et al. (2008) used ACE data (McComas et al., 1998a; Smith et al., 1998) collected from 1998 to 2004 at the Lagrangian point L1 in the ecliptic solar wind to test the P&P law, equation (54), here called ${}^{ISO}D_3^{\pm} = \langle \Delta z_{\ell}^{\mp} \left| \Delta z_i^{\pm} \right|^2 \rangle = \frac{4}{3}\varepsilon^{\pm} \langle v_R \rangle_t \tau$, and its analogues above, equations (66) and (65). Each 28-day solar rotation was divided into 14 sub-intervals of 2 days from which third-order moments of the Elsasser variables were computed and ensemble-averaged. In Figure 22, the plot of ${}^{ISO}D_3^{\pm}$ shows estimates of the classical P&P third-order tensor. The same figure shows the energy transfer rate per unit mass for outward-propagating (blue lines) and inward-propagating (red lines) fluctuations, as well as their mean, giving the total energy transfer rate (solid black lines). The outward-traveling fluctuations display higher cascade rate to small scales than the inward-traveling fluctuations. The structure function analysis for an isotropic geometry yields a heating rate of 6.5 kJ (kg s)$^{-1}$, with the sample including both fast and slow solar wind streams. Figure 22 shows also the plot of ${}^{2D}D_3^{\pm}$, where ${}^{2D}D_3^{\pm}/\tau$ is the energy transfer rate associated with the cascade perpendicular to the mean field direction. Even in this case, the outward-propagating fluctuations (blue lines) produce higher energy transfer rate than the inward-propagating fluctuations (red lines). The solid black lines indicates again the total energy transfer rate, 5.6 kJ (kg s)$^{-1}$. The third pair of panels from the top in Figure 22 show the plot of ${}^{1D}D_3^{\pm}$, together with the rate of the energy cascade along

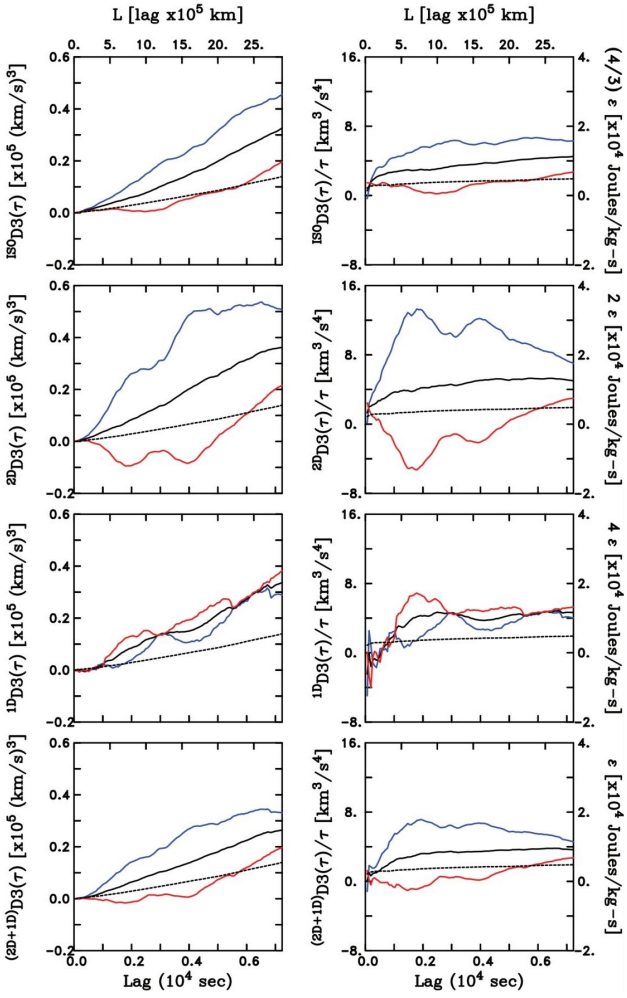

Figure 22: Left panels, from top to bottom: third-order mixed structure function as a function of the scale, for the isotropic ($^{ISO}D3$, corresponding to the P&P law, equation 54), 2D ($^{2D}D3$, equation 65), 1D ($^{1D}D3$, equation 66), and 2D+1D composite geometry ($^{2D+1D}D3$) models. Blue, red and black curves refer to the outward, inward and total third-order moment, respectively. The spatial lag scale, in units of km, visible on the top x-axis, is $L = \langle v_R \rangle_t \tau$, τ being the time lag, reported on the bottom x-axis. The right panels show the same quantity normalized to the time scale, and the corresponding energy transfer rate, ε (right vertical axes). Figure adapted from MacBride et al. (2008).

the mean field direction $^{1D}D_3^{\pm}/\tau$ (dashed lines). Finally, an additional third-order structure function for the composite $2D + 1D$ geometry is computed and displayed in the bottom row of Figure 22, $^{2D+1D}D_3^{\pm}$, together with the

corresponding energy transfer rate per unit of mass, ${}^{2D}D_3^{\pm}/\tau$ (dashed lines). The heating rate for this composite geometry is 7.9 kJ (kg s)$^{-1}$, interestingly very close (within one standard deviation) to the isotropic calculation performed using the original P&P law (${}^{ISO}D_3^{\pm}$).

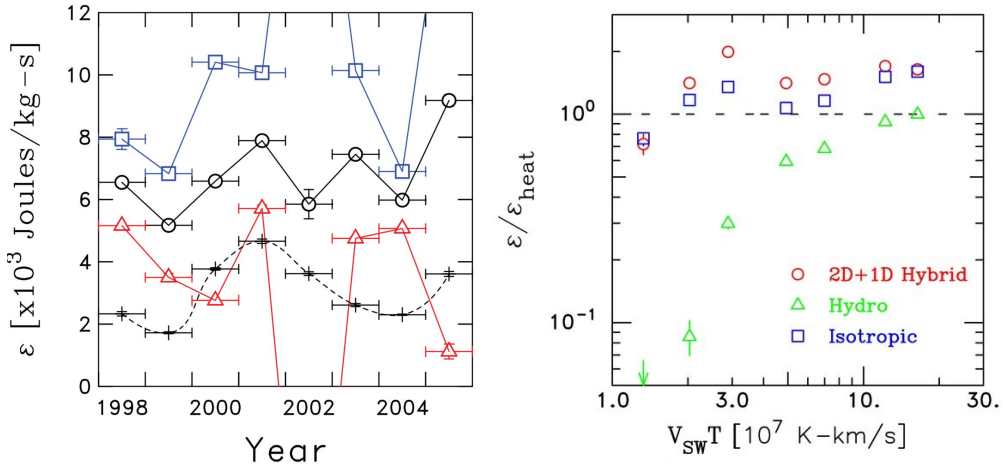

Figure 23: Left panel: Yearly average of the dissipation rates estimated from ACE data using the isotropic and anisotropic relations as in MacBride et al. (2008) (same color code as in Figure 22). Figure adapted from MacBride et al. (2008). Right panel: ratio of energy transfer rate, measured through different structure functions formulations method for MHD (see legend), to the heating rate ε_{heat}, estimated using the Vasquez et al. (2007) analysis of thermal protons, versus the product $V_{SW}T$. Figure adapted from Stawarz et al. (2009).

Using a similar analysis of the ACE database, extended to 2008 in order to encompass both solar maximum and minimum, Stawarz et al. (2009) computed the energy transfer rate, estimated in 12-hour subsets, through both the isotropic (${}^{ISO}D_3^{\pm}$) and hybrid (${}^{2D+1D}D_3^{\pm}$) third-order structure functions. Yearly averages, shown in the left panel of Figure 23, reveal again the dominance of the outward propagating mode, and a marked variability with the solar cycle. The energy transfer rate was then compared with the Vasquez et al. (2007) model for solar wind heating rate (see equation 64), extending to the ecliptic wind the analysis previously performed in polar wind (Marino et al., 2008). Yearly averages, shown by crosses and dahsed line in the left panel of Figure 23, are systematically smaller than the total energy transfer rate, confirming previous results (MacBride et al., 2008). The ratio between the total energy transfer and the heating rates is then shown in the right

panel of Figure 23. In this representation, both values were averaged in bins of similar values of the product $V_{SW}T$, which was shown to be a good ordering parameter for the energy transfer rate. The estimated MHD energy cascade rate is again clearly systematically greater than ε_{heat}, except for the samples with smaller values of $V_{SW}T$, disregarding of the formulation of the third-order structure function used (the isotropic and anisotropic versions give comparable values). This behaviour is opposite to what observed in polar wind using the isotropic formulation (Marino et al., 2008). However, the order of magnitude of the energy transfer rate is comparable in the two studies. A purely hydrodynamic version (green markers), computed for comparison, gives insufficient energy for heating the solar wind, probably since it completely neglects the magnetic contribution to the energy transfer. These results clearly indicate that turbulence transfers more energy to small scales than required to account for the observed proton heating. This would leave energy available for heating electrons and for other forms of particle energization that are not accounted for in the model. For example, it was claimed by several authors that the observed non-adiabatic radial decay of the electron temperature requires between 20% and 40% of the total plasma heating (Leamon et al., 1999; Breech et al., 2009; Cranmer et al., 2009). Quantitatively evaluating other forms of energization is more complicated and not yet determined (see for instance the attempts to determine the processes responsible for particle energization described in Howes et al., 2022).

4.6. Role of cross-helicity in the ecliptic solar wind

Analyzing the same ACE database used in Stawarz et al. (2009), again partitioned in 12 hours intervals, Smith et al. (2009) and Stawarz et al. (2010) performed further statistics of the pseudo-energy transfer rate obtained through the P&P law and combinations of equations 66 and 65, following the approach described in the previous section. In particular, time-averaged values of $\varepsilon^{\pm}$ have been conditioned to the normalized cross-helicity, σ_c, and to the solar activity level. In this analysis, Δz^- (Δz^+) corresponds to fluctuations propagating parallel (anti-parallel) to the mean solar-wind magnetic field, which can be directed sunward (in) or anti-sunward (out), and ${}^{ISO}D_3^{\pm}$ (as well as ${}^{1D}D_3^{\pm}$ and ${}^{2D}D_3^{\pm}$) were collected so as to average D_3^{out} and D_3^{in} according to the direction propagation of the fluctuations relative to the Sun. The left panel of Figure 24 shows that as $|\sigma_c|$ increases all the cascade rates estimates reported in the plot decrease as well (Smith et al., 2009). The pseudo-energy cascade rate for the outward-propagating compo-

nent, D_3^{out}, becomes negative for large $|\sigma_c|$. This would correspond to a back transfer of energy from small to large scales. The pseudo-energy transfer rate in the MHD cascade estimated for the inward-propagating component, D_3^{in}, does not seem to turn negative, though this analysis shows it becomes smaller for increasing values of $|\sigma_c|$. The total pseudo-energy cascade rate, $D_3^{in}+D_3^{in}/2$, becomes instead negative for $|\sigma_c| > 0.75$ (Coburn et al., 2012). The evidence of negative values of the fluxes in the ecliptic solar wind, as well ass the negative values of $\varepsilon^{\pm}$ previously estimated in the fast polar wind (Sorriso-Valvo et al., 2007; Marino et al., 2008), suggests that an inverse cascade might be developing in some cases within the solar wind plasma. Following on Smith et al. (2009), negative fluxes are associated to high cross-helicity states in the ecliptic solar wind. On the other hand, no studies other than those based on the P&P law have so far confirmed unambiguously this possibility. In general, high values of the cross-helicity would lead to a depletion of the non-linear interactions in MHD turbulent plasmas (see Sec. 2.2), which makes the correlation of this quantity with the energy flux physically meaningful.

The right panel of Figure 24 shows the number of sunspots (top) together with values of the energy transfer rate averaged for each each year of the ACE database from 1998 to 2009 (bottom) (Coburn et al., 2012). This analysis seems to indicate that the turbulent energy transfer rate at 1 au during the solar minimum is comparable with (or exceeds) the average cascade during the solar maximum. The authors speculate that this trend might be due to the admixture of solar wind streams, thus high-latitude winds together with the wind originating at low heliolatitude. In other words, it is argued that the greater turbulence level associated with solar minimum might be simply a selection effect resulting from sampling ecliptic wind as well as the wind coming from high-latitude sources (Coburn et al., 2012). However, as is shown in Section 4.2.1, in purely high-latitude, fast, polar wind a clear modulation of both the intensity and occurrence of the MHD turbulent cascade with the solar activity was actually detected Marino et al. (2012). In that case, lower solar activity was associated with weaker energy cascade rates. The discrepancy between those observations is likely due to the different nature of polar and ecliptic wind.

Given the variety of solar wind conditions and dataset considered in the analyses presented in this section, as well the hypotheses and caveats of the various implemented approaches, one aspect clearly emerges from the pioneering investigations based on the original P&P law: the systematic as-

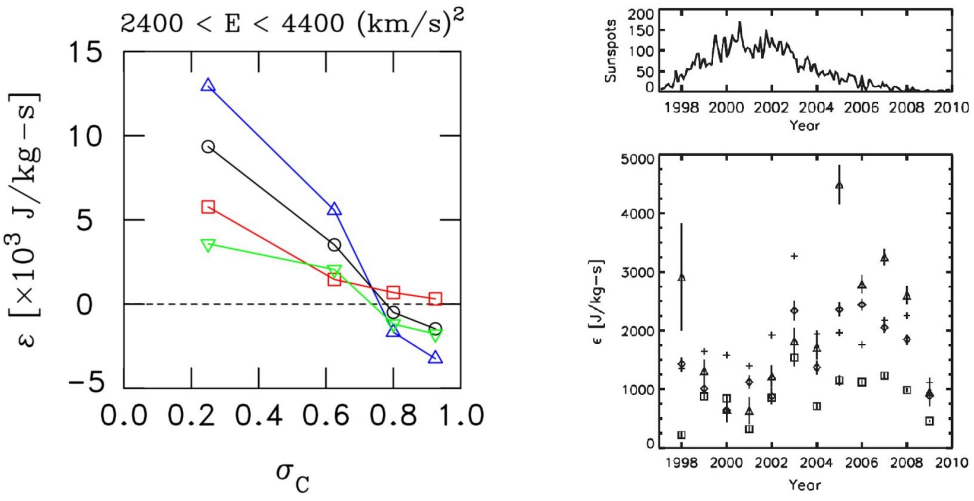

Figure 24: Left panel: average cascade rates, ε, estimated from third-moment analysis versus the absolute value of the normalized cross-helicity, σ_C: for outward propagation (blue triangles), inward propagation (red squares), and total energy T (black circles). Figure adapted from Smith et al. (2009). Right panel: the top sub-panel shows the monthly sunspot number as a function of time. The bottom sub-panel displays the yearly average energy cascade rate estimated through the third-order moment analysis as a function of time, throughout the ACE database. Diamonds refer to the MHD formalism for the isotropic law, triangles to the hybrid geometry (both defined in the text), squares to the Navier-Stokes formalism (the exact law for classical hydrodynamics). "+" symbols refer to estimates obtained through the heating model by Vasquez et al. (2007). Figure adapted from Coburn et al. (2012).

sessment of the third-order moment offers a great number of opportunities to gain insights on fundamental aspects of the energy transfer in space plasmas. On the other hand, these studies suggested caution when high-order statistics are built over extended samples of solar wind, since coronal origin and turbulent state of the plasma may significantly vary over time.

5. Generalized scaling laws in space plasmas

The multiple hypotheses behind the P&P law were thoroughly described in previous sections, including the assessment of their validity in the solar wind. As a matter of fact, in real physical systems some of these hypotheses may not be verified to a sufficient degree for all the simplification performed in obtaining the P&P law to be applicable, preventing also its validation in data from observations. In this section, various cases are reviewed for which

it was possible to relax one or more of the hypotheses proposed in the original P&P law derivation (Politano and Pouquet, 1998; Politano and Pouquet, 1998), together with the related modifications to the mathematical developments and inclusions of extra terms in the third-order exact law. As we shall see, in some instances, as in the presence of strong magnetic fields, it is necessary to model the effects of the resulting anisotropy, in order to include them in the third-order scaling law. In other cases, such as in compressive and/or Hall MHD plasmas, the derivation has been performed retaining mathematical rigour, without resorting to models. As is often the case, some of the generalizations obtained for plasmas followed approaches previously developed for neutral fluids. However, the richer variety of modifications required for turbulent plasmas with respect to the case of neutral fluids reflects the greater complexity of the former, showing how the plasma community is strongly engaged in obtaining maximum results from the analyses performed through the third-order scaling laws. This is due to the fundamental importance of such laws in nearly-collisionless plasmas, for which they represent the only accessible mean to estimate turbulent energy dissipation, which is crucial to properly describe the dynamics of the space plasmas.

5.1. Modified cascade for anisotropic turbulence

As we have seen in the previous section, simple models based on the rotation of the structure functions in a field-aligned reference frame have allowed preliminary analysis of the anisotropic properties of the turbulence cascade. This is fundamental for solar wind turbulence, which is known to be anisotropic (Bieber et al., 1996). Successive studies have introduced more or less sophisticated models to account for anisotropy, at least under specific conditions of relevance for space plasmas. Here we will review some of those models, and their application to space plasmas.

5.1.1. Characterization of MHD anisotropy through the third-order structure functions

Estimating the turbulent cascade rate in the solar wind through the P&P law requires to make assumptions on the unknown anisotropy of the third order structure function. The initial approach in this direction for the analysis of in-situ spacecraft data was to assume isotropic turbulence, therefore using equation (54), which was mainly employed for fast polar wind on Ulysses measurements (Sorriso-Valvo et al., 2007; Marino et al., 2008; Marino et al., 2011; Marino et al., 2012). Alternatively, some form of axisymmetric anisotropy

was considered. As discussed in previous section, given the impossibility to compute derivatives along parallel and perpendicular directions with respect the solar wind flow, MacBride et al. (2008); Stawarz et al. (2009); Stawarz et al. (2010) resorted to simplified geometrical models of an hybrid $2D + 1D$ turbulence, as described by equations (66) and (65), implemented using Wind and ACE data collected in the ecliptic solar wind. This method assumes that the third-order structure function has parallel and perpendicular components depending only on parallel and perpendicular increments, respectively, and that the cascades in the two directions are independent from each other. The total energy transfer can then be investigated by combining the two independent equations for 1D-parallel and for 2D-perpendicular cascades, given by equations (66) and (65) respectively for ${}^{1D}D_3^{\pm}$ and ${}^{2D}D_3$, so that the cascade rate for the composite geometry, $\varepsilon_{hybrid} = {}^{1D}\ \varepsilon + {}^{2D}\ \varepsilon$, is given by the composite structure function ${}^{2D+1D}D_3^{\pm}$.

Obviously, a correct description of anisotropy effects can be obtained using numerical simulations, where all gradients can be computed. Verdini et al. (2015) investigated the process of bi-dimensionalization and the anisotropy of the turbulent energy transfer in plasmas through direct numerical simulations, by integrating the incompressible MHD equations on grids up to 1024^3 points. These authors computed for the first time the third-order structure functions in a fully 3D MHD plasmas, in the presence of large-scale forcing and mean magnetic field B_0. Among other things, they tested the anisotropic mixed third-order moments introduced in MacBride et al. (2008); Stawarz et al. (2009), exploring their range of validity for the investigation for the slow solar wind. In particular, estimates of the energy cascade rate obtained through equations (66) and (65) were compared with values of the cascade rate retrieved from the direct computation of the divergence of $Y = \langle \Delta z^{\mp} (\Delta z^{\pm})^2 \rangle$, which is possible in simulations given the availability of the point-wise velocity and magnetic fields. Starting from equation (26), without assuming isotropy, it is indeed possible to retrieve a relation between the divergence of the mixed tensor and what can be considered the true cascade rate of the energy transfer at intermediate scales: $\nabla \cdot Y = -4\varepsilon_{true}$. In Figure 25, ε_{true} is compared with ε_{hybrid} obtained from third-order structure function for the composite $2D + 1D$ geometry, normalized by a cascade rate ε obtained from the spectra. The comparison was performed for a weakly compressible MHD run (B), with an imposed mean magnetic field and anisotropic forcing (applied to components perpendicular to the mean field and to wavevectors mainly perpendicular to the mean field), and for an

incompressible MHD run (C), again with an imposed mean magnetic field and a forcing that is isotropic in both components and wavevectors. In both cases, the forcing injects energy in the largest scales of the system (see details in Verdini et al., 2015). Each panel in Figure 25 is a cut in the $(\ell_{||}, \ell_{\perp})$ plane taken along a fixed direction, the latter forming an angle, θ, with the direction of the mean field, B_0. ε_{hybrid} turns out to be consistent with ε_{true} at all the angles considered, yielding the correct cascade rate at oblique angles $\theta \geq 20$. However, in the nearly parallel direction, the hybrid method has the tendency to underestimate the true cascade rate by a factor $\gtrsim 10$. Though based on numerical simulations reproducing the plasma in regimes different than in the heliosphere, this analysis suggests that together with avoiding mixtures of fast and slow solar wind streams, as well as of samples observed in different periods of the solar cycle, third-order scaling analysis accounting for anisotropy might be better verified also in space plasmas, providing more accurate estimates of the energy transfer rate.

5.2. Shear-induced anisotropy

One of the possible ways to break isotropy is when large-scale velocity shears are present in the flow, which is a common scenario in space plasmas. For example, in the solar wind stream-interaction regions, the wind speed changes with a transition of the wind from slow to fast, or vice-versa, generating respectively rarefaction or compression regions. The validity of

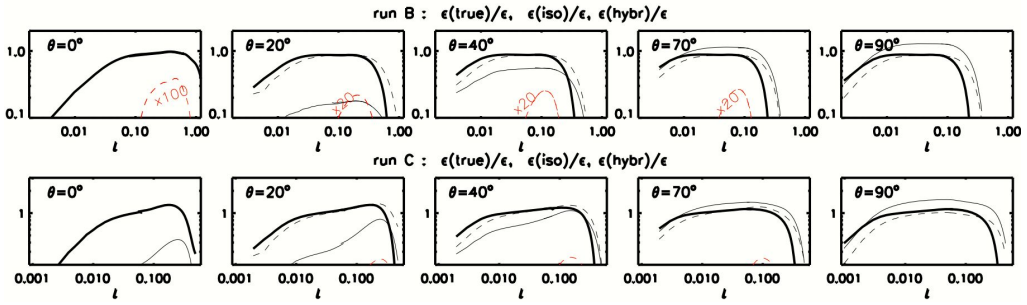

Figure 25: Comparison of $\varepsilon_{true} = (\boldsymbol{\nabla} \cdot \mathbf{Y})/4$ (solid thick line) with the hybrid cascade rate, $\varepsilon_{hybrid} = {}^{1D}\varepsilon + {}^{2D}\varepsilon$ (dashed black line). The red dashed line is the 1D (parallel) cascade rate obtained within the hybrid method. All cascade rates are normalized by the dissipation rate, ε Top panels refer to run B, bottom panels to run C. From left to right, different panels refer to increasing angle θ between the sampling direction and the mean field B_0. Figure adapted from Verdini et al. (2015).

the third-order moment scaling law in shear-dominated flows has been extensively explored in neutral fluids turbulence (Lindborg, 1996). The basic idea is that shears act as energy sources for the turbulence, and being superposed to the velocity fluctuations they must be explicitly included in the standard Richardson decomposition of the flow. The energy flux scaling relation is modified accordingly by introducing additional terms to the standard third-order moment of the velocity fluctuations. In particular, the modified third-order law for the velocity includes two contributions of different nature: one accounting for the energy transfer associated with the mean (sheared) flow, and an additional term accounting for the energy associated to the velocity fluctuations produced by the shear (Casciola et al., 2003). These terms are indicated as transfer and production terms, respectively. Numerical simulations have been used to validate the law. These also demonstrated that, typically, the modified third-order transfer term will dominate at smaller scales, while the production term will be relevant at larger scales, where the shear gradient has characteristic scale comparable with that of the turbulent fluctuations.

A similar procedure has been implemented for the MHD case, as will be described in the following. In a series of papers, a theoretical derivation was provided for three-dimensional plasma flows (Wan et al., 2009), then validated using 2D MHD turbulence numerical simulations (Wan et al., 2010), and finally adapted to the specific case of solar wind single- and multi-spacecraft time series (Stawarz et al., 2011; Osman et al., 2011).

5.2.1. Theoretical modeling of shear-driven anisotropy of the turbulent energy transfer rate

Following the derivation for neutral fluids (Casciola et al., 2003), Wan et al. (2009) considered a homogeneous velocity shear that is constant in time. The first step of the procedure is to separate the velocity field $\mathbf{v}$ in its mean and fluctuating components, $\mathbf{v} = \mathbf{u} + \mathbf{U}$, where $\mathbf{U}(\mathbf{r})$ is the time-averaged velocity profile and $\mathbf{u}(\mathbf{r}, t)$ the fluctuations. Assuming that $\mathbf{U}(\mathbf{r})$ is non-randomly and slowly varying, the turbulence can be seen as locally homogeneous, which allows to perform the standard third-order moment law derivation. Once this is done, and under the other usual assumptions, additional terms arise in the energy conservation equation that cannot be eliminated invoking isotropy. Assuming a homogeneous, linear velocity shear, the reference system can be set to obtain the simple background velocity expression $\mathbf{U} = \alpha y \hat{\mathbf{x}}$, so that the bulk flow is in the x axis direction and

the velocity gradient of magnitude α is along the y direction. The general equation for the energy transfer law is expressed using MHD variables here defined as $\mathbf{Z}^{\pm} = \mathbf{z}^{\pm} + \alpha y \hat{\mathbf{x}} \pm \mathbf{B_0}/(\mathbf{4}\pi\rho)^{\mathbf{1/2}}$, where $\mathbf{z}^{\pm}$ indicate the Richardson-decomposed fluctuation part of the standard Elsasser variables.

The equations obtained by Wan et al. (2009) integrating the energy flux and source terms over a spherical volume can be written as:

$$S^{\pm} + S_U^{\pm} + S_P^{\pm} = -(4/3)\varepsilon^{\pm} r. \tag{67}$$

Here $S^{\pm}$ is the standard isotropic mixed third-order moment. $S_U^{\pm}$ and $S_P^{\pm}$ are the aforementioned anisotropic terms, respectively accounting for the energy transfer due to the convection by the shear (a flux term) and for the energy production by the shear (a source term). Note that, in order to keep the notation used in the original papers and in the figures reproduced here, $r \equiv \ell$ now indicates the spatial scale, and not the vector position. With the notation introduced here, the three left-hand-side terms are

$$S^{\pm} = \frac{1}{4\pi} \int \langle (\Delta z^{\pm})^2 \Delta \mathbf{z}^{\mp} \rangle \cdot \hat{\mathbf{r}} \, d\Omega \tag{68}$$

$$S_U^{\pm} = \frac{\alpha r}{4\pi} \int \sin^2\theta \sin\phi \cos\phi \langle (\Delta z^{\pm})^2 \rangle d\Omega \tag{69}$$

$$S_P^{\pm} = \frac{2\alpha}{4\pi r^2} \int \int \langle (\Delta z_x^{\pm} \Delta z_y^{\mp}) \rangle r^2 dr d\Omega \tag{70}$$

where θ, ϕ and r are spherical coordinates, and Ω is the solid angle. Integration is intended over all angles and over all spherical volume. The two anisotropic terms, $S_U^{\pm}$ and $S_P^{\pm}$, have both explicit (linear) and implicit (undetermined) proportionality to the scale, r. This implies that the isotropic term is not necessarily a linear function of the scale. In neutral fluids, numerical studies showed that the two first terms, associated with energy cascading across scales and proportional to the shear amplitude, are typically dominating in the inertial range, while the third term, associated with the large-scale energy injection by the shear, is mostly relevant at the shear scale (see, e.g., Casciola et al., 2003, and references therein).

5.2.2. Validation of the shear-driven anisotropic third-order moment scaling in two-dimensional MHD numerical simulations

In order to test the modified law for sheared plasmas, a numerical study was performed using a standard two-dimensional simulations of the MHD

equations with low cross-helicity and a superimposed homogeneous velocity shear (Wan et al., 2010). The top panel of Figure 26 displays a snapshot

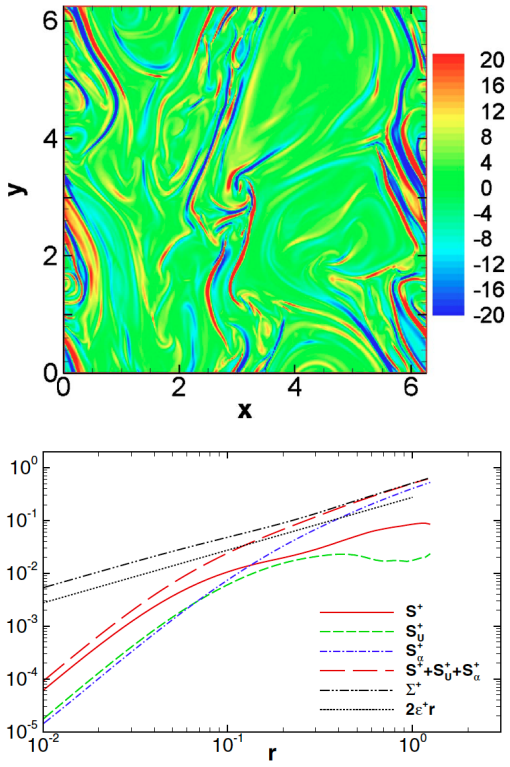

Figure 26: Top panel: a snapshot of the out-of-plane electric current, j, for the simulation with he velocity shear, whose effect is visible as elongated structures in the y direction. Bottom panel: the scaling of the third-order law estimated using a 2D MHD numerical simulation with large-scale, homogeneous velocity shear. The three terms S^+ (full red line, equation 68), S_U^+ (dashed green line, equation 69), and $S_\alpha^+ = S_P^+$ (dashed-dot blue line, equation 70) are shown along with their sum, $S^+ + S_U^+ + S_\alpha^+$ (long-dashed red line, equation 67). Σ^+ (dashed-dot-dot black line) represents the total flux with an additional viscous correction, and $2\varepsilon^+ r$ (dotted black line, equation 67) is the standard right-hand side of the third-order law for two-dimensional MHD turbulence. Figure from Wan et al. (2010).

of the out-of-plane current, j, taken in the steady state of the turbulence for the 2D-MHD simulation with superimposed velocity shear. The same figure shows, in the bottom panel, the scaling of the individual terms in the modified law, $S^\pm$, $S_U^\pm$ and $S_\alpha^\pm = S_P^\pm$, their total sum (also including the

case with additional viscous correction, Σ^+), and the right-hand side, $2\varepsilon^+ r$. The isotropic contribution shows a good linear scaling in the inertial range ($0.1 < r < 1$ in adimensional simulation units), but its amplitude is considerably smaller than the actual transfer rate. The additional shear terms, and in particular the production term, account for such difference. Note that the figure presented here refers to a sub-region of the simulation domain that shows homogeneous turbulence. When considering the whole domain, the linear scaling of $S^{\pm}$ is no longer present. This suggests that the shear affects the linear scaling of the third-order moment to a large extent. The above analysis is based on a theoretical derivation that uses the Reynolds-decomposed field, so that the fluctuations have been detrended to eliminate the background shear, as customary. However, a similar derivation can be performed using instead the whole field v, explicitly separating the mean and fluctuating components, $\mathbf{u} + \mathbf{U}$, but without subtracting the background shear. In this case, the additional terms S_U^+ and S_P^+ are not estimated independently, but rather are embedded in the standard third-order moment. Using the relation obtained without separating the background to analyze the same numerical simulation, the linear scaling and the correct amplitude are restored, suggesting that the effects of the shear are well captured by the complete third-order law, at least when the shear is periodic Wan et al. (2010). This is an important indication for the analysis of solar wind time series. Indeed, it suggests that mean fields should not be removed when performing the analysis, particularly in the presence of zero-mean large-scale velocity shears, unless the geometry of the shear is known with accuracy.

5.2.3. Single-spacecraft validation of the anisotropic third-order moment in solar wind turbulence

The study of the effects of large-scale velocity shears was extended to the case of solar wind flow. In the solar wind, the large-scale dynamics is dominated by the plasma flow, and quasi-linear velocity shears are often observed (Marino et al., 2012). In order to account for their effects on the turbulent cascade, the derivation briefly described above (Wan et al., 2009, 2010) should be extended to one-dimensional measurements, such as those obtained by spacecraft in the solar wind. This carries the known limitation that it is impossible to estimate gradients in directions other than the sampling line, via the Taylor hypothesis. Stawarz et al. (2011) performed such extension by modeling the anisotropy generated by the shear in the three terms of equation (67). It was additionally assumed that the anisotropy due

to the large-scale magnetic field is negligible with respect to the shear-driven anisotropy, a reasonable approximation in the solar wind (MacBride et al., 2008; Stawarz et al., 2010). Based on geometrical considerations, Stawarz et al. (2011) described the effects of the shear-induced vortex stretching as acting along preferential axes, which are in turn determined by the geometry of the shear. In particular, a scale-independent ellipsoidal anisotropy was assumed, so that the fluctuation energy is $[\Delta z^{\pm}(r,\theta,\phi)]^2 = [\Delta z^{\pm}(r)]^2 f(\theta,\phi)$. The angular dependence can be described by the ellipsoid of anisotropy with principal axes radii a, b on the shear plane x–y, and c perpendicular to it, given by

$$\begin{aligned} f(\theta,\phi) &= \frac{3}{1/a^2+1/b^2+1/c^2}\left[\frac{\sin^2\theta(1/2+\cos\phi\sin\phi)}{a^2}\right. \\ &+ \left.\frac{\sin^2\theta(1/2-\cos\phi\sin\phi)}{b^2}+\frac{\cos^2\theta}{c^2}\right]. \end{aligned}$$

Since in solar wind only the streamwise fluctuations, $[\Delta z^{\pm}(r)]_s$, are accessible, the anisotropy model can be used to retrieve the general fluctuations as $\langle[\Delta z^{\pm}(r)]\rangle = A_s\langle[\Delta z^{\pm}(r)]_s\rangle$, where the coefficient $A_s = [2c^2(a^2+b^2) + a^2b^2)]/[3c^2(a^2+b^2)]$ accounts for the geometry of the modeled anisotropic fluctuations. With this assumption, solid angle integration of the three energy flux and source terms in equations (68)-(70) provides expressions that use the streamwise increments, available from time series data, and which depend explicitly on the principal anisotropy axis radii a, b and c. In particular, the following expressions hold:

$$S^{\pm} = A_s^{3/2}\langle[(\Delta z^{\pm})^2\Delta z_x^{\mp}]_s\rangle \tag{71}$$

$$S_U^{\pm} = -\frac{2|\alpha|r}{15}\frac{|b^2-a^2|}{a^2+b^2}\langle[\Delta z^{\pm}(r)]_s^2\rangle \tag{72}$$

$$S_P^{\pm} = \frac{2\alpha A_s}{r^2}\int_0^r \langle[\Delta z_x^{\pm}\Delta z_y^{\mp}]_s\rangle r^2 dr\,. \tag{73}$$

After estimating the effects on each term for various geometries, it is possible to conclude that: (i) the S_U^{+} term is sensitive to small departures from isotropy but insensitive to large departures; (ii) large anisotropy in the direction perpendicular to the shear plane can affect the values of $S^{\pm}$ and S_P^{+}. Using equations (71)-(73) adapted to specific geometry of solar wind flow, spacecraft data were used to explore the validity of the model and to assess

the effects of shear anisotropy in the evaluation of the energy transfer rate. To this aim, ten years of ACE measurements were accurately selected and divided in 12-hour sub-intervals. For each interval, the presence of velocity shears was evaluated. The shear gradient magnitude was crudely estimated using large-scale features of the interval velocity, upon simplifying assumptions on the shear geometry and orientation. After discussing the dependence of the energy flux and source terms upon the anisotropy geometry (Stawarz et al., 2011), for the solar wind study this was assumed by assigning specific values of the three radii, $a = c = 1$ and $b = 2$. Two versions of scaling laws are used, namely the original isotropic P&P law, equation (54), providing the total energy transfer rate $\varepsilon_{\mathrm{NOSH}}$ and the modified shear-anisotropy version, giving $\varepsilon_{\mathrm{SH}}$. Note that these are total values, obtained averaging the two inward and outward mode rates. An estimate of the turbulence heating rate, $\varepsilon_{\mathrm{heat}}$, based on the solar wind temperature and velocity is used as reference (Vasquez et al., 2007). While using the heating rate as reference may be questionable due to the model limitations (e.g., electron heating and other forms of energy conversion are not included), this parameter can provide a qualitative estimate of the effects of the shear on turbulence. Figure 27 shows the two energy transfer rates and the heating rate as a function of the estimated shear amplitude. Values from 12-hours sub-intervals from the ACE database were averaged in each of eight shear magnitude bins, as indicated. The heating rate (black) is always positive and shows no dependency of the shear magnitude. Similarly, the shear-modified total energy transfer rate (red) shows values compatible with the modeled heating rate, and relatively weak variability with the shear properties. On the contrary, the P&P isotropic version (blue) reveals a strong dependency on the shear, suggesting that the shear is contaminating the third-order moment, which might therefore be unreliable. In particular, the sign of the third-order moment follows that of the shear, suggesting that the presence of strong shears could be one possible reason to observe change of sign in the energy transfer rate. While the analysis presented by Stawarz et al. (2011) is based on a realistic but strongly approximated modeling of the shear effects, and the ACE database includes a broad variety of solar wind conditions, the results suggest that caution should be used in the analysis of third-order moment analysis, in particular when large-scale velocity shears are present in the sample. The approximated inclusion of these effects, described above, may help to provide better estimates of the energy transfer rate, and could be considered reliable if the shear geometry is specifically assessed for each case. This might be

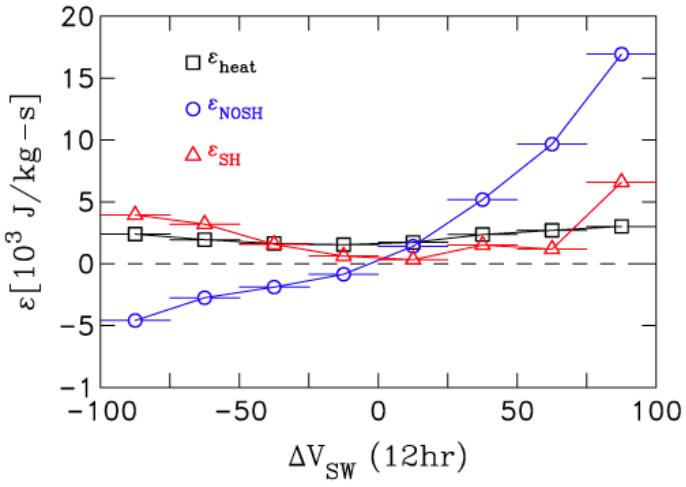

Figure 27: Mean energy transfer rate, ε, for the isotropic P&P law (ε_{NOSH}, blue circles), the anisotropic law (ε_{SH}, red triangles) and heating rate (ε_{heat}, black squares) versus the shear intensity, ΔV_{SW}, obtained using a partition in 12-hour intervals of 10 years of ACE measurements. Intervals were divided in eight bins according to the shear magnitude, and the energy transfer or heating values were averaged over each bin. Figure from Stawarz et al. (2011).

unpractical for systematic large statistical analyses, but possibly relevant for more accurate case studies, or when a precise energy budget is desired. It is obvious to imagine that the use of multi-spacecraft missions, such as ESA Cluster, NASA MMS or the upcoming NASA Helioswarm and the proposed ESA Plasma Observatory, could considerably improve the description of the velocity shears geometry, and for the cases in which this can be modeled, allow a more precise integration of the three terms and, therefore, a more accurate estimate of the turbulent energy transfer rate.

5.2.4. Multi-spacecraft validation of anisotropic third-order moment in solar wind turbulence

In order to explore the actual anisotropy of the cascade, a multi-spacecraft technique has been adopted to estimate the third order P&P law. This enables to account for arbitrary axisymmetric rotations about the mean magnetic field direction. In particular, using the Cluster 1 and Cluster 3 spacecraft (see Section 7), separated by a distance $\mathbf{d_{13}}$, Osman et al. (2011) computed the Elsasser field time series $\mathbf{z}_1^{\pm}(t)$ and $\mathbf{z}_3^{\pm}(t)$ along the flow direc-

tion, the subscript indicating the respective spacecraft. Assuming validity of the Taylor's hypothesis, the spacecraft time series correspond to the spatial time series in the plasma frame, $\mathbf{z}_1^{\pm}(-\mathbf{v}_{sw}t)$ and $\mathbf{z}_3^{\pm}(\mathbf{d_{13}} - \mathbf{v}_{sw}t)$. Varying the time lag Δt is thus equivalent to changing the separation between pairs of sampling points in the plasma frame, which permits to sample a range of scales and angular dependencies of the mixed third-order using a single data interval, namely $\mathbf{r}(\Delta t) = \mathbf{d_{13}} - \mathbf{v}_{sw}\Delta t$. In a magnetic field-aligned, right-handed, orthogonal coordinate system, it is thus possible to define the flux density, $F^{\pm} = (\hat{\mathbf{r}} \cdot \Delta\mathbf{z}^{\mp})|\Delta\mathbf{z}^{\pm}|^2$, and the acute angle between the time-lagged spacecraft separation vector and the magnetic field direction, θ_{SB}. During the period from January to March of 2006, the two Cluster spacecraft were orbiting with a separation $d_{13} \simeq 10000$ km. Their relative position with respect to the mean magnetic field changed along the orbit, resulting in a good coverage in θ_{SB} provided by an ensemble of $\gtrsim 1$ hour intervals, suitable for studying anisotropy. The choice of the specific separation was motivated by two facts. First of all, given the typical solar-wind speed, it correspond to scales well within the inertial range, of interest for studying the cascade. Secondly, it had the greatest θ_{SB} coverage in the whole Cluster database, and is therefore more suitable for the anisotropy analysis.

As shown in the left panel of Figure 28, the database was used to integrate the flux over a sphere (Wan et al., 2009):

$$\int_0^{\pi/2} \langle F^{\pm} sin\theta_{SB} d\theta_{SB} \rangle = -\frac{4}{3}\varepsilon^{\pm}\mathbf{r} \tag{74}$$

This multi-spacecraft technique was used to compute estimates of $F^{\pm}$ at two scales, namely the spacecraft separation and a shorter scale (4000 km), obtained using two spacecraft and the Taylor hypothesis. At separation of 10000 km, the two integrated flux functions, divided by the separation distance and the constant factor, provided single-scale estimates of the pseudo-energy transfer rates, $\varepsilon^{+} = 5.2$ kJ (kg s)$^{-1}$ and $\varepsilon^{-} = 5.7$ kJ (kg s)$^{-1}$, respectively for the sunward and the anti-sunward components of the mixed third-order moment. For spacecraft separations $\simeq$4000 km, a second set of single-scale pseudo-energy transfer rates was obtained, $\varepsilon^{+} = 4.9$ kJ (kg s)$^{-1}$ and $\varepsilon^{-} = 5.8$ kJ (kg s)$^{-1}$. For each component, the pair of single-scale third-order moments was finally fitted by a linear law, equation (74), obtaining the pseudo-energy transfer rates within the solar wind turbulent inertial range. This is shown in the right panel of Figure 28, where the values obtained

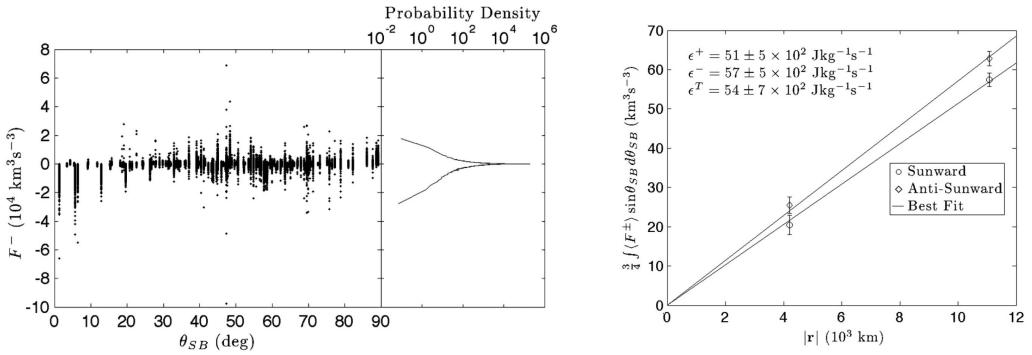

Figure 28: Left panel: estimates of the anti-sunward normalized flux density $F^- = (\hat{\mathbf{r}} \cdot \Delta\mathbf{z}^+)|\Delta\mathbf{z}^-|^2$ versus the angle between the magnetic field and the bulk flow direction, θ_{SB}, together with the corresponding probability distribution function. Similar results were obtained for F^+. Right panel: linear scaling of the sunward (circles) and anti-sunward (diamonds) components of the third-order law, equation (74). The solid lines are least squares fits to the data, the gradients of these lines correspond to the mean volume averaged cascade rates. The total energy transfer rate is the average of the sunward and anti-sunward components. Figure adapted from Osman et al. (2011).

though this procedure are also indicated. Since only two points are used for the fit, it obviously cannot inform about the goodness of the linear model, but it can still provide relatively uncertain, yet indicative values of the parameters upon imposing linear scaling. Note that the energy transfer rate values are broadly consistent with estimates of the studies conducted in the ecliptic (MacBride et al., 2008).

5.3. Additional terms for radial solar-wind expansion

An important factor that can impact the validity of the original version of the P&P law in heliospheric plasmas is the intrinsic radial expansion of the solar wind. For example, the isotropy assumption needs to be revised, since expansion affects in a different manner the radial and tangential components of mean fields and their fluctuations. An extensive literature exists that describes studies devoted to the correct analysis of the properties of the radially expanding solar wind, including turbulence. Theory, models, numerical simulations and data analysis provide frameworks and constraints for this complex dynamical problem, which to date is still open. Understanding the effects of expansion on solar wind dynamics is critical for the correct modeling of the global heliosphere, for characterizing physical processes such as waves, instabilities and dissipation occurring in the plasma, as well as to

achieve an accurate prediction of the CME transit time. In this review, we limit the focus on the effects of the solar wind expansion on the validity of the P&P law and on the quantities estimated from it, presenting the modifications proposed to the original P&P law approach, equation (54), in order to account for it in the energy evolution equation. The general concept is that, like for velocity shears, the expansion can be viewed as a source of energy, and should therefore be included in the dynamical equation. Hellinger et al. (2013) derived the modified equations considering the expanding box approximation (Grappin et al., 1993), where the expansion is assumed supersonic, radial and uniform, for example $|\mathbf{v}_{SW}| = |(v_{SW}, 0, 0)| \gg v_A$ in the RTN coordinate system, and the plasma volume under study is smaller than the expansion scale, so that the local mean field can be assumed constant. With these approximations, it is possible to write the MHD equations for a plasma volume comoving with the expanding solar wind, which results in two additional forcing terms. Accordingly, additional terms appear in the modified P&P law, which, in divergence form, can be written as

$$\begin{aligned} \frac{\partial\langle|\Delta\mathbf{z}^{\pm}|^2\rangle}{\partial t} &+ \nabla\cdot\langle\Delta\mathbf{z}^{\mp}|\Delta\mathbf{z}^{\pm}|^2\rangle = -4\varepsilon^{\pm} + 2\nu\nabla^2|\Delta\mathbf{z}^{\pm}|^2 \\ &- \frac{v_{SW}}{R}\langle|\Delta\mathbf{z}^{\pm}|^2 + \Delta\mathbf{z}^{+}\cdot\Delta\mathbf{z}^{-} - 2\Delta\mathbf{z}_L^{+}\Delta\mathbf{z}_L^{-}\rangle\,, \end{aligned} \tag{75}$$

where the subscript L indicates the radial component and R is the distance from the center of expansion. The three terms on the second line of equation (75) represent the forcing contribution to the energy budget due to expansion. In particular, the first of the three terms accounts for the standard Wentzel–Kramers–Brillouin (WKB) evolution of the Elsasser fluctuations (see, e.g., Matthaeus et al., 1994, and references therein). The second and third terms describe the effects of the coupling between the inward and outward modes, which arise due to mode reflection caused by the inhomogeneity associated with the solar wind expansion. It effectively couples the large-scale expanding fields with the small-scale cross-correlation of the Elsasser fields, therefore modifying the nonlinear interactions. Ideally, equation (75) should be validated by numerical simulations that use the expanding box approximation (see, e.g., Verdini and Grappin, 2015). At the time of writing, no such validation exists in the literature, although preliminary comforting results were presented at a conference (A. Verdini, private communication, see Verdini et al., 2014).

In order to test the ability of the modified P&P law to capture the ad-

ditional energy injection provided by the expansion, a similar relation was derived by Gogoberidze et al. (2013) in an integral form, more suitable for application to solar wind data. In such form, the law was written as

$$\langle \Delta \mathbf{z}^{\mp} |\Delta \mathbf{z}^{\pm}|^2 \rangle + \frac{v_{SW}}{R\ell^2} \int_0^{\ell} y^2 \left[\frac{\partial}{\partial R} (R |\Delta \mathbf{z}^{\pm}|^2) - \langle \Delta \mathbf{z}^{+} \cdot \Delta \mathbf{z}^{-} \rangle \right] dy = -\frac{4}{3} \varepsilon^{\pm} \ell \,, \tag{76}$$

where, as usual, the Taylor hypothesis is used to convert spatial to temporal scales, $\ell = -v_{SW} \Delta t$. Gogoberidze et al. (2013) erroneously identify only two extra terms (instead of three, as in Hellinger et al., 2013), which appear in the definite integral in equation (76). Nevertheless, validation against solar wind data was performed, and even in this possibly slightly incorrect form, useful indications can be obtained. In order to evaluate the corrective term accounting for possible large-scale fields effects on the cross-correlation of the Elsasser fluctuations (namely the second term under the integral, labeled as M by the authors), an interval of data measured by the Wind spacecraft was used. As shown in Figure 29, top panel, this provided evidence that the M term (dashed line) is relatively smaller, but not fully negligible, in most of the inertial range with respect to the standard P&P term (full line), with some larger effect at larger scales. In fact, an average factor $\simeq 3$ between the two terms was found using several data intervals. On the other hand, in order to determine the radial gradients in the WKB expansion term (the first of the two terms in the integral, labeled as D), Helios 2 data were used. In particular, two intervals measured at two different distances from the Sun, $R = 0.65$ and $R = 0.87$, at nearly one month distance were used. The two streams were observed to proceed from the same solar coronal hole, so that the turbulence can be reasonably considered as stationary (see more on this topic and on the specific Helios data in Section 6.2). The radial derivative was then obtained as two-point increment, and this allowed to obtain an estimate for the D term, as shown in the bottom panel of Figure 29. In this case, the M term gives smaller contribution, but the D term is comparable with the standard third-order moment term at all scales.

The above estimate might be approximate to many effects, including the partly incorrect equation used, the crude approximation on estimating the derivative, the use of solar wind intervals separated by a month, and the use of the absolute value in plotting the energy transfer rate and the other flux or source terms. Nevertheless, the conclusion of these works is that expansion terms should be considered when studying solar wind data, since they can

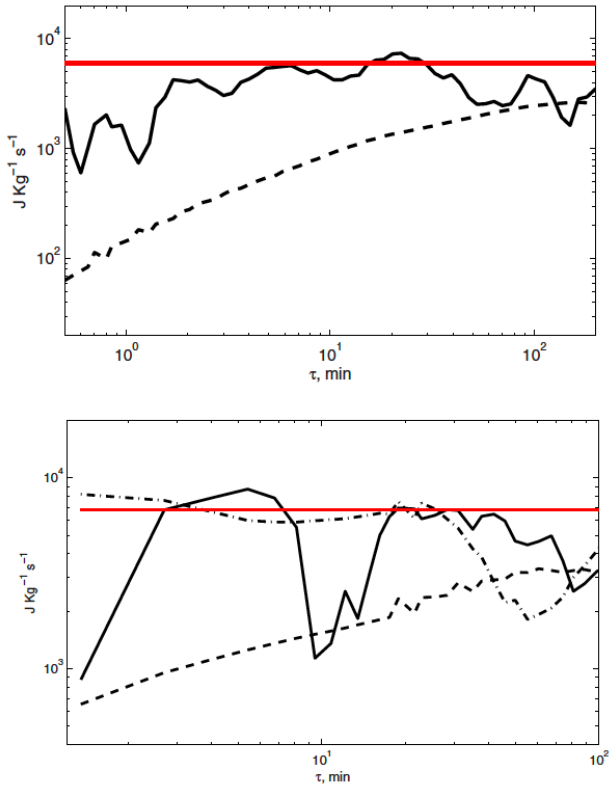

Figure 29: Scale (labeled as τ) dependence of the total mixed third-order moment term (full black line, see equation 76), the cross-correlation term (M, dashed line, see text), and the expansion term (D, dot-dashed black line, bottom panel only, see text), together with the turbulent heating rate estimated using the model by Vasquez et al. (2007) (red line, equation 64). Top panel: Wind data; bottom panel: Helios 2 data. Figure adapted from Gogoberidze et al. (2013).

provide additional energy that is not sufficiently captured in the isotropic version of the P&P law. Like in the case of velocity shears, the anisotropic contribution appears as terms that depend on the geometry of the system, providing a nontrivial contribution to the scaling. The increasing availability of radially aligned spacecraft in the inner heliosphere should allow a prompt improvement of the above study, allowing to evaluate with better precision the effects of radial expansion in solar wind turbulence.

5.4. Reaching down to sub-ion scales: incompressible Hall MHD

As recalled previously, for many purposes the macroscopic description of solar wind fields at the scales where the heliospheric plasma can be considered quasi-neutral and at the local thermal equilibrium, can be done in the frame of the classical magnetohydrodynamics (MHD). Using the one-fluid MHD equations is indeed equivalent to treat the plasma as a single neutral fluid with conductive properties (Galtier, 2016). In the ideal MHD description, it is assumed that ions and electrons move essentially along the magnetic field, with the same velocity. However, this assumption is no longer valid if one is interested in exploring the plasma evolution at scales close to or below the characteristic ion scales, for which other effects must be taken into account. In collisionless space plasmas, the physics of sub-MHD scales is extremely rich and interesting, since at those scales the turbulence entangle with sub-ion kinetic physics, and all contribute to the energy conversion. It is therefore crucial to be able to describe as accurately as possible the cross-scale energy flux in the presence of non-MHD effects. Such extension is the topic of this Section.

5.4.1. Hall-MHD description of plasmas

Perhaps the simplest extension of the ideal MHD, which allows to investigate scales smaller the the characteristic separation scale between ions and electrons, is the Hall-MHD model. In the Hall-MHD framework, the generalized Ohm's law is modified with the introduction of the Hall electric field, a term proportional to $\mathbf{J} \times \mathbf{B}$, $\mathbf{J}$ and $\mathbf{B}$ being the electric current density and the magnetic field, respectively. The adimensional formulation of the Hall-MHD equations in the incompressible framework, in Alfvén units, reads as follows:

$$\boldsymbol{\nabla} \cdot \mathbf{U} = 0 \tag{77}$$

$$\partial_t \mathbf{U} + (\mathbf{U} \cdot \boldsymbol{\nabla})\mathbf{U} = \mathbf{J} \times \mathbf{B} - \boldsymbol{\nabla} p + \nu \boldsymbol{\nabla}^2 \mathbf{U} \tag{78}$$

$$\partial_t \mathbf{B} = \boldsymbol{\nabla} \times [(\mathbf{U} - \xi_H \mathbf{J}) \times \mathbf{B}] + \eta \boldsymbol{\nabla}^2 \mathbf{B} \tag{79}$$

$$\boldsymbol{\nabla} \cdot \mathbf{B} = 0 \tag{80}$$

where $\mathbf{U}$ and $\mathbf{B}$ are fluid velocity and magnetic field, $\mathbf{J} = \boldsymbol{\nabla} \times \mathbf{B}$ is the electric current density, p the pressure, ν and η the kinematic viscosity and magnetic diffusivity, respectively. The strength of the so called Hall term $\xi_H \mathbf{J} \times \mathbf{B}$ depends on the Hall parameter $\xi_H = L_H/L_0$ (often indicated by ε_H in the literature), given by the ratio between the integral scale of the

system L_0 and the Hall characteristic length scale L_H. The latter is defined in turn as $L_H = cV_A/(\omega_{pi}U_0)$, where V_A is the Alfvén speed, ω_{pi} is the ion frequency and U_0 the characteristic bulk velocity. It is worth noticing that when $U_0 = V_A$, then the Hall length scale is equal to the ion inertial length, $L_H = d_i = c/\omega_{pi}$. The Hall term is a measure of the difference in velocity between ions and electrons, assuming that the former are decoupled from the magnetic field while the latter are guided by it. The mechanism responsible for the decoupling of the ions is not always the same, depending on the level of ionization of plasma. In highly ionized plasmas the Hall effect arises from the unbalance between ions and electrons inertia, while in partially ionized plasmas neutral collisions can be more efficient in decoupling the ions (Pandey and Wardle, 2008). Differences between the two mechanisms are significant in terms of the scales at which the Hall effect becomes important, affecting the plasma dynamics. Indeed, in the case of a fully ionized plasma, the reference characteristic length scales is the ion inertial length, $d_i = c/\omega_\pi$ (Huba, 2003), whereas in partially ionized plasmas the Hall effect can act also at scales of the order of the energy containing structures of the system (i.e., the integral scale) (Pandey and Wardle, 2008). Another feedback on the MHD plasma dynamics, due the introduction of the Hall term in the equations, is the propagation of two wave modes in addition to the Alfvén waves, namely the whistler and Hall drift waves. Their phase speed is inversely proportional to the ion cyclotron frequency, $\Omega_i = eB/m_ic$, and is instead proportional to the square of the Alfvén speed, thus resulting significantly faster than the classical MHD Alfvén waves (Huba, 2003). The Hall-MHD model has been successfully utilized to describe the dynamics of many astrophysical settings, including heliospheric plasmas. Star formation (Norman and Heyvaerts, 1985; Marchand et al., 2019; Wurster et al., 2021), solar atmosphere and the solar wind at Earth distance (Galtier and Buchlin, 2007; González-Morales et al., 2019), dynamo action (Mininni et al., 2002, 2005; Gómez et al., 2010) and the Earth and planetary magnetospheres (Liu et al., 2013; Dorelli et al., 2015; Xie et al., 2015; Tóth et al., 2016), are only some of the frameworks and science cases tackled in the literature employing the Hall-MHD model. Several studies have also shown that the Hall term enhances the rate of magnetic reconnection (Wang et al., 2001; Morales et al., 2005; Ma et al., 2014; Ma et al., 2018), though there is an ongoing discussion on the role of the Hall current in the emergence of magnetic structures (Mininni et al., 2007). In particular, claims are made that the Hall effect may help amplifying the large-scale magnetic field (Mininni et al., 2005) and the

emergence of self-organized structures (Numata et al., 2004; Ohsaki, 2006), while some authors argue it helps instead with the generation of small-scale structures and filaments (Rheinhardt and Geppert, 2002; Miura and Araki, 2014; Martin et al., 2013).

The effect of the Hall current is sizable also in the power spectrum of the magnetic field. In case of fully developed turbulence, the latter is characterized by the usual power-law slope close to -5/3 at large (MHD) scales, followed by a steeper power law regime at scales below the ion scale, though the prediction of the spectral slope for this ion inertial range is still matter of debate. Some theoretical and numerical work anticipate a value of the spectral index close to -7/3 (Galtier and Buchlin, 2007; Howes et al., 2008; Alexandrova et al., 2008), which would result from the feedback of the faster wave modes on the non-linear interactions, entering the MHD phenomenology through the Hall term. However, most of spacecraft observations (mainly in the near-Earth solar wind) show a steeper value, between -2.6 and -3 (Leamon et al., 1998; Alexandrova et al., 2008; Kiyani et al., 2015), which is also reported in numerical studies (Franci et al., 2015; Cerri et al., 2017; Foldes et al., 2022).

Exploring the Hall-MHD regime by means of numerical simulations is rather a challenging task, as it requires large scale separation in case of highly turbulent space plasmas, in order to resolve both the MHD and the ion inertial range, and all the characteristic scales involved in the problem. Moreover, in order to resolve the fastest wave modes (whistler and Hall-drift waves) the time step of the simulations needs to be very small, and since its value decreases quadratically with the grid resolution (Gómez et al., 2010) that increases by much the computational cost of Hall MHD simulations. Though, driven by the need to understand the small-scale plasma dynamics, especially in the context of the space investigations, several attempts have been made to numerically solve the Hall-MHD equations. As a result, many codes have been developed adopting different numerical methods, from pseudo-spectral (Mininni et al., 2003) to finite-volume (Tóth et al., 2008) and particle-in-cell (PIC). The latter reproduce the dynamics of the kinetic scale, assuming electrons as a mass-less charged fluid while ions are described as particles (Ma et al., 2018; Cerri et al., 2017; Papini et al., 2019). Large-eddy simulation schemes parametrizing the Hall effect have also been developed for the aim of reducing the computational cost (Miura and Hamba, 2022). More recently, Lattice Boltzmann codes have been developed and employed to perform high-resolution 3D Hall-MHD simulations, exploiting their very

good scalability on large parallel machines as well as on Graphical Processing Units (GPUs), with very good performances in terms of accuracy of the numerical solutions and excellent speed-ups (Foldes et al., 2022). When dealing with the simulation of turbulent flows, pseudo-spectral methods are recognized as the best option allowing for an equally-accurate representation of all scales of the dynamics (Patterson and Orszag, 1971), and of all the fields integrated.

The remarkable efforts the space community as a whole is putting in developing codes able to exploit modern supercomputer architectures to simulate the plasma dynamics beyond the ion scales, is also motivated by the latest and upcoming space missions, carrying high-resolution plasma and magnetic field instruments able to investigate solar wind and magnetospheric plasma at unprecedented resolutions, such as Solar Orbiter, Parker Solar Probe and the Magnetospheric Multi-Scale Mission, to name a few. The availability of space plasma observations in the Hall regime and the output of state-of-the-art simulations reproducing the Hall scales in a parameter space compatible with a variety of phenomena observed in the heliosphere, will allow major breakthroughs in a not too distant future, including an exhaustive characterisation of the turbulent cascade by means of the scaling laws approach, and the mechanisms leading to dissipation in non-collisional plasmas.

5.4.2. Additional terms for Hall-MHD

In space plasmas like the solar wind and the terrestrial magnetosheath, fluctuations exist on an extremely broad range of scales, which reach well beyond the typical ion scales. Near and below the ion inertial length, solar wind and magnetospheric magnetic spectra consistently show a transition region, marking a steepening in the power-law scaling, which in turn suggests a change in the dynamics. At sub-ion scales, spectra typically show scaling exponents between -2 and -4, with average close to -7/3 (Leamon et al., 1998; Alexandrova et al., 2008; Kiyani et al., 2015). Intermittency was observed to extend to sub-ion scales (Alexandrova et al., 2008; Perrone et al., 2016; Sorriso-Valvo et al., 2017), although not consistently. Several observations showed that intermittency measures, such as the flatness, stop increasing as the scale decreases, which is typically associated to return to self-similarity (Kiyani et al., 2009b; Kiyani et al., 2013; Wu et al., 2013; Chen et al., 2014). However, different diagnostic tools have given different results (see, e.g., Sorriso-Valvo et al., 2017; Roberts et al., 2022, and references therein), suggesting that the accuracy of measurements and validity of

the Taylor hypothesis might be important factors determining the statistical properties of small-scale fluctuations. The observations described above broadly suggest that a more complex cascade, resulting from nonlinear interactions, is active in that range of scales, at least in the proximity of the ion break. On the other hand, alternative models of ion-scale waves have been invoked to explain the observed spectra. These include, for example, a cascade of kinetic Alfvén waves, the sub-ion scale version of MHD Alfvén waves (Howes, 2010). For this reason, going beyond phenomenology can help understanding the role of the nonlinear interactions in shaping the sub-ion range.

The first attempts to write an exact relation for the energy transfer for Hall MHD that could be used for space measurements dates back to the theoretical work by Galtier (2008). In a crucial paper, this author initiated the quest for a compact form for the Hall-MHD version of the P&P law, deriving a version of it that uses two-points correlators, similarly to the P&P derivation proposed in (Politano and Pouquet, 1998). At present, consensus was reached on an elegant yet complete form of the equation, which is currently being used with solar wind and magnetospheric data. Without loss of generality, we briefly describe here only the latest version, which was initially suggested by Hellinger et al. (2018) in a slightly incorrect form, and promptly corrected by Ferrand et al. (2019). For the reader interested in the rigorous details of the derivation, a thorough description can be found in the PhD thesis of Ferrand (2021).

The procedure for the derivation is analogous to that for the P&P law based on the second-order structure function (Danaila et al., 2001b; Sorriso-Valvo et al., 2007), which we rewrite here as $\langle S \rangle = \langle |\Delta \mathbf{v}|^2 + |\Delta \mathbf{b}|^2 \rangle$, with the usual meaning of the spatial increment, Δ. Here the magnetic field is given in velocity units. After writing the evolution equation for $\langle S \rangle$ using the Hall MHD equations, exploiting incompressibility to remove the pressure terms, performing some non-trivial vector calculation, and finally assuming that forcing and dissipation can be neglected (thus assuming large Reynolds numbers), the following simple exact relation can be obtained:

$$\begin{aligned} \boldsymbol{\nabla}_{\boldsymbol{\ell}} \cdot \langle (|\Delta \mathbf{u}|^2 + |\Delta \mathbf{b}|^2) \Delta \mathbf{u} \;&-\; 2(\Delta \mathbf{u} \cdot \Delta \mathbf{b}) \Delta \mathbf{b} + \\ d_i (\Delta \mathbf{b} \cdot \Delta \mathbf{j}) \Delta \mathbf{b} \;&-\; \frac{1}{2} d_i |\Delta \mathbf{b}|^2 \Delta \mathbf{j} \rangle = -4\varepsilon \end{aligned} \tag{81}$$

where the first term divergence is intended in the direction of the spatial

increment vector, $\boldsymbol{\ell}$.

The above equation, given in divergence form, includes the three well-known terms of the MHD contribution to the energy flux, $\mathbf{Y}$, and two new terms that, together, account for Hall effects, $\mathbf{H}$. These are defined as

$$\mathbf{Y} = \langle(|\Delta\mathbf{u}|^2 + |\Delta\mathbf{b}|^2)\Delta\mathbf{u} - 2(\Delta\mathbf{u}\cdot\Delta\mathbf{b})\Delta\mathbf{b}\rangle \quad (82)$$

$$\mathbf{H} = -d_i\langle|\Delta\mathbf{b}|^2\Delta\mathbf{j} - 2(\Delta\mathbf{b}\cdot\Delta\mathbf{j})\Delta\mathbf{b}\rangle\,, \quad (83)$$

The two new terms in $\mathbf{H}$ describe the decoupling of ion and electron flows. The similarity between the purely MHD and Hall-MHD contributions is evident by replacing the current, $\mathbf{j}$, with the electron velocity in the ion flow frame, $\mathbf{u}_e$. The Hall term is in fact the analogous of the $\mathbf{Y}$ term that explicitly accounts for the magnetic field coupling to the electron flow, represented by the current. Defining the two contributions as above allows to write the Hall-P&P law in a conveniently compact form, $\boldsymbol{\nabla}_\ell\cdot(\mathbf{Y}+\mathbf{H}/2) = -4\varepsilon$. Finally, assuming isotropy and a constant energy flux in the inertial range, the usual integration gives an equation for the projection along the displacement direction, $\boldsymbol{\ell}$:

$$Y_\ell + \frac{1}{2}H_\ell = -\frac{4}{3}\varepsilon\ell\,. \quad (84)$$

This formulation, based on two-point increments, allows to estimate the third-order moment scaling law for Hall MHD using single-spacecraft time series, provided a measure of the current $\mathbf{j}$ is available. For this reason, high resolution, high-cadence measurements of ion and electron distribution functions are necessary for the correct estimate of the current as $\mathbf{j} = e(n_i\mathbf{u}_i - n_e\mathbf{u}_e)$, where e is the positive fundamental electric charge. An alternative way to compute the current is to use multi-spacecraft missions with tetrahedral configuration, such as Cluster and MMS, which allow estimating three-dimensional gradients of the magnetic field (using the so-called "curlometer" technique; see, e.g., Dunlop et al., 2021). For single-spacecraft measurements where accurate electron and ion distributions are not available, the magnetic gradient could provide a reasonable proxy for the current, at least for rough order-of-magnitude estimates of the Hall contributions to the energy transfer.

As mentioned above, two alternative formulations of the Hall-MHD P&P law were previously proposed, that make use of the plasma vorticity, $\mathbf{w} = \nabla\times\mathbf{u}$. These can be useful for implementations based on high-resolution numerical simulations, where the point-wise vorticity is known with sufficient accuracy (Galtier, 2008; Banerjee and Galtier, 2017). For the sake of completeness, we give here the version of the Hall-P&P law found in Banerjee

and Galtier (2017), which in its integral form reads:

$$\langle \Delta[\mathbf{u} \times \omega + \mathbf{j} \times \mathbf{b}] \rangle + \langle \Delta[(\mathbf{u} - d_i \mathbf{j}) \times \mathbf{b}] \cdot \Delta \mathbf{j}] \rangle = 2\varepsilon \,. \tag{85}$$

The above relation contains, again, only two-points increments, and is therefore suitable for spacecraft time series analysis, provided the current and vorticity can be measured with sufficient accuracy. While the current can be estimated using sufficiently good plasma measurements, only multi-spacecraft missions give access to the vorticity, which needs three-dimensional gradients to be estimated. As noted above, and with the same caveats, in some cases a crude approximation for the vorticity could be obtained by using small-scale velocity gradients. Conversely, the original version formulated in Galtier (2008) includes explicit divergence in the increment direction, similar to equation (81), and therefore cannot easily be used for single-spacecraft time series. However, the three formulations are mathematically equivalent, so that all of them can be used to estimate energy transfer rates according to the specific details of the database. Moreover, the Hall contributions to the energy transfer rate from the three different versions were compared using high resolution numerical simulations of electron MHD turbulence (equivalent to the Hall MHD equations with the velocity set to zero). Results are illustrated in the left panel of Figure 30, where the three different colors indicate the different formulations for the Hall terms, **H**, and show that they are convincingly equivalent (Ferrand et al., 2019). Some discrepancies were noticed when using different techniques to implement the calculation on the 3D numerical simulation domains, which also suggests that the version proposed in Banerjee and Galtier (2017) provides the best possible result (Ferrand, 2021). It was also pointed out that an additional uniform background magnetic field would not appear explicitly in the scaling law, although it would be expected to affect the plasma dynamics (Banerjee and Galtier, 2017). This is exemplified in the right panel of Figure 30, where the ratio between the Hall contribution to the energy transfer rate for a run without and the one for a similar run with external field is shown (Ferrand, 2021). In their paper introducing the formalism used for the derivation of equation (81), Hellinger et al. (2018) use two-dimensional particle-in-cell numerical simulations of the hybrid Vlasov-Maxwell system of equations, which fully includes the Hall physics. Three runs with different values of the plasma β (1/16, 1/2, 4) were used to explore the role of the Hall contribution as the transition scale, d_i, moves in the spectrum. Indeed, while for $\beta \sim 1$ the ion

gyroradius, $\rho_i = v_{T,i}/\Omega_{ci}$ ($v_{T,i}$ being ion thermal speed and Ω_{ci} the ion cyclotron frequency), and the ion inertial length, d_i, are comparable, larger $\beta \sim 1$ values result in larger d_i. In such cases, the Hall terms become relevant at larger scale, within the inertial range (Alexandrova et al., 2008, 2009; Sahraoui et al., 2009). To this aim, the two terms, $\mathbf{Y}$ and $\mathbf{H}$, were computed separately and then summed up. A term describing the dissipation, called $\eta\nabla^2 S_b/2$, and a large-scale forcing terms, called $-(\partial S/\partial t)/4$, were also computed, in order to account for possible deviations from the strictly stationary state and for finite Reynolds number effects. Figure 31 shows one example for $\beta = 1/16$ of the four terms, together with their sum. As evident, the total flux (black solid line) is reasonably constant over a broad range. This results from the combined action of different dominating contributions in different ranges, namely: the forcing term at large scales, the MHD term in the inertial range, the Hall term at sub-ion scales, and finally the dissipation term at the smallest scale. Despite the equation given in Hellinger et al. (2018) contains a small error in one of the terms (the Hall term), this figure illustrates very clearly the role of the various nonlinear couplings across the whole range of scales, and represents a benchmark of the technique for the Hall MHD case.

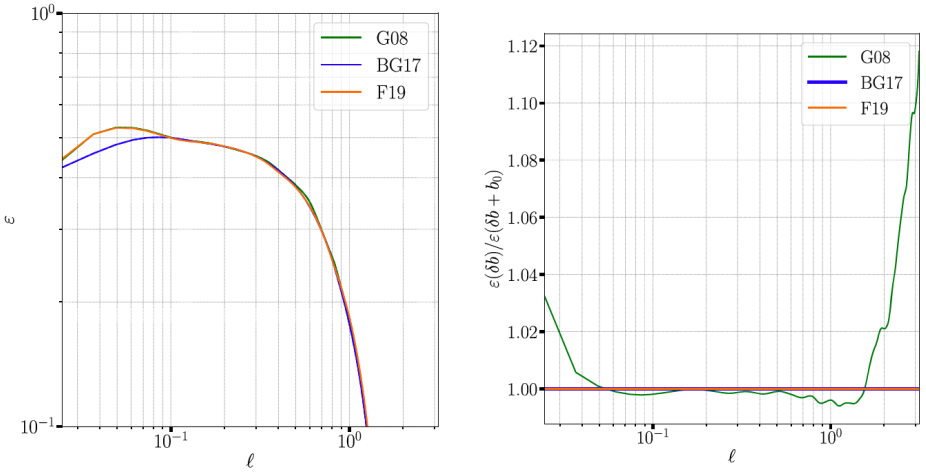

Figure 30: Left panel: Hall contribution to the energy transfer rate obtained from a numerical simulation of electron MHD turbulence, for the three alternative formulations (G08 being the formulation by Galtier (2008), BG17 that by Banerjee and Galtier (2017), equation 85, and F19 that by Ferrand et al. (2019)). Right panel: for the same three formulations, the ratio between the Hall contribution with or without an external magnetic field. Figure from Ferrand et al. (2019).

Finally, Vásconez et al. (2021) examined the different prominence of the Hall effect in different numerical models. To this aim, these authors used a set of two-dimensional numerical simulations with out-of-plane ambient magnetic field, including: (i) a Hall-MHD DNS (Perrone et al., 2018); (ii) a Landau Fluid model, which retains part of the low-frequency kinetic physics, such as the Landau damping, but uses a weakly nonlinear approximation (for a detailed description of the model, see Passot et al., 2014); and (iii) a hybrid Vlasov-Maxwell DNS, which describes the ion kinetic physics (including the Hall physics) at the expenses of scale separation in the MHD range (Valentini et al., 2007). Initial conditions, forcing and other parameters were identical, as to ensure the best possible comparison among the runs. The three top

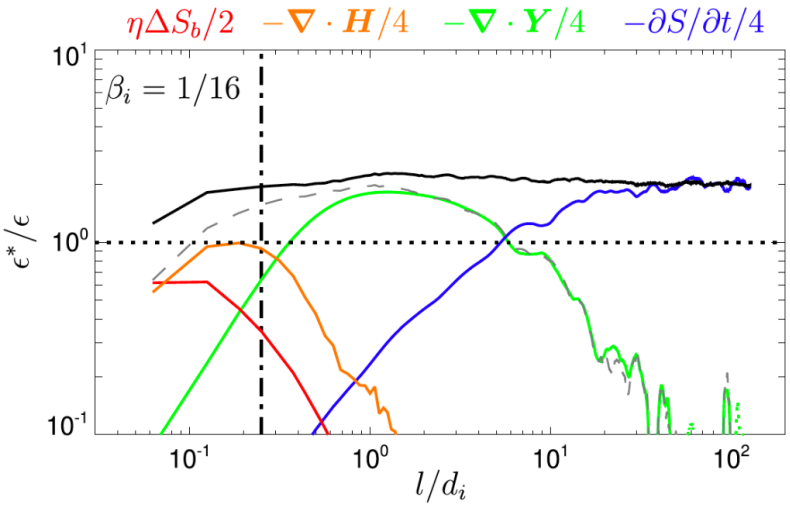

Figure 31: Energy transfer rate that includes the large scale, inertial range and dissipation contributions, $\varepsilon^* = -\frac{1}{4}\frac{\partial S}{\partial t} - \frac{1}{4}\boldsymbol{\nabla}\cdot(\mathbf{Y}+\mathbf{H}) + \frac{1}{2}\eta\Delta S_b$ (for details see equation 7 in Hellinger et al., 2018), normalized to the actual viscous-resistive dissipation rate, $\varepsilon = \nu\langle\boldsymbol{\nabla}\mathbf{u} : \boldsymbol{\nabla}\mathbf{u}\rangle + \eta\langle\boldsymbol{\nabla}\mathbf{b} : \boldsymbol{\nabla}\mathbf{b}\rangle$ (where ":" indicates double contraction of the two second-order tensors, see Section 2 in Hellinger et al., 2018). Both rates are obtained using the scaling law of the Hall MHD third-order moment from a two-dimensional PIC simulation of the hybrid Vlasov-Maxwell system. The different contributions are marked with colors as indicated, while their sum is in black. Solid and dotted lines indicate positive and negative values, respectively. The dashed gray line shows the energy transfer for the inertial range only, $-\frac{1}{4}\boldsymbol{\nabla}\cdot(\mathbf{Y}+\mathbf{H})$. The vertical dash-dotted black line indicates the ion gyroradius, ρ_i, and the dotted horizontal line indicates $\varepsilon^* = \varepsilon$. Figure from Hellinger et al. (2018).

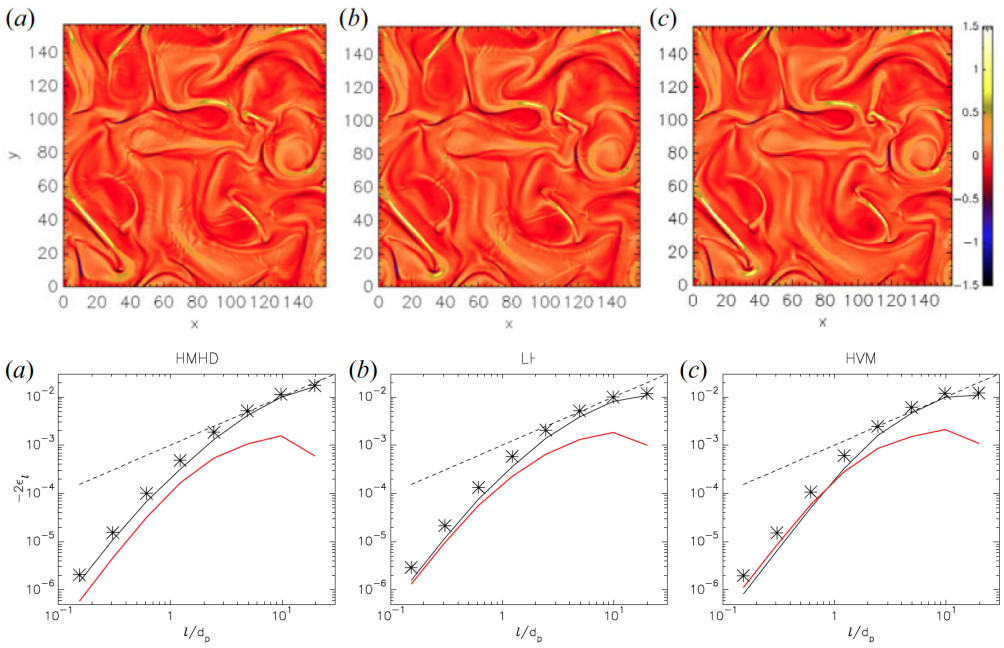

Figure 32: Top panels: contour plots (color bar on the right) of the out-of-plane current density, $j_z(x, y)$, for the HMHD (top panel a), LF (top panel b) and HVM (top panel c) numerical simulations, at the time of maximal turbulence activity estimated as the peak of the mean squared current, $\langle j_z^2 \rangle$). Bottom panels: mixed third-order moment (stars), indicated as $-2\varepsilon_l$, as a function of the scale l, for the HMHD (bottom panel a), LF (bottom panel b) and HVM (bottom panel c) simulations. The separated contributions from MHD terms, Y (black solid line, equation 82), and Hall terms, H (red solid line, equation 83), are shown. The dashed line indicates a reference linear scaling. In all panels the spatial coordinates, (x, y), and the scale are normalized to the proton skin depth, d_p. Figure adapted from Vásconez et al. (2021).

panels of Figure 32 show a snapshot of each of the simulations in the fully turbulent steady state: from left to right, Hall MHD (HMHD), Landau Fluid (LF), and Hybrid Vlasov-Maxwell (HVM). Visual inspection of the current plots shows little or no evident differences among the three models, so that any difference in the diagnostics shall be included in the small-scale fine details of the fluctuations and in the coupling among the different fields. The three snapshots were analyzed using the Hall-MHD P&P law, thus using equation (81), and the resulting scaling laws are shown in the corresponding bottom panels of the same figure. The MHD and Hall terms are represented with black and red lines, respectively, while the total scaling, labeled as $-2\varepsilon_l$,

is given by the black asterisks. An approximately linear scaling of the total third-order moment is only present at scales larger than d_i, and is very similar for the three runs. The cross-scale energy transfer does not seem to depend critically on the model used for the description. However, looking at the different contributions reveals that for the two fluid models the MHD term dominates at all scales, although the two terms become closer at scales smaller than d_i. This is more evident in the LF case, where the two terms are comparable. On the other hand, in the kinetic run the Hall term becomes slightly dominant below d_i. A possible reason for this difference is that Hall effects introduce compressible activity, which is not properly captured by the incompressible form of the P&P law used here. In the LF model, and even more so in the HVM case, compressible fluctuations are suppressed by in-plane Landau damping and/or cyclotron resonances, which excite Alfvénic fluctuations, therefore transferring energy from compressible to incompressible fluctuations and enhancing the strength of the Hall contribution. After examining the local properties of the nonlinear coupling (see Section 8) and the role of the five different terms of the Hall-MHD P&P law, the authors of the study concluded that the turbulent energy transfer is similar for the three models, yet not precisely identical. This suggests the presence of a cross-scale seeding between the fluid and kinetic scales. In this sense, the turbulent cascade drives the small-scale kinetic processes, but at the same time the kinetic processes provide feedback to the inertial range cascade to some extent, acting as dynamical dissipation. Direct evidence of the non-locality of the transfer and of an increase of both the local transfer of magnetic energy to smaller scales and of a non-local back-scatter of magnetic energy to large scales due to the Hall effect, were provided in Mininni et al. (2007). These authors have shown how Hall currents have an impact on the coupling between magnetic and velocity fields, emphasizing that the way energy is exchanged between them is different than in the MHD case. This behavior is explained by the fact that the Hall term modifies the nature of the non-dispersive MHD Alfvén waves into dispersive and circularly polarized waves. Consequently, the nonlinear coupling between magnetic field and velocity field is also changed. The non-local back-scatter of magnetic energy was observed at scales larger than the Hall scale, thus connecting two regimes, one involving the fluid scales and the other closer to the kinetic scales. Further studies using larger numerical simulations and more detailed descriptors of the cascade (e.g. including compressive effects, see next subsection) will be required to understand in depth the observed differences. However, this

preliminary result illustrates the powerful diagnostic capacities of the exact third-order scaling laws in the complex realm of weakly collisional plasma turbulence.

5.5. Towards a major challenge: relaxing the incompressibility hypothesis

The extension of the P&P law to Hall-MHD physics represents a first important step towards a generalized description of turbulence in collisionless plasmas. The subsequent and so far most challenging step is to relax the incompressibility hypothesis. This endeavour was initially performed in the frame of neutral flows, revealing the complexity of the energy budget when density fluctuations are significantly large and shocks may form. As always, and even more so in this case, extending fluid paradigms to plasmas is not at all straightforward. The intricate interplay between plasma flows and magnetic field fluctuations becomes extremely complex in the compressible case, so that the quest for a valid formulation of the compressible Hall MHD third-order moment exact law, suitable for the validation in space plasmas, is still ongoing. Here we propose a brief overview of the initial steps undertaken in this direction, presenting the two most interesting versions of the third-order scaling law for MHD plasmas available to date. Examples from both numerical simulations and spacecraft data will be used to illustrate the effects of compressibility on the global energy budget of the turbulent cascade in plasmas as seen with this approach, issues of the model equations presented will be pointed out.

5.5.1. Compressible MHD: a phenomenological approach

The initial approach to compressible fluctuations in plasma turbulence was attempted using a simple phenomenological argument. This was stimulated by an early model for three-dimensional compressible turbulence, where the intermittent, scale-invariant hierarchy of density fluctuations was described using a geometrical compression coefficient (von Weizsäcker, 1951). In this scenario, since the density fluctuations would admit scaling laws, Lighthill (1955) proposed to use the fact that, if the flow is compressible, the energy transfer rate per volume rather than per mass unit will be constant. This concept was introduced by coupling the density fluctuations to the velocity fluctuations when phenomenologically estimating the time derivative of the kinetic energy, $(\rho v^2)v/\ell$, so that the scaling law describing such fluctuations becomes $v\rho^{1/3} \sim \ell$. Using the arguments above, Fleck (1996) derived a complete Kolmogorov-like phenomenology for spectra and structure functions

of compressible hydrodynamic turbulence, including the description of intermittency. These relations were eventually adapted to MHD, and validated using high-resolution numerical simulations of three-dimensional, compressible MHD (Kowal and Lazarian, 2007; Kritsuk et al., 2007). Carbone et al. (2009a) used the same heuristic argument proposed by Lighthill (1955) to obtain an adaptation of the P&P law to compressible plasmas. In particular, by introducing density-weighted Elsasser variables, defined as $\mathbf{w}^{\pm} = \rho^{1/3}\mathbf{z}^{\pm}$, an equivalent phenomenological compressible version of the P&P law, yet intended for the MHD, was obtained

$$W^{\pm}(\ell) = \langle |\Delta \mathbf{w}^{\pm}|^2 \Delta w_{\parallel}^{\mp} \rangle \langle \rho \rangle^{-1} = -\frac{4}{3}\varepsilon^{\pm}\ell \,. \tag{86}$$

Despite its purely phenomenological nature, thus its intrinsically approximated character, equation (86), hereafter C09, was used to estimate the compressible energy transfer rate in solar wind data. The same Ulysses measurements of fast, polar solar wind as in Sorriso-Valvo et al. (2007) were used, again split in 11-day sub-intervals. The top panel of Figure 33 shows a comparison of the scaling in the standard incompressible (P&P law) version, and in the phenomenological compressible version, C09, in one of the samples. The compressible version reveals a good linear scaling over a broad inertial range, and a remarkable increase in the mean energy transfer rate estimated from the Ulysses data-set. It was reported that the fraction of samples presenting a linear scaling of the third order increased considerably (from roughly 25% to 33%), showing that the compressible correction, although only approximate, increases the probability to observe a scaling of the third-order moment. The bottom panel of Figure 33 shows the radial evolution of the measured energy transfer rate for the compressible (red full squares for ε^{+}, blue open squares for ε^{-}) and for the incompressible (green full circles for ε_I^{+}, violet open circles for ε_I^{-}) cases. The enhancement observed when including the compressible contribution is evident.

5.5.2. Compressible MHD and Hall MHD: isothermal closure

The phenomenological attempt to include compressive effects described above stimulated efforts for a derivation of exact laws for the description of compressible MHD, and later of compressible Hall MHD. Some of these efforts were based, in different measure, upon analogous works in neutral fluid turbulence (see, e.g., Aluie, 2011, 2013; Eyink and Drivas, 2018; Lai et al., 2018). Here we will not give a strictly chronological description of the

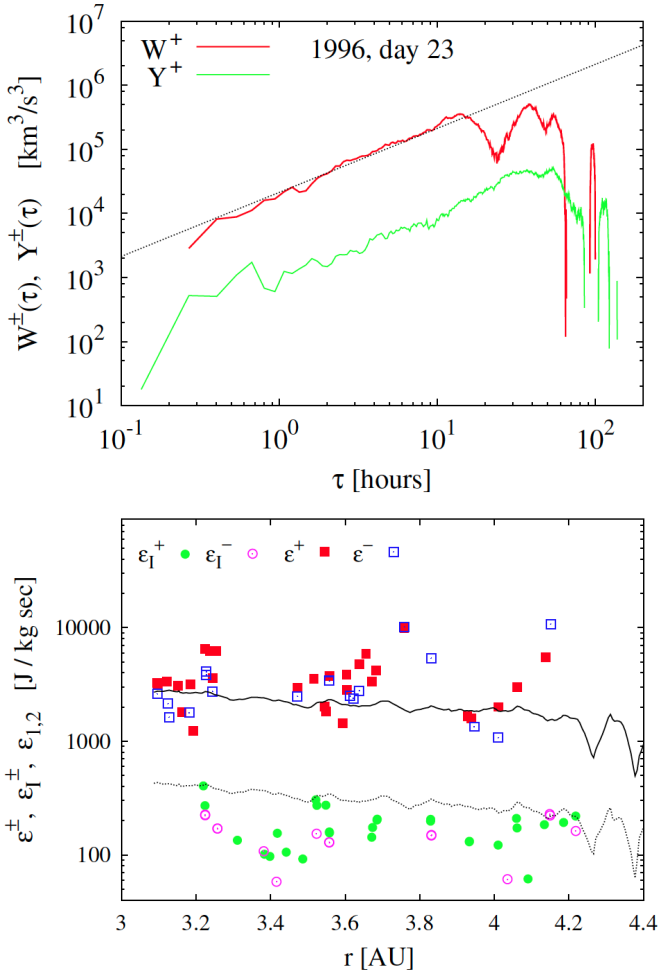

Figure 33: Top panel: scaling of the third-order law for a 11-day interval of Ulysses measurements in the polar solar wind, for the incompressible (PP, Y^+, green line) and compressible (C09, W^+, red line) versions. The dashed black line indicates the linear fit for the compressible case. Bottom panel: the radial evolution of the energy transfer rate obtained using 6 months of Ulysses data. Red, full squares indicate the compressible ε^+, blue open squares the compressible ε^-, green, full circles indicate the incompressible (PP) version ε_I^+, and violet, open circles ε_I^-. The two full and dashed lines indicate the two estimates of the modeled heating rate (equation 64, Vasquez et al., 2008), obtained using the two different dataset of plasma temperature provided by Ulysses, see Section 4.3. Figure from Carbone et al. (2009a).

various works, all useful and functional to reach the most recent and updated

forms. Instead, we will briefly describe the logic of the derivation of some of the forms, including approximated forms that have been largely used to study space plasmas turbulence, and we will finish with the most complete equation, which, as a matter of fact, is not fully suitable for single-probe time series analysis.

As in the case of Hall MHD, the endeavour was initiated by Galtier and Banerjee (2011), who approached compressible hydrodynamics and set the basis of the general derivation the third-order moment scaling law. This was promptly followed by the extension to compressible MHD (Banerjee and Galtier, 2013). These authors addressed the specific case of isothermal turbulence (see also Banerjee and Galtier, 2014), a common assumption in numerical studies of interstellar plasma turbulence (see, e.g, Kritsuk et al., 2007). The same approach was later revisited (Galtier, 2016; Andrés and Sahraoui, 2017) and extended to Hall MHD (Andrés et al., 2018; Andrés et al., 2018; Ferrand et al., 2021a). Here we go through the compressible Hall MHD version presented by Andrés et al. (2018), since the purely MHD versions (e.g., Banerjee and Galtier, 2013) can then be easily obtained by suppressing the Hall terms. For the sake of completeness, we report the set of the compressible MHD equations

$$\frac{\partial \rho}{\partial t} + \boldsymbol{\nabla} \cdot (\rho \mathbf{v}) = 0 \tag{87}$$

$$\begin{aligned} \rho \left(\frac{\partial \mathbf{v}}{\partial t} + (\mathbf{v} \cdot \boldsymbol{\nabla}) \mathbf{v} \right) &= -\boldsymbol{\nabla} P_{tot} + \frac{(\mathbf{B} \cdot \boldsymbol{\nabla})\, \mathbf{B}}{4\pi} + \eta \nabla^2 \mathbf{v} \\ &+ \left(\frac{\eta}{3} + \xi \right) \boldsymbol{\nabla} (\boldsymbol{\nabla} \cdot \mathbf{v}) \end{aligned} \tag{88}$$

$$\frac{\partial \mathbf{B}}{\partial t} = \boldsymbol{\nabla} \times (\mathbf{v} \times \mathbf{B}) + \frac{c^2}{4\pi\sigma} \nabla^2 \mathbf{B}\,, \tag{89}$$

σ being the conductivity, η the absolute viscosity and $P_{tot} = (P + \frac{B^2}{8\pi})$ the total (kinetic and magnetic) pressure. Assuming the isothermal closure, the pressure term in equation (88) can be written as $P = c_s^2 \rho$, where $c_s^2 = k_B T_i / m_i$ is the (constant) ion sound speed at constant mass density $\rho_0 = n_0 m_i$. The work is then $dW = PdV = -mc_s^2 d\rho/\rho$, which can be integrated to give the variation in internal energy associated with the work done by pressure forces, $e = c_s^2 \ln(\rho/\rho_0)$. This corresponds to neglecting the heat associated with entropy variations, a fair assumption when dissipation is negligible. With this assumption, the total energy reads $E_{tot} = \rho/2[v^2 + B^2/(4\pi\rho) + 2e]$, the last term representing the internal compressible energy for an isothermal plasma.

Note that Ferrand et al. (2021a) derivation also uses the isothermal description of the pressure term. However, explicit internal energy terms disappear in the fully developed turbulence regime and do not appear in the final exact relation.

Without dwelling in the details of the complex derivation of the isothermal version, we simply remind that it starts from the above definition of total energy and follows similar steps as for the cases already described (for a detailed description of the derivation see Andrés et al., 2018). The derivation uses the two-point correlator associated to the total energy, which in the notation of Ferrand et al. (2022) is $R_E = (\rho/2)(\mathbf{v}\cdot\mathbf{v}' + \mathbf{v}_A\cdot\mathbf{v}'_A + \rho e')$, and after lengthy and nontrivial calculation leads to the third-order moment equation for compressible, isothermal Hall MHD:

$$
\begin{aligned}
-2\varepsilon &= \frac{1}{2}\boldsymbol{\nabla}_{\boldsymbol{\ell}}\cdot\big\langle[\Delta(\rho\mathbf{v})\cdot\Delta\mathbf{v} + \Delta(\rho\mathbf{v}_A)\cdot\Delta\mathbf{v}_A + 2\Delta e\Delta\rho]\Delta\mathbf{v} \\
&- [\Delta(\rho\mathbf{v})\cdot\Delta\mathbf{v}_A + \Delta\mathbf{v}\cdot\Delta(\rho\mathbf{v}_A)]\Delta\mathbf{v}_A\big\rangle \\
&+ \left\langle\left[R'_E - \frac{1}{2}(R'_B + R_B) + \frac{1}{2}(P'_M - P') - E'_{tot}\right](\boldsymbol{\nabla}\cdot\mathbf{v})\right\rangle \\
&+ \left\langle\left[R_E - \frac{1}{2}(R'_B + R_B) + \frac{1}{2}(P_M - P) - E_{tot}\right](\boldsymbol{\nabla}'\cdot\mathbf{v}')\right\rangle \\
&+ \left\langle\left[(R_H - R'_H) - \overline{\rho}(\mathbf{v}'\cdot\mathbf{v}_A) + H' + \frac{\lambda}{2}\Delta\rho(\mathbf{J}_c\cdot\mathbf{v}'_A)\right](\boldsymbol{\nabla}\cdot\mathbf{v}_A)\right\rangle \\
&+ \left\langle\left[(R'_H - R_H) - \overline{\rho}(\mathbf{v}\cdot\mathbf{v}'_A) + H - \frac{\lambda}{2}\Delta\rho(\mathbf{J}'_c\cdot\mathbf{v}_A)\right](\boldsymbol{\nabla}'\cdot\mathbf{v}'_A)\right\rangle \\
&+ \frac{1}{2}\left\langle\left(e' + \frac{v'^2_A}{2}\right)[\boldsymbol{\nabla}\cdot(\rho\mathbf{v})] + \left(e + \frac{v^2_A}{2}\right)[\boldsymbol{\nabla}'\cdot(\rho'\mathbf{v}')]\right\rangle \\
&- \frac{1}{2}\big\langle\beta^{-1'}\boldsymbol{\nabla}'\cdot(e'\rho\mathbf{v}) + \beta^{-1}\boldsymbol{\nabla}\cdot(e\rho'\mathbf{v}')\big\rangle \\
&+ \frac{1}{2}\boldsymbol{\nabla}_{\boldsymbol{\ell}}\cdot\big\langle 2\lambda[(\overline{\rho\mathbf{J}_c\times\mathbf{v}_A})\times\Delta\mathbf{v}_A - \Delta(\mathbf{J}_c\times\mathbf{v}_A)\times\overline{\rho\mathbf{v}_A}]\big\rangle \\
&+ \frac{\lambda}{2}\big\langle(R_B - R'_B)(\boldsymbol{\nabla}\cdot\mathbf{J}_c) + (R'_B - R_B)(\boldsymbol{\nabla}'\cdot\mathbf{J}'_c)\big\rangle\,. \qquad (90)
\end{aligned}
$$

Over-lined quantities indicates the two-points average of a variable ψ at scale $\boldsymbol{\ell}$, $\overline{\psi} = [\psi(\mathbf{x}+\boldsymbol{\ell}) + \psi(\mathbf{x})]/2$, $\mathbf{J}_c = \mathbf{J}/\rho$ is the normalized current, $H = \rho(\mathbf{v}\cdot\mathbf{v}_A)$

is the local cross-helicity, $R_H = (\rho/2)(\mathbf{v}\cdot\mathbf{v}'_A + \mathbf{v}'\cdot\mathbf{v}_A)$ the associated two-point correlator, $R_B = (\rho/2)(\mathbf{v}_A\cdot\mathbf{v}'_A)$ the magnetic two-point correlator, $\beta = 2c_s^2/v_A^2$ the usual kinetic-to-magnetic pressure ratio, and $\lambda = m_i/q_e$ is the ratio between the ion mass, m_i, and the electron charge, q_e. If various terms representing different physical contributions are grouped together, the above equation can be recast in a compact form as follows:

$$-2\varepsilon = \frac{1}{2}\boldsymbol{\nabla}_{\boldsymbol{\ell}}\cdot(\boldsymbol{\mathcal{F}}^{\rm MHD}+\lambda\boldsymbol{\mathcal{F}}^{\rm HMHD})+(\mathcal{S}^{\rm MHD}+\lambda\mathcal{S}^{\rm HMHD})+\mathcal{H}^{\rm MHD}+\mathcal{M}_\beta^{\rm MHD}\,. \quad (91)$$

The six terms in the right-hand side of equation (91) include:

- a purely MHD flux term, $\boldsymbol{\mathcal{F}}^{\rm MHD}$, which represents the compressible extension of the standard MHD scaling law and that appears as local divergence of two-points increments:

$$\begin{aligned}\boldsymbol{\mathcal{F}}^{\rm MHD} &= \big\langle[\Delta(\rho\mathbf{v})\cdot\Delta\mathbf{v}+\Delta(\rho\mathbf{v}_A)\cdot\Delta\mathbf{v}_A+2\Delta e\Delta\rho]\Delta\mathbf{v}\\ &- [\Delta(\rho\mathbf{v})\cdot\Delta\mathbf{v}_A+\Delta\mathbf{v}\cdot\Delta(\rho\mathbf{v}_A)]\Delta\mathbf{v}_A\big\rangle\,; \end{aligned} \quad (92)$$

- a flux term representing the Hall contributions, $\boldsymbol{\mathcal{F}}^{\rm HMHD}$, which, as the MHD one, can be expressed as divergence of fields increments and vector products (Banerjee and Galtier, 2013):

$$\begin{aligned}\boldsymbol{\mathcal{F}}^{\rm HMHD} &= 2\big\langle\overline{\rho}[(\mathbf{J}_c\times\mathbf{v}_A)\times\Delta\mathbf{v}'_A-(\mathbf{J}'_c\times\mathbf{v}'_A)\times\Delta\mathbf{v}_A]\\ &+ 2[\overline{(\rho\mathbf{J}_c\times\mathbf{v}_A)}\times\Delta\mathbf{v}_A-\Delta(\mathbf{J}_c\times\mathbf{v}_A)\times\overline{\rho\mathbf{v}_A}]\big\rangle\,; \end{aligned} \quad (93)$$

- a MHD source term, $\mathcal{S}^{\rm MHD}$, accounting for dilatation and compression of the plasma, which is proportional to the divergence of the MHD fields and cannot be expressed as divergence of increments (therefore requiring multi-spacecraft measurements for its evaluation),

$$\begin{aligned}\mathcal{S}^{\rm MHD} &= \left\langle\left[R'_E-\frac{1}{2}(R'_B+R_B)\right](\boldsymbol{\nabla}\cdot\mathbf{v})\right\rangle\\ &+ \left\langle\left[R_E-\frac{1}{2}(R'_B+R_B)\right](\boldsymbol{\nabla}'\cdot\mathbf{v}')\right\rangle\\ &+ \big\langle[(R_H-R'_H)-\overline{\rho}(\mathbf{v}'\cdot\mathbf{v}_A)]\,(\boldsymbol{\nabla}\cdot\mathbf{v}_A)\big\rangle\\ &+ \big\langle[(R'_H-R_H)-\overline{\rho}(\mathbf{v}\cdot\mathbf{v}'_A)]\,(\boldsymbol{\nabla}'\cdot\mathbf{v}'_A)\big\rangle\,; \end{aligned} \quad (94)$$

- a similar purely Hall-MHD source term, $\mathcal{S}^{\rm HMHD}$, again not simply expressed as divergence of increments,

$$\begin{aligned}\mathcal{S}^{\rm HMHD} &= \frac{1}{2}\big\langle \Delta\rho(\mathbf{J}_c\cdot\mathbf{v}_A)(\boldsymbol{\nabla}\cdot\mathbf{v}'_A) - \Delta\rho(\mathbf{J}'_c\cdot\mathbf{v}_A)(\boldsymbol{\nabla}'\cdot\mathbf{v}'_A)\big\rangle \\ &+ \big\langle (R_B - R'_B)(\boldsymbol{\nabla}\cdot\mathbf{J}_c) + (R'_B - R_B)(\boldsymbol{\nabla}'\cdot\mathbf{J}'_c)\big\rangle\,; \end{aligned} \tag{95}$$

- a hybrid term, $\mathcal{H}^{\rm MHD}$, which provides pressure gradients, cross-helicity, and internal energy contributions, and include both source and flux terms,

$$\begin{aligned}\mathcal{H}^{\rm MHD} &= \frac{1}{2}\big\langle [(P'_M - P') - 2E'_{tot}]\,(\boldsymbol{\nabla}\cdot\mathbf{v}) + [(P_M - P) - 2E_{tot}]\,(\boldsymbol{\nabla}'\cdot\mathbf{v}')\big\rangle \\ &+ \frac{1}{2}\left\langle \left(e' + \frac{v'^2_A}{2}\right)[\boldsymbol{\nabla}\cdot(\rho\mathbf{v})] + \left(e + \frac{v^2_A}{2}\right)[\boldsymbol{\nabla}'\cdot(\rho'\mathbf{v}')]\right\rangle \\ &+ \big\langle H'(\boldsymbol{\nabla}\cdot\mathbf{v}_A) + H(\boldsymbol{\nabla}'\cdot\mathbf{v}'_A)\big\rangle\,; \end{aligned} \tag{96}$$

- and finally a plasma-β-dependent term, $\mathcal{M}^{\rm MHD}_\beta$, which accounts for effects of the magnetic pressure gradients, and cannot be easily transformed into simple flux or source terms,

$$\mathcal{M}^{\rm MHD}_\beta = -\frac{1}{2}\big\langle \beta^{-1\prime}\boldsymbol{\nabla}'\cdot(e'\rho\mathbf{v}) + \beta^{-1}\boldsymbol{\nabla}\cdot(e\rho'\mathbf{v}')\big\rangle\,. \tag{97}$$

In addition to the above terms, Ferrand et al. (2022) pointed out that, when relaxing the assumptions of stationarity and large Reynolds number (corresponding to sufficient scale separation as to ignore the forcing and dissipative terms), equation (90) can be extended to include a dissipative term, $\mathcal{D}$, and a forcing term, $\mathcal{F}$, whose expressions read:

$$\begin{aligned}\mathcal{D} = &- \frac{1}{2}\big\langle [1 + (\rho/\rho')]\,\mathbf{v}'\cdot\mathbf{d}_\nu + [1 + (\rho'/\rho)]\,\mathbf{v}\cdot\mathbf{d}'_\nu\big\rangle \\ &- \frac{1}{2}\big\langle \left[(\rho/\rho')^{1/2} + (\rho'/\rho)^{1/2}\right](\mathbf{b}\cdot\mathbf{d}'_\eta + \mathbf{b}'\cdot\mathbf{d}_\eta)\big\rangle \end{aligned} \tag{98}$$

$$\mathcal{F} = - \frac{1}{2}\big\langle [1 + (\rho/\rho')]\,\mathbf{v}'\cdot\mathbf{f} + [1 + (\rho'/\rho)]\,\mathbf{v}\cdot\mathbf{f}'\big\rangle\,, \tag{99}$$

where $\mathbf{d}_\nu$, $\mathbf{d}_\eta$, $\mathbf{f}$ represent respectively kinetic dissipation, resistive dissipation, and forcing terms in the Hall-MHD equations.

It was shown in several works that the compressible MHD equations (Banerjee and Galtier, 2013, 2017) can be simply obtained suppressing the Hall terms in equation (91). We will not give the explicit equations here.

The reader should keep in mind that the major underlying isothermal assumption is in evident disagreement with the highly fluctuating temperature of the out-of-equilibrium space plasmas. The isothermal closure used to simplify the effect of pressure-dilation contributions may not generally apply to space plasmas. As pointed out by Hellinger et al. (2021a), at MHD and Hall-MHD scales there are no net exchanges between internal energy and total energy (intended as kinetic plus magnetic), so that inclusion of an internal-energy related term may be questionable and unnecessary. Moreover, how the scale redistribution of the internal energy and its exchange with mechanic energy can be described by structure functions, and if and how it affects the plasma heating rate, are not straightforward problems (Hellinger et al., 2021b).

In light of these considerations, we should bear in mind that the isothermal version must be considered as an approximation that uses some degree of modeling. Nevertheless, such version can provide a useful characterization of the turbulent cascade in space plasmas, where more complete and model-free descriptions are not successfully estimated yet. Furthermore, the equation derived by Andrés et al. (2018) is complex and include a large number of terms, whose role in not always easy to interpret in terms of the underlying physical mechanisms. It is formally equivalent to the simpler descriptions given by Hellinger et al. (2021a) and Ferrand et al. (2021a) (see below), and in case of fully dimensional numerical simulations all the terms can in principle be evaluated. However, the limitations of using the complete equation (91) for space data are obvious. Even in the presence of multi-spacecraft missions that enable estimates of vector gradients and cross-products, it is expected that instrumental noise and gradient computation uncertainties could affect the total energy budget in ways that might not be easy to estimate. Nevertheless, as we shall see in the following, not all terms are expected to carry significant contributions, in which case approximations can be done to mitigate the noise issues.

5.5.3. Isothermal compressible MHD and Hall MHD: numerical simulations

The validity and equivalence of various isothermal versions of the exact law for compressible MHD and Hall MHD were tested thoroughly with numerical simulations. Andrés et al. (2018) used various three-dimensional

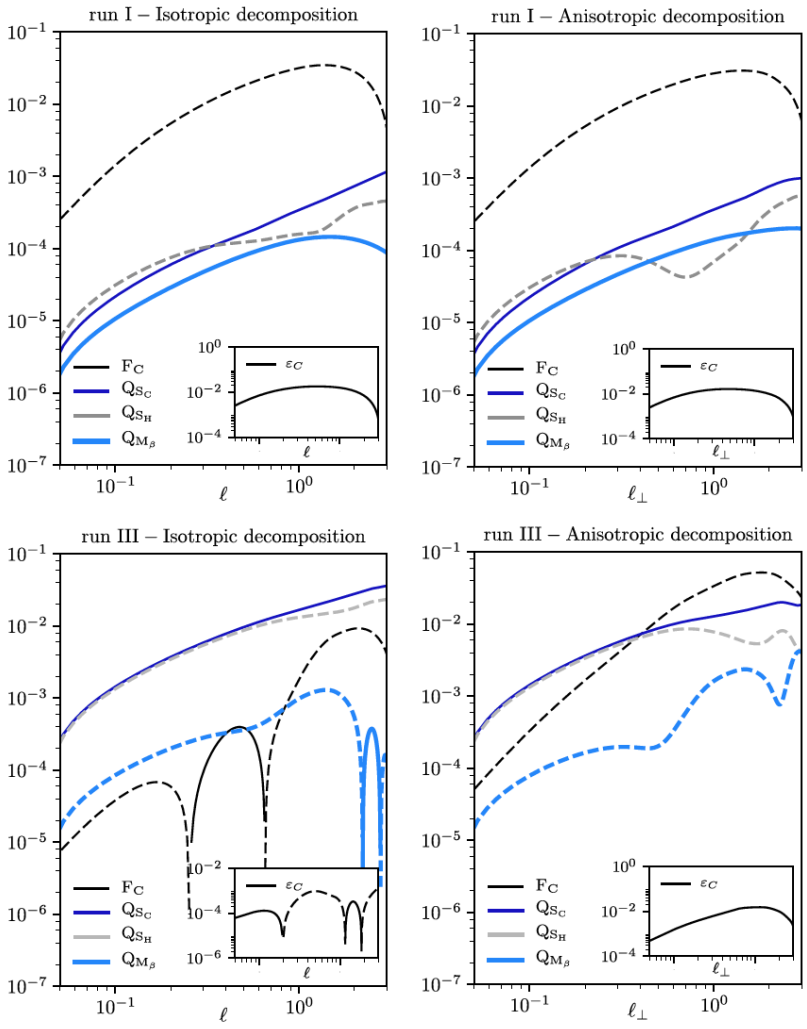

Figure 34: Isotropic (left panels) and anisotropic (right panels) scaling of the compressible MHD energy transfer rate, equation (91), for run I (top panels) and run III (bottom panels). Different colors (see legend) indicate contributions from different terms: the MHD flux term $F_C \equiv \mathcal{F}^{MHD}$, equation (92), the MHD source term, $Q_{S_C} \equiv \mathcal{S}^{MHD}$, equation (94), the MHD hybrid term, $Q_{S_H} \equiv \mathcal{H}^{MHD}$, equation (96), and the MHD plasma β related term, $Q_{M_\beta} \equiv \mathcal{M}_\beta^{MHD}$, equation (97). Full (dashed) lines indicate positive (negative) scaling. The inset shows the total transfer rate, ε_C, equation (91). The dimensionless scale, ℓ, spans from the grid size, $2\pi/512$, up to the simulation box size, 2π, is shown in a slightly reduced range. Figure from Andrés et al. (2018).

(512^3) compressible MHD numerical simulations (Mininni et al., 2011b) to validate the compressible MHD exact law (Andrés and Sahraoui, 2017), obtained suppressing the Hall terms in equation (91). The simulations are driven with random, uncorrelated force, and an external magnetic field, B_0, can be imposed in the z direction. Two different projections were used to estimate the two-point increments of the fields. An isotropic estimate was obtained using the SO(3) decomposition of the simulation field (Taylor et al., 2003), and then averaging over all possible angles (in the specific case, 73 directions were identified). This procedure gives an isotropic law that depends only on the scale, ℓ. Since the introduction of an external magnetic field likely produces anisotropy in the turbulence (Biskamp, 1993), an anisotropic decomposition was also used. This was based on a SO(2) polar decomposition in the plane perpendicular to the ambient magnetic field, and a translation (R) decomposition in the field direction. The resulting third-order moments can therefore be estimated separately in the field direction, $\ell_\parallel$, and in the perpendicular plane, where they are averaged over all possible (planar) angles, $\ell_\perp$. Consequently, for each simulation the three energy transfer rates ε, $\varepsilon_\parallel$ and $\varepsilon_\perp$ were computed, in order to study the anisotropic properties of the energy flux.

The insets in the four panels of Figure 34 show the total anisotropic (perpendicular) and isotropic energy transfer rate for two runs of the simulation. In run I (top panels), where there is no external field ($B_0 = 0$), a broad inertial range (constant ε_C) is present, and the two estimates are equivalent, as expected in the absence of a preferential direction. In run III, where a strong guide field is present($B_0 = 8$), the anisotropic estimate (right panel) provides a reduced but sign-defined scaling, with similar energy transfer rate as in the isotropic case. However, the isotropic estimate gives a non converging scaling, with several sign changes at different scales, likely artificially arising because of the isotropic assumption. The breakdown of the contributions from the flux term, F_C, from the source term, Q_{S_C}, from the hybrid term, Q_{S_H}, and from the β-dependent term, Q_{M_β}, reveals that the source term largely dominates when no external field is present. In run III, according to the isotropic description the source and hybrid terms, which are opposite in sign, are of the same order and dominating, so that their difference determines the alternating sign of the energy transfer. In the anisotropic description, the flux term dominates at large scales, where the linear scaling is actually observed. This observation shows that the compressible law is able to capture the energy transfer in compressible MHD turbulence, but

also that using isotropy in a strongly anisotropic medium can result in erroneous estimates. The analysis then turns to the sub-terms of each of the four terms described in Figure 34. Here we briefly mention the result about the flux sub-terms, which are relevant to spacecraft data (the source terms being hard to estimate using one-dimensional time series). In particular, the flux term can be separated in three contributions, $F_C \equiv \boldsymbol{\mathcal{F}}^{\rm MHD} = F_{1a} + F_{1b} + F_2$, where

$$F_{1a} \equiv F_v = \langle [\Delta(\rho \mathbf{v}) \cdot \Delta \mathbf{v} + \Delta(\rho \mathbf{v}_A) \cdot \Delta \mathbf{v}_A] \Delta \mathbf{v} \rangle \quad (100)$$

$$F_{1b} \equiv F_b = -\langle [\Delta(\rho \mathbf{v}) \cdot \Delta \mathbf{v}_A + \Delta \mathbf{v} \cdot \Delta(\rho \mathbf{v}_A)] \Delta \mathbf{v}_A \rangle \quad (101)$$

$$F_2 \equiv F_e = 2 \langle \Delta e \Delta \rho \Delta \mathbf{v} \rangle \quad (102)$$

are the velocity-gradient related contribution, the magnetic-gradient related contribution, and internal energy contribution, respectively. Figure 35 shows

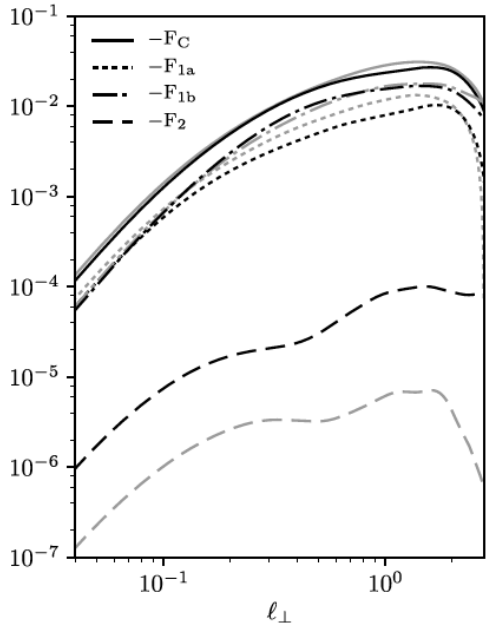

Figure 35: For two isotropic runs (run I, black, and run IV, grey), the total MHD flux term, $F_C \equiv \mathcal{F}^{MHD}$, equation (92), and its breakdown in the flux sub-terms F_{1a}, F_{1b}, F_2, equations (100-102). Figure from Andrés et al. (2018). The dimensionless scale, ℓ, spans from the grid size, $2\pi/512$, up to the simulation box size, 2π, is shown in a slightly reduced range.

the breakdown of the flux term in the above contributions, for two isotropic

runs (run I in black and run IV, having no external field and higher level of compressibility, in grey). The internal energy sub-term is clearly subdominant with respect to the kinetic and magnetic sub-terms, suggesting that the role of the energy exchange does not affect the energy transfer associated with the turbulent cascade. More comments on this point will be given in the next subsection.

A thorough description of the compressible Hall MHD scaling law in numerical simulations was given by Ferrand et al. (2022), who also discussed the comparison between the two isothermal forms given by Andrés et al. (2018) and Ferrand et al. (2021a) (the latter, not presented in this review, is formally similar to the case that will be discussed in Section 5.5.4, but with the additional assumption of isothermal plasma). The two versions provided the same results, confirming that, despite some differences in their derivation, the two expressions correctly describe the same physical processes. One additional conclusion of this study concerned the role of non-stationarity, approached by including time derivatives of the total energy, namely relaxing the time stationarity hypothesis (see a similar approach in Hellinger et al., 2021a). Figure 36 shows an example of comparison among the energy transfer rate of the isothermal compressible Hall MHD model obtained using the derivation by Andrés et al. (2018) (red line), the complete time derivative of the two-point correlator, defined as described in Ferrand et al. (2021a) (brown line), the purely dissipative term (pink line, see Ferrand et al., 2021a) and the sum of these (black line). The latter is hence a measure of the error introduced by neglecting the non-stationary effects. The analysis of numerical simulations allowed to conclude that even in the absence of an external forcing (in decaying turbulence case) non-stationarity can be seen as a scale-dependent reservoir of energy. Such energy is either injected in the turbulent cascade (at larger scales) or also directly dissipated (at smaller scales). The error in neglecting the non-stationary terms was evaluated to be negligible in the simulations. These results confirm that, in the inertial range, the exact scaling laws, which are usually valid under the assumption of time stationarity, remain valid for decaying turbulence. This is an important confirmation for the study of completely or partially decaying systems, such as the the expanding solar wind (Sorriso-Valvo et al., 2022).

5.5.4. Compressible Hall MHD: a complete description

In two companion papers, Hellinger et al. (2021b,a) provided a thorough description of the procedure used to obtain the full von Kármán-Howarth-

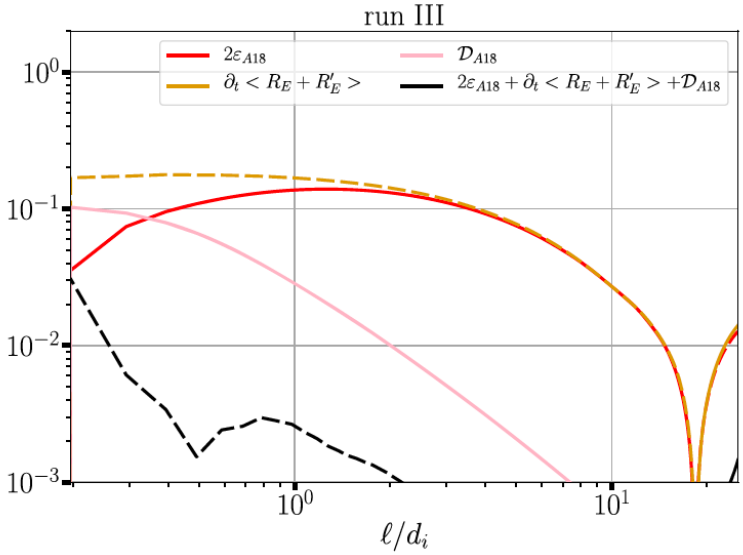

Figure 36: Comparison between the energy transfer rate of the isothermal compressible Hall MHD model, $2\varepsilon_{A18}$ (red line, equation 91, see Andrés et al., 2018), the complete time derivative of the two-point correlator, $\partial_t\langle R_E + R'_E\rangle$ (brown line, see described in Section 5.5.2, Ferrand et al., 2021a), the dissipation term, $\mathcal{D}_{A18}$ (pink line, equation 98, see Ferrand et al., 2021a) and the sum of these (black line). Solid and dashed lines refer to positive and negative values, respectively. The scale, ℓ, is normalized to the ion inertial scale, d_i. Figure from Ferrand et al. (2022).

Monin (KHM) equation for hydrodynamic and Hall magnetohydrodynamic turbulence. The same approach was used independently in the isothermal approximation by Ferrand et al. (2021a), who obtained a similar relation. Using the same notation as in Hellinger et al. (2021a), the compressible Hall MHD equations can be written as follows:

$$\frac{\partial \rho}{\partial t} + (\mathbf{u}\cdot\boldsymbol{\nabla})\rho = -\rho\boldsymbol{\nabla}\cdot\mathbf{u} \tag{103}$$

$$\rho\frac{\partial \mathbf{u}}{\partial t} + \rho(\mathbf{u}\cdot\boldsymbol{\nabla})\mathbf{u} = (\boldsymbol{\nabla}\times\mathbf{B})\times\mathbf{B} - \boldsymbol{\nabla}p + \boldsymbol{\nabla}\cdot\boldsymbol{\tau} \tag{104}$$

$$\frac{\partial \mathbf{B}}{\partial t} = \boldsymbol{\nabla}\times[(\mathbf{u}-\mathbf{j})\times\mathbf{B}] + \eta\nabla^2\mathbf{B}\,, \tag{105}$$

where $\boldsymbol{\tau}$ is the viscous stress tensor of components $\tau_{ij} = \mu(\partial u_i/\partial x_j + \partial u_j/\partial x_i - 2/3\delta_{ij}\partial u_k/\partial x_k)$, η is the dynamic viscosity, $\mathbf{j} = \mathbf{J}/\rho_c = \mathbf{u} - \mathbf{u}_e$ is the electric current density in velocity units, ρ_c the charge density and $\mathbf{u}_e$ the electron ve-

locity, and the magnetic permeability μ_0 is set to 1. Introducing the density-weighed velocity $\mathbf{w} = \rho^{1/2}\mathbf{u}$ (see, e.g., Kida and Orszag, 1990; Aluie, 2013), it is possible to write the evolution equations for the sum of the second-order magnetic and kinetic structure functions, $\mathcal{S}_w = \langle|\Delta\mathbf{w}|^2\rangle$ and $\mathcal{S}_B = \langle|\Delta\mathbf{B}|^2\rangle$, namely for the total structure function $\mathcal{S} = \mathcal{S}_w + \mathcal{S}_B$. The latter allows to obtain a dynamic KHM equation, as is briefly described below. Note that in this formulation the weight factor is $\rho^{1/2}$, which is consistent with the definition of the kinetic energy using the second-order structure function of $\mathbf{w}$, as opposed to the $\rho^{1/3}$ used in the phenomenological approach described in Section 5.5.1 (Carbone et al., 2009a; Marino et al., 2011).

Following the usual procedure of subtracting the dynamical equations for velocity and magnetic field (equations 104 and 105) written at two points in space (say $\mathbf{x}$ and $\mathbf{x}'$, whose vector difference defines the increment scale $\boldsymbol{\ell}$), then summing the two equations, using statistical homogeneity, and finally performing substantial manipulation, allows one to obtain the KHM equation for compressible Hall MHD (for the details of the derivation, see Hellinger et al., 2021a):

$$\frac{\partial\mathcal{S}}{\partial t} + \boldsymbol{\nabla}\cdot(\mathcal{Y}+\mathcal{H}) + \mathcal{R} = \mathcal{C} + 2\langle\Delta\theta\Delta p\rangle - 2\langle\Delta\boldsymbol{\Sigma} : \Delta\boldsymbol{\tau}\rangle - 4Q_\eta + 2\eta\nabla^2_{\boldsymbol{\ell}}\mathcal{S}_B\,. \quad (106)$$

In the above equation, $\theta = \boldsymbol{\nabla}\cdot\mathbf{u}$ is the plasma dilatation, $\boldsymbol{\Sigma} = \boldsymbol{\nabla}\mathbf{u}$ indicates the usual stress tensor, and the Laplacian $\nabla^2_{\boldsymbol{\ell}}$ is intended along the separation vector $\boldsymbol{\ell}$. The two flux terms,

$$\mathcal{Y} = \langle\Delta\mathbf{u}(|\Delta\mathbf{w}|^2 + |\Delta\mathbf{B}|^2) - 2\Delta\mathbf{B}(\mathbf{u}\cdot\mathbf{B})\rangle \quad (107)$$

and

$$\mathcal{H} = \langle\Delta\mathbf{B}(\Delta\mathbf{j}\cdot\Delta\mathbf{B}) - (1/2)\Delta\mathbf{j}|\mathbf{B}|^2\rangle\,, \quad (108)$$

are the analogous of the usual MHD and Hall contributions to the energy transfer rate, with the only difference of introducing the density-weighted kinetic energy accounting for density fluctuations. The fluid source term

$$\mathcal{R} = \langle\Delta\mathbf{w}\cdot(\theta'\mathbf{w} - \theta\mathbf{w}')\rangle\,, \quad (109)$$

where the primed variables are estimated at $\mathbf{x}'$, explicitly contains the two-point variation of the dilatation or compression, θ, and represents therefore a purely compressible contribution to the energy transfer rate. This term obviously vanishes in the incompressible limit, where $\theta = 0$. The remaining

source and flux terms that depend explicitly of the density, and are therefore compressible in nature, can be collected in one single term, which the authors call correction term. A relatively compact form can be written by introducing the density correction operator $C_\rho[\mathbf{a},\mathbf{b}] = \langle(\rho'/\rho - 1)\mathbf{a}'\cdot\mathbf{b} + (\rho/\rho' - 1)\mathbf{a}\cdot\mathbf{b}'\rangle$, where $\mathbf{a}$ and $\mathbf{b}$ are generic vectors. Note that for constant density the operator C_ρ is identically zero, so that the correction term vanishes in the incompressible limit. With this notation, the correction term,

$$\mathcal{C} = 2C_{\sqrt{\rho}}[\mathbf{u},\boldsymbol{\nabla}p] - 2C_{\sqrt{\rho}}[\mathbf{u},\boldsymbol{\nabla}\cdot\boldsymbol{\tau}] + 2C_{\sqrt{\rho}}[\mathbf{u},\mathbf{B}\times\mathbf{J} + 2C_\rho[\mathbf{B}\times\mathbf{j},\mathbf{J}]\,,$$

includes effects of the coupling between the density fluctuations and various terms in the compressible Hall MHD equations, such as the pressure gradient, the stress tensor and the $\mathbf{J}\times\mathbf{B}$ term, which are in turn coupled to velocity, magnetic field and electric current. Finally, the remaining terms account for energy dissipation due to viscosity in the compressible case, $\langle\Delta\boldsymbol{\Sigma}:\Delta\boldsymbol{\tau}\rangle$, and resistivity, $4Q_\eta - 2\eta\nabla^2_{\boldsymbol{\ell}}\mathcal{S}_B$, where $4Q_\eta = \eta\langle|\mathbf{J}|^2\rangle$.

Equation (106) is the most general version of the KHM relation for compressible Hall MHD turbulence, and is written in terms of divergences of third-order structure functions, which in principle does not require isotropy, stationary steady state or negligible dissipation. However, while the above form is complete and can be correctly computed using multi-dimensional numerical simulations, its use for single-spacecraft time series is limited by the impossibility to estimate three-dimensional derivatives, necessary to compute divergences. This can be partially approximated by replacing the full divergence with its projection along the direction of sampling, which although will require some assumptions of isotropy. We will see in the following that such approximation is only partially acceptable.

As we have briefly mentioned before, an alternative derivation for the incompressible Hall MHD exact law was obtained using the second-order structure functions instead of third-order ones. This was achieved using increments of vector products between velocity, magnetic field, vorticity and current (Banerjee and Galtier, 2017; Banerjee and Kritsuk, 2018). The same approach was then used by Hellinger et al. (2021a) to obtain a similar form for the compressible Hall MHD equations, which is formally close to equation (106):

$$\frac{\partial\mathcal{S}}{\partial t} + \tilde{\mathcal{Y}} + \tilde{\mathcal{H}} + \tilde{\mathcal{R}} = +\tilde{\mathcal{C}} + 2\langle\Delta\theta\Delta p\rangle - 2\langle\Delta\boldsymbol{\Sigma}:\Delta\boldsymbol{\tau}\rangle - 4Q_\eta + 2\eta\nabla^2_{\boldsymbol{\ell}}\mathcal{S}_B\,. \quad (110)$$

In this formulation, the various terms retain the physical meaning of those

described above, but some of them, marked by a tilde, are given by the following expressions:

$$\tilde{\mathcal{Y}} = -2\langle \Delta\mathbf{w} \cdot \Delta(\mathbf{u} \times \boldsymbol{\omega}^\star)\rangle - 2\langle \Delta\mathbf{w} \cdot \Delta(\mathbf{J} \times \mathbf{B}/\sqrt{\rho})\rangle - 2\langle \Delta\mathbf{J} \times \Delta(\mathbf{u} \times \mathbf{B})\rangle$$
$$\tilde{\mathcal{H}} = 2\langle \Delta\mathbf{J} \times \Delta(\mathbf{j} \times \mathbf{B})\rangle$$
$$\tilde{\mathcal{R}} = \langle \Delta\mathbf{w} \cdot \Delta(\mathbf{w}\theta)\rangle + 2\langle \Delta\mathbf{w} \cdot \Delta[(\boldsymbol{\nabla}\mathbf{w}) \cdot \mathbf{u}]\rangle$$
$$\tilde{\mathcal{C}} = 2C_{\sqrt{\rho}}[\mathbf{u}, \boldsymbol{\nabla}p] - 2C_{\sqrt{\rho}}[\mathbf{u}, \boldsymbol{\nabla} \cdot \boldsymbol{\tau}]\,,$$

where $\boldsymbol{\omega}^\star = \boldsymbol{\nabla} \times \mathbf{w}$ is the density-weighted vorticity. The divergence does not appear in the above terms. Note, however, that still single-spacecraft time series might not provide sufficient information to estimate correctly the curl, which is necessary for the vorticity, while the current can be computed using high-resolution plasma moments for both ions and electrons, if these are available.

In order to verify the validity of the KHM relation, equation (106), a standard two-dimensional Hall-MHD high-resolution numerical simulation of decaying turbulence was used. A moderate external constant magnetic field, such that $\delta B/B_0 = 0.17$, is applied in the out-of-plane direction, and the initial conditions include low-wavenumber Alfvénic fluctuations and zero cross-helicity (for details of the numerical simulation, see Hellinger et al., 2021a). After the initial growth of nonlinear interactions, a clear transition to turbulence is observed when current sheets start forming. The volume-averaged squared current reaches a saturation level, probably due to the onset of small-scale magnetic reconnection, so that the system reaches a steady state. The analysis was performed during the whole time evolution, in order to describe the interplay of the various terms of equation (106). Note that, for a more logical separation of the different contributions at different scales or from different general physical mechanisms, a reordering of the terms was performed. The energy variations can indeed be rewritten as the sum of a purely MHD term,

$$\mathcal{K}_{MHD} = -1/4\boldsymbol{\nabla} \cdot \mathcal{Y} - 1/4\mathcal{R} + 1/2C_{\sqrt{\rho}}[\mathbf{u}, \mathbf{B} \times \mathbf{J}]\,, \tag{111}$$

a fully Hall term,

$$\mathcal{K}_H = -1/4\boldsymbol{\nabla} \cdot \mathcal{H} + 1/4C_\rho[\mathbf{B} \times \mathbf{j}, \mathbf{J}]\,, \tag{112}$$

a pressure dilation term,

$$\Psi = 1/2\langle \Delta p \Delta\theta\rangle + 1/2C_{\sqrt{\rho}}[\mathbf{u}, \boldsymbol{\nabla}p]\,, \tag{113}$$

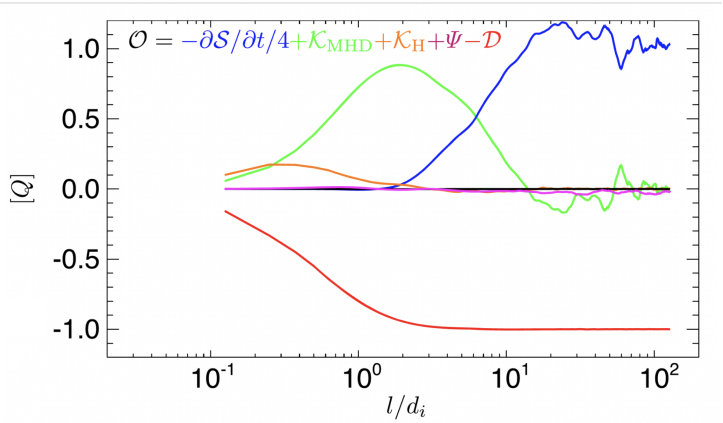

Figure 37: Scaling law of the Hall MHD third-order moment law, equation (106), from a two-dimensional simulation of the equations, generally indicated as $[Q]$. The different contributions $\mathcal{K}_{MHD}$, $\mathcal{K}_H$, Ψ and $\mathcal{D}$, defined by equations (111)-(114), are marked with colors as indicated, while their sum, $\mathcal{O}$, equation (115) is in black. The scale l is normalized to the ion inertial length d_i. All the quantities are given in units of the total heating rate, Q, defined by equation (116). Figure from Hellinger et al. (2021a).

and a dissipation term,

$$-\mathcal{D} = Q_\eta - \eta/2\nabla^2\mathcal{S}_B + 1/2\langle\Delta\boldsymbol{\tau} : \Delta\boldsymbol{\Sigma}\rangle + 1/2C_{\sqrt{\rho}}[\mathbf{u}, \boldsymbol{\nabla}\cdot\boldsymbol{\tau}]\,. \tag{114}$$

The scale-dependent behaviour of the four terms was estimated using the numerical data, and the results are shown in different colors in Figure 37. In the same figure, the black line indicates the sum of all terms (whose sum should ideally be zero),

$$\mathcal{O} = -(1/4)\partial S/\partial t + \mathcal{K}_{MHD} + \mathcal{K}_H + \Psi - \mathcal{D}\,, \tag{115}$$

which represents a validity test for the exact law. $\mathcal{O}$ is observed to be a tiny fraction ($< 0.3\%$) of the total heating rate, defined as the sum of the viscous and resistive dissipation rate,

$$Q = \langle\boldsymbol{\tau} : \boldsymbol{\Sigma}\rangle + \eta\langle|\mathbf{J}|^2\rangle\,, \tag{116}$$

demonstrating the validity of the law. The time fluctuations of the total energy provide a dominating contribution at energy containing scales, as expected, and gradually reduce and vanish going towards smaller scales. The MHD term dominates the inertial range, being negligible at both large and

small scales. Note that the simulation configuration did not allow sufficient scale separation as to obtain a broad linear scaling of the MHD term in the inertial range. This was not, however, the goal of the paper. The Hall term gives negligible contribution at large and intermediate scales, and at sufficiently small scales it become comparable to or slightly larger than the MHD term. The small Hall contribution was attributed by the authors to the limited Hall range and to the resulting dissipation. The pressure dilation term is negligible everywhere, suggesting that it is acceptable to omit it in the calculation when using one-dimensional time series. Finally, the (negative) contribution of the total dissipation term balances the sum of the other terms at all scales. However, more detailed analysis showed that the viscous-resistive dissipation only acts at small scales, as one should expect in the fully nonlinear regime. It is interesting to notice that the different dynamical regimes are well separated in scales, suggesting that the interactions might be local in scale.

Similar results were obtained using the alternative version of the exact law, equation (110), showing that the two are indeed equivalent. The authors also used Fourier filtering (see, e.g., Mininni et al., 2007, and the general discussion in Section 1) to obtain an independent, alternative and precise estimate of the spectral energy transfer in the wavevector space (see the review by Alexakis and Biferale, 2018). When using the full two-dimensional simulations, these give the same result as the two KHM equations, further supporting the robustness of the latter (Hellinger et al., 2021a). In order to determine the approximation resulting from reducing dimensionality to time series, such as single spacecraft data, one-dimensional cuts of the simulation domain were considered and the comparison was repeated. Since the divergence cannot be fully estimated with one dimensional cut only, all divergence terms in equations (106) were approximated using one single gradient direction, corresponding to the sampling direction in space data time series. On the other hand, the spectral filtering evaluation was performed by computing the Fourier transform in one direction only, but computing two-dimensional derivatives, therefore retaining part of the original dimensionality. Similarly, fully two-dimensional curls were used to estimate current and vorticity in the alternative version of the KHM equation. The comparison among the three techniques is illustrated in the two panels of Figure 38. In the top panel, the comparison between the spectral transfer (S terms, full lines) and the estimate from equations (106) ($\mathcal{K}$, dashed lines) is shown, separately for the MHD (green) and Hall MHD (orange) terms. It is evident that, in the inertial

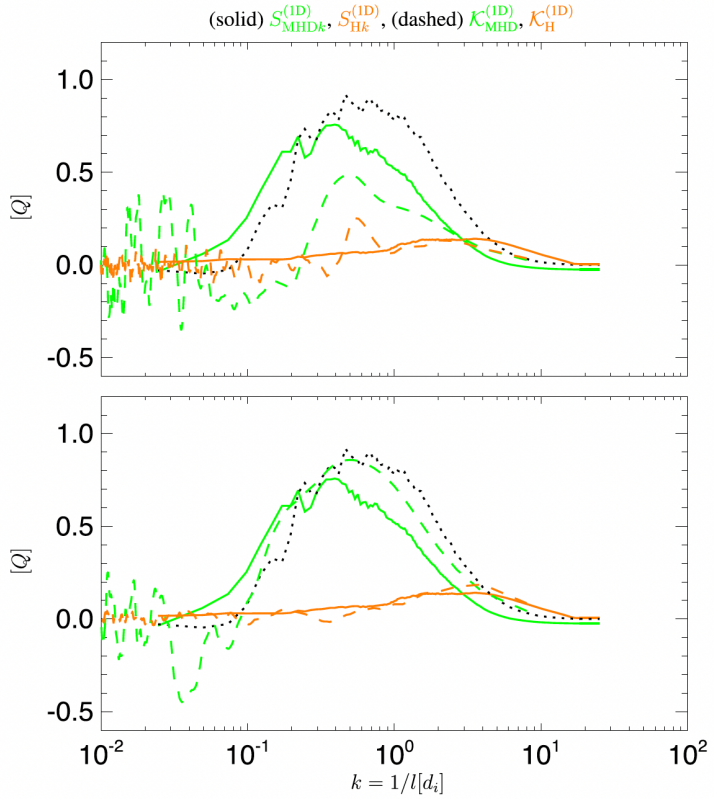

Figure 38: Comparison among different estimates of the scale-dependent energy transfer rate, indicated as $[Q]$, in one-dimensional cuts of two-dimensional Hall-MHD numerical simulations. Top panel: comparison between the von Kármán-Howarth-Monin scaling relation in its divergence form, $\mathcal{K}_{MHD}$ and $\mathcal{K}_H$ (equations 111 and 112, dashed lines), and the Fourier spectral transfer, S (full lines, see equation 19 in Hellinger et al., 2021a), for the MHD (green) and Hall MHD (orange) contribution. Bottom panel: same as top panel, but using the alternative KHM formulation, equation (110). In both panels, the black-dotted line indicates the MHD cascade rate, S_{MHD}, obtained from the spectral transfer analysis (see details in Section 4 of Hellinger et al., 2021a), shown here for for comparison. All the quantities are given in units of the total heating rate, Q, defined by equation (116). Figure from Hellinger et al. (2021a).

range, the KHM equation in divergence form fails to correctly capture the full cascade rate, as the MHD term underestimates by a considerable factor the actual energy transfer. The issue is not so evident for the Hall contribution, for which stronger fluctuations are observed in the KHM form. In the bottom panel of the same figure, the same representation allows to compare the spectral transfer with the alternative version of the KHM equations (dashed lines). In this case, very good agreement is found between the two representations. Note, however, that both these versions use one-dimensional cuts but full two-dimensional derivatives. The two panels of Figure 38 together seem to indicate that, at least for the compressible case, reducing dimensionality may give incorrect estimates of the transfer rate, and illustrates the need for multi-spacecraft measurements, which should enable the correct estimation of the divergence terms.

The extensive work presented by Hellinger et al. (2021a); Ferrand et al. (2021a) demonstrates that exact laws provide excellent estimates of the energy transfer rate in turbulent compressible flows. It is able to separate the contribution from different terms of the dynamical interactions details, which of course can be performed to a finer detail than done in the work described here. The approach was also successfully used to describe the time evolution of the system, capturing the various transitions to a high degree of precision (Hellinger et al., 2021a). In addition, it highlights the importance of the possible error when the estimate is preformed using time series. As we pointed out above, the conclusion given in the article that spectral transfer or the alternative KHM version might provide better results in space data is however misleading, since using multi-spacecraft missions is equally necessary for computing divergence, curl and the space derivative included in the spectral transfer description. This should be tested using three-dimensional simulations and virtual multi-spacecraft cuts simulating realistic spacecraft missions (Servidio et al., 2011), and/or performing similar fully one-dimensional approximations for the three different versions, which should enable a fairer comparison.

5.6. Solar wind observations of the compressible MHD and Hall MHD turbulent cascade

Despite of their inherent difficult evaluation from one-dimensional time series, the compressible models of turbulent cascade rate were abundantly used to analyse spacecraft measurements.

The first studies (Banerjee and Galtier, 2016) tested a modified version of the scaling law presented in Banerjee and Galtier (2013) (not reported explicitly in this review but fundamentally similar to the MHD limit of the alternative version by Hellinger et al. (2021a)), which uses the Elsasser fields. After isotropic integration, incorporating part of the β-dependent term in the flux term (under the assumption of constant β), and neglecting all the source terms (under the assumption that they are likely negligible in subsonic turbulence, such as in the solar wind), the exact law can be re-written as follows:

$$-\frac{4}{3}\varepsilon_C \ell = \mathcal{F}_1 + \mathcal{F}_2 + \mathcal{F}_3\,, \tag{117}$$

where the three flux terms are

$$\mathcal{F}_1 = \frac{1}{2}\Big\langle [\Delta(\rho \mathbf{z}^-)\cdot\Delta\mathbf{z}^-]\Delta z_L^+ + [\Delta(\rho\mathbf{z}^+)\cdot\Delta\mathbf{z}^+]\Delta\mathbf{z}_L^-\Big\rangle \tag{118}$$

$$\mathcal{F}_2 = \Big\langle 2\Delta\rho\,\Delta e\,\Delta v_L\Big\rangle \tag{119}$$

$$\mathcal{F}_3 = \frac{1}{2}\Big\langle [4\overline{[(1+\beta^{-1})e + v_A^2]}\delta(\delta\rho v_L)\Big\rangle\,. \tag{120}$$

We remind the reader that $\overline{\psi}$ indicates two-point average of the quantity ψ at scale separation ℓ. Moreover, the subscript L indicates the component along the bulk flow, and $\delta\rho = \rho - \langle\rho\rangle$ are the density fluctuations. All the terms in equation (117) can be easily computed from solar wind time series.

The NASA THEMIS mission (see Figure 39) is a five-spacecraft constellation launched in 2007 and still operational, which originally aimed at studying the terrestrial magnetotail (Angelopoulos, 2008). In the nominal phase of the mission, the spacecraft had a geocentric orbit that sampled the terrestrial magnetosphere and magnetotail, and occasionally the upstream free streaming solar wind. Starting in 2008, NASA started an extended mission where two of the spacecraft, THEMIS-B and THEMIS-C, would be placed in lunar orbit. In that occasion, the two spacecraft were renamed respectively ARTEMIS-P1 and ARTEMIS-P2, and reached lunar orbit in 2011 (Angelopoulos, 2011). During the transition, THEMIS-B/ARTEMIS-P1 collected a large fraction of data in the near-Earth solar wind, at 1 au from the Sun. Banerjee and Galtier (2016) used THEMIS-B/ARTEMIS-P1 magnetic field and plasma measurements with 3 s cadence measured between 2008 and 2011 in the fast solar wind. After careful selection, intervals with solar disturbances, changes of mean magnetic field direction, evident non-stationarity, highly variable plasma β and slow mean speed were rejected.

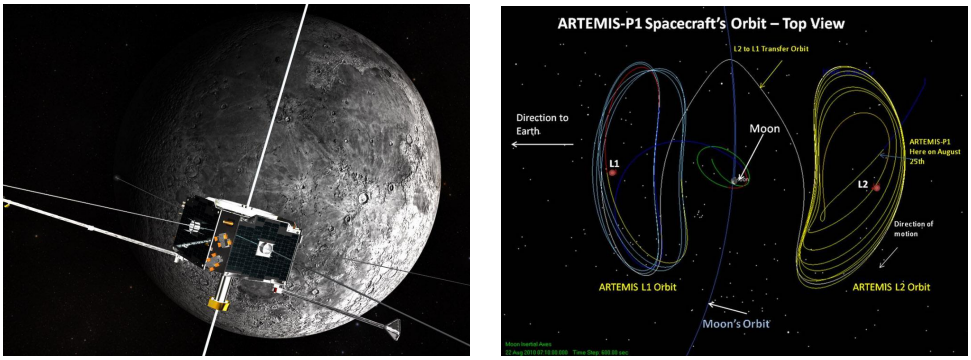

Figure 39: Left panel: artist's illustration of one ARTEMIS spacecraft orbiting the Moon. Right panel: the complex transition from geocentric to selenocentric orbit. Credits: NASA/Goddard/Conceptual Image Lab (left) and NASA/Goddard (right), both available at `https://www.nasa.gov/mission_pages/THEMIS/news/artemis-orbit.html`.

Out of four years of data, 170 intervals of 35-minute length were finally selected and used for the analysis. Although those intervals are relatively short, they cover at least one correlation scale of the MHD fields, which the authors deem sufficient to perform the analysis. Indeed, the linear scaling is observed on a sufficient range of scales, enabling estimates of the energy transfer rate. The left panel of Figure 40 shows the compressible energy flux $Y_1 + Y_2 + Y_3$, equation (117), computed from one interval from the extensive database of the study (red line). Note that the authors used the absolute value. This procedure is in general incorrect, since sign changes that could disrupt the linear scaling are hidden in this representation. However, the linear scaling appears evident, as also shown when dividing the flux by the scale to obtain the energy transfer rate ε_C (right panel). Converting the energy transfer rate to the units used here, the values found by Banerjee and Galtier (2016) are $\varepsilon_C \sim 50$ kJ kg^{-1} s^{-1}, namely of the same order of magnitude as in previous observations at the same distance from the Sun. The black line in both panels shows the incompressible version of the energy flux and energy transfer rate (P&P law, equation 54), again using the absolute value. The inset in the right panel shows four additional intervals. In the majority of the cases, the compressible and incompressible estimates of the energy transfer rate were found to be similar. Only in a limited number of cases one of the two was larger than the other, with a slight predominance of larger compressible energy transfer. This is not surprising, since the fast, Alfvénic solar wind intervals studied here do not show strong density fluc-

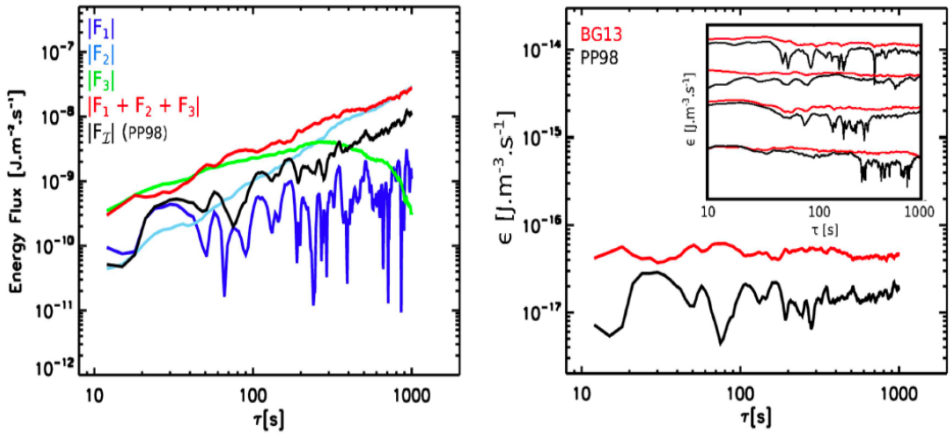

Figure 40: Left panel: one example of the scaling of the total compressible energy flux $F_1 + F_2 + F_3$ (equation 117, red line) and its three terms separately (see legend for colors) for one 35 m solar wind interval measured by THEMIS B. The incompressible scaling, $F_I \equiv Y$ is also shown (equation 54, black line). Right panel: for the same interval, the energy transfer rate for the compressible (ε_C, equation 117, red line) and incompressible (ε, equation 54, black line) models. The inset shows the same quantities for four additional intervals. Figure adapted from Banerjee et al. (2016).

tuations, and are therefore mostly incompressible. In the left panel of the same figure, the blue, cyan and green lines indicate the contributions of the three sub-terms, equations (118)-(120), showing that the $\mathcal{F}_2$ and $\mathcal{F}_3$ terms dominate this particular case. This explains the difference between the compressible and incompressible scaling, and highlights that the difference is not related to the compressive correction to the standard third-order P&P term ($\mathcal{F}_1$), but rather to the two purely compressible terms. Based on this remark, the authors argue that, even including density fluctuations corrections, the incompressible scaling would provide a poor approximation of the compressible turbulent energy transfer rate. However, since this observation is based on one single case, these conclusions were perhaps premature.

In a follow-up paper, Hadid et al. (2017) extended the analysis to include slow solar wind intervals, where the compressible contributions can be expected to be more relevant. Based on similar criteria as Banerjee and Galtier (2016), and using data from the same spacecraft, these authors selected 148 fast and 182 slow solar wind intervals and repeated the analysis of the same energy flux equations. An example of their results for one interval of slow

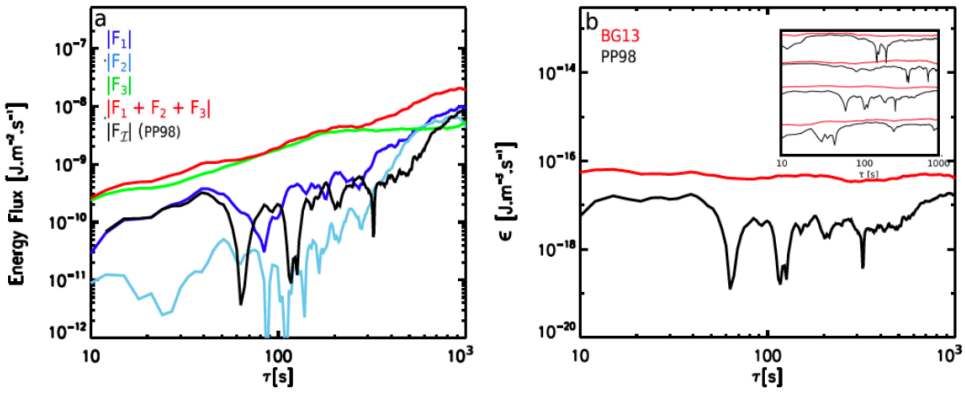

Figure 41: Left panel: one example of the scaling of the total compressible energy flux $F_1 + F_2 + F_3$ (equation 117, red line) and its three terms separately (see legend for colors) for one 35 m solar wind interval measured by THEMIS B. The incompressible scaling, $F_I \equiv Y$ is also shown (equation 54, black line). Right panel: for the same interval, the energy transfer rate for the compressible (ε_C, equation 117, red line) and incompressible (ε, equation 54, black line) models. The inset shows the same quantities for four additional intervals. Figure from Hadid et al. (2017).

solar wind is given in Figure 41, which has the same structure as Figure 40. The results confirmed the overall conclusions of the previous work for fast solar wind, and extended the same to slow solar wind intervals. Even for slow wind, compressible effects are limited, and estimates of the energy transfer rate done with the compressible exact law is in most cases comparable to the estimates based on the incompressible P&P law. This confirms that the contribution of the internal energy to the cascade is often negligible. The order of magnitude of the measured values of the energy transfer rate are in agreement with previous observations at 1 au, with an average value $\varepsilon \simeq 55$ kJ kg^{-1} s^{-1} for the fast solar wind and $\varepsilon \simeq 27$ kJ kg^{-1} s^{-1} for the slow one. Similarly to the fast solar wind, but slightly more often, in some of the slow intervals the compressible energy cascade is stronger, like in the case depicted in Figure 41. However, the increase is again mostly due to a strong flux $\mathcal{F}_3$ that includes the internal energy contribution, so that it is not easy to directly compare the compressible and incompressible transfer rates. By comparing the heating rates, ε_C and ε, in fast and slow solar wind, it emerged that fast wind has stronger energy transfer than slow wind for both compressible and incompressible models, in agreement with previous observations (MacBride et al., 2008; Stawarz et al., 2009; Coburn et al., 2012). In the slow solar wind,

the compressible cascade is slightly more likely to be stronger than the incompressible one. A scaling relation was identified between the energy transfer rate, ε_C, estimated with the compressible P&P law, equation (118), and the kinetic ($E_k = \rho_0 \delta v^2/2$, where δv is the root-mean-square of the velocity fluctuations), magnetic ($E_b = \delta B^2/(2\mu_0)$, where δB is the root-mean-square of the magnetic field fluctuations) and internal ($E_e = \rho_0 c_s^2 \ln(1 + \delta\rho/\rho_0)$) fluctuation energies, as well as with their sum, $E_T = E_k + E_b + E_e$, namely $\varepsilon_C \sim E_i^{1/\alpha}$ with $i = k, b, e, T$. This is visible in the four panels of Figure 42, which show such dependency (but with reversed axes) for fast (left panels) and slow (right panels) solar wind intervals separately. Power-law fits show the following dependencies: $\varepsilon_C \sim E_k^{1.72} \sim E_b^{1.69} \sim E_e^{2.38} \sim E_T^{1.79}$ for the fast intervals; $\varepsilon_C \sim E_k^{1.75} \sim E_b^{1.59} \sim E_e^{3.13} \sim E_T^{1.64}$ for the slow intervals. These scaling exponents are generally in agreement with previous solar wind observations (MacBride et al., 2008). Note that the Kolmogorov phenomenology (see, e.g., Frisch, 1995) predicts $\varepsilon \sim E_T^{3/2}$, which is much closer to the exponents for the kinetic and magnetic energy than to those for the internal energy. On the other hand, the prediction of the 3/2 exponent assumes that the density is constant, thus it is not surprising that the internal energy scaling slightly departs from the incompressible case. The relatively good agreement between phenomenological predictions and observations suggests that the estimates obtained using the compressible or incompressible exact laws are correct, or at least can capture the variability of the cascade in response to the fields fluctuations. However, the less consistent scaling with the internal energy seems to indicate a minor relevance of the associated terms for the energy budget of the turbulent cascade.

The analysis also revealed a scaling relation between the sonic Mach number, $M_S = \sqrt{\delta v^2/c_s^2}$, and the energy transfer rate, $\varepsilon_C \sim M_S^\gamma$, where the fitted exponents are $\gamma \simeq 2.7$ for slow solar wind and $\gamma \simeq 1.5$ for fast solar wind. Since no theoretical prediction for such scaling exist, these observations might be used to constrain theories and models of the role of compressive fluctuations in solar wind turbulence and heating. Hadid et al. (2017) further studied the sign of the cascade rate, whose histograms are shown in Figure 43, in the two groups of solar wind intervals. While in both types of wind positive and negative scaling was observed with similar occurrence, in fast solar wind there is a slight predominance of negative scaling, suggesting that an inverse cascade might be active more often than in the slow wind samples. This is in agreement with previous observations (Smith et al., 2009), whose

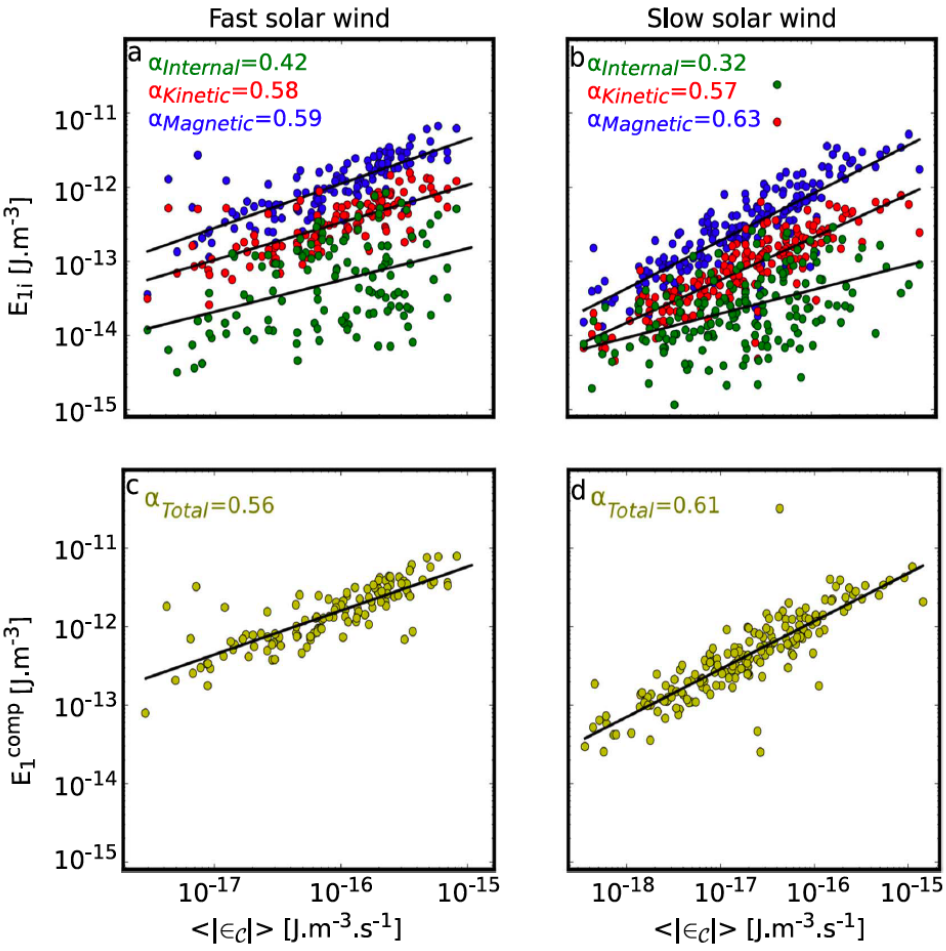

Figure 42: Top panels: scaling relation between the kinetic, magnetic and internal energy (indicated with E_{1i}, where i stands for internal, kinetic and magnetic) and the absolute value of the energy transfer rate $|\varepsilon_C|$ (equation 117), for fast (left) and slow (right) intervals. The power-law fitting exponents, α_i, are indicated. Note that in the text we have given $1/\alpha_i$. Bottom panels: the scaling of the total energy E_1^{comp}, sum of the three contributions above. The fitting exponents α_{Total} are indicated. In all panels, black lines indicate power-law fits. Figure from Hadid et al. (2017).

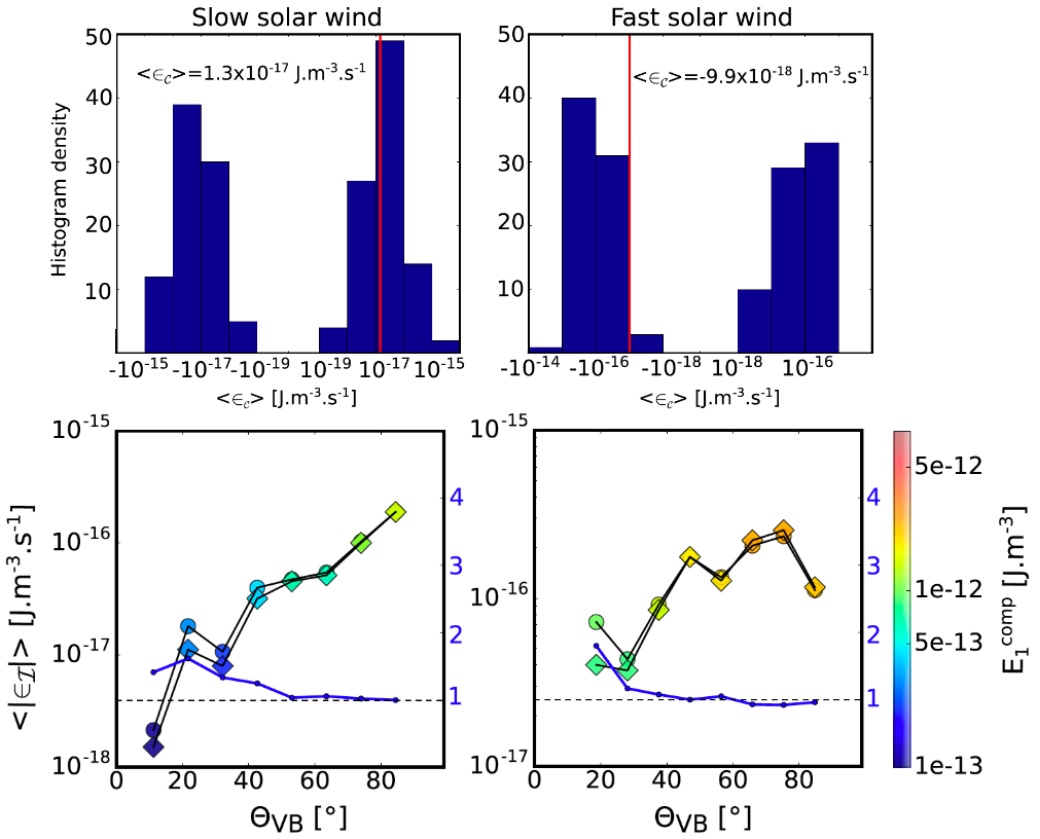

Figure 43: For slow (left panels) and fast (right panels) solar wind intervals, the top panels show histograms of the compressible energy transfer rate, ε_C. The vertical red lines indicate the mean, which is also given in each panel. Note the different sign for the mean in fast (negative) and slow (positive) wind, possibly related to the different cross-helicity normally observed in fast and slow streams. The bottom panels show the angle-bin averaged compressible (circles) and incompressible (diamonds) energy transfer rate as a function of the angle between the bulk solar wind speed and the interplanetary magnetic field, θ_{VB}, color-coded according to the total fluctuation energy (increasing from blue to red, color bar not shown). The blue lines indicate the ratio between compressible and incompressible energy transfer rates. Figure from Hadid et al. (2017).

interpretation suggested that the inverse cascade may be responsible for the long-term survival of cross-helicity in fast solar wind. However, we remark that the actual physical meaning of the sign of the cascade might be more complex than in the ideal version of the law, since, as we saw in Section 5.1, other factors, related for example to expansion or anisotropy, might concur in changing the sign of the energy flux terms.

Finally, the dependence on the angle between the solar wind bulk speed and the large-scale magnetic field, θ_{VB}, was discussed. For both types of wind, the energy transfer is clearly larger when the field is perpendicular to the flow, namely when the spacecraft is sampling fluctuations in the plane perpendicular to the field. For the fast intervals, this is in agreement with previous analysis by MacBride et al. (2008), while for the slow wind the strong angular dependence was not observed before. It should be pointed out that MacBride et al. (2008) used a modified version of the P&P law that included anisotropy effects, while in the present case the separation in the two directions was not performed. This might explain the discrepancy between the two observations. In the same panels, the ratio between compressible and incompressible energy transfer rates is also indicated. In the fast streams, the ratio is close to unity for most angles, with the exception of the cases closer to parallel sampling, where the cascade is not easily measured (see also the smaller transfer rate). This indicates that compressive effects are negligible in most cases. In slow streams, the two rates are again comparable for large angles, but there is a remarkable dominance of the compressible estimate for parallel angles $\theta_{VB} < 45°$, probably arising from the more compressive nature of the slow wind, and associated again with smaller energy transfer rate.

6. Origin and evolution of turbulence in the inner heliosphere: from Helios to Parker Solar Probe

One outstanding question in the space plasma community concerns the origin and evolution of turbulence as the solar wind expands in the heliosphere. For example, whether turbulence is generated at coronal level, then decays during the solar wind expansion, or rather is sustained by local energy injection mechanisms, is yet not fully established. Consequently, the way turbulence and kinetic processes interact may also evolve with the heliocentric distance, resulting in a complex dynamical scale-coupling of fundamental processes. The appropriate description of turbulence is crucial for the detailed

modeling of the global heliospheric dynamics (Usmanov et al., 2018; Gombosi et al., 2018), of the propagation of transients or impulsive events, such as CMEs or CIRs (see, e.g., Poedts, Stefaan et al., 2020), and to understand the mechanisms producing solar wind heating and particle energization.

The properties of the turbulence developing in the expanding solar wind have been studied since the early stage of space exploration. This was made possible by the in-situ measurements of spacecraft such as the Helios 1 and Helios 2 missions in the inner heliosphere, and Voyager, Pioneer and, later on, Ulysses in the outer heliosphere. More recently, various spacecraft, including, the dedicated ESA Solar Orbiter (Müller et al., 2020; Zouganelis et al., 2020) and NASA Parker Solar Probe (Fox et al., 2016), provided access to high-resolution, continuous sampling of plasma fields and statistical moments, allowing for more accurate studies of solar wind turbulence in the inner heliosphere.

6.1. Early results on solar wind turbulence evolution: the Helios missions

Until recently, studies on solar wind turbulence in the inner heliosphere relied heavily on spectral and structure function analysis of the plasma and fields measured by the two Helios spacecraft, which in 1975 and 1976 approached as close as 0.3 au from the Sun. An archive picture of the spacecraft Helios 2 and a schematics of the two Helios orbits are illustrated in Figure 44. During three different solar rotations, in 1976, Helios 2 measured plasma and fields of three fast solar wind streams at three different distances from the sun (0.9, 0.7 and 0.3 au, see Figure 45), holding the record at the time for the closest flyby of the Sun. It was soon established that those streams were originating from the same stable coronal hole. Therefore, assuming that the coronal source was steady enough, the three streams are of particular relevance to the study of the radial evolution of turbulence, since the initial conditions can be considered as stationary. Similarly, the preceding slow wind streams were extensively used as a sample of evolving slow solar wind, although in that case the originating region might have evolved during the time span of the observation. Using these streams, as well as several other Helios 1 and 2 data, it was highlighted that striking differences exist between the radial evolution of fast and slow solar wind turbulence (Bruno et al., 2003; Bruno et al., 2004, 2014).

Fast wind plasma, normally characterized by strongly Alfvénic fluctuations (as evidenced by the associated large cross-helicity state) and by the

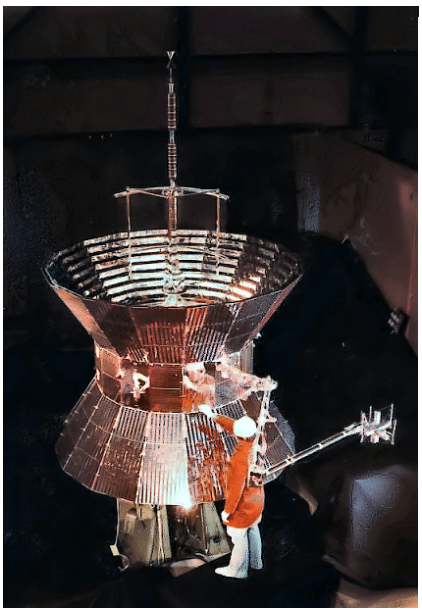

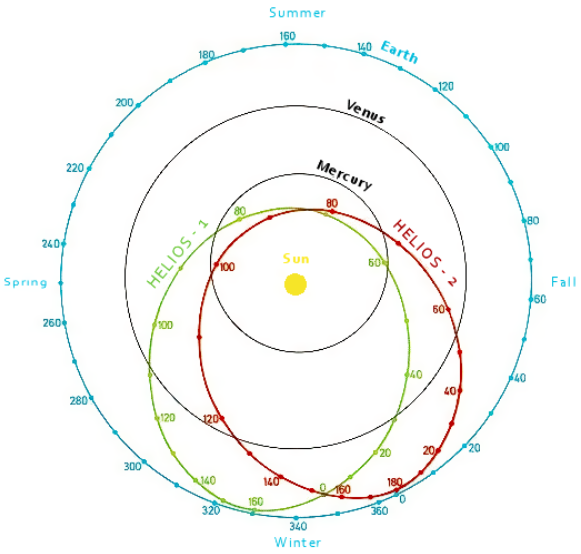

Figure 44: Left panel: a picture of the Helios 2 spacecraft during testing. Right panel: the orbit of Helios 1 and Helios 2. Credits: NASA/Max Plank Institute. Available at: left: `https://en.wikipedia.org/wiki/Helios_(spacecraft)`; right: `https://heasarc.gsfc.nasa.gov/docs/heasarc/missions/images/helios2_images.html`

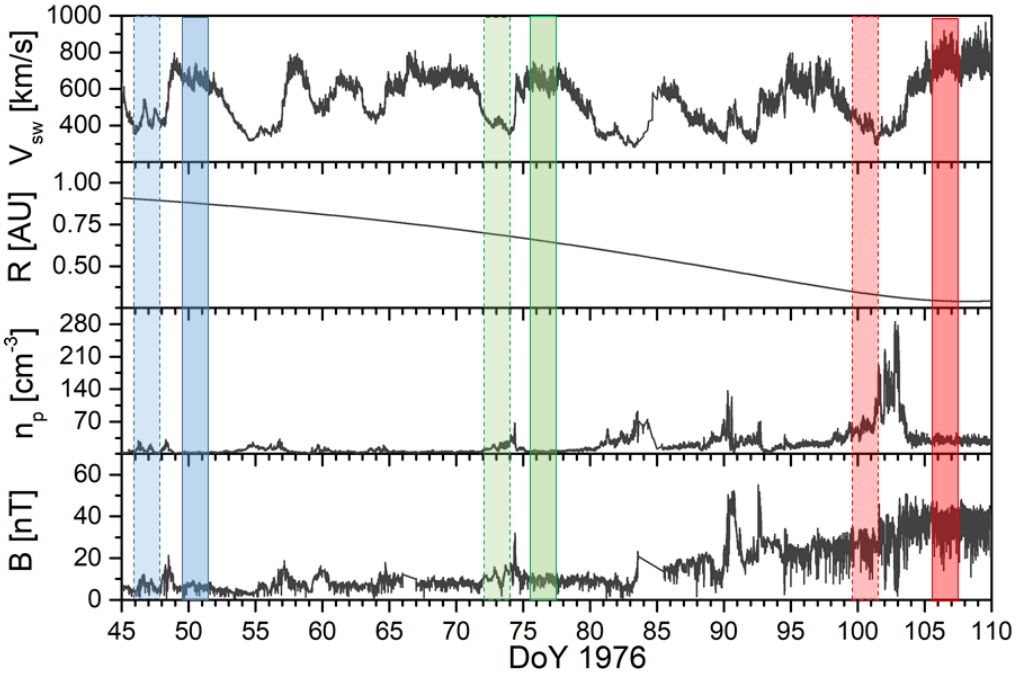

Figure 45: The six streams measured by Helios 2 in 1976 used for the study of radial evolution of solar wind turbulence: three fast streams, indicated with darker-colored and full-line bordered shaded areas, and three preceding slow streams, indicated using lighter colors and dashed-line borders. From top to bottom, the figure shows the solar wind speed, V_{sw}, the heliocentric radial distance, R, the solar wind density, n_p, and the magnitude of the magnetic field, B. Figure from Sorriso-Valvo et al. (2022).

presence of $1/f$ large-scale magnetic spectra, evolves radially in the heliosphere, showing clear decrease of the v-b alignment, broader inertial range (and/or reduced $1/f$ range), smaller spectral amplitude, and stronger intermittency as the radial distance from the Sun increases. The top panels of Figure 46, based on Helios 2 and Ulysses data, show the trace of the magnetic power spectral density measured at different distances from the Sun, separately for fast (left panel) and slow (right panel) stream. In both fast and slow streams, a broad inertial range, with Kolmogorov scaling $\sim f^{-5/3}$, is present on the whole frequency range (slow streams) or on the higher-frequency part (fast streams) of the spectrum. In the fast solar wind, the low-frequency $1/f$ range is also clearly visible. In the left panel, the blue dot indicates the frequency of the break separating the two ranges. Its drift

towards lower frequencies, indicating the expansion of the inertial range with the radial distance, is evident. The bottom panels of Figure 46 show the scale-dependent flatness of the magnetic field magnitude, $F(\Delta t) = \langle \Delta B^4 \rangle / \langle \Delta B^2 \rangle^2$, for the same three fast (right panel) and three slow (left panel) solar wind streams measured by Helios 2. As normally observed in turbulent flows, the flatness increases as a negative power-law of the scale, from its large-scale Gaussian value, $F = 3$, until other non-turbulent processes modify the scaling. Steeper power-law increase indicates that the turbulent cascade is more rapidly generating small-scale structures, and hence dissipating the energy more efficiently. In the fast wind, the flatness clearly increases with the radial distance, indicating stronger intermittency. In the slow wind, however, there is no similar evidence of radial evolution. The observation of the differences in the spectral properties of the inward and outward Elsasser modes (not shown) also corroborated the picture of a strongly evolving fast solar wind (for a thorough description of radial evolution of solar wind turbulence, see: Tu and Marsch, 1995; Bruno and Carbone, 2013).

The above characteristics are generally interpreted as the signature of the fast wind turbulence being still evolving towards a fully developed state during the expansion. In one possible instance of a scenario, Bruno et al. (2003) proposed that the observations could be explained by the competing action between a correlated, coherent component (the intermittent structures generated by the turbulent cascade in the early stage of the turbulence onset, and populating the Kolmogorov 5/3 or 3/2 spectral region, see Bruno et al., 2019), and an uncorrelated, stochastic component (the propagating Alfvénic fluctuations, populating the large-scale $1/f$ portion of the spectrum). In the early stage of the radial expansion, the two components, possibly originating in the corona (Bruno et al., 2001; Chang et al., 2004; Borovsky, 2008), are overlapping, so that the large-amplitude Alfvénic fluctuations partially hide the coherent component. This would explain the initially reduced inertial range and intermittency of the fluctuations. As the solar wind expands, the inward and outward Alfvénic fluctuations interact nonlinearly, consequently losing their Alfvénic alignment, reducing their amplitude, and feeding the turbulent cascade with supplementary energy. On the other hand, the coherent component would be advected by the wind without losing amplitude. Hence, it would progressively emerge from the decreasing uncorrelated Alfvénic background, resulting in the observed extended Kolmogorov spectrum and increasing intermittency. Moreover, the presence of the large-scale Alfvénic fluctuations could justify the spectral indices observed in fast wind,

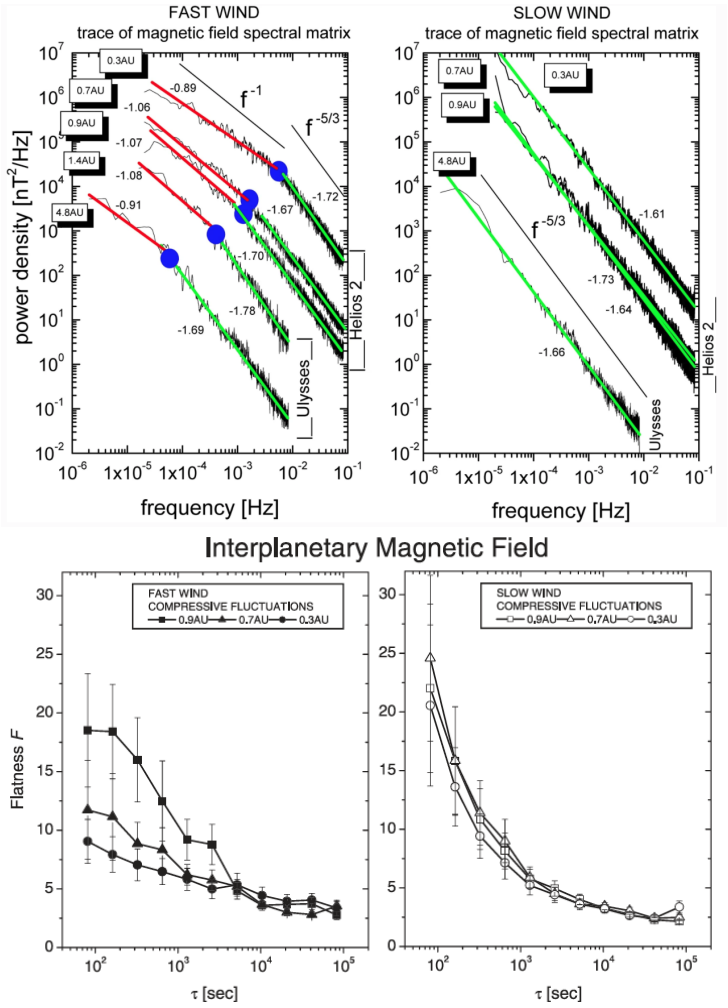

Figure 46: Top panels: Trace of the power spectral density of the interplanetary magnetic field, estimated at different distances from the Sun using Helios 2 and Ulysses data. Top-left and top-right panel show results for fast and slow streams, respectively. Power-law fits and spectral indices are indicated in the relevant ranges. Bottom panels: the flatness of the magnetic field magnitude, for three fast (bottom-left panel) and three slow (bottom-right panel) Helios 2 streams. Figure from Bruno and Carbone (2013) (top) and Bruno et al. (2003) (bottom).

often closer to the Kraichnan value, 3/2, rather than the Kolmogorov's, 5/3 (Bruno and Carbone, 2013). The slow solar wind milder evolution was ascribed to the relative absence of Alfvénic fluctuations (at least further out

than 0.3 au, where Helios measurements were taken), with no decorrelating effect inhibiting the nonlinear turbulent interactions (see, again, Tu and Marsch, 1995; Bruno and Carbone, 2013, and references therein).

A visualization of the fluctuations of the tip of the magnetic field vector (small red dots), connected by a black line to highlight the vector displacements, is presented in Figure 47. Left panels refer to fast wind, and right panels to slow wind. Top panels are measured at 0.3 au, while bottom panels at 0.9 au. It is evident that in the 0.3 au fast stream the vector randomly covers the whole space, suggesting the stochastic nature of the Alfvénic fluctuations. On the contrary, at larger distance patches of small fluctuations are alternated with large fluctuations, resulting in more clustered intermit-

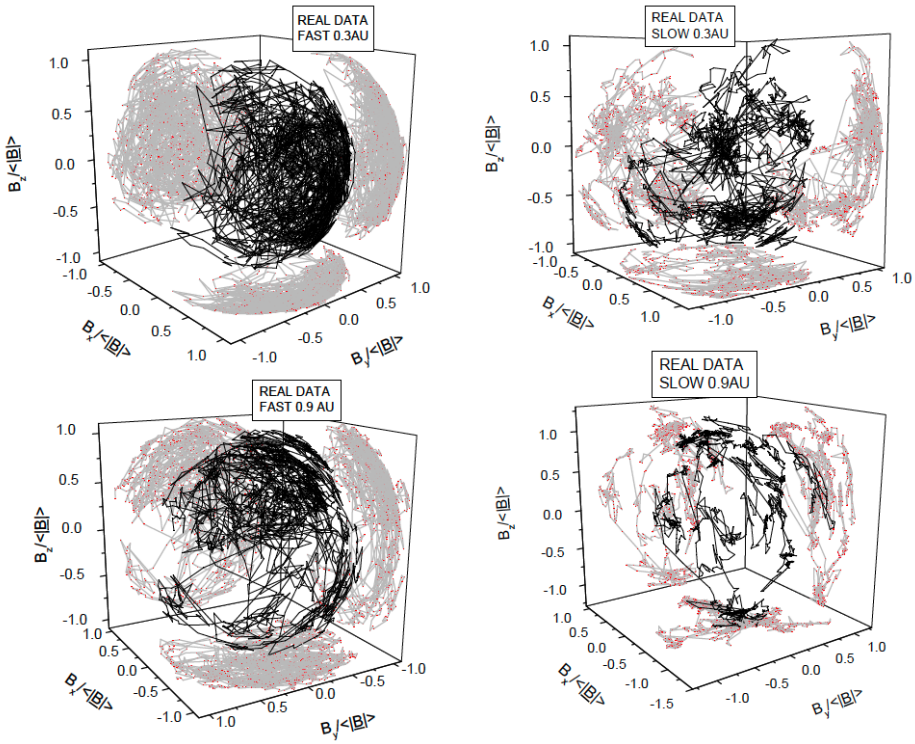

Figure 47: Visualization of the displacement of the tip of the magnetic field vector normalized to the mean field magnitude (red dots, connected by a black line) obtained using 6-second cadence measurements of 3.3 hour intervals extracted from the fast (left panels) and slow (right panels) streams measured by Helios 2 at 0.3 au (top panels) and 0.9 au (bottom panels). Figure from Bruno et al. (2004)

tent fluctuations. The slow wind streams do not present the same stochastic fluctuations, so that the clustering of intermittent fluctuations is already emerging at 0.3 au.

The above observations, corroborated by more observations of Helios data, were initially used to support the evolving nature of the solar wind turbulence in the inner heliosphere, and to constrain global solar wind models and their energy budget.

6.2. Observation of decaying turbulence in the inner heliosphere: revisiting half-century old Helios 2 measurements using the Politano & Pouquet law.

For a more detailed evaluation of the solar wind turbulence evolution, it is interesting to examine the scaling of the third-order moment in the samples described above. To this aim, the six Helios 2 recurring fast and slow streams (Bavassano et al., 1982; Bruno et al., 2003) were used to estimate the P&P law for incompressible, isotropic MHD turbulence (Sorriso-Valvo et al., 2022). The intervals, each including nearly two days of data, were long enough as to ensure statistical convergence, which was additionally verified using the standard tests (Dudok de Wit, 2004; Kiyani et al., 2009a). The mixed third-order moments are displayed in the top panels of Figure 48 for the six intervals, separated according to the wind speed (left panel: fast streams; right panel: slow streams). The distance from the sun is marked by the different colors and symbols, with the 0.9 au intervals in blue triangles, the 0.7 ones in green circles, and the 0.3 ones in red diamonds. An inertial range is identified for each case for timescales between 81 s (the plasma data resolution) and $\sim$ 20 minutes, although the linear scaling is more extended in the samples at 0.3 au. Note that for the fast streams such range unexpectedly extends within the $1/f$ spectral range (see Figure 46). The fit of the linear P&P law provides, as usual, the values of the mean energy transfer rate for each sample. Values are given in colors next to each fitted line in Figure 48. It is immediately evident from the amplitude of the third-order moments, Y, that the energy transfer rate decreases with the distance from the Sun. This is observed consistently for both fast and slow wind streams. The slow solar wind has always smaller energy transfer than the fast solar wind. Plotting the energy transfer rate versus the radial distance reveals a possible power-law dependence, as shown in the bottom-left panel of Figure 48. Despite having only three points, power-law fits, $\varepsilon \sim R^{-\alpha}$, can be reasonably performed. These provide slightly different exponents for fast and

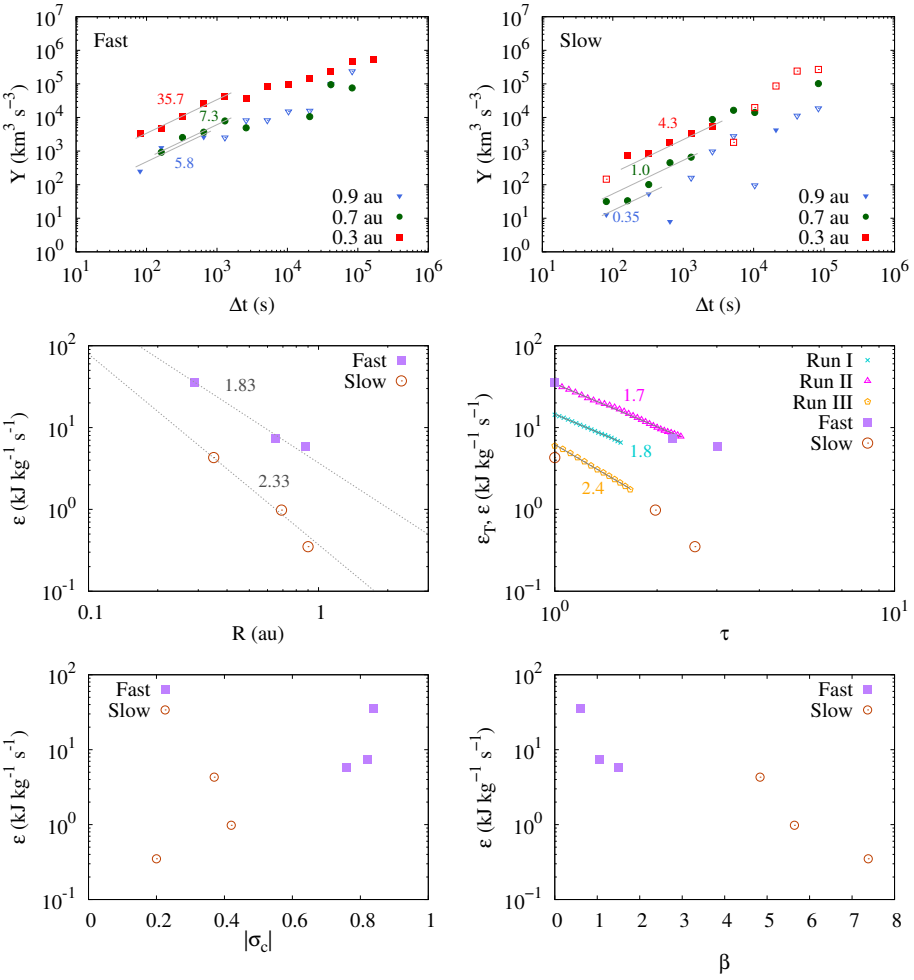

Figure 48: P&P scaling for fast (top-left) and slow (top-right) streams, at three different distances from the sun (colors, see legend). Linear fits in the inertial range are indicated (grey lines), and the corresponding energy transfer rate, ε, is given (color coded). ε is then displayed as a function of the radial distance R (center-left panel, also showing power-law fits and the fitted exponents), of the unsigned normalized cross-helicity $|\sigma_c|$ (bottom-left) and of the plasma β (bottom-right). The decay of ε in a 512^3 lattice Boltzmann numerical simulation of the weakly compressible MHD turbulence is shown in the center-right panel. The time is normalized to the peak of the turbulence. Top and central panels are adapted from Sorriso-Valvo et al. (2022).

slow wind, respectively $\alpha_F = 1.84 \pm 0.2$ and $\alpha_S = 2.34 \pm 0.2$. From the bottom panels of the same figure, note that the dependency on the normalized cross helicity is opposite with respect to the standard expectation from the decorrelation effect (Dobrowolny et al., 1980) and to observations at 1 au (Smith et al., 2009). A clear decrease with the plasma β is also observed, against the intuitive expectation of stronger turbulence for less magnetized plasmas. This indicates that the decay is controlling the radial evolution of turbulence, while the decorrelation due to Alfvénic fluctuations is a subdominant effect, which can only order turbulence for intervals at a similar decay stage. According to the above observation of decreasing turbulent energy transfer, and assuming that the three streams are freely expanding without further interactions with the surrounding plasma, it could be suggested that the turbulence is decaying as the wind travels away from the Sun. Therefore, turbulent energy, mostly injected at coronal level (or at least in the region with $R < 0.3$ au, see Kasper et al., 2021; Bandyopadhyay et al., 2022; Sorriso-Valvo and Yordanova, 2022), is depleted during the expansion. This is also consistent with recent Ulysses observations in the outer heliosphere, where the observation of the energy transfer rate radial decrease was statistically robust (Watson et al., 2022). The faster decay observed in the slow streams could be due to the absence of the $1/f$ reservoir, which in the fast streams provides an energy injection during the expansion. The above interpretation was supported by comparison with numerical simulations of decaying MHD turbulence, which show strikingly similar power-law decay of the energy dissipation (center-right panel of Figure 48). Additionally, the intermittency was observed to increase with radial distance (for the solar wind) and with time (for the simulation) in a similar fashion (Sorriso-Valvo et al., 2022), which further supports the possible decaying turbulence scenario for the solar wind radial evolution.

Although the analysis of Sorriso-Valvo et al. (2022) needs to be confirmed by more events, it shows that using the third-order scaling law may reveal important details that can point to substantial revision of the currently accepted paradigms of the processes regulating the evolving nature of solar wind turbulence. The observed behaviour and parameters values can be relevant to constrain models of turbulence in the expanding solar wind.

6.3. New frontiers of inner heliosphere exploration: Parker Solar Probe and Solar Orbiter

Forty years after Helios measurements, novel space missions have been launched in the inner heliosphere to allow continuing the observation of the evolution of turbulence as it leaves the Sun. The Parker Solar Probe (PSP) was launched by NASA in August 2018, and is currently operating in the inner heliosphere (Fox et al., 2016; Verscharen, 2019). Thanks to gravitational assists at Venus, it has rapidly reached a highly elliptic orbit that grazes the Sun at a short distance. The first solar encounter occurred in late 2018, when the PSP closest approach reached the record distance of 0.17 au (36 $R_\odot$, with $R_\odot$ =696340 km being the solar radius) from the solar surface. At the time of writing, thirteen orbits were covered, with the latest perihelion sitting at about 0.062 au (13.3 $R_\odot$). In the next phases, which will extend at least till late 2025, it will reach as close as 0.046 au (9.9 $R_\odot$). Among other instruments, PSP is equipped with payload for in-situ particle (SWEAP, Kasper et al., 2016) and fields (FIELDS, Bale et al., 2016) detectors, protected by the heat shield, and technologically developed to operate in the challenging near-Sun environment. These instrument suits provide measurements of density, velocity and temperature of protons, as well as of electric and magnetic field. The wealth of data collected by PSP in these previously unexplored regions of the near-Sun space have already provided a large amount of scientific discoveries (Bale et al., 2019; Kasper et al., 2019; McComas et al., 2019; Howard et al., 2019).

On the other side of the Atlantic ocean, in February 2020 the European Space Agency has launched Solar Orbiter (Müller et al., 2020; Zouganelis et al., 2020), a spacecraft equipped with both *in situ* and remote payload, able to produce simultaneous observations of the solar environment (including the photosphere and the corona) and in-situ measurements of plasma and fields. Solar Orbiter has an elliptical orbit that, exploiting several flybys at Venus and at the Earth, will reach its closest perihelion at 0.28 au (60 $R_\odot$), and at this time has reached as close as 0.32 au (69 $R_\odot$). The Solar Wind Analyser (SWA, Owen et al., 2020), the Magnetometers (MAG, Horbury et al., 2020) and the Radio Plasma Waves suite (RPW Maksimovic et al., 2020) provide, respectively, high-resolution, high-cadence ion and electron distribution functions and moments, magnetic field, and high frequency magnetic and electric fields.

The two state-of-the-art probes represents successful challenges, mostly due to the proximity with the Sun and the consequent extreme environ-

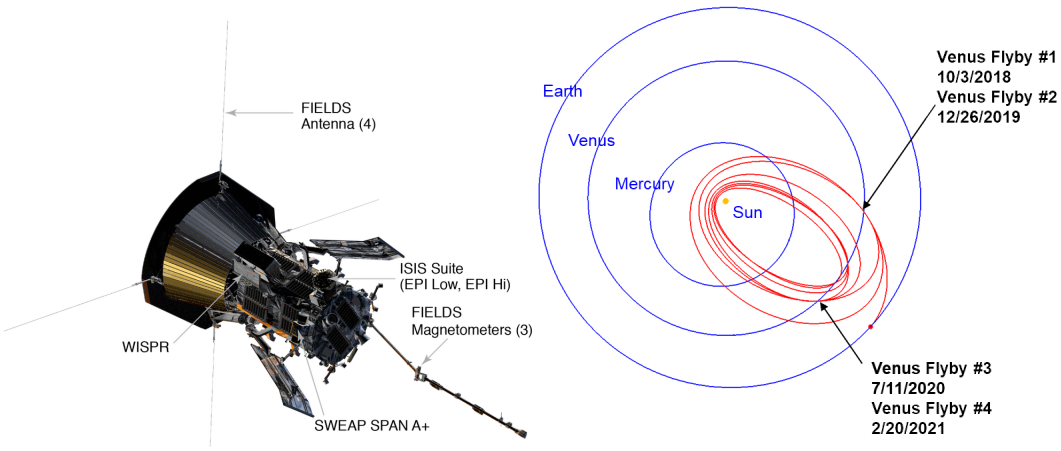

Figure 49: Left: rendering of the Parker Solar Probe, with the indication of the paylod location (source: JPL, available at `http://parkersolarprobe.jhuapl.edu/index.php`). Right: a graphical view of the typical PSP orbits (source: NASA, available at `https://blogs.nasa.gov/parkersolarprobe/2019/12/23/parker-solar-probe-heads-toward-second-venus-flyby`).

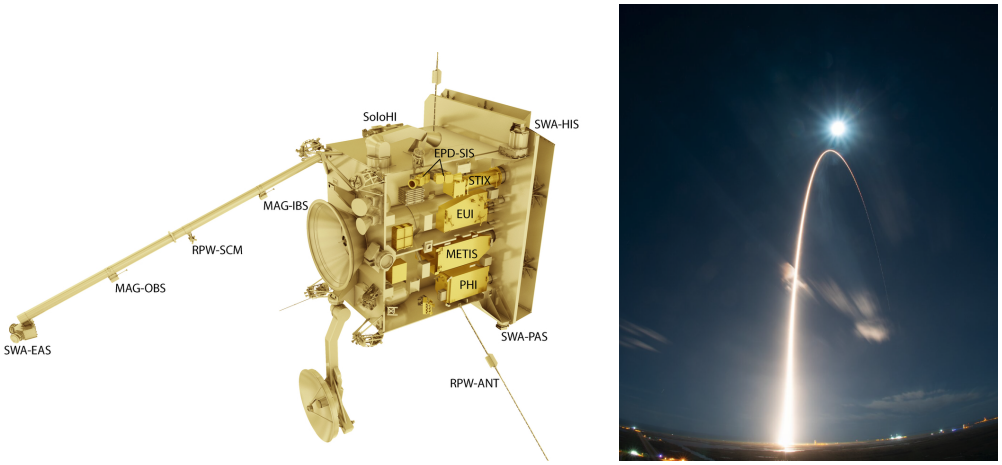

Figure 50: Left: rendering of the Solar Orbiter spacecraft, with labels indicating the payload (source: IRF, available at `https://www.irf.se/sv/irf-i-rymden/solar-orbiter`). Right: a picture of the Solar Orbiter launch from the Cape Canaveral site (source: ESA, available at `https://www.esa.int/Science_Exploration/Space_Science/Solar_Orbiter/Liftoff_for_Solar_Orbiter_ESA_s_mission_to_face_the_Sun_up_close`).

mental conditions that the spacecraft and their payload must survive. Heat shields were specifically designed using innovative materials, and the payload electronics was protected from the severe temperature gradients that the missions are bound to experience. As a result, both missions are currently exploring the inner heliosphere, offering an unprecedented opportunity to study the turbulence in the young solar wind and the way it evolves in its radial expansion. Additional science will benefit from alignments of the two probes, which could provide a series of two-point measurements of the evolving turbulence in the same plasma (Velli et al., 2020; Telloni et al., 2021).

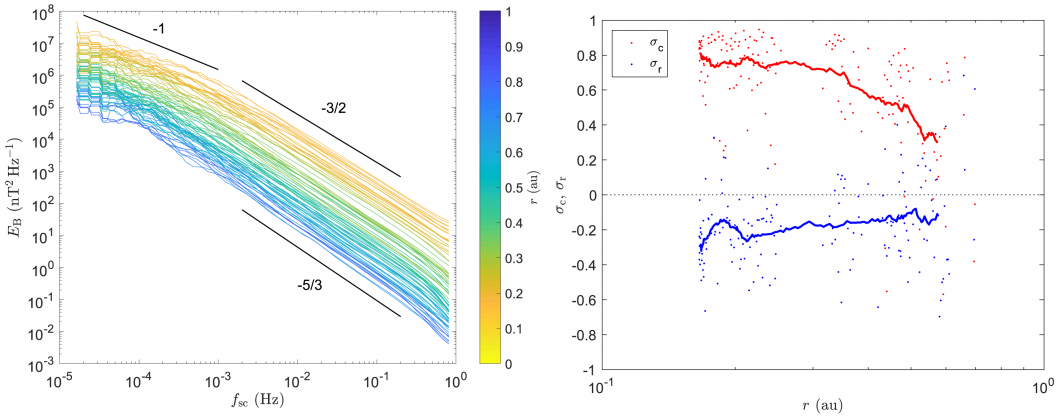

Figure 51: Left panel: radial evolution of the power spectral density of the interplanetary magnetic field as measured by Parker Solar Probe in the inner heliosphere during the first solar encounter. The radial distance is color-coded. The typical power-law scaling with exponents -1, -3/2 and -5/3 are indicated for reference. Right panel: radial evolution of the normalized cross-helicity σ_c (red dots: 6 hr average, red line: 30-point running average; for the definition see the last paragraph of Section 2.2) and residual energy σ_r (blue dots: 6 hr average, blue line: 30-point running average; for the definition see the last paragraph of Section 2.2). Figures from Chen et al. (2020).

We shall limit here to the topics of relevance to this review. Among these, several studies focused on the properties of turbulence and their radial evolution in the expanding solar wind. For example, Chen et al. (2020) studied PSP data and observed that the spectral power density of magnetic fluctuations gradually changes from a -3/2 power-law scaling (most of the time associated with the typical additional 1/f low-frequency range) at 0.16 au, typical of strongly Alfvénic turbulence, to a -5/3 scaling (with shorter or no 1/f range) at 1 au. This evolution is shown in the left panel of Figure 51.

Similarly, magnetic fluctuation power and Alfvénicity (see the right panel of the same figure) decrease with distance, while the magnetic compressibility increases (not shown). All these observations confirms the results from Helios measurements of an evolution towards more fully developed turbulence as the solar wind expands, corresponding to reducing the sweeping effect typically associated with Alfvénic fluctuations or to the depletion of the uncorrelated large-scale Alfvénic fluctuations, as described in Sections 6 and 6.2.

Using a more complete database which included eleven PSP orbits as well as one year of data from Solar Orbiter, Sioulas et al. (2022a) described the radial evolution of intermittency by means of the high-order moments of the scale-dependent fluctuations. In agreement with Helios observations, it was shown that intermittency generally increases with the radial distance (see for example the radial evolution of the flatness shown in Figure 52). Other parameters, such as the time of travel from the Sun, the angle between the magnetic field and the wind speed, and the solar wind bulk speed, also contribute to different degrees to determining the intermittency.

6.4. Mixed third-order moment scaling laws in the inner heliosphere

The spectral and structure function analysis was complemented by the study of the energy injection and transfer rates of the turbulent cascade. In Bandyopadhyay et al. (2020), the von Kármán decay law, equation (17), and the Politano-Pouquet linear scaling of the mixed third-order moment, equation (54), were used to estimate the turbulent energy injection and transfer rates, respectively. In order to capture signatures of radial evolution, the PSP first encounter measurements were divided in about 34 eight-hour disjoint intervals, each sufficiently larger than the typical observed correlation time ($\tau_c \simeq 300$—600 s, see Parashar et al., 2020; Bandyopadhyay et al., 2020). For each interval, the two relations above were computed. While the large-scale energy input is easily estimated for all intervals, for only 27 cases it was possible to find a linear scaling of the P&P law, and therefore estimate the energy transfer rate. Note that the authors use a convergence criterion that imposes negative scaling of the Taylor-transformed third-order moment, implying positive energy transfer rate and hence a direct turbulent cascade. Two examples of mixed third-order moment scaling are shown in the two top panels of Figure 53, for two different intervals at 36 $R_\odot$ (top) and 54 $R_\odot$ (center). A roughly linear scaling range is observed. This important observation supports the existence of a well developed turbulent cascade already as close to the Sun as 36 $R_\odot$ (top). This suggests that, even in the presence of

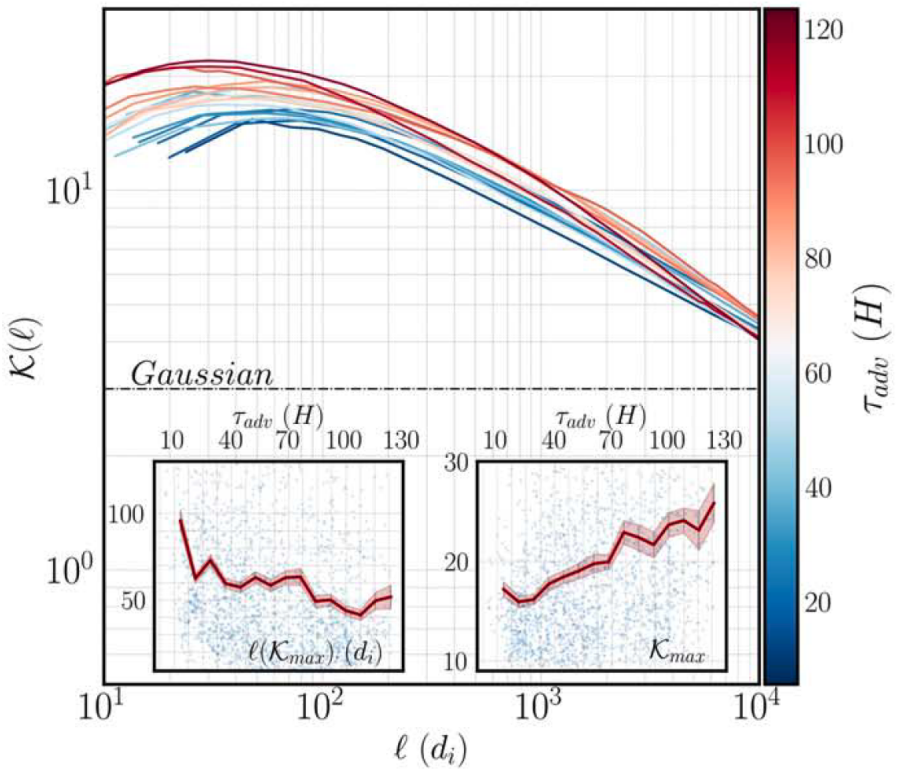

Figure 52: Main panel: scale-dependent kurtosis (namely the reduced flatness, $\mathcal{K} = F - 3$) of the magnetic field fluctuations, estimated at different heliocentric distance, here represented through the advection time τ_{adv}, namely the transit time from the Sun to the observation point (color coded). The two insets (points) show the scale of the maximum kurtosis (left) and the maximum value (right), while the red lines and shaded areas indicate the mean and standard deviation over a binned partition. Figure adapted from Sioulas et al. (2022a).

highly Alfvénic fluctuations with the typical -3/2 power spectral index, the turbulence should be considered as fully developed at those distances from the Sun. In the examples shown in the aforementioned paper, a linear fit to equation (54) is indicated (red line). The fit allows to rigorously identify the inertial range of turbulence, which in the two cases illustrated in Figure 53 lies between 10^2 and 10^4 d_i. Additionally, and more importantly, it provides the values of the energy transfer rate, ε, within each interval.

The energy injection and transfer rates can then be used to observe the variation of the turbulent cascade energization during the early stages of the

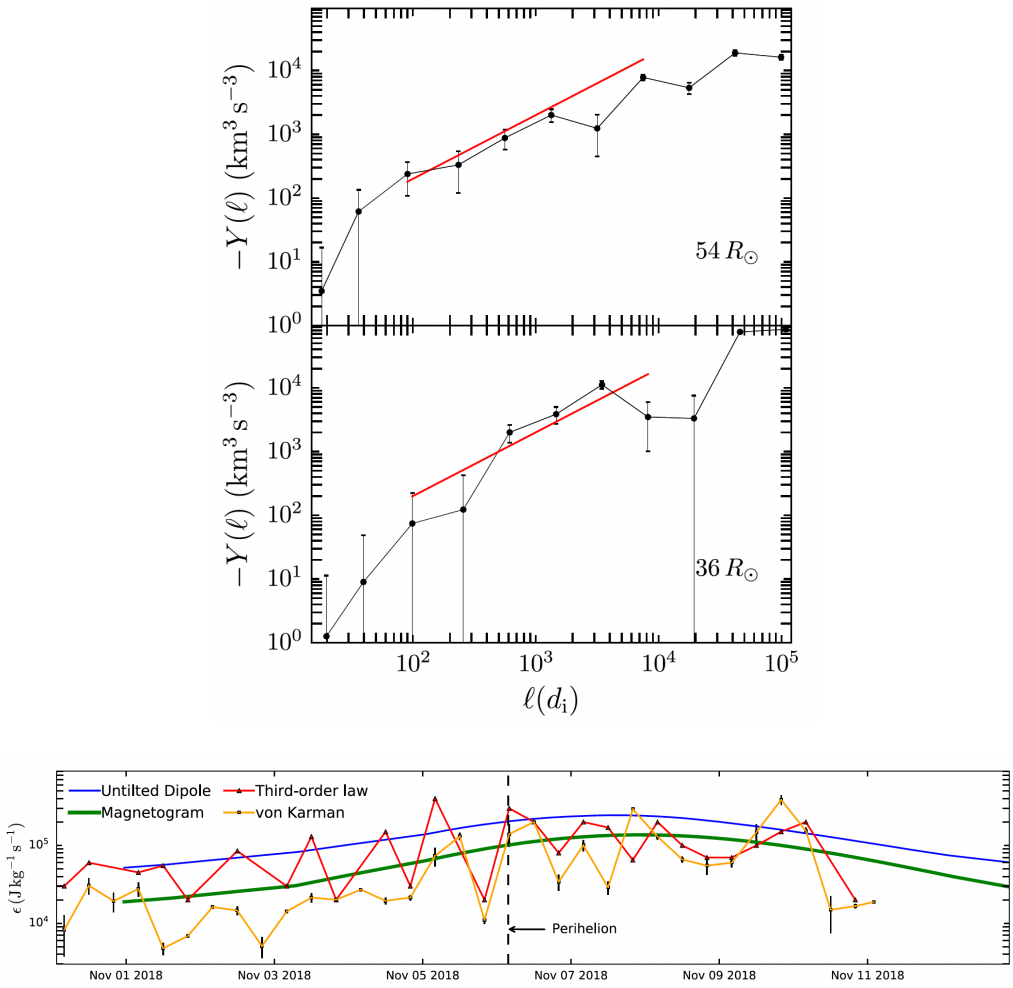

Figure 53: Top panels: P&P law estimated in two 8 hr intervals extracted from the first solar encounter of Parker Solar Probe. Linear fits in the inertial range are indicated by a red line. Bottom panel: turbulent energy transfer (red) and injection (yellow) rates obtained using 8 hr intervals from the first solar encounter of Parker Solar Probe. A comparison with two different global heliospheric models is also superposed (blue and green lines, respectively based on an untilted solar dipole and on measured solar magnetograms; for details see Bandyopadhyay et al., 2020). Figures from Bandyopadhyay et al. (2020).

solar wind expansion. The bottom panel of Figure 53 shows the values obtained from the data time series, which range between 10^4 and 10^5 J kg^{-1} s^{-1}. The closest approach of the probe. tothe Sun (perihelion) is indicated by a vertical black dashed line, while the right and left portions of the plot

refer to larger distances from the Sun. It is immediately evident that the two parameters are closely correlated within reasonable approximations, so that the energy transfer rate follows the energy injection rate quite closely. For both parameters, a common trend is visible indicating that the turbulent cascade is transferring more energy closer to the Sun, while some decay is visible at larger distance, particularly in the approaching phase (left part of the plot). Note that the values typically observed at 1 au are one or more order of magnitude smaller (see Section 4.4), in agreement with the interpretation that the turbulence may be in a decaying phase, and its energetic content is depleted during the expansion (Sorriso-Valvo et al., 2022). To confirm the goodness of the observation, a comparison was performed with two different realizations of a global solar corona and solar wind model. The simulations use a MHD-based model that include self-consistent turbulence transport and heating (Usmanov et al., 2018; Chhiber et al., 2019). Results, providing large-scale solar wind parameters, were then used to estimate the large-scale energy content, using the von Kármán approach as for the PSP data. Two different magnetic field boundary condition at the coronal base were used, namely a standard untilted Sun-centered dipole (blue line in the bottom panel of Figure 53), and the extrapolation of a photospheric magnetogram observed at the time of PSP measurements (green line in the bottom panel of Figure 53). Both simulations reproduce satisfactorily the overall profile of the energy injection rate, with the one based on the observed magnetograms slightly better capturing the values of the experimental data and its radial evolution. Whether the observed radial profile is due to the actual decay of the turbulence, or rather to expansion effects and/or other instabilities, is still an open question that needs to be addressed with the appropriate tools. To this aim, we recall that additional expansion terms can be evaluated in the P&P law (Hellinger et al., 2013; Gogoberidze et al., 2013), and numerical simulations can be used to test their relevance (Velli et al., 1990; Grappin et al., 1993; Tenerani and Velli, 2017). Moreover, the availability of data from successive PSP encounters will provide a much larger database, and reaching in closer to the Sun, allowing a deeper analysis. Synergistic studies using multiple spacecraft can also improve the detail of the interpretation, as attempted, for example, in Andres et al. (2021), where data from PSP, THEMIS (see Section 5.6) and MAVEN (see Section 7.4) were used. The third-order moment approach can and will still be crucial to effectively determining the nature and evolution of the turbulent cascade in the expanding solar wind.

6.5. Magnetic switchbacks and turbulence

One distinctive phenomenon observed by PSP is the frequent presence of sudden momentary reversals of the interplanetary magnetic field direction, commonly referred to as magnetic switchbacks (Bale et al., 2019). Figure 54 shows a popular pictorial view of a magnetic switchback.

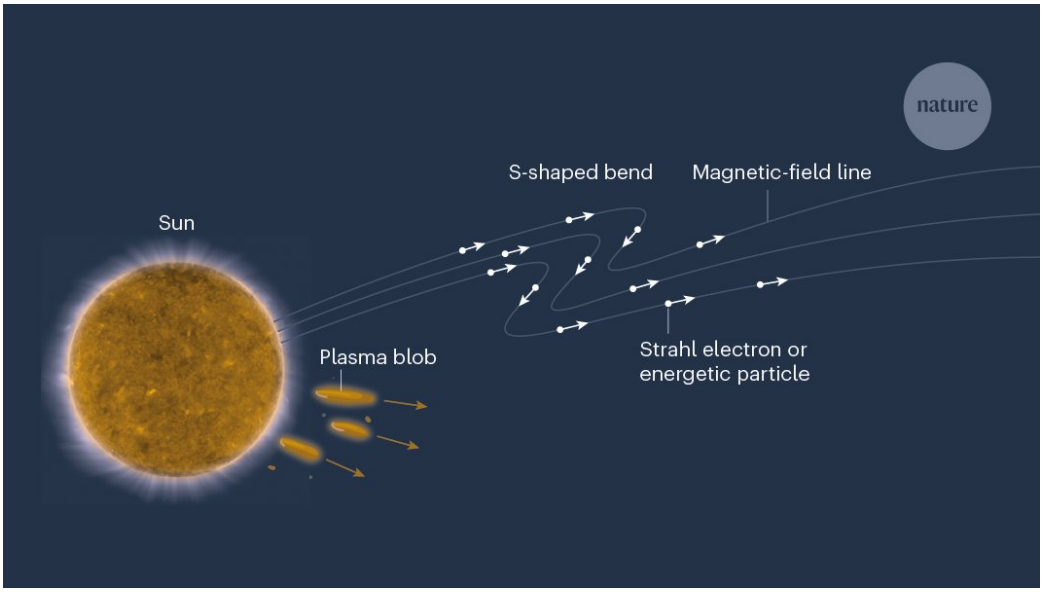

Figure 54: A pictorial representation of magnetic switchbacks. Figure from Verscharen (2019).

Early observations of fast solar wind streams in the outer heliosphere by the Ulysses spacecraft first revealed the existence of such structures (Balogh et al., 1999; Yamauchi et al., 2004; Neugebauer and Goldstein, 2013). However, these are increasingly visible closer to the Sun. The characteristics of the switchbacks have been studied in depth using PSP data as well as numerical simulations (e.g., Horbury et al., 2020; Bandyopadhyay et al., 2021b), yet their origin is still being debated and several models, not mutually exclusive, have been proposed. For example, it was proposed that switchbacks could be the signature of flux ropes produced by interchange reconnection in the solar corona (Fisk and Kasper, 2020; Zank et al., 2020; Sterling and Moore, 2020; Drake et al., 2021; Liang et al., 2021) or that they might be associated with the motion of magnetic field footpoints from the slow to the fast wind sectors (Schwadron and McComas, 2021). Magnetohydrodynamic numeri-

cal simulations suggest they may be Alfvénic structures originated in the lower corona and propagating out in the heliosphere (Matteini et al., 2015; Tenerani et al., 2020), or be related with a velocity shear-driven dynamics (Landi et al., 2006; Ruffolo et al., 2020). Bale et al. (2021) observed that switchbacks are not homogeneously distributed in the solar wind, but rather clustered in patches, whose size and distance is compatible with the coronal magnetic structure determined by the solar suprergranulation. This seems to suggest that switchbacks are nonlinear Alfvénic structures somehow associated with the global circulation of open magnetic flux at the solar surface (Fisk and Kasper, 2020; Zank et al., 2021). A different approach considers switchbacks as self-consistently generated during the solar wind expansion of turbulent fluctuations (Ruffolo et al., 2020; Squire et al., 2020; Shoda et al., 2021). However, the overall switchbacks occurrence characteristics observed by PSP better support their origin in the transition region rather than *in situ* (Mozer et al., 2021; Bale et al., 2021; Fargette et al., 2021). The latter view is also supported by a recent remote observation of one switchback propagating in the solar corona (Telloni et al., 2022a). The switchback, shown in Figure 55 was observed in the visible light channel of the METIS coronagrapher onboard Solar Orbiter (Antonucci et al., 2020),

The relationship between the presence of switchbacks and turbulence represent a novel, interesting problem that has been explored in recent studies. According to their originating mechanisms, these structures can either be considered as simply superposed to the underlying turbulence, not excluding their possible role as additional energy injection source for the nonlinear turbulent cascade, or, on the contrary, as being dynamically generated self-consistently by the turbulence. Dudok de Wit et al. (2020) studied the spectral properties of magnetic fluctuations separately for periods of high and low incidence of switchbacks, showing that the magnetic spectra have Kolmogorov-like scaling $f^{-3/2}$ only in intervals populated by switchbacks. Intervals poor in switchback showed a limited Kolmogorov inertial range, whereas the low-frequency end is characterized by a $1/f$ uncorrelated noise, routinely seen in fast solar wind (Bavassano et al., 1982; Verdini et al., 2012; Chandran, 2018; Matteini et al., 2018). According to this observation, it was concluded that in the quiet samples the turbulence is not yet developed, while the intervals with presence of switchbacks have fully developed turbulence. This suggests that switchbacks are a driver of the turbulence, and are responsible for accelerating its evolution as the solar wind expands (Bourouaine et al., 2020). Other authors suggested that the switchbacks

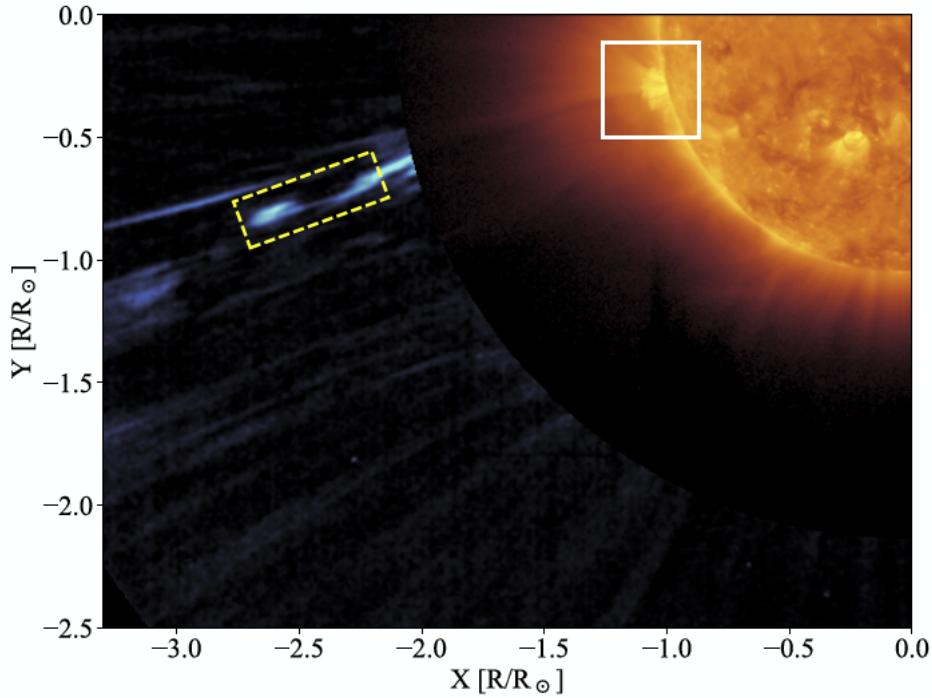

Figure 55: First Solar Orbiter observation of a switchback in the solar corona (yellow-dashed line box), shown in a composite image of the solar corona (METIS) and disk (EUI, Extreme-Ultraviolet Imager). Figure from Telloni et al. (2022b).

dynamics is more complex and includes both their depletion through turbulent fluctuations, and their generation through nonlinear processes (Tenerani et al., 2021). Further observations have added more indications, for example highlighting that switchbacks are sites of enhanced intermittency (Perrone et al., 2020; Martinović et al., 2021). Independent of the origin of the switchbacks, the above observations are well consistent with the typical low-frequency broadening of the spectral inertial range as the distance from the sun increases (Bavassano et al., 1982; Bruno and Carbone, 2013; Chen et al., 2020).

It is well known, however, that spectral properties are not sufficient to describe the nature of turbulence. Instead, the P&P law can help assessing more robustly the presence of a fully developed cascade, the extension of its inertial range, and the associated energy transfer rate. To this aim, the PSP first encounter was recently used to study possible relations between presence

of switchbacks and the characteristics of turbulent cascade (Hernández et al., 2021). An overview of the plasma and magnetic field data used for the study are shown in the three top panels of Figure 56, and the radial distance from the sun is shown in the bottom panel of the same figure. Switchbacks are visible as sharp jumps of the B_x component (black line). Hernández et al. (2021) used the parameter introduced by Dudok de Wit et al. (2020) to detect their presence

$$\mathrm{z} = 0.5(1 - \cos\alpha)\,, \tag{121}$$

where $\alpha = \cos^{-1}(\mathbf{B} \cdot \langle\mathbf{B}\rangle/(B\langle B\rangle))$ is the angle of deflection of the local magnetic field $\mathbf{B}$ with respect to the mean field $\langle\mathbf{B}\rangle$, the mean being estimated over 6 h intervals. The parameter z is plotted in the fourth panel from the top of Figure 56 as a gray line. The richness of switchbacks in the dataset is evident, as well as their clustering (Dudok de Wit et al., 2020; Bale et al., 2021). Relying on an arbitrary threshold for the parameter z, specific intervals where manually selected with maximal (S, for switchbacks) or minimal (Q, for quiet) occurrence of switchbacks. Further imposing the requirement of intervals larger than about three times the correlation timescale, $\tau_c \simeq 1$ h (Parashar et al., 2020; Bandyopadhyay et al., 2020), six S and six Q intervals were eventually used. These are indicated by the purple open circles and the olive-green full circles in the same panel as z. Additionally, a statistical and quantitative approach complemented the study. The mean value of the switchback parameter, $\langle\mathrm{z}\rangle$, was indeed used to estimate the quantity of switchbacks in non-overlapping running windows of 6 hours, therefore providing a discrete measure of the presence of switchback during the whole encounter. The mean switchback parameter is shown as blue diamonds, labeled with R, for running, in Figure 56, along with the values for S and Q samples. The spectral properties, intermittency and mixed third-order scaling law were then determined in the S, Q and R intervals. The analysis revealed interesting and unexpected features. The first important observation was that the P&P law is validated in several intervals (as already shown by Bandyopadhyay et al., 2020), but its presence does not depend on the incidence of switchbacks. Both Q and S samples presented well-developed scaling ranges, on some occasions with changes of sign in the third-order moment, Y. Two examples are given in Figure 57, one for a quiet interval (left panel), and one for an intervals with high occurrence of switchbacks (right panel). In the case with switchbacks, a clear change of sign is observed at a scale that corresponds to the break in the power-law scaling of the struc-

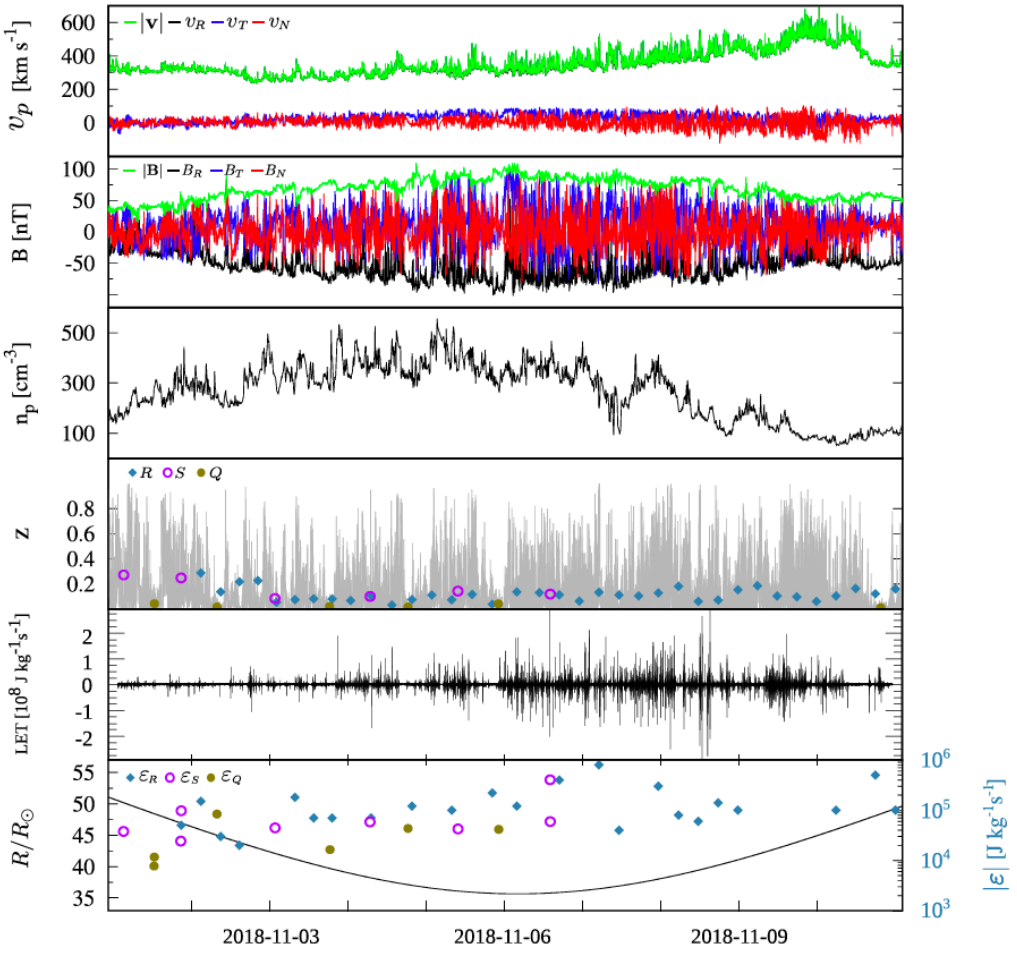

Figure 56: Overview plot of the first encounter measurements by PSP. From top to bottom: proton velocity v_p (500 s average); magnetic field, **B** (500 s average); proton density n_p (500 s average); switchback parameter, z, (equation (121), gray line) and its average values in 6 hr running windows, $\langle z \rangle$ (color-coded points, see the legend, where R, S and Q stand for running, switchback and quiet intervals, respectively); local energy transfer rate proxy, LET (see Section 8), estimated for $\Delta t = 16$ s; absolute value of the mean energy transfer rate, $|\varepsilon|$ (color-coded points indicating values ε_R, ε_S and ε_Q corresponding to R, S and Q intervals, see the legend), along with the radial distance from the Sun in solar radii units, $R/R_\odot$ (black line). Figure from Hernández et al. (2021).

ture functions (not shown here, see Figure 3 of Hernández et al., 2021). The nature of such change of sign is still unclear, although it may suggest the possibility of an inverse cascade occurring as the result of the energy injec-

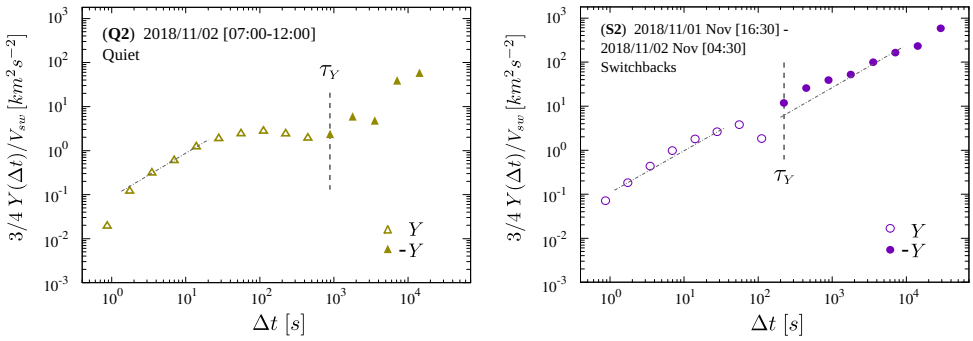

Figure 57: Two examples of the P&P law in PSP data. The third-order moment is normalized to $3/(4V_{sw})$ for a more direct comparison. Left panel: a quiet interval (green symbols). Right panel: an interval with switchbacks (purple symbols). Open and full symbols indicate positive and negative values, respectively. Linear fits are shown as dashed lines, and the vertical lines indicate the timescale τ_Y of the sign reversal. Figure from Hernández et al. (2021).

tion from switchbacks, whose size roughly corresponds to the break scale. Numerical simulations and a more extensive statistical study of solar wind data could help clarifying the nature of change of sign, and the possible role of the switchbacks and of other large-scale structures. After evaluating the energy transfer rate by fitting the P&P law as usual, three more important observations emerged, corroborating the scenario of evolution of turbulence described in the previous sections. These are illustrated in Figure 58. First of all (top panel), there is a weak but non negligible decrease of the energy transfer rate with the increasing radial distance from the Sun. This confirms previous PSP observations (Bandyopadhyay et al., 2020) and the recent Helios 2 results (Sorriso-Valvo et al., 2022). Secondly (central panel), positive energy transfer rates are moderately correlated with the number of switchbacks, suggesting that these may be associated to more energetic cascades, and also in agreement with the observations of Dudok de Wit et al. (2020). Finally (bottom panel), as also observed for the Helios 2 recurring streams (Sorriso-Valvo et al., 2022), the energy transfer rate increases with the cross-helicity. This confirms that the inverse proportionality inferred from the statistical analysis at 1 au (Smith et al., 2009), which captures the expected inhibiting effect of the large-scale Alfvénic decorrelation on the nonlinear interactions (Dobrowolny et al., 1980), is probably a subdominant effect with respect to the radial decay of the turbulence. It is interesting to remember that an inverse relation was found between the cross-helicity and the number

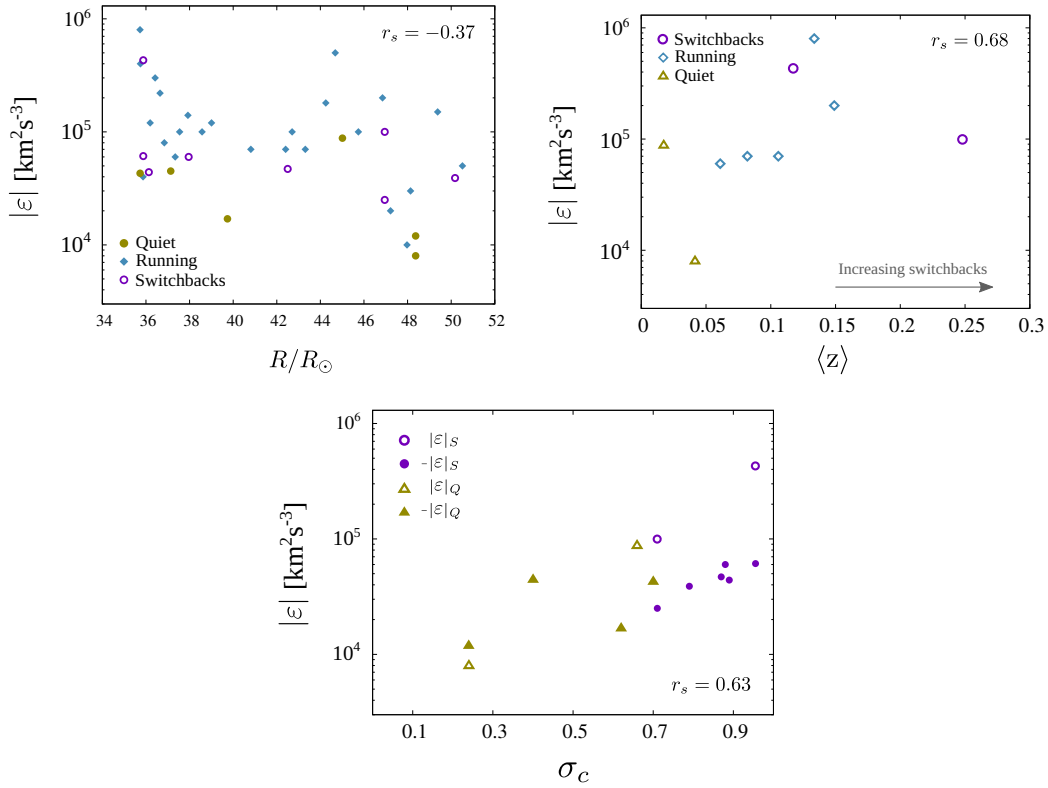

Figure 58: Variation of the energy transfer rate with various parameters. Top-left panel: radial distance from the Sun. Top-right panel: mean number of switchbacks (in this case, only positive values of ε were considered). Bottom panel: normalized cross-helicity. Green, purple and blue symbols refer to quiet, switchbacks and running intervals, respectively. Open (full) symbols indicate positive (negative) values. Figure from Hernández et al. (2021).

of intervals where the P&P law was validated using polar Ulysses data in the outer heliosphere (Marino et al., 2012). This is not in contrast with the above analysis, since it does not examine the energy transfer of the cascade, but only the validity of the P&P law, which is a more direct expression of the decorrelation effect. The results of this preliminary study support the idea that switchbacks are an important source of energy for the turbulent cascade, and therefore may represent one of he crucial mechanisms leading to the onset of turbulence in the solar corona.

6.6. First observations of turbulence in the proximity of the Alfvén surface.

Observations in the inner heliosphere provide a detailed description of the way the turbulence evolves as the solar wind expands away from the Sun. It reveals that spectra and intermittency are ubiquitous. Furthermore, we have seen using the P&P law that the radial profile of the energy transfer rate suggests that the turbulence may be decaying in the solar wind expansion. Still, the question about the birthplace of turbulence remains unanswered. PSP observations close to the sun showed an active and highly energetic cascade as close as $\sim 30R_\odot$ (Bandyopadhyay et al., 2020; Andres et al., 2021). In order to determine if the turbulence is first generated inside the corona or rather at its boundary, and with which energy, it is necessary to analyze data from the frontier separating the corona from the solar wind. Such frontier, called the Alfvén critical surface, is predicted to be irregular and highly variable, being directly modulated by the solar activity and by the coronal magnetic structure. The critical surface marks the transition from the magnetically-dominated solar coronal plasma to the freely streaming solar wind. Conditions on two parameters can be used to determine the position of the frontier, the Alfvén radius, r_A, so that the coronal plasma is where $\beta < 1$ and the Alfvénic Mach number is $M_A = v_{sw}/v_A > 1$. On April 28, 2021, PSP crossed the coronal boundaries for nearly 5 hours, while skimming the Alfvén surface in its sixth perihelion approach around 19 $R_\odot$ (Kasper et al., 2021). An overview of the PSP measurements is shown in Figure 59, along with the angle between the magnetic field and the wind velocity, θ_{BV}, the mean plasma β and the radial Alfvén Mach number, and the wavelet power spectrogram of the magnetic field fluctuations parallel and perpendicular to the mean field (Sorriso-Valvo and Yordanova, 2022). In order to study the properties of the turbulence in the frontier region, three sub-intervals were selected for the analysis, as indicated by the color-shaded areas in 59: (i) one sub-Alfvénic interval (SC, from solar corona, blue area) Kasper et al. (2021) with $M_A < 1$, assumed to be inside the solar corona; (ii) a superalfvénic interval preceding SC (SW1, red area), with $M_A > 1$ and therefore assumed to be in the streaming solar wind, although occasionally crossing the Alfvén surface; (iii) a super-Alfvénic interval following the sub-Alfvénic interval (SW2, yellow area), again with $M_A > 1$ and in the streaming solar wind.

In the three intervals, most of the solar wind parameters shown in Figure 59 were comparable. In particular, they were characterized by quasi-sunward magnetic field, considerable velocity and magnetic field fluctuations, $\delta v/v_0 \simeq \delta B/B_0 \simeq 0.2$—$0.3$, and high Alfvénicity, $\sigma_c \simeq 0.85$. A major differ-

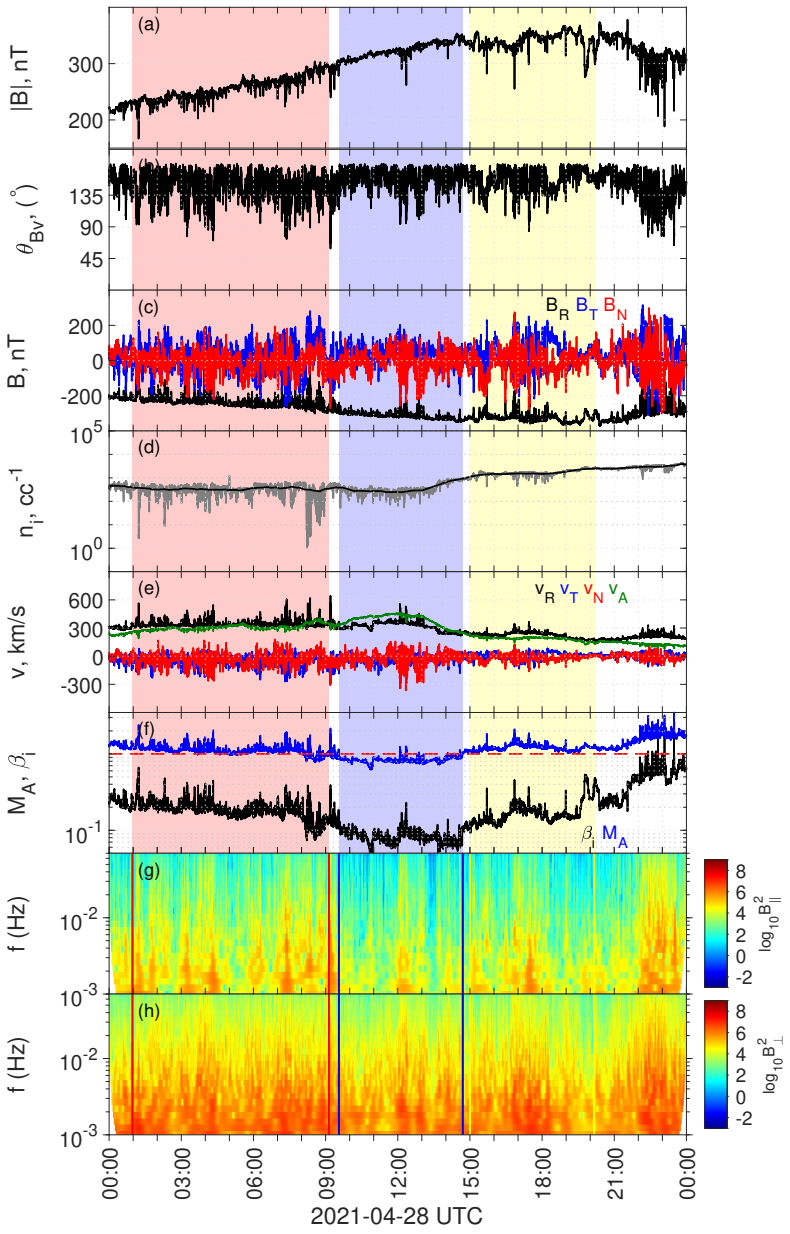

Figure 59: Overview plot of the event measured by PSP on April 28, 2021. From top to bottom: (a) magnetic field magnitude $|\mathbf{B}|$; (b) angle between the magnetic field and the (radial) velocity, θ_{BV}; (c) RTN magnetic field components; (d) ion density n_i (grey) along with its one-hour average $\tilde{n}_i$ (black); (e) RTN velocity components v_i and Alfvén speed, V_A; (f) ion plasma β and Alfvénic Mach number, M_A; (g) parallel ($||$) and (h) perpendicular ($\perp$) magnetic spectral power (in nT^2 Hz^{-1}). Figure from Sorriso-Valvo and Yordanova (2022).

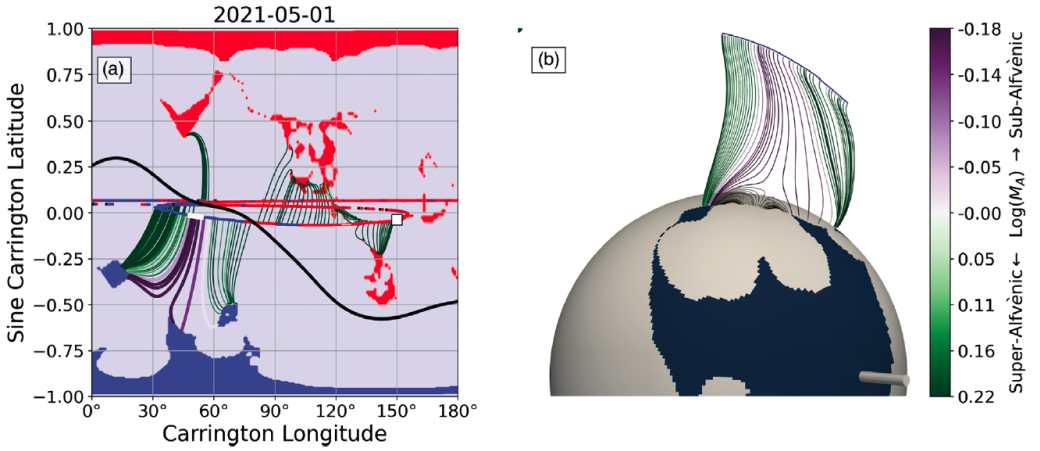

Figure 60: Mapping of solar wind plasma from PSP to the solar surface based on a PFSS magnetic field model. The left panel shows a two-dimensional Carrington projection of the photospheric magnetic field, based on an observed ADAPT-GONG magnetogram recorded on 1 May 2021. Red and blue areas represent coronal hole regions with outward and inward field polarities, respectively. The black line indicates the position of the the heliospheric current sheet measured *in situ* by PSP and projected at the height of 2 $R_\odot$ above the photosphere. The red and blue lines show the spacecraft trajectory for an extended period centered on April 28, projected at 2 $R_\odot$ (the colors indicating the magnetic polarity measured *in situ* by PSP). Green and purple lines indicate the magnetic field lines connecting the projected trajectory at 2 $R_\odot$ to the photosphere, with the Alfvén Mach number given by colors (described by the color bar on the right hand of the left panel). The short white portion of trajectory indicate the sub-Alfvénic period of study, and the white square indicates its position at the beginning of 1 May 2021. In the right panel, a 3D reconstruction is presented for the day 28. Figure from Kasper et al. (2021).

ence between the samples was revealed tracing back the plasma of the three intervals to their originating region on the solar surface. This was clearly highlighted by the three-dimensional reconstruction of the magnetic field connecting the spacecraft to the solar photosphere (Kasper et al., 2021), performed using the potential field source surface model (PFSS, Badman et al., 2020). The reconstruction is shown in the left panel of Figure 60 for an extended interval, and in the right panel for the day 28, under analysis here. The reconstruction allowed to identify the reasons for the differences in Mach number. In fact, it emerged that the solar wind intervals SW1 and SW2 were magnetically connected to two separate low- and mid-latitude coronal holes in the southern solar hemisphere. These regions are characterized by nearly radial open magnetic field lines, indicated in green in Figure 60 (green in-

dicating connectivity with plasma flowing with $M_A > 1$). They are usually associated to Alfvén waves propagating outward, which interact nonlinearly with an inward component generated by reflection by the strong radial density gradient. Such interaction is one of the possible mechanisms generating the turbulence in the corona. The two SW intervals show indeed large-scale Alfvénic fluctuations, as evidenced by the strong power in the perpendicular magnetic fluctuations in the 100—1000 s range (panel h of Figure 59). Such power is also associated with the presence of switchbacks, which are Alfvénic in nature, and are also visible as large-scale structures in the parallel magnetic fluctuations (panel g of Figure 59). Note that the above range is compatible with the 100—500 s period of the outward-propagating Alfvénic motions observed in the lower corona and in the transition region (McIntosh et al., 2011), considered as possible agents of coronal plasma heating and solar wind acceleration. On the other hand, the mapping provided by the PFSS modeling showed that for interval SC the photospheric magnetic footpoint was initially located in the same southern coronal hole generating SW1 (see Figure 60, where the purple magnetic field lines indicate connectivity with the flow with $M_A > 1$), but then rapidly jumped to a mid-latitude extension of the southern polar coronal hole. Such sudden change was interpreted as a pseudostreamer region, where closed magnetic loops (visible in the three-dimensional reconstruction represented in the right panel of Figure 60) are enveloped by the neighbouring open lines (Kasper et al., 2021). Few or no switchbacks were present in this sample, and the associated large-scale magnetic power is smaller (panel g of Figure 59), consistently with the properties of a region above a pseudostreamer. Therefore, despite the overall similarity of the plasma and fields parameters, the two SW and the SC intervals were connected to two fundamentally different solar source regions, which explains the difference in the Mach number and in the turbulence, as will be shown in the following.

The properties of turbulence were initially evaluated using resampled 7-second plasma and magnetic field measurements to perform the classical structure functions analysis. In particular the second-order structure function, S_2, was considered as an alternative to the power spectral density. The Flatness, $F(\Delta t) = S_4/S_2^2 \sim \Delta t^{-\kappa}$, and its scaling exponent κ, were used to evaluate the intermittency, as an alternative to the whole set of scaling exponents of the structure functions. The above quantities were estimated for ion velocity, magnetic field and ion density, for the three selected intervals, and are shown in Figure 61. The possibility to estimate structure functions

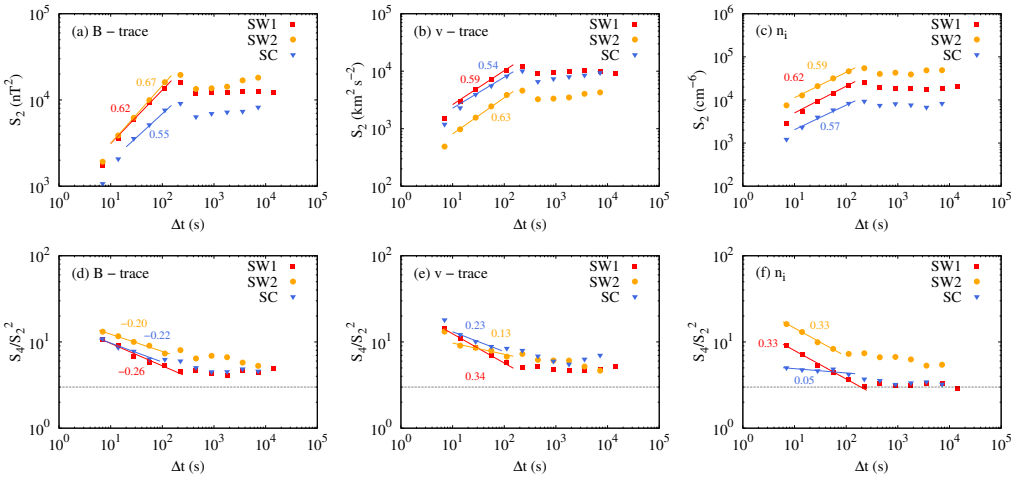

Figure 61: Panels *a*-*c*: second-order structure functions of magnetic field, velocity and proton number density, for the three intervals (color-coded in each panel). For vector field, the sum over the three components is plotted, corresponding to the spectral trace. Panels *d*-*f*: the flatness of the same fields. For the vector fields, the average over the three components is shown. For each case, a power-law fit and the fitted scaling exponent is indicated with color-coded lines and numbers. Figure from Sorriso-Valvo and Yordanova (2022).

up to the fourth order was confirmed by the convergence test described in Dudok de Wit (2004). The results were observed to be qualitatively similar for the three components of the vector fields. Therefore, for a simpler visualization, the three components of velocity and magnetic vectors were summed (for the spectra, obtaining the equivalent trace) or averaged (for the flatness, obtaining the mean intermittency scaling). The same colors of the shaded regions in Figure 59 were used to identify the three intervals. Power-law fits (lines) in the appropriate ranges of scales provided the scaling exponents, ζ_2 and κ, which are indicated in the figure using the same colors. The second-order structure function S_2 scaling (panels *a*-*c*) reveals a robust inertial range for all the fields, which extends approximately between 10 and 100 s. Such range is compatible with previous spectral estimates (Kasper et al., 2021) and with the estimated correlation scale (of the order of 200 s, as estimated as the e-folding scale of the autocorrelation function, and roughtly in agreement with independent values given in Zhao et al., 2022). Additionally, they correspond to the range of the large-scale Alfvénic structures visible in the spectrograms described above (panels g and h of Figure 59). For all intervals,

the spectral exponents are between 5/3 and 3/2, which is compatible with the standard Kolmogorov or Kraichnan phenomenology. It might be noted that the coronal (SC) interval has slightly smaller exponent for all the fields. This could be interpreted as a less developed status of the turbulence with respect to the two adjacent SW intervals. The flatness (panels *d*-*f*) shows similar power-law and intermittency exponents for all cases (with the exception of density in the SW2 interval). At large scales, $\Delta t > 100$ s, both the second-order structure functions and the flatness are nearly constant. This is consistent with the $1/f$ spectrum being associated with the broad presence of large-scale Alfvénic fluctuations (Bruno and Carbone, 2013; D'Amicis et al., 2021; Chandran, 2018), a reservoir for the solar wind turbulence (Verdini et al., 2012)

In order to capture the subtle differences in the turbulent cascade possibly associated with the different origin of the coronal and solar wind samples, the scaling of the mixed third-order moment, equation (54), and the associated energy transfer rate ε were evaluated for the three intervals. The scaling laws are shown in Panels *a*-*c* of Figure 62, where positive and negative Y are indicated by full and open symbols, respectively. Unlike the structure functions analysis, the P&P law is able to capture a striking, fundamental difference between the solar wind and coronal plasma. In the two solar wind samples (panels *a* and *c*), the P&P scaling law is valid in a range compatible with the structure functions inertial range (cf. Figure 61). On the contrary, the coronal interval (panels *b*) does not show any linear scaling, with Y changing sign erratically and the moments considerably scattered along the scales. This simple observation carries two important results. First, it shows that solar wind turbulence can be already fully developed in the proximity of the solar corona (19 $R_\odot$) when the plasma is connected to coronal holes. In that configuration, it is likely that the Alfvénic fluctuations and the associated switchbacks provide the necessary energy to sustains the turbulent cascade. Second, it suggests that if the flow is not connected with coronal holes, as in the SC sample, and if the Alfvénic fluctuations and switchbacks are limited, the cascade may have not yet reach a fully developed state at the Alfvén surface. We will comment more on this possible consequence in the following. The structure of the coronal plasma can therefore drive the inhomogeneous properties of turbulence in the solar wind (Bale et al., 2021; Hernández et al., 2021). A third important result relies upon the measured energy transfer rate. The observed values, $\varepsilon = 520$ kJ kg^{-1} s^{-1} in SW1 and $\varepsilon = 100$ kJ kg^{-1} s^{-1} in SW2, are comparable with those measured at

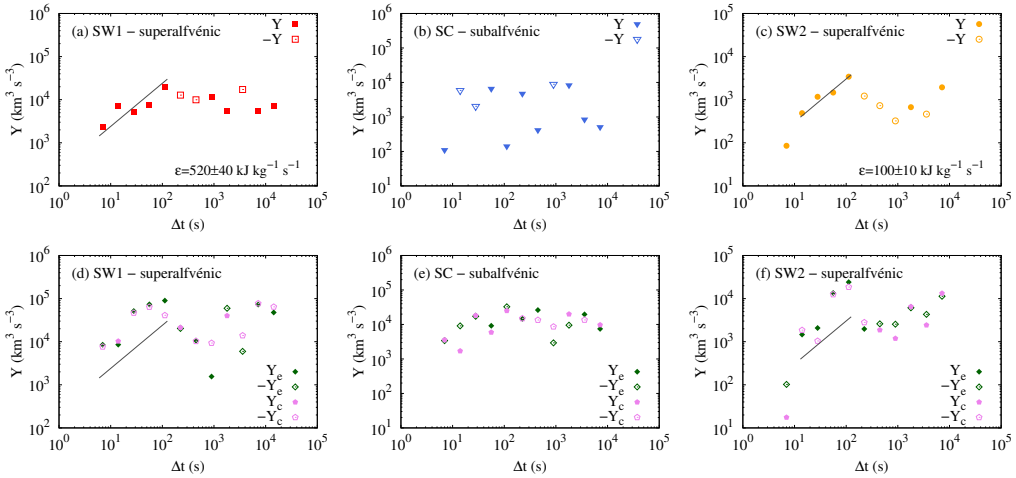

Figure 62: Panels *a-c*: third-order moments, $Y(\Delta t)$, for the three samples. In SW1 and SW2 samples, linear fits and the associated energy transfer rate are indicated. In the SC sample, no linear scaling was observed, probably due to underdeveloped turbulence (see discussion in the main text). Panels *d-f*: breakdown of the mixed third-order moment in its energy (Y_e, green diamonds) and cross-helicity (Y_c, violet pentagons) components. In all panels, full (open) symbols show positive (negative) values. Figure from Sorriso-Valvo and Yordanova (2022).

larger distance form the sun (36 $R_\odot$, Bandyopadhyay et al., 2020; Hernández et al., 2021), indicating that the turbulence is fully energized at the corona frontier and does not necessarily require further in-situ energization during the expansion.

Finally, more subtle differences can be highlighted by looking at the contribution to the moment Y from each term of the P&P law: the energy contribution, $Y_e = \langle \Delta v_L(|\Delta \mathbf{v}|^2 + |\Delta \mathbf{b}|^2)\rangle$, and the cross-helicity one, $Y_c = -2\langle \Delta b_L(\Delta \mathbf{v} \cdot \Delta \mathbf{b})\rangle$. These are shown separately in panels *d*-*f* of Figure 62. In SW1 and SW3, the contribution to the linear scaling is positive and have roughly linear scaling for the energy term, but it is mostly negative and with less clear linear scaling for the cross-helicity term. In the SC interval, the energy term, Y_e, carries mostly negative contribution, while the cross-helicity term, Y_c, is positive, suggesting a different dynamics in which the Alfvénic fluctuations are transferring energy to small scales, but velocity and magnetic field individually are not able to generate appropriately correlated intermittent structures yet, possibly representing an earlier stage of the turbulence. More data analysis and comparison with numerical simulations will be necessary to interpret such observations in terms of dynamical properties of the turbulence.

A note on the validity of the Taylor hypothesis is necessary at this point. (Bandyopadhyay et al., 2022) pointed out that, given the mean flow speed the Alfvén speed, and the typical fluctuations, the Taylor hypothesis may be failing in these intervals. Furthermore, the presence of large-scale Alfvénic fluctuations may result in doppler-shifted frequencies which are different for inward and outward fluctuations. This may represent a major issue when estimating scale-dependent increments through time series, since it could result in some mixing of space structure and time dynamics. In a separate analysis of the same data, Zhao et al. (2022) used a modified Taylor hypothesis (Zank et al., 2022) that involves using a different speed for inward and outward modes, each obtained combining the solar wind speed with the Alfvén speed of the corresponding mode. Such procedure should ensure a better implementation of the Taylor hypothesis-based transformation from time to space scales. In their paper, Zhao et al. (2022) estimate the power spectral density of the Elsasser fields, which have well-developed power-law range, and largely dominant outward modes. They also estimate the compressible (Andres et al., 2021) and incompressible (Politano and Pouquet, 1998) third-order scaling laws, separately for the inward and outward modes (after using the modified Taylor hypothesis), and then sum them to obtain

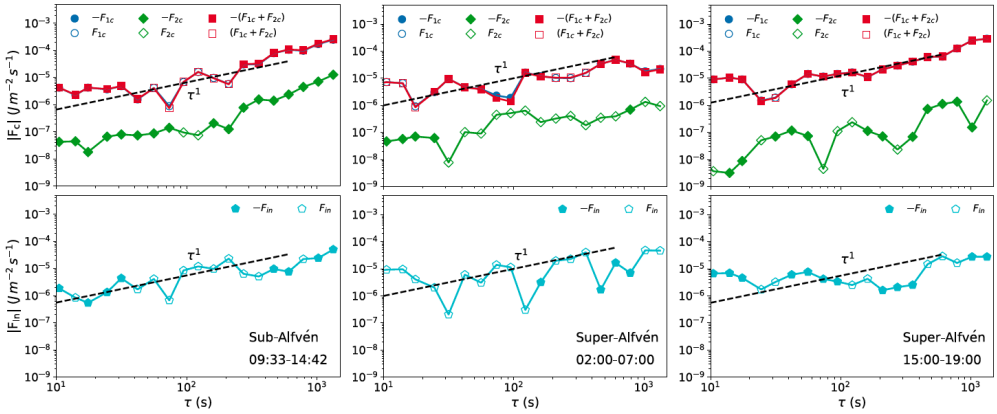

Figure 63: Top panels: compressible energy flux terms F_{1c} (flux terms, blue, equivalent to $F_{1a} + F_{1b}$, equations (100-101)) and F_{2c} (internal-energy term, equivalent to F_2, equation (102)), together with their sum (red), estimated as in Andres et al. (2021). Bottom panels: the same but using the standard incompressible P&P relation, equation (54). Left panels: sub-Alfvénic interval SC; central panels: superalfvénic interval SW1; right panels: superalfvénic interval SW2. Figure adapted from Zhao et al. (2022).

the mean energy transfer rate. As shown in Figure 63, there is evidence of relatively good compressible scaling (with definite sign) in the second of the two super-Alfvénic intervals (spanning from 15:00 to 19:00, equivalent to SW2), while the scaling is less clear in the other one (from 02:00 to 07:00 equivalent to SW1). The scaling is even less clear, with non convergent sign, in the sub-Alfvénic interval (09:33 to 14:42, equivalent to SC). The incompressible scaling gives slightly less converging results, but have a comparable energy transfer rate, showing that the overall compressible contribution is small. The compressible energy transfer rate, estimated for the three cases by means of a linear fit of the absolute values of the third-order moments, was $\varepsilon \simeq 150$ kJ kg^{-1} s^{-1} for the two SW intervals, which are in good agreement with those found using the incompressible case and without applying the modified Taylor hypothesis. On the other hand, a higher energy transfer rate, of the order of 570 kJ kg^{-1} s^{-1}, was obtained for the coronal sample.

The conclusions of the study in this specific sample that turbulence is already developed, although the difficult experimental conditions do not allow a robust claim based on observations. The dubious validity of the Taylor hypothesis seems to be alleviated by the positive comparison with the results obtained using a modified Taylor hypothesis. However, even the modified

version could not be sufficiently accurate as to draw strong conclusions from the results. The observation of a linear scaling seems to be the stronger indication that the analysis is, in fact, feasible, since it is hard to build a sign-definite third-order moment from randomized fluctuations.

The mixed third-order moment results on the nature of the turbulence in previously unexplored regions of the solar surrounding seem to suggest that the onset of turbulence happens close to the corona or inside of it, and that the inhomogeneity of solar wind turbulence has roots in the solar coronal structure. However, with all the above caveats in mind, it is clear that the near-Sun results presented in this section should be taken with the due precaution. A more extended statistical investigation is obviously necessary to confirm their validity.

7. Third-order scaling laws in near-Earth and planetary space, and in other exotic environments

Most planets of the solar system have an intrinsic magnetic field, probably frozen in their metallic cores and sustained by dynamo effects. Typically dipolar, such magnetic fields have normally slow dynamics, and can be considered as static compared to the subjects of study in this report (Davies and Constable, 2020). The magnetosphere refers to the region where the planet's magnetic field is dominant and controls the dynamics of the particles, as opposed to the interplanetary plasma, controlled by the heliospheric magnetic field. Being embedded in the solar wind, magnetospheres continuously interact with the interplanetary plasma and magnetic field. The solar wind blows on the planetary magnetospheres, considerably modifying their undisturbed dipolar configuration (Akasofu, 1981; Pulkkinen, 2007; Borovsky, 2021). The complex dynamical coupling between magnetosphere and solar wind is driven by the solar activity, and in fact determines a large part of the star-planet interaction. Such interaction is extremely important as it controls space weather conditions, which modulate the magnetic and radiation balance of the planet, and hence affect its habitability (Cohen et al., 2014; Airapetian et al., 2020). A schematic view of the terrestrial magnetosphere is presented in Figure 64, with the solar wind blowing from left to right indicated with yellow arrows, the magnetosphere indicated by the blue-black region, and the Earth (not in scale) in the deformed dipole center. The solar wind pressure deforms the planetary dipole, pushing the day-side lobe towards the planet, and stretching the night-side in the flow direction, generating an extended

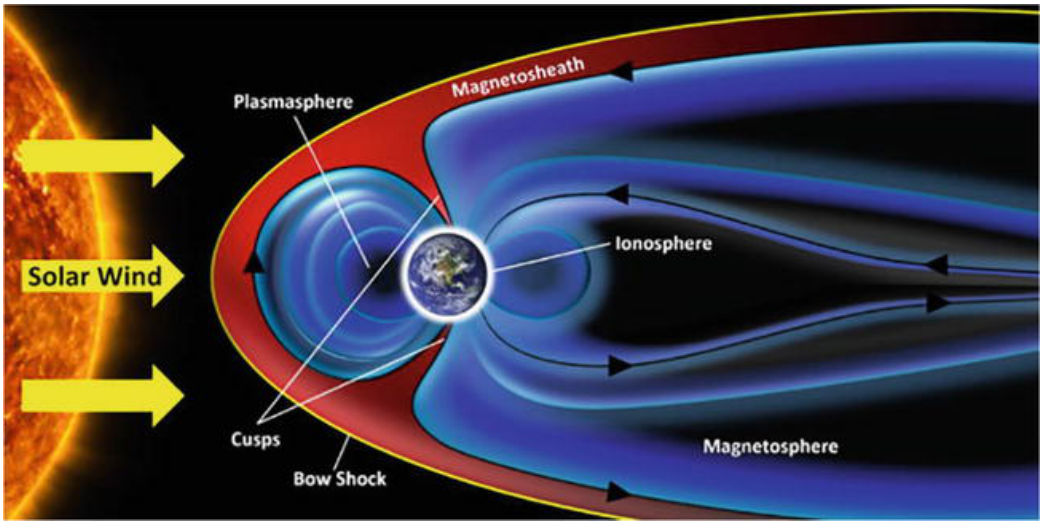

Figure 64: A schematic diagram of the terrestrial magnetosphere and the embedding solar wind. Figure from Belisheva (2019).

tail. The frontier between the planetary magnetosphere and the solar wind, called magnetopause, is located where the magnetic pressure from the planetary magnetosphere is balanced with the solar wind kinetic pressure. Called the Chapman–Ferraro distance, this can be roughly estimated imposing the balance between the two pressures, $R_{CF} = R_P(B_P^2/\mu_0\rho V_{SW}^2)^{1/6}$, where B_P is the planet magnetic field at the surface at the equator (Chapman and Ferraro, 1931). If the planet's magnetic field is strong enough, resulting in $R_{CF} \gg R_P$, the magnetosphere is said intrinsic, while for weakly magnetized bodies it can be induced by the interaction with the solar wind. Under normal solar wind conditions, the sunward extremity of the terrestrial magnetosphere, called the nose, can extend as far as $\simeq 10R_E$ (where $R_E = 6371$ km is the mean Earth radius), but it may considerably reduce its distance under high solar wind pressure conditions. On the other side, the dipole magnetotail can be stretched as far as $\simeq 1000R_E$. Since the solar wind is supersonic, the impact on the planetary magnetosphere will generate a shock wave, called bow shock (indicated by a thin yellow line in Figure 64). The transition region between the bow shock and the magnetopause is called magnetosheath (region in red in Figure 64), characterized by shocked plasma and extremely large magnetic field fluctuations. For this reason, the magnetosheath is a region of interest for turbulence studies. The complex coupling occurring at the bow shock

and the highly dynamical solar driver make the conditions in this region particularly rich and diverse. This results in a strongly inhomogeneous medium, whose turbulence properties must to be examined with care and can provide important knowledge about various cross-scale, multi-physics coupling mechanisms.

Several space missions have been launched to study the various magnetospheric dynamical processes. Among these, turbulence is a key process for the energy transport and for the magnetosphere-solar wind coupling. Massive advances in the description of turbulence were recently obtained thanks to the analysis of spacecraft data collected by the multispacecraft missions ESA/Cluster (launched in 2000, see Escoubet et al., 1997)) and NASA/MMS (Magnetospheric Multiscale Mission, launched in 2015, see Burch et al., 2016), both still active today. Figures 65 and 66 present images of the two missions along with schematics of their highly elliptical orbits. These were carefully designed to change with time, thoroughly exploring the diverse subregions of near-Earth space under different conditions, therefore offering a unique laboratory for the study of space plasmas turbulence. For example, Cluster collected data during two solar cycles, and both spacecraft formations sampled the pristine solar wind, the magnetosheath, the magnetosphere and the magnetotail. Spectral and structure function analysis of magnetic field

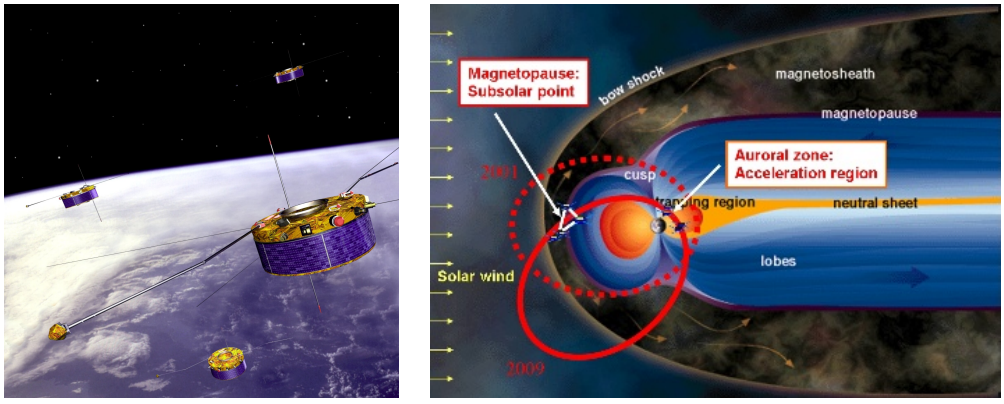

Figure 65: Left panel: artistic representation of the four Cluster spacecraft in tetrahedral constellation. Credits: ESA-CC BY-SA 3.0 IGO (available at `https://www.esa.int/About_Us/ESA_history/Cluster_s_20_years_of_studying_Earth_s_magnetosphere`). Right panel: representation of two examples of Cluster orbit in 2009 and 2011 (red lines). Credits: ESA (available at `https://sci.esa.int/web/cluster/-/36560-orbit-evolution-after-extension`).

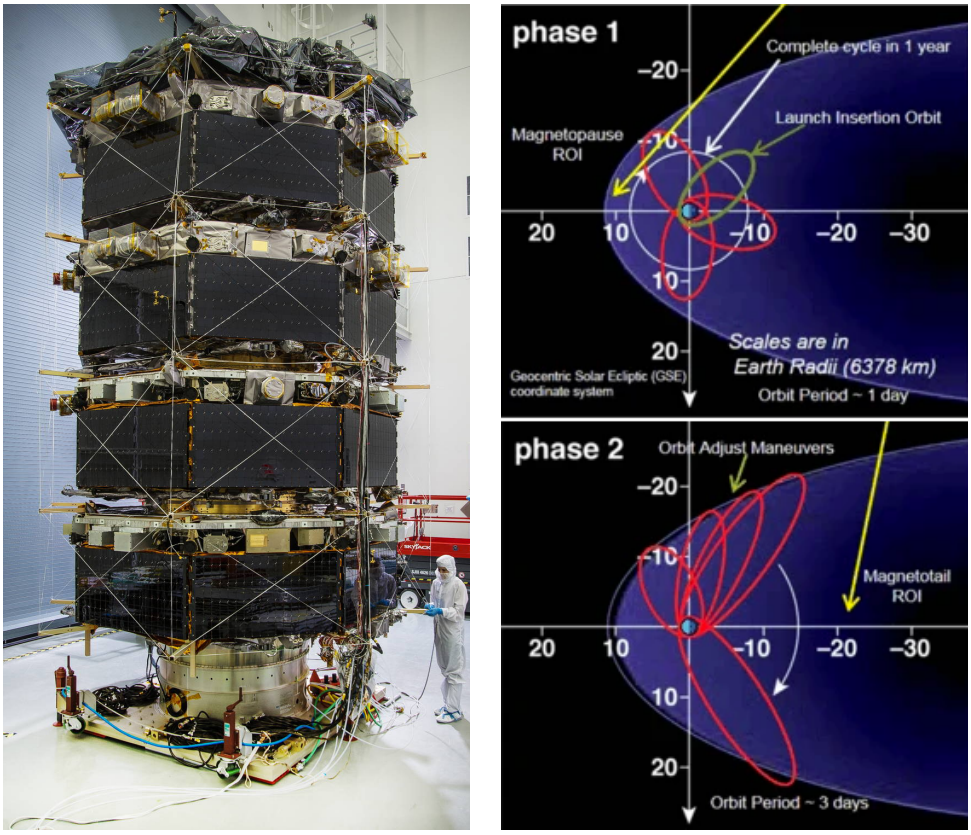

Figure 66: Left panel: The four MMS spacecraft stacked for launch being tested at the NASA's Goddard Space Flight Center in Greenbelt, Md., USA. Credits: NASA/Chris Gunn (available at `https://www.nasa.gov/content/goddard/mms-stacked-for-environmental-testing`). Right panel: schematic view of the orbit of MMS in two different moments of the mission. The yellow arrows indicate the regions of interest for the mission science objectives. Adapted from Tooley et al. (2016).

and plasma measurements were used to map the properties of turbulence in the different regions and under different conditions of the magnetosphere. In the dayside magnetosheath region, the shocked solar wind plasma tends to lose its correlation properties, since the strong shock destroys the turbulent structures and reshuffles their phases. In the region directly downstream of the bow shock, the fluctuations are extremely large but there is no clear evidence of Kolmogorov spectra. Moving away from the bow shock, sub-ion scale turbulence starts forming well defined power-law spectra, with typical steep spectral exponents $\sim$2.3—3.5 (Yordanova et al., 2008; Huang et al.,

2014; Hadid et al., 2015). As the turbulence ages, nonlinear interactions may generate an MHD inertial range on scales larger than the typical ion scales. This is observed to develop a broader scaling range and intermittency as the distance from the shock increases (Yordanova et al., 2008), indicating a clear evolution of the turbulence. An example of magnetic spectrum is shown in the top panel Figure 67, where the sub-ion range is clearly visible, but the inertial range is still not well developed (Yordanova et al., 2008). The bottom panel of the same figure shows the evolution of the intermittency p-model parameter P (Meneveau and Sreenivasan, 1987) and of the spectral exponent α with the distance from the bow shock, clearly pointing to an increase of intermittency and formation of a ion-scale spectrum away from the shock crossing (Yordanova et al., 2008). At the magnetopause and inside the magnetosphere, turbulence is occasionally observed, mostly driven by the magnetospheric boundary layer and by instabilities forming in the frontier region (Di Mare et al., 2019; Quijia et al., 2021). The properties of turbulence in the proximity of the bow shock are also strongly dependent of the shock geometry. If the normal to the shock is perpendicular to the solar wind magnetic field (quasi-perpendicular conditions), reflected ions cannot cross the magnetic field lines and are confined by cyclotron gyration to the proximity of the shock. On the other hand, when the shock is quasi-parallel, reflected ions can travel long distances upstream of the solar wind along the filed lines, interacting with the incoming flow and generating a region of strong turbulence and intermittency, called foreshock region. Examples of these different conditions can be seen in Figure 68, where the structure functions and their scaling exponents are shown for three different shock geometries, as indicated by the angle between the shock and the solar wind magnetic field, θ. Additionally, the shock crossing also enhances the plasma compressibility. Therefore, density fluctuations in the magnetosheath can be as large as 50—100%, generating highly turbulent fluctuations whose nature differs from the quieter solar wind turbulence, where the fluctuations are typically of the order of 5—20%. The above examples of variety of magnetosheath turbulence clearly highlight the richness and complexity of the processes in near-Earth space. Studies of the third-order moment are therefore important to discriminate between different dynamical regimes, and to determine the actual role of the nonlinear interaction in sustaining the turbulence and generating the small scale structures, to explore their interplay with waves and instabilities, and to investigate the cross-scale balance between fluid and kinetic processes.

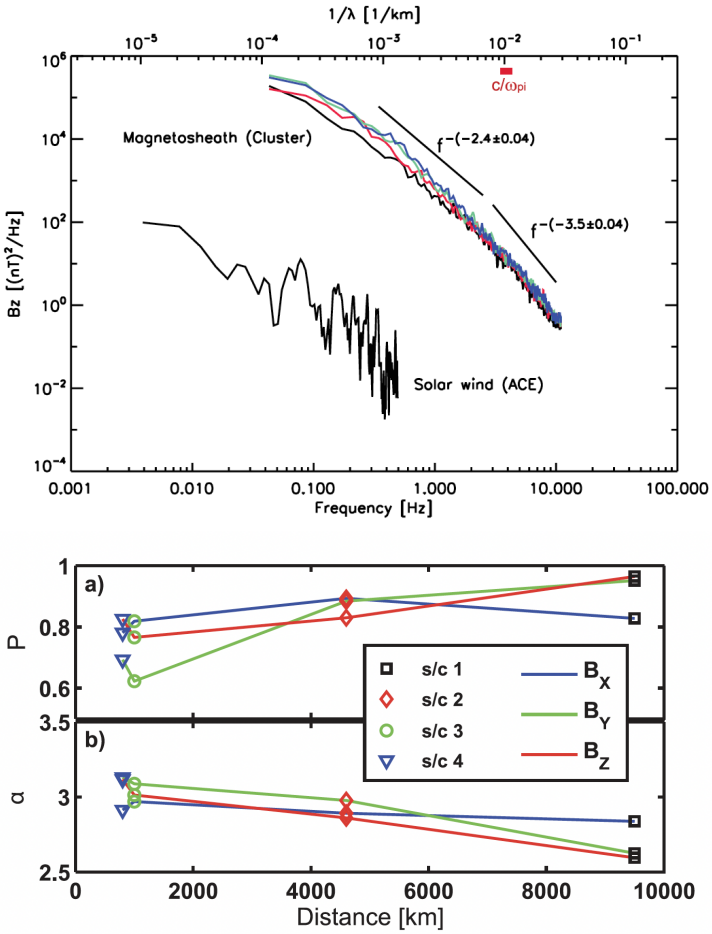

Figure 67: Top: power spectral density of the magnetic field component B_z in the magnetosheath, as measured by the four Cluster spacecraft (colored lines), and in the upstream solar wind (measured by ACE, black line). Fitted power laws are indicated. Bottom: evolution of the intermittency p-model parameter P (top, see equation 18, Meneveau and Sreenivasan, 1987) and fitted spectral exponent α (bottom) with the distance from the bow shock, for the three magnetic field components (colored lines) and four Cluster spacecraft (colored symbols). Figure from Yordanova et al. (2008).

7.1. Third-order scaling law in the terrestrial magnetosheath: from incompressible MHD to compressible Hall MHD

The complex structure of the magnetosphere and the strongly elliptical orbits of the dedicated missions do not generally allow collecting long samples of homogeneous plasma. However, in various occasions magnetosheath

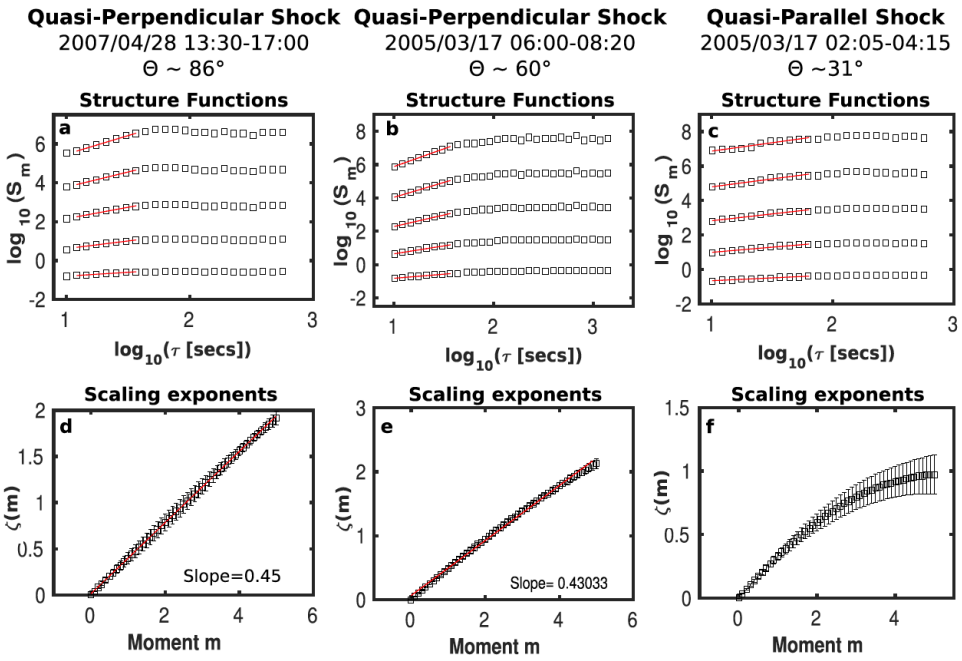

Figure 68: Structure functions of order m, $S_m = \langle \Delta B^m \rangle$ (top panels), and the corresponding anomalous scaling exponents $\zeta(m)$ (bottom panels) for three samples of magnetosheath plasma at three different angles, θ, between the shock normal and the solar wind magnetic field (indicated above each column). Red lines indicate power-law fits of the structure functions (top panels), or linear fits of the scaling exponents (bottom panels). Figure from Hadid et al. (2015).

crossings were sufficiently long so that statistically robust analysis was possible. Far enough from the bow shock, the occasional presence of a short but well defined MHD spectral range suggested that the turbulence could be developed enough as to observe the linear scaling of the third-order moment. Several studies have been carried out using various versions of the P&P law, including compressive and Hall terms. While the results discussed below are not presented in chronological order of publication, they account for the increasing complexity of the third-order moment scaling law versions, which progressively include additional terms for compressive effects and Hall physics. The various versions allow to highlight different properties and reveal important features of turbulence, representing therefore an outstanding source of information on the near-Earth plasma physics.

The simplest analysis was carried out by Bandyopadhyay et al. (2018a),

who used the basic incompressible MHD version, equation (54), to validate the P&P law in one sample of magnetosheath plasma sampled by the MMS spacecraft on 2017-01-18. Figure 69 shows an example of scaling of $Y^{\pm}$, computed for the Elsasser variables $\mathbf{z}^{\pm}$ (bottom panel), along with the magnetic spectral trace (top panel). The absolute value used here does not allow to evaluate correctly the convergence of the sign of the third-order moment over the whole range of scales. Large excursions in the large-scale end (where the spectrum becomes shallower, indicating a broad-band injection region) suggest frequent changes of sign, which do not prove the extended-range validity of the P&P law. However, the sign appears stabilized at least in the typical range of the $f^{-5/3}$ MHD scaling, 1—10 s (Bandyopadhyay et al., 2018a; Quijia et al., 2021), allowing a rough estimate of the energy transfer rate, $\varepsilon \simeq 10$ MJ kg^{-1} s^{-1}. The value observed in this sample is three orders of magnitude larger than in the solar wind at 1 au, demonstrating the strong energization of the turbulence at the bow-shock crossing. This observation is of high relevance for the studies of the coupling and the energy flux between solar wind and magnetosphere, and therefore for space weather applications. In order to examine the energy balance in the various spectral ranges, the large-scale energy injection rate, $\varepsilon_1 \simeq 10$ MJ kg^{-1} s^{-1}, was evaluated using the von Kármán decay law, equation (17), obtaining values extremely similar to the transfer rate, ε. Furthermore, the energy balance was explored at kinetic scales, where a $f^{-8/3}$ spectrum indicates the typical ion-scale turbulence. A modified scaling law based on Gauss integration of the Yaglom divergence, on multi-spacecraft spatial increments, and neglecting Hall and pressure anisotropy contributions, leads to the kinetic range energy transfer rate, $\varepsilon_3 \simeq 1$ MJ kg^{-1} s^{-1}, which clearly underestimates the actual energy transfer.

Since the shock crossing introduces a high degree of compressibility of the magnetosheath fluctuations, Hadid et al. (2018) attempted a study of the compressible MHD version of the third-order scaling law, which was described in Section 5.6. In particular, they use the version from Banerjee and Galtier (2013), analogous of the updated version given here, equations (117)-(120), and labeled as BG13. In their study, these authors identified 47 intervals of THEMIS and Cluster measurements, each sufficiently extended (~ 50 minutes) as to perform accurate statistical analysis. These intervals were separated in two groups, according to the compressibility level: 29 weakly compressive intervals, labeled as Alfvénic-like events, and 18 more strongly compressive ones, associated with magnetosonic-like fluctuations. Two ex-

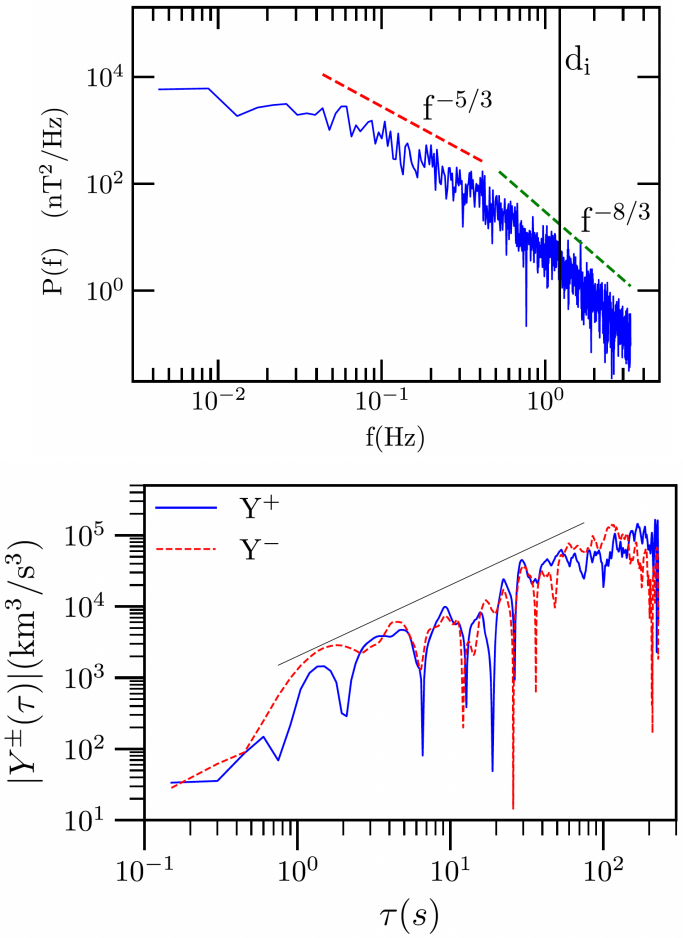

Figure 69: Top panel: magnetic power spectrum (trace, blue line) for the MMS1 measurements in the terrestrial magnetosheath. Kolmogorov (red dashed line) and sub-ion (green dashed line) typical power-laws are indicated, as well as the ion inertial length, d_i (vertical line). Bottom panel: for the same sample, absolute value of the mixed third-order moments, $Y^{\pm}$ (equation 54, blue and red lines), versus the time scale, $\tau \equiv \Delta t$. A reference linear scaling (dotted black line) is shown for reference. Figure from Bandyopadhyay et al. (2018a).

amples are presented in Figure 70, where the top panels show magnetic field magnitude, B_0, magnetic fluctuations, $|\delta B|/B_0$, ion density n_i and the associate fluctuations, $|\delta n|/n_0$, as well as the plasma β. The insets in the bottom panels show the total magnetic power spectral density (PSD) for the two categories, revealing a broad Kolmogorov-like power-law scaling in the

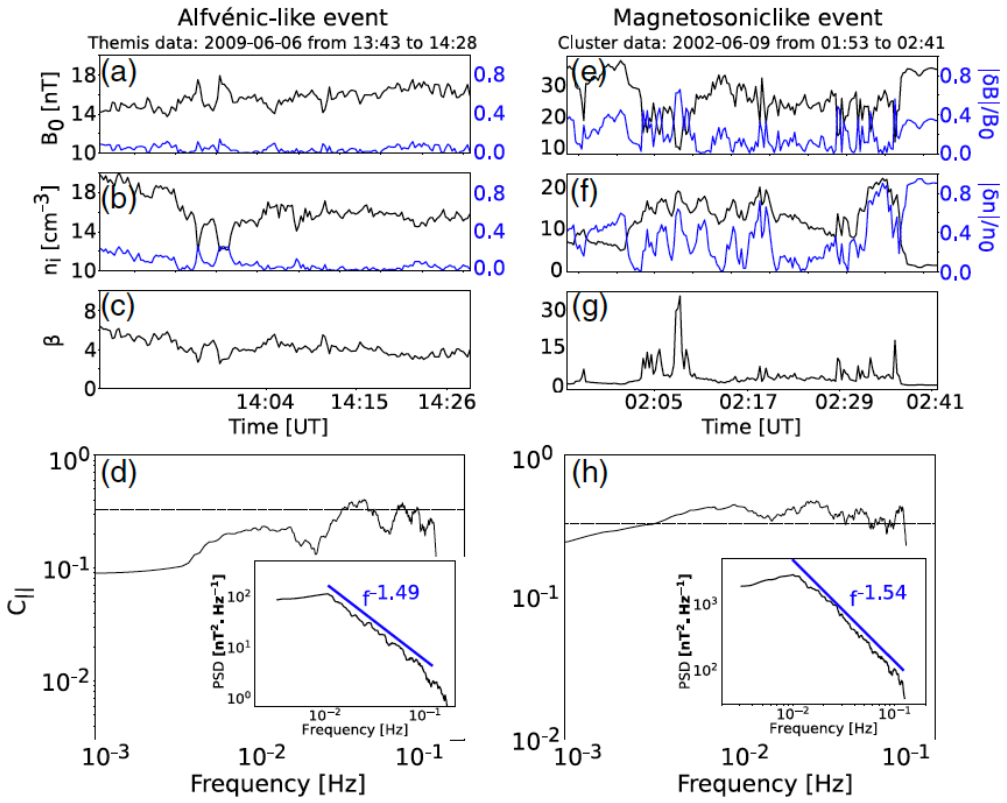

Figure 70: Examples of Alfvénic (left) and Magnetosonic (right) events, with respective compressibility spectra $C_{\parallel}$ (bottom panels, main windows, indicating the parallel to total magnetic power spectral density ratio) and total magnetic power spectral densities (bottom panels, insets). Figure from Hadid et al. (2018).

range of timescales 10—100 s (power-law fits are indicated along with the corresponding exponent). The main windows of the same panels show the compressibility spectra $C_{\parallel} = \delta B_{\parallel}^2/\delta B^2$, namely the ratio between the parallel and the total power magnetic spectral density (where parallel refers to the mean field B_0).

Figure 71 shows two examples of the third-order moment in the BG13 form (red lines), normalized to the scale and to the constant coefficient, so that a flat region indicates linear scaling. Although the absolute value was used in the figure, the authors checked the sign convergence of the moments before computing the mean energy transfer rate, $\langle|\varepsilon|\rangle$, which however does

not distinguish between positive and negative values. Direct comparison with the incompressible version of the P&P law (black lines, labeled as PP98) suggests that the contributions of the density fluctuations enhance the estimate of the energy transfer rate by nearly one order of magnitude in the compressive intervals, while the difference is much smaller for the Alfvénic intervals.

Finally, in order to exploit the information on the energy transfer rate ob-

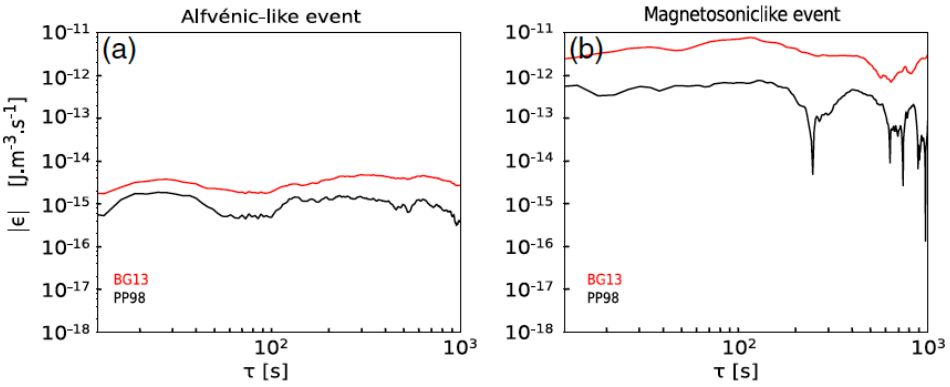

Figure 71: Examples of normalized mixed third-order moments, ε, for compressible (indicated as BG13, red) and incompressible (PP98, black) MHD, for Alfvénic (left) and Magnetosonic (right) events. Figure from Hadid et al. (2018).

tained through the third-order scaling, a statistical analysis was performed comparing the values of the energy transfer rate of the two groups of intervals with several parameters. Figure 72 shows some examples. In the top row, a comparison with the sonic Mach number, M_S, is presented separately for the two types of intervals. In both cases, an empirical power-law relation, $\langle|\varepsilon|\rangle \sim M_S^4$, was identified. Such relation does not fully agree with similar solar wind observations that were previously modeled by a M_S^3 dependency (Hadid et al., 2017), highlighting the specificity of the magnetosheath fluctuations and the enhanced role of the compressive fluctuations therein. The above observed relation can be relevant to constrain models of the magnetosheath or, more generally, of compressive plasma turbulence. In the central panels, the dependency on the angle between the velocity and the magnetic field, θ_{VB}, is shown for those intervals that had relatively constant values. Since the angle describes the sampling direction with respect to the magnetic field, this allows to explore the role of compressive fluctuations in the anisotropy of the turbulence. In the Alfvénic events, the energy transfer rate

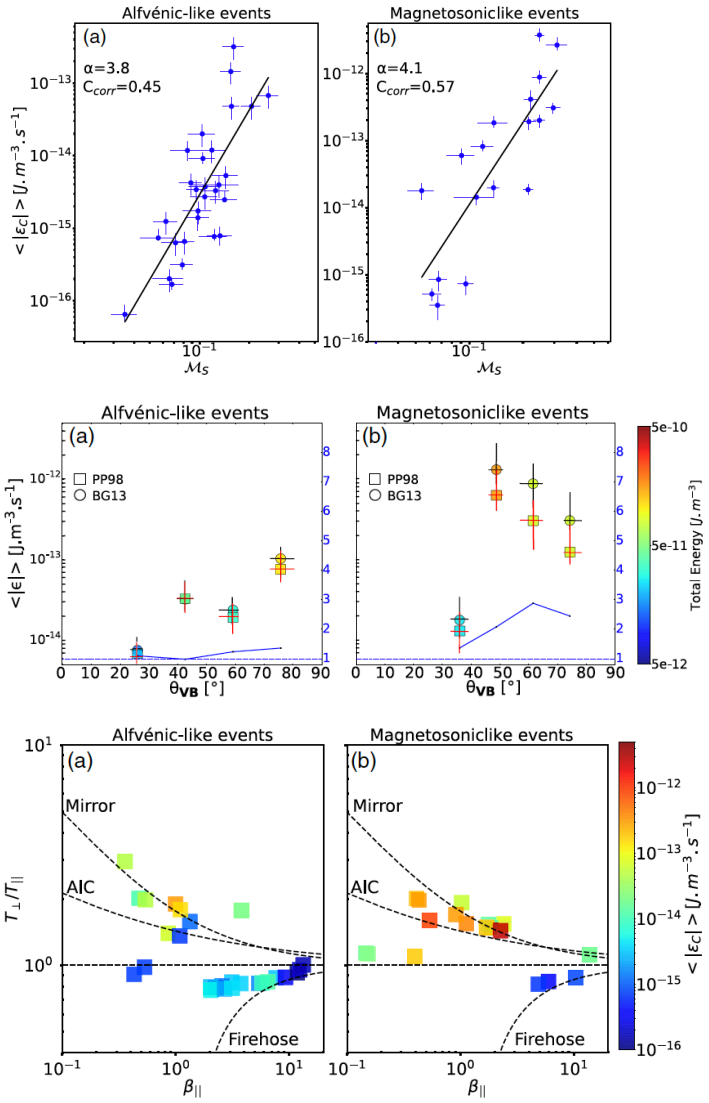

Figure 72: Top panels: absolute value of the compressible energy cascade rate, $\langle|\varepsilon_C|\rangle$, versus the sonic Mach number M_S. Power-law fits, resulting exponents α and correlation coefficients C_{corr} are indicated. Central panels: compressible (circles, BG13) and incompressible (squares, PP98) cascade rate and their ratio (blue lines) versus the mean θ_{VB} angle, and versus the total energy (colors). Bottom panels: compressible energy transfer rate averaged in bins of proton temperature anisotropy, $T_\perp/T_\parallel$, and $\beta_\parallel$. Dashed liens represent the indicated instability thresholds. Left (a) and right (b) panels refer to the Alfvénic and magnetosonic intervals, respectively. Figure from Hadid et al. (2018).

increases with the angle, so that fluctuations parallel to the mean field are less energetic, in agreement with predictions and solar wind observations (Osman et al., 2011). Again, the difference between compressible and incompressible laws is limited. On the other hand, for magnetosonic-like events, where the difference between the two versions is larger, a maximum of the transfer rate appears near $\sim 45°$, which was explained as possible energy injection due to the mirror instability. Finally, in the bottom panels of 72 the energy transfer rate (color coded) is represented in the standard instability plot, where the plain shows the proton temperature anisotropy $T_\perp/T_\parallel$ versus the proton parallel $\beta_\parallel$, useful to identify the parameter regions for the thresholds of the mirror, Alfvénic ion cyclotron and firehose instabilities (Hellinger et al., 2006). This representation reveals that the Alfvénic events are mostly seen near the firehose instability threshold, while the magnetosonic ones lie closer to the mirror instability threshold, confirming the anisotropy observation described above. These observations show that estimating the energy transfer rate is crucial for understanding the nature of turbulence and its possible sources in complex environments such as the terrestrial magnetosheath.

In a combined study of solar wind, magnetosheath and hybrid-kinetic numerical simulations, Bandyopadhyay et al. (2020) used MMS data to explore the role of Hall terms in the turbulent energy cascade. These authors used the simple version of the Hall-MHD scaling law, equation (84), which include the Hall term, H, in addition to the MHD Yaglom term, Y (Ferrand et al., 2019). Examples of analysis are shown in Figure 73, where solar wind and magnetosheath data (left column) and hybrid-kinetic simulations with similar plasma β (right column) are compared. In all panels, the total third-order moment is shown (black-dashed lines) together with the separated MHD (full green) and Hall-MHD (full red) contributions. Observing the scaling of the third-order moment, it was found that at fluid scales the inertial range is dominated by the MHD contribution, as expected. On the other hand, at sub-ion scales the cascade is not completely sustained by the Hall term, so that a clear linear scaling is not observed. Comparison with numerical simulations reveal good agreement for the magnetosheath samples, while in the solar wind some differences emerge. This indicates that the energy is probably removed from the cascade by other processes, perhaps of kinetic nature, not fully captured by the Hall-MHD approximation. This observation represents an important step towards understanding the interplay between turbulence and dissipative processes (to be intended in a broad sense), and suggests that those are already active in the sub-ion range.

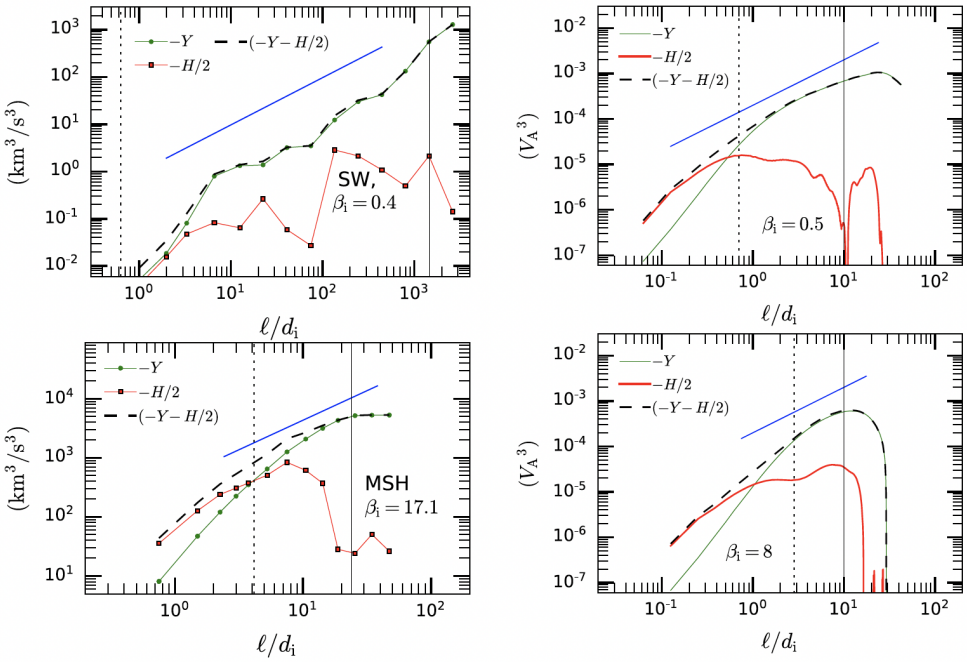

Figure 73: Mixed third-order moments contributions from the MHD (Y, green lines) and Hall-MHD ($H/2$, red liens) terms, and their sum (black dashed lines). Linear relation are shown for reference (blue lines). Vertical dotted and full lines indicate the ion gyroradius and the correlation scale, respectively. Left panels refer to MMS measurements in the solar wind (SW, top-lef) and in the terrestrial magnetosheath (MS, left-bottom), with the plasma ion β parameter indicated. Right panels show analogous results for two runs of a two-dimensional hybrid-kinetic simulation with similar plasma β. For the simulation results, the velocity is given in Alfvén speed units (V_A). Figure from Bandyopadhyay et al. (2020).

To close the overview of studies targeting the Earth's magnetosheath region, we describe the work of Andrés et al. (2019). These authors used a complete compressible Hall-MHD version of the third order moment scaling, equation (106), to attempt an accurate description of the energy transfer rate accounting for all inertial range and sub-ion scale terms, with no (or limited) approximations. As we have seen in Section 5.5.2, the long list of terms in equation (90) can be condensed in four different terms, so that the compressive energy transfer rate is $\varepsilon_C = \varepsilon^{flux}_{CMHD} + \varepsilon^{nonflux}_{CMHD} + \varepsilon^{flux}_{CHMHD} + \varepsilon^{nonflux}_{CHMHD}$, each term referring to MHD or Hall-MHD, flux and non-flux terms. Comparing the compressible to the incompressible rate (the standard MHD P&P law, equation 54), and the contribution from the four terms in ε_C can provide

important information on the processes dominating the cascade in different scale ranges and plasma conditions. In order to evaluate the non-flux and the Hall contributions appearing in equation (106), spatial gradients and sufficiently precise measures of the current density are needed. Therefore, high-resolution, accurate measurements of fields and plasma from the four-spacecraft MMS mission in the magnetosheath were used. Gradients were estimated using multi-spacecraft techniques, exploiting the tetrahedral configuration of the four MMS spacecraft, which provides two-point measurements in three dimensions (Paschmann and Schwartz, 2000). The reduced (electron-scale) inter-spacecraft distance enables estimating vector gradients with adequate precision. Similarly, the current density associated with the Hall terms was obtained using the highly accurate MMS measurements of electron and ion moments, at 150 ms cadence. 72 intervals of about 300 s were selected in the magnetosheath region towards the flanks of the magnetopause, where a Kolmogorov-like inertial range was observed. Figure 74 shows two examples of intervals from the database. In the left panel, an example of nearly-incompressible fluctuations; in the right panels, one with largely compressible fluctuations (see the magnetic field magnitude and density plots in the top panels). After verifying that a Kolmogorov-like spectrum is present (see the compensated spectra in the central panels), the bottom panel shows the third-order moment normalized to the scale, so that a constant value indicates linear scaling. The four different versions (compressible and incompressible MHD and Hall MHD, labeled respectively CMHD, IMHD, CHMHD, IHMHD) are plotted in different colors and compared.
Note that the values are presented using the absolute value, so that changes of sign are not visible. The authors argue that the sign of the cascade is not relevant to their analysis, which is acceptable as long as sign convergence is achieved. Changes of sign are possibly present, mostly in the compressible Hall-MHD version, but reduced scaling ranges can be identified in the two cases. In the Kolmogorov range, for the nearly incompressible interval the CMHD and IMHD versions are nearly superposed, while in the compressible interval the IMHD version is slightly larger, indicating a limited but effective role of density fluctuations in enhancing the global cascade rate. On the other hand, at sub-ion scales the difference between the two estimates increases for both intervals, suggesting that the Hall terms are affected by compressible fluctuations more than the MHD terms. By comparing quantitatively the ratios between compressible and incompressible transfer rates (Figure 75), the authors conclude that density fluctuations enhance the cas-

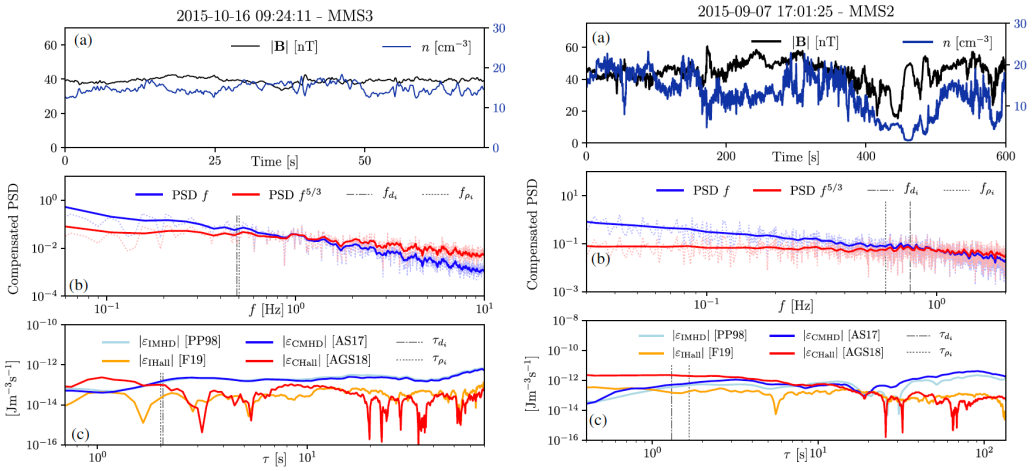

Figure 74: Two characteristic MMS magnetosheath intervals among the 72 studied by Andrés et al. (2019). Left panels: poorly compressible interval; right panels: highly compressible interval. For each interval: top panels show the magnetic field magnitude and density; central panels the compensated magnetic power spectral density; bottom panels show the magnitude of the scale-normalized third-order moments for compressible (ε_C) and incompressible (ε_I) MHD and Hall-MHD P&P law. Figure from Andrés et al. (2019).

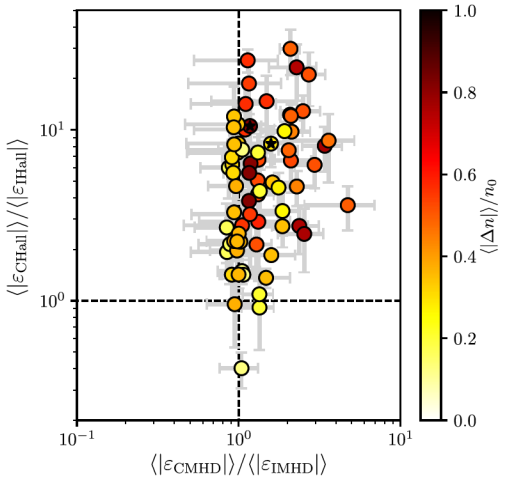

Figure 75: Scatter plot of the ratios between the compressible and incompressible cascade rates for the Hall-MHD and MHD versions of the P&P law. Colors indicate the level of density fluctuation. Figure from Andrés et al. (2019).

cade rate at sub-ion scales, particularly when Hall terms are considered, and this demonstrates the inherently compressible nature of the magnetosheath turbulence.

Magnetosheath particles and fields measurements from MMS and Cluster are among the most accurate and highest resolution in space plasmas. Moreover, the multi-spacecraft mission configuration allows uniquely to estimate ion- and electron-scale spatial gradients to a high precision. Finally, the magnetosheath offers a broad variety of plasma conditions, with young and more developed turbulence as well as various degrees of compressibility. For these reasons, using different versions of the third-order scaling laws with magnetosheath measurements allowed to obtain a number of important details on the nature of the turbulent cascade in such environment. In particular, it was determined the the turbulence can reach a fully developed state quite rapidly after the bow shock crossing, and is largely more energetic than in the upstream solar wind. The role of the Hall terms and of the compressive fluctuations in enhancing the cascade in different ranges of scales was highlighted by the works presented above, providing insight in the properties of the fluctuations that will eventually drive small-scale kinetic processes, ultimately dissipating the cascading energy. In order to gain further knowledge about the particle heating and energization problem, a local approach will be probably necessary, as will be discussed in Section 8.

7.2. Turbulence driven by a Kelvin-Helmholtz instability event at the terrestrial magnetopause

As evidenced by spectral analysis, in the terrestrial magnetosheath the turbulence becomes more developed as the plasma blows away from the bow shock, where it is processed and strongly reshuffled. Additionally, several fluid instabilities or large-scale structures can locally enhance the turbulence by injecting further energy in the cascade. One interesting case is occasionally observed at the magnetopause. Under specific conditions (Chandrasekhar, 1961; Faganello and Califano, 2017), the plasma shear forming between the magnetosheath plasma and the magnetopause may trigger the Kelvin-Helmholtz instability (KHI), which initially generates large-scale rolled-up vortices (Sundberg et al., 2012). The instability rapidly grows to a turbulent state, where the rolls mix up and merge, transporting plasma and energy from the denser magnetosheath to the rarefied magnetosphere (Mitchell et al., 1987; Bavassano Cattaneo et al., 2010; Nakamura et al., 2017). The KHI is a powerful driver of turbulence, providing an injection

of energy since the early stage, when the large-scale shear is broken down in smaller rolls which nonlinearly interact (Karimabadi et al., 2013). These were observed in the flanks of the Earth's magnetosphere (Chen and Kivelson, 1993; Hasegawa et al., 2004; Eriksson et al., 2016), and effects on the fluctuations were studied, revealing the expected increase of turbulence (Stawarz et al., 2016; Di Mare et al., 2019; Sorriso-Valvo et al., 2019a; Franci et al., 2020).

Quijia et al. (2021) used MMS measurements to perform an in-depth study of the statistical properties of turbulence in the KHI event of 8 September 2015, when the four-spacecraft formation was crossing the transition between the magnetosheath and the magnetospheric boundary layer, which was identified by Eriksson et al. (2016). The KHI event, lasting nearly 80 minutes, showed the alternation of magnetosheath and magnetospheric boundary layer plasma, evidenced by the differences in speed, magnetic field, density and temperature. A two-minute sub-interval is shown in Figure 76, where the alternation between the two regions (where the red and blue shaded areas indicate the boundary layer and the magnetosheath, respectively) and the sharp boundary separating them are evident. The authors identified nearly stationary sub-intervals on each side of the KHI boundary (specifically, 59 in the magnetosheath, MS, and 24 in the magnetospheric boundary layer, BL), carefully excluding the interaction regions, so that they could be considered as individual samples of turbulence in two different environments. Sub-intervals were relatively short, their length averaging 2.35 minutes. The spectral analysis of magnetic field, velocity, Elsasser fields and pressure, performed using compressed sensing, a novel technique enabling the combined study of the separated sub-intervals (Fraternale et al., 2016, 2019), revealed a peak, clearly appearing near 1 minute, which was identified as the KHI large-scale rolls, and supposed to represent the major driver of the turbulence in this interval. A robust Kolmogorov spectrum was observed in both samples, in a range extending between 2.5 and 25 s, clearly visible in top panels of Figure 77. The boundary layer (top-left panel) shows relatively shallow spectra, with exponents close to 3/2, while a slightly steeper spectrum, with exponent closer to 5/3, was observed in the magnetosheath. This seems to indicate the presence of a moderately more developed turbulence in the magnetosheath. This conclusion was not confirmed by comparing the intermittency of the ensembles of MS and BL intervals. Indeed, as shown in the bottom panels of Figure 77, the BL intervals has larger intermittency parameter, P, obtained from a p-model fit of the structure functions scal-

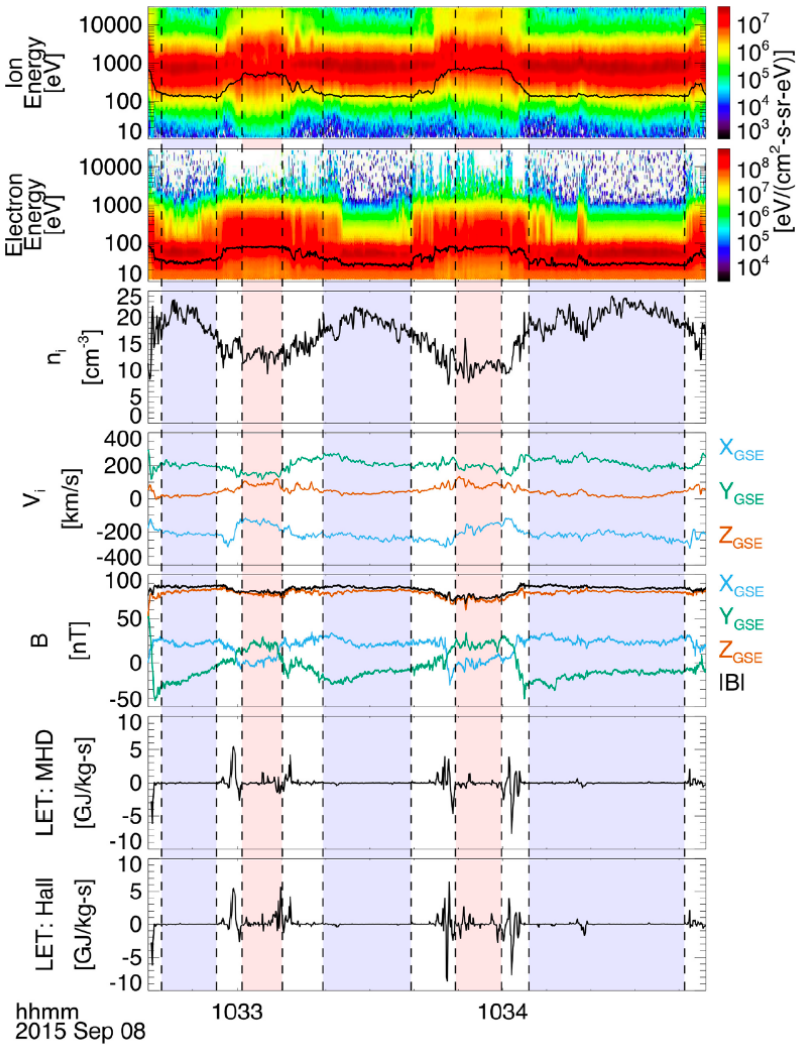

Figure 76: MMS measurements of a Kelvin-Helmholtz instability crossing at the magnetopause. From top to bottom: ion energy distribution and temperature (black line); electron energy distribution and temperature (black line); ion density; ion velocity components; magnetic field components and magnitude; the MHD and Hall-MHD local energy trasnfer (LET) time series (see Section 8). Vectors are in the geocentric solar ecliptic (GSE) reference system, with the x axis towards the Sun and the z axis perpendicular to the plane of the Earth's orbit around the Sun (positive North). Figure from Quijia et al. (2021).

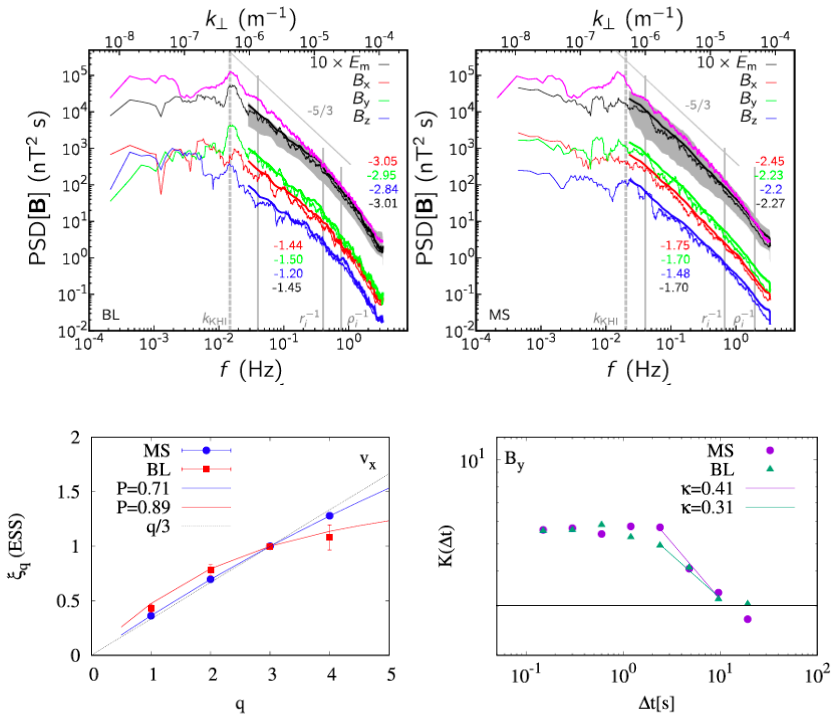

Figure 77: Top panels: power spectral density (PSD) of the magnetic field components fluctuations (color-coded) in the magnetospheric boundary layer (BL, left panel) and in the magnetosheath (MS, right panel), estimated using the compressed sensing technique (Fraternale et al., 2016, 2019). The black curves refers to the total magnetic energy, E_m (trace), and are vertically shifted for clarity. Power-law exponents, obtained fitting the compressed sensing spectra, are indicated in colors. For comparison, thicker lines show the spectra estimated from each short sub-interval and then ensemble-averaged, and the magenta lines the total magnetic energy estimated using the whole interval. The vertical dashed grey line indicates the Kelvin-Helmholtz waves period estimated independently (Eriksson et al., 2016). Vertical full grey lines indicate the boundaries of the inertial range and the typical ion scales. Bottom-left panel: anomalous scaling of the q-th order structure function exponents, indicated here as ξ_q, shown for the BL (red symbols) and for the MS (blue symbols). p-model fits (Meneveau and Sreenivasan, 1987, see Section 3.2) and the resulting parameter P are indicated, along with a reference linear relation for non-intermittent Kolmogorov turbulence ($q/3$). Bottom-right panel: for the two ensembles, scale dependent flatness (here indicated as K, color-coded markers), with inertial-range power-law fit (lines) and the resulting exponents κ, for the B_y magnetic field component. The horizontal line indicates the Gaussian value $K = 3$. Note the plateau below $\Delta t \simeq 2$ s, suggesting monofractal scaling in the sub-ion region. Figure from Quijia et al. (2021).

ing exponents (see Section 3.2). On the contrary, the scaling exponent of the flatness, κ, is moderately larger for the MS interval. These contradictory observations suggest that the fluctuations are not simply generated by turbulent nonlinear interactions, but rather structures exist that are pre-existing or generated by alternative processes. The interaction of solar wind turbulence with the bow-shock, as well as the disrupted KHI large-scale structures, could be examples of such non-turbulent features.

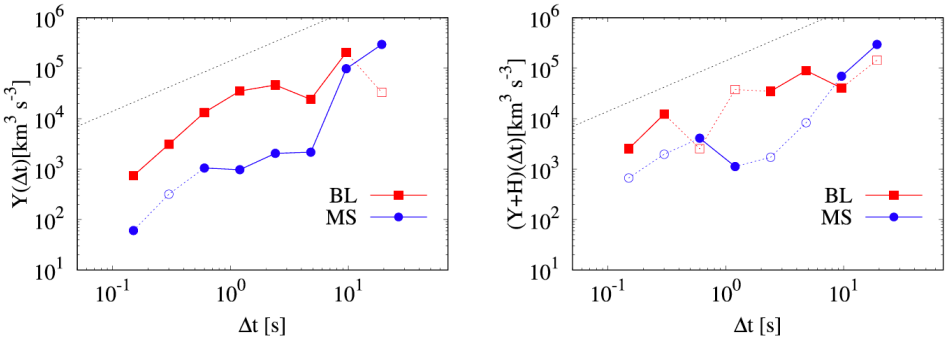

Figure 78: The P&P law for MHD (left) and Hall-MHD (right). Blue and red symbols refer to the terrestrial magnetospheric boundary layer region (BL) and to the magnetosheath (MS), respectively. Full lines and symbols indicate positive Y, while dashed lines and open symbols indicate negative Y. Figure from Quijia et al. (2021)

.

In order to clarify the above observations, the nature and development state of the turbulence was finally examined using the P&P law, in both the MHD and Hall-MHD versions, respectively equations (54) and (84). Despite the limited overall sample size, it was possible to observe a convincing MHD third-order moment linear scaling in the BL intervals, while this was not the case for the MS, as shown in the left panel of Figure 78. According to this observations, turbulence is well developed in the BL, while in the MS the P&P law does not converge yet. In light of the results of spectral and structure function analysis, determining whether the lack of linear scaling in the MS samples is due to finite-size effects or to underdevelopment of the turbulence is still an open question that would require the analysis of more events. As usual, a rough estimate of the energy transfer rate for the BL samples provided values in line with those observed in the magnetosheath (see, e.g., Franci et al., 2020), demonstrating a high energization of the turbulent cascade. On the other hand, the measured energy transfer rate in the

magnetospheric boundary layer was $\varepsilon \simeq 60 \pm 10$ MJ kg^{-1} s-1, the largest value measured in space plasmas so far. The right panel of Figure 78 shows the lack of scaling of the Hall-MHD version of the P&P law, suggesting that Hall-physics effects are largely present in both regions. In agreement with the spectral and intermittency analysis, it appears that current structures of non-turbulent origin may populate the plasma, disrupting the possibility to observe a linear law.

In a complex environment such as the KHI observed at the magnetopause, the P&P law allowed to determine the nature of the fluctuations, highlighting the coexistence of an active turbulent cascade with structures of different origin, and revealing differences between the two plasma populations that are not yet mixed by the instability. Moreover, it showed that the instability can drive extremely strong turbulence in the boundary layer region.

7.3. The onset of turbulence in a magnetic reconnection exhaust in the Earth's magnetotail

Among many possible mechanisms that can drive turbulence in space plasmas, magnetic reconnection is one of the most intriguing and complex. Magnetic reconnection is a fundamental process occurring in plasmas when two oppositely directed magnetic field lines are pushed together (see a simplified schematic view in Figure 79). Being unable to cross each other, they reconfigure their topology, breaking the frozen-in condition (Burch and Drake, 2009; Yamada et al., 2010). The reconnection process often results in the explosive conversion of magnetic energy into particle energization (Zenitani et al., 2011). It is believed to be a major mechanism producing solar flares and coronal mass ejections (Sweet, 1958; Parker, 1957), favouring the plasma exchange and driving auroral substorms at planetary magnetospheres (Paschmann et al., 1979; Sonnerup et al., 1981; Akasofu, 2019), regulating astrophysical plasma processes (Lazarian et al., 2015) and resulting in the loss of confinement in fusion devices (Lawrence and Gekelman, 2009). Examples of some of those processes are illustrated in the bottom panels of Figure 79. Magnetic reconnection may be strictly related with turbulence mostly in two different ways, according to the relative typical scales (Matthaeus and Velli, 2011). The small-scale current sheets generated by turbulence can provide conditions for initiating reconnection, as routinely observed in space plasma measurements (Sundkvist et al., 2007; Retinò et al., 2007; Burch et al., 2016) and in numerical simulations (Matthaeus and Lamkin, 1986; Servidio et al., 2009; Karimabadi et al., 2013). On the other hand, large-scale reconnection

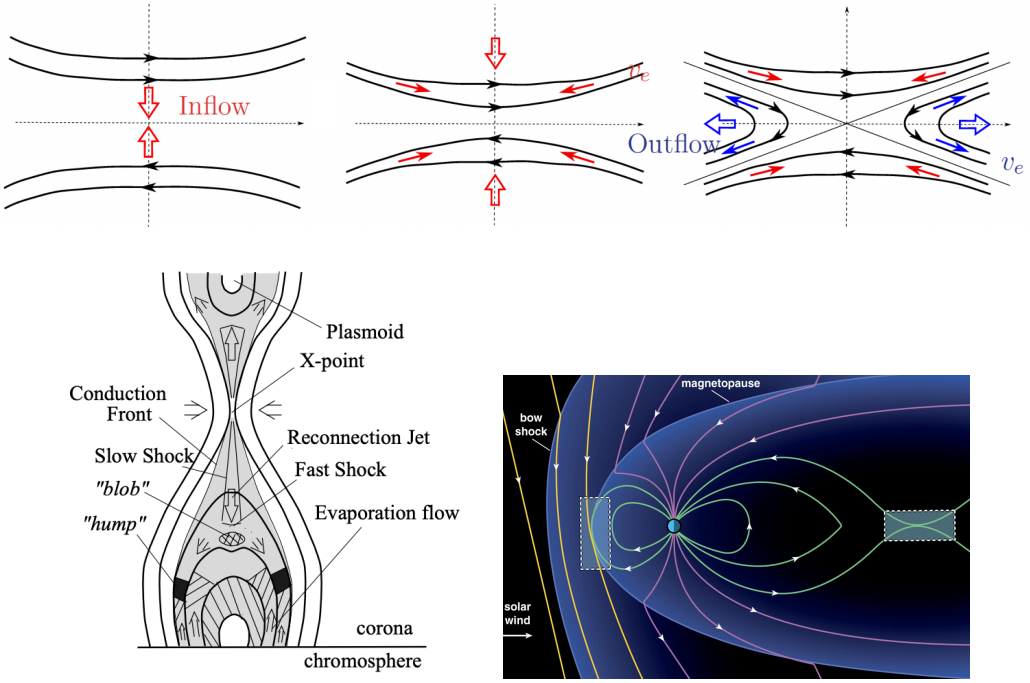

Figure 79: Top: a simplified schematic view of two-dimensional magnetic reconnection. Black lines indicate reconnecting magnetic field lines, red and blue arrows show respectively plasma inflows and outflows. In the right panel, the diagonal dashed lines indicate the location of the x-point, where the actual reconnection (breakup of the frozen-in condition) occurs. Figure adapted from Cozzani (2020). Bottom-left: an example of model of a reconnection event in the solar corona, producing a solar flare and a coronal mass ejection. Figure adapted from Yokoyama and Shibata (2001). Bottom right: schematic view of the terrestrial magnetosphere and the embedding solar wind. Likely reconnection events locations, marked by two shaded box, are located at the nose and in the tail. Figure adapted from Burch et al. (2016).

events are associated with fast plasma exhausts (Gosling et al., 1986; Phan et al., 2000), which can in turn generate turbulence at the interface with the surrounding plasma (Pucci et al., 2018).

The latter configuration may be conveniently studied in the terrestrial magnetotail region, where the ambient plasma is typically drifting at low speed, and the turbulence level is low (Borovsky et al., 1997; Vörös et al., 2004; Zimbardo et al., 2010; Ergun et al., 2018). A recent example of the was provided by Bandyopadhyay et al. (2021a). These authors used MMS magnetic field and particle measurements of a reconnection exhaust at the edge

of the plasma sheet in the terrestrial magnetotail, recorded on 2017 June 16 from 18:10:03 to 18:29:33 UTC. The presence of a stable, fast jet of plasma, generated by the reconnection event, enables the use of the Taylor hypothesis and therefore to use the time series of data as a sample of turbulence. Figure 80 shows an overview of the event, where it is possible to appreciate that the X component of the velocity was about 170 km s^{-1}. After discussing

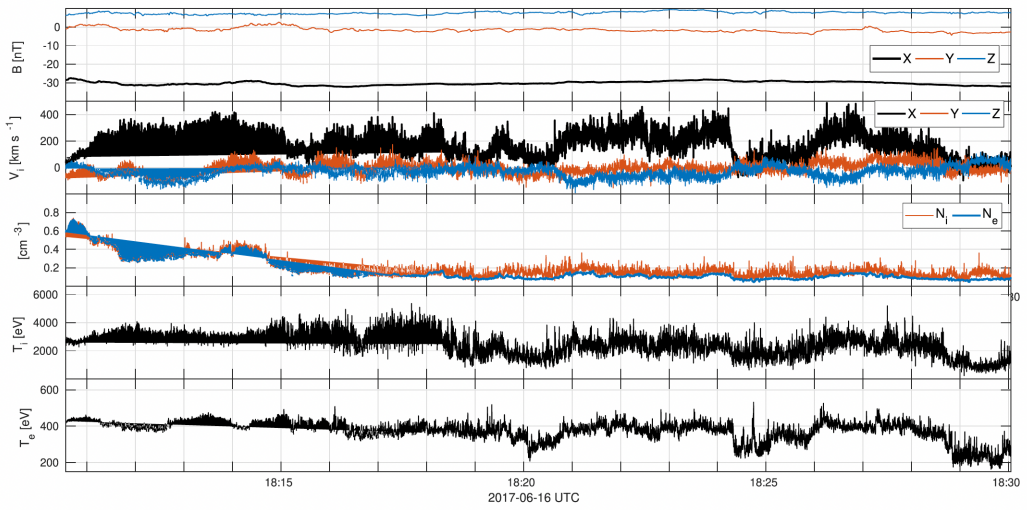

Figure 80: The data interval measured by the MMS spacecraft in the terrestrial magnetotail on June 16th 2017, and identified as the exhaust of a magnetic reconnection event. From top to bottom: magnetic field components, velocity components, ion and electron density, ion temperature and electron temperature. Figure from Bandyopadhyay et al. (2021a).

in detail the validity of the Taylor hypothesis, the authors performed the spectral analysis of the magnetic field and proton velocity fluctuations, revealing the presence of clear power-law turbulent inertial and kinetic ranges (top and central panels of Figure 81). In addition, as shown in the bottom panel of Figure 81, the incompressible P&P law was validated, providing evidence that the exhaust turbulence is fully developed, and allowing to estimate the mean energy transfer rate, $\varepsilon = 24$ MJ kg^{-1} s^{-1}, a large value not dissimilar from those observed in the inner heliosphere at small distance from the solar corona (Bandyopadhyay et al., 2020; Hernández et al., 2021; Zhao et al., 2022) and in the terrestrial magnetosheath (Bandyopadhyay et al., 2018a; Quijia et al., 2021). The observation of Bandyopadhyay et al. (2021a) demonstrates once more the importance of assessing the existence of a tur-

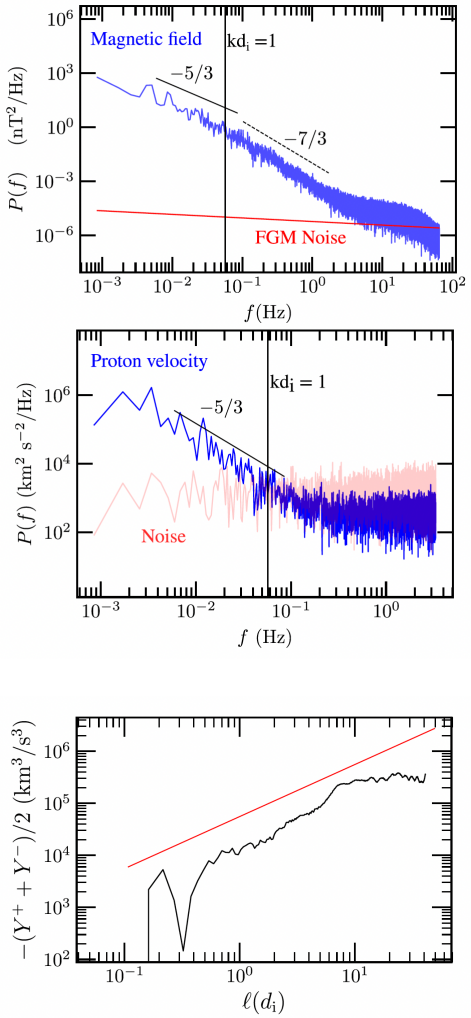

Figure 81: In blue, the power spectral density of magnetic field (top panel) and proton velocity (central panel) in the reconnection exhaust. The noise floor is also indicated (red lines). Vertical lines identify the wavevector associated with the ion inertial scale. Power laws with typical scaling exponents are indicated for reference. The bottom panel shows the scaling of the mixed third-order moment Y for incompressible MHD (black line) in the reconnection exhaust observed by MMS in the terrestrial magnetotail. A linear scaling is indicated for reference (red line). Figure from Bandyopadhyay et al. (2021a).

bulent cascade, which also enables to estimate the equivalent of the energy dissipation rate in collisionless space plasmas. The high energy transfer rate

found in the reconnection exhaust shows that large-scale reconnection events in the terrestrial magnetotail are able to locally generate strong turbulence, and may ultimately contribute to shape the temperature profile observed in the magnetotail region. The P&P law can therefore help constraining models of the Earth's magnetosphere. More generally, it can shed light on the complex interplay between turbulence and magnetic reconnection in energizing collisionless plasmas particles.

7.4. Exploring planetary environments: turbulence upstream of the Martian bow shock

The properties of turbulence near 1 au have been thoroughly studied for several decades (Bruno and Carbone, 2013). Similarly, good quality measurements in the inner heliosphere have allowed a robust characterization of turbulence (Marsch and Tu, 1997; Bruno et al., 2003; Sorriso-Valvo et al., 2018; Chen et al., 2020; Bandyopadhyay et al., 2020; Hernández et al., 2021; David et al., 2022). Conversely, in the outer heliosphere most of the studies only addressed magnetic field turbulence. With the notable exception of the Ulysses spacecraft (Sorriso-Valvo et al., 2007; Marino et al., 2012), plasma instruments were so far not tailored for accurate turbulence studies, so that the time resolution of the measurements from, for example, the Voyager probes (see, e.g., Fraternale et al., 2016) or most planetary missions was not sufficient to explore the scaling properties in the inertial range.

A recent opportunity to explore the heliospheric medium in the region around $\sim$1.5 au is provided by several NASA and ESA missions targeting Mars, which are often equipped with fields and plasma instruments. The near-Mars space environment is of great interest, not only for heliospheric science, but also to understand how the solar wind has impacted the Martian atmospheric gases escape in the past, and how the planet's magnetic weak crustal field couples with the interplanetary magnetic field. The induced magnetosphere of Mars is generated by the interaction between the solar wind and the planet's magnetic fields (see, e.g., Acuña et al., 1998, 1999). This results in a complex system, fundamentally different from the terrestrial environment, with stronger coupling between the planet's atmosphere and the surrounding solar wind (see a schematic representation of the near-Mars space in the left panel of Figure 82). A broad variety of instabilities are generated by such coupling, resulting in waves on a broad range of frequencies. Among these, proton cyclotron waves (PCWs) are observed near the Doppler-shifted local proton cyclotron frequency (Russell et al., 1990).

These waves have shown strong seasonal variability, which was associated to the orbital modulation of the martian atmospheric particle escape (Romanelli et al., 2013).

The NASA MAVEN spacecraft (Figure 82, right panel) was launched in 2013 to explore the loss of Martian atmospheric gases to space and, among other things, the interactions of the Sun and the solar wind with the Mars magnetosphere and upper atmosphere (Jakosky et al., 2015). Equipped with magnetic field and plasma sensors, MAVEN orbits Mars (at heliocentric distance of ∼1.38—1.67 au) with a ∼4.5 h period at an altitude varying from about 150 km to 6220 km from the planet surface. While the magnetic field is accurately sampled with 0.031 s cadence, the plasma instrument measures the moments of the proton distribution functions with 4 s cadence. At that distance from the Sun, such temporal resolution is enough to study the inertial range turbulence. A detailed analysis of magnetic turbulent spectra showed a wide range of spectral exponents in the solar wind upstream of the martian bow shock and in the magnetosheath, as displayed in the two panels of Figure 83. The left panel refers to MHD-scale spectral exponents, ranging from -0.5 to -2 in different regions of the Martian environment, with steeper spectra observed in the upstream solar wind and in the magnetosheath, and shallower, non-turbulent spectra mostly at and downstream of the bow shock. The kinetic range exponents, shown in the right panel, are larger and close to typical values for space plasmas sub-ion scales (see, e.g, Leamon et al., 1998; Chen, 2016). In the region downstream of the magnetosheath, one single

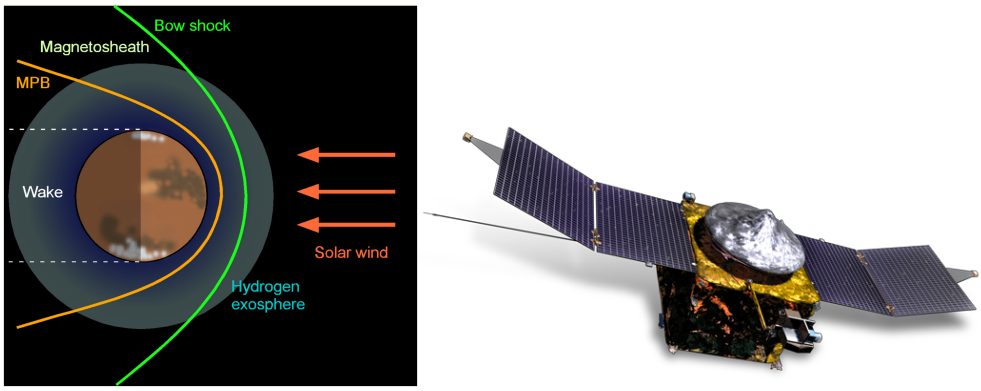

Figure 82: Left: A schematic representation of the near-mars space environment, from Ruhunusiri et al. (2017). Right: the NASA MAVEN orbiter, from the NASA/MAVEN official web page (https://mars.nasa.gov/maven).

scaling law with index close to -2 was found. A marked seasonal variability was also observed (not shown here), which was associated to the seasonal variability of proton cyclotron waves (Ruhunusiri et al., 2017).

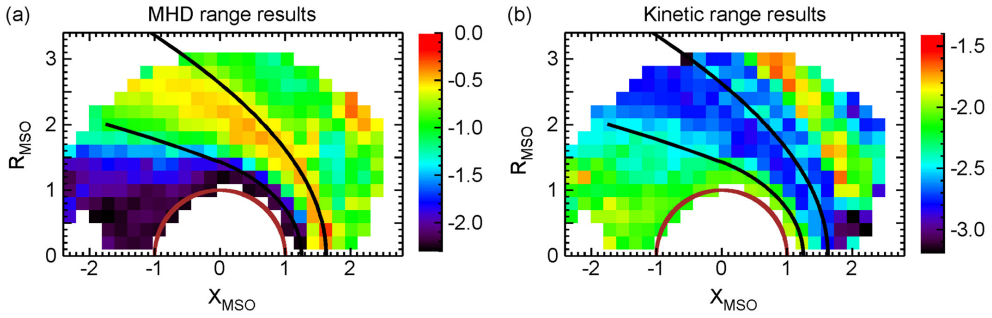

Figure 83: Mapping of the spectral indices of the magnetic fluctuations in a planar projection perpendicular to the ecliptic plane of the near-Mars space. Colors indicate the values of the spectral index, shown separately for the MHD range (left panel) and at kinetic scales (right panel). The Mars-centered Solar Orbital (MSO) coordinate system is used, where the x-axis points from Mars to the Sun, the z-axis is perpendicular to the plan containing Mars orbit (positive in the direction of the ecliptic north) and the y-axis completes the right-handed system. Figure from Ruhunusiri et al. (2017).

The properties of the MHD turbulence energy cascade and the possible effect of PCWs have been the subject of a thorough study performed by Andrés et al. (2020) using MAVEN data. These authors have selected about three hundred 30-minute intervals in the region upstream of the martian bow-shock, characterized by stable large-scale magnetic field direction and low density fluctuations, at the locations described in the top panels of Figure 84. After separating intervals with and without presence of PCWs (respectively indicated by the blue points in the top-left panel and by the red points in the top-right panel of Figure 84), the energy transfer rate was estimated using the P&P law for incompressible MHD, equation (54). The two plots in the bottom-right panels of Figure 84 show the mean energy transfer rate, $\langle|\varepsilon|\rangle$, estimated as the mixed third-order moment, Y, divided by the scale, Δt, and by the constant factor (including the solar wind speed, V_{sw}). Unfortunately, the presentation of the figure does not allow evaluating the actual presence of a clear linear scaling range (which would correspond to constant $\langle|\varepsilon|\rangle$) in each single interval. Moreover, using the magnitude at this level prevents to detect possible sign changes, which would imply lack of convergence of the moment and of linear scaling. It is therefore possi-

ble that, for some of the intervals, the estimate of the mean energy transfer rate is incorrect, since the linear scaling might not be observed at all. With these caveats in mind, the authors use a statistical approach to observe differences in their estimates. The statistical analysis should indeed reduce the possible effect of the presence of ill-defined linear scaling in some of the intervals. The measured energy transfer rate is found to be of the order of

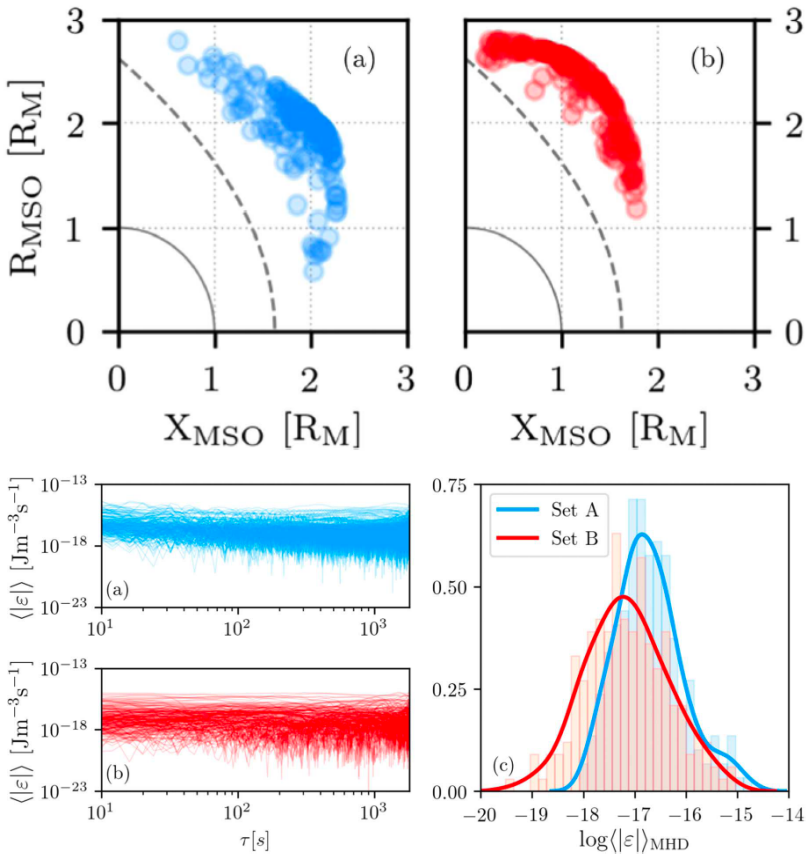

Figure 84: Top panels: the location of the intervals selected for the analysis, separated according to the presence (top-left panel, blue points, set A) or absence (top-right panel, red points, set B) of proton cyclotron waves. Bottom-left panel: the scale-dependent magnitude of the energy transfer rate for the two sets of intervals (color coded as in the top panels). Bottom-right: histograms of the logarithm of the mean energy transfer rate magnitude, separately for the two sets (same colors). The MSO coordinate system is used (see Figure 83). Figures from Andrés et al. (2020).

$\sim 10^{-16}$—10^{-17} J m^{-3} s^{-1}, namely at least one order of magnitude smaller

than at 1 au (see Section 4.4). This seems to suggest that the solar wind turbulence may be decaying during its expansion, also in agreement with the much larger rates observed in the near-Sun environment (Bandyopadhyay et al., 2020; Hernández et al., 2021). It would be interesting to explore the values in the ecliptic solar wind further out in the heliosphere, which could be done, to some extent, using the Voyager data. Future planetary or interstellar missions, such as Juice (to be launched in 2023, Grasset et al., 2013) or interstellar probes (proposed but not yet selected for launch by space agencies, McNutt et al., 2022), will help determining the radial evolution of solar wind turbulent cascade with better accuracy. Finally, the red and blue histograms in Figure 84 indicate that the two sets with and without PCWs have slightly different energy transfer rate. In particular, the intervals with waves appear to have larger energy transfer rate. The authors suggest that the ion-scale waves may play a role in modulating the inertial range cascade, through instabilities or inverse cascade mechanisms, therefore explaining the seasonality of the spectral indices previously observed. The causality relation between the two observations is harder to assess. The enhanced turbulence might indeed be the cause for observation of the PCWs, or, more likely, both features could be associated with the same driver, possibly related with the seasonal changes in the Mars exosphere and magnetosphere connection with the solar wind. Previous observations of ion-scale cyclotron waves was typically associated with periods of reduced turbulence (Khotyaintsev et al., 2021; Carbone et al., 2021). This suggest that the MAVEN observations are in fact demonstrating a different feature, more strictly connected with the specific Mars environment, and which will deserve more accurate studies.

The P&P law is therefore extremely useful to constrain the modeling of the interaction between the solar wind and the planetary environments. In the case of Mars, this is of great importance for a correct understanding of the history of the planet atmosphere, and for the modeling of electromagnetic and radiation seasonal variations, with relevance for its habitability.

7.5. Enhanced turbulent cascade in interplanetary coronal mass ejections

One of the most impressive features of the solar activity is the sudden expulsion of massive blobs of strongly magnetized plasma form the corona, called coronal mass ejections (CMEs, Howard, 2011). CMEs are generated during powerful releases of energy in the corona, usually associated with solar flares and solar active regions. They are typically the result of magnetic reconnection events that reconfigure and relax regions of highly stressed,

twisted magnetic field structures, called flux ropes. These usually entrap colder and denser coronal plasma, which may fall back to the solar surface or be violently released outward. In the latter case, once the expelled plasma structures are released from the corona in the heliosphere, they are often indicated as interplanetary coronal mass ejections (ICMEs, Kilpua et al., 2017). The expelled bubble of plasma carries the associated magnetic flux rope out in the interplanetary medium, expanding vigorously while it travels away from the sun with speed usually between 250 and 3000 km/s. Such speed is often larger than the speed of the embedding solar wind. If the ICME speed in the solar wind reference frame exceeds the local magnetosonic speed, a shock wave may form ahead of the expanding plasma bubble. Needless to

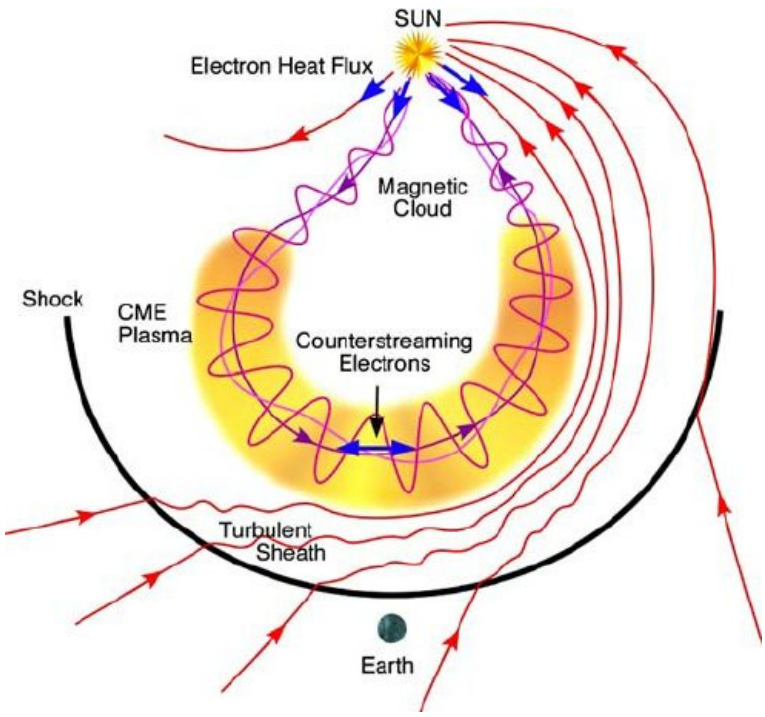

Figure 85: A schematic view of an expanding interplanetary coronal mass ejection. Figure from Zurbuchen and Richardson (2006).

say, from the point of view of turbulence, ICMEs are the equivalent of a dynamic obstacle in the solar wind flow, possibly causing modification on the fields fluctuations inside the ICME and in its trail. When ICMEs impact the terrestrial magnetosphere, they cause abrupt changes in the solar wind

dynamic pressure, in the magnetic configuration at the bow shock, in the flux of particles accelerated by the shock, and in several more parameters of the solar wind and of its fields fluctuations. These are usually associated with modifications of the global magnetospheric current system and configuration, therefore driving hazardous yet spectacular space weather events such as geomagnetic storms and auroras (Pulkkinen et al., 2007).

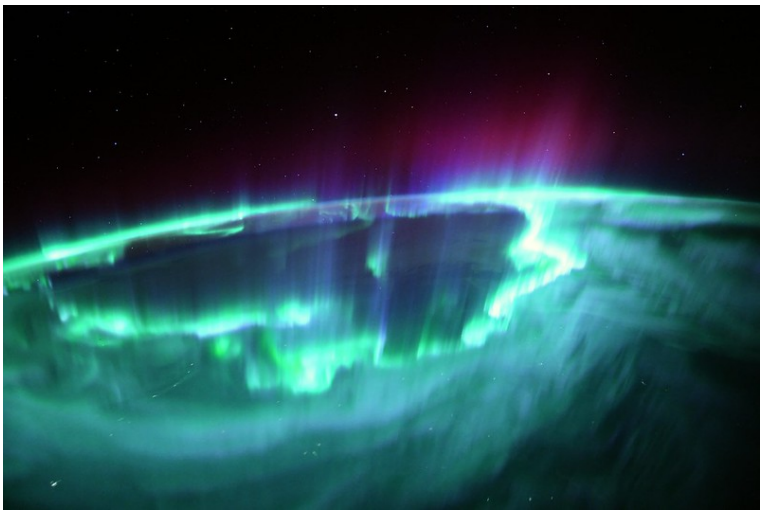

Figure 86: The aurora produced by the impact of an interplanetary coronal mass ejection on the terrestrial magnetosphere on November 4th, 2021, photographed from space by the ISS astronaut Thomas Pesquet. Credits: ESA/NASA—T. Pesquet.

Predictive modeling of CME expansion are expected to depend on the nature of the turbulent fluctuations of the solar wind and interplanetary magnetic field, and possibly of the ICME itself. This is manifestly clear when considering, for example, the effects of drag that the interplanetary medium applies on the ICME expansion (Maloney and Gallagher, 2010). Knowing the properties of solar wind fluctuations associated with ICMEs, and the way those interact with the surrounding solar wind and IMF, is therefore of extreme strategic importance for space weather purposes.

Recently, the statistical properties of turbulence in ICMEs have been studied using standard data analysis tools such as spectra and structure functions. Observations of larger magnetic field fluctuation power, steeper power spectra and enhanced intermittency suggest that ICME-driven sheaths have stronger but less developed turbulence than the surrounding solar wind (Kilpua et al., 2020; Kilpua et al., 2021; Pitňa et al., 2021). This is produced

by the strong compression of the plasmas crossing the ICME shock, which increases the fluctuations amplitude and inject fresh energy that needs to be transferred across scales by the turbulent cascade. A similar process is commonly observed at the terrestrial bow shock (Yordanova et al., 2008).

The P&P law can provide further and more solid information about the status, strength and development of the turbulence in various sectors of ICMEs, and in the surrounding solar wind. To exploit the strength of the diagnostics, preliminary studies were performed using a few largely examined ICME events. Sorriso-Valvo et al. (2021) analysed Wind measurements of an ICME crossing occurred in July, 2012, a "textbook" event with clear separation between the various sectors and presenting all the typical features of ICMEs (Webb and Nitta, 2017). The data were split in five intervals: two in the solar wind ahead of the ICME, one in the ICME sheath between the shock and the ICME flux rope, one in the hearth of the flux rope, and one in the solar wind behind the ICME (see the color-shaded areas in the panels of Figure 87). For each interval, the general conditions of turbulence were assessed using the solar wind parameters (the bulk speed, V_{sw}, the plasma β parameter, the magnetic fluctuations amplitude, $\delta B/B_0$, the angle between the solar wind velocity and the magnetic field, θ_{VB}, and the normalized cross-helicity, σ_c) and the standard turbulence properties (the spectral index, α, and the scaling exponent of the flatness, κ, estimated for the velocity and magnetic field components, as well as for the density and temperature). For this event, the scaling exponent of the second-order structure function (equivalent to the power spectral density) and of the flatness do not change substantially in the different regions, suggesting that the overall turbulence properties were not affected by the shock compression. The only exception was observed for the density fluctuations (see panel (c) of Figure 88), which are intermittent only in the ICME sheath, where the shock compression produces a nonlinear cascade that generates small-scale density structures.

The P&P law was then evaluated for each interval, using equation (54). Results, shown in Figure 89, indicate that the P&P law is verified, as expected, in the solar wind ahead (SW-1) and behind (SW-2) the ICME. This was not the case for the SW-2 interval, probably a magnetic cloud with low turbulence level, where statistical convergence of the mixed third-order moment was not attained, so that Y repeatedly changes sign with the scale. In the ICME sheath and cloud, a stable, broad linear scaling range was identified, so that the P&P law was correctly validated. This result shows that the turbulent cascade is already fully developed in the ICME regions. This

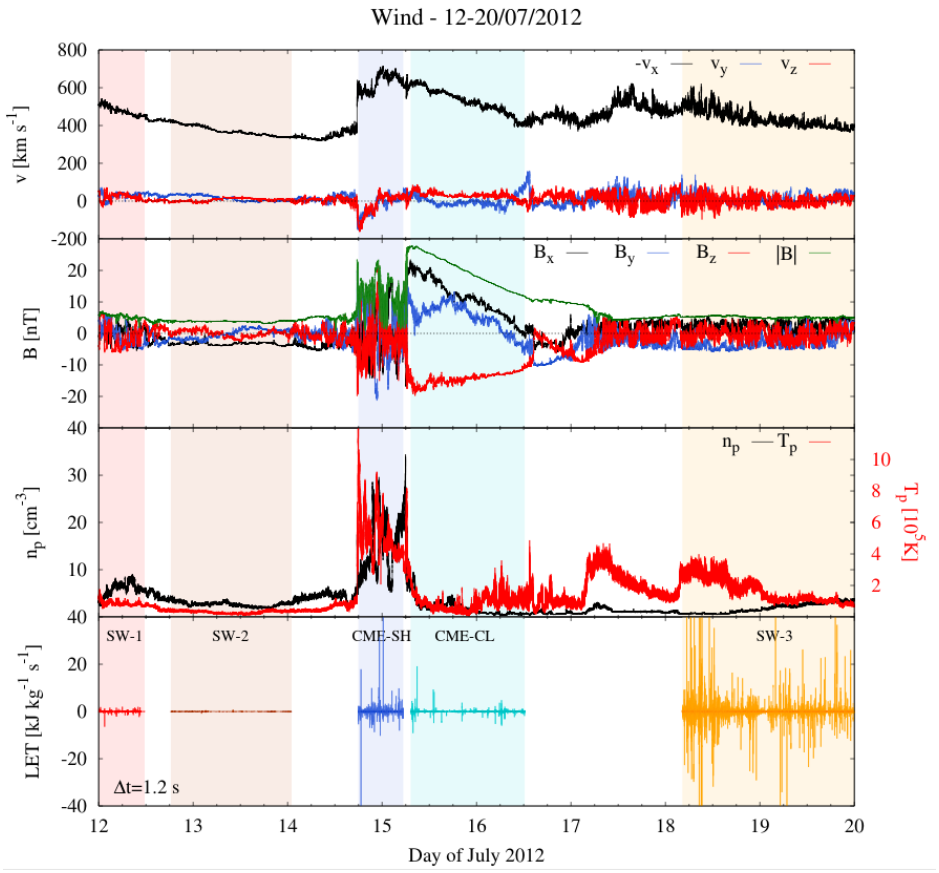

Figure 87: The Wind measurements during the interplanetary coronal mass ejection (CME) crossing of 12—20 July, 2012. From top to bottom: velocity components in RTN; magnetic field components and magnitude; proton density and temperature; the proxy of the local energy transfer rate, LET (see Section 8). The color-shaded areas indicate the five intervals selected for the study. Shades of blue represent the two CME portions, namely the sheath (CME-SH) and the magnetic cloud (CME-CL), while the solar wind sub-intervals are indicated by SW-1, SW-2 and SW-3. Figure from Sorriso-Valvo et al. (2021).

is in contrast with the conclusions of Kilpua et al. (2021), where a young turbulence was invoked to explain the different spectra and flatness. The same conclusion arises when observing the estimated values of the mean energy transfer rate ε (see the legends in each panel of Figure 89, which is largest in the ICME sheath, suggesting a fully developed, strong turbulence. Two possible scenarios can explain this observation. On the one hand, it is pos-

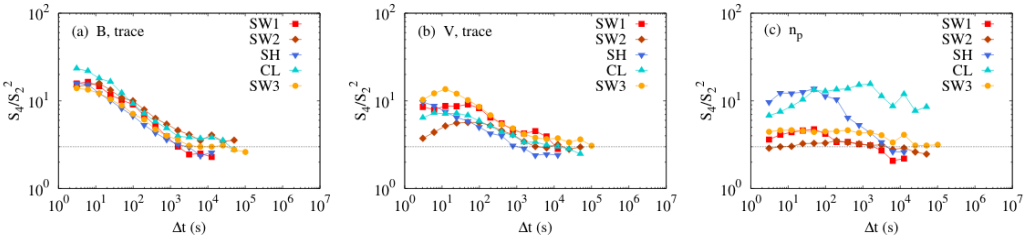

Figure 88: The flatness $F = S_4/S_2^2$, estimated for magnetic field (panel a) and velocity (panel b) fluctuations averaged over the three components and labeled as "trace", and for density fluctuations (panel c), for all five regions (same color-code as in Figure 87. The gray horizontal line indicate the Gaussian reference value $F = 3$. Figure from Sorriso-Valvo et al. (2021).

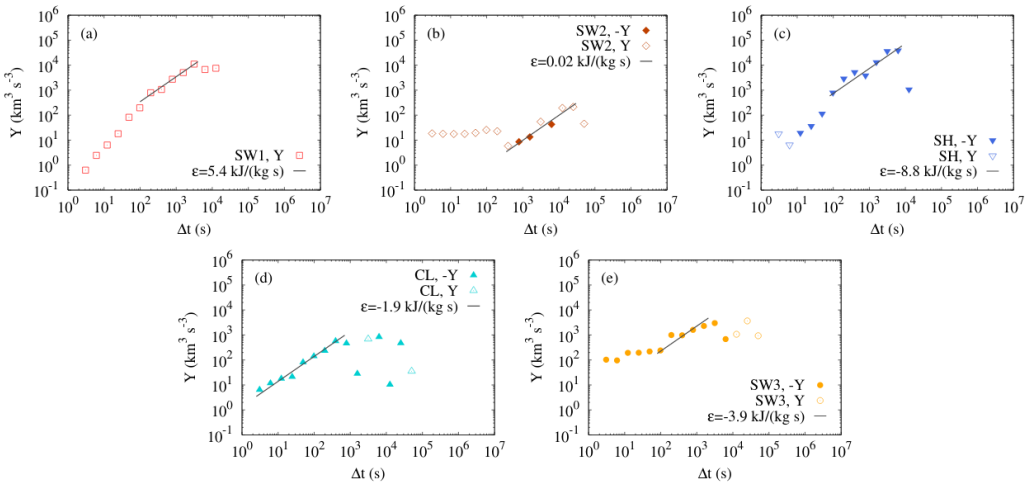

Figure 89: Scaling of the mixed third-order moment for incompressible MHD (PP-law) in the five intervals studied. Linear fits are indicated. Figure from Sorriso-Valvo et al. (2021).

sible that the onset of turbulence downstream of the ICME shock is rapid and efficient, and allows the turbulent cascade to immediately build up. On the other hand, it is also possible that the preexisting solar wind turbulence is not fundamentally affected by the shock crossing, which adds compression but leaves the fields correlations (i.e. the intermittent structures) robustly well defined. However, this second possibility is in contrast with the observations of underdeveloped turbulence in the magnetosheath, downstream of the terrestrial bow shock, where the cascade is not immediately recovered

after the strong compression. A statistical analysis of several events will be necessary to further understand the properties of turbulence in ICMEs and in the surrounding solar wind.

7.6. A phenomenological Yaglom law for proton density and temperature

An interesting phenomenological extension of the P&P law was recently proposed to describe the energy cascade associated to scalar quantities that are passively advected by the active solar wind turbulent fluctuations (Yaglom, 1949). In the solar wind flow, proton density and temperature are turbulent quantities whose fluctuations display spectral and intermittency properties not dissimilar to those of velocity and magnetic field. Their study is, however, less commonly found in the literature. Some exceptions are represented by a series of works that revealed the possible passive nature of both those quantities (Consolini, 2012; Consolini et al., 2020), suggesting similarities with passive scalar turbulence in ordinary flows (see for example Shraiman and Siggia, 2000; Warhaft, 2000, and references therein). Such behaviour was not always confirmed by other studies of density fluctuations, which instead pointed to a broader variety of dynamical properties, not simply associated to active or passive role, particularly in the more compressive slow solar wind (Hnat et al., 2005; Bruno et al., 2014; Riazantseva et al., 2016; Sorriso-Valvo et al., 2017; Carbone et al., 2021). Nevertheless, at least in those cases where density and temperature actually behave like passive scalars, the analogous of the von Kármán-Howarth relation for passive scalars, better known as Yaglom law (Yaglom, 1949), can be recovered. In its hydrodynamic version, such equation predicts the linear scaling of the mixed third-order moment involving the passive scalar ϕ, and can be written as

$$Y_\phi(\ell) = \langle \Delta \mathbf{v}_L (\Delta\phi)^2 \rangle = -\frac{4}{3}\varepsilon_\phi \ell \,, \tag{122}$$

where the advecting field is assumed to be the velocity (purely fluid model), and ε_ϕ is the energy transfer rate associated to the density or temperature variance. This represents the rate at which the temperature or density fluctuations are transferred towards smaller scales and depleted by some specific mechanisms, clearly yet undetermined in the solar wind. Under the usual assumptions of homogeneity, stationarity and local isotropy, the Yaglom law for density and temperature was recently validated in solar wind data (Consolini et al., 2020). In particular, the Empirical Mode Decomposition-based Dominant Amplitude Multifractal Formalism (Welter and Esquef, 2013) was

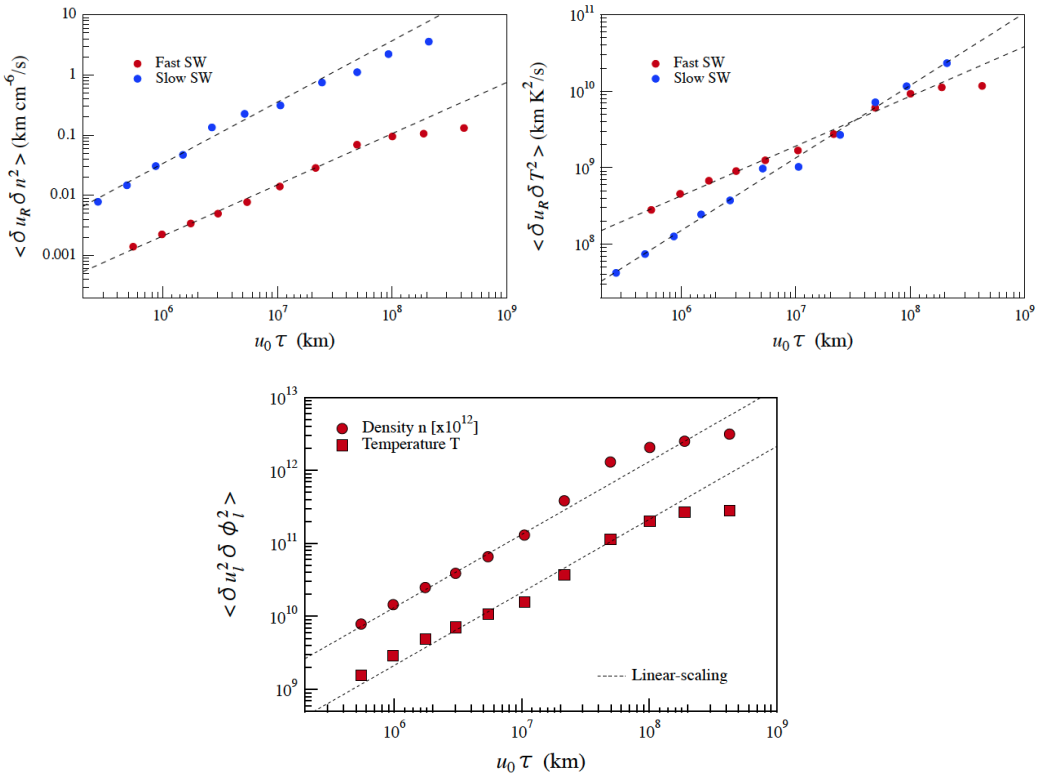

Figure 90: Top panels: the third-order scaling law for solar wind proton temperature (left panel) and density (right panel), see equation (122). In both of the top panels, fast and slow solar wind data are indicated by red and blue markers, respectively. Bottom panel: for the fast wind stream, the mixed fourth-order moment scaling law for density (circles) and temperature (squares), see equation (123). The timescale $\tau = \ell/V_{sw}$ is obtained, as usual, transforming the spatial scale r via the Taylor hypothesis. Power-law fits $Y_\phi(\ell) \propto \ell^\alpha$ are superposed (black dashed lines). The fitted scaling exponents for the slow wind samples are $\alpha = 0.95 \pm 0.05$ (temperature) and $\alpha = 1.02 \pm 0.05$ (density), compatible with the predicted linear scaling, while for fast wind samples are not linear, with $\alpha = 0.65 \pm 0.02$ (temperature) and $\alpha = 0.85 \pm 0.03$ (density). Figures from Consolini et al. (2020).

used for one fast (Alfvénic) and one slow (non-Alfvénic) solar wind streams measured by the Ulysses spacecraft. Results, illustrated in the top panels of Figure 90 showed that in the more compressive slow solar wind (blue symbols), for both variables the linear prediction of equation (122) was verified to a large extent and on a broad range of scales, extending from the data resolution (12 m) to several hours. The associated energy transfer rates resulted

$\varepsilon_n \simeq 10^{-8}\mathrm{cm}^{-6}\mathrm{s}^{-1}$ and $\varepsilon_T \simeq 10^2$ $\mathrm{K}^2\mathrm{s}^{-1}$ for density and temperature fluctuations, respectively. Conversely, for the fast solar wind sample (red symbols) the linear law was not observed, although a power-law scaling $Y_\phi(\ell) \propto \ell^\alpha$ with exponents $\alpha = 0.65$ (temperature) and $\alpha = 0.85$ (density) was present (Consolini et al., 2020). Such observation was used to support the passive nature of the two quantities in the slow solar wind sample.

As mentioned above, equation (122) is purely fluid and does not include magnetohydrodynamic effects. Although the analytical derivation of the MHD equivalent of the Yaglom law for the passive scalar has not been explored yet, an alternative scaling law based on phenomenological considerations was proposed by the authors of the study in order to explain the fast stream observation. Fast solar wind turbulence is often highly Alfvénic, with correlated v-b fluctuations over a broad range of scales (Bruno and Carbone, 2013). Therefore, the decorrelation produced by the sweeping of Alfvénic fluctuations reduces the nonlinear interactions, resulting in the Kraichnan scaling and spectrum of the Elsasser fields, $\Delta\mathbf{z}^\pm \sim \ell^{1/4}$ (Kraichnan, 1965). In analogy with the Kraichnan scaling for the Elsasser fields fluctuations, a simple phenomenological analysis can be used to introduce the Alfvénic decorrelation associated with the Alfvén time-scale also for the passive scalar. This results in the phenomenological analogous of the passive-scalar Yaglom law for Alfvénic turbulence,

$$\langle \Delta v^2 \Delta\phi^2 \rangle \sim \varepsilon_\phi \ell \, c_A \,, \tag{123}$$

which predicts the linear scaling of the mixed fourth-order moment instead of the third-order one. The bottom panel of Figure 90 shows that in the fast solar wind the modified phenomenological MHD Yaglom law, equation (123), is verified to a good extent, over more than two decades of scales, for both density and temperature (Consolini et al., 2020). Although the observed fourth-order scaling is remarkable, it should be stressed once more that the above relation (123) is not derived from the dynamical equations, and is therefore not an exact law, but rather a dimensional, phenomenological relation. Further studies should be devoted to the exact law describing the passive scalar in MHD flows, both by seeking the equivalent formal Yaglom law for MHD plasmas, and by performing more complete solar wind data statistical analysis. In particular, the dependence of the temperature and density behaviour could be examined as a function of the specific plasma conditions (e.g. radial distance from the Sun, compressibility, Alfvénicity, magnetic fluctuation level). This could help understanding the passive or

active nature of the proton parameters in the global energy transfer process as well as their role in the solar wind heating mechanisms.

7.7. Energy cascade in the interstellar medium

In some space and astrophysical systems, the role of the magnetic field can be considered marginal, and other force terms can appear in the Newton equation of the plasma. In other cases, for example when dealing with supersonic turbulence, the dynamics is modeled neglecting the magnetic field contribution in order to optimize computationally challenging numerical solutions. One clear example is the turbulent interstellar medium (ISM, see for example McKee and Ostriker, 2007; Federrath and Klessen, 2012; Hennebelle and Falgarone, 2012). Studying the interstellar medium is crucial for understanding processes such as star formation and cosmic ray transport. For example, intermittency generated by turbulence is considered an important ingredient leading to mass clustering and the subsequent star formation (Falgarone and Puget, 1995; Elmegreen and Scalo, 2004; Scalo and Elmegreen, 2004; Falgarone et al., 2009). In the absence of in-situ measurements, the ISM has been studied numerically (see, e.g., McKee and Ostriker, 2007; Federrath and Klessen, 2012; Hennebelle and Falgarone, 2012) and using remote observations. For instance, Orkisz et al. (2017) found that, while large-scale motions of the Orion B nebula are solenoidal, at smaller scales and within specific regions they are compressive, which highlighted the supersonic nature of the turbulence (Elmegreen and Scalo, 2004). While some authors have approached the MHD description (Federrath, 2016), in many cases the supersonic turbulence in the ISM is described using numerical simulations of the compressible, isothermal hydrodynamic equations (e.g., Kritsuk et al., 2007; Federrath, 2016). This is mostly motivated by numerical constraints and by the requirement of high Mach numbers.

7.7.1. A third-order relation for supersonic hydrodynamic turbulence

In a recent work, Ferrand et al. (2020) has adapted the compressible MHD exact law to the purely hydrodynamic case for the description of supersonic interstellar turbulence. The governing equations are

$$\frac{\partial \rho}{\partial t} + \boldsymbol{\nabla} \cdot (\rho \mathbf{u}) = 0 \tag{124}$$

$$\frac{\partial (\rho \mathbf{u})}{\partial t} + \boldsymbol{\nabla} \cdot (\rho \mathbf{u}\mathbf{u}) = -\boldsymbol{\nabla} P + \mathbf{d} + \mathbf{f}\,, \tag{125}$$

where $\mathbf{d}$ and $\mathbf{f}$ are respectively the dissipation term and the forcing. Following the same approach as in Hellinger et al. (2021b), additionally using an isothermal closure for the pressure, $P = c_s^2 \rho$ (Ferrand et al., 2019), a simple relation for the energy transfer rate ε was obtained assuming homogeneity, stationarity, and the existence of a well defined inertial range (i.e., the forcing only act at large scales and dissipation occurs at small scales). In divergence form, and within the inertial range of scales, the exact law is then:

$$\boldsymbol{\nabla}_{\boldsymbol{\ell}} \cdot \langle \overline{\Delta} \rho |\Delta \mathbf{u}|^2 \Delta \mathbf{u} \rangle - \frac{1}{2} \langle (\rho \theta' + \rho' \theta) |\Delta \mathbf{u}|^2 \rangle = -4\varepsilon \,, \tag{126}$$

where, as already described in Section 5.5.2, primed quantities are estimated at the point $\mathbf{r} + \boldsymbol{\ell}$, $\overline{\Delta}$ indicates average between values of a quantity at the two point $\mathbf{r}$ and $\mathbf{r} + \boldsymbol{\ell}$, and $\theta = \boldsymbol{\nabla} \cdot \mathbf{u}$ is the plasma dilatation. The left-hand side of equation (126) includes two simple terms. The first one, indicated as $\boldsymbol{\nabla}_{\boldsymbol{\ell}} \cdot \mathbf{F}$, is a pure divergence (flux) term, which is similar to the standard incompressible one with the (smooth) additional contribution from the density fluctuations. This signed term can remain finite at small scales, since the divergence operator grows as the scale decreases (Ferrand et al., 2020). The second term, indicated as S, is a simple source term that involves (smooth, finite) dilatation variations, which should therefore vanish as the velocity fluctuation energy as the scale decreases, and is absent in the incompressible limit ($\theta = 0$). Note that for an expanding plasma ($\theta > 0$) the source term is negative, and a direct cascade generated by the flux term is reduced or inhibited. If the plasma is being compressed ($\theta < 0$), the source term is positive, and contributes to enhance the cascade towards the small scales. The formulation of equation (126) therefore allows to describe the role of compression in the global cross-scale energy flux. The scaling law can be expressed in a practical way as the sum of the two terms, $\boldsymbol{\nabla}_{\boldsymbol{\ell}} \cdot \mathbf{F} + S = -4\varepsilon$.

7.7.2. Energy transfer in a numerical simulation of supersonic interstellar turbulence

Since there are currently no in-situ plasma measurements in the interstellar medium, and remote observations do not allow accurate estimates of the velocity (although proxies can be inferred), studies of the turbulent energy transfer rate can be only performed using numerical simulations. To this aim, Ferrand et al. (2020) used one high-resolution (1048^3 grid points in a periodic cubic box) direct numerical simulation of the isothermal, compressible Navier-Stokes equations in the regime of supersonic turbulence, namely with

turbulent Mach number $\mathcal{M} = u_{rms}/c_s = 4$, where u_{rms} is the velocity dispersion estimated using the fluctuations at the scale of the forcing (for details of the simulation, see Federrath et al., 2021). The left panels of Figure 91 show one two-dimensional slice of a snapshot of the density dilatation $\theta\rho$ (top-left panel) and magnitude of the vorticity (bottom-left panel) during the steady state of the turbulence. The highly turbulent nature of the fluctuations of those quantities is evident. The two terms of equation (126) have been estimated over the entire volume, and averaged over four snapshots in order to improve statistical convergence. The results are shown in Figure 92. The total energy transfer rate, ε (red line), is reasonably constant over a broad range of scales, indicating that the law correctly captures the cascade properties of the flow. The positive flux term (blue line) can be interpreted as an effective cascade rate, composed of the combined contribution of the actual dissipation rate, ε, and of the dilatation term, S. The resulting effective rate is increased by the smaller negative source term (green dashed line) over the whole range of scales. This indicates that the dilatation of the plasma is not negligible, and is contributing to generate small scale fluctuations.

The study then focuses on the role of the filamentary vorticity structures, highlighted in the magnifications in the right panels of Figure 91, in driving the dilatation contribution. Conditional analysis of regions with and without vorticity/compression filaments confirms the obvious expectation that most of the energy flux comes from the structures, a known property of intermittency (Frisch, 1995). The typical size of the structures is observed to correspond to the sonic scale, which has been previously estimated by Federrath et al. (2021). These structures appear therefore as the joint result of the supersonic nonlinear interactions and dilatation/compression. Smaller scales seems to be characterized by standard subsonic turbulence, so that dilatation structures are not observed.

Finally, in order to understand the role of nonlinear interactions and dilatation in the dynamics, the authors explore the different regimes by estimating the root mean square, rather than the average, of the flux and source terms. To do so, the average of the absolute value of the two terms is computed. This obviously invalidate the exact law, so that no scaling is expected or predicted, and no direct relationship with the energy transfer rate may be inferred. Nevertheless, this representation can highlight the intensity of the two-way cross-scale energy transfer, or in some sense the activity of the nonlinear interactions and of the compressive energy exchanges. Figure 93 shows, for one snapshot of the simulation, the modified unsigned flux term,

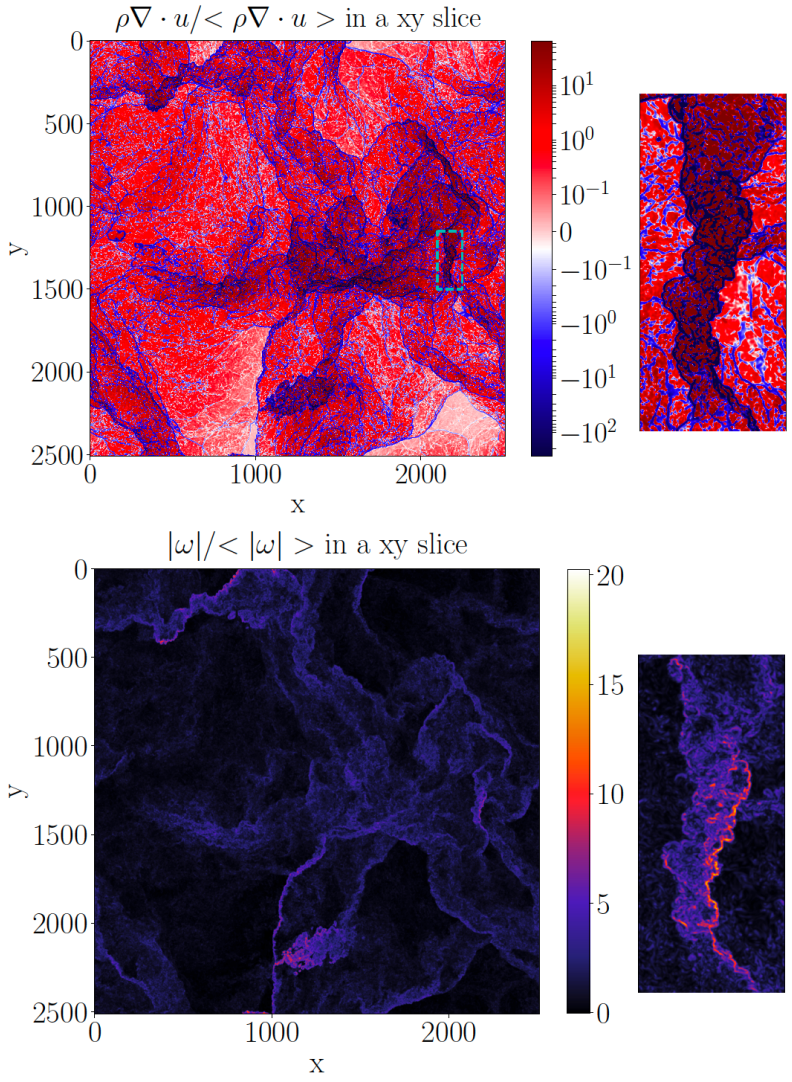

Figure 91: Left panels: two-dimensional cuts of the normalized density dilatation (top, see color bar) and vorticity magnitude (bottom, see color bar) obtained from one snapshot of the three-dimensional isothermal, supersonic hydrodynamic turbulence numerical simulation described in the text. The two axes are given in number of grid points. Right panels: magnification of a filament of strong compressive and vorticity activity (the location of the magnified area is indicated by the cyan dashed box in the top-left panel, and the magnified box is 150×400 grid points). Figure adapted from Ferrand et al. (2020).

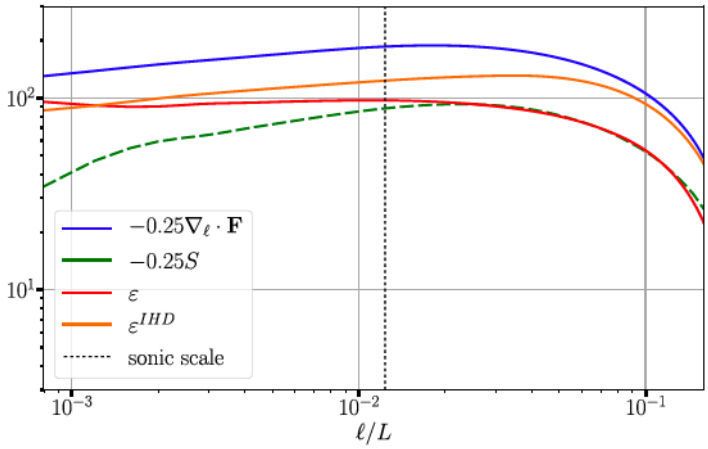

Figure 92: Scaling of the energy transfer rate, ε (red line, equation 126), flux term, $-1/4\boldsymbol{\nabla}_\ell \cdot \mathbf{F}$ (blue), source term, $-1/4S$ (green), and the simple incompressible hydrodynamic (IHD) energy transfer rate, ε^{IHD} (orange). Full or dashed lines indicate respectively positive and negative values. The vertical dashed black line identifies the sonic scale as estimated in (Federrath et al., 2021). The scale ℓ is normalized to the simulation box size, L. Figure from Ferrand et al. (2020).

$\tilde{\mathbf{F}} = \langle \bar{\Delta}\rho(\Delta\mathbf{u})^2|\Delta\mathbf{u}|\rangle$ (cyan), and source term, $\tilde{S} = 1/2\langle|\rho\theta' + \rho'\theta|(\Delta\mathbf{u})^2$ (green), both labeled with a tilde. The flux term, like for the signed case, is approximately constant across the scales. On the other hand, the source term clearly increases, approximately as the square root of the scale. A crossover is observed precisely at the sonic scale, which therefore separate two ranges characterized by different dominant dynamics. At supersonic scales, the dynamics is dominated by strong compression (such as shock structures), and the energy transfer rate is not constant. These produce filaments whose typical size is of the order of the sonic scale. Below such scale, namely at subsonic scales, a standard compressible energy cascade takes place, generates small-scale vortices and waves, and has constant energy transfer rate.

Notwithstanding all the caveats and limitations of the proposed numerical modeling, this result may be useful in the interpretation of remote observations of star formation regions, where the role of compressive modes dominates the dynamics (Orkisz et al., 2017).

7.8. From the stars to the lab: electrostatic turbulence in fusion plasmas

While plasma is the most common state of visible matter in the universe, it is practically absent in the Earth environment below the ionosphere. Spo-

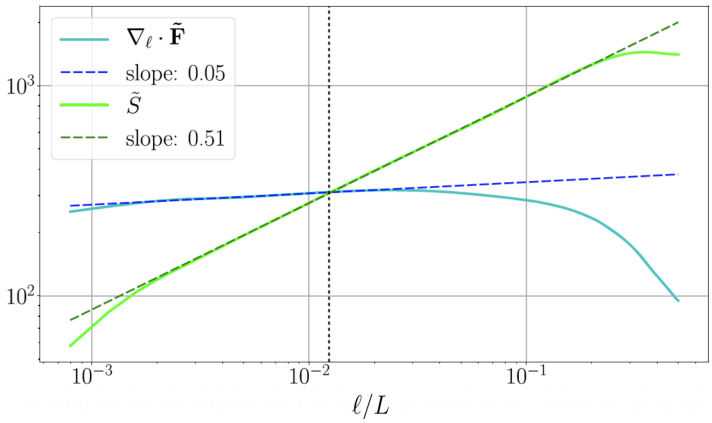

Figure 93: Scaling of the averaged unsigned flux term, $\tilde{\mathbf{F}} = \langle \bar{\Delta}\rho(\Delta\mathbf{u})^2|\Delta\mathbf{u}|\rangle$ (cyan), and source term, $\tilde{S} = 1/2\langle|\rho\theta' + \rho'\theta|(\Delta\mathbf{u})^2\rangle$ (green), see equation (126). The vertical dashed black line identifies the sonic scale (Federrath et al., 2021). Blue and green dashed lines indicate power-laws, and are shown for reference. The scale ℓ is normalized to the simulation box size, L. Figure adapted from Ferrand et al. (2020).

radic natural examples are found in lightnings (see for example Bazelyan and Raizer, 2000; Becker et al., 2005, and references therein) and in exceptionally hot flames. On the other hand, artificial plasmas are commonly produced and studied in a broad range of laboratory systems, ranging from fusion devices to industrial treatment of materials. Among those, fusion plasmas are relevant to this review, allowing to investigate several aspects of interest also for space and astrophysical plasmas. Besides their paramount importance for energy production purposes, their accessibility in laboratory provides otherwise inaccessible direct experimental measurements of the dynamical fields, though in conditions often very different than in space. With the necessary caution in considering the different plasma regimes and parameters, these can be used to help understanding fundamental plasma physics mechanisms (see Stacey, 2005). In particular, turbulence plays a crucial role in driving cross-field energy losses in magnetized plasmas. In their typical configurations, toroidal fusion devices such as tokamaks, stellarators, and reversed field pinches host strong electrostatic fluctuations in their edge regions (Horton, 1999; Zweben et al., 2007; Scott, 2007). In equilibrium with the $\mathbf{E} \times \mathbf{B}$ drift velocity shear, these drive enhanced particle transport across the plasma column (Antoni et al., 1998), often in the form of intermittent, localized high-density structures propagating from the hot plasma core to-

wards the device external wall. This represents one of the most disruptive effects driving energy losses and thus limiting the plasma confinement (Terry, 2000; Carbone et al., 2003). Understanding the fundamental properties of intermittent turbulence in fusion devices is therefore necessary to try to enhance the confinement properties of fusion plasma, and ultimately achieve the goal of using controlled thermonuclear fusion for energetic purposes.

7.8.1. A Yaglom-like equation for electrostatic turbulence in fusion plasmas

A simplified model to simulate two-dimensional electrostatic turbulence in a cylindrical domain configuration, without magnetic field curvature and background density gradient, was proposed by Servidio et al. (2008). These authors described the dynamics of the plasma by modeling a spatially localized and randomized source of space charge (vorticity) and mass number density (a passive scalar) at the center of the domain. This setup produces intermittent plasma "blobs" that are ejected into a low-density region at the cylinder edge, then radially advected by the drift velocity $\mathbf{u} = \mathbf{E}\times\mathbf{B}/B^2$. The radial motion of these structures is thus driven by the poloidal electric field fluctuations. The model was built to describe what happens, for instance, in the two-dimensional cross-section of a plasma column of a tokamak machine, in cylindrical coordinates (r, θ, z), with constant magnetic field directed perpendicular to the plane, $\mathbf{B} = B\mathbf{e}_z$. Under some standard approximations (for details, see Servidio et al., 2008), the model describes the dynamics in the (r, θ) plane by solving the continuity equation for the plasma density n, the Euler equation for the flow stream function $\psi = \phi/B$ (with ϕ the electrostatic potential, such that the drift velocity is $\mathbf{u} = \mathbf{e}_z \times \boldsymbol{\nabla}\psi$) and vorticity $\omega = \nabla^2\psi$, and the Poisson equation for the stream function:

$$\frac{\partial n}{\partial t} + (\mathbf{u}\cdot\boldsymbol{\nabla})n = f_n \tag{127}$$

$$\frac{\partial \omega}{\partial t} + (\mathbf{u}\cdot\boldsymbol{\nabla})\omega = f_\omega \tag{128}$$

$$\nabla^2\psi = \omega \tag{129}$$

The forcing term f_n represents some ionization mechanism, while f_ω is a source of vorticity in the central region of the plasma column that can be related to the plasma perturbations f_n. Equations (128) and (129) are sufficient to determine the dynamics of the system. Therefore, the density n behaves as a passive scalar transported by the drift velocity $\mathbf{u}$, as described by

equation (127). The dynamics equations are then used to drive the density, which is a passive scalar quantity advected by the drift velocity.

Starting from this model equations, the authors derive a Yaglom-like relation for the cascade associated to the density fluctuations, through a procedure similar to that for the classical Yaglom law for the passive scalar in fluid turbulence (Monin and Yaglom, 1971; Danaila et al., 2001b; Antonia et al., 1997). In particular, starting from the evolution equation (127) for the density written at two points $\mathbf{x} = (r, \theta)$ and $\mathbf{x}' = (r', \theta')$ radially separated by the distance $\mathbf{r} = \mathbf{x}' - \mathbf{x}$ of length $|\mathbf{r}| \equiv \ell$, under the hypotheses of statistically steady state, isotropy, local homogeneity (rather than global), and incompressibility for the drift velocity, a relation for the third-order moment can be obtained in the following form:

$$S_3(\ell, r) = \langle (\Delta n)^2 \Delta u_r \rangle = -\frac{1}{\ell} \int_0^\ell y F(r, y) dy \,, \tag{130}$$

where ℓ is the separation length, y is an integration variable, and the generalized input rate of density turbulence is defined as

$$F(r, y) = \frac{1}{2} \left\langle u_r \left[\frac{\partial}{\partial r} + \frac{\partial}{\partial r'} \right] (\Delta n)^2 \right\rangle - \langle \Delta n \Delta f_n \rangle \,. \tag{131}$$

In this geometry, and in particular because of the presence of structures that propagate radially, the third-order correlations also depend on the radial position and not just on the increment length. Therefore, the mixed moment in equation (130) includes an additional term that does not vanish and is not linear in the scale. Equation (130) can be considered as an equivalent of the Yaglom equation, here for case of electrostatic turbulence. The third-order mixed correlation, $S_3(\ell, r)$, represents the flux of density variance, $\epsilon(r)$.

It is possible to expand $F(r, y)$ around its local maximum in scale ℓ_m (assuming its existence) in terms of the (logarithmic) relative distance from the maximum ($y = \ell_m$), which at first order results in

$$S_3(\ell, r) = -\epsilon(r) \psi(1) \ell \,. \tag{132}$$

A range of scales showing the scaling predicted by relation (132) is indicative of an electrostatic turbulent cascade in the plasma. Values of $\epsilon(r)$ can be estimated from numerical and laboratory experiments after comparing equation (132) with the Yaglom law for the passive scalar in two-dimensional fluid

turbulence (for instance, $\langle(\Delta T)^2 \Delta u_r\rangle = -(4/d)\chi_\kappa \ell$, with d=2, χ_κ being the generalized transfer rate associated with the temperature) which allows to infer $\psi(1) = 2$, so that:

$$S_3(\ell, r) \simeq -2\ell\epsilon(r)\,. \tag{133}$$

The second- and fourth-order logarithmic expansion terms can also be retained, in analogy to the typical procedure for low Reynolds number turbulence where the inertial range is not yet extended, resulting in:

$$S_3(\ell, r) \simeq -2\ell\epsilon(r)\left\{1 - H_2(r)[\ln(\ell/\ell_m)]^2 + H_4(r)[\ln(\ell/\ell_m)]^4 + \cdots\right\}, \tag{134}$$

This relation can then be used to fit the third-order mixed correlations (at different radial positions) obtained from both numerical simulations and laboratory runs, as shown here this and the next section.

Without giving details of the numerical scheme implemented, snapshots obtained from integrating the model equations (127)-(129) are presented in the top panels of Figure 94, where both the number density (top-left) and flow vorticity (top-right) show clearly the formation of bursty turbulent structures that drift radially and outward. The system seems thus to satisfactorily reproduce the desired process observed in toroidal devices for plasma fusion. The third-order mixed correlations were estimated from the numerical results, using three different radial positions and averaging over the angle θ and in time. Results are given in the bottom panel of Figure 94. Finally, estimates of $S_3(\ell, r)$ were fitted to the relation (134) (see Figure 94, bottom), providing experimental values of the parameters $H_2(r)$ and $H_4(r)$, from which to infer important physical information, such as the flux of the density density variance, $\epsilon(r)$.

7.8.2. Scaling of the mixed third-order moment of the density in a fusion device

The mixed third-order scaling law for the density fluctuations in the inhomogeneous, cylindrical plasma column derived and validated in two-dimensional numerical simulations (Servidio et al., 2008) was also verified in experimental data. Lepreti et al. (2009) used measurements collected in the edge region of the RFX-mod (Piovesan et al., 2013), a large toroidal fusion plasma device in the reversed field pinch configuration (Spolaore et al., 2004) located in Padova, Italy (see a picture of the device in the top panel of Figure 95). The device has 2 m major radius, and minor radius a =0.46

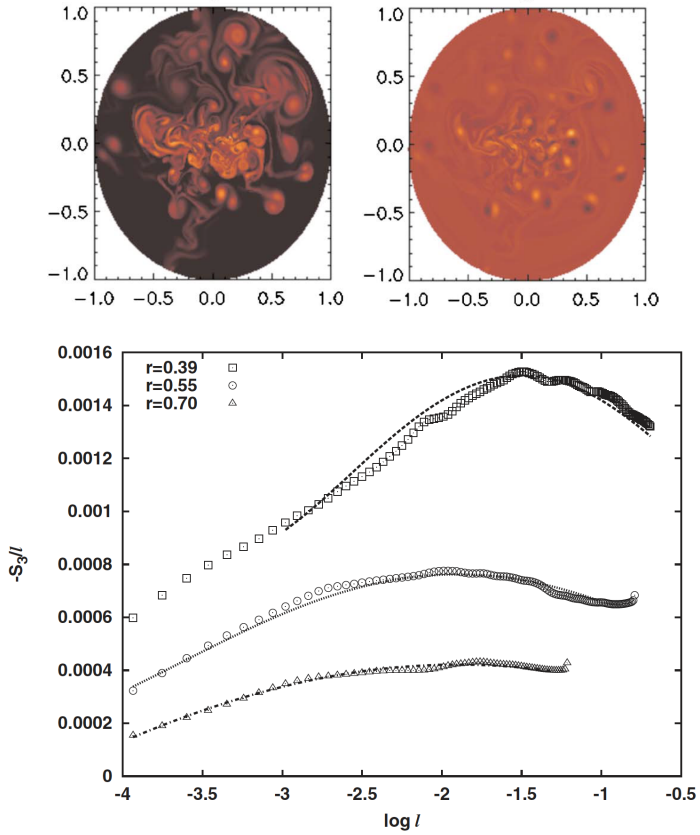

Figure 94: Top panel: snapshots of the model simulation used to verify the mixed third-order moment for the density $S_3(\ell, r)$ developed to investigate electrostatic turbulence in laboratory plasmas. The number density (top-left panel) and flow vorticity (top-right panel) show clear formation of bursty turbulent structures. Bottom panel: $S_3(\ell, r)$ estimated at three different radial distances from the center. The dashed line are fits done with the Yaglom-like model given by equation (134). Figure from Servidio et al. (2008).

m. For the study of electrostatic turbulence, a low-current discharge was considered, with average plasma density around $2{\cdot}10^{19}$ m^{-3}. The diagnostic probes (Spolaore et al., 2009), located at two different radial positions near the external wall (r/a =0.953 and r/a =0.966), measure high resolution magnetic and electrostatic fluctuations. From these, the poloidal component of the drift velocity u_r and the plasma density n_e are obtained. The sampling frequency is 5 MHz, and the sample length 170 ms. From the time series, scale-dependent increments Δu_r and Δn_e were computed, and from the latter

the mixed third-order moment, $S_3(\ell, r)$, was estimated. The Taylor hypothesis was used to convert temporal (Δt) to spatial scales (ℓ) through the average poloidal speed, $\ell = \langle v_r \rangle \Delta t$ (Taylor, 1938). The resulting quantity, rescaled by ℓ for better visualization, is plotted in the bottom panel of Figure 95 for two realizations of the measurement, at the two different positions indicated above. In the intermediate range of scales, a constant ratio S_3/ℓ, corresponding to the linear scaling prediction of the Yaglom law, is clearly visible. This shows that the electrostatic turbulence observed in RFX-mod is characterized by the typical features of fully developed turbulence: an inertial range is formally present, and the plasma density follows the prescription for a passive scalar advected by the drift velocity. All the other standard diagnostics for intermittent turbulence were estimated, and showed typical properties: power-law spectra, anomalous scaling of the structure functions, increasing flatness of the fluctuations' distribution. This observation could be useful in the modeling of the turbulent transport process that affects the confinement of plasma in devices for plasma fusion.

8. Local and regional description of the energy transfer

8.1. Can exact laws for fluid turbulence help understanding kinetic dissipation mechanisms?

For many decades, the study of turbulent plasmas has been focusing mostly on the global statistical properties of the fields and plasma fluctuations (Bruno and Carbone, 2013). Power spectra, anomalous scaling of the structure functions, variance and wavevector anisotropy were abundantly studied in space plasmas and in numerical simulations. All these studies rely on the solid basic assumption that inertial-range fluctuations are independent of the small-scale processes replacing viscous dissipation in collisionless plasmas. Higher-resolution space plasma measurements have recently pushed the focus towards smaller-scale features, possibly including a secondary turbulent cascade that encompasses field-particle interaction effects (Leamon et al., 1998; Alexandrova et al., 2008; Kiyani et al., 2009b). The variety of phenomena that have been observed in the kinetic range of scales (Gary, 1993; Marsch, 2006; Alexandrova et al., 2013; Goldstein et al., 2015; Bruno, 2019; Verscharen et al., 2019; Khotyaintsev et al., 2019; Matteini et al., 2020) raises questions on the corresponding variety of possible dissipation process.

As we have described in previous sections, the exact law approach permits to obtain one fundamental ingredient for understanding how dissipation

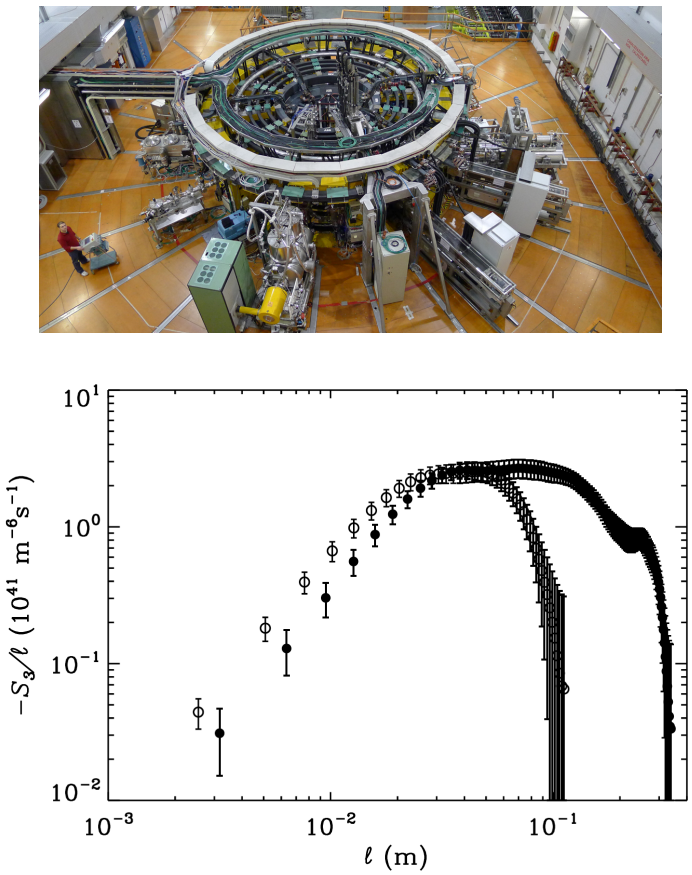

Figure 95: Top panel: a view of the RFX device in Padova (picture courtesy of the RFX consortium, available at `https://www.igi.cnr.it/en`). Bottom: the rescaled mixed third-order moment, S_3, divided by the scale, ℓ, for the electron density measured in the RFX decvice, for two different radial distances from the edge, $r/a = 0.953$ (open circles) and $r/a = 0.966$ (filled circles), where $a = 0.459$ m is the minor radius of the toroidal chamber. Figure from Lepreti et al. (2009).

works in the collisionless solar wind: the turbulent energy transfer rate. Ultimately, this represents the energy that the turbulence is transforming from the large-scale injection to small scales, where it can be transformed in internal energy, or heating. While the thermodynamics of non-equilibrium plasmas is finally being investigated (Liang et al., 2020; Pezzi et al., 2021), the possible pathways to dissipation are also being explored (Matthaeus et al., 2020). In this sense, being able to quantify the energy transported through the fluid (MHD) and sub-ion (Hall MHD) scales is a crucial step forward to

understand energy dissipation in nearly-collisionless space plasmas. An example given in the following section can demonstrate how exact laws can be successfully used to evaluate the effectiveness of kinetic dissipative processes.

8.2. Landau damping and the turbulent cascade

One possible strategy to tackle the complexity and diversity of sub-ion kinetic processes in weakly collisional plasmas consists of studying a system where one single process is active. While this is a promising strategy for the analysis of space plasma measurements, numerical simulations can help assessing its validity. To this aim, Ferrand et al. (2021b) performed a thorough study of the scaling of the Hall-MHD energy cascade rate in a series of numerical simulations of a Landau Fluid model (LF, Passot and Sulem, 2007). LF models are designed to retain the nonlinear dynamics of the parallel and perpendicular pressures and heat fluxes, with a closure based on a low-frequency linear kinetic description. By disregarding finite Larmor radius effects, the model effectively includes Landau damping as the sole kinetic process. In the numerical simulation, turbulence is forced with counter-propagating kinetic Alfvén waves (KAWs), injected at different scales and at different angles, θ, with the mean magnetic field (Passot et al., 2014). The different angles were used to control the intensity of the Landau damping, which is essentially transverse. Hyperviscous and hyperdiffusive dissipation is used to remove the energy at small scales. Through a detailed description of the energetics of the simulation, it was possible to show quantitatively that the Landau damping at small scales is associated with a steady decrease of the energy cascade rate. Furthermore, the effective energy removed via Landau damping should be added to the hyperviscous dissipation and to the nonlinear energy transfer in order to obtain a constant energy cascade rate. In other words, if ε is the nonlinear energy transfer rate obtained through the Hall-MHD usual relation (Ferrand et al., 2019), ε_{diss} the visco-resistive dissipation, and ε_{LD} the energy removed through Landau damping (estimated through appropriate modeling in Ferrand et al., 2021b), then their sum, $\varepsilon^{corr} = \varepsilon + \varepsilon_{diss} + \varepsilon_{LF}$ should give the actual constant energy transfer rate. This is clearly visible in Figure 96, where the above quantities are plotted for one run with the magnetic field angle $\theta = 75^\circ$ (LF3). Therefore, the deviation from constant of the exact law provided an indirect but correct estimate of the energy dissipated into particle heating by Landau damping.

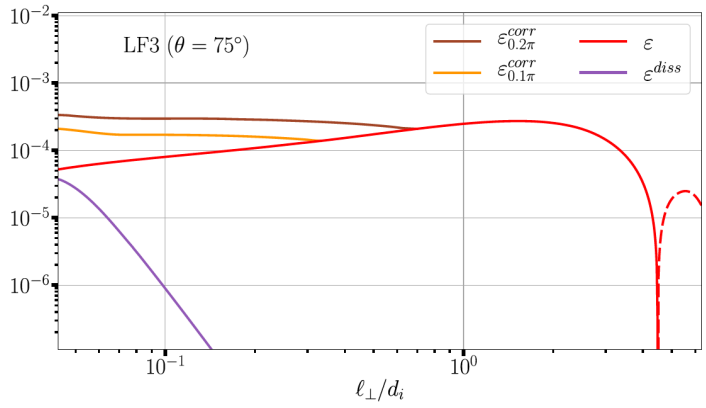

Figure 96: Comparison between the energy transfer rate (red), the dissipation rate (purple), and the corrected energy transfer rate that includes Landau damping (dark and light orange), using a Landau fluid model numerical simulation. The angle $\theta = 75°$ between the magnetic field and the injected kinetic Alfvén wave propagation direction is indicated. Figure adapted from Ferrand et al. (2021b).

8.3. From global to local description of the cascade

The numerical experiment described above illustrates the tight connection between fluid scale cascades and energy conversion in systems that are not limited to viscous-resistive dissipation and dispersion. However, experimental conditions in real plasmas cannot be controlled as easily, and in most cases the energy conversion cannot be attributed to one single kinetic process, nor be quantitatively estimated. In those cases where the plasma conditions permit an accurate estimate of the turbulent cascade rate, deviations from constant energy transfer rate can still be used to predict the energy dissipated by non-fluid processes. However, understanding which processes are active in a specific plasma sample, how they contribute to heating and energization of particles, and how they are activated by the fluctuations is still a complicate issue. In this perspective, it is natural to opt for a change of paradigm, and focus on the local or regional details of the fluctuations, rather than global. Such approach, for which modeling, predictability and a phenomenological descriptions are challenging, has the advantage of illuminating the physics of the cross-scale connection between the turbulence-generated fluctuations and the kinetic plasma processes. Small-scale processes such as plasma resonances, instabilities, magnetic reconnection, collisions and resistive dissipation, all require specific conditions in order to be effective.The

local or regional characteristics of small-scale turbulent fluctuations are often the main discriminating factor for the activation of these processes. Knowing the specific nature of the fluctuations at a given point in space can therefore help identifying the corresponding local "dissipative" process, so that the particle energization mechanism can be understood.

As we shall see in this Section, the local approach to the description of the turbulent cascade through third-order moment scaling laws is supported by theoretical considerations, which were first developed for Navier-Stokes turbulence, and later adapted to magnetohydrodynamics. On the other hand, solar-wind data analysis provided increasing insight on the dissipative mechanisms, as also confirmed by numerical simulations. In the remainder of this Section, data analysis techniques based on the local approach to exact scaling laws are reviewed. The most recent observational and numerical studies in such framework are described, along with the resulting advances in understanding the physics of dissipation in space plasmas.

8.4. The filtered approach

As was shown in the previous sections, the P&P law proved to be an invaluable tool for the investigation of the turbulent cascade in plasmas, in particular in the outer space, where assessing the inter-scale transfer by computing spatial variations of velocity and magnetic field is currently not attainable. Together with the information provided by the third-order exact laws, concerning the mean energy transfer rate over the inertial range, one would like to know how the irregular occurrence of shears, reconnection points, magnetic switchbacks, and other phenomena that may develop at intermediate MHD scales, feeds back on the energy transfer. One possibility to achieve a scale decomposition of second-order quantities —locally in the physical space— to ultimately be able to characterize the turbulent energy transfer even when inhomogeneities are present in the plasma due to localized events, is the well known space-filter approach (Camporeale et al., 2018), routinely applied to the governing equations of fluids and plasmas. First introduced by Leonard (1975) to model turbulent flows with large-eddy simulations (LES), then further developed by Germano (1992), this approach has been successfully applied in a variety of turbulent frameworks. Eyink (2005) and Aluie and Eyink (2009) used space filters to prove the locality of turbulent cascades. The same authors then extended the space-filter applications to geophysical flows, whose dynamics is well described by the Boussinesq equations (Aluie and Kurien, 2011), as well as to compressible flows (Aluie et al., 2012) and to

astrophysical plasmas in the magnetohydrodynamics (MHD) regime (Aluie and Eyink, 2010). Hellinger et al. (2020) made a step forward, performing a quantitative comparison between the fluxes obtained through the application of filters and those retrieved from a version of the Kármán-Howarth-Monin (KHM) equation in the hydrodynamic case that takes into account compressibility, at high Mach number. Various studies utilized the space-filter techniques to investigate how the presence of coherent structures affects the transfer of the energy between scales both in neutral and electrically conductive fluids. Foldes et al. (2022) implemented a refined space-filter approach to characterize the local energy release by extreme vertical drafts in stratified geophysical flows, whereas Camporeale et al. (2018) combined the space-filter approach with wavelet analysis to prove that coherent structures in plasmas, described by 2.5D Hall-MHD simulations, correlate with regions where the energy transfer is enhanced, in a particular range of scales. Space filters were also used by Manzini et al. (2022) to emphasize, in fully 3D Hall-MHD simulations, how magnetic reconnection sites do affect energy dissipation. The concept of space filtering has been also implemented to obtain a local version of the third-order law hydrodynamic turbulence and in MHD, which makes it relevant for the purpose of this review. This approach was first formalized by Duchon and Robert (1999), introducing a local version of the KHM relation, later on extended in Eyink (2007–2008, 2008) to the derivation of a local 4/3 law, where statistical averages are replaced with averages over a sphere of radius ℓ and no assumption of isotropy or homogeneity is made. The results from Duchon and Robert (1999) have been generalized to MHD case in Galtier (2018), while Kuzzay et al. (2019) reformulate the local version of the 4/3 law in terms of the Elsasser variables. Here we emphasise how the approach taken in Camporeale et al. (2018), aiming at obtaining the energy transfer rate, at a given scale ℓ, from the MHD equations, compares with that of Kuzzay et al. (2019), in which the energy transfer at the scale ℓ obtains from a local version of the P&P law.

Starting from the incompressible MHD framework:

$$\boldsymbol{\nabla} \cdot \mathbf{v} = 0 \tag{135}$$

$$\partial_t \mathbf{v} + (\mathbf{v} \cdot \boldsymbol{\nabla})\mathbf{v} - (\mathbf{b} \cdot \boldsymbol{\nabla})\mathbf{b} = -\boldsymbol{\nabla} P + \mathcal{D}_\nu + \mathbf{f} \tag{136}$$

$$\partial_t \mathbf{b} = \boldsymbol{\nabla} \times (\mathbf{v} \times \mathbf{b}) + \mathcal{D}_\eta \tag{137}$$

(with $\mathcal{D}_\nu = \nu \boldsymbol{\nabla}^2 \mathbf{v}$ and $\mathcal{D}_\eta = \eta \boldsymbol{\nabla}^2 \mathbf{b}$), following Camporeale et al. (2018) the physical quantities are modulated by a kernel G (here applied to the velocity

$\widetilde{\mathbf{v}}(\mathbf{x},t) \doteq \int_V G(\mathbf{x}-\xi)\mathbf{u}(\xi,t)\mathrm{d}^3\xi$, where V is the domain volume) which allows to obtain the filtered equations:

$$\boldsymbol{\nabla}\cdot\widetilde{\mathbf{v}} = 0 \tag{138}$$

$$\partial_t\widetilde{\mathbf{v}} + (\widetilde{\mathbf{v}}\cdot\boldsymbol{\nabla})\widetilde{\mathbf{v}} - (\widetilde{\mathbf{b}}\cdot\boldsymbol{\nabla})\widetilde{\mathbf{b}} = -\boldsymbol{\nabla}P + \widetilde{\mathcal{D}}_\nu + \widetilde{\mathbf{f}} - \boldsymbol{\nabla}\cdot\mathcal{T}_{ub} \tag{139}$$

$$\partial_t\widetilde{\mathbf{b}} = \boldsymbol{\nabla}\times(\widetilde{\mathbf{v}}\times\widetilde{\mathbf{b}}) + \widetilde{\mathcal{D}}_\eta + \boldsymbol{\nabla}\times\boldsymbol{\varepsilon}_{\mathrm{MHD}} \tag{140}$$

with

$$\mathcal{T}_{vb} = \widetilde{\mathbf{v}\mathbf{v}} - \widetilde{\mathbf{v}}\widetilde{\mathbf{v}} - (\widetilde{\mathbf{b}\mathbf{b}} - \widetilde{\mathbf{b}}\widetilde{\mathbf{b}}) \tag{141}$$

and the sub-grid electric field

$$\boldsymbol{E}_{\mathrm{MHD}} = \widetilde{\mathbf{v}\times\mathbf{b}} - \widetilde{\mathbf{v}}\times\widetilde{\mathbf{b}} \tag{142}$$

The filtering kernel G can be chosen as any real-valued even function of a variable x with the following features: being characterized by a sufficiently rapid and smooth decay for large values of x; being normalized (meaning that the integral of G over the whole domain is equal to 1) and positive definite (such that $G(x) \geq 0$ for any x). From these, multiplying equation (139) by $\widetilde{\mathbf{v}}$ and equation (140) by $\widetilde{\mathbf{b}}$, one obtains the equations for the variation in time of the filtered kinetic ($\widetilde{\mathcal{E}}_u = |\widetilde{\mathbf{v}}|^2/2$) and magnetic ($\widetilde{\mathcal{E}}_M = |\widetilde{\mathbf{b}}|^2/2$) energies:

$$\partial_t\widetilde{\mathcal{E}}_u = -\boldsymbol{\nabla}\cdot\left[\widetilde{\mathcal{E}}_u\widetilde{\mathbf{v}} + \widetilde{P}\widetilde{\mathbf{v}} - (\widetilde{\mathbf{v}}\cdot\widetilde{\mathbf{b}})\widetilde{\mathbf{b}} + \mathcal{T}_{ub}\cdot\widetilde{\mathbf{v}}\right] - \widetilde{\mathbf{b}}\cdot(\widetilde{\mathbf{b}}\cdot\boldsymbol{\nabla})\widetilde{\mathbf{v}} + \widetilde{\mathbf{v}}\cdot\widetilde{\mathcal{D}}_\nu + \mathcal{S}_u + \boldsymbol{\varepsilon}_{inj} \tag{143}$$

$$\partial_t\widetilde{\mathcal{E}}_M = \boldsymbol{\nabla}\cdot\left[\widetilde{\mathcal{E}}_M\widetilde{\mathbf{v}} - \boldsymbol{\varepsilon}_{\mathrm{MHD}}\times\widetilde{\mathbf{b}}\right] + \widetilde{\mathbf{b}}\cdot(\widetilde{\mathbf{b}}\cdot\boldsymbol{\nabla})\widetilde{\mathbf{v}} + \widetilde{\mathbf{b}}\cdot\widetilde{\mathcal{D}}_\eta + \mathcal{S}_b \tag{144}$$

with $\mathcal{S}_b = \widetilde{\mathbf{j}}\cdot\boldsymbol{\varepsilon}_{\mathrm{MHD}}$, $\mathcal{S}_v = \mathcal{T}_{vb} : \boldsymbol{\nabla}\widetilde{\mathbf{v}}$, and with a term indicating the conversion between kinetic and potential energy:

$$\mathcal{S}_{vb} = \widetilde{\mathbf{b}}\cdot(\widetilde{\mathbf{b}}\cdot\boldsymbol{\nabla})\widetilde{\mathbf{v}} \tag{145}$$

The equation of the filtered total energy, defined as $\widetilde{\mathcal{E}} = (|\widetilde{\mathbf{v}}|^2 + |\widetilde{\mathbf{b}}|^2)/2$, obtains from gathering equations (143) and (144)

$$\begin{aligned}\partial_t\widetilde{\mathcal{E}} + \boldsymbol{\nabla}\cdot\left[\widetilde{\mathcal{E}}\widetilde{\mathbf{v}} + \widetilde{P}\widetilde{\mathbf{v}} - (\widetilde{\mathbf{v}}\cdot\widetilde{\mathbf{b}})\widetilde{\mathbf{b}} + \mathcal{T}_{vb}\cdot\widetilde{\mathbf{v}} - (\widetilde{\mathbf{v}}\cdot\widetilde{\mathbf{b}})\widetilde{\mathbf{b}} - \varepsilon_{\mathrm{MHD}}\times\widetilde{\mathbf{b}}\right] = \\ = \widetilde{\mathbf{v}}\cdot\widetilde{\mathcal{D}}_\nu + \widetilde{\mathbf{b}}\cdot\widetilde{\mathcal{D}}_\eta + \mathcal{S}_v + \mathcal{S}_b + \boldsymbol{\varepsilon}_{inj}\end{aligned} \tag{146}$$

If we perform a volume average, considering periodic or vanishing boundary conditions, the divergence term in the above equation vanishes, thus it reads as

$$\partial_t \langle \widetilde{\mathcal{E}} \rangle = \langle \widetilde{\mathbf{v}} \cdot \widetilde{\mathcal{D}}_\nu \rangle + \langle \widetilde{\mathbf{b}} \cdot \widetilde{\mathcal{D}}_\eta \rangle + \langle \mathcal{S}_v \rangle + \langle \mathcal{S}_b \rangle + \langle \boldsymbol{\varepsilon}_{inj} \rangle \tag{147}$$

The first two terms on the RHS are the dissipative contributions to the energy loss, the last term is the energy injection and the sub-grid terms (third and fourth) represent the energy exchange between different scales across the filtering one. From equation (147), the total sub-grid energy term is defined as:

$$\mathcal{S} = \mathcal{S}_v + \mathcal{S}_b = \mathcal{T}_{ub} : \boldsymbol{\nabla} \widetilde{\mathbf{v}} + \widetilde{\mathbf{j}} \cdot \varepsilon_{\mathrm{MHD}} \tag{148}$$

A similar approach, based on the space-filtering technique, was proposed in Kuzzay et al. (2019), where a local (in space) version of the KHM equation is first developed then assessed in three-dimensional MHD simulations. The main difference with the approach by Camporeale et al. (2018) consists in the different definition used for the filtered energy, leading in turn to a different definition for the nonlinear energy flux. In Kuzzay et al. (2019) the latter is given in terms of Elsasser variables and it is based on the point-split energy density of a field $\phi(\mathbf{x}, t)$, $\phi(\mathbf{x}, t)\phi(\mathbf{x} + \mathbf{r}, t)/2$, reading as

$$\widetilde{E}^{\pm} = \frac{\mathbf{z}^{\pm} \widetilde{\mathbf{z}}^{\pm}}{2} \tag{149}$$

Alternatively, the same expression in terms of $\mathbf{u}$ and $\mathbf{b}$, is proposed in Galtier (2018),

$$\widetilde{E} = \frac{\mathbf{v} \cdot \widetilde{\mathbf{v}} + \mathbf{b} \cdot \widetilde{\mathbf{b}}}{2} \tag{150}$$

In the approach adopted in Camporeale et al. (2018), mainly based on the LES technique, the large-scale energy is again defined as the square of the filtered fields $\tilde{\mathcal{E}} = (|\widetilde{\mathbf{v}}|^2 + |\widetilde{\mathbf{b}}|^2)/2$ which, in terms of equation (150), leads to $\widetilde{\mathcal{E}}^{\pm} = \widetilde{E}^{\pm} + \widetilde{\delta \mathbf{z}}^{\pm} \cdot \widetilde{\mathbf{z}}^{\pm}$. The definition of energy given in Kuzzay et al. (2019) does not guarantee that $\widetilde{E} \geq 0$, but is preferred as it leads to the formulation of a local version of the P&P law. The local version of the KHM equation obtains from an equation for the energy conservation resembling equation (147),

$$\partial_t E_\ell + \boldsymbol{\nabla} \cdot \mathbf{J}_\ell = -\Pi_\ell^T - \mathcal{D}_\ell^{\nu,\eta} - \mathbf{F}_\ell \tag{151}$$

The first right-hand-side term is an analogous of the third and forth sub-grid terms in equation (147)) but it does not depend on the sub-grid Reynolds stress tensor $\mathcal{T}$, defined in terms of Elsasser variables as $\mathcal{T}^{\pm} = \widetilde{\mathbf{z}^{\pm} \mathbf{z}^{\pm}} - \widetilde{\mathbf{z}}^{\pm} \widetilde{\mathbf{z}}^{\pm}$.

Equation (151) obtains from the filtered MHD system, multiplying the momentum equation by $\mathbf{u}$ and the induction equation by $\mathbf{b}$. The term indicating the cross-scale energy transfer, Π_ℓ^T, can be expressed as the divergence of the third-order structure function of velocity and magnetic fields:

$$\begin{aligned}\Pi_\ell^T &= \frac{1}{4}\int \boldsymbol{\nabla}\mathbf{G}(\mathbf{r})_\ell \cdot \left[\left((\Delta\mathbf{v})^2 + (\Delta\mathbf{b})^2\right)\Delta\mathbf{v} - 2(\Delta\mathbf{v}\cdot\Delta\mathbf{b})\Delta\mathbf{b}\right] d\mathbf{r} \\ &= -\frac{1}{4}\int \mathbf{G}(\mathbf{r})_\ell \boldsymbol{\nabla} \cdot \left[\left((\Delta\mathbf{v})^2 + (\Delta\mathbf{b})^2\right)\Delta\mathbf{v} - 2(\Delta\mathbf{v}\cdot\Delta\mathbf{b})\Delta\mathbf{b}\right] d\mathbf{r} \end{aligned} \quad (152)$$

Equation (151) can be seen as a local version of the KHM equation for MHD in the physical space. Thus, the energy flux provided by equation (152) through a filtering operated at the scale ℓ can be used to obtain a local version of the P&P law, equation (54), that does not require isotropy and homogeneity assumptions:

$$\Pi_\ell^{\pm} = -\frac{\langle \Delta_\ell z^{\mp} |\Delta_\ell \mathbf{z}^{\pm}|^2\rangle_\Omega}{4/3\ell} \quad (153)$$

Equation 153 is given in terms of both longitudinal and vector increments of the Elsasser variables, where ℓ is both the filtering scale and the scale of the field increments. The brackets indicate an averaging operation performed over a spherically symmetric support Ω. Expression (153) is suitable to investigate the cross-scale energy transfer in turbulent systems characterized by strong anisotropy, such as the interplanetary space plasma, which is characterized by a background magnetic field. ${\Pi_\ell}^T = (\Pi_\ell^+ + \Pi_\ell^-)/2$, obtained from equation (153), is a point-wise quantity, whose statistics depend on the scale. In Kuzzay et al. (2019), ${\Pi_\ell}^T$ is computed within the domain of a DNS of the incompressible MHD equations, integrated on a cubic grid of 1024^3 points and size 2π, with periodic boundary conditions, in the presence of a Taylor-Green forcing. The energy is injected at the scale $L = \pi/2$. The local flux, ${\Pi_\ell}^T$ (shown in Figure 97, left, for a scale ℓ close to the forcing scale, so that $\ell/L = 0.996$), was then averaged over the entire volume, $\mathcal{V}$, for each scale ℓ, as is reported in Figure 97, right panel. The same plot shows $\varepsilon_\ell^T = (\varepsilon^+ + \varepsilon^-)/2$, which is the energy transfer rate computed from the third-order structure functions (blue dash-dotted curve in Figure 97), which allows for a comparison between the original P&P law (equation 54) and its local version (equation 153). The plots show that $\langle {\Pi_\ell}^T\rangle_\mathcal{V}$ and ε_ℓ^T are consistent at intermediate scales, where homogeneity and isotropy are expected,

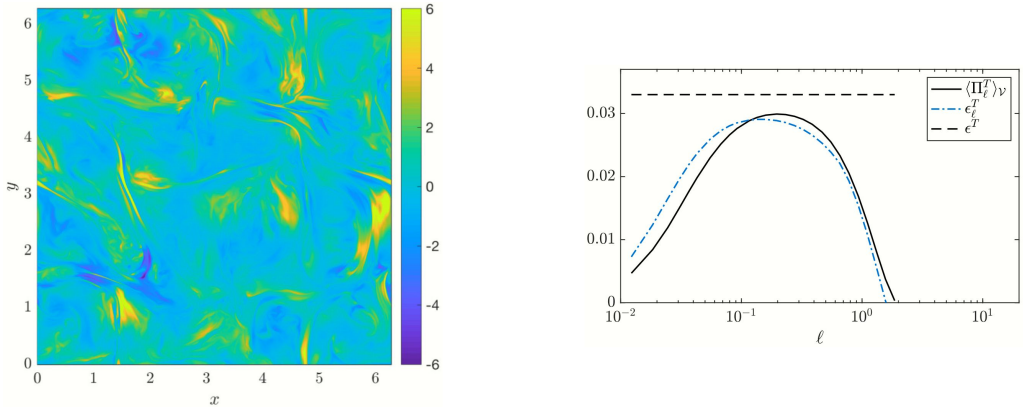

Figure 97: Left panel: horizontal cut of the total energy flux Π_ℓ^T (color scale on the right of the panel), computed through (152) for a given scale ℓ close to the forcing scale $L(\ell/L = 0.996)$. Right panel: Volume-averaged scale-to-scale transfer $\langle \Pi_\ell^T \rangle_\mathcal{V}$ and ε_ℓ^T (obtained from the P&P law, equation 54). The dashed horizontal line is total energy dissipation rate. Figure adapted from Kuzzay et al. (2019).

demonstrating the equivalence between spatial and ensemble averages within the MHD turbulent inertial range, in the simulation under study. The authors point out that since the original P&P law assumes homogeneity and isotropy, its application to this DNS would not provide a correct estimate of the energy cascade rate in the inertial range, emphasizing the usefulness of the local approach (Kuzzay et al., 2019).

8.5. Local proxies of dissipative processes.

While turbulence is one of the evoked mechanisms, the nature of the solar wind heating processes is not yet fully established. Inspired by standard studies on intermittency, solar wind data have been used to determine the role of turbulence in heating the plasma. The general approach is to identify the location of small-scale, intermittent structures generated by the turbulent cascade, and to selectively estimate the heating occurring at those locations, to be compared with other regions of less intense turbulent activity. Various techniques have been used to this goal, all aimed at establishing a link between the turbulence-generated structures and the plasma heating, thus supporting the role of turbulence in the heating process.

8.5.1. LIM and PVI: local proxies for the scale-dependent fluctuation energy

In fluid turbulence, the intermittent structures have been identified by mapping the local energy associated to the scale-dependent field fluctuations. One notable example is given by the Local Intermittency Measure (LIM) (Farge, 1991), a wavelet-based quantity estimating the squared amplitude of velocity fluctuations, and thus indicating the spatial distribution of kinetic energy at each scale. Given a field $v(r)$, its wavelet transform is $w(r,\ell) = \ell^{-1/2} \int_{-\infty}^{\infty} v(r)\psi^{\star}[(t-x)/\ell]\, dt$, where r is a spatial coordinate, ℓ a spatial scale, and ψ a suitably defined base function, called mother wavelet. The wavelet coefficients are formally equivalent to two-point spatial increments of the field, and strictly so if a square wavelet function, the Haar mother wavelet, is chosen. Therefore, all of the statistical tools defined for the two-point increments can be adapted to wavelets. Furthermore, as usual, the Taylor hypothesis can be used to transform spatial coordinates and scales to their time equivalents. The LIM is defined as $LIM = |w(r,\ell)|^2$. An arbitrary or recursive threshold can be set to separate the stronger structures from the turbulent, more uncorrelated (e.g. Gaussian, Veltri, 1999) background. This techniques has been used extensively in fluid turbulence, both in experiments and in numerical simulations, to identify and study the local and statistical properties of the structures generated by the turbulent cascade. When focusing on scales near the dissipative range, the LIM indicator is a good proxy for the dissipation, being related to a power of the velocity gradients.

Likewise, solar wind data and MHD numerical simulations have been studied using the LIM, providing evidence of the intermittent nature of the turbulence and allowing a detailed study of the characteristics and evolution of the intermittent structures with the expansion of the solar wind (Veltri, 1999; Sorriso-Valvo et al., 2005; Salem et al., 2009).

While wavelets provide a rigorous determination of the local power, it is sometimes faster and more convenient to use directly the field fluctuations in the physical space. A proxy called Partial Variance of Increments (PVI) has been introduced to identify solar wind locations of turbulent magnetic structures (Greco et al., 2008). It is the equivalent of the LIM in the physical space, the main difference being a normalization to the local variance of the field, to account for the poor stationarity of space plasmas. For a time series of solar wind magnetic field component $B_i(t)$, the adimensional PVI at time scale Δt is defined as $PVI(t,\Delta t) = |\Delta B_i(t,\Delta t)|/|\Delta B_i(\Delta t)|_{rms}$, where the

rms is computed on a sub-interval of the order of or larger than the correlation timescale $\tau_c \gg \Delta t$ centered at t. It is evident that the PVI represents a proxy for current structures, and other magnetic discontinuities (Greco and Perri, 2014). Note that PVI^2 and LIM are strictly related, and they indeed coincide if the wavelet transform is performed using the Haar mother wavelet (Farge, 1991). A similar proxy was also defined for the velocity components, representing vorticity structures and shocks, but also for other turbulent quantities such as proton density and temperature (Servidio et al., 2014).

It is well known that viscous-resistive dissipation is concentrated on the small-scale intermittent structures. In order to verify whether this holds for weakly collisional plasmas as well, the proxies described above can be used to identify the intermittent structures. Those can then be selected to perform conditional analysis of quantities that can be related to dissipation. One notable example is the solar wind proton temperature, which is expected to increase where the turbulent kinetic and magnetic energies are being converted into particle energization. Osman et al. (2012) performed such analysis using solar wind measurements, exploiting several years of data from the ACE spacecraft. The resulting averaged temperature profile, estimated using only data from short intervals centered at the local maxima of the magnetic PVI, displays a clear peak, whose amplitude depends on the selected PVI threshold (see Figure 98). This illustrates that proton heating is being produced preferentially at the magnetic discontinuities. Further works used PSP data to extend the results to the inner heliosphere (Qudsi et al., 2020) and to compare the differential heating of ions and electrons (Sioulas et al., 2022b). Similar results were also found by conditionally looking at highly energized electrons around small-scale magnetic structures (Tessein et al., 2013). A general conclusion is that the energy accumulated in the intermittent structures at the bottom of the turbulent cascade is being transformed into particle energization via the kinetic plasma processes occurring at small scale. Such transfer effectively represents a dynamical form of dissipation.

8.5.2. LET: a proxy for the local energy transfer rate

Since the energy transfer in MHD plasmas is related to the scaling of mixed fluctuations, a more detailed proxy of energy has been obtained using a quantity based on the P&P law, estimating the local contribution of the fluctuations to the global energy flux. The unaveraged third-order mixed fluctuations, as they appear in the right-hand side of equation (55), provide indeed a proxy of the local energy transfer (LET, Marsch and Tu, 1997;

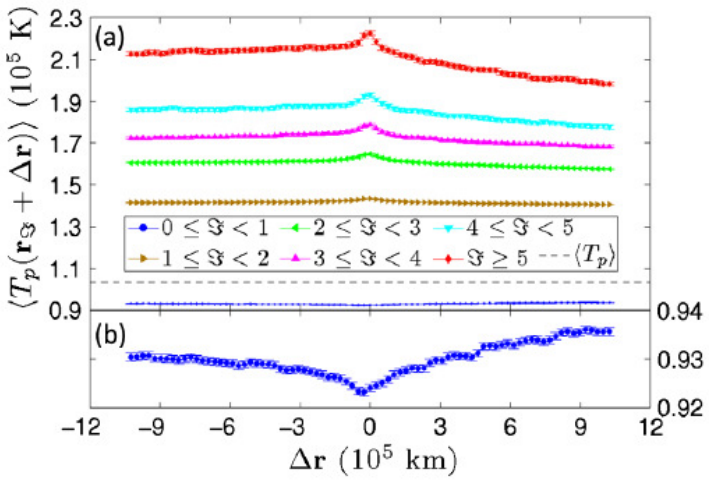

Figure 98: Panel (a): the conditionally averaged solar wind proton temperature profiles T_p in the proximity of peaks of the partial variance of increments (PVI, see text for the definition), considered as a proxy of the turbulent magnetic structures. The different color-coded curves refer to different thresholds (see legend). While far from the structures the random temperature fluctuations average out, a clear peak centered at the strongest structures indicates persistent heating. Panel (b): a magnification of the background average. Measurements refer to a sample of several years of 64 s resolution magnetic field data collected from the ACE spacecraft. Figure from Osman et al. (2012).

Sorriso-Valvo et al., 2000; Sorriso-Valvo et al., 2005; Sorriso-Valvo et al., 2015):

$$\varepsilon(t,\tau) = \frac{3}{4\langle v\rangle \Delta t}\left[(|\Delta\mathbf{v}|^2 + |\Delta\mathbf{b}|^2)\Delta v_\parallel - 2(\Delta\mathbf{v}\cdot\Delta\mathbf{b})\Delta b_\parallel\right] . \qquad (154)$$

Note that, assuming the validity of the Taylor hypothesis, the mean bulk speed estimated over the sample, $\langle v\rangle$, has been used to convert spatial scales, ℓ, to time scales, Δt, via the standard relation $\ell = -\langle v\rangle \Delta t$. Equation (154) defines a time-dependent, scale-dependent quantity, $\varepsilon(t, \Delta t)$, as opposed to the constant (in both time and scale) global energy transfer rate, ε, which appears in equation (55). Such proxy is composed of three signed elements, whose sum determines the local contribution to the energy made available for dissipation. In particular, it enables to separate the contribution to the energy flux coming from the velocity structures (e.g. plasma eddies), which are coupled to the velocity gradients, that of the magnetic structures (e.g. current sheets, discontinuities), also transported by velocity gradients, and

that of the correlated, Alfvén wave-like velocity and magnetic fluctuations, transported by the magnetic gradients. In a work based on the same technique as in Osman et al. (2012), the LET-conditioned temperature analysis has been used with Helios 2 data to identify locations of enhanced energy transfer. As shown in Figure 99, strong peaks of proton temperature were observed (Sorriso-Valvo et al., 2018), demonstrating the effectiveness of the LET proxy in identifying regions of enhanced dissipative activity. The large width of the temperature peak, of the order of 200 s, is in agreement with recent estimates of patches of heated plasmas in turbulent space plasmas (Yordanova et al., 2021), suggesting that the LET correctly captures the clustering properties of the heating structures in the solar wind. Moreover, since the LET effectively acts as a proxy for local dissipation, it was possible to use models to describe the dissipation time series. For example, as visible in the left panel of Figure 100, the scale-dependent probability distribution function of the LET was successfully modeled using a stretched exponential function, as predicted by Frisch and Sornette (1997) for systems whose dynamics is controlled by extreme events (Extreme Deviation Theory). Furthermore, the stretched exponential fitting parameter, $c(\Delta t)$, which measures deviations from Gaussian, was shown to scale as a double power law (right panel of Figure 100), which was interpreted as a quantitative measure of the intermittency based on the dissipation (Sorriso-Valvo et al., 2018).

As a further example of use of the LET, the multifractal spectrum (Parisi and Frisch, 1985; Paladin and Vulpiani, 1987; Sreenivasan, 1991) of $\varepsilon(t)$ near the ion-scale break was estimated (see the q-th order singularity exponents τ_q in Figure 101), and a fit to a standard p-model (Meneveau and Sreenivasan, 1987) showed a remarkably strong intermittency, with intermittency parameter $P = 0.87$ (Sorriso-Valvo et al., 2018). For comparison, standard values for Navier-Stokes fully developed turbulence are typically of the order of $P \simeq 0.7$ (Meneveau and Sreenivasan, 1987), while for samples of space plasmas values as large as $P = 0.89$ have been observed in the terrestrial magnetosphere (corresponding to extremely strong intermittency, see e.g. Quijia et al., 2021).

As we have underlined, in addition to the PVI and LIM indicators, the LET provides more complete information on all relevant MHD fluctuations responsible for the energy transfer, including wave-like fluctuations. While these observations do not identify directly the specific dissipating mechanism, they may suggest that particle energization takes places mostly where the turbulent energy is being concentrated on small-scale structures, therefore es-

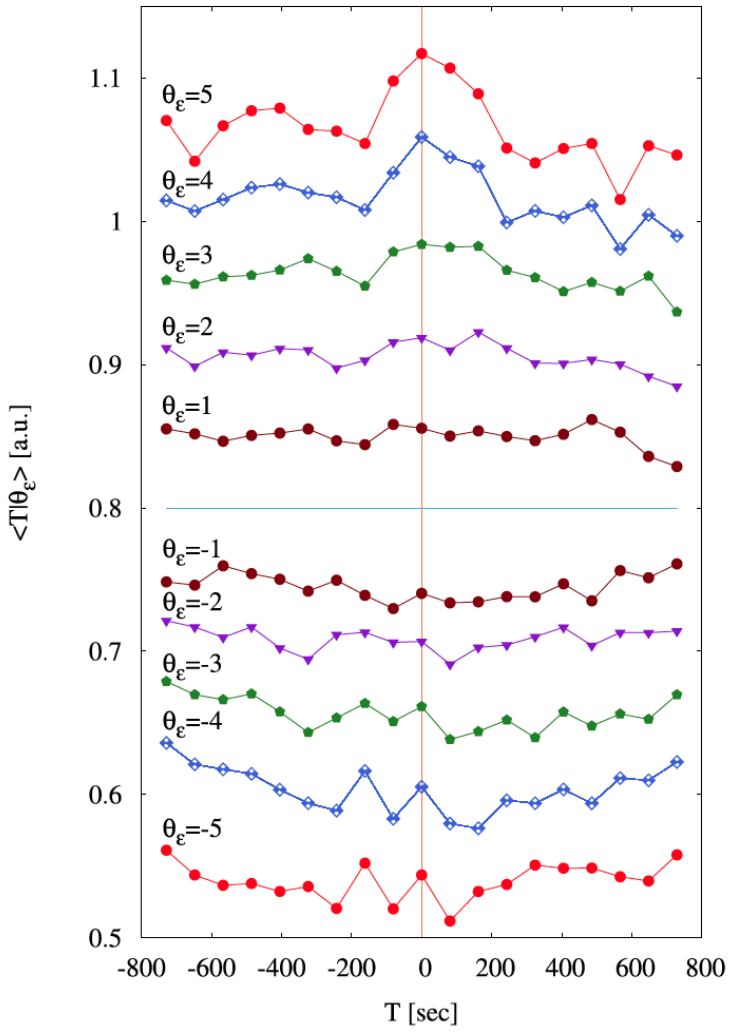

Figure 99: Conditionally averaged solar wind proton temperature profiles $T = T_p$ (note that the subscript p is missing in the y-axis label). Each curve is built by averaging the 1500 s windows centered ($T = 0$) on the peaks of the local energy transfer ε (i.e, when ε exceeds a variable threshold θ_ε). The resulting profiles therefore describe the averaged temperature in the proximity of positive (top curves) and negative (bottom curves) peaks of ε. The different color-coded curves refer to different thresholds θ_ε (see legend), used to identify the peaks of the local energy transfer. A clear, broad peak centered at the strongest positive structures indicates persistent heating. Figure adapted from Sorriso-Valvo et al. (2018).

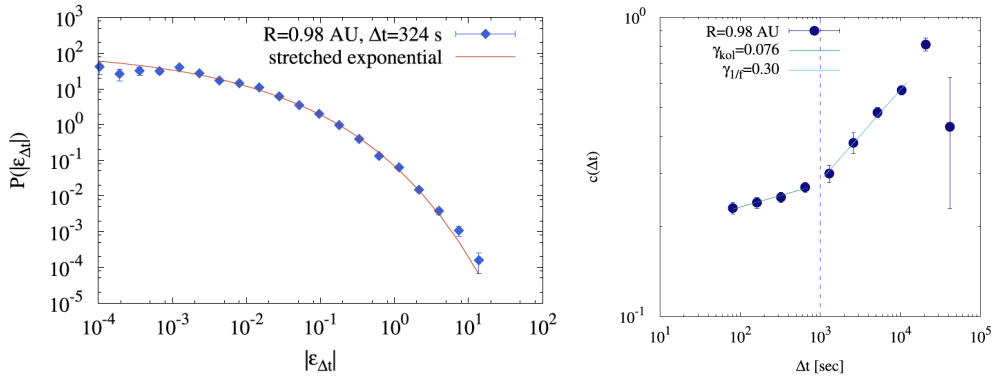

Figure 100: Left panel: probability distribution function of the absolute value of the LET, $|\varepsilon_{\Delta t}|$, at scale $\Delta t = 324$ s, estimated using Helios 2 data at 0.98 au (blue markers). The red line is a stretched exponential fit $P(|\varepsilon_{\Delta t}|) \sim e^{-b\Delta t^c}$, where the fitting parameters $c(\Delta t)$ and $b(\Delta t)$ describe the scale-dependent shape of the distribution (Frisch and Sornette, 1997). Right panel: scaling of the shape parameter, showing clear double power-law scaling $c \sim \Delta t^{\gamma}$, with a break near the correlation scale (vertical dashed line, where the spectrum transitions from Kolmogorov to $1/f$). The two corresponding scaling exponents, γ_{kol} and $\gamma_{1/f}$, are indicated. Figure adapted from Sorriso-Valvo et al. (2018).

tablishing a link between the scaling properties of the fluctuations generated by the turbulent cascade, and the processes leading to solar wind heating.

The LET being a signed quantity, it also carries information about the local direction of the energy flux in the scale space. Exploiting this unique characteristic, the LET was studied using sign-singularity analysis (Ott et al., 1992), obtaining a quantitative description of the differences among various space plasmas, including the free solar wind, the terrestrial magnetosheath, and a Kelvin-Helmholtz instability region at the magnetopause (Sorriso-Valvo et al., 2019b).

It is of course easy to imagine the extension of the LET to the more complete versions of the exact laws described in this review, for example to include anisotropy, Hall terms, and compressibility, and how this approach could provide crucial information on the specific locally dominating process or processes that drive the dissipation. Initial attempts in this direction were performed using numerical simulations of the Hall-MHD equations or of the Vlasov-Maxwell system (Yang et al., 2018; Vásconez et al., 2021; Pezzi et al., 2021). One example of a map of the LET for the Hall-MHD exact law, simply

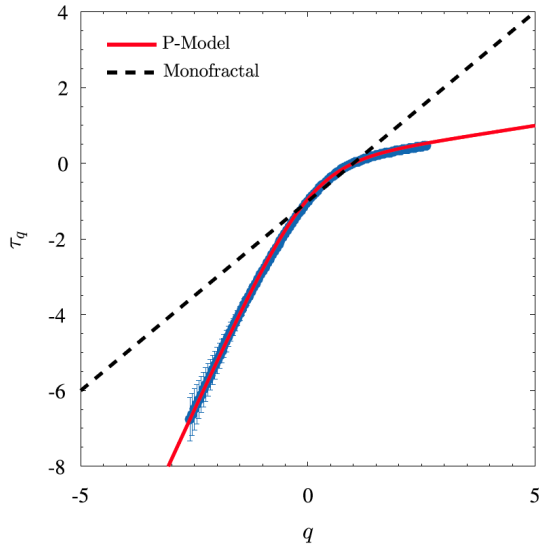

Figure 101: Multifractal singularity exponents τ_q of the LET from Helios data, seen as a proxy of the dissipation field (blue crosses). A p-model fit for the multifractal description of intermittency (red line, Meneveau and Sreenivasan, 1987, see Section 3.2) and a reference monofractal scaling are also shown. Figure adapted from Sorriso-Valvo et al. (2018).

defined as

$$\begin{aligned} -2\ell\varepsilon_H(\mathbf{r},\ell) &= (\Delta\mathbf{v}\cdot\Delta\mathbf{v}+\Delta\mathbf{b}\cdot\Delta\mathbf{b})\Delta v_\ell - 2(\Delta\mathbf{v}\cdot\Delta\mathbf{b})\Delta b_\ell \\ &- \frac{d_p}{2}(\Delta\mathbf{b}\cdot\Delta\mathbf{b})\Delta j_\ell + d_p(\Delta\mathbf{b}\cdot\Delta\mathbf{j})\Delta b_\ell\,, \end{aligned} \tag{155}$$

(with the obvious notation) is shown in Figure 102 for a two-dimensional hybrid kinetic simulation. The regions that mostly contribute to the cross-scale energy transfer can be so identified and studied in detail, for example using the local particle distribution functions to investigate the presence of waves, resonances, instabilities and other kinetic processes. The approach described above, still not completely developed in the community, represents one of the possible routes for improving our understanding of dissipative processes in space plasmas.

8.6. Making the local cross-scale connection: turbulence-driven kinetic processes

The LET representation of the turbulent MHD fluctuations provides the breakdown of the energy content among different forms: gradients of velocity

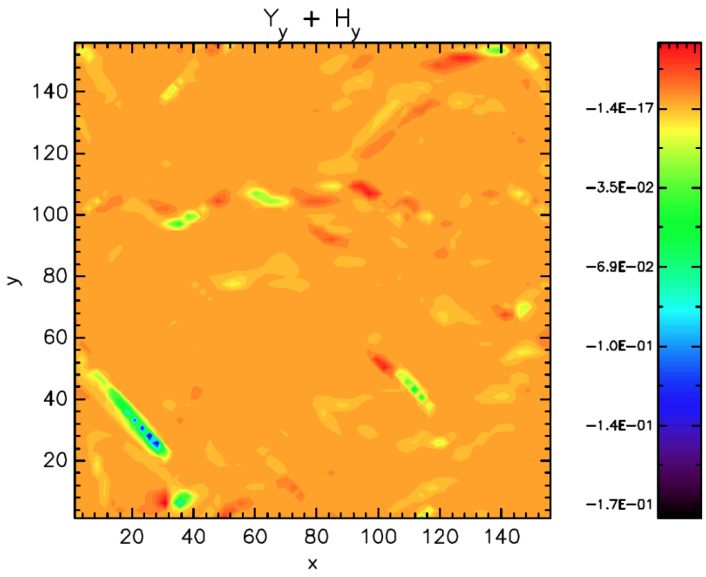

Figure 102: A snapshot of a two-dimensional Hybrid Vlasov-Maxwell numerical simulation of kinetic turbulence. The quantity represented here (see color bar) is the y component of the Hall-MHD LET, equation (155), estimated at the proton inertial length scale $\ell \simeq d_p$. Figure adapted from Vásconez et al. (2021).

(e.g. vortices) and magnetic field (e.g. current structures), which transfer energy towards smaller scales, and wave-like correlated fluctuations, which generally inhibit such transfer. Yet, a fundamental point is that the presence of correlated fluctuations may still result in the activation of kinetic processes, therefore effectively resulting in some form of dissipation. This represents a considerable difference with respect to the MHD case, where $\nabla^2\mathbf{v}$-type dissipation terms require strong gradients, and are not effective for wave-like fluctuations. The enhanced information contained in the LET can therefore be exploited to investigate the energization mechanisms occurring in the kinetic range of scales. While plasma heating and energized particles are the effect of the energization processes, only more appropriate diagnostic tools for kinetic processes can help identifying the specific processes that cause them. The most notable is the particle velocity distribution function, whose shape may inform on processes such as, for example, Landau damping and wave-particle resonances, or temperature anisotropy instabilities.

An opportunity to test such technique using experimental data was provided by the high-resolution ion distribution functions (VDFs) measured

in the near-Earth space by the NASA Magnetospheric MultiScale mission (MMS). Using 150 ms cadence MMS magnetic field, ion velocity and ion density measurements, Sorriso-Valvo et al. (2019a) estimated the LET for a series of short magnetospheric boundary layer turbulent intervals selected during the spacecraft crossing of a Kelvin-Helmoltz instability region (Eriksson et al., 2016; Stawarz et al., 2016). After validating the global third-order moment scaling law, thus confirming the turbulent nature of the fluctuations in those intervals, the LET was used to identify the location of stronger small-scale energy transfer. This procedure, based on an arbitrary threshold on the LET magnitude, resulted in the selection of about one hundred peaks. One hundred more events were randomly selected at locations of nearly-zero LET, to be used as reference. For each selected event, the LET contributions were evaluated separately and compared. In particular, the dominant between the sum of the two energy-related terms and the cross-helicity term was identified. Figure 103 shows various fields extracted from the data, and in particular the selected peaks of LET (bottom panel), separated according to the dominant component. The ion VDFs were then extracted for those two-hundred locations, and classified according to their specific features. In particular, the classification resulted in the following categories: (i) quasi-Maxwellian VDFs with no apparent features; (ii) presence of heating (either isotropic or field-perpendicular); (iii) presence of one or two evident ion beams (observed near the Alfvén speed and parallel to the magnetic field); (iv) other features. Examples of VDFs with various features is shown in Figure 104. A statistical survey revealed that the low-LET positions were mostly (57%) characterized by quasi-Maxwellian VDFs, indicating the absence of kinetic processes. On the contrary, high-LET positions had the totality (100%) of VDFs with heating, beams or other non-Maxwellian features, which is expected since the available energy could activate dissipative processes. Most of the VDFs with ion beams (73%) were observed when the cross-helicity component of the LET was dominating or large. In addition, the beams were always moving at the Alfvén speed with respect to the bulk, and associated to regions showing ion-cyclotron waves (as determined through the observation of left- and right-handed polarized magnetic fluctuations). Finally, at the same locations, strong electrostatic activity was evidenced by the presence of high-frequency peaks in the electric field power spectra. Together with the characteristics of the beams, all these observations suggested the presence of a resonance process between the Alfvén wave-like fluctuations and the ions. The resulting transfer of energy between

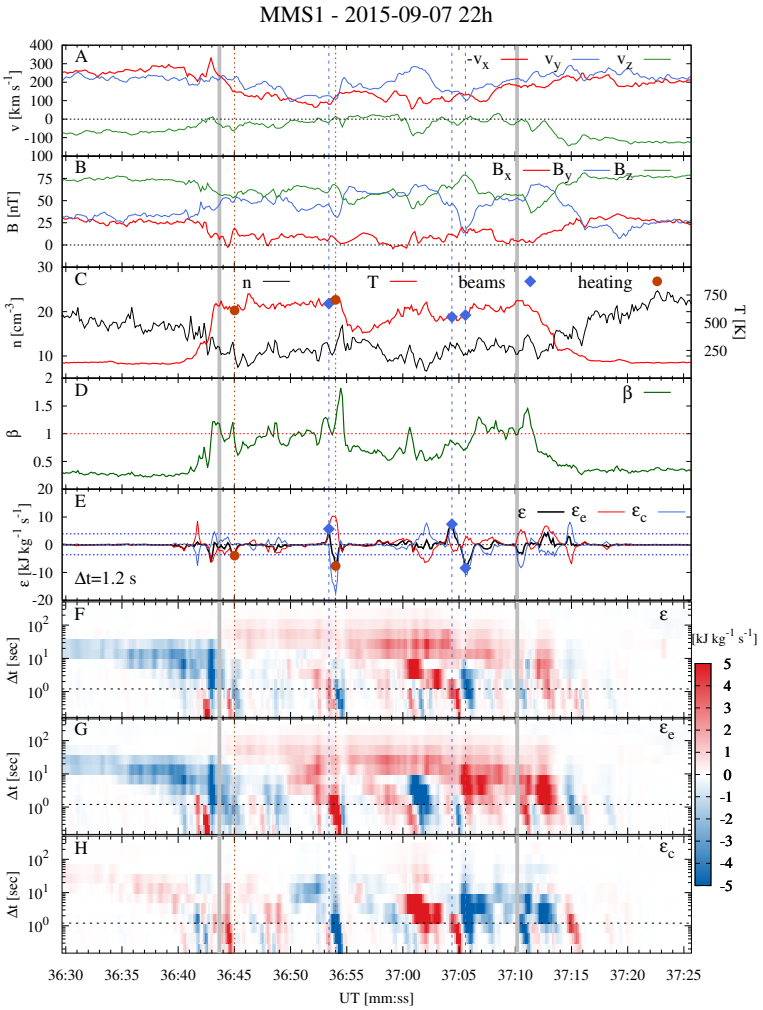

Figure 103: Overview plot of the event studied in Sorriso-Valvo et al. (2019a). From top to bottom: GSE components of the plasma velocity; magnetic field components; plasma density; plasma ion β; LET (black line) and its two energy (red) and cross-helicity (blue) components, with indication of the threshold used to select bursts of intense transfer of total energy (horizontal lines) and the location of the peaks (with red and blue bullets indicating peaks dominated by the energy or cross-helicity term, respectively); scalogram of the LET (see color bar); scalogram of the energy-related LET; scalogram of the cross-helicity related LET.

the fluid fluctuations and the particles provided the acceleration of the beam. In turn, the accelerated beam quickly becomes unstable and therefore excites

high-frequency, electrostatic waves. High-resolution hybrid Vlasov-Maxwell numerical simulations of plasma turbulence were also used to validate the results. The features observed in the simulations were similar to those observed in the magnetospheric plasma, where the resonance process was finally identified as Landau damping of small-scale Alfvén waves resonating with ions moving at the Alfvén speed.

The use of the LET technique allowed the identification of a specific

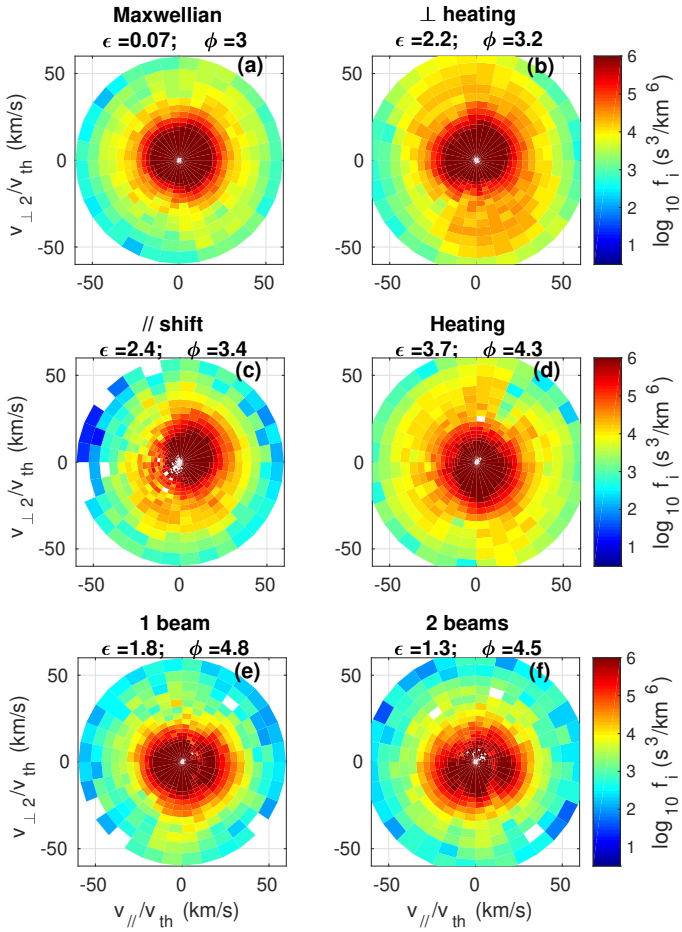

Figure 104: Examples of ion two-dimensional cuts (the x-axis being parallel to the mean magnetic field) of the MMS ion distribution functions corresponding to specific values of the LET. The LET value (ε) and the type of distribution function are displayed above each panel. Each distribution function was averaged over 1.2 s. The two distribution functions in panels b and f were already published in Sorriso-Valvo et al. (2019a).

process of conversion of energy from the turbulent cascade to the plasma particles, in this case the Landau damping of Alfvén waves generating a beam of accelerated ions.

The complex interplay between sub-ion scale wave packets and local properties of turbulence remains an interesting open question (Khotyaintsev et al., 2021; Carbone et al., 2021). Such work demonstrated that the investigation of the details of the turbulent cascade, and in particular the local contributions to the scaling laws, may help answering one of the most crucial open questions in space plasma physics, namely, what are the mechanisms that dissipate the turbulent energy and provide the observed particle energization. It is impossible not to wonder whether the approach described above, as well as the other local approaches, could be useful in other physical systems. For instance, it would be interesting to apply the LET analysis to measurements of laboratory plasmas or in fusion devices, where it could yield supplementary information on the disruptive processes that prevent the plasma confinement. In fact, it is also tempting to ask whether similar techniques could be used for fluid turbulence, where they could reveal important details of the turbulent cascade and allow us to go beyond the global laws.

9. Perspectives and future developments

The efforts of the space plasma community are currently focused on a number of fundamental issues, all boldly stated in programmatic documents and calls for new mission proposals and research projects from space agencies and academic institutions. Major puzzles are encompassed under the following broad science case: How does the solar system work? Questions concerning the origin, acceleration and heating of the solar wind, as well as its coupling with planetary environments, and of course the mechanics of the Sun, are central to this international quest. Among the topics covered by this review, the role of turbulence in the dynamics of the interplanetary medium and the complex interplay of waves and turbulent fluctuations in space plasmas are questions that remains without an exhaustive answer.

In the present work we have described the development of theoretical, numerical and observational studies produced in the last quarter of a century around the magnetohydrodynamic turbulent energy cascade in space plasmas. The focus of this review was on the derivation, validation and application of a scaling relation between the third-order structure-function of plasma fields and the turbulent energy transfer rate at intermediate scale,

which is intimately connected, if not equal, to the small-scale dissipation, whose first derivation is known as the Politano & Pouquet law. This scaling law, proposed in 1998 (Politano and Pouquet, 1998; Politano and Pouquet, 1998), and its extensions, describe the turbulent cross-scale flux of energy in plasmas in the MHD regime, down to the Hall-MHD and kinetic scales, and by now represents the backbone of one of the most prolific domain of investigation of the modern space physics.

Starting from the initial scaling relation developed for the incompressible MHD —assuming homogeneity and isotropy— the inclusion to the original P&P law of Hall physics, compressibility, anisotropy, isothermal closure and of various other effects, enabled to extend the range of validity of this invaluable tool to the investigation of space plasmas, thus making it suitable for exploration of variety of complex phenomena in the outer space. In many cases, the theoretical developments of variants of the third-order scaling laws presented here was adapted from previous hydrodynamics studies, which date back to the mid or late XX century. However, the quest for more complete versions describing increasingly realistic approximations required autonomous development in the more complex framework of plasma physics. Sometimes hydrodynamic equivalent for the velocity field only were obtained as a preliminary and more attainable effort, mostly to open the way and set the logic of the derivation. Subsequently, the same authors extended the work to obtain a version of the exact scaling law for plasmas. This illustrates to which extent the space plasma community has grasped the potential of the third-order moment approach in order to obtain a detailed description of the statistical properties of turbulence in a medium, the interplanetary and near-Earth space, where observations are challenging and the experimental conditions cannot be fully known, let alone controlled. Most importantly, theories and models of solar wind require some knowledge of the turbulent energy dissipation, which controls heating, particle acceleration, as well as diffusion and transport of various quantities. Since in the nearly-collisionless space plasmas dissipation is not visco-resistive and cannot be easily or directly estimated (Matthaeus et al., 2020), measuring the cross-scale energy transfer produced by the nonlinear interactions, among plasma fluctuations and waves, at intermediate scales, is the next available option. The added value of this approach for the space plasma community is therefore enormous, as demonstrated by the explosive increase in the number of publications and researchers using it to describe solar wind and near Earth plasmas.

As is often the case, the original theoretical derivation of the third-order

scaling law for incompressible MHD was not immediately followed-up by numerical or experimental validations, with the sole exception of one numerical study (Sorriso-Valvo et al., 2002), though not purposed to this aim. The first applications to data only appeared in 2005 (MacBride et al., 2005) and 2007 (Sorriso-Valvo et al., 2007), nearly one decade after the publication of the P&P law. We should emphasize that this was likely due to the difficult observation of the P&P scaling, whose computation requires extensive data-sets to ensure statistical convergence and at the same time short enough sampling windows for stationarity and homogeneity to hold, together with a number of other conditions (most notably isotropy and incompressibility). All that must be granted in order to enable sufficient scale separation to compellingly identify the MHD inertial range, when the space plasma conditions fulfill the assumptions prescribed in equation (54). Nevertheless, after the first solar wind data validations, a surge of observations in space plasmas and, to some extent, in numerical simulations, emerged in the community, which motivated this review work. To date, the P&P law and its many extensions have been increasingly used to describe the status of turbulence in specific plasma intervals (e.g., MacBride et al., 2005; Sorriso-Valvo et al., 2007; Marino et al., 2011; Marino et al., 2012; Sorriso-Valvo et al., 2015; Bandyopadhyay et al., 2019), to compare different plasma conditions and different regions of space (e.g., Marino et al., 2008; Smith et al., 2009; Stawarz et al., 2010; Coburn et al., 2012; Banerjee et al., 2016; Hadid et al., 2017; Andrés et al., 2019), to explore the onset of turbulence (e.g., Bandyopadhyay et al., 2021a; Quijia et al., 2021; Sorriso-Valvo et al., 2021; Zhao et al., 2022), to study its radial evolution (e.g., Marino et al., 2012; Bandyopadhyay et al., 2020; Wu et al., 2022a,b), to validate solar wind models (Marino et al., 2012; Coburn et al., 2012; Coburn et al., 2014; Wu et al., 2022b; Sorriso-Valvo et al., 2022), and to explore the pathway to dissipation in collisionless plasmas (Sorriso-Valvo et al., 2018, 2019a; Pezzi et al., 2021; Ferrand et al., 2021b; David et al., 2022).

The third-order scaling laws presented here are derived through rigorous mathematical steps from the equations governing the dynamics of plasmas and can therefore be considered exact to a large extent. In fact, as for the case of the Kolmogorov 4/5 law, they may be mathematically presented as theorems (Frisch, 1995). However, the various derivations rely on a number of assumptions, necessary to suppress or neglect various terms, for instance to reduce the dimensionality of the approach, though some of them could possibly contribute to the actual energy flux. In most cases, it is possible to

relax some of the working hypotheses and write equations that include the corresponding contributions, approximations to the more complete model equations being made in general in order to exploit single-point spacecraft time series and therefore to cope with lack of the point-wise (or at least multi-point) knowledge of the dynamical fields in space plasmas. For example, divergence terms and gradients cannot be estimated using one-dimensional cuts of a three-dimensional turbulence. Likewise, electric current estimates may be tricky without sufficiently accurate plasma instrumentation, or multi-spacecraft formations. In any case, it is worth noting that many of the scaling relations we examined, stemming from the original P&P, have been tested in high-resolution numerical simulations and are ready for the implementation using future multi-spacecraft measurements in the heliosphere, and also in the interstellar plasmas. The description of space plasma turbulence has therefore acquired and consolidated a novel tool to expand the details of our understanding of how the heliosphere works. With most theoreticians, modelers, data analysers and instrumentation designers only recently becoming aware of its potential contribution, the full extent of the P&P law approach is still far from being achieved.

9.1. Theoretical and numerical modeling perspectives

The history of the third-order scaling laws for plasma turbulence suggests that there is broad margin for future developments and implementations of this approach. From a theoretical standpoint, several are the possible directions for obtaining more detailed versions of the P&P law by further pushing the key mathematical developments away from ideal conditions. Another fascinating perspective is that of extending its range of applicability incorporating the non-collisional nature of space plasmas, to obtain scaling laws able to model the energy transfer in space plasmas at increasingly smaller (and less fluid) scales. A first step in that direction has been recently undertaken in Banerjee and Andrés (2020); Pan and Banerjee (2020), where a derivation of the KHM equation for a two-fluid description of plasmas was presented. This formulation implies a separate description of ions and electrons and may in future be adapted to model the energetics of other particles, such as the α or other minor ion species, exploiting the high-resolution observations provided by the Solar Orbiter spacecraft (Forveille and Shore, 2020). A critical leap forward in the investigation of space plasmas will be made once a direct investigation of wave-particle interactions and collisions will be possible. At the time of writing of this review, we are aware that a scaling law was recently

obtained for the Vlasov-Maxwell equations (S. Servidio, private communication; see also the preliminary phenomenological results in Servidio et al., 2017; Adkins and Schekochihin, 2018; Pezzi et al., 2018). As is obvious, the conservation of the Vlasov invariants (e.g., the enstrophy) is used, and the derivation is made in the six-dimensional $(\mathbf{v}, \mathbf{r})$ phase space, which adds to the complexity of the calculation. The validation of this law with observational data will be a major development to be expected in the near future. As a matter of fact, being able to describe the cascade in the Vlasov regime will provide access to sub-ion scale phenomena that control the actual dissipation and particle energization in space plasmas. Important preliminary analyses in this direction were already performed. Klein and Howes (2016) introduced a phenomenological correlator based on the Vlasov-Maxwell equation, that approaches yet does not fully describe the enstrophy cascade. However, applications of the method revealed enormous potential (Chen et al., 2019) in helping the identification of the active dissipative processes. An automated implementation is currently being developed in order to be uploaded on the processing unit onboard the upcoming NASA space mission HelioSwarm (`https://www.lpl.arizona.edu/missions/helioswarm`), with the aim of providing real-time diagnostics of the physical processes occurring at the bottom of the cascade (Verniero et al., 2021; Verniero et al., 2021; Howes et al., 2022).

The next step forward in the theoretical advance of the exact laws approach would be to include weak collisions, whose role may be enhanced in the proximity of specific plasma structures. This requires the extension of the scaling laws to the full description given by the Boltzmann model. Finally, it would be desirable to obtain a cross-scale integration of the three descriptions (MHD, Vlasov and Boltzmann), encompassing all physical scales of space plasma processes.

Another direction for theoretical developments is represented by the local description of the turbulent cascade. We have already discussed how this was attempted using a purely heuristic approach (Sorriso-Valvo et al., 2019a). However, novel approaches are being proposed that use local (in space) versions of the scaling laws, which promise to provide extremely important information about the local contribution of turbulent fluctuations to the onset of kinetic plasma processes (see for example the preliminary studies by Kuzzay et al., 2019; David et al., 2022). At first, the goal will be to describe how the fluid-scale turbulence manages to transport energy to specific locations in space, through localized phenomena (e.g. coherent structures or

wave-like fluctuations), and how this triggers or inhibits kinetic processes. In the long term, should a Vlasov description of the cascade become available, it is easy to imagine the potential impact of a local description in the phase-space, which may enable a complete diagnostics of the processes at play at any position in space, at all scales, and concerning all particle species. The local approach to exact scaling laws in turbulent space plasmas can therefore become a valuable tool to understand as well how plasma particles are heated and energized, how waves and instabilities are excited, and more in general how energy is transported and exchanged in space, across scales, and among different particle species.

From the point of view of numerical simulations, the developments are easily stated. All the theoretical predictions must be validated using numerical simulations. These should also provide ways to determine the degree of approximation and error that is unavoidably made when using reduced dimensionality data, as happens in space. The increasing computational power, associated with the use of virtual spacecraft techniques, should be pushed to the point of enabling a correct evaluation of errors, placing boundaries and limitations to the use of experimental data. In addition, simulations permit to study the physical processes under controlled conditions and with complete knowledge of the system. Therefore, the implications of the scaling laws on dissipation, energy flux, and the role of all possible deviations from the ideal conditions can be assessed thoroughly. In this sense, the basic requirement is to increase the simulation performances, as to obtain more extended scaling ranges, but also more dynamical range for the physics to develop in full. This is even more the case if sub-ion (e.g. Hall or Vlasov) physics is included. Given the multi-scale, multi-physics nature of space plasmas, achieving large enough scale separation in numerical simulations will be critical to identify regimes in which different physical phenomena dominate. For instance, various type of waves within the different regimes that can be identified in the kinetic and magnetic energy spectra. Scale separation is also needed to investigate the transition from the MHD to the Hall-MHD regime, allowing the latter a sufficient range in the spectrum for the Hall term to become important at smaller scales (see Figure 105). Novel numerical codes designed to exploit graphics processing units (GPU) will allow to fully resolve the transition from the fluid to the kinetic scales in space plasmas, and in three-dimension, dimensionality being critical in order to capture the correct dynamics (Mininni et al., 2011a; Rosenberg et al., 2020; Foldes et al., 2022).

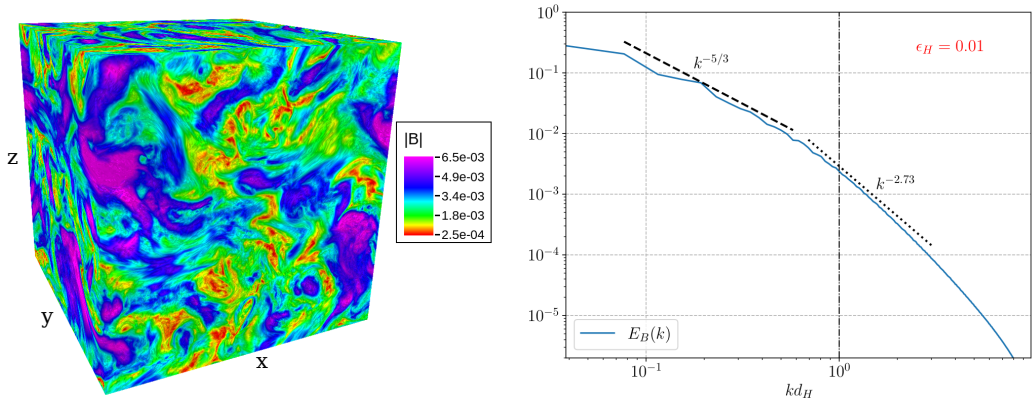

Figure 105: Left panel: three-dimensional rendering of the magnetic field magnitude at the peak of the current density of a Hall-MHD simulation performed with the Lattice-Boltzmann code FLAME (Foldes et al., 2022, Fast Lattice-Boltzmann Algorithm for Magnetohydrodynamic Experiments,), with grid resolution of 512^3 points. No background magnetic field is applied. Right panel: Isotropic magnetic energy spectrum computed at the same time of the snapshot in the left panel. The wavenumber has been rescaled with the Hall length scale, with $\varepsilon_H = d_H/L_0$, $L_0 = 2\pi \int E_V(k)k^{-1}dk / \int E(k)dk$ the integral scale computed using the kinetic energy spectral density $E_V(k)$. The black dash-dotted vertical line corresponds thus to the Hall length scale, that in case the bulk speed is equal to the Alfvèn speed (namely $v_0 = v_A$), coincides with the ion skin depth $d_H = d_i$.

A long-standing open question in the solar wind community, only partially addressed with the scaling laws approach, concerns the existence of a dual energy cascade in heliospheric plasmas. This could be due, for instance, to local processes that alter the energy flux and generate an inverse cascade, like a shock propagating in the plasma and injecting additional energy. Clear answers may arise from next generation high-resolution simulations —performed in a parameter space of interest for the heliosphere— able to handle the injection of energy at intermediate scales and to resolve, simultaneous and compellingly, upscale and downscale constant flux energy transfers in the MHD regime, if existent, as well as the downscale energy transfer towards the kinetic scales.

9.2. Observational perspectives

Finally, the hardest of the paths to take in order to maximize the return from the scaling laws approach, but probably the most promising, involves the design and development of novel space missions. These should and will provide estimates of the quantities and in the geometries that will enable the implementation of the most detailed structure functions equations. For example, multi-spacecraft missions should be designed as to provide multi-scale, three-dimensional geometries. In the past, the Cross-Scale concept was proposed to collect data on three nested tetrahedra, each covering a different range of scales (fluid, ion, and electron). Figure 106 shows the spacecraft configuration (left) and a rendering of the possible launch system of the 12 spacecraft (right). However, the Cross-Scale mission, proposed to ESA more than 15 years ago, was never funded since it was deemed too expensive. Fortunately, a similar concept was recently accepted by NASA, which is going to launch a multi-scale, multi-point observatory, Helioswarm (see the mission concept in the image in Figure 107). In this case, the budget was met by adopting limited plasma diagnostics, which may affect the quality of the observations for specific third-order moment investigation, yet allowing to advance the implementation of the methodology under study here. The mission will represent a step forward in the direction of controlling the physics of space plasma turbulence.

Alternative or additional space mission developments concern the exploration of different regions, such as the outer heliosphere and the interstellar medium (see, e.g., the Interstellar Probe white paper, available at `https://www.cosmos.esa.int/documents/1866264/3219248/Wimmer-SchweingruberR_2019-08-04-interstellar-whitepaper.pdf`, and Fraternale et al., 2022).

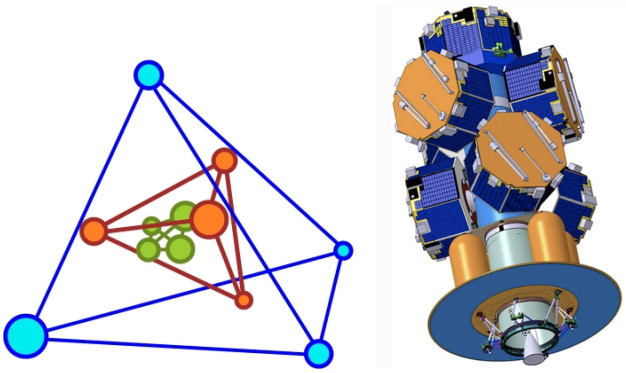

Figure 106: Left panel: the ESA/Cross-Scale mission proposal logo, representing the nested-triple tetrahedron spacecraft configuration. Figure from (Schwartz et al., 2009). Right panel: a rendering of the mission launching configuration, with the 12 spacecraft stacked on a bus. Figure from the ESA Cross-Scale Assessment Study Report (SRE-2009-1), Publication date: 01 December 2009, available at `https://sci.esa.int/documents/34697/35949/1567257732515-SRE-2009-1_Cross-Scale21.pdf`.

Those regions were poorly explored so far, and the probes that reached out beyond Jupiter's orbit could not provide quality plasma data. With modern and tailored payload, it is envisaged that outer heliospheric and interstellar missions could help understanding the way the solar plasma interacts with the interstellar medium, and the turbulence properties of the latter. Such understanding is of paramount importance for studies of cosmic ray and energetic particle transport and diffusion in the heliosphere, with the associated relevance to space weather and, more generally, the sciences of the universe.

Besides novel space mission concepts, data analysis tools need to be developed to incorporate as many elements as possible from the theoretical laws. It will be necessary to provide ways to describe the three-dimensional nature of turbulence, account for anisotropy and for the solar variability, and improve the quality and cadence of the plasma measurements. Preliminary tools, such as the wave-particle correlator (Klein and Howes, 2016; Howes et al., 2017; Chen et al., 2019), the LET (Sorriso-Valvo et al., 2019a), and the local transfer (David et al., 2022) will need to be further developed to include all possible physics, and to better understand the transition from fluid- to ion- and then electron-physics regimes.

Importantly, discussions about the uncertainty and the level of approximation when using exact laws to estimate the energy transfer rate should complete the toolkit for a correct description of the turbulence (Podesta

et al., 2009). Finally, the use of the scaling laws approach should be ef-

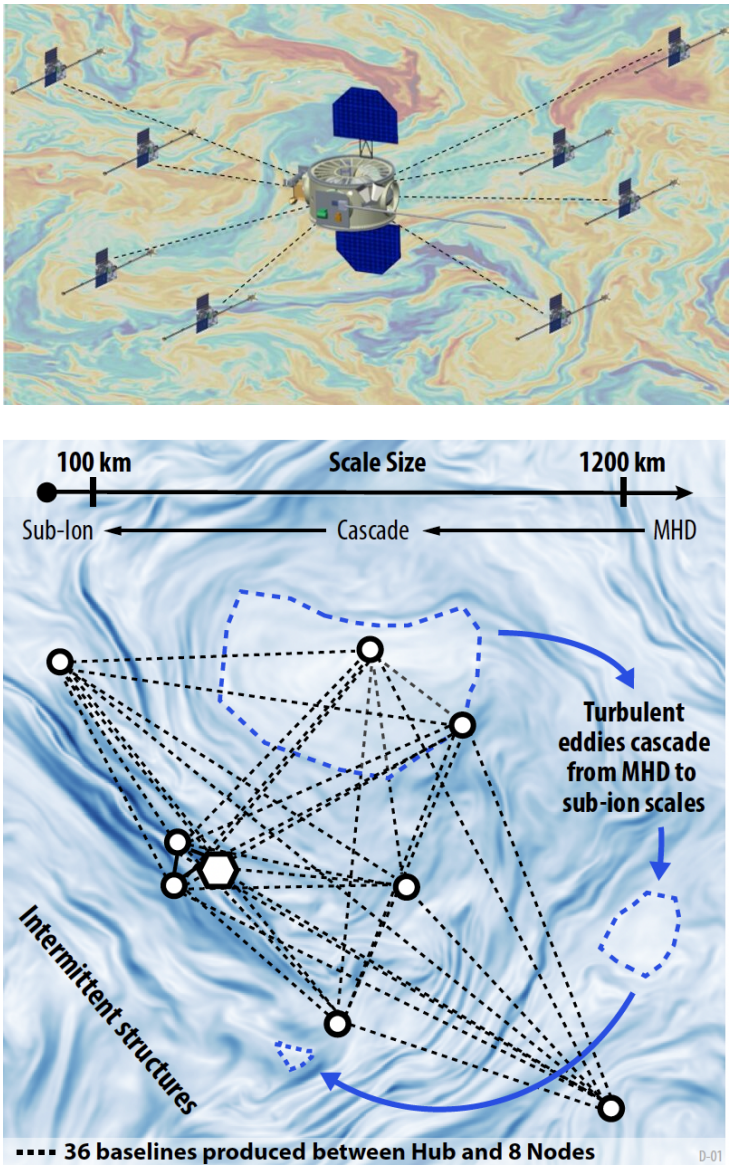

Figure 107: Top panel: illustration of the NASA/Helioswarm 9 spacecraft configuration. Credits: UNH EOS (available at `https://www.unh.edu/unhtoday/2022/02/solar-windfall`). Bottom panel: a rendering of the mission concept, with possible 36 baselines covering scales Figure from `https://www.lpl.arizona.edu/missions/helioswarm`.

ficiently paired with coordinated multi-spacecraft observations (e.g., a list of radial alignment events between Solar Orbiter and Parker Solar Probe is presented in Velli et al., 2020), in order to describe, for example, the radial evolution of plasma turbulence in the expansion from the corona to the solar wind, as well as the dynamical evolution in the neighborhoods of transition regions, such as planetary bow-shocks, interplanetary shocks, comet tails and other planetary environments.

9.3. Potential for application to space weather and astrophysical observations

The better understanding of local properties of turbulence achieved through the third order law approach is critical to improve the predictive power of space weather models. This field received growing attention in recent years, for its relevant societal applications, with major progresses being made thanks to the implementation of artificial intelligence and machine learning techniques. The latter allowed significant steps forward in the forecasting of solar extreme events (e.g., solar flares and Coronal Mass Ejections, Napoletano et al., 2022) that contribute to inject energy into the heliospheric plasma, reverberating on the dynamics of the near-Earth environment (Camporeale, 2019), of the Earth's magnetosphere (Zhelavskaya et al., 2017; Foldes et al., 2021) and of the solar wind itself (Amaya et al., 2020).

On the outer side of the solar system, interstellar plasma density has been both estimated in different ranges of scales using Earth-based observations (mainly scintillation of pulsar radio emission generated by interstellar electrons turbulence and observation of interstellar clouds, Lee and Jokipii, 1976; Armstrong et al., 1995; Chepurnov and Lazarian, 2010), and measured *in situ* by the two Voyager spacecraft (Lee and Lee, 2019). Amazingly, the joint power spectral density of the inferred or measured plasma density shows a nearly single power-law scaling, spanning over 16 orders of magnitude, from 50 m to 10^{18} m, with exponent compatible with Kolmogorov turbulence. This unparalleled broad-range turbulent power-law spectrum, shown in the left panel of Figure 108, has been appropriately called *The Big Power Law in the Sky*[1] (Armstrong et al., 1995). As it is well known, spectra are not

[1]After the recent extension to even larger wavevectors obtained using the Voyager in-situ measurements, the nickname of the combined power-law was upgraded to *The Grand Power Law in the Milky Way* (right panel of Figure 108, Lee and Lee, 2019). The new name adequately conveys the desired, unavoidable feeling of awe and wonder. Unfortunately, this comes at the price of the loss of the idealistic interconnection between

a sufficient descriptor of turbulence, and cannot capture fine details of the cascade process, in particular the spatial distribution of the fluctuations, the rate at which energy is transferred across the scales and the direction of the transfer. In this respect, the Big Power Law in the Sky needs to be examined using more detailed tools. These should be able to capture, for example, the actual dynamical regimes, the properties of the structures generated by nonlinear interactions, and their clustering. Third-order scaling laws represent a possible route, which will require novel and more precise remote observations and *in situ* measurements, a challenge for future generations of scientists. Ultimately, understanding the interplay of nonlinear interactions and compression in the turbulent interstellar medium could shed light on how these control processes such as star formation and cosmic ray diffusion. Similar reasoning applies to the study of other turbulent astrophysical systems, such as, for example, galaxy clusters (Zhuravleva et al., 2014), black holes (Wielgus et al., 2020) and gravitational waves. In the latter example, initial attempts to derive exact laws from the governing Einstein's general relativity equations have been already performed (Galtier and Nazarenko, 2017). The ubiquitous observation of turbulence and the universal nature of the associated scaling laws explored in this review highlight the fundamental relevance of these studies.

Acknowledgments

R.M. acknowledges support from the project "EVENTFUL" (ANR-20-CE30-0011), funded by the French "Agence Nationale de la Recherche" - ANR through the program AAPG-2020. L.S.-V. was supported by SNSA grants 86/20 and 145/18.

Acronyms and Abbreviations

ACE: Advanced Composition Explorer

ARTEMIS: Acceleration, Reconnection, Turbulence and Electrodynamics

BG13: Banjaree andc Galtier 2013

scientific amazement and artistic creativity that undoubtedly inspired the original name (Wright and Torry, 1973).

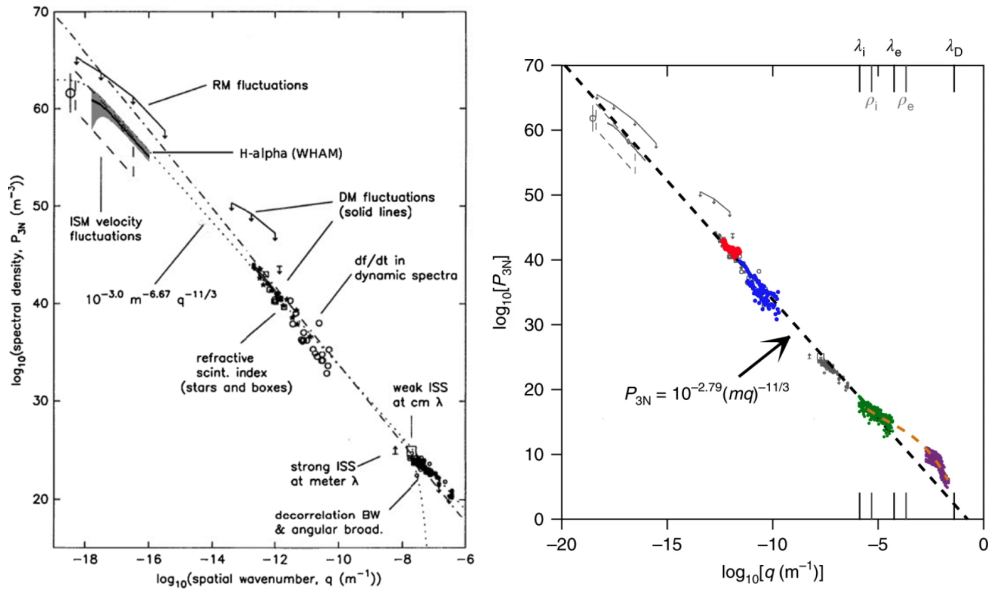

Figure 108: Left panel: *The Big Power Law in the Sky*, or the spectral power density of interstellar electron density, P_{3N}, inferred using radio scintillation and interstellar clouds observations (Armstrong et al., 1995; Chepurnov and Lazarian, 2010). Right panel: *The Grand Power Law in the Milky Way*, obtained adding Voyager density spectra from in-situ measurements (colored markers). Figure adapted from Chepurnov and Lazarian (2010) (left) and Lee and Lee (2019).

BG17: Banjaree and Galtier 2017

BL: Boundary Layer

CHMHD: Compressible Hall-MagnetoHydroDynamics

CIR: Corotating Interaction Region

CME: Coronal Mass Ejections

CMHD: Compressible MagnetoHydroDynamics

CNR: Centro Nazionale della Ricerca

CNRS: Centre National de la Recherche Scientifique

DNS: Direct Numerical Simulation

DoY: Day of the Year

EIT: Extreme ultraviolet Imaging Telescope

EM: ElectroMagnetic

ESA: European Space Agency

EUI: Extreme Ultraviolet Imager

F19: Ferrand et al. 2019

FLAME: Fast Lattice-Boltzmann Algorithm for MHD Experiments

G08: Galtier 2008

GHOST: Geophysical High-Order Suite for Turbulence

GPU: Graphics Processing Unit

GSE: Geocentric Solar Ecliptic

HAO: Mauna Loa High Altitude Observatory

HMHD: Hall-MagnetoHydroDynamics

HVM: Hybrid Vlasov-Maxwell

ICME: Interplanetary Coronal Mass Ejections

IHMHD: Incompressible Hall-MagnetoHydroDynamics

IK: Iroshnikov-Kraichnan

IMF: Interplanetary Magnetic Field

IMHD: Incompressible Magneto-HydroDynamics

INSA: Institut National des Sciences Appliquées

IRF: Institutet för Rymdfysik

ISEE: International Sun-Earth Explorer

ISM: InterStellar Medium

ISS: International Space Station

ISTP: Instituto per la Scienza e Tecnologia dei Plasmi

ITER: International Thermonuclear Experimental Reactor

JPL: Jet Propulsion Laboratory

K41: Kolmogorov theory 1941

KAW: Kinetic Alfén Wave

KH: Kelvin-Helmholtz

KHI: Kelvin-Helmholtz instability

KHM: Kármán-Howarth-Monin

L1: Lagrangian point 1

LASCO: Large Angle and Spectrometric Coronagraph

LES: Large-Eddy Simulation

LET: Local Energy Transfer

LF: Landau Fluid

LIM: Local Intermittency Measure

MAVEN: Mars Atmosphere and Volatile Evolution

MHD: Magneto-HydroDynamics

MMS: Magnetospheric Multiscale Mission

MS: MagnetoSheath

NASA: National Aeronautics and Space Administration

NRL: Naval Research Laboratory

P&P: Politano-Pouquet

PCW: Proton Cyclotron Wave

PFSS: Potential-Field Source-Surface Models

PIC: Particle-In-Cell

PP: Politano-Pouquet

PP98: Compressible Politano-Pouquet law, 1998

PSD: Power Spectral Density

PSP: Parker Solar Probe

PVI: Partial Variance of Increments

RFX: Reversed-Field eXperiment

RHS: Right-Hand Side

RPW: Radio Plasma Waves

RTN: Radial Tangential Normal

SC: Solar corona

STEREO: Solar Terrestrial Relations Observatory

SW: Solar Wind

SW1: Solar Wind interval 1

SW2: Solar Wind interval 2

SW3: Solar Wind interval 3

SWA: Solar Wind plasma Analyser

SWEAP: Solar Wind Electrons Alphas and Protons

THEMIS: Time History of Events and Macroscale Interactions during Substorms

UNH: University of New Hampshire

UT: Universal time

UTC: Universal time coordinated

VDF: Velocity Distribution Function

VKH: von Kármán–Howarth

WKB: Wentzel–Kramers–Brillouin

Main mathematical symbols

α: Spectral exponent | scaling exponent | particle species;

$\mathbf{B}_0$, B_0: Ambient magnetic field vector (magnitude);

β, β_p, β_i, β_e: Plasma beta parameter (proton, ion, electron);

$\mathbf{D_3}^{\pm}$: Third-order moment vector field for outward/inward modes;

${}^{ISO}D_3^{\pm}$, ${}^{1D}D_3^{\pm}$, ${}^{2D}D_3^{\pm}$: isotropic (ISO) and anisotropic projection of $\mathbf{D_3}^{\pm}$ along ($1D$) or perpendicular to ($2D$) the mean magnetic field;

$\mathcal{D}$: Dissipation term;

d_p, d_i, d_e: Proton/ion/electron inertial length;

Δt: Time increment;

E, E_v or E_k, E_b, E_e, E_{tot} or E_T: Energy (kinetic, magnetic, internal, total);

$E^{\pm}$: Outward/inward mode pseudo-energy;

ε, ε_ℓ^T, $\langle|\varepsilon|\rangle$: Total energy injection/transfer/dissipation rate;

ε_e, ε_c, ε_H: Energy transfer rate (kinetic+magnetic energy terms, cross-helicity term, Hall terms);

ε_I: Incompressible energy transfer rate;

$\varepsilon^{\pm}$, $\varepsilon_I^{\pm}$: Pseudo-energy injection/transfer rate of outward/inward mode (incompressible);

ε_C, $\langle|\varepsilon_C|\rangle$: Compressible energy transfer rate;

$\varepsilon_{CMHD}^{flux}$, $\varepsilon_{CMHD}^{nonflux}$, $\varepsilon_{CHMHD}^{flux}$, $\varepsilon_{CHMHD}^{nonflux}$: Compressible energy transfer rate contributions from MHD/Hall-MHD and flux/non-flux terms;

ε_ϕ: Energy transfer rate rate for a passive scalar ϕ;

ε_{heat}: Heating rate;

ε_1: Energy injection rate, Heating rate;

ε_2: Heating rate

ε_3: Sub-ion-scale energy transfer rate;

$\varepsilon(t, \Delta t)$, $\varepsilon_{\Delta t}$: MHD local energy transfer rate (LET);

$\varepsilon_H(t, \Delta t)$: Hall-MHD local energy transfer rate (LET);

ζ_q: Scaling exponent of the structure function of order q;

θ_{VB}, θ_{BV}, θ_{RB}, θ_{BR}, θ_{SB}: acute angle between magnetic field and velocity (VB, BV), radial (RB, BR) or sampling (SB) direction;

θ: plasma dilation (divergence of the velocity);

f, f_s, f_p, f_e: frequency | velocity; distribution function (specie s, proton, electron);

f_{EM}: Laplace force;

$F(\ell)$, $F(\Delta t)$: Scale-dependent flatness;

$\mathcal{F}^{MHD}$, $\mathcal{F}^{HMHD}$: MHD and Hall-MHD flux terms;

$\mathcal{F}$: Forcing term;

h: scaling exponent of MHD fields fluctuations;

$\mathbf{H}$: Vector third-order moment Hall term;

$\mathcal{H}^{MHD}$: Hybrid MHD term;

κ: scaling exponent of the flatness;

L, L_0: Outer/integral/large scale | box size/sample length;

L_H: Characteristic Hall scale;

ℓ: Spatial scale;

λ_D: Debye length;

$\lambda^{\pm}$: Taylor microscale;

M_S, $\mathcal{M}$: Sonic Mach number;

M_A, $\mathcal{M}$: Alfvénic Mach number;

$\mathcal{M}_{\beta}^{MHD}$: β-dependent MHD term;

ξ_q: Scaling exponent of the structure function of order q using Extended Self Similarity;

P, P_k, P_m, P_{tot}: Pressure (kinetic, magnetic, total);

P: P-model parameter;

Π, $\Pi^{\pm}$: Energy flux (total, outward/inward modes);

Π_ℓ, Π_ℓ^T: Energy flux at scale ℓ;

R_E: Earth radius;

$R_\odot$: Solar radius;

r_A: Alfvén ratio;

S_q: Structure function of order q;

$\mathcal{S}$, $\mathcal{S}_w$, $\mathcal{S}_B$: Second-order structure function (total, kinetic and magnetic);

$\mathcal{S}^{MHD}$, $\mathcal{S}^{HMHD}$: MHD and Hall-MHD source terms;

σ_c: Normalized cross-helicity;

σ_r: Residual energy;

V_{SW}, v_A: Solar wind bulk speed, Alfvén speed;

v_R, v_L: Velocity component along the longitudinal direction (ℓ);

T, $T_\parallel$, $T_\perp$: Temperature (total, parallel, perpendicular with respect to the ambient magnetic field);

τ, τ_A, τ_{NL}: Time scale, characteristic time (Alfvén, nonlinear);

τ_c: Correlation time scale;

τ_q: Multifractal scaling exponents of the partition functions of order q;

$Y(\ell)$, $Y^{\pm}(\ell)$, $Y(\Delta t)$, $Y^{\pm}(\Delta t)$: Space- or time-scale-dependent mixed third-order structure function (total, outward/inward modes);

Y_e, Y_c: kinetic+magnetic energy and cross-helicity components of the mixed third-order structure function;

$Y_\phi(\ell)$: scale dependent mixed third-order structure function for a passive scalar ϕ;

$\mathbf{Y}$: Vector third-order moment MHD term;

Ω_P: Plasma frequency;

$\mathbf{z}^{\pm}$: Elsasser field vectors for outward/inward Alfvén modes.

References

Acuña, M.H., Connerney, J.E.P., F., N., Ness, Lin, R.P., Mitchell, D., Carlson, C.W., McFadden, J., Anderson, K.A., Rème, H., Mazelle, C., Vignes, D., Wasilewski, P., Cloutier, P., 1999. Global distribution of crustal magnetization discovered by the Mars global surveyor mag/er experiment. Science 284, 790–793. URL: https://www.science.org/doi/abs/10.1126/science.284.5415.790, doi:10.1126/science.284.5415.790.

Acuña, M.H., Connerney, J.E.P., Wasilewski, P., Lin, R.P., Anderson, K.A., Carlson, C.W., McFadden, J., Curtis, D.W., Mitchell, D., Reme, H., Mazelle, C., Sauvaud, J.A., d'Uston, C., Cros, A., Medale, J.L., Bauer, S.J., Cloutier, P., Mayhew, M., Winterhalter, D., Ness, N.F., 1998. Magnetic field and plasma observations at mars: Initial results of the Mars global surveyor mission. Science 279, 1676–1680. URL: https://www.science.org/doi/abs/10.1126/science.279.5357.1676, doi:10.1126/science.279.5357.1676.

Adhikari, L., Zank, G.P., Bruno, R., Telloni, D., Hunana, P., Dosch, A., Marino, R., Hu, Q., 2015a. The transport of low-frequency turbulence in the super-Alfvénic solar wind. Journal of Physics: Conference Series 642, 012001. URL: https://dx.doi.org/10.1088/1742-6596/642/1/012001, doi:10.1088/1742-6596/642/1/012001.

Adhikari, L., Zank, G.P., Bruno, R., Telloni, D., Hunana, P., Dosch, A., Marino, R., Hu, Q., 2015b. The trasport of low-frequency turbulence

in astrophysical flows. II. Solutions for the super-Alfvénic solar wind. The Astrophysical Journal 805, 63. URL: https://doi.org/10.1088/0004-637x/805/1/63, doi:10.1088/0004-637x/805/1/63.

Adkins, T., Schekochihin, A.A., 2018. A solvable model of Vlasov-kinetic plasma turbulence in Fourier–Hermite phase space. Journal of Plasma Physics 84, 905840107. doi:10.1017/S0022377818000089.

Airapetian, V.S., Barnes, R., Cohen, O., Collinson, G.A., Danchi, W.C., Dong, C.F., Del Genio, A.D., France, K., Garcia-Sage, K., Glocer, A., et al., 2020. Impact of space weather on climate and habitability of terrestrial-type exoplanets. International Journal of Astrobiology 19, 136–194. doi:10.1017/S1473550419000132.

Akasofu, S.I., 1981. Energy coupling between the solar wind and the magnetosphere. *Space Sci. Rev.* 28, 121–190. doi:10.1007/BF00218810.

Akasofu, S.I., 2019. The explosive characteristics of the aurora: The electric current line approach. Frontiers in Astronomy and Space Sciences 6. URL: https://www.frontiersin.org/article/10.3389/fspas.2019.00001, doi:10.3389/fspas.2019.00001.

Alexakis, A., Biferale, L., 2018. Cascades and transitions in turbulent flows. Physics Reports 767-769, 1–101. URL: https://www.sciencedirect.com/science/article/pii/S0370157318301935, doi:https://doi.org/10.1016/j.physrep.2018.08.001.

Alexandrova, O., Carbone, V., Veltri, P., Sorriso-Valvo, L., 2007. Solar wind Cluster observations: Turbulent spectrum and role of Hall effect. Planetary and Space Science 55, 2224–2227. URL: https://www.sciencedirect.com/science/article/pii/S0032063307001754, doi:https://doi.org/10.1016/j.pss.2007.05.022.

Alexandrova, O., Carbone, V., Veltri, P., Sorriso-Valvo, L., 2008. Small-scale energy cascade of the solar wind turbulence. *Astrophys. J.* 674, 1153–1157. doi:10.1086/524056, arXiv:0710.0763.

Alexandrova, O., Chen, C.H.K., Sorriso-Valvo, L., Horbury, T.S., Bale, S.D., 2013. Solar wind turbulence and the role of ion instabilities. *Space Sci. Rev.* 178, 101–139. arXiv:1306.5336.

Alexandrova, O., Lacombe, C., Mangeney, A., 2008. Spectra and anisotropy of magnetic fluctuations in the earth's magnetosheath: Cluster observations. Annales Geophysicae 26, 3585–3596. doi:10.5194/angeo-26-3585-2008.

Alexandrova, O., Saur, J., Lacombe, C., Mangeney, A., Mitchell, J., Schwartz, S.J., Robert, P., 2009. Universality of solar-wind turbulent spectrum from mhd to electron scales. Phys. Rev. Lett. 103, 165003. URL: https://link.aps.org/doi/10.1103/PhysRevLett.103.165003, doi:10.1103/PhysRevLett.103.165003.

Alfvén, H., 1942. Existence of electromagnetic-hydrodynamic waves. *Nature* 150, 405–406. doi:10.1038/150405d0.

Aluie, H., 2011. Compressible turbulence: The cascade and its locality. Phys. Rev. Lett. 106, 174502. URL: https://link.aps.org/doi/10.1103/PhysRevLett.106.174502, doi:10.1103/PhysRevLett.106.174502.

Aluie, H., 2013. Scale decomposition in compressible turbulence. Physica D: Nonlinear Phenomena 247, 54–65. URL: https://www.sciencedirect.com/science/article/pii/S0167278912003132, doi:https://doi.org/10.1016/j.physd.2012.12.009.

Aluie, H., Eyink, G.L., 2009. Localness of energy cascade in hydrodynamic turbulence. II. Sharp spectral filter. Physics of Fluids 21, 115108. doi:10.1063/1.3266948.

Aluie, H., Eyink, G.L., 2010. Scale locality of magnetohydrodynamic turbulence. Physics Review Letters 104, 081101. doi:10.1103/PhysRevLett.104.081101, arXiv:0912.3752.

Aluie, H., Kurien, S., 2011. Joint downscale fluxes of energy and potential enstrophy in rotating stratified boussinesq flows. EPL (Europhysics Letters) 96, 44006. doi:10.1209/0295-5075/96/44006.

Aluie, H., Li, S., Li, H., 2012. Conservative cascade of kinetic energy in compressible turbulence. The Astrophysical Journal 751, L29. doi:10.1088/2041-8205/751/2/l29.

Amaya, J., Dupuis, R., Innocenti, M.E., Lapenta, G., 2020. Visualizing and interpreting unsupervised solar wind classifications. Frontiers

in Astronomy and Space Sciences 7. URL: https://www.frontiersin.org/articles/10.3389/fspas.2020.553207, doi:10.3389/fspas.2020.553207.

Andrés, N., Galtier, S., Sahraoui, F., 2018. Exact law for homogeneous compressible Hall magnetohydrodynamics turbulence. Phys. Rev. E 97, 013204. URL: https://link.aps.org/doi/10.1103/PhysRevE.97.013204, doi:10.1103/PhysRevE.97.013204.

Andrés, N., Romanelli, N., Hadid, L.Z., Sahraoui, F., DiBraccio, G., Halekas, J., 2020. Solar wind turbulence around mars: Relation between the energy cascade rate and the proton cyclotron waves activity. *Astrophys. J.* 902, 134. doi:10.3847/1538-4357/abb5a7, arXiv:2007.09476.

Andrés, N., Sahraoui, F., 2017. Alternative derivation of exact law for compressible and isothermal magnetohydrodynamics turbulence. Phys. Rev. E 96, 053205. URL: https://link.aps.org/doi/10.1103/PhysRevE.96.053205, doi:10.1103/PhysRevE.96.053205.

Andrés, N., Sahraoui, F., Galtier, S., Hadid, L.Z., Ferrand, R., Huang, S.Y., 2019. Energy cascade rate measured in a collisionless space plasma with mms data and compressible Hall magnetohydrodynamic turbulence theory. *Phys. Rev. Lett.* 123, 245101. doi:10.1103/PhysRevLett.123.245101, arXiv:1911.09749.

Andres, N., Sahraoui, F., Hadid, L.Z., Huang, S.Y., Romanelli, N., Galtier, S., DiBraccio, G., Halekas, J., 2021. The Evolution of Compressible Solar Wind Turbulence in the Inner Heliosphere: PSP, THEMIS, and MAVEN Observations. Astrophysical Journal 919. doi:{10.3847/1538-4357/ac0af5}.

Andrés, N., Sahraoui, F., Galtier, S., Hadid, L.Z., Dmitruk, P., Mininni, P.D., 2018. Energy cascade rate in isothermal compressible magnetohydrodynamic turbulence. Journal of Plasma Physics 84, 905840404. doi:10.1017/S0022377818000788.

Angelopoulos, V., 2008. The themis mission. *Space Sci. Rev.* 141, 5–34. doi:10.1007/s11214-008-9336-1.

Angelopoulos, V., 2011. The artemis mission. *Space Sci. Rev.* 165, 3–25. doi:10.1007/s11214-010-9687-2.

Anselmet, F., Gagne, Y., Hopfinger, E.J., Antonia, R.A., 1984. High-order velocity structure functions in turbulent shear flow. *J. Fluid Mech.* 140, 63–89.

Antoni, V., Cavazzana, R., Desideri, D., Martines, E., Serianni, G., Tramontin, L., 1998. Electrostatic turbulence and transport in the velocity shear layer of a reversed field pinch plasma. Phys. Rev. Lett. 80, 4185–4188. URL: https://link.aps.org/doi/10.1103/PhysRevLett.80.4185, doi:10.1103/PhysRevLett.80.4185.

Antonia, R.A., Ould-Rouis, M., Anselmet, F., Zhu, Y., 1997. Analogy between predictions of kolmogorov and yaglom. Journal of Fluid Mechanics 332, 395–409. doi:10.1017/S0022112096004090.

Antonucci, E., Romoli, M., Andretta, V., Fineschi, S., Heinzel, P., Moses, J.D., Naletto, G., Nicolini, G., Spadaro, D., Teriaca, L., Berlicki, A., Capobianco, G., Crescenzio, G., Da Deppo, V., Focardi, M., Frassetto, F., Heerlein, K., Landini, F., Magli, E., Marco Malvezzi, A., Massone, G., Melich, R., Nicolosi, P., Noci, G., Pancrazzi, M., Pelizzo, M.G., Poletto, L., Sasso, C., Schühle, U., Solanki, S.K., Strachan, L., Susino, R., Tondello, G., Uslenghi, M., Woch, J., Abbo, L., Bemporad, A., Casti, M., Dolei, S., Grimani, C., Messerotti, M., Ricci, M., Straus, T., Telloni, D., Zuppella, P., Auchère, F., Bruno, R., Ciaravella, A., Corso, A.J., Alvarez Copano, M., Aznar Cuadrado, R., D'Amicis, R., Enge, R., Gravina, A., Jejčič, S., Lamy, P., Lanzafame, A., Meierdierks, T., Papagiannaki, I., Peter, H., Fernandez Rico, G., Giday Sertsu, M., Staub, J., Tsinganos, K., Velli, M., Ventura, R., Verroi, E., Vial, J.C., Vives, S., Volpicelli, A., Werner, S., Zerr, A., Negri, B., Castronuovo, M., Gabrielli, A., Bertacin, R., Carpentiero, R., Natalucci, S., Marliani, F., Cesa, M., Laget, P., Morea, D., Pieraccini, S., Radaelli, P., Sandri, P., Sarra, P., Cesare, S., Del Forno, F., Massa, E., Montabone, M., Mottini, S., Quattropani, D., Schillaci, T., Boccardo, R., Brando, R., Pandi, A., Baietto, C., Bertone, R., Alvarez-Herrero, A., García Parejo, P., Cebollero, M., Amoruso, M., Centonze, V., 2020. Metis: the solar orbiter visible light and ultraviolet coronal imager. *Astron. Astrophys.* 642, A10. doi:10.1051/0004-6361/201935338.

Armstrong, J.W., Rickett, B.J., Spangler, S.R., 1995. Electron density power spectrum in the local interstellar medium. *Astrophys. J.* 443, 209. doi:10.1086/175515.

Badman, S.T., Bale, S.D., Oliveros, J.C.M., Panasenco, O., Velli, M., Stansby, D., Buitrago-Casas, J.C., Réville, V., Bonnell, J.W., Case, A.W., de Wit, T.D., Goetz, K., Harvey, P.R., Kasper, J.C., Korreck, K.E., Larson, D.E., Livi, R., MacDowall, R.J., Malaspina, D.M., Pulupa, M., Stevens, M.L., Whittlesey, P.L., 2020. Magnetic connectivity of the ecliptic plane within 0.5 AU: Potential field source surface modeling of the first Parker Solar Probe encounter. The Astrophysical Journal Supplement Series 246, 23. URL: https://doi.org/10.3847/1538-4365/ab4da7, doi:10.3847/1538-4365/ab4da7.

Bale, S.D., Badman, S.T., Bonnell, J.W., Bowen, T.A., Burgess, D., Case, A.W., Cattell, C.A., Chandran, B.D.G., Chaston, C.C., Chen, C.H.K., Drake, J.F., de Wit, T.D., Eastwood, J.P., Ergun, R.E., Farrell, W.M., Fong, C., Goetz, K., Goldstein, M., Goodrich, K.A., Harvey, P.R., Horbury, T.S., Howes, G.G., Kasper, J.C., Kellogg, P.J., Klimchuk, J.A., Korreck, K.E., Krasnoselskikh, V.V., Krucker, S., Laker, R., Larson, D.E., MacDowall, R.J., Maksimovic, M., Malaspina, D.M., Martinez-Oliveros, J., McComas, D.J., Meyer-Vernet, N., Moncuquet, M., Mozer, F.S., Phan, T.D., Pulupa, M., Raouafi, N.E., Salem, C., Stansby, D., Stevens, M., Szabo, A., Velli, M., Woolley, T., Wygant, J.R., 2019. Highly structured slow solar wind emerging from an equatorial coronal hole. *Nature* 576, 237–242. doi:10.1038/s41586-019-1818-7.

Bale, S.D., Goetz, K., Harvey, P.R., Turin, P., Bonnell, J.W., Dudok de Wit, T., Ergun, R.E., MacDowall, R.J., Pulupa, M., Andre, M., Bolton, M., Bougeret, J.L., Bowen, T.A., Burgess, D., Cattell, C.A., Chandran, B.D.G., Chaston, C.C., Chen, C.H.K., Choi, M.K., Connerney, J.E., Cranmer, S., Diaz-Aguado, M., Donakowski, W., Drake, J.F., Farrell, W.M., Fergeau, P., Fermin, J., Fischer, J., Fox, N., Glaser, D., Goldstein, M., Gordon, D., Hanson, E., Harris, S.E., Hayes, L.M., Hinze, J.J., Hollweg, J.V., Horbury, T.S., Howard, R.A., Hoxie, V., Jannet, G., Karlsson, M., Kasper, J.C., Kellogg, P.J., Kien, M., Klimchuk, J.A., Krasnoselskikh, V.V., Krucker, S., Lynch, J.J., Maksimovic, M., Malaspina, D.M., Marker, S., Martin, P., Martinez-Oliveros, J., McCauley, J., McComas, D.J., McDonald, T., Meyer-Vernet, N., Moncuquet, M., Monson, S.J., Mozer, F.S., Murphy, S.D., Odom, J., Oliverson, R., Olson, J., Parker, E.N., Pankow, D., Phan, T., Quataert, E., Quinn, T., Ruplin, S.W., Salem, C., Seitz, D., Sheppard, D.A., Siy, A., Stevens, K., Summers, D., Szabo, A., Tim-

ofeeva, M., Vaivads, A., Velli, M., Yehle, A., Werthimer, D., Wygant, J.R., 2016. The FIELDS instrument suite for Solar Probe Plus. measuring the coronal plasma and magnetic field, plasma waves and turbulence, and radio signatures of solar transients. *Space Sci. Rev.* 204, 49–82. doi:10.1007/s11214-016-0244-5.

Bale, S.D., Horbury, T.S., Velli, M., Desai, M.I., Halekas, J.S., McManus, M.D., Panasenco, O., Badman, S.T., Bowen, T.A., Chandran, B.D.G., Drake, J.F., Kasper, J.C., Laker, R., Mallet, A., Matteini, L., Phan, T.D., Raouafi, N.E., Squire, J., Woodham, L.D., Woolley, T., 2021. A solar source of Alfvénic magnetic field switchbacks: In situ remnants of magnetic funnels on supergranulation scales. *Astrophys. J.* 923, 174. doi:10.3847/1538-4357/ac2d8c, arXiv:2109.01069.

Balogh, A., Forsyth, R.J., Lucek, E.A., Horbury, T.S., Smith, E.J., 1999. Heliospheric magnetic field polarity inversions at high heliographic latitudes. Geophysical Research Letters 26, 631–634. URL: https://agupubs.onlinelibrary.wiley.com/doi/abs/10.1029/1999GL900061, doi:https://doi.org/10.1029/1999GL900061.

Balogh, A., Southwood, D.J., Forsyth, R.J., Horbury, T.S., Smith, E.J., Tsurutani, B.T., 1995. The heliospheric magnetic field over the south polar region of the Sun. Science 268, 1007–1010. URL: https://www.science.org/doi/abs/10.1126/science.268.5213.1007, doi:10.1126/science.268.5213.1007.

Bandyopadhyay, R., Chasapis, A., Chhiber, R., Parashar, T.N., Matthaeus, W.H., Shay, M.A., Maruca, B.A., Burch, J.L., Moore, T.E., Pollock, C.J., Giles, B.L., Paterson, W.R., Dorelli, J., Gershman, D.J., Torbert, R.B., Russell, C.T., Strangeway, R.J., 2018a. Incompressive energy transfer in the earth's magnetosheath: Magnetospheric multiscale observations. *Astrophys. J.* 866, 106. doi:10.3847/1538-4357/aade04, arXiv:1806.04275.

Bandyopadhyay, R., Chasapis, A., Gershman, D.J., Giles, B.L., Russell, C.T., Strangeway, R.J., Le Contel, O., Argall, M.R., Burch, J.L., 2021a. Observation of an inertial-range energy cascade within a reconnection jet in the earth's magnetotail. *Mon. Not. Roy. Astron. Soc.* 500, L6–L10. doi:10.1093/mnrasl/slaa171, arXiv:2010.01782.

Bandyopadhyay, R., Goldstein, M.L., Maruca, B.A., Matthaeus, W.H., Parashar, T.N., Ruffolo, D., Chhiber, R., Usmanov, A., Chasapis, A., Qudsi, R., Bale, S.D., Bonnell, J.W., Dudok de Wit, T., Goetz, K., Harvey, P.R., MacDowall, R.J., Malaspina, D.M., Pulupa, M., Kasper, J.C., Korreck, K.E., Case, A.W., Stevens, M., Whittlesey, P., Larson, D., Livi, R., Klein, K.G., Velli, M., Raouafi, N., 2020. Enhanced energy transfer rate in solar wind turbulence observed near the Sun from Parker Solar Probe. *Astrophys. J. Suppl.* 246, 48. doi:10.3847/1538-4365/ab5dae, arXiv:1912.02959.

Bandyopadhyay, R., Matthaeus, W.H., McComas, D.J., Chhiber, R., Usmanov, A.V., Huang, J., Livi, R., Larson, D.E., Kasper, J.C., Case, A.W., Stevens, M., Whittlesey, P., Romeo, O.M., Bale, S.D., Bonnell, J.W., de Wit, T.D., Goetz, K., Harvey, P.R., MacDowall, R.J., Malaspina, D.M., Pulupa, M., 2022. Sub-Alfvénic solar wind observed by the Parker Solar Probe: Characterization of turbulence, anisotropy, intermittency, and switchback. The Astrophysical Journal Letters 926, L1.

Bandyopadhyay, R., Matthaeus, W.H., McComas, D.J., Joyce, C.J., Szalay, J.R., Christian, E.R., Giacalone, J., Schwadron, N.A., Mitchell, D.G., Hill, M.E., McNutt, R.L., Desai, M.I., Bale, S.D., Bonnell, J.W., Dudok de Wit, T., Goetz, K., Harvey, P.R., MacDowall, R.J., Malaspina, D.M., Pulupa, M., Kasper, J.C., Stevens, M., 2021b. Energetic particle behavior in near-sun magnetic field switchbacks from psp. *Astron. Astrophys.* 650, L4. doi:10.1051/0004-6361/202039800.

Bandyopadhyay, R., Matthaeus, W.H., Oughton, S., Wan, M., 2019. Evolution of similarity lengths in anisotropic magnetohydrodynamic turbulence. Journal of Fluid Mechanics 876, 5–18. doi:10.1017/jfm.2019.513, arXiv:1906.07764.

Bandyopadhyay, R., Oughton, S., Wan, M., Matthaeus, W.H., Chhiber, R., Parashar, T.N., 2018b. Finite dissipation in anisotropic magnetohydrodynamic turbulence. Physical Review X 8, 041052. doi:10.1103/PhysRevX.8.041052, arXiv:1812.02379.

Bandyopadhyay, R., Sorriso-Valvo, L., Chasapis, A., Hellinger, P., Matthaeus, W.H., Verdini, A., Landi, S., Franci, L., Matteini, L., Giles,

B.L., Gershman, D.J., Moore, T.E., Pollock, C.J., Russell, C.T., Strangeway, R.J., Torbert, R.B., Burch, J.L., 2020. In situ observation of Hall magnetohydrodynamic cascade in space plasma. Phys. Rev. Lett. 124, 225101. URL: https://link.aps.org/doi/10.1103/PhysRevLett.124.225101, doi:10.1103/PhysRevLett.124.225101.

Banerjee, S., Andrés, N., 2020. Scale-to-scale energy transfer rate in compressible two-fluid plasma turbulence. Phys. Rev. E 101, 043212. URL: https://link.aps.org/doi/10.1103/PhysRevE.101.043212, doi:10.1103/PhysRevE.101.043212.

Banerjee, S., Galtier, S., 2013. Exact relation with two-point correlation functions and phenomenological approach for compressible magnetohydrodynamic turbulence. Phys. Rev. E 87, 013019. URL: https://link.aps.org/doi/10.1103/PhysRevE.87.013019, doi:10.1103/PhysRevE.87.013019.

Banerjee, S., Galtier, S., 2014. A Kolmogorov-like exact relation for compressible polytropic turbulence. Journal of Fluid Mechanics 742, 230–242. doi:10.1017/jfm.2013.657.

Banerjee, S., Galtier, S., 2016. Chiral exact relations for helicities in Hall magnetohydrodynamic turbulence. Phys. Rev. E 93, 033120. URL: https://link.aps.org/doi/10.1103/PhysRevE.93.033120, doi:10.1103/PhysRevE.93.033120.

Banerjee, S., Galtier, S., 2017. An alternative formulation for exact scaling relations in hydrodynamic and magnetohydrodynamic turbulence. Journal of Physics A: Mathematical and Theoretical 50, 015501. URL: https://doi.org/10.1088/1751-8113/50/1/015501, doi:10.1088/1751-8113/50/1/015501.

Banerjee, S., Hadid, L.Z., Sahraoui, F., Galtier, S., 2016. Scaling of compressible magnetohydrodynamic turbulence in the fast solar wind. The Astrophysical Journal 829, L27. URL: https://doi.org/10.3847/2041-8205/829/2/l27, doi:10.3847/2041-8205/829/2/l27.

Banerjee, S., Kritsuk, A.G., 2018. Energy transfer in compressible magnetohydrodynamic turbulence for isothermal self-gravitating fluids. Phys. Rev.

E 97, 023107. URL: https://link.aps.org/doi/10.1103/PhysRevE.97.023107, doi:10.1103/PhysRevE.97.023107.

Basu, S., 2016. Global seismology of the sun. Living Reviews in Solar Physics 13, 2. doi:10.1007/s41116-016-0003-4, arXiv:1606.07071.

Bavassano, B., Dobrowolny, M., Mariani, F., Ness, N., 1982. Radial evolution of power spectra of interplanetary Alfvénic turbulence. J. Geophys. Res. 87, 3617–3622. doi:10.1029/JA087iA05p03617.

Bavassano, B., Pietropaolo, E., Bruno, R., 2000. Alfvénic turbulence in the polar wind: A statistical study on cross helicity and residual energy variations. Journal of Geophysical Research: Space Physics 105, 12697–12704. URL: https://agupubs.onlinelibrary.wiley.com/doi/abs/10.1029/2000JA900004, doi:https://doi.org/10.1029/2000JA900004.

Bavassano Cattaneo, M.B., Marcucci, M.F., Bogdanova, Y.V., Rème, H., Dandouras, I., Kistler, L.M., Lucek, E., 2010. Global reconnection topology as inferred from plasma observations inside Kelvin-Helmholtz vortices. Annales Geophysicae 28, 893–906. URL: https://angeo.copernicus.org/articles/28/893/2010/, doi:10.5194/angeo-28-893-2010.

Bazelyan, E.M., Raizer, Y.P., 2000. Lightning Physics and Lightning Protection. Bristol/Philadelphia: Institute of Physics Publishing.

Becker, K.H., Kogelschatz, U., Schoenbach, K.H., Barker, R.J.E., 2005. Non-Equilibrium Air Plasmas at Atmospheric Pressure (1st ed.). CRC Press, Boca Raton, Florida, United States.

Belisheva, N.K., 2019. The effect of space weather on human body at the spitsbergen archipelago, in: Kanao, M., Kakinami, Y., Toyokuni, G. (Eds.), Arctic Studies. IntechOpen, Rijeka. chapter 5. URL: https://doi.org/10.5772/intechopen.85021, doi:10.5772/intechopen.85021.

Benzi, R., Ciliberto, S., Tripiccione, R., Baudet, C., Massaioli, F., Succi, S., 1993. Extended self-similarity in turbulent flows. *Phys. Rev. E* 48, 29.

Bieber, J.W., Wanner, W., Matthaeus, W.H., 1996. Dominant two-dimensional solar wind turbulence with implications for cosmic ray transport. Journal of Geophysical Research: Space Physics 101, 2511–2522.

URL: https://agupubs.onlinelibrary.wiley.com/doi/abs/10.1029/95JA02588, doi:https://doi.org/10.1029/95JA02588.

Biermann, L., 1951. Kometenschweife und solare korpuskularstrahlung. *Zeitschrift für Astrophysik* 29, 274.

Birkeland, K., 1913. The Norwegian Aurora Polaris Expedition. Publ. H. Aschehoug & Co.

Birkeland, K., 1916. Are the solar corpuscular rays that penetrate the earth's atmosphere negative or positive rays? in: Videnskapsselskapets Skrifter, I Mat - Naturv. Klasse No. 1, Christiania .

Biskamp, D., 1993. Magnetohydrodynamic Turbulence. Cambridge University Press.

Boldyrev, S., 2005. On the spectrum of magnetohydrodynamic turbulence. The Astrophysical Journal 626, L37–L40.

Boldyrev, S., 2006. Spectrum of magnetohydrodynamic turbulence. Phys. Rev. Lett. 96, 115002. URL: https://link.aps.org/doi/10.1103/PhysRevLett.96.115002, doi:10.1103/PhysRevLett.96.115002.

Borovsky, J.E., 2008. Flux tube texture of the solar wind: Strands of the magnetic carpet at 1 AU? Journal of Geophysical Research: Space Physics 113. URL: https://agupubs.onlinelibrary.wiley.com/doi/abs/10.1029/2007JA012684, doi:https://doi.org/10.1029/2007JA012684.

Borovsky, J.E., 2021. Is our understanding of solar-wind/magnetosphere coupling satisfactory? Frontiers in Astronomy and Space Sciences 8. URL: https://www.frontiersin.org/article/10.3389/fspas.2021.634073, doi:10.3389/fspas.2021.634073.

Borovsky, J.E., Elphic, R.C., Funsten, H.O., Thomsen, M.F., 1997. The earth's plasma sheet as a laboratory for flow turbulence in high-β MHD. Journal of Plasma Physics 57, 1–34. doi:10.1017/S0022377896005259.

Bourouaine, S., Perez, J.C., Klein, K.G., Chen, C.H.K., Martinović, M., Bale, S.D., Kasper, J.C., Raouafi, N.E., 2020. Turbulence characteristics of switchback and nonswitchback intervals observed by Parker Solar Probe. *Astrophys. J. Lett.* 904, L30. doi:10.3847/2041-8213/abbd4a, arXiv:2010.00936.

Breech, B., Matthaeus, W.H., Cranmer, S.R., Kasper, J.C., Oughton, S., 2009. Electron and proton heating by solar wind turbulence. Journal of Geophysical Research: Space Physics 114. URL: https://agupubs.onlinelibrary.wiley.com/doi/abs/10.1029/2009JA014354, doi:https://doi.org/10.1029/2009JA014354, arXiv:https://agupubs.onlinelibrary.wiley.com/doi/pdf/10.1029/2009JA014354.

Bruno, R., 2019. Intermittency in solar wind turbulence from fluid to kinetic scales. Earth and Space Science 6, 656–672. URL: https://agupubs.onlinelibrary.wiley.com/doi/abs/10.1029/2018EA000535, doi:https://doi.org/10.1029/2018EA000535, arXiv:https://agupubs.onlinelibrary.wiley.com/doi/pdf/10.1029/2018EA000535.

Bruno, R., Carbone, V., 2013. The solar wind as a turbulence laboratory. *Liv. Rev. in Solar Phys.* 10, 2.

Bruno, R., Carbone, V., Primavera, L., Malara, F., Sorriso-Valvo, L., Bavassano, B., Veltri, P., 2004. On the probability distribution function of small-scale interplanetary magnetic field fluctuations. Annales Geophysicae 22, 3751–3769. doi:10.5194/angeo-22-3751-2004, arXiv:physics/0409056.

Bruno, R., Carbone, V., Sorriso-Valvo, L., Bavassano, B., 2003. Radial evolution of solar wind intermittency in the inner heliosphere. J. of Geophys. Res.: Space Phys. 108, 1130.

Bruno, R., Carbone, V., Veltri, P., Pietropaolo, E., Bavassano, B., 2001. Identifying intermittent events in the solar wind. Planet. Space Sci. 49, 1201–1210. doi:10.1016/S0032-0633(01)00061-7.

Bruno, R., Telloni, D., Primavera, L., Pietropaolo, E., D'Amicis, R., Sorriso-Valvo, L., Carbone, V., Malara, F., Veltri, P., 2014. Radial evolution of the intermittency of density fluctuations in the fast solar wind. *Astrophys. J.* 786, 53. doi:10.1088/0004-637X/786/1/53, arXiv:1411.3473.

Bruno, R., Telloni, D., Sorriso-Valvo, L., Marino, R., De Marco, R., D'Amicis, R., 2019. The low-frequency break observed in the slow solar wind magnetic spectra. *Astron. Astrophys.* 627, A96. doi:10.1051/0004-6361/201935841.

Buaria, D., Pumir, A., Feraco, F., Marino, R., Pouquet, A., Rosenberg, D., Primavera, L., 2020. Single-particle Lagrangian statistics from direct numerical simulations of rotating stratified turbulence. Phys. Rev. Fluids 5, 064801.

Burch, J.L., Drake, J.F., 2009. Reconnecting magnetic fields: The huge amounts of energy released from the relinking of magnetic fields in outer space are both mysterious and potentially destructive. American Scientist 97, 392–399. URL: http://www.jstor.org/stable/27859391.

Burch, J.L., Moore, T.E., Torbert, R.B., Giles, B.L., 2016. Magnetospheric multiscale overview and science objectives. *Space Sci. Rev.* 199, 5–21. doi:10.1007/s11214-015-0164-9.

Burch, J.L., Torbert, R.B., Phan, T.D., Chen, L.J., Moore, T.E., Ergun, R.E., Eastwood, J.P., Gershman, D.J., Cassak, P.A., Argall, M.R., Wang, S., Hesse, M., Pollock, C.J., Giles, B.L., Nakamura, R., Mauk, B.H., Fuselier, S.A., Russell, C.T., Strangeway, R.J., Drake, J.F., Shay, M.A., Khotyaintsev, Y.V., Lindqvist, P.A., Marklund, G., Wilder, F.D., Young, D.T., Torkar, K., Goldstein, J., Dorelli, J.C., Avanov, L.A., Oka, M., Baker, D.N., Jaynes, A.N., Goodrich, K.A., Cohen, I.J., Turner, D.L., Fennell, J.F., Blake, J.B., Clemmons, J., Goldman, M., Newman, D., Petrinec, S.M., Trattner, K.J., Lavraud, B., Reiff, P.H., Baumjohann, W., Magnes, W., Steller, M., Lewis, W., Saito, Y., Coffey, V., Chandler, M., 2016. Electron-scale measurements of magnetic reconnection in space. Science 352, aaf2939. URL: https://www.science.org/doi/abs/10.1126/science.aaf2939, doi:10.1126/science.aaf2939, arXiv:https://www.science.org/doi/pdf/10.1126/science.aaf2939.

Camporeale, E., 2019. The challenge of machine learning in space weather: Nowcasting and forecasting. Space Weather 17, 1166–1207. URL: https://agupubs.onlinelibrary.wiley.com/doi/abs/10.1029/2018SW002061, doi:https://doi.org/10.1029/2018SW002061.

Camporeale, E., Sorriso-Valvo, L., Califano, F., Retinò, A., 2018. Coherent structures and spectral energy transfer in turbulent plasma: A space-filter approach. Phys. Rev. Lett. 120, 125101. doi:10.1103/PhysRevLett.120.125101.

Carbone, F., Sorriso-Valvo, L., Khotyaintsev, Y.V., Steinvall, K., Vecchio, A., Telloni, D., Yordanova, E., Graham, D.B., Edberg, N.J.T., Eriksson, A.I., Johansson, E.P.G., Vásconez, C.L., Maksimovic, M., Bruno, R., D'Amicis, R., Bale, S.D., Chust, T., Krasnoselskikh, V., Kretzschmar, M., Lorfèvre, E., Plettemeier, D., Soucek, J., Steller, M., Štverák, Š., Trávnícek, P., Vaivads, A., Horbury, T.S., O'Brien, H., Angelini, V., Evans, V., 2021. Statistical study of electron density turbulence and ion-cyclotron waves in the inner heliosphere: Solar orbiter observations. arXiv e-prints , arXiv:2105.07790arXiv:2105.07790.

Carbone, V., Lepreti, F., Veltri, P., 2003. Barriers for transport in turbulent plasmas. Phys. Rev. Lett. 90, 055001. URL: https://link.aps.org/doi/10.1103/PhysRevLett.90.055001, doi:10.1103/PhysRevLett.90.055001.

Carbone, V., Marino, R., Sorriso-Valvo, L., Noullez, A., Bruno, R., 2009a. Scaling laws of turbulence and heating of fast solar wind: The role of density fluctuations. Phys. Rev. Lett. 103, 061102. URL: https://link.aps.org/doi/10.1103/PhysRevLett.103.061102, doi:10.1103/PhysRevLett.103.061102.

Carbone, V., Sorriso-Valvo, L., Marino, R., 2009b. On the turbulent energy cascade in anisotropic magnetohydrodynamic turbulence. Europhysics Letters 88, 25001. URL: https://dx.doi.org/10.1209/0295-5075/88/25001, doi:10.1209/0295-5075/88/25001.

Carbone, V., Telloni, D., Lepreti, F., Vecchio, A., 2022. High-frequency Magnetic Fluctuations in Space Plasmas and the Role of Electron Landau Damping. *Astrophys. J. Lett.* 924, L26. doi:10.3847/2041-8213/ac4740.

Carrington, R.C., 1859. Description of a singular appearance seen in the Sun on september 1, 1859. *Mon. Not. Roy. Astron. Soc.* 20, 13–15. doi:10.1093/mnras/20.1.13.

Casciola, C.M., Gualtieri, P., Benzi, R., Piva, R., 2003. Scale-by-scale budget and similarity laws for shear turbulence. Journal of Fluid Mechanics 476, 105–114. doi:10.1017/S0022112002003142.

Cerri, S.S., Franci, L., Califano, F., Landi, S., Hellinger, P., 2017. Plasma turbulence at ion scales: a comparison between particle in cell and eule-

rian hybrid-kinetic approaches. Journal of Plasma Physics 83, 705830202. doi:10.1017/S0022377817000265.

Chandran, B.D.G., 2018. Parametric instability, inverse cascade and the $1/f$ range of solar-wind turbulence. Journal of Plasma Physics 84, 905840106. doi:10.1017/S0022377818000016.

Chandrasekhar, S., 1951. The Invariant Theory of Isotropic Turbulence in Magneto-Hydrodynamics. Proc. R. Soc. Lond. A 204, 435–449.

Chandrasekhar, S., 1961. Hydrodynamic and hydromagnetic stability.

Chang, T., Tam, S.W.Y., Wu, C.c., 2004. Complexity induced anisotropic bimodal intermittent turbulence in space plasmas. Physics of Plasmas 11, 1287–1299. URL: https://doi.org/10.1063/1.1667496, doi:10.1063/1.1667496, arXiv:https://doi.org/10.1063/1.1667496.

Chapman, S., Ferraro, V.C.A., 1931. A new theory of magnetic storms. Terrestrial Magnetism and Atmospheric Electricity 36, 171–186. URL: https://agupubs.onlinelibrary.wiley.com/doi/abs/10.1029/TE036i003p00171, doi:https://doi.org/10.1029/TE036i003p00171.

Chapman, S., Zirin, H., 1957. Notes on the solar corona and the terrestrial ionosphere. Smithsonian Contributions to Astrophysics 2, 1–14.

Chen, C.H.K., 2016. Recent progress in astrophysical plasma turbulence from solar wind observations. Journal of Plasma Physics 82, 535820602. doi:10.1017/S0022377816001124, arXiv:1611.03386.

Chen, C.H.K., Bale, S.D., Bonnell, J.W., Borovikov, D., Bowen, T.A., Burgess, D., Case, A.W., Chandran, B.D.G., de Wit, T.D., Goetz, K., Harvey, P.R., Kasper, J.C., Klein, K.G., Korreck, K.E., Larson, D., Livi, R., MacDowall, R.J., Malaspina, D.M., Mallet, A., McManus, M.D., Moncuquet, M., Pulupa, M., Stevens, M.L., Whittlesey, P., 2020. The evolution and role of solar wind turbulence in the inner heliosphere. *Astrophys. J. Suppl.* 246, 53. doi:10.3847/1538-4365/ab60a3, arXiv:1912.02348.

Chen, C.H.K., Klein, K.G., Howes, G.G., 2019. Evidence for electron landau damping in space plasma turbulence. Nature Communications 10, 740. doi:10.1038/s41467-019-08435-3, arXiv:1902.05785.

Chen, C.H.K., Sorriso-Valvo, L., Šafránková, J., Němeček, Z., 2014. Intermittency of solar wind density fluctuations from ion to electron scales. The Astrophysical Journal Letters 789, L8. URL: http://stacks.iop.org/2041-8205/789/i=1/a=L8.

Chen, S.H., Kivelson, M.G., 1993. On nonsinusoidal waves at the earth's magnetopause. Geophysical Research Letters 20, 2699–2702. URL: https://agupubs.onlinelibrary.wiley.com/doi/abs/10.1029/93GL02622, doi:https://doi.org/10.1029/93GL02622.

Chepurnov, A., Lazarian, A., 2010. Extending the big power law in the sky with turbulence spectra from wisconsin hα mapper data. The Astrophysical Journal 710, 853–858. URL: https://doi.org/10.1088/0004-637x/710/1/853, doi:10.1088/0004-637x/710/1/853.

Chhiber, R., Usmanov, A.V., Matthaeus, W.H., Parashar, T.N., Goldstein, M.L., 2019. Contextual predictions for Parker Solar Probe. II. turbulence properties and Taylor hypothesis. The Astrophysical Journal Supplement Series 242, 12. URL: https://doi.org/10.3847/1538-4365/ab16d7, doi:10.3847/1538-4365/ab16d7.

Coburn, J.T., Forman, M.A., Smith, C.W., Vasquez, B.J., Stawarz, J.E., 2015. Third-moment descriptions of the interplanetary turbulent cascade, intermittency and back transfer. Philosophical Transactions of the Royal Society A: Mathematical, Physical and Engineering Sciences 373, 20140150. URL: https://royalsocietypublishing.org/doi/abs/10.1098/rsta.2014.0150, doi:10.1098/rsta.2014.0150.

Coburn, J.T., Smith, C.W., Vasquez, B.J., Forman, M.A., Stawarz, J.E., 2014. Variable cascade dynamics and intermittency in the solar wind at 1 AU. The Astrophysical Journal 786, 52. URL: https://doi.org/10.1088/0004-637x/786/1/52, doi:10.1088/0004-637x/786/1/52.

Coburn, J.T., Smith, C.W., Vasquez, B.J., Stawarz, J.E., Forman, M.A., 2012. The turbulent cascade and proton heating in the solar wind during solar minimum. *Astrophys. J.* 754, 93. doi:10.1088/0004-637X/754/2/93.

Cohen, O., Drake, J.J., Glocer, A., Garraffo, C., Poppenhaeger, K., Bell, J.M., Ridley, A.J., Gombosi, T.I., 2014. Magnetospheric structure and

atmospheric Joule heating of habitable planets orbiting M-dwarf stars. The Astrophysical Journal 790, 57. URL: https://doi.org/10.1088/0004-637x/790/1/57, doi:10.1088/0004-637x/790/1/57.

Coleman, Jr., P.J., 1968. Turbulence, viscosity, and dissipation in the solar-wind plasma. *Astrophys. J.* 153, 371. doi:10.1086/149674.

Consolini, G., 2012. On the passive nature of proton temperature in solar wind turbulence, in: Leubner, M.P., Vörös, Z. (Eds.), Multi-scale Dynamical Processes in Space and Astrophysical Plasmas, Springer Berlin Heidelberg, Berlin, Heidelberg. pp. 187–193.

Consolini, G., Alberti, T., Carbone, V., 2020. On Yaglom's law for the interplanetary proton density and temperature fluctuations in solar wind turbulence. Entropy 22. URL: https://www.mdpi.com/1099-4300/22/12/1419, doi:10.3390/e22121419.

Consolini, G., De Michelis, P., Alberti, T., Coco, I., Giannattasio, F., Tozzi, R., Carbone, V., 2020. Intermittency and passive scalar nature of electron density fluctuations in the high-latitude ionosphere at swarm altitude. *Geophys. Res. Lett.* 47, e89628. doi:10.1029/2020GL089628.

Costa, A., Osborne, A.R., Resio, D.T., Alessio, S., Chrivì, E., Saggese, E., Bellomo, K., Long, C.E., 2014. Soliton turbulence in shallow water ocean surface waves. Phys. Rev. Lett. 113, 108501. URL: https://link.aps.org/doi/10.1103/PhysRevLett.113.108501, doi:10.1103/PhysRevLett.113.108501.

Cozzani, G., 2020. Microphysics of magnetic reconnection in near-Earth space – Spacecraft observations and numerical simulations. Springer International Publishing. doi:10.1007/978-3-030-56142-0.

Cranmer, S.R., Matthaeus, W.H., Breech, B.A., Kasper, J.C., 2009. Empirical constraints on proton and electron heating in the fast solar wind. The Astrophysical Journal 702, 1604. URL: https://dx.doi.org/10.1088/0004-637X/702/2/1604, doi:10.1088/0004-637X/702/2/1604.

Danaila, L., Anselmet, F., Zhou, T., Antonia, R.A., 2001a. Turbulent energy scale budget equations in a fully developed channel flow. Journal of Fluid Mechanics 430, 87–109.

Danaila, L., Anselmet, F., Zhou, T., Antonia, R.A., 2001b. Turbulent energy scale budget equations in a fully developed channel flow. Journal of Fluid Mechanics 430, 87–109. doi:10.1017/S0022112000002767.

David, V., Galtier, S., Sahraoui, F., Hadid, L.Z., 2022. Energy Transfer, Discontinuities, and Heating in the Inner Heliosphere Measured with a Weak and Local Formulation of the Politano-Pouquet Law. *Astrophys. J.* 927, 200. doi:10.3847/1538-4357/ac524b, arXiv:2201.02377.

Davies, C.J., Constable, C.G., 2020. Rapid geomagnetic changes inferred from earth observations and numerical simulations. Nature Communications 11, 3371. doi:10.1038/s41467-020-16888-0.

de Karman, T., Howarth, L., 1938. On the statistical theory of isotropic turbulence. Proceedings of the Royal Society of London Series A 164, 192–215. doi:10.1098/rspa.1938.0013.

Di Mare, F., Sorriso-Valvo, L., Retinò, A., Malara, F., Hasegawa, H., 2019. Evolution of turbulence in the Kelvin-Helmholtz instability in the terrestrial magnetopause. Atmosphere 10, 561. doi:10.3390/atmos10090561.

Dmitruk, P., Matthaeus, W.H., 2007. Low-frequency 1/f fluctuations in hydrodynamic and magnetohydrodynamic turbulence. Phys. Rev. E 76, 036305. URL: https://link.aps.org/doi/10.1103/PhysRevE.76.036305, doi:10.1103/PhysRevE.76.036305.

Dmitruk, P., Mininni, P., Pouquet, A., Servidio, S., Matthaeus, W., 2011. Emergence of very long time fluctuations and 1 / f noise in ideal flows. Physical review. E, Statistical, nonlinear, and soft matter physics 83, 066318. doi:10.1103/PHYSREVE.83.066318.

Dobrowolny, M., Mangeney, A., Veltri, P., 1980. Fully developed anisotropic hydromagnetic turbulence in interplanetary space. *Phys. Rev. Lett.* 45, 144–147.

Dorelli, J.C., Glocer, A., Collinson, G., Tóth, G., 2015. The role of the Hall effect in the global structure and dynamics of planetary magnetospheres: Ganymede as a case study. Journal of Geophysical Research: Space Physics 120, 5377–5392. doi:https://doi.org/10.1002/2014JA020951.

Drake, J.F., Agapitov, O., Swisdak, M., Badman, S.T., Bale, S.D., Horbury, T.S., Kasper, J.C., MacDowall, R.J., Mozer, F.S., Phan, T.D., Pulupa, M., Szabo, A., Velli, M., 2021. Switchbacks as signatures of magnetic flux ropes generated by interchange reconnection in the corona. *Astron. Astrophys.* 650, A2. doi:10.1051/0004-6361/202039432, arXiv:2009.05645.

Duchon, J., Robert, R., 1999. Inertial energy dissipation for weak solutions of incompressible euler and navier-stokes equations. Nonlinearity 13, 249–255. doi:10.1088/0951-7715/13/1/312.

Dudok de Wit, T., 2004. Can high-order moments be meaningfully estimated from experimental turbulence measurements? *Phys. Rev. E* 70, 055302.

Dudok de Wit, T., Krasnoselskikh, V.V., Bale, S.D., Bonnell, J.W., Bowen, T.A., Chen, C.H.K., Froment, C., Goetz, K., Harvey, P.R., Jagarlamudi, V.K., Larosa, A., MacDowall, R.J., Malaspina, D.M., Matthaeus, W.H., Pulupa, M., Velli, M., Whittlesey, P.L., 2020. Switchbacks in the near-sun magnetic field: Long memory and impact on the turbulence cascade. *Astrophys. J. Suppl.* 246, 39. doi:10.3847/1538-4365/ab5853, arXiv:1912.02856.

Dunlop, M.W., Dong, X.C., Wang, T.Y., Eastwood, J.P., Robert, P., Haaland, S., Yang, Y.Y., Escoubet, P., Rong, Z.J., Shen, C., Fu, H.S., De Keyser, J., 2021. Curlometer technique and applications. Journal of Geophysical Research: Space Physics 126, e2021JA029538. URL: https://agupubs.onlinelibrary.wiley.com/doi/abs/10.1029/2021JA029538, doi:https://doi.org/10.1029/2021JA029538. e2021JA029538 2021JA029538.

D'Amicis, R., Perrone, D., Bruno, R., Velli, M., 2021. On Alfvénic slow wind: A journey from the Earth back to the Sun. Journal of Geophysical Research: Space Physics 126, e2020JA028996. URL: https://agupubs.onlinelibrary.wiley.com/doi/abs/10.1029/2020JA028996, doi:https://doi.org/10.1029/2020JA028996, arXiv:https://agupubs.onlinelibrary.wiley.com/doi/pdf/10.1029/2020JA028996. e2020JA028996 2020JA028996.

Elmegreen, B.G., Scalo, J., 2004. Interstellar turbulence i: Observations and processes. Annu. Rev. Astron. Astrophys. 42, 211–273. doi:10.1146/annurev.astro.41.011802.094859, arXiv:astro-ph/0404451.

Elsasser, W.M., 1950. The hydromagnetic equations. Phys. Rev. 79, 183–183. URL: https://link.aps.org/doi/10.1103/PhysRev.79.183, doi:10.1103/PhysRev.79.183.

Ergun, R.E., Goodrich, K.A., Wilder, F.D., Ahmadi, N., Holmes, J.C., Eriksson, S., Stawarz, J.E., Nakamura, R., Genestreti, K.J., Hesse, M., Burch, J.L., Torbert, R.B., Phan, T.D., Schwartz, S.J., Eastwood, J.P., Strangeway, R.J., Le Contel, O., Russell, C.T., Argall, M.R., Lindqvist, P.A., Chen, L.J., Cassak, P.A., Giles, B.L., Dorelli, J.C., Gershman, D., Leonard, T.W., Lavraud, B., Retino, A., Matthaeus, W., Vaivads, A., 2018. Magnetic reconnection, turbulence, and particle acceleration: Observations in the earth's magnetotail. Geophysical Research Letters 45, 3338–3347. URL: https://agupubs.onlinelibrary.wiley.com/doi/abs/10.1002/2018GL076993, doi:https://doi.org/10.1002/2018GL076993.

Eriksson, S., Lavraud, B., Wilder, F.D., Stawarz, J.E., Giles, B.L., Burch, J.L., Baumjohann, W., Ergun, R.E., Lindqvist, P.A., Magnes, W., Pollock, C.J., Russell, C.T., Saito, Y., Strangeway, R.J., Torbert, R.B., Gershman, D.J., Khotyaintsev, Y.V., Dorelli, J.C., Schwartz, S.J., Avanov, L., Grimes, E., Vernisse, Y., Sturner, A.P., Phan, T.D., Marklund, G.T., Moore, T.E., Paterson, W.R., Goodrich, K.A., 2016. Magnetospheric multiscale observations of magnetic reconnection associated with Kelvin-Helmholtz waves. Geophysical Research Letters 43, 5606–5615. URL: https://agupubs.onlinelibrary.wiley.com/doi/abs/10.1002/2016GL068783, doi:https://doi.org/10.1002/2016GL068783.

Escoubet, C.P., Schmidt, R., Goldstein, M.L., 1997. Cluster - science and mission overview. *Space Sci. Rev.* 79, 11–32. doi:10.1023/A:1004923124586.

Eyink, G.L., 2005. Locality of turbulent cascades. Physica D: Nonlinear Phenomena 207, 91–116. doi:https://doi.org/10.1016/j.physd.2005.05.018.

Eyink, G.L., 2007–2008. Turbulence theory, course notes. The John Hopkins University.

Eyink, G.L., 2008. Dissipative anomalies in singular euler flows. Physica D: Nonlinear Phenomena 237, 1956–1968. doi:https://doi.org/10.1016/j.physd.2008.02.005.

Eyink, G.L., Drivas, T.D., 2018. Cascades and dissipative anomalies in compressible fluid turbulence. Phys. Rev. X 8, 011022. URL: https://link.aps.org/doi/10.1103/PhysRevX.8.011022, doi:10.1103/PhysRevX.8.011022.

Faganello, M., Califano, F., 2017. Magnetized Kelvin–Helmholtz instability: theory and simulations in the earth's magnetosphere context. Journal of Plasma Physics 83, 535830601. doi:10.1017/S0022377817000770.

Fahr, H.J., 2002. Solar wind heating by an embedded quasi-isothermal pick-up ion fluid. Annales Geophysicae 20, 1509–1518. doi:10.5194/angeo-20-1509-2002.

Falgarone, E., Pety, J., Hily-Blant, P., 2009. Intermittency of interstellar turbulence: extreme velocity-shears and co emission on milliparsec scale. *Astron. Astrophys.* 507, 355–368. doi:10.1051/0004-6361/200810963, arXiv:0910.1766.

Falgarone, E., Puget, J.L., 1995. The intermittency of turbulence in interstellar clouds: implications for the gas kinetic temperature and decoupling of heavy particles from the gas motions. *Astron. Astrophys.* 293, 840–852.

Fan, S., He, J., Yan, L., Tomczyk, S., Tian, H., Song, H., Wang, L., Zhang, L., 2018. Turbulence and heating in the flank and wake regions of a coronal mass ejection. *Solar Phys.* 293, 6. doi:10.1007/s11207-017-1221-1.

Farge, M., 1991. Wavelet analysis of coherent structures in two-dimensional turbulent flows. Physics of Fluids A 3, 2029–2029. doi:10.1063/1.4738850.

Fargette, N., Lavraud, B., Rouillard, A.P., Réville, V., Dudok De Wit, T., Froment, C., Halekas, J.S., Phan, T.D., Malaspina, D.M., Bale, S.D., Kasper, J.C., Louarn, P., Case, A.W., Korreck, K.E., Larson, D.E., Pulupa, M., Stevens, M.L., Whittlesey, P.L., Berthomier, M., 2021. Characteristic scales of magnetic switchback patches near the sun and their possible association with solar supergranulation and granulation. *Astrophys. J.* 919, 96. doi:10.3847/1538-4357/ac1112, arXiv:2109.01519.

Federrath, C., 2016. On the universality of interstellar filaments: theory meets simulations and observations. Monthly Notices of the Royal Astro-

nomical Society 457, 375–388. URL: https://doi.org/10.1093/mnras/stv2880, doi:10.1093/mnras/stv2880.

Federrath, C., Klessen, R.S., 2012. The star formation rate of turbulent magnetized clouds: comparing heory, simulations and observations. The Astrophysical Journal 761, 156. URL: https://doi.org/10.1088/0004-637x/761/2/156, doi:10.1088/0004-637x/761/2/156.

Federrath, C., Klessen, R.S., Iapichino, L., Beattie, J.R., 2021. The sonic scale of interstellar turbulence. Nature Astronomy 5, 365–371. doi:10.1038/s41550-020-01282-z, arXiv:2011.06238.

Feraco, F., Marino, R., Primavera, L., Pumir, A., Mininni, P.D., Rosenberg, D., Pouquet, A., Foldes, R., Lévêque, E., Camporeale, E., Cerri, S., Asokan, H.C., Chau, J., Bertoglio, J., Salizzoni, P., Marro, M., 2021. Connecting large-scale velocity and temperature bursts with small-scale intermittency in stratified turbulence. Eur. Phys. Lett. 135, 14001.

Feraco, F., Marino, R., Pumir, A., Primavera, L., Mininni, P.D., Pouquet, A., Rosenberg, D., 2018. Vertical drafts and mixing in stratified turbulence: sharp transition with Froude number. Eur. Phys. Lett. 123, 44002.

Ferrand, R., 2021. Multi-scale compressible turbulence in astrophysical plasmas viewed through theoretical, numerical and observational methods. Ph.D. thesis. Université Paris-Saclay. URL: https://tel.archives-ouvertes.fr/tel-03545797.

Ferrand, R., Galtier, S., Sahraoui, F., 2021a. A compact exact law for compressible isothermal Hall magnetohydrodynamic turbulence. Journal of Plasma Physics 87, 905870220. doi:10.1017/S0022377821000374.

Ferrand, R., Galtier, S., Sahraoui, F., Federrath, C., 2020. Compressible turbulence in the interstellar medium: New insights from a high-resolution supersonic turbulence simulation. The Astrophysical Journal 904, 160. URL: https://doi.org/10.3847/1538-4357/abb76e, doi:10.3847/1538-4357/abb76e.

Ferrand, R., Galtier, S., Sahraoui, F., Meyrand, R., Andrés, N., Banerjee, S., 2019. On exact laws in incompressible Hall magnetohydrodynamic turbulence. *Astrophys. J.* 881, 50. doi:10.3847/1538-4357/ab2be9, arXiv:1905.06110.

Ferrand, R., Sahraoui, F., Galtier, S., Andrés, N., Mininni, P., Dmitruk, P., 2022. An in-depth numerical study of exact laws for compressible Hall magnetohydrodynamic turbulence. The Astrophysical Journal 927, 205. URL: https://doi.org/10.3847/1538-4357/ac517a, doi:10.3847/1538-4357/ac517a.

Ferrand, R., Sahraoui, F., Laveder, D., Passot, T., Sulem, P.L., Galtier, S., 2021b. Fluid energy cascade rate and kinetic damping: New insight from 3d landau-fluid simulations. The Astrophysical Journal 923, 122. URL: https://doi.org/10.3847/1538-4357/ac2bfb, doi:10.3847/1538-4357/ac2bfb.

Fisk, L.A., Kasper, J.C., 2020. Global circulation of the open magnetic flux of the sun. The Astrophysical Journal Letters 894, L4. URL: https://doi.org/10.3847/2041-8213/ab8acd, doi:10.3847/2041-8213/ab8acd.

Fleck, R.C.J., 1996. Scaling relations for the turbulent, non–self-gravitating, neutral component of the interstellar medium. *Astrophys. J.* 458, 739. doi:10.1086/176853.

Foldes, R., Del Corpo, A., Pietropaolo, E., Vellante, M., 2021. Assessing machine learning techniques for identifying field line resonance frequencies from cross-phase spectra. Journal of Geophysical Research: Space Physics 126, e2020JA029008. URL: https://agupubs.onlinelibrary.wiley.com/doi/abs/10.1029/2020JA029008, doi:https://doi.org/10.1029/2020JA029008.

Foldes, R., Lévêque, E., Marino, R., Pietropaolo, E., De Rosis, A., Telloni, D., Feraco, F., 2022. Efficient kinetic lattice Boltzmann simulation of three-dimensional Hall-mhd. Journal of Plasma Physics (in preparation) .

Forveille, T., Shore, S., 2020. The solar orbiter mission. Astronomy & Astrophysics 642, E1.

Foullon, C., Verwichte, E., Nakariakov, V.M., Nykyri, K., Farrugia, C.J., 2011. Magnetic Kelvin-Helmholtz instability at the Sun. *Astrophys. J. Lett.* 729, L8. doi:10.1088/2041-8205/729/1/L8.

Fox, N.J., Velli, M.C., Bale, S.D., Decker, R., Driesman, A., Howard, R.A., Kasper, J.C., Kinnison, J., Kusterer, M., Lario, D., Lockwood, M.K.,

McComas, D.J., Raouafi, N.E., Szabo, A., 2016. The Solar Probe Plus mission: humanity's first visit to our star. *Space Sci. Rev.* 204, 7–48. doi:10.1007/s11214-015-0211-6.

Fraedrich, K., Blender, R., 2003. Scaling of atmosphere and ocean temperature correlations in observations and climate models. Phys. Rev. Lett. 90, 108501. URL: https://link.aps.org/doi/10.1103/PhysRevLett.90.108501, doi:10.1103/PhysRevLett.90.108501.

Franci, L., Stawarz, J.E., Papini, E., Hellinger, P., Nakamura, T., Burgess, D., Landi, S., Verdini, A., Matteini, L., Ergun, R., Contel, O.L., Lindqvist, P.A., 2020. Modeling MMS observations at the earth's magnetopause with hybrid simulations of Alfvénic turbulence. The Astrophysical Journal 898, 175. URL: https://doi.org/10.3847/1538-4357/ab9a47, doi:10.3847/1538-4357/ab9a47.

Franci, L., Verdini, A., Matteini, L., Landi, S., Hellinger, P., 2015. Solar wind turbulence from MHD to sub-ion scales: high-resolution hybrid simulations. The Astrophysical Journal 804, L39. URL: https://doi.org/10.1088/2041-8205/804/2/l39, doi:10.1088/2041-8205/804/2/l39.

Fraternale, F., Gallana, L., Iovieno, M., Opher, M., Richardson, J.D., Tordella, D., 2016. Turbulence in the solar wind: spectra from voyager 2 data at 5 AU. Physica Scripta 91, 023011. URL: https://doi.org/10.1088/0031-8949/91/2/023011, doi:10.1088/0031-8949/91/2/023011.

Fraternale, F., Pogorelov, N.V., Richardson, J.D., Tordella, D., 2019. Magnetic turbulence spectra and intermittency in the heliosheath and in the local interstellar medium. The Astrophysical Journal 872, 40. URL: https://doi.org/10.3847/1538-4357/aafd30, doi:10.3847/1538-4357/aafd30.

Fraternale, F., Zhao, L., Pogorelov, N.V., Sorriso-Valvo, L., Redfield, S., Zhang, M., Ghanbari, K., Florinski, V., Chen, T.Y., 2022. Exploring turbulence from the sun to the local interstellar medium: Current challenges and perspectives for future space missions. Frontiers in Astronomy and Space Sciences 9. URL: https://www.frontiersin.org/articles/10.3389/fspas.2022.1064098, doi:10.3389/fspas.2022.1064098.

Freeman, J.W., Totten, T., Arya, S., 1992. A determination of the polytropic index of the free streaming solar wind using improved temperature and density radial power-law indices. EOS Trans. AGU 73.

Friedrich, J., 2020. Probability density functions in homogeneous and isotropic magneto-hydrodynamic turbulence. Atmosphere 11. URL: https://www.mdpi.com/2073-4433/11/4/382, doi:10.3390/atmos11040382.

Friedrich, J., Homann, H., Schäfer, T., Grauer, R., 2016. Longitudinal and transverse structure functions in high reynolds-number magneto-hydrodynamic turbulence. New J. Phys. 18, 125008.

Frisch, U., 1995. Turbulence: The Legacy of A.N. Kolmogorov. Cambridge University Press.

Frisch, U., Sornette, D., 1997. Extreme deviations and applications. J. Phys. I France 7, 1155–1171. URL: https://doi.org/10.1051/jp1:1997114, doi:10.1051/jp1:1997114.

Frisch, U., Sulem, P.L., Nelkin, M., 1978. A simple dynamical model of intermittent fully developed turbulence. *J. Fluid Mech.* 87, 719–736.

Galtier, S., 2008. von Kármán-Howarth equations for Hall magnetohydrodynamic flows. Phys. Rev. E 77, 015302. URL: https://link.aps.org/doi/10.1103/PhysRevE.77.015302, doi:10.1103/PhysRevE.77.015302.

Galtier, S., 2011. Third-order Elsässer moments in axisymmetric MHD turbulence. Comptes Rendus Physique 12, 151–159. URL: https://www.sciencedirect.com/science/article/pii/S1631070510001581, doi:https://doi.org/10.1016/j.crhy.2010.11.006.

Galtier, S., 2016. Introduction to Modern Magnetohydrodynamics.

Galtier, S., 2018. On the origin of the energy dissipation anomaly in (Hall) magnetohydrodynamics. Journal of Physics A: Mathematical and Theoretical 51, 205501. URL: https://doi.org/10.1088/1751-8121/aabbb5, doi:10.1088/1751-8121/aabbb5.

Galtier, S., Banerjee, S., 2011. Exact relation for correlation functions in compressible isothermal turbulence. Phys. Rev. Lett. 107, 134501.

URL: https://link.aps.org/doi/10.1103/PhysRevLett.107.134501, doi:10.1103/PhysRevLett.107.134501.

Galtier, S., Buchlin, E., 2007. Multiscale Hall-magnetohydrodynamic turbulence in the solar wind. The Astrophysical Journal 656, 560–566. URL: https://doi.org/10.1086/510423, doi:10.1086/510423.

Galtier, S., Nazarenko, S.V., 2017. Turbulence of weak gravitational waves in the early universe. Phys. Rev. Lett. 119, 221101. URL: https://link.aps.org/doi/10.1103/PhysRevLett.119.221101, doi:10.1103/PhysRevLett.119.221101.

Gary, S.P., 1993. Theory of Space Plasma Microinstabilities.

Germano, M., 1992. Turbulence: the filtering approach. Journal of Fluid Mechanics 238, 325–336. doi:10.1017/S0022112092001733.

Gogoberidze, G., Perri, S., Carbone, V., 2013. The Yaglom law in the expanding solar wind. The Astrophysical Journal 769, 111. URL: https://doi.org/10.1088/0004-637x/769/2/111, doi:10.1088/0004-637x/769/2/111.

Goldstein, B.E., Neugebauer, M., Phillips, J.L., Bame, S., Gosling, J.T., McComas, D., Wang, Y.M., Sheeley, N.R., Suess, S.T., 1996. Ulysses plasma parameters: Latitudinal, radial, and temporal variations. Astron. Astrophys. 316.

Goldstein, B.E., Smith, E.J., Balogh, A., Horbury, T.S., Goldstein, M.L., Roberts, D.A., 1995. Properties of magnetohydrodynamic turbulence in the solar wind as observed by ulysses at high heliographic latitudes. Geophysical Research Letters 22, 3393–3396. URL: https://agupubs.onlinelibrary.wiley.com/doi/abs/10.1029/95GL03183, doi:https://doi.org/10.1029/95GL03183.

Goldstein, M.L., Roberts, D.A., Deane, A., 2003. The effect of microstreams on Alfvénic fluctuations in the solar wind, in: Solar Wind Ten, pp. 405–408. doi:10.1063/1.1618622.

Goldstein, M.L., Wicks, R.T., Perri, S., Sahraoui, F., 2015. Kinetic scale turbulence and dissipation in the solar wind: key observational results and future outlook. Philosophical Transactions of

the Royal Society A: Mathematical, Physical and Engineering Sciences 373, 20140147. URL: https://royalsocietypublishing.org/doi/abs/10.1098/rsta.2014.0147, doi:10.1098/rsta.2014.0147, arXiv:https://royalsocietypublishing.org/doi/pdf/10.1098/rsta.2014.0147.

Gombosi, T.I., van der Holst, B., Manchester, W.B., Sokolov, I.V., 2018. Extended MHD modeling of the steady solar corona and the solar wind. Living Reviews in Solar Physics 15, 4. doi:10.1007/s41116-018-0014-4.

Gómez, D.O., Mininni, P.D., Dmitruk, P., 2010. Hall-magnetohydrodynamic small-scale dynamos. Phys. Rev. E 82, 036406. doi:10.1103/PhysRevE.82.036406.

González-Morales, P.A., Khomenko, E., Cally, P.S., 2019. Fast-to-Alfvén mode conversion mediated by Hall current. II. application to the solar atmosphere. Astrophysical Journal 870, 94. doi:10.3847/1538-4357/aaf1a9.

Gosling, J.T., Thomsen, M.F., Bame, S.J., Russell, C.T., 1986. Accelerated plasma flows at the near-tail magnetopause. *J. Geophys. Res.* 91, 3029–3041. doi:10.1029/JA091iA03p03029.

Grappin, R., Velli, M., Mangeney, A., 1993. Nonlinear wave evolution in the expanding solar wind. *Phys. Rev. Lett.* 70, 2190–2193. doi:10.1103/PhysRevLett.70.2190.

Grasset, O., Dougherty, M., Coustenis, A., Bunce, E., Erd, C., Titov, D., Blanc, M., Coates, A., Drossart, P., Fletcher, L., Hussmann, H., Jaumann, R., Krupp, N., Lebreton, J.P., Prieto-Ballesteros, O., Tortora, P., Tosi, F., Van Hoolst, T., 2013. JUpiter ICy moons Explorer (JUICE): An ESA mission to orbit ganymede and to characterise the jupiter system. Planetary and Space Science 78, 1–21. URL: https://www.sciencedirect.com/science/article/pii/S0032063312003777, doi:https://doi.org/10.1016/j.pss.2012.12.002.

Greco, A., Chuychai, P., Matthaeus, W.H., Servidio, S., Dmitruk, P., 2008. Intermittent MHD structures and classical discontinuities. Geophysical Research Letters 35. URL: https://agupubs.onlinelibrary.wiley.com/doi/abs/10.1029/2008GL035454, doi:https://doi.org/10.1029/2008GL035454.

Greco, A., Perri, S., 2014. Identification of high shears and compressive discontinuities in the inner heliosphere. The Astrophysical Journal 784, 163. URL: https://doi.org/10.1088/0004-637x/784/2/163, doi:10.1088/0004-637x/784/2/163.

Gringauz, K.I., Bezrukikh, V.V., Ozerov, V.D., Rybshinskiy, R.E., 1960. Soviet Phys. Docklady, English version 5, 361.

Hadid, L.Z., Sahraoui, F., Galtier, S., 2017. Energy cascade rate in compressible fast and slow solar wind turbulence. *Astrophys. J.* 838, 9. doi:10.3847/1538-4357/aa603f, arXiv:1612.02150.

Hadid, L.Z., Sahraoui, F., Galtier, S., Huang, S.Y., 2018. Compressible magnetohydrodynamic turbulence in the Earth's magnetosheath: Estimation of the energy cascade rate using in situ spacecraft data. *Phys. Rev. Lett.* 120, 055102. doi:10.1103/PhysRevLett.120.055102, arXiv:1710.04691.

Hadid, L.Z., Sahraoui, F., Kiyani, K.H., Retinò, A., Modolo, R., Canu, P., Masters, A., Dougherty, M.K., 2015. Nature of the MHD and kinetic scale turbulence in the magnetosheath of Saturn: Cassini observations. The Astrophysical Journal 813, L29. URL: https://doi.org/10.1088/2041-8205/813/2/l29, doi:10.1088/2041-8205/813/2/l29.

Hansteen, V.H., Velli, M., 2012. Solar wind models from the chromosphere to 1 AU. *Space Sci. Rev.* 172, 89–121. doi:10.1007/s11214-012-9887-z.

van Haren, H., Cimatoribus, A., Gostiaux, L., 2015. Where large deep-ocean waves break. Geophysical Research Letters 42, 2351–2357. URL: https://agupubs.onlinelibrary.wiley.com/doi/abs/10.1002/2015GL063329, doi:https://doi.org/10.1002/2015GL063329, arXiv:https://agupubs.onlinelibrary.wiley.com/doi/pdf/10.1002/2015GL063329.

Hasegawa, H., Fujimoto, M., Phan, T.D., Rème, H., Balogh, A., Dunlop, M.W., Hashimoto, C., TanDokoro, R., 2004. Transport of solar wind into Earth's magnetosphere through rolled-up Kelvin-Helmholtz vortices. *Nature* 430, 755–758. doi:10.1038/nature02799.

Hellinger, P., Papini, E., Verdini, A., Landi, S., Franci, L., Matteini, L., Montagud-Camps, V., 2021a. Spectral transfer and Karman-Howarth-Monin equations for compressible Hall magnetohydrodynamics. The Astro-

physical Journal 917, 101. URL: https://doi.org/10.3847/1538-4357/ac088f, doi:10.3847/1538-4357/ac088f.

Hellinger, P., Trávníček, P.M., Štverák, Š., Matteini, L., Velli, M., 2013. Proton thermal energetics in the solar wind: Helios reloaded. Journal of Geophysical Research (Space Physics) 118, 1351–1365. doi:10.1002/jgra.50107.

Hellinger, P., Trávníček, P., Kasper, J.C., Lazarus, A.J., 2006. Solar wind proton temperature anisotropy: Linear theory and WIND/SWE observations. Geophysical Research Letters 33. URL: https://agupubs.onlinelibrary.wiley.com/doi/abs/10.1029/2006GL025925, doi:https://doi.org/10.1029/2006GL025925.

Hellinger, P., Verdini, A., Landi, S., Franci, L., Matteini, L., 2018. von Kármán–Howarth equation for Hall magnetohydrodynamics: Hybrid simulations. The Astrophysical Journal 857, L19. URL: https://doi.org/10.3847/2041-8213/aabc06, doi:10.3847/2041-8213/aabc06.

Hellinger, P., Verdini, A., Landi, S., Franci, L., Papini, E., Matteini, L., 2020. On cascade of kinetic energy in compressible hydrodynamic turbulence. arXiv e-prints , arXiv:2004.02726arXiv:2004.02726.

Hellinger, P., Verdini, A., Landi, S., Papini, E., Franci, L., Matteini, L., 2021b. Scale dependence and cross-scale transfer of kinetic energy in compressible hydrodynamic turbulence at moderate Reynolds numbers. Phys. Rev. Fluids 6, 044607. URL: https://link.aps.org/doi/10.1103/PhysRevFluids.6.044607, doi:10.1103/PhysRevFluids.6.044607.

Hennebelle, P., Falgarone, E., 2012. Turbulent molecular clouds. *Astron. Astrophys. Rev.* 20, 55. doi:10.1007/s00159-012-0055-y, arXiv:1211.0637.

Herault, J., Pétrélis, F., Fauve, S., 2015. Experimental observation of 1/f noise in quasi-bidimensional turbulent flows. Europhysics Letters 111, 44002. URL: https://dx.doi.org/10.1209/0295-5075/111/44002, doi:10.1209/0295-5075/111/44002.

Herbert, C., Marino, R., Rosenberg, D., Pouquet, A., 2016. Waves and vortices in the inverse cascade regime of stratified turbulence with or without rotation. Journal of Fluid Mechanics 806, 165–204.

Hernández, C.S., Sorriso-Valvo, L., Bandyopadhyay, R., Chasapis, A., Vásconez, C.L., Marino, R., Pezzi, O., 2021. Impact of switchbacks on turbulent cascade and energy transfer rate in the inner heliosphere. The Astrophysical Journal Letters 922, L11. URL: https://doi.org/10.3847/2041-8213/ac36d1, doi:10.3847/2041-8213/ac36d1.

Hill, R.J., 1997. Applicability of Kolmogorov's and Monin's equations of turbulence. J. Fluid Mech. 353, 67–81.

Hnat, B., Chapman, S.C., Rowlands, G., 2005. Compressibility in solar wind plasma turbulence. *Phys. Rev. Lett.* 94, 204502.

Hollweg, J.V., 1973. Alfvén waves in a two-fluid model of the solar wind. *Astrophys. J.* 181, 547–566. doi:10.1086/152072.

Horbury, T.S., O'Brien, H., Carrasco Blazquez, I., Bendyk, M., Brown, P., Hudson, R., Evans, V., Oddy, T.M., Carr, C.M., Beek, T.J., Cupido, E., Bhattacharya, S., Dominguez, J.A., Matthews, L., Myklebust, V.R., Whiteside, B., Bale, S.D., Baumjohann, W., Burgess, D., Carbone, V., Cargill, P., Eastwood, J., Erdös, G., Fletcher, L., Forsyth, R., Giacalone, J., Glassmeier, K.H., Goldstein, M.L., Hoeksema, T., Lockwood, M., Magnes, W., Maksimovic, M., Marsch, E., Matthaeus, W.H., Murphy, N., Nakariakov, V.M., Owen, C.J., Owens, M., Rodriguez-Pacheco, J., Richter, I., Riley, P., Russell, C.T., Schwartz, S., Vainio, R., Velli, M., Vennerstrom, S., Walsh, R., Wimmer-Schweingruber, R.F., Zank, G., Müller, D., Zouganelis, I., Walsh, A.P., 2020. The solar orbiter magnetometer. *Astron. Astrophys.* 642, A9. doi:10.1051/0004-6361/201937257.

Horbury, T.S., Wicks, R.T., Chen, C.H.K., 2012. Anisotropy in space plasma turbulence: Solar wind observations. *Space Sci. Rev.* 172, 325–342. doi:10.1007/s11214-011-9821-9.

Horbury, T.S., Woolley, T., Laker, R., Matteini, L., Eastwood, J., Bale, S.D., Velli, M., Chandran, B.D.G., Phan, T., Raouafi, N.E., Goetz, K., Harvey, P.R., Pulupa, M., Klein, K.G., de Wit, T.D., Kasper, J.C., Korreck, K.E., Case, A.W., Stevens, M.L., Whittlesey, P., Larson, D., MacDowall, R.J., Malaspina, D.M., Livi, R., 2020. Sharp Alfvénic impulses in the near-sun solar wind. The Astrophysical Journal Supplement Series 246, 45. URL: https://doi.org/10.3847/1538-4365/ab5b15, doi:10.3847/1538-4365/ab5b15.

Horton, W., 1999. Drift waves and transport. Rev. Mod. Phys. 71, 735–778. URL: https://link.aps.org/doi/10.1103/RevModPhys.71.735, doi:10.1103/RevModPhys.71.735.

Hossain, M., Gray, P.C., Pontius, Duane H., J., Matthaeus, W.H., Oughton, S., 1995. Phenomenology for the decay of energy-containing eddies in homogeneous MHD turbulence. Physics of Fluids 7, 2886–2904. doi:10.1063/1.868665.

Howard, R.A., Vourlidas, A., Bothmer, V., Colaninno, R.C., DeForest, C.E., Gallagher, B., Hall, J.R., Hess, P., Higginson, A.K., Korendyke, C.M., Kouloumvakos, A., Lamy, P.L., Liewer, P.C., Linker, J., Linton, M., Penteado, P., Plunkett, S.P., Poirier, N., Raouafi, N.E., Rich, N., Rochus, P., Rouillard, A.P., Socker, D.G., Stenborg, G., Thernisien, A.F., Viall, N.M., 2019. Near-sun observations of an f-corona decrease and k-corona fine structure. *Nature* 576, 232–236. doi:10.1038/s41586-019-1807-x.

Howard, T., 2011. Coronal Mass Ejections: An Introduction. volume 376. doi:10.1007/978-1-4419-8789-1.

Howes, G.G., 2010. A prescription for the turbulent heating of astrophysical plasmas. Monthly Notices of the Royal Astronomical Society: Letters 409, L104–L108. URL: https://doi.org/10.1111/j.1745-3933.2010.00958.x, doi:10.1111/j.1745-3933.2010.00958.x.

Howes, G.G., Cowley, S.C., Dorland, W., Hammett, G.W., Quataert, E., Schekochihin, A.A., 2008. A model of turbulence in magnetized plasmas: Implications for the dissipation range in the solar wind. Journal of Geophysical Research (Space Physics) 113, A05103. doi:10.1029/2007JA012665, arXiv:0707.3147.

Howes, G.G., Klein, K.G., Li, T.C., 2017. Diagnosing collisionless energy transfer using field–particle correlations: Vlasov–Poisson plasmas. Journal of Plasma Physics 83, 705830102. doi:10.1017/S0022377816001197.

Howes, G.G., Tenbarge, J.M., Dorland, W., Quataert, E., Schekochihin, A.A., Numata, R., Tatsuno, T., 2011. Gyrokinetic simulations of solar wind turbulence from ion to electron scales. Physical Review Letters 107, 035004. doi:10.1103/PhysRevLett.107.035004, arXiv:1104.0877.

Howes, G.G., Verniero, J.L., Larson, D.E., Bale, S.D., Kasper, J.C., Goetz, K., Klein, K.G., Whittlesey, P.L., Livi, R., Rahmati, A., Chen, C.H.K., Wilson, L.B., Alterman, B.L., Wicks, R.T., 2022. Revolutionizing our understanding of particle energization in space plasmas using on-board wave-particle correlator instrumentation. Frontiers in Astronomy and Space Sciences 9, 912868. doi:10.3389/fspas.2022.912868.

Huang, S.Y., Sahraoui, F., Deng, X.H., He, J.S., Yuan, Z.G., Zhou, M., Pang, Y., Fu, H.S., 2014. Kinetic turbulence in the terrestrial magnetosheath: Cluster observations. The Astrophysical Journal 789, L28. URL: https://doi.org/10.1088/2041-8205/789/2/l28, doi:10.1088/2041-8205/789/2/l28.

Huba, J.D., 2003. Hall magnetohydrodynamics - a tutorial, in: Büchner, J., Dum, C., Scholer, M. (Eds.), Space Plasma Simulation. volume 615, pp. 166–192.

Hundhausen, A.J., 1972. Coronal Expansion and Solar Wind. Springer-Verlag Berlin Heidelberg.

Hwang, K.J., Goldstein, M.L., Kuznetsova, M.M., Wang, Y., ViñAs, A.F., Sibeck, D.G., 2012. The first in situ observation of Kelvin-Helmholtz waves at high-latitude magnetopause during strongly dawnward interplanetary magnetic field conditions. Journal of Geophysical Research (Space Physics) 117, A08233. doi:10.1029/2011JA017256.

Iroshnikov, P.S., 1964. Turbulence of a conducting fluid in a strong magnetic field. *Sov. Astron.* 7, 566.

Isenberg, P.A., 1986. Interaction of the solar wind with interstellar neutral hydrogen: three-fluid model. *J. Geophys. Res.* 91, 9965–9972. doi:10.1029/JA091iA09p09965.

Jakosky, B.M., Lin, R.P., Grebowsky, J.M., Luhmann, J.G., Mitchell, D.F., Beutelschies, G., Priser, T., Acuna, M., Andersson, L., Baird, D., Baker, D., Bartlett, R., Benna, M., Bougher, S., Brain, D., Carson, D., Cauffman, S., Chamberlin, P., Chaufray, J.Y., Cheatom, O., Clarke, J., Connerney, J., Cravens, T., Curtis, D., Delory, G., Demcak, S., DeWolfe, A., Eparvier, F., Ergun, R., Eriksson, A., Espley, J., Fang, X., Folta, D., Fox, J., Gomez-Rosa, C., Habenicht, S., Halekas, J., Holsclaw, G., Houghton,

M., Howard, R., Jarosz, M., Jedrich, N., Johnson, M., Kasprzak, W., Kelley, M., King, T., Lankton, M., Larson, D., Leblanc, F., Lefevre, F., Lillis, R., Mahaffy, P., Mazelle, C., McClintock, W., McFadden, J., Mitchell, D.L., Montmessin, F., Morrissey, J., Peterson, W., Possel, W., Sauvaud, J.A., Schneider, N., Sidney, W., Sparacino, S., Stewart, A.I.F., Tolson, R., Toublanc, D., Waters, C., Woods, T., Yelle, R., Zurek, R., 2015. The Mars atmosphere and volatile evolution (MAVEN) mission. *Space Sci. Rev.* 195, 3–48. doi:10.1007/s11214-015-0139-x.

Karimabadi, H., Roytershteyn, V., Wan, M., Matthaeus, W.H., Daughton, W., Wu, P., Shay, M., Loring, B., Borovsky, J., Leonardis, E., Chapman, S.C., Nakamura, T.K.M., 2013. Coherent structures, intermittent turbulence, and dissipation in high-temperature plasmas. Physics of Plasmas 20, 012303. doi:10.1063/1.4773205.

Kasper, J.C., Abiad, R., Austin, G., Balat-Pichelin, M., Bale, S.D., Belcher, J.W., Berg, P., Bergner, H., Berthomier, M., Bookbinder, J., Brodu, E., Caldwell, D., Case, A.W., Chandran, B.D.G., Cheimets, P., Cirtain, J.W., Cranmer, S.R., Curtis, D.W., Daigneau, P., Dalton, G., Dasgupta, B., DeTomaso, D., Diaz-Aguado, M., Djordjevic, B., Donaskowski, B., Effinger, M., Florinski, V., Fox, N., Freeman, M., Gallagher, D., Gary, S.P., Gauron, T., Gates, R., Goldstein, M., Golub, L., Gordon, D.A., Gurnee, R., Guth, G., Halekas, J., Hatch, K., Heerikuisen, J., Ho, G., Hu, Q., Johnson, G., Jordan, S.P., Korreck, K.E., Larson, D., Lazarus, A.J., Li, G., Livi, R., Ludlam, M., Maksimovic, M., McFadden, J.P., Marchant, W., Maruca, B.A., McComas, D.J., Messina, L., Mercer, T., Park, S., Peddie, A.M., Pogorelov, N., Reinhart, M.J., Richardson, J.D., Robinson, M., Rosen, I., Skoug, R.M., Slagle, A., Steinberg, J.T., Stevens, M.L., Szabo, A., Taylor, E.R., Tiu, C., Turin, P., Velli, M., Webb, G., Whittlesey, P., Wright, K., Wu, S.T., Zank, G., 2016. Solar wind electrons alphas and protons (sweap) investigation: design of the solar wind and coronal plasma instrument suite for Solar Probe Plus. *Space Sci. Rev.* 204, 131–186. doi:10.1007/s11214-015-0206-3.

Kasper, J.C., Bale, S.D., Belcher, J.W., Berthomier, M., Case, A.W., Chandran, B.D.G., Curtis, D.W., Gallagher, D., Gary, S.P., Golub, L., Halekas, J.S., Ho, G.C., Horbury, T.S., Hu, Q., Huang, J., Klein, K.G., Korreck, K.E., Larson, D.E., Livi, R., Maruca, B., Lavraud, B., Louarn, P., Maksimovic, M., Martinovic, M., McGinnis, D., Pogorelov, N.V., Richardson,

J.D., Skoug, R.M., Steinberg, J.T., Stevens, M.L., Szabo, A., Velli, M., Whittlesey, P.L., Wright, K.H., Zank, G.P., MacDowall, R.J., McComas, D.J., McNutt, R.L., Pulupa, M., Raouafi, N.E., Schwadron, N.A., 2019. Alfvénic velocity spikes and rotational flows in the near-sun solar wind. *Nature* 576, 228–231. doi:10.1038/s41586-019-1813-z.

Kasper, J.C., Klein, K.G., Lichko, E., Huang, J., Chen, C.H.K., Badman, S.T., Bonnell, J., Whittlesey, P.L., Livi, R., Larson, D., Pulupa, M., Rahmati, A., Stansby, D., Korreck, K.E., Stevens, M., Case, A.W., Bale, S.D., Maksimovic, M., Moncuquet, M., Goetz, K., Halekas, J.S., Malaspina, D., Raouafi, N.E., Szabo, A., MacDowall, R., Velli, M., Dudok de Wit, T., Zank, G.P., 2021. Parker Solar Probe enters the magnetically dominated solar corona. *Phys. Rev. Lett.* 127, 255101. doi:10.1103/PhysRevLett.127.255101.

Khotyaintsev, Y.V., Graham, D.B., Norgren, C., Vaivads, A., 2019. Collisionless magnetic reconnection and waves: Progress review. Frontiers in Astronomy and Space Sciences 6, 70. URL: https://www.frontiersin.org/article/10.3389/fspas.2019.00070, doi:10.3389/fspas.2019.00070.

Khotyaintsev, Y.V., Graham, D. B., Vaivads, A., Steinvall, K., Edberg, N. J. T., Eriksson, A. I., Johansson, E. P. G., Sorriso-Valvo, L., Maksimovic, M., Bale, S. D., Chust, T., Krasnoselskikh, V., Kretzschmar, M., Lorfèvre, E., Plettemeier, D., Soucek, J., Steller, M., Stverák, S., Trávnícek, P., Vecchio, A., Horbury, T. S., O´Brien, H., Evans, V., Angelini, V., 2021. Density fluctuations associated with turbulence and waves - first observations by solar orbiter. A&A 656, A19. URL: https://doi.org/10.1051/0004-6361/202140936, doi:10.1051/0004-6361/202140936.

Kida, S., Orszag, S.A., 1990. Energy and spectral dynamics in forced compressible turbulence. Journal of Scientific Computing 5, 85–125.

Kieokaew, R., Lavraud, B., Yang, Y., Matthaeus, W. H., Ruffolo, D., Stawarz, J. E., Aizawa, S., Foullon, C., Génot, V., Pinto, R. F., Fargette, N., Louarn, P., Rouillard, A., Fedorov, A., Penou, E., Owen, C. J., Horbury, T. S., O´Brien, H., Evans, V., Angelini, V., 2021. Solar Orbiter observations of the Kelvin-Helmholtz waves in the solar wind. A&A 656, A12. URL: https://doi.org/10.1051/0004-6361/202140915, doi:10.1051/0004-6361/202140915.

Kilpua, E., Koskinen, H.E.J., Pulkkinen, T.I., 2017. Coronal mass ejections and their sheath regions in interplanetary space. Living Reviews in Solar Physics 14, 5. doi:10.1007/s41116-017-0009-6.

Kilpua, E.K.J., Fontaine, D., Good, S.W., Ala-Lahti, M., Osmane, A., Palmerio, E., Yordanova, E., Moissard, C., Hadid, L.Z., Janvier, M., 2020. Magnetic field fluctuation properties of coronal mass ejection-driven sheath regions in the near-earth solar wind. Annales Geophysicae 38, 999–1017. URL: https://angeo.copernicus.org/articles/38/999/2020/, doi:10.5194/angeo-38-999-2020.

Kilpua, E.K.J., Good, S.W., Ala-Lahti, M., Osmane, A., Fontaine, D., Hadid, L., Janvier, M., Yordanova, E., 2021. Statistical analysis of magnetic field fluctuations in CME-driven sheath regions. Frontiers in Astronomy and Space Sciences 7, 109. doi:10.3389/fspas.2020.610278.

Kivelson, M.G., Russel, C.T., 1995. Introduction to Space Physics. Cambridge University Press.

Kiyani, K., Chapman, S.C., Watkins, N.W., 2009a. Global scale-invariant dissipation in collisionless plasma turbulence. Phys. Rev. E 79, 036109.

Kiyani, K.H., Chapman, S.C., Khotyaintsev, Y.V., Dunlop, M.W., Sahraoui, F., 2009b. Global scale-invariant dissipation in collisionless plasma turbulence. *Phys. Rev. Lett.* 103, 075006.

Kiyani, K.H., Chapman, S.C., Sahraoui, F., Hnat, B., Fauvarque, O., Khotyaintsev, Y.V., 2013. Enhanced magnetic compressibility and isotropic scale invariance at sub-ion larmor scales in solar wind turbulence. *Astrophys. J.* 763, 10. doi:10.1088/0004-637X/763/1/10, arXiv:1008.0525.

Kiyani, K.H., Osman, K.T., Chapman, S.C., 2015. Dissipation and heating in solar wind turbulence: from the macro to the micro and back again. Philosophical Transactions of the Royal Society A: Mathematical, Physical and Engineering Sciences 373, 20140155. doi:10.1098/rsta.2014.0155.

Klein, K.G., Howes, G.G., 2016. Measuring collisionless damping in heliospheric plasmas using field-particle correlations. The Astrophysical Journal 826, L30. URL: https://doi.org/10.3847/2041-8205/826/2/l30, doi:10.3847/2041-8205/826/2/l30.

Klymak, J.M., Pinkel, R., Rainville, L., 2008. Direct breaking of the internal tide near topography: Kaena Ridge and Hawaii. J. Phys. Oceano. 38, 380–399.

Kolmogorov, A.N., 1941. Dissipation of energy in locally isotropic turbulence. *Dokl. Akad. Nauk SSSR* 32, 16–18.

Kolmogorov, A.N., 1962. A refinement of previous hypotheses concerning the local structure of turbulence in a viscous incompressible fluid at high reynolds number. *J. Fluid Mech.* 13, 82–85.

Kowal, G., Lazarian, A., 2007. Scaling relations of compressible MHD turbulence. The Astrophysical Journal 666, L69–L72. URL: https://doi.org/10.1086/521788, doi:10.1086/521788.

Kraichnan, R.H., 1965. Inertial-range spectrum of hydromagnetic turbulence. *Phys. of Fluids* 8, 1385–1387.

Kraichnan, R.H., Nagarajan, S., 1967. Growth of turbulent magnetic fields. Phys. Fluids 10, 859–870.

Kritsuk, A.G., Norman, M.L., Padoan, P., Wagner, R., 2007. The statistics of supersonic isothermal turbulence. The Astrophysical Journal 665, 416–431. URL: https://doi.org/10.1086/519443, doi:10.1086/519443.

Kuzzay, D., Alexandrova, O., Matteini, L., 2019. Local approach to the study of energy transfers in incompressible magnetohydrodynamic turbulence. Phys. Rev. E 99, 053202. URL: https://link.aps.org/doi/10.1103/PhysRevE.99.053202, doi:10.1103/PhysRevE.99.053202.

Lai, C.C.K., Charonko, J.J., Prestridge, K., 2018. A Kármán–Howarth–Monin equation for variable-density turbulence. Journal of Fluid Mechanics 843, 382–418. doi:10.1017/jfm.2018.125.

Landau, L., 1936. Kinetic equation for the Coulomb effect. Phys. Z. Sowjet. 10, 154.

Landi, S., Hellinger, P., Velli, M., 2006. Heliospheric magnetic field polarity inversions driven by radial velocity field structures. Geophysical Research Letters 33. URL: https://agupubs.onlinelibrary.wiley.com/doi/abs/10.1029/2006GL026308, doi:https://doi.org/10.1029/2006GL026308.

Lawrence, E.E., Gekelman, W., 2009. Identification of a quasiseparatrix layer in a reconnecting laboratory magnetoplasma. Phys. Rev. Lett. 103, 105002. URL: https://link.aps.org/doi/10.1103/PhysRevLett.103.105002, doi:10.1103/PhysRevLett.103.105002.

Lazarian, A., Eyink, G.L., Vishniac, E.T., Kowal, G., 2015. Magnetic Reconnection in Astrophysical Environments. Springer Berlin Heidelberg, Berlin, Heidelberg. pp. 311–372. URL: https://doi.org/10.1007/978-3-662-44625-6_12, doi:10.1007/978-3-662-44625-6_12.

Leamon, R.J., Smith, C.W., Ness, N.F., Matthaeus, W.H., Wong, H.K., 1998. Observational constraints on the dynamics of the interplanetary magnetic field dissipation range. *J. Geophys. Res.* 103, 4775. doi:10.1029/97JA03394.

Leamon, R.J., Smith, C.W., Ness, N.F., Wong, H.K., 1999. Dissipation range dynamics: Kinetic Alfvén waves and the importance of β_e. Journal of Geophysical Research: Space Physics 104, 22331–22344. URL: https://agupubs.onlinelibrary.wiley.com/doi/abs/10.1029/1999JA900158, doi:https://doi.org/10.1029/1999JA900158, arXiv:https://agupubs.onlinelibrary.wiley.com/doi/pdf/10.1029/1999JA900158.

Lee, K.H., Lee, L.C., 2019. Interstellar turbulence spectrum from in situ observations of voyager 1. Nature Astronomy 3, 154–159. doi:10.1038/s41550-018-0650-6.

Lee, L.C., Jokipii, J.R., 1976. The irregularity spectrum in interstellar space. *Astrophys. J.* 206, 735–743. doi:10.1086/154434.

Leonard, A., 1975. Energy cascade in large-eddy simulations of turbulent fluid flows, in: Frenkiel, F., Munn, R. (Eds.), Turbulent Diffusion in Environmental Pollution. Elsevier. volume 18 of *Advances in Geophysics*, pp. 237–248. doi:https://doi.org/10.1016/S0065-2687(08)60464-1.

Lepreti, F., Carbone, V., Spolaore, M., Antoni, V., Cavazzana, R., Martines, E., Serianni, G., Veltri, P., Vianello, N., Zuin, M., 2009. Yaglom law for electrostatic turbulence in laboratory magnetized plasmas. EPL (Europhysics Letters) 86, 25001. doi:10.1209/0295-5075/86/25001.

Liang, H., Barbhuiya, M.H., Cassak, P.A., Pezzi, O., Servidio, S., Valentini, F., Zank, G.P., 2020. Kinetic entropy-based measures of distribution function non-Maxwellianity: theory and simulations. Journal of Plasma Physics 86, 825860502. doi:10.1017/S0022377820001270, arXiv:2008.06669.

Liang, H., Zank, G.P., Nakanotani, M., Zhao, L.L., 2021. Assessing the role of interchange reconnection in forming switchbacks. *Astrophys. J.* 917, 110. doi:10.3847/1538-4357/ac0a73.

Lighthill, M.J., 1955. The effect of compressibility on turbulence, in: Gas Dynamics of Cosmic Clouds, p. 121.

Lindborg, E., 1996. A note on Kolmogorov's third-order structure-function law, the local isotropy hypothesis and the pressure–velocity correlation. Journal of Fluid Mechanics 326, 343–356. doi:10.1017/S0022112096008348.

Linkmann, M.F., Berera, A., McComb, W.D., McKay, M.E., 2015. Nonuniversality and finite dissipation in decaying magnetohydrodynamic turbulence. *Phys. Rev. Lett.* 114, 235001. doi:10.1103/PhysRevLett.114.235001, arXiv:1502.06439.

Liu, C., Feng, X., Guo, J., Ye, Y., 2013. Study of small-scale plasmoid structures in the magnetotail using Cluster observations and Hall MHD simulations. Journal of Geophysical Research (Space Physics) 118, 2087–2100. doi:10.1002/jgra.50248.

Loomis, E., 1860. The great auroral exhibition of aug. 28th to sept. 4th, 1859; and the geographical distribution of auroras and thunder storms. American Journal of Science 30, 79–100. doi:10.2475/ajs.s2-30.88.79.

Loomis, E., 1862. On electrical currents circulating near the earth's surface and their connection with the phenomena of the aurora polaris. American Journal of Science 34, 34–45. doi:10.2475/ajs.s2-34.100.34.

Louarn, P., Fedorov, A., Prech, L., Owen, C.J., Bruno, R., Livi, S., Lavraud, B., Rouillard, A.P., Génot, V., André, N., Fruit, G., Réville, V., Kieokaew, R., Plotnikov, I., Penou, E., Barthe, A., Khataria, D., Berthomier, M., D'Amicis, R., Sorriso-Valvo, L., Allegrini, F., Raines, J., Verscharen, D.,

Fortunato, V., Mele, G., Horbury, T.S., O'brien, H., Evans, V., Angelini, V., Maksimovic, M., Kasper, J.C., Bale, S.D., 2021. Multiscale views of an Alfvénic slow solar wind: 3d velocity distribution functions observed by the proton-alpha sensor of solar orbiter. *Astron. Astrophys.* 656, A36. doi:10.1051/0004-6361/202141095.

Ma, Y., Russell, C.T., Toth, G., Chen, Y., Nagy, A.F., Harada, Y., McFadden, J., Halekas, J.S., Lillis, R., Connerney, J.E.P., Espley, J., DiBraccio, G.A., Markidis, S., Peng, I.B., Fang, X., Jakosky, B.M., 2018. Reconnection in the martian magnetotail: Hall-mhd with embedded particle-in-cell simulations. Journal of Geophysical Research: Space Physics 123, 3742–3763. doi:https://doi.org/10.1029/2017JA024729.

Ma, Z.W., Wu, L.N., Li, L.J., Wang, L.C., 2014. Bursty magnetic reconnection under slow shock-generated whistler waves. Journal of Geophysical Research (Space Physics) 119, 7495–7500. doi:10.1002/2014JA020190.

MacBride, B.T., Forman, M.A., Smith, C.W., 2005. Turbulence and third moment of fluctuations: Kolmogorov's 4/5 law and its mhd analogues in the solar wind, in: Fleck, B., Zurbuchen, T.H., Lacoste, H. (Eds.), Solar Wind 11/SOHO 16, Connecting Sun and Heliosphere, p. 613.

MacBride, B.T., Smith, C.W., Forman, M.A., 2008. The turbulent cascade at 1 AU: Energy transfer and the third-order scaling for MHD. The Astrophysical Journal 679, 1644–1660. URL: https://doi.org/10.1086/529575, doi:10.1086/529575.

Maksimovic, M., Bale, S.D., Chust, T., Khotyaintsev, Y., Krasnoselskikh, V., Kretzschmar, M., Plettemeier, D., Rucker, H.O., Souček, J., Steller, M., Štverák, Š., Trávníček, P., Vaivads, A., Chaintreuil, S., Dekkali, M., Alexandrova, O., Astier, P.A., Barbary, G., Bérard, D., Bonnin, X., Boughedada, K., Cecconi, B., Chapron, F., Chariet, M., Collin, C., de Conchy, Y., Dias, D., Guéguen, L., Lamy, L., Leray, V., Lion, S., Malac-Allain, L.R., Matteini, L., Nguyen, Q.N., Pantellini, F., Parisot, J., Plasson, P., Thijs, S., Vecchio, A., Fratter, I., Bellouard, E., Lorfèvre, E., Danto, P., Julien, S., Guilhem, E., Fiachetti, C., Sanisidro, J., Laffaye, C., Gonzalez, F., Pontet, B., Quéruel, N., Jannet, G., Fergeau, P., Brochot, J.Y., Cassam-Chenai, G., Dudok de Wit, T., Timofeeva, M., Vincent, T., Agrapart, C., Delory, G.T., Turin, P., Jeandet, A., Leroy, P., Pellion, J.C.,

Bouzid, V., Katra, B., Piberne, R., Recart, W., Santolík, O., Kolmašová, I., Krupař, V., Krupařová, O., Píša, D., Uhlíř, L., Lán, R., Baše, J., Ahlèn, L., André, M., Bylander, L., Cripps, V., Cully, C., Eriksson, A., Jansson, S.E., Johansson, E.P.G., Karlsson, T., Puccio, W., Břínek, J., Öttacher, H., Panchenko, M., Berthomier, M., Goetz, K., Hellinger, P., Horbury, T.S., Issautier, K., Kontar, E., Krucker, S., Le Contel, O., Louarn, P., Martinović, M., Owen, C.J., Retino, A., Rodríguez-Pacheco, J., Sahraoui, F., Wimmer-Schweingruber, R.F., Zaslavsky, A., Zouganelis, I., 2020. The solar orbiter radio and plasma waves (rpw) instrument. *Astron. Astrophys.* 642, A12. doi:10.1051/0004-6361/201936214.

Malara, F., Primavera, L., Veltri, P., 2000. Nonlinear evolution of parametric instability of a large-amplitude nonmonochromatic Alfvén wave. Physics of Plasmas 7, 2866–2877. URL: https://doi.org/10.1063/1.874136, doi:10.1063/1.874136, arXiv:https://doi.org/10.1063/1.874136.

Malara, F., Primavera, L., Veltri, P., 2001. Nonlinear evolution of the parametric instability: numerical predictions versus observations in the heliosphere. Nonlinear Processes in Geophysics 8, 159–166. doi:10.5194/npg-8-159-2001.

Maloney, S.A., Gallagher, P.T., 2010. Solar wind drag and the kinematics of interplanetary coronal mass ejections. The Astrophysical Journal 724, L127–L132. URL: https://doi.org/10.1088/2041-8205/724/2/l127, doi:10.1088/2041-8205/724/2/l127.

Manchester, W. B., I., Gombosi, T.I., De Zeeuw, D.L., Sokolov, I.V., Roussev, I.I., Powell, K.G., Kóta, J., Tóth, G., Zurbuchen, T.H., 2005. Coronal mass ejection shock and sheath structures relevant to particle acceleration. *Astrophys. J.* 622, 1225–1239. doi:10.1086/427768.

Manzini, D., Sahraoui, F., Califano, F., Ferrand, R., 2022. Local cascade and dissipation in incompressible Hall magnetohydrodynamic turbulence: the coarse-graining approach. arXiv e-prints , arXiv:2203.01050arXiv:2203.01050.

Marchand, P., Tomida, K., Commerçon, B., Chabrier, G., 2019. Impact of the Hall effect in star formation, improving the angular momentum conservation. Astronomy and Astrophysics 631, A66. doi:10.1051/0004-6361/201936215, arXiv:1909.09025.

Marino, R., Feraco, F., Primavera, L., Pumir, A., Pouquet, A., Rosenberg, D., Mininni, P.D., 2022. Turbulence generation by large-scale extreme vertical drafts and the modulation of local energy dissipation in stably stratified geophysical flows. Phys. Rev. Fluids 7, 033801.

Marino, R., Mininni, P.D., Rosenberg, D., Pouquet, A., 2013. Inverse cascades in rotating stratified turbulence: Fast growth of large scales. EPL (Europhysics Letters) 102, 44006. doi:10.1209/0295-5075/102/44006.

Marino, R., Mininni, P.D., Rosenberg, D.L., Pouquet, A., 2014. Large-scale anisotropy in stably stratified rotating flows. Phys. Rev. E 90, 023018. URL: https://link.aps.org/doi/10.1103/PhysRevE.90.023018, doi:10.1103/PhysRevE.90.023018.

Marino, R., Pouquet, A., Rosenberg, D., 2015a. Resolving the paradox of oceanic large-scale balance and small-scale mixing. Phys. Rev. Lett. 114, 114504. URL: https://link.aps.org/doi/10.1103/PhysRevLett.114.114504, doi:10.1103/PhysRevLett.114.114504.

Marino, R., Rosenberg, D., Herbert, C., Pouquet, A., 2015b. Interplay of waves and eddies in rotating stratified turbulence and the link with kinetic-potential energy partition. Eur. Phys. Lett. 112, 49001.

Marino, R., Sorriso-Valvo, L., Carbone, V., Noullez, A., Bruno, R., Bavassano, B., 2008. Heating the solar wind by a magnetohydrodynamic turbulent energy cascade. *Astrophys. J. Lett.* 677, L71–L74.

Marino, R., Sorriso-Valvo, L., Carbone, V., Veltri, P., Noullez, A., Bruno, R., 2011. The magnetohydrodynamic turbulent cascade in the ecliptic solar wind: Study of ulysses data. Planetary and Space Science 59, 592–597. URL: https://www.sciencedirect.com/science/article/pii/S0032063310001789, doi:https://doi.org/10.1016/j.pss.2010.06.005. cross-Scale Coupling in Plasmas.

Marino, R., Sorriso-Valvo, L., D'Amicis, R., Carbone, V., Bruno, R., Veltri, P., 2012. On the occurrence of the third-order scaling in high latitude solar wind. *Astrophys. J.* 750, 41. doi:10.1088/0004-637X/750/1/41.

Marsch, E., 2006. Kinetic physics of the solar corona and solar wind. Living Reviews in Solar Physics 3, 1. doi:10.12942/lrsp-2006-1.

Marsch, E., Muehlhaeuser, K.H., Rosenbauer, H., Schwenn, R., 1983. On the equaton of state of solar wind ions derived from Helios measurements. *J. Geophys. Res.* 88, 2982–2992. doi:10.1029/JA088iA04p02982.

Marsch, E., Schwenn, R., Rosenbauer, H., Muehlhaeuser, K.H., Pilipp, W., Neubauer, F.M., 1982. Solar wind protons: Three-dimensional velocity distributions and derived plasma parameters measured between 0.3 and 1 AU. *J. Geophys. Res.* 87, 52–72. doi:10.1029/JA087iA01p00052.

Marsch, E., Tu, C., 1997. Intermittency, non-Gaussian statistics and fractal scaling of MHD fluctuations in the solar wind. *Nonlinear Processes in Geophys.* 4, 101–124.

Martin, L.N., De Vita, G., Sorriso-Valvo, L., Dmitruk, P., Nigro, G., Primavera, L., Carbone, V., 2013. Cancellation properties in Hall magnetohydrodynamics with a strong guide magnetic field. Phys. Rev. E 88, 063107. URL: https://link.aps.org/doi/10.1103/PhysRevE.88.063107, doi:10.1103/PhysRevE.88.063107.

Martinović, M.M., Klein, K.G., Huang, J., Chandran, B.D.G., Kasper, J.C., Lichko, E., Bowen, T., Chen, C.H.K., Matteini, L., Stevens, M., Case, A.W., Bale, S.D., 2021. Multiscale solar wind turbulence properties inside and near switchbacks measured by the Parker Solar Probe. The Astrophysical Journal 912, 28. URL: https://doi.org/10.3847/1538-4357/abebe5, doi:10.3847/1538-4357/abebe5.

Matteini, L., 2012. Parametric decay of Alfvén waves at parallel and oblique propagation: Kinetic effects and transverse couplings, in: Sulem, P.L., Mond, M. (Eds.), Waves and Instabilities in Space and Astrophysical Plasmas, pp. 83–93. doi:10.1063/1.3701353.

Matteini, L., Franci, L., Alexandrova, O., Lacombe, C., Landi, S., Hellinger, P., Papini, E., Verdini, A., 2020. Magnetic field turbulence in the solar wind at sub-ion scales: In situ observations and numerical simulations. Frontiers in Astronomy and Space Sciences 7, 83. URL: https://www.frontiersin.org/article/10.3389/fspas.2020.563075, doi:10.3389/fspas.2020.563075.

Matteini, L., Horbury, T.S., Pantellini, F., Velli, M., Schwartz, S.J., 2015. Ion kinetic energy conservation and magnetic field strength constancy

in multi-fluid solar wind Alfévnic turbulence. The Astrophysical Journal 802, 11. URL: https://doi.org/10.1088/0004-637x/802/1/11, doi:10.1088/0004-637x/802/1/11.

Matteini, L., Stansby, D., Horbury, T.S., Chen, C.H.K., 2018. On the 1/f spectrum in the solar wind and its connection with magnetic compressibility. The Astrophysical Journal 869, L32. URL: https://doi.org/10.3847/2041-8213/aaf573, doi:10.3847/2041-8213/aaf573.

Matthaeus, W.H., 2021. Turbulence in space plasmas: Who needs it? Physics of Plasmas 28, 032306. URL: https://doi.org/10.1063/5.0041540, doi:10.1063/5.0041540.

Matthaeus, W.H., Goldstein, M.L., Roberts, D.A., 1990. Evidence for the presence of quasi-two-dimensional nearly incompressible fluctuations in the solar wind. *J. Geophys. Res.* 95, 20673–20683. doi:10.1029/JA095iA12p20673.

Matthaeus, W.H., Lamkin, S.L., 1986. Turbulent magnetic reconnection. Physics of Fluids 29, 2513–2534. doi:10.1063/1.866004.

Matthaeus, W.H., Minnie, J., Breech, B., Parhi, S., Bieber, J.W., Oughton, S., 2004. Transport of cross helicity and radial evolution of Alfvénicity in the solar wind. *Geophys. Res. Lett.* 31, L12803. doi:10.1029/2004GL019645.

Matthaeus, W.H., Velli, M., 2011. Who needs turbulence?. a review of turbulence effects in the heliosphere and on the fundamental process of reconnection. *Space Sci. Rev.* 160, 145–168.

Matthaeus, W.H., Yang, Y., Wan, M., Parashar, T.N., Bandyopadhyay, R., Chasapis, A., Pezzi, O., Valentini, F., 2020. Pathways to dissipation in weakly collisional plasmas. *Astrophys. J.* 891, 101. doi:10.3847/1538-4357/ab6d6a.

Matthaeus, W.H., Zank, G.P., Smith, C.W., Oughton, S., 1999. Turbulence, spatial transport, and heating of the solar wind. *Phys. Rev. Lett.* 82, 3444–3447. doi:10.1103/PhysRevLett.82.3444.

Matthaeus, W.H., Zhou, Y., Zank, G.P., Oughton, S., 1994. Transport theory and the wkb approximation for interplanetary mhd fluctuations. *J. Geophys. Res.* 99, 23421–23430. doi:10.1029/94JA02326.

McComas, D., Bame, S., Barker, P., Feldman, W., Phillips, J., Riley, P., Griffee, J., 1998a. Solar wind electron proton alpha monitor (swepam) for the advanced composition explorer. Space Science Reviews 86, 563–612.

McComas, D.J., Bame, S.J., Barraclough, B.L., Feldman, W.C., Funsten, H.O., Gosling, J.T., Riley, P., Skoug, R., Balogh, A., Forsyth, R., Goldstein, B.E., Neugebauer, M., 1998b. Ulysses' return to the slow solar wind. Geophysical Research Letters 25, 1–4. URL: https://agupubs.onlinelibrary.wiley.com/doi/abs/10.1029/97GL03444, doi:https://doi.org/10.1029/97GL03444.

McComas, D.J., Christian, E.R., Cohen, C.M.S., Cummings, A.C., Davis, A.J., Desai, M.I., Giacalone, J., Hill, M.E., Joyce, C.J., Krimigis, S.M., Labrador, A.W., Leske, R.A., Malandraki, O., Matthaeus, W.H., McNutt, R.L., Mewaldt, R.A., Mitchell, D.G., Posner, A., Rankin, J.S., Roelof, E.C., Schwadron, N.A., Stone, E.C., Szalay, J.R., Wiedenbeck, M.E., Bale, S.D., Kasper, J.C., Case, A.W., Korreck, K.E., MacDowall, R.J., Pulupa, M., Stevens, M.L., Rouillard, A.P., 2019. Probing the energetic particle environment near the sun. *Nature* 576, 223–227. doi:10.1038/s41586-019-1811-1.

McComas, D.J., Velli, M., Lewis, W.S., Acton, L.W., Balat-Pichelin, M., Bothmer, V., Dirling Jr., R.B., Feldman, W.C., Gloeckler, G., Habbal, S.R., Hassler, D.M., Mann, I., Matthaeus, W.H., McNutt Jr., R.L., Mewaldt, R.A., Murphy, N., Ofman, L., Sittler Jr., E.C., Smith, C.W., Zurbuchen, T.H., 2007. Understanding coronal heating and solar wind acceleration: Case for in situ near-sun measurements. Reviews of Geophysics 45. URL: https://agupubs.onlinelibrary.wiley.com/doi/abs/10.1029/2006RG000195, doi:https://doi.org/10.1029/2006RG000195.

McIntosh, S.W., de Pontieu, B., Carlsson, M., Hansteen, V., Boerner, P., Goossens, M., 2011. Alfvénic waves with sufficient energy to power the quiet solar corona and fast solar wind. *Nature* 475, 477–480. doi:10.1038/nature10235.

McKee, C.F., Ostriker, E.C., 2007. Theory of star formation. *Annu. Rev. Astron. Astrophys.* 45, 565–687. doi:10.1146/annurev.astro.45.051806.110602, arXiv:0707.3514.

McNutt, R.L., Wimmer-Schweingruber, R.F., Gruntman, M., Krimigis, S.M., Roelof, E.C., Brandt, P.C., Vernon, S.R., Paul, M.V., Stough, R.W., Kinnison, J.D., 2022. Interstellar probe – destination: Universe! Acta Astronautica 196, 13–28. URL: https://www.sciencedirect.com/science/article/pii/S0094576522001503, doi:https://doi.org/10.1016/j.actaastro.2022.04.001.

Meneveau, C., Sreenivasan, K.R., 1987. Simple multifractal cascade model for fully developed turbulence. *Phys. Rev. Lett.* 59, 1424–1427.

Mininni, P., Rosenberg, D., Reddy, R., Pouquet, A., 2011a. A hybrid MPI-OpenMP scheme for scalable parallel pseudospectral computations for fluid turbulence. Parallel Computing 37, 316–326.

Mininni, P.D., Alexakis, A., Pouquet, A., 2007. Energy transfer in Hall-MHD turbulence: cascades, backscatter, and dynamo action. Journal of Plasma Physics 73, 377–401. doi:10.1017/S0022377806004624.

Mininni, P.D., Gómez, D.O., Mahajan, S.M., 2002. Dynamo action in Hall magnetohydrodynamics. Astrophysical Journal 567, L81–L83. doi:10.1086/339850.

Mininni, P.D., Gomez, D.O., Mahajan, S.M., 2003. Dynamo action in magnetohydrodynamics and Hall-magnetohydrodynamics. Astrophysical Journal 587, 472–481. doi:10.1086/368181.

Mininni, P.D., Gomez, D.O., Mahajan, S.M., 2005. Direct simulations of helical Hall-MHD turbulence and dynamo action. Astrophysical Journal 619, 1019–1027. doi:10.1086/426534.

Mininni, P.D., Pouquet, A., 2009. Finite dissipation and intermittency in magnetohydrodynamics. Phys. Rev. E 80, 025401. URL: https://link.aps.org/doi/10.1103/PhysRevE.80.025401, doi:10.1103/PhysRevE.80.025401.

Mininni, P.D., Rosenberg, D., Reddy, R., Pouquet, A., 2011b. A hybrid mpi–openmp scheme for scalable parallel pseudospectral

computations for fluid turbulence. Parallel Computing 37, 316–326. URL: https://www.sciencedirect.com/science/article/pii/S0167819111000512, doi:https://doi.org/10.1016/j.parco.2011.05.004.

Mishin, V.V., Tomozov, V.M., 2016. Kelvin-Helmholtz instability in the solar atmosphere, solar wind and geomagnetosphere. *Solar Phys.* 291, 3165–3184. doi:10.1007/s11207-016-0891-4.

Mitchell, D.G., Kutchko, F., Williams, D.J., Eastman, T.E., Frank, L.A., Russell, C.T., 1987. An extended study of the low-latitude boundary layer on the dawn and dusk flanks of the magnetosphere. Journal of Geophysical Research: Space Physics 92, 7394–7404. URL: https://agupubs.onlinelibrary.wiley.com/doi/abs/10.1029/JA092iA07p07394, doi:https://doi.org/10.1029/JA092iA07p07394.

Miura, H., Araki, K., 2014. Structure transitions induced by the Hall term in homogeneous and isotropic magnetohydrodynamic turbulence. Physics of Plasmas 21, 072313. doi:10.1063/1.4890857.

Miura, H., Hamba, F., 2022. Sub-grid-scale model for studying Hall effects on macroscopic aspects of magnetohydrodynamic turbulence. Journal of Computational Physics 448, 110692. doi:10.1016/j.jcp.2021.110692.

Monin, A.S., Yaglom, A.M., 1971. Statistical Fluids Mechanics: Mechanics of Turbulence. The MIT Press.

Montgomery, D., Turner, L., 1982. Two-and-a-half-dimensional magnetohydrodynamic turbulence. The Physics of Fluids 25, 345–349.

Morales, L., Dasso, S., Gómez, D., 2005. Hall effect in incompressible magnetic reconnection. Journal of Geophysical Research 110. doi:10.1029/2004JA010675.

Morton, R.J., Tomczyk, S., Pinto, R., 2015. Investigating Alfvénic wave propagation in coronal open-field regions. Nature Communications 6, 7813. doi:10.1038/ncomms8813.

Mozer, F.S., Bale, S.D., Bonnell, J.W., Drake, J.F., Hanson, E.L.M., Mozer, M.C., 2021. On the origin of switchbacks observed in the solar wind. *Astrophys. J.* 919, 60. doi:10.3847/1538-4357/ac110d, arXiv:2105.07601.

Müller, D., St. Cyr, O.C., Zouganelis, I., Gilbert, H.R., Marsden, R., Nieves-Chinchilla, T., Antonucci, E., Auchère, F., Berghmans, D., Horbury, T.S., Howard, R.A., Krucker, S., Maksimovic, M., Owen, C.J., Rochus, P., Rodriguez-Pacheco, J., Romoli, M., Solanki, S.K., Bruno, R., Carlsson, M., Fludra, A., Harra, L., Hassler, D.M., Livi, S., Louarn, P., Peter, H., Schühle, U., Teriaca, L., del Toro Iniesta, J.C., Wimmer-Schweingruber, R.F., Marsch, E., Velli, M., De Groof, A., Walsh, A., Williams, D., 2020. The solar orbiter mission. science overview. *Astron. Astrophys.* 642, A1. doi:10.1051/0004-6361/202038467, arXiv:2009.00861.

Nakamura, T.K.M., Hasegawa, H., Daughton, W., Eriksson, S., Li, W.Y., Nakamura, R., 2017. Turbulent mass transfer caused by vortex induced reconnection in collisionless magnetospheric plasmas. Nature Communications 8, 1582. doi:10.1038/s41467-017-01579-0.

Napoletano, G., Foldes, R., Camporeale, E., de Gasperis, G., Giovannelli, L., Paouris, E., Pietropaolo, E., Teunissen, J., Tiwari, A.K., Del Moro, D., 2022. Parameter distributions for the drag-based modeling of CME propagation. Space Weather , e2021SW002925URL: https://agupubs.onlinelibrary.wiley.com/doi/abs/10.1029/2021SW002925, doi:https://doi.org/10.1029/2021SW002925.

Neugebauer, M., Alexander, C.J., Schwenn, R., Richter, A.K., 1986. Tangential discontinuities in the solar wind: Correlated field and velocity changes in the Kelvin-Helmholtz instability. *J. Geophys. Res.* 91, 13694–13698. doi:10.1029/JA091iA12p13694.

Neugebauer, M., Goldstein, B.E., 2013. Double-proton beams and magnetic switchbacks in the solar wind, in: Zank, G.P., Borovsky, J., Bruno, R., Cirtain, J., Cranmer, S., Elliott, H., Giacalone, J., Gonzalez, W., Li, G., Marsch, E., Moebius, E., Pogorelov, N., Spann, J., Verkhoglyadova, O. (Eds.), Solar Wind 13, pp. 46–49. doi:10.1063/1.4810986.

Neugebauer, M., Goldstein, B.E., McComas, D.J., Suess, S.T., Balogh, A., 1995. Ulysses observations of microstreams in the solar wind from coronal holes. *J. Geophys. Res.* 100, 23389–23396. doi:10.1029/95JA02723.

Neugebauer, M., Snyder, C.W., 1962. Solar plasma experiment. Science 138, 1095–1097.

Norman, C., Heyvaerts, J., 1985. Anomalous magnetic field diffusion during star formation. Astronomy & Astrophysics 147, 247–256.

Numata, R., Yoshida, Z., Hayashi, T., 2004. Nonlinear three-dimensional simulation for self-organization and flow generation in two-fluid plasmas. Computer Physics Communications 164, 291–296. doi:https://doi.org/10.1016/j.cpc.2004.06.041. proceedings of the 18th International Conferene on the Numerical Simulation of Plasmas.

Ofman, L., 2010. Wave modeling of the solar wind. Living Reviews in Solar Physics 7, 4. doi:10.12942/lrsp-2010-4.

Ofman, L., Thompson, B.J., 2011. SDO/AIA observation of Kelvin-Helmholtz instability in the solar corona. *Astrophys. J. Lett.* 734, L11. doi:10.1088/2041-8205/734/1/L11, arXiv:1101.4249.

Ohsaki, S., 2006. Publisher's note: "hall effect on relaxation process of flowing plasmas" [phys. plasmas 12, 032306 (2005)]. Physics of Plasmas 13, 029901. doi:10.1063/1.2172413.

Orkisz, J.H., Pety, J., Gerin, M., Bron, E., Guzmán, V.V., Bardeau, S., Goicoechea, J.R., Gratier, P., Le Petit, F., Levrier, F., Liszt, H., Öberg, K., Peretto, N., Roueff, E., Sievers, A., Tremblin, P., 2017. Turbulence and star formation efficiency in molecular clouds: solenoidal versus compressive motions in orion b. *Astron. Astrophys.* 599, A99. doi:10.1051/0004-6361/201629220, arXiv:1701.00962.

Osman, K.T., Matthaeus, W.H., Wan, M., Rappazzo, A.F., 2012. Intermittency and local heating in the solar wind. Phys. Rev. Lett. 108, 261102. URL: https://link.aps.org/doi/10.1103/PhysRevLett.108.261102, doi:10.1103/PhysRevLett.108.261102.

Osman, K.T., Wan, M., Matthaeus, W.H., Weygand, J.M., Dasso, S., 2011. Anisotropic third-moment estimates of the energy cascade in solar wind turbulence using multispacecraft data. Phys. Rev. Lett. 107, 165001. URL: https://link.aps.org/doi/10.1103/PhysRevLett.107.165001, doi:10.1103/PhysRevLett.107.165001.

Ott, E., Du, Y., Sreenivasan, K.R., Juneja, A., Suri, A.K., 1992. Sign-singular measures: Fast magnetic dynamos, and high-

reynolds-number fluid turbulence. Phys. Rev. Lett. 69, 2654–2657. URL: https://link.aps.org/doi/10.1103/PhysRevLett.69.2654, doi:10.1103/PhysRevLett.69.2654.

Oughton, S., Matthaeus, W.H., 2020. Critical balance and the physics of magnetohydrodynamic turbulence. The Astrophysical Journal 897, 37. URL: https://doi.org/10.3847/1538-4357/ab8f2a, doi:10.3847/1538-4357/ab8f2a.

Owen, C.J., Bruno, R., Livi, S., Louarn, P., Al Janabi, K., Allegrini, F., Amoros, C., Baruah, R., Barthe, A., Berthomier, M., Bordon, S., Brockley-Blatt, C., Brysbaert, C., Capuano, G., Collier, M., DeMarco, R., Fedorov, A., Ford, J., Fortunato, V., Fratter, I., Galvin, A.B., Hancock, B., Heirtzler, D., Kataria, D., Kistler, L., Lepri, S.T., Lewis, G., Loeffler, C., Marty, W., Mathon, R., Mayall, A., Mele, G., Ogasawara, K., Orlandi, M., Pacros, A., Penou, E., Persyn, S., Petiot, M., Phillips, M., Přech, L., Raines, J.M., Reden, M., Rouillard, A.P., Rousseau, A., Rubiella, J., Seran, H., Spencer, A., Thomas, J.W., Trevino, J., Verscharen, D., Wurz, P., Alapide, A., Amoruso, L., André, N., Anekallu, C., Arciuli, V., Arnett, K.L., Ascolese, R., Bancroft, C., Bland, P., Brysch, M., Calvanese, R., Castronuovo, M., Čermák, I., Chornay, D., Clemens, S., Coker, J., Collinson, G., D'Amicis, R., Dandouras, I., Darnley, R., Davies, D., Davison, G., De Los Santos, A., Devoto, P., Dirks, G., Edlund, E., Fazakerley, A., Ferris, M., Frost, C., Fruit, G., Garat, C., Génot, V., Gibson, W., Gilbert, J.A., de Giosa, V., Gradone, S., Hailey, M., Horbury, T.S., Hunt, T., Jacquey, C., Johnson, M., Lavraud, B., Lawrenson, A., Leblanc, F., Lockhart, W., Maksimovic, M., Malpus, A., Marcucci, F., Mazelle, C., Monti, F., Myers, S., Nguyen, T., Rodriguez-Pacheco, J., Phillips, I., Popecki, M., Rees, K., Rogacki, S.A., Ruane, K., Rust, D., Salatti, M., Sauvaud, J.A., Stakhiv, M.O., Stange, J., Stubbs, T., Taylor, T., Techer, J.D., Terrier, G., Thibodeaux, R., Urdiales, C., Varsani, A., Walsh, A.P., Watson, G., Wheeler, P., Willis, G., Wimmer-Schweingruber, R.F., Winter, B., Yardley, J., Zouganelis, I., 2020. The solar orbiter solar wind analyser (swa) suite. *Astron. Astrophys.* 642, A16. doi:10.1051/0004-6361/201937259.

Pagel, C., Balogh, A., 2003. Radial dependence of intermittency in the fast polar solar wind magnetic field using ulysses. J. Geophys. Res. (Space Physics) 108, 1012.

Paladin, G., Vulpiani, A., 1987. Anomalous scaling laws in multifractal objects. *Phys. Reports* 156, 147–225.

Palmroth, M., Ganse, U., Pfau-Kempf, Y., Battarbee, M., Turc, L., Brito, T., Grandin, M., Hoilijoki, S., Sandroos, A., von Alfthan, S., 2018. Vlasov methods in space physics and astrophysics. Living Reviews in Computational Astrophysics 4, 1. doi:10.1007/s41115-018-0003-2, arXiv:1808.05885.

Pan, N., Banerjee, S., 2020. Energy transfer in simple and active binar fluid turbulence. Phys. Rev. E .

Pandey, B.P., Wardle, M., 2008. Hall magnetohydrodynamics of partially ionized plasmas. Monthly Notices of the Royal Astronomical Society 385, 2269–2278. doi:10.1111/j.1365-2966.2008.12998.x.

Papini, E., Franci, L., Landi, S., Verdini, A., Matteini, L., Hellinger, P., 2019. Can Hall magnetohydrodynamics explain plasma turbulence at sub-ion scales? Astrophysical Journal 870, 52. doi:10.3847/1538-4357/aaf003.

Parashar, T.N., Goldstein, M.L., Maruca, B.A., Matthaeus, W.H., Ruffolo, D., Bandyopadhyay, R., Chhiber, R., Chasapis, A., Qudsi, R., Vech, D., Roberts, D.A., Bale, S.D., Bonnell, J.W., de Wit, T.D., Goetz, K., Harvey, P.R., MacDowall, R.J., Malaspina, D., Pulupa, M., Kasper, J.C., Korreck, K.E., Case, A.W., Stevens, M., Whittlesey, P., Larson, D., Livi, R., Velli, M., Raouafi, N., 2020. Measures of scale-dependent Alfvénicity in the first PSP solar encounter. The Astrophysical Journal Supplement Series 246, 58. URL: https://doi.org/10.3847/1538-4365/ab64e6, doi:10.3847/1538-4365/ab64e6.

Parisi, G., Frisch, U., 1985. On the singularity structure of fully developed turbulence, in: Ghil, N., Benzi, R., Parisi, G. (Eds.), Proc. Intl School of Physics E. Fermi: Turbulence and Predictability of Geophysical Flows and Climatic Dynamics, North Holland Amsterdam. p. 84.

Parker, E.N., 1957. Sweet's mechanism for merging magnetic fields in conducting fluids. *J. Geophys. Res.* 62, 509–520.

Parker, E.N., 1958. Dynamics of the interplanetary gas and magnetic fields. *Astrophys. J.* 128, 664.

Paschmann, G., Papamastorakis, I., Sckopke, N., Haerendel, G., Sonnerup, B.U.O., Bame, S.J., Asbridge, J.R., Gosling, J.T., Russel, C.T., Elphic, R.C., 1979. Plasma acceleration at the earth's magnetopause - evidence for reconnection. *Nature* 282, 243–246. doi:10.1038/282243a0.

Paschmann, G., Schwartz, S.J., 2000. Issi book on analysis methods for multispacecraft data, in: Harris, R.A. (Ed.), Cluster-II Workshop Multiscale / Multipoint Plasma Measurements, p. 99.

Passot, T., Henri, P., Laveder, D., Sulem, P.L., 2014. Fluid simulations of ion scale plasmas with weakly distorted magnetic fields. flr-landau fluid simulations. European Physical Journal D 68, 207. doi:10.1140/epjd/e2014-50160-1.

Passot, T., Sulem, P.L., 2007. Collisionless magnetohydrodynamics with gyrokinetic effects. Physics of Plasmas 14, 082502. URL: https://doi.org/10.1063/1.2751601, doi:10.1063/1.2751601, arXiv:https://doi.org/10.1063/1.2751601.

Patterson, G.S., Orszag, S.A., 1971. Spectral calculations of isotropic turbulence: Efficient removal of aliasing interactions. The Physics of Fluids 14, 2538–2541. doi:10.1063/1.1693365.

Pereira, M., Gissinger, C., Fauve, S., 2019. 1 / f noise and long-term memory of coherent structures in a turbulent shear flow. Physical Review E 99. doi:10.1103/PhysRevE.99.023106.

Perez, J.C., Bourouaine, S., Chen, C.H.K., Raouafi, N.E., 2021a. Applicability of Taylor's hypothesis during Parker Solar Probe perihelia. *Astron. Astrophys.* 650, A22. doi:10.1051/0004-6361/202039879, arXiv:2103.12022.

Perez, J.C., Chandran, B.D.G., Klein, K.G., Martinović, M.M., 2021b. How Alfvén waves energize the solar wind: heat versus work. Journal of Plasma Physics 87, 905870218. doi:10.1017/S0022377821000167, arXiv:2103.09365.

Perri, S., Servidio, S., Vaivads, A., Valentini, F., 2017. Numerical study on the validity of the taylor hypothesis in space plasmas. The Astrophysical Journal Supplement Series 231, 4. URL: https://doi.org/10.3847/1538-4365/aa755a, doi:10.3847/1538-4365/aa755a.

Perrone, D., Alexandrova, O., Mangeney, A., Maksimovic, M., Lacombe, C., Rakoto, V., Kasper, J.C., Jovanovic, D., 2016. Compressive coherent structures at ion scales in the solar wind. The Astrophysical Journal 826, 196. URL: https://doi.org/10.3847/0004-637x/826/2/196, doi:10.3847/0004-637x/826/2/196.

Perrone, D., Bruno, R., D'Amicis, R., Telloni, D., Marco, R.D., Stangalini, M., Perri, S., Pezzi, O., Alexandrova, O., Bale, S.D., 2020. Coherent events at ion scales in the inner heliosphere: Parker Solar Probe observations during the first encounter. The Astrophysical Journal 905, 142. URL: https://doi.org/10.3847/1538-4357/abc480, doi:10.3847/1538-4357/abc480.

Perrone, D., Passot, T., Laveder, D., Valentini, F., Sulem, P.L., Zouganelis, I., Veltri, P., Servidio, S., 2018. Fluid simulations of plasma turbulence at ion scales: Comparison with Vlasov-Maxwell simulations. Physics of Plasmas 25, 052302. URL: https://doi.org/10.1063/1.5026656, doi:10.1063/1.5026656, arXiv:https://doi.org/10.1063/1.5026656.

Pezzi, O., Liang, H., Juno, J.L., Cassak, P.A., Vásconez, C.L., Sorriso-Valvo, L., Perrone, D., Servidio, S., Roytershteyn, V., TenBarge, J.M., Matthaeus, W.H., 2021. Dissipation measures in weakly collisional plasmas. Monthly Notices of the Royal Astronomical Society 505, 4857–4873. URL: https://doi.org/10.1093/mnras/stab1516, doi:10.1093/mnras/stab1516.

Pezzi, O., Perrone, D., Servidio, S., Valentini, F., Sorriso-Valvo, L., Veltri, P., 2019. Proton–proton collisions in the turbulent solar wind: Hybrid Boltzmann–Maxwell simulations. The Astrophysical Journal 887, 208. URL: https://doi.org/10.3847/1538-4357/ab5285, doi:10.3847/1538-4357/ab5285.

Pezzi, O., Servidio, S., Perrone, D., Valentini, F., Sorriso-Valvo, L., Greco, A., Matthaeus, W.H., Veltri, P., 2018. Velocity-space cascade in magnetized plasmas: Numerical simulations. Physics of Plasmas 25, 060704. URL: https://doi.org/10.1063/1.5027685, doi:10.1063/1.5027685, arXiv:https://doi.org/10.1063/1.5027685.

Pezzi, O., Valentini, F., Veltri, P., 2016. Collisional relaxation of fine velocity structures in plasmas. Phys. Rev. Lett. 116, 145001. URL: https:

//link.aps.org/doi/10.1103/PhysRevLett.116.145001, doi:10.1103/PhysRevLett.116.145001.

Phan, T.D., Kistler, L.M., Klecker, B., Haerendel, G., Paschmann, G., Sonnerup, B.U.Ö., Baumjohann, W., Bavassano-Cattaneo, M.B., Carlson, C.W., DiLellis, A.M., Fornacon, K.H., Frank, L.A., Fujimoto, M., Georgescu, E., Kokubun, S., Moebius, E., Mukai, T., Øieroset, M., Paterson, W.R., Reme, H., 2000. Extended magnetic reconnection at the earth's magnetopause from detection of bi-directional jets. *Nature* 404, 848–850. doi:10.1038/35009050.

Piovesan, P., Bonfiglio, D., Auriemma, F., Bonomo, F., Carraro, L., Cavazzana, R., De Masi, G., Fassina, A., Franz, P., Gobbin, M., Marrelli, L., Martin, P., Martines, E., Momo, B., Piron, L., Valisa, M., Veranda, M., Vianello, N., Zaniol, B., Agostini, M., Baruzzo, M., Bolzonella, T., Canton, A., Cappello, S., Chacón, L., Ciaccio, G., Escande, D.F., Innocente, P., Lorenzini, R., Paccagnella, R., Puiatti, M.E., Scarin, P., Soppelsa, A., Spizzo, G., Spolaore, M., Terranova, D., Zanca, P., Zanotto, L., Zuin, M., 2013. Rfx-mod: A multi-configuration fusion facility for three-dimensional physics studies. Physics of Plasmas 20, 056112. URL: https://doi.org/10.1063/1.4806765, doi:10.1063/1.4806765, arXiv:https://doi.org/10.1063/1.4806765.

Pitňa, A., Šafránková, J., Němeček, Z., Ďurovcová, T., Kis, A., 2021. Turbulence upstream and downstream of interplanetary shocks. Frontiers in Physics 8, 654. URL: https://www.frontiersin.org/article/10.3389/fphy.2020.626768, doi:10.3389/fphy.2020.626768.

Podesta, J.J., Forman, M.A., Smith, C.W., Elton, D.C., Malécot, Y., Gagne, Y., 2009. Accurate estimation of third-order moments from turbulence measurements. Nonlinear Processes in Geophysics 16, 99–110. URL: https://npg.copernicus.org/articles/16/99/2009/, doi:10.5194/npg-16-99-2009.

Poedts, Stefaan, Lani, Andrea, Scolini, Camilla, Verbeke, Christine, Wijsen, Nicolas, Lapenta, Giovanni, Laperre, Brecht, Millas, Dimitrios, Innocenti, Maria Elena, Chané, Emmanuel, Baratashvili, Tinatin, Samara, Evangelia, Van der Linden, Ronald, Rodriguez, Luciano, Vanlommel, Petra, Vainio, Rami, Afanasiev, Alexandr, Kilpua, Emilia, Pomoell, Jens,

Sarkar, Ranadeep, Aran, Angels, Sanahuja, Blai, Paredes, Josep M., Clarke, Ellen, Thomson, Alan, Rouilard, Alexis, Pinto, Rui F., Marchaudon, Aurélie, Blelly, Pierre-Louis, Gorce, Blandine, Plotnikov, Illya, Kouloumvakos, Athanasis, Heber, Bernd, Herbst, Konstantin, Kochanov, Andrey, Raeder, Joachim, Depauw, Jan, 2020. European heliospheric forecasting information asset 2.0. J. Space Weather Space Clim. 10, 57. URL: https://doi.org/10.1051/swsc/2020055, doi:10.1051/swsc/2020055.

Politano, H., Pouquet, A., 1998. Dynamical length scales for turbulent magnetized flows. *Geophys. Res. Lett.* 25, 273–276. doi:10.1029/97GL03642.

Politano, H., Pouquet, A., 1998. von Kármán-Howarth equation for magnetohydrodynamics and its consequences on third-order longitudinal structure and correlation functions. Phys. Rev. E 57, R21–R24. doi:10.1103/PhysRevE.57.R21.

Pouquet, A., Marino, R., 2013. Geophysical turbulence and the duality of the energy flow across scales. Phys. Rev. Lett. 111, 234501. URL: https://link.aps.org/doi/10.1103/PhysRevLett.111.234501, doi:10.1103/PhysRevLett.111.234501.

Pouquet, A., Rosenberg, D., Marino, R., 2019a. Linking dissipation and anisotropy and intermittency in rotating stratified turbulence. Phys. Fluids 31, 105116.

Pouquet, A., Rosenberg, D., Stawarz, J., Marino, R., 2019b. Helicity dynamics, inverse, and bidirectional cascades in fluid and magnetohydrodynamic turbulence: A brief review. Earth Space Sci. 6, 1–19.

Primavera, L., Malara, F., Servidio, S., Nigro, G., Veltri, P., 2019. Parametric instability in two-dimensional Alfvénic turbulence. The Astrophysical Journal 880, 156. doi:10.3847/1538-4357/ab29f5.

Pucci, F., Matthaeus, W.H., Chasapis, A., Servidio, S., Sorriso-Valvo, L., Olshevsky, V., Newman, D.L., Goldman, M.V., Lapenta, G., 2018. Generation of turbulence in colliding reconnection jets. *Astrophys. J.* 867, 10. doi:10.3847/1538-4357/aadd0a, arXiv:1810.13318.

Pulkkinen, T., 2007. Space weather: Terrestrial perspective. Living Reviews in Solar Physics 4, 1. doi:10.12942/lrsp-2007-1.

Pulkkinen, T., Palmroth, M., Tanskanen, E., Ganushkina, N., Shukhtina, M., Dmitrieva, N., 2007. Solar wind—magnetosphere coupling: A review of recent results. Journal of Atmospheric and Solar-Terrestrial Physics 69, 256–264. URL: https://www.sciencedirect.com/science/article/pii/S1364682606002653, doi:https://doi.org/10.1016/j.jastp.2006.05.029. global Aspects of Magnetosphere-Ionosphere Coupling.

Qudsi, R.A., Maruca, B.A., Matthaeus, W.H., Parashar, T.N., Bandyopadhyay, R., Chhiber, R., Chasapis, A., Goldstein, M.L., Bale, S.D., Bonnell, J.W., de Wit, T.D., Goetz, K., Harvey, P.R., MacDowall, R.J., Malaspina, D., Pulupa, M., Kasper, J.C., Korreck, K.E., Case, A.W., Stevens, M., Whittlesey, P., Larson, D., Livi, R., Velli, M., Raouafi, N., 2020. Observations of heating along intermittent structures in the inner heliosphere from psp data. The Astrophysical Journal Supplement Series 246, 46. URL: https://doi.org/10.3847/1538-4365/ab5c19, doi:10.3847/1538-4365/ab5c19.

Quijia, P., Fraternale, F., Stawarz, J.E., Vásconez, C.L., Perri, S., Marino, R., Yordanova, E., Sorriso-Valvo, L., 2021. Comparing turbulence in a Kelvin-Helmholtz instability region across the terrestrial magnetopause. *Mon. Not. Roy. Astron. Soc.* 503, 4815–4827. doi:10.1093/mnras/stab319.

Rebut, P.H., 1995. Iter: the first experimental fusion reactor. Fusion Engineering and Design 30, 85–118. URL: https://www.sciencedirect.com/science/article/pii/092037969400403T, doi:https://doi.org/10.1016/0920-3796(94)00403-T.

Retinò, A., Sundkvist, D., Vaivads, A., Mozer, F., André, M., Owen, C.J., 2007. In situ evidence of magnetic reconnection in turbulent plasma. Nature Physics 3, 236–238. doi:10.1038/nphys574.

Rheinhardt, M., Geppert, U., 2002. Hall-drift induced magnetic field instability in neutron stars. Phys. Rev. Lett. 88, 101103. URL: https://link.aps.org/doi/10.1103/PhysRevLett.88.101103, doi:10.1103/PhysRevLett.88.101103.

Riazantseva, M.O., Budaev, V.P., Rakhmanova, L.S., Zastenker, G.N., Šafránková, J., Němeček, Z., Přech, L., 2016. Comparison of properties of small-scale ion flux fluctuations in the flank magnetosheath and in the

solar wind. Advances in Space Research 58, 166–174. doi:10.1016/j.asr.2015.12.022.

Richardson, I.G., 2018. Solar wind stream interaction regions throughout the heliosphere. Living Reviews in Solar Physics 15, 1. doi:10.1007/s41116-017-0011-z.

Richardson, J.D., Paularena, K.I., Lazarus, A.J., Belcher, J.W., 1995. Evidence for a solar wind slowdown in the outer heliosphere? *Geophys. Res. Lett.* 22, 1469–1472. doi:10.1029/95GL01421.

Richardson, J.D., Smith, C.W., 2003. The radial temperature profile of the solar wind. *Geophys. Res. Lett.* 30, 1206. doi:10.1029/2002GL016551.

Roberts, D.A., Goldstein, M.L., Matthaeus, W.H., Ghosh, S., 1992. Velocity shear generation of solar wind turbulence. Journal of Geophysical Research: Space Physics 97, 17115–17130. URL: https://agupubs.onlinelibrary.wiley.com/doi/abs/10.1029/92JA01144, doi:https://doi.org/10.1029/92JA01144.

Roberts, O., Alexandrova, O., Sorriso-Valvo, L., et al., 2022. Scale-dependent kurtosis of magnetic field fluctuations in the solar wind: A multi-scale study with Cluster 2003-2015. JGR: Space Physics, submitted .

Robertson, H.P., 1940. The invariant theory of isotropic turbulence, in: Math. Proc. Cambridge Philos. Soc., Cambridge Univ Press. pp. 209–223.

Romanelli, N., Bertucci, C., Gómez, D., Mazelle, C., Delva, M., 2013. Proton cyclotron waves upstream from Mars: Observations from Mars global surveyor. Planetary and Space Science 76, 1–9. URL: https://www.sciencedirect.com/science/article/pii/S0032063312003029, doi:https://doi.org/10.1016/j.pss.2012.10.011.

Rorai, C., Mininni, P.D., Pouquet, A., 2014. Turbulence comes in bursts in stably stratified flows. Phys. Rev. E 89, 043002.

Rosenberg, D., Mininni, P., Reddy, R., Pouquet, A., 2020. GPU parallelization of a hybrid pseudospectral geophysical turbulence framework using CUDA. Atmosphere 11, 178.

Rosenbluth, M.N., MacDonald, W.M., Judd, D.L., 1957. Fokker-Planck equation for an inverse-square force. Phys. Rev. 107, 1–6. URL: https://link.aps.org/doi/10.1103/PhysRev.107.1, doi:10.1103/PhysRev.107.1.

Ruffolo, D., Matthaeus, W.H., Chhiber, R., Usmanov, A.V., Yang, Y., Bandyopadhyay, R., Parashar, T.N., Goldstein, M.L., DeForest, C.E., Wan, M., Chasapis, A., Maruca, B.A., Velli, M., Kasper, J.C., 2020. Shear-driven transition to isotropically turbulent solar wind outside the Alfvén critical zone. *Astrophys. J.* 902, 94. doi:10.3847/1538-4357/abb594, arXiv:2009.06537.

Ruhunusiri, S., Halekas, J.S., Espley, J.R., Mazelle, C., Brain, D., Harada, Y., DiBraccio, G.A., Livi, R., Larson, D.E., Mitchell, D.L., Jakosky, B.M., Howes, G.G., 2017. Characterization of turbulence in the Mars plasma environment with MAVEN observations. Journal of Geophysical Research: Space Physics 122, 656–674. URL: https://agupubs.onlinelibrary.wiley.com/doi/abs/10.1002/2016JA023456, doi:https://doi.org/10.1002/2016JA023456.

Russell, C.T., Luhmann, J.G., Schwingenschuh, K., Riedler, W., Yeroshenko, Y., 1990. Upstream waves at mars: Phobos observations. *Geophys. Res. Lett.* 17, 897–900. doi:10.1029/GL017i006p00897.

Rybanský, M., Rušin, V., Minarovjech, M., Gašpar, P., 1994. Coronal index of solar activity: Years 1939–1963. Solar Physics 152, 153–159.

Sahraoui, F., Goldstein, M.L., Robert, P., Khotyaintsev, Y.V., 2009. Evidence of a cascade and dissipation of solar-wind turbulence at the electron gyroscale. Phys. Rev. Lett. 102, 231102. URL: https://link.aps.org/doi/10.1103/PhysRevLett.102.231102, doi:10.1103/PhysRevLett.102.231102.

Salem, C., Mangeney, A., Bale, S.D., Veltri, P., 2009. Solar wind magnetohydrodynamic turbulence: anomalous scaling and role of intermittency. The Astrophysical Journal 702, 537–553. URL: https://doi.org/10.1088/0004-637x/702/1/537, doi:10.1088/0004-637x/702/1/537.

Sasunov, Y.L., Semenov, V.S., Heyn, M.F., Kubyshkin, I.V., Biernat, H.K., 2012. Kelvin-Helmholtz stability of reconnection exhausts in the solar wind. *Geophys. Res. Lett.* 39, L06104. doi:10.1029/2012GL051273.

Scalo, J., Elmegreen, B.G., 2004. Interstellar turbulence ii: Implications and effects. Annu. Rev. Astron. Astrophys. 42, 275–316. doi:10.1146/annurev.astro.42.120403.143327, arXiv:astro-ph/0404452.

Schwadron, N.A., McComas, D.J., 2021. Switchbacks explained: Super-Parker fields—the other side of the sub-Parker spiral. *Astrophys. J.* 909, 95. doi:10.3847/1538-4357/abd4e6, arXiv:2102.03696.

Schwartz, S.J., Horbury, T., Owen, C., Baumjohann, W., Nakamura, R., Canu, P., Roux, A., Sahraoui, F., Louarn, P., Sauvaud, J.A., Pinçon, J.L., Vaivads, A., Marcucci, M.F., Anastasiadis, A., Fujimoto, M., Escoubet, P., Taylor, M., Eckersley, S., Allouis, E., Perkinson, M.C., 2009. Cross-scale: multi-scale coupling in space plasmas. Experimental Astronomy 23, 1001–1015. doi:10.1007/s10686-008-9085-x.

Schwenn, R., 1983. The average solar wind in the inner heliosphere: Structures and slow variations. JPL Solar Wind Five .

Scott, B.D., 2007. Tokamak edge turbulence: background theory and computation. Plasma physics and controlled fusion 49, S25–S41. URL: https://doi.org/10.1088/0741-3335/49/7/s02, doi:10.1088/0741-3335/49/7/s02.

Servidio, S., Chasapis, A., Matthaeus, W.H., Perrone, D., Valentini, F., Parashar, T.N., Veltri, P., Gershman, D., Russell, C.T., Giles, B., Fuselier, S.A., Phan, T.D., Burch, J., 2017. Magnetospheric multiscale observation of plasma velocity-space cascade: Hermite representation and theory. Phys. Rev. Lett. 119, 205101. URL: https://link.aps.org/doi/10.1103/PhysRevLett.119.205101, doi:10.1103/PhysRevLett.119.205101.

Servidio, S., Greco, A., Matthaeus, W.H., Osman, K.T., Dmitruk, P., 2011. Statistical association of discontinuities and reconnection in magnetohydrodynamic turbulence. Journal of Geophysical Research: Space Physics 116. URL: https://agupubs.onlinelibrary.wiley.com/doi/abs/10.1029/2011JA016569, doi:https://doi.org/10.1029/2011JA016569.

Servidio, S., Matthaeus, W.H., Shay, M.A., Cassak, P.A., Dmitruk, P., 2009. Magnetic reconnection in two-dimensional magnetohydrodynamic turbulence. Phys. Rev. Lett. 102, 115003. URL: https:

//link.aps.org/doi/10.1103/PhysRevLett.102.115003, doi:10.1103/PhysRevLett.102.115003.

Servidio, S., Osman, K.T., Valentini, F., Perrone, D., Califano, F., Chapman, S., Matthaeus, W.H., Veltri, P., 2014. Proton kinetic effects in Vlasov and solar wind turbulence. *Astrophys. J. Lett.* 781, L27. doi:10.1088/2041-8205/781/2/L27, arXiv:1306.6455.

Servidio, S., Primavera, L., Carbone, V., Noullez, A., Rypdal, K., 2008. A model for two-dimensional bursty turbulence in magnetized plasmas. Physics of Plasmas 15, 012301. URL: https://doi.org/10.1063/1.2825656, doi:10.1063/1.2825656, arXiv:https://doi.org/10.1063/1.2825656.

Shaikh, Z., Raghav, A., Bhaskar, A., 2017. The presence of turbulent and ordered local structure within the ICME shock-sheath and its contribution to Forbush decrease. *Astrophys. J.* 844, 121. doi:10.3847/1538-4357/aa729f.

She, Z.S., Leveque, E., 1994. Universal scaling laws in fully developed turbulence. *Phys. Rev. Lett.* 72, 336–339.

Shi, C., Velli, M., Tenerani, A., Rappazzo, F., Réville, V., 2020. Propagation of Alfvén waves in the expanding solar wind with the fast-slow stream interaction. *Astrophys. J.* 888, 68. doi:10.3847/1538-4357/ab5fce.

Shoda, M., Chandran, B.D.G., Cranmer, S.R., 2021. Turbulent generation of magnetic switchbacks in the Alfvénic solar wind. The Astrophysical Journal 915, 52. URL: https://doi.org/10.3847/1538-4357/abfdbc, doi:10.3847/1538-4357/abfdbc.

Shraiman, B.I., Siggia, E.D., 2000. Scalar turbulence. *Nature* 405, 639–646. doi:10.1038/35015000.

Sioulas, N., Huang, Z., Velli, M., Chhiber, R., Cuesta, M.E., Shi, C., Matthaeus, W.H., Bandyopadhyay, R., Vlahos, L., Bowen, T.A., Qudsi, R.A., Bale, S.D., Owen, C.J., Louarn, P., Fedorov, A., Maksimović, M., Stevens, M.L., Case, A., Kasper, J., Larson, D., Pulupa, M., Livi, R., 2022a. Magnetic field intermittency in the solar wind: Parker Solar Probe and SolO observations ranging from the Alfvén region up to 1 AU.

The Astrophysical Journal 934, 143. URL: https://doi.org/10.3847/1538-4357/ac7aa2, doi:10.3847/1538-4357/ac7aa2.

Sioulas, N., Shi, C., Huang, Z., Velli, M., 2022b. Preferential heating of protons over electrons from coherent structures during the first perihelion of the Parker Solar Probe. The Astrophysical Journal Letters 935, L29. URL: https://doi.org/10.3847/2041-8213/ac85de, doi:10.3847/2041-8213/ac85de.

Smith, C., L'Heureux, J., Ness, N., Acuña, M., Burlaga, L., Scheifele, J., 1998. The ACE magnetic fields experiment. Space Science Reviews 86, 613–632.

Smith, C.W., Isenberg, P.A., Matthaeus, W.H., Richardson, J.D., 2006. Turbulent heating of the solar wind by newborn interstellar pickup protons. *Astrophys. J.* 638, 508–517. doi:10.1086/498671.

Smith, C.W., Stawarz, J.E., Vasquez, B.J., Forman, M.A., MacBride, B.T., 2009. Turbulent cascade at 1 AU in high cross-helicity flows. *Phys. Rev. Lett.* 103, 201101. doi:10.1103/PhysRevLett.103.201101.

Smith, C.W., Tessein, J.A., Vasquez, B.J., Skoug, R.M., 2011. Turbulence associated with corotating interaction regions at 1 AU: Inertial range cross-helicity spectra. Journal of Geophysical Research: Space Physics 116. URL: https://agupubs.onlinelibrary.wiley.com/doi/abs/10.1029/2011JA016645, doi:https://doi.org/10.1029/2011JA016645.

Smith, C.W., Vasquez, B.J., 2021. Driving and dissipation of solar-wind turbulence: What is the evidence? Frontiers in Astronomy and Space Sciences 7, 114. doi:10.3389/fspas.2020.611909.

Smith, E.J., 2001. The heliospheric current sheet. Journal of Geophysical Research: Space Physics 106, 15819–15831. URL: https://agupubs.onlinelibrary.wiley.com/doi/abs/10.1029/2000JA000120, doi:https://doi.org/10.1029/2000JA000120.

Smith, E.J., Balogh, A., Neugebauer, M., McComas, D., 1995a. Ulysses observations of Alfvén waves in the southern and northern solar hemispheres. Geophysical Research Letters 22, 3381–3384. URL: https://agupubs.onlinelibrary.wiley.com/doi/abs/10.1029/95GL03268, doi:https://doi.org/10.1029/95GL03268.

Smith, E.J., Marsden, R.G., Page, D.E., 1995b. Ulysses above the Sun's south pole: An introduction. Science 268, 1005–1007. URL: https://www.science.org/doi/abs/10.1126/science.7754377, doi:10.1126/science.7754377.

Sonnerup, B.U.O., Paschmann, G., Papamastorakis, I., Sckopke, N., Haerendel, G., Bame, S.J., Asbridge, J.R., Gosling, J.T., Russell, C.T., 1981. Evidence for magnetic field reconnection at the earth's magnetopause. *J. Geophys. Res.* 86, 10049–10067. doi:10.1029/JA086iA12p10049.

Sorriso-Valvo, L., Carbone, F., Leonardis, E., Chen, C.H.K., Šafránková, J., Němeček, Z., 2017. Multifractal analysis of high resolution solar wind proton density measurements. Advances in Space Research 59, 1642–1651. doi:10.1016/j.asr.2016.12.024.

Sorriso-Valvo, L., Carbone, F., Perri, S., Greco, A., Marino, R., Bruno, R., 2018. On the statistical properties of turbulent energy transfer rate in the inner heliosphere. *Solar Phys.* 293, 10. doi:10.1007/s11207-017-1229-6, arXiv:1712.09825.

Sorriso-Valvo, L., Carbone, V., Bruno, R., 2005. On the origin of the strong intermittent nature of interplanetary magnetic field. *Space Sci. Rev.* 121, 49–53. doi:10.1007/s11214-006-5559-1.

Sorriso-Valvo, L., Carbone, V., Marino, R., Noullez, A., Bruno, R., Veltri, P., 2010. Sorriso-valvo et al. reply:. Phys. Rev. Lett. 104, 189002. URL: https://link.aps.org/doi/10.1103/PhysRevLett.104.189002, doi:10.1103/PhysRevLett.104.189002.

Sorriso-Valvo, L., Carbone, V., Noullez, A., Politano, H., Pouquet, A., Veltri, P., 2002. Analysis of cancellation in two-dimensional magnetohydrodynamic turbulence. Physics of Plasmas 9, 89–95. doi:10.1063/1.1420738, arXiv:nlin/0111053.

Sorriso-Valvo, L., Carbone, V., Veltri, P., Consolini, G., Bruno, R., 1999. Intermittency in the solar wind turbulence through probability distribution functions of fluctuations. *Geophys. Res. Lett.* 26, 1801–1804.

Sorriso-Valvo, L., Carbone, V., Veltri, P., Politano, H., Pouquet, A., 2000. Non-Gaussian probability distribution functions in two-dimensional

magnetohydrodynamic turbulence. Europhysics Letters (EPL) 51, 520–526. URL: https://doi.org/10.1209/epl/i2000-00369-6, doi:10.1209/epl/i2000-00369-6.

Sorriso-Valvo, L., Catapano, F., Retinò, A., Le Contel, O., Perrone, D., Roberts, O.W., Coburn, J.T., Panebianco, V., Valentini, F., Perri, S., Greco, A., Malara, F., Carbone, V., Veltri, P., Pezzi, O., Fraternale, F., Di Mare, F., Marino, R., Giles, B., Moore, T.E., Russell, C.T., Torbert, R.B., Burch, J.L., Khotyaintsev, Y.V., 2019a. Turbulence-driven ion beams in the magnetospheric Kelvin-Helmholtz instability. *Phys. Rev. Lett.* 122, 035102. doi:10.1103/PhysRevLett.122.035102, arXiv:1901.11482.

Sorriso-Valvo, L., De Vita, G., Fraternale, F., Gurchumelia, A., Perri, S., Nigro, G., Catapano, F., Retinò, A., Chen, C.H.K., Yordanova, E., Pezzi, O., Chargazia, K., Kharshiladze, O., Kvaratskhelia, D., Vásconez, C.L., Marino, R., Le Contel, O., Giles, B., Moore, T.E., Torbert, R.B., Burch, J.L., 2019b. Sign singularity of the local energy transfer in space plasma turbulence. Frontiers in Physics 7, 108. doi:10.3389/fphy.2019.00108, arXiv:1907.11108.

Sorriso-Valvo, L., Foldes, R., Marino, R., D'Amicis, R., Telloni, D., Yordanova, E., Bruno, R., 2022. Observation of decaying solar wind turbulence in the inner heliosphere. submitted to Astron. & Astrophys. .

Sorriso-Valvo, L., Marino, R., Carbone, V., Noullez, A., Lepreti, F., Veltri, P., Bruno, R., Bavassano, B., Pietropaolo, E., 2007. Observation of inertial energy cascade in interplanetary space plasma. *Phys. Rev. Lett.* 99, 115001.

Sorriso-Valvo, L., Marino, R., Lijoi, L., Perri, S., Carbone, V., 2015. Self-consistent Castaing distribution of solar wind turbulent fluctuations. The Astrophysical Journal 807, 86. URL: https://doi.org/10.1088/0004-637x/807/1/86, doi:10.1088/0004-637x/807/1/86.

Sorriso-Valvo, L., Yordanova, E., 2022. Where does solar wind turbulence break free? Astronomy & Astrophysics, submitted .

Sorriso-Valvo, L., Yordanova, E., Dimmock, A.P., Telloni, D., 2021. Turbulent cascade and energy transfer rate in a solar coronal mass ejection. *Astrophys. J. Lett.* 919, L30. doi:10.3847/2041-8213/ac26c5.

Spolaore, M., Antoni, V., Spada, E., Bergsåker, H., Cavazzana, R., Drake, J.R., Martines, E., Regnoli, G., Serianni, G., Vianello, N., 2004. Vortex-induced diffusivity in reversed field pinch plasmas. Phys. Rev. Lett. 93, 215003. URL: https://link.aps.org/doi/10.1103/PhysRevLett.93.215003, doi:10.1103/PhysRevLett.93.215003.

Spolaore, M., Vianello, N., Agostini, M., Cavazzana, R., Martines, E., Serianni, G., Scarin, P., Spada, E., Zuin, M., Antoni, V., 2009. Magnetic and electrostatic structures measured in the edge region of the rfx-mod experiment. Journal of Nuclear Materials 390-391, 448–451. URL: https://www.sciencedirect.com/science/article/pii/S0022311509001548, doi:https://doi.org/10.1016/j.jnucmat.2009.01.132. proceedings of the 18th International Conference on Plasma-Surface Interactions in Controlled Fusion Device.

Squire, J., Chandran, B.D.G., Meyrand, R., 2020. In-situ switchback formation in the expanding solar wind. *Astrophys. J. Lett.* 891, L2. doi:10.3847/2041-8213/ab74e1, arXiv:2001.08422.

Sreenivasan, K.R., 1991. Fractals and multifractals in fluid turbulence. Annual Review of Fluid Mechanics 23, 539–604. URL: https://doi.org/10.1146/annurev.fl.23.010191.002543, doi:10.1146/annurev.fl.23.010191.002543.

Stacey, W.M., 2005. Fusion plasma physics. Whiley-VCH, Weinheim, Germany.

Stawarz, J.E., Eriksson, S., Wilder, F.D., Ergun, R.E., Schwartz, S.J., Pouquet, A., Burch, J.L., Giles, B.L., Khotyaintsev, Y., Contel, O.L., Lindqvist, P.A., Magnes, W., Pollock, C.J., Russell, C.T., Strangeway, R.J., Torbert, R.B., Avanov, L.A., Dorelli, J.C., Eastwood, J.P., Gershman, D.J., Goodrich, K.A., Malaspina, D.M., Marklund, G.T., Mirioni, L., Sturner, A.P., 2016. Observations of turbulence in a Kelvin-Helmholtz event on 8 september 2015 by the magnetospheric multiscale mission. Journal of Geophysical Research: Space Physics 121, 11,021–11,034. URL: https://agupubs.onlinelibrary.wiley.com/doi/abs/10.1002/2016JA023458, doi:https://doi.org/10.1002/2016JA023458.

Stawarz, J.E., Smith, C.W., Vasquez, B.J., Forman, M.A., MacBride, B.T.,

2009. The turbulent cascade and proton heating in the solar wind at 1 AU. The Astrophysical Journal 697, 1119–1127.

Stawarz, J.E., Smith, C.W., Vasquez, B.J., Forman, M.A., MacBride, B.T., 2010. The turbulent cascade for high cross-helicity states at 1 AU. *Astrophys. J.* 713, 920–934. doi:10.1088/0004-637X/713/2/920.

Stawarz, J.E., Vasquez, B.J., Smith, C.W., Forman, M.A., Klewicki, J., 2011. Third moments and the role of anisotropy from velocity shear in the solar wind. The Astrophysical Journal 736, 44. URL: https://doi.org/10.1088/0004-637x/736/1/44, doi:10.1088/0004-637x/736/1/44.

Stein, R.F., 2012. Solar surface magneto-convection. Living Reviews in Solar Physics 9, 4. doi:10.12942/lrsp-2012-4.

Sterling, A.C., Moore, R.L., 2020. Coronal-jet-producing minifilament eruptions as a possible source of Parker Solar Probe switchbacks. *Astrophys. J. Lett.* 896, L18. doi:10.3847/2041-8213/ab96be, arXiv:2006.04990.

Stewart, B., 1861. On the great magnetic disturbance which extended from august 28 to september 7, 1859, as recorded by photography at the kew observatory. Philosophical Transactions of the Royal Society of London 151, 423–430. URL: http://www.jstor.org/stable/108745.

Stix, M., 2002. The Sun. Springer-Verlag Berlin Heidelberg.

Sundberg, T., Boardsen, S.A., Slavin, J.A., Anderson, B.J., Korth, H., Zurbuchen, T.H., Raines, J.M., Solomon, S.C., 2012. Messenger orbital observations of large-amplitude Kelvin-Helmholtz waves at mercury's magnetopause. Journal of Geophysical Research: Space Physics 117. URL: https://agupubs.onlinelibrary.wiley.com/doi/abs/10.1029/2011JA017268, doi:https://doi.org/10.1029/2011JA017268.

Sundkvist, D., Retinò, A., Vaivads, A., Bale, S.D., 2007. Dissipation in turbulent plasma due to reconnection in thin current sheets. Phys. Rev. Lett. 99, 025004. URL: https://link.aps.org/doi/10.1103/PhysRevLett.99.025004, doi:10.1103/PhysRevLett.99.025004.

Sweet, P.A., 1958. The neutral point theory of solar flares, in: Lehnert, B. (Ed.), IAU Symp. 6, Electromagnetic phenomena in cosmical physics, New York: Cambridge Univ. Press. p. 123.

Tang, B.B., Li, W.Y., Graham, D.B., Rager, A.C., Wang, C., Khotyaintsev, Y.V., Lavraud, B., Hasegawa, H., Zhang, Y.C., Dai, L., Giles, B.L., Dorelli, J.C., Russell, C.T., Lindqvist, P.A., Ergun, R.E., Burch, J.L., 2019. Crescent-shaped electron distributions at the nonreconnecting magnetopause: Magnetospheric multiscale observations. Geophysical Research Letters 46, 3024–3032. URL: https://agupubs.onlinelibrary.wiley.com/doi/abs/10.1029/2019GL082231, doi:https://doi.org/10.1029/2019GL082231.

Taylor, G.I., 1938. The spectrum of turbulence. *Royal Society of London Proceedings Series A* 164, 476–490.

Taylor, M.A., Kurien, S., Eyink, G.L., 2003. Recovering isotropic statistics in turbulence simulations: The Kolmogorov 4/5th law. Phys. Rev. E 68, 026310. URL: https://link.aps.org/doi/10.1103/PhysRevE.68.026310, doi:10.1103/PhysRevE.68.026310.

Telloni, D., Adhikari, L., Zank, G.P., Zhao, L., Sorriso-Valvo, L., Antonucci, E., Giordano, S., Mancuso, S., 2022a. Possible evidence for shear-driven kelvin–helmholtz instability along the boundary of fast and slow solar wind in the corona. The Astrophysical Journal 929, 98. URL: https://doi.org/10.3847/1538-4357/ac5cc3, doi:10.3847/1538-4357/ac5cc3.

Telloni, D., Sorriso-Valvo, L., Woodham, L.D., Panasenco, O., Velli, M., Carbone, F., Zank, G.P., Bruno, R., Perrone, D., Nakanotani, M., Shi, C., D'Amicis, R., Marco, R.D., Jagarlamudi, V.K., Steinvall, K., Marino, R., Adhikari, L., Zhao, L., Liang, H., Tenerani, A., Laker, R., Horbury, T.S., Bale, S.D., Pulupa, M., Malaspina, D.M., MacDowall, R.J., Goetz, K., de Wit, T.D., Harvey, P.R., Kasper, J.C., Korreck, K.E., Larson, D., Case, A.W., Stevens, M.L., Whittlesey, P., Livi, R., Owen, C.J., Livi, S., Louarn, P., Antonucci, E., Romoli, M., O'Brien, H., Evans, V., Angelini, V., 2021. Evolution of solar wind turbulence from 0.1 to 1 AU during the first Parker Solar Probe–Solar Orbiter radial alignment. The Astrophysical Journal Letters 912, L21. URL: https://doi.org/10.3847/2041-8213/abf7d1, doi:10.3847/2041-8213/abf7d1.

Telloni, D., Zank, G.P., et al., 2022b. Observation of magnetic switchback in the solar corona. The Astrophysical Journal Letters, in press .

Telloni, D., Zhao, L., Zank, G.P., Liang, H., Nakanotani, M., Adhikari, L., Carbone, F., D'Amicis, R., Perrone, D., Bruno, R., Dasso, S., 2020. Magnetohydrodynamic turbulent evolution of a magnetic cloud in the outer heliosphere. *Astrophys. J. Lett.* 905, L12. doi:10.3847/2041-8213/abcb03.

Tenerani, A., Sioulas, N., Matteini, L., Panasenco, O., Shi, C., Velli, M., 2021. Evolution of switchbacks in the inner heliosphere. *Astrophys. J. Lett.* 919, L31. doi:10.3847/2041-8213/ac2606, arXiv:2109.06341.

Tenerani, A., Velli, M., 2017. Evolving waves and turbulence in the outer corona and inner heliosphere: The accelerating expanding box. *Astrophys. J.* 843, 26. doi:10.3847/1538-4357/aa71b9.

Tenerani, A., Velli, M., Matteini, L., Réville, V., Shi, C., Bale, S.D., Kasper, J.C., Bonnell, J.W., Case, A.W., de Wit, T.D., Goetz, K., Harvey, P.R., Klein, K.G., Korreck, K., Larson, D., Livi, R., MacDowall, R.J., Malaspina, D.M., Pulupa, M., Stevens, M., Whittlesey, P., 2020. Magnetic field kinks and folds in the solar wind. The Astrophysical Journal Supplement Series 246, 32. URL: https://doi.org/10.3847/1538-4365/ab53e1, doi:10.3847/1538-4365/ab53e1.

Terry, P.W., 2000. Suppression of turbulence and transport by sheared flow. Rev. Mod. Phys. 72, 109–165. URL: https://link.aps.org/doi/10.1103/RevModPhys.72.109, doi:10.1103/RevModPhys.72.109.

Tessein, J.A., Matthaeus, W.H., Wan, M., Osman, K.T., Ruffolo, D., Giacalone, J., 2013. Association of suprathermal particles with coherent structures and shocks. The Astrophysical Journal 776, L8. URL: https://doi.org/10.1088/2041-8205/776/1/l8, doi:10.1088/2041-8205/776/1/l8.

Tooley, C.R., Black, R.K., Robertson, B.P., Stone, J.M., Pope, S.E., Davis, G.T., 2016. The magnetospheric multiscale constellation. *Space Sci. Rev.* 199, 23–76. doi:10.1007/s11214-015-0220-5.

Tu, C.Y., Marsch, E., 1995. Magnetohydrodynamic structures waves and turbulence in the solar wind - observations and theories. *Space Sci. Rev.* 73, 1–210. doi:10.1007/BF00748891.

Tóth, G., Jia, X., Markidis, S., Peng, I.B., Chen, Y., Daldorff, L.K.S., Tenishev, V.M., Borovikov, D., Haiducek, J.D., Gombosi, T.I., Glocer, A., Dorelli, J.C., 2016. Extended magnetohydrodynamics with embedded particle-in-cell simulation of ganymede's magnetosphere. Journal of Geophysical Research: Space Physics 121, 1273–1293. doi:https://doi.org/10.1002/2015JA021997.

Tóth, G., Ma, Y., Gombosi, T.I., 2008. Hall magnetohydrodynamics on block-adaptive grids. Journal of Computational Physics 227, 6967–6984. doi:https://doi.org/10.1016/j.jcp.2008.04.010.

Usmanov, A.V., Matthaeus, W.H., Goldstein, M.L., Chhiber, R., 2018. The steady global corona and solar wind: A three-dimensional MHD simulation with turbulence transport and heating. The Astrophysical Journal 865, 25. URL: https://doi.org/10.3847/1538-4357/aad687, doi:10.3847/1538-4357/aad687.

Valentini, F., Trávníček, P., Califano, F., Hellinger, P., Mangeney, A., 2007. A hybrid-Vlasov model based on the current advance method for the simulation of collisionless magnetized plasma. Journal of Computational Physics 225, 753–770. doi:10.1016/j.jcp.2007.01.001.

Vasquez, B.J., Smith, C.W., Hamilton, K., MacBride, B.T., Leamon, R.J., 2007. Evaluation of the turbulent energy cascade rates from the upper inertial range in the solar wind at 1 AU. Journal of Geophysical Research (Space Physics) 112, A07101. doi:10.1029/2007JA012305.

Vasquez, L.J., Rodriguez, A., Römer, R.A., 2008. Multifractal analysis of the metal-insulator transition in the three-dimensional Anderson model. I. Symmetry relation under typical averaging. *Phys. Rev. B* 78, 195106.

Vecchio, A., Carbone, V., Lepreti, F., Primavera, L., Sorriso-Valvo, L., Veltri, P., Alfonsi, G., Straus, T., 2005. Proper orthogonal decomposition of solar photospheric motions. *Phys. Rev. Lett.* 95, 061102. doi:10.1103/PhysRevLett.95.061102, arXiv:astro-ph/0506641.

Velli, M., Grappin, R., Mangeney, A., 1990. Solar wind expansion effects on the evolution of hydromagnetic turbulence in the interplanetary medium. Computer Physics Communications 59, 153–162. doi:10.1016/0010-4655(90)90165-W.

Velli, M., Harra, L.K., Vourlidas, A., Schwadron, N., Panasenco, O., Liewer, P.C., Müller, D., Zouganelis, I., St Cyr, O.C., Gilbert, H., Nieves-Chinchilla, T., Auchère, F., Berghmans, D., Fludra, A., Horbury, T.S., Howard, R.A., Krucker, S., Maksimovic, M., Owen, C.J., Rodríguez-Pacheco, J., Romoli, M., Solanki, S.K., Wimmer-Schweingruber, R.F., Bale, S., Kasper, J., McComas, D.J., Raouafi, N., Martinez-Pillet, V., Walsh, A.P., De Groof, A., Williams, D., 2020. Understanding the origins of the heliosphere: integrating observations and measurements from Parker Solar Probe, Solar Orbiter, and other space- and ground-based observatories. *Astron. Astrophys.* 642, A4. doi:10.1051/0004-6361/202038245.

Veltri, P., 1999. MHD turbulence in the solar wind: self-similarity, intermittency and coherent structures. *Plasma Phys. and Controlled Fusion* 41, 787.

Verdini, A., Grappin, R., 2015. IMPRINTS OF EXPANSION ON THE LOCAL ANISOTROPY OF SOLAR WIND TURBULENCE. The Astrophysical Journal 808, L34. URL: https://doi.org/10.1088/2041-8205/808/2/l34, doi:10.1088/2041-8205/808/2/l34.

Verdini, A., Grappin, R., Hellinger, P., Landi, S., Müller, W.C., 2015. ANISOTROPY OF THIRD-ORDER STRUCTURE FUNCTIONS IN MHD TURBULENCE. The Astrophysical Journal 804, 119. URL: https://doi.org/10.1088/0004-637x/804/2/119, doi:10.1088/0004-637x/804/2/119.

Verdini, A., Grappin, R., Pinto, R., Velli, M., 2012. On the origin of the 1/f spectrum in the solar wind magnetic field. The Astrophysical Journal 750, L33. URL: https://doi.org/10.1088/2041-8205/750/2/l33, doi:10.1088/2041-8205/750/2/l33.

Verdini, A., Landi, S., Hellinger, P., 2014. Measuring the cascade rate in anisotropic turbulence through 3rd order structure functions., in: EGU General Assembly 2014, pp. EGU2014–2197.

Verma, M.K., 2022. Taylor's frozen-in hypothesis for magnetohydrodynamic turbulence and solar wind. Physics of Plasmas 29, 082902. URL: https://doi.org/10.1063/5.0096743, doi:10.1063/5.0096743, arXiv:https://doi.org/10.1063/5.0096743.

Verma, M.K., Roberts, D.A., Goldstein, M.L., 1995. Turbulent heating and temperature evolution in the solar wind plasma. *J. Geophys. Res.* 100, 19839–19850. doi:10.1029/95JA01216.

Verniero, J.L., Howes, G.G., Stewart, D.E., Klein, K.G., 2021. Determining threshold instrumental resolutions for resolving the velocity-space signature of ion landau damping. Journal of Geophysical Research: Space Physics 126, e2020JA028361. URL: https://agupubs.onlinelibrary.wiley.com/doi/abs/10.1029/2020JA028361, doi:https://doi.org/10.1029/2020JA028361. e2020JA028361 2020JA028361.

Verniero, J.L., Howes, G.G., Stewart, D.E., Klein, K.G., 2021. Patch: Particle arrival time correlation for heliophysics. Journal of Geophysical Research (Space Physics) 126, e28940. doi:10.1029/2020JA028940.

Verscharen, D., 2019. A step closer to the Sun's secrets. *Nature* 576, 219–220. doi:10.1038/d41586-019-03665-3.

Verscharen, D., Klein, K.G., Maruca, B.A., 2019. The multi-scale nature of the solar wind. Living Reviews in Solar Physics 16, 5. doi:10.1007/s41116-019-0021-0, arXiv:1902.03448.

Viall, N.M., Borovsky, J.E., 2020. Nine outstanding questions of solar wind physics. Journal of Geophysical Research: Space Physics 125, e2018JA026005. doi:https://doi.org/10.1029/2018JA026005.

von Weizsäcker, C.F., 1951. The evolution of galaxies and stars. *Astrophys. J.* 114, 165. doi:10.1086/145462.

Vásconez, C.L., Perrone, D., Marino, R., Laveder, D., Valentini, F., Servidio, S., Mininni, P., Sorriso-Valvo, L., 2021. Local and global properties of energy transfer in models of plasma turbulence. Journal of Plasma Physics 87, 825870101. doi:10.1017/S0022377820001567.

Vörös, Z., Baumjohann, W., Nakamura, R., Volwerk, M., Runov, A., Zhang, T.L., Eichelberger, H.U., Treumann, R., Georgescu, E., Balogh, A., Klecker, B., Réme, H., 2004. Magnetic turbulence in the plasma sheet. Journal of Geophysical Research: Space Physics 109. URL: https://agupubs.onlinelibrary.wiley.com/doi/abs/10.1029/2004JA010404, doi:https://doi.org/10.1029/2004JA010404.

Wan, M., Servidio, S., Oughton, S., Matthaeus, W.H., 2009. The third-order law for increments in magnetohydrodynamic turbulence with constant shear. Physics of Plasmas 16, 090703. URL: https://doi.org/10.1063/1.3240333, doi:10.1063/1.3240333, arXiv:https://doi.org/10.1063/1.3240333.

Wan, M., Servidio, S., Oughton, S., Matthaeus, W.H., 2010. The third-order law for magnetohydrodynamic turbulence with shear: Numerical investigation. Physics of Plasmas 17, 052307. URL: https://doi.org/10.1063/1.3398481, doi:10.1063/1.3398481, arXiv:https://doi.org/10.1063/1.3398481.

Wang, X., Bhattacharjee, A., Ma, Z.W., 2001. Scaling of collisionless forced reconnection. Phys. Rev. Lett. 87, 265003. doi:10.1103/PhysRevLett.87.265003.

Wang, Y.M., Robbrecht, E., Sheeley, N.R., 2009. On the weakening of the polar magnetic fields during solar cycle 23. The Astrophysical Journal 707, 1372–1386. URL: https://doi.org/10.1088/0004-637x/707/2/1372, doi:10.1088/0004-637x/707/2/1372.

Warhaft, Z., 2000. Passive scalars in turbulent flows. Annual Review of Fluid Mechanics 32, 203–240. doi:10.1146/annurev.fluid.32.1.203.

Warmuth, A., 2015. Large-scale globally propagating coronal waves. Living Reviews in Solar Physics 12, 3. doi:10.1007/lrsp-2015-3.

Watson, A.S., Smith, C.W., Marchuk, A.V., Argall, M.R., Joyce, C.J., Isenberg, P.A., Vasquez, B.J., Schwadron, N.A., Bzowski, M., Kubiak, M.A., Murphy, N., 2022. High-latitude observations of inertial-range turbulence by the ulysses spacecraft during the solar minimum of 1993–96. The Astrophysical Journal 927, 43. URL: https://doi.org/10.3847/1538-4357/ac4588, doi:10.3847/1538-4357/ac4588.

Webb, D., Nitta, N., 2017. Understanding problem forecasts of ISEST campaign flare-CME events. *Solar Phys.* 292, 142. doi:10.1007/s11207-017-1166-4.

Welter, G.S., Esquef, P.A.A., 2013. Multifractal analysis based on amplitude extrema of intrinsic mode functions. Phys. Rev. E 87, 032916. doi:10.1103/PhysRevE.87.032916.

Wielgus, M., Akiyama, K., Blackburn, L., Chan, C.k., Dexter, J., Doeleman, S.S., Fish, V.L., Issaoun, S., Johnson, M.D., Krichbaum, T.P., Lu, R.S., Pesce, D.W., Wong, G.N., Bower, G.C., Broderick, A.E., Chael, A., Chatterjee, K., Gammie, C.F., Georgiev, B., Hada, K., Loinard, L., Markoff, S., Marrone, D.P., Plambeck, R., Weintroub, J., Dexter, M., MacMahon, D.H.E., Wright, M., Alberdi, A., Alef, W., Asada, K., Azulay, R., Baczko, A.K., Ball, D., Baloković, M., Barausse, E., Barrett, J., Bintley, D., Boland, W., Bouman, K.L., Bremer, M., Brinkerink, C.D., Brissenden, R., Britzen, S., Broguiere, D., Bronzwaer, T., Byun, D.Y., Carlstrom, J.E., Chatterjee, S., Chen, M.T., Chen, Y., Cho, I., Christian, P., Conway, J.E., Cordes, J.M., Crew, G.B., Cui, Y., Davelaar, J., Laurentis, M.D., Deane, R., Dempsey, J., Desvignes, G., Dzib, S.A., Eatough, R.P., Falcke, H., Fomalont, E., Fraga-Encinas, R., Friberg, P., Fromm, C.M., Galison, P., García, R., Gentaz, O., Goddi, C., Gold, R., Gómez, J.L., Gómez-Ruiz, A.I., Gu, M., Gurwell, M., Hecht, M.H., Hesper, R., Ho, L.C., Ho, P., Honma, M., Huang, C.W.L., Huang, L., Hughes, D.H., Inoue, M., James, D.J., Jannuzi, B.T., Janssen, M., Jeter, B., Jiang, W., Jimenez-Rosales, A., Jorstad, S., Jung, T., Karami, M., Karuppusamy, R., Kawashima, T., Keating, G.K., Kettenis, M., Kim, J.Y., Kim, J., Kim, J., Kino, M., Koay, J.Y., Koch, P.M., Koyama, S., Kramer, M., Kramer, C., Kuo, C.Y., Lauer, T.R., Lee, S.S., Li, Y.R., Li, Z., Lindqvist, M., Lico, R., Liu, K., Liuzzo, E., Lo, W.P., Lobanov, A.P., Lonsdale, C., MacDonald, N.R., Mao, J., Marchili, N., Marscher, A.P., Martí-Vidal, I., Matsushita, S., Matthews, L.D., Medeiros, L., Menten, K.M., Mizuno, Y., Mizuno, I., Moran, J.M., Moriyama, K., Moscibrodzka, M., Müller, C., Musoke, G., Nagai, H., Nagar, N.M., Nakamura, M., Narayan, R., Narayanan, G., Natarajan, I., Nathanail, A., Neri, R., Ni, C., Noutsos, A., Okino, H., Olivares, H., Ortiz-León, G.N., Oyama, T., Özel, F., Palumbo, D.C.M., Park, J., Patel, N., Pen, U.L., Piétu, V., PopStefanija, A., Porth, O., Prather, B., Preciado-López, J.A., Psaltis, D., Pu, H.Y., Ramakrishnan, V., Rao, R., Rawlings, M.G., Raymond, A.W., Rezzolla, L., Ripperda, B., Roelofs, F., Rogers, A., Ros, E., Rose, M., Roshanineshat, A., Rottmann, H., Roy, A.L., Ruszczyk, C., Ryan, B.R., Rygl, K.L.J., Sánchez, S., Sánchez-Arguelles, D., Sasada, M., Savolainen, T., Schloerb, F.P., Schuster, K.F., Shao, L., Shen, Z., Small, D., Sohn, B.W., SooHoo, J., Tazaki, F., Tiede, P., Tilanus, R.P.J., Titus, M., Toma, K., Torne, P., Trent, T., Traianou, E., Trippe, S., Tsuda, S., Bemmel, I.v., van Langevelde, H.J., van Rossum, D.R., Wagner, J., Wardle, J., Ward-Thompson, D., Wex, N., Wharton, R., Wu, Q., Yoon,

D., Young, A., Young, K., Younsi, Z., Yuan, F., Yuan, Y.F., Zensus, J.A., Zhao, G., Zhao, S.S., Zhu, Z., 2020. Monitoring the morphology of m87* in 2009-2017 with the event horizon telescope. *Astrophys. J.* 901, 67. doi:10.3847/1538-4357/abac0d, arXiv:2009.11842.

Wright, R., Torry, C., 1973. The great gig in the sky, in: Pink Floyd: The Dark Side of the Moon, Harvest Records.

Wu, H., Tu, C., He, J., Wang, X., Yang, L., 2022a. Consistency of von kármán decay rate with the energy supply rate and heating rate observed by Parker Solar Probe. The Astrophysical Journal 926, 116. URL: https://doi.org/10.3847/1538-4357/ac4413, doi:10.3847/1538-4357/ac4413.

Wu, H., Tu, C., He, J., Wang, X., Yang, L., 2022b. The Yaglom scaling of the third-order structure functions in the inner heliosphere observed by Helios 1 and 2. The Astrophysical Journal 927, 113. URL: https://doi.org/10.3847/1538-4357/ac4fcc, doi:10.3847/1538-4357/ac4fcc.

Wu, P., Perri, S., Osman, K., Wan, M., Matthaeus, W.H., Shay, M.A., Goldstein, M.L., Karimabadi, H., Chapman, S., 2013. Intermittent heating in solar wind and kinetic simulations. The Astrophysical Journal Letters 763, L30. URL: http://stacks.iop.org/2041-8205/763/i=2/a=L30.

Wurster, J., Bate, M.R., Bonnell, I.A., 2021. The impact of non-ideal magnetohydrodynamic processes on discs, outflows, counter-rotation, and magnetic walls during the early stages of star formation. Monthly Notices of the Royal Astronomical Society 507, 2354–2372. doi:10.1093/mnras/stab2296, arXiv:2108.02787.

Xie, L., Li, L., Zhang, Y., Feng, Y., Wang, X., Zhang, A., Kong, L., 2015. Three-dimensional Hall MHD simulation of lunar minimagnetosphere: General characteristics and comparison with Chang'E-2 observations. Journal of Geophysical Research: Space Physics 120, 6559–6568. doi:https://doi.org/10.1002/2015JA021647.

Yaglom, A.M., 1949. Local structure of the temperature field in a turbulent flow. Dokl. Akad. Nauk SSSR 69, 743–746.

Yamada, M., Kulsrud, R., Ji, H., 2010. Magnetic reconnection. Rev. Mod. Phys. 82, 603–664. URL: https://link.aps.org/doi/10.1103/RevModPhys.82.603, doi:10.1103/RevModPhys.82.603.

Yamauchi, Y., Suess, S.T., Steinberg, J.T., Sakurai, T., 2004. Differential velocity between solar wind protons and alpha particles in pressure balance structures. Journal of Geophysical Research: Space Physics 109. URL: https://agupubs.onlinelibrary.wiley.com/doi/abs/10.1029/2003JA010274, doi:https://doi.org/10.1029/2003JA010274.

Yang, Y., Wan, M., Matthaeus, W.H., Sorriso-Valvo, L., Parashar, T.N., Lu, Q., Shi, Y., Chen, S., 2018. Scale dependence of energy transfer in turbulent plasma. Monthly Notices of the Royal Astronomical Society 482, 4933–4940. URL: https://doi.org/10.1093/mnras/sty2977, doi:10.1093/mnras/sty2977.

Yokoyama, T., Shibata, K., 2001. Magnetohydrodynamic simulation of a solar flare with chromospheric evaporation effect based on the magnetic reconnection model. *Astrophys. J.* 549, 1160–1174. doi:10.1086/319440.

Yordanova, E., Vaivads, A., André, M., Buchert, S.C., Vörös, Z., 2008. Magnetosheath plasma turbulence and its spatiotemporal evolution as observed by the Cluster spacecraft. Phys. Rev. Lett. 100, 205003. URL: https://link.aps.org/doi/10.1103/PhysRevLett.100.205003, doi:10.1103/PhysRevLett.100.205003.

Yordanova, E., Vörös, Z., Sorriso-Valvo, L., Dimmock, A.P., Kilpua, E., 2021. A possible link between turbulence and plasma heating. The Astrophysical Journal 921, 65. URL: https://doi.org/10.3847/1538-4357/ac1942, doi:10.3847/1538-4357/ac1942.

Zank, G.P., Adhikari, L., Zhao, L.L., Mostafavi, P., Zirnstein, E.J., McComas, D.J., 2018. The pickup ion-mediated solar wind. *Astrophys. J.* 869, 23. doi:10.3847/1538-4357/aaebfe.

Zank, G.P., Dosch, A., Hunana, P., Florinski, V., Matthaeus, W.H., Webb, G.M., 2011. The transport of low-frequency turbulence in astrophysical flows. I. Governing equations. The Astrophysical Journal 745, 35. URL: https://doi.org/10.1088/0004-637x/745/1/35, doi:10.1088/0004-637x/745/1/35.

Zank, G.P., Matthaeus, W.H., Smith, C.W., 1996. Evolution of turbulent magnetic fluctuation power with heliospheric distance. Journal of Geophysical Research: Space Physics 101, 17093–17107.

Zank, G.P., Nakanotani, M., Zhao, L.L., Adhikari, L., Kasper, J., 2020. The origin of switchbacks in the solar corona: Linear theory. *Astrophys. J.* 903, 1. doi:10.3847/1538-4357/abb828.

Zank, G.P., Zhao, L.L., Adhikari, L., Telloni, D., Kasper, J.C., Bale, S.D., 2021. Turbulence transport in the solar corona: Theory, modeling, and Parker Solar Probe. Physics of Plasmas 28, 080501. URL: https://doi.org/10.1063/5.0055692, doi:10.1063/5.0055692, arXiv:https://doi.org/10.1063/5.0055692.

Zank, G.P., Zhao, L.L., Adhikari, L., Telloni, D., Kasper, J.C., Stevens, M., Rahmati, A., Bale, S.D., 2022. Turbulence in the sub-Alfvénic solar wind. The Astrophysical Journal Letters 926, L16. URL: https://doi.org/10.3847/2041-8213/ac51da, doi:10.3847/2041-8213/ac51da.

Zenitani, S., Hesse, M., Klimas, A., Kuznetsova, M., 2011. New measure of the dissipation region in collisionless magnetic reconnection. Phys. Rev. Lett. 106, 195003. URL: https://link.aps.org/doi/10.1103/PhysRevLett.106.195003, doi:10.1103/PhysRevLett.106.195003.

Zhao, L.L., Zank, G.P., Telloni, D., Stevens, M., Kasper, J.C., Bale, S.D., 2022. The turbulent properties of the sub-Alfvénic solar wind measured by the Parker Solar Probe. The Astrophysical Journal Letters 928, L15. URL: https://doi.org/10.3847/2041-8213/ac5fb0, doi:10.3847/2041-8213/ac5fb0.

Zhelavskaya, I.S., Shprits, Y.Y., Spasojević, M., 2017. Empirical modeling of the plasmasphere dynamics using neural networks. Journal of Geophysical Research: Space Physics 122, 11,227–11,244. doi:https://doi.org/10.1002/2017JA024406.

Zhou, Y., Matthaeus, W.H., 1990. Remarks on transport theories of interplanetary fluctuations. Journal of Geophysical Research: Space Physics 95, 14863–14871.

Zhuravleva, I., Churazov, E., Schekochihin, A.A., Allen, S.W., Arévalo, P., Fabian, A.C., Forman, W.R., Sanders, J.S., Simionescu, A., Sunyaev, R., Vikhlinin, A., Werner, N., 2014. Turbulent heating in galaxy clusters brightest in x-rays. *Nature* 515, 85–87. doi:10.1038/nature13830, arXiv:1410.6485.

Zimbardo, G., Greco, A., Sorriso-Valvo, L., Perri, S., Vörös, Z., Aburjania, G., Chargazia, K., Alexandrova, O., 2010. Magnetic turbulence in the geospace environment. *Space Sci. Rev.* 156, 89–134. doi:10.1007/s11214-010-9692-5.

Zouganelis, I., De Groof, A., Walsh, A.P., Williams, D.R., Müller, D., St Cyr, O.C., Auchère, F., Berghmans, D., Fludra, A., Horbury, T.S., Howard, R.A., Krucker, S., Maksimovic, M., Owen, C.J., Rodríguez-Pacheco, J., Romoli, M., Solanki, S.K., Watson, C., Sanchez, L., Lefort, J., Osuna, P., Gilbert, H.R., Nieves-Chinchilla, T., Abbo, L., Alexandrova, O., Anastasiadis, A., Andretta, V., Antonucci, E., Appourchaux, T., Aran, A., Arge, C.N., Aulanier, G., Baker, D., Bale, S.D., Battaglia, M., Bellot Rubio, L., Bemporad, A., Berthomier, M., Bocchialini, K., Bonnin, X., Brun, A.S., Bruno, R., Buchlin, E., Büchner, J., Bucik, R., Carcaboso, F., Carr, R., Carrasco-Blázquez, I., Cecconi, B., Cernuda Cangas, I., Chen, C.H.K., Chitta, L.P., Chust, T., Dalmasse, K., D'Amicis, R., Da Deppo, V., De Marco, R., Dolei, S., Dolla, L., Dudok de Wit, T., van Driel-Gesztelyi, L., Eastwood, J.P., Espinosa Lara, F., Etesi, L., Fedorov, A., Félix-Redondo, F., Fineschi, S., Fleck, B., Fontaine, D., Fox, N.J., Gandorfer, A., Génot, V., Georgoulis, M.K., Gissot, S., Giunta, A., Gizon, L., Gómez-Herrero, R., Gontikakis, C., Graham, G., Green, L., Grundy, T., Haberreiter, M., Harra, L.K., Hassler, D.M., Hirzberger, J., Ho, G.C., Hurford, G., Innes, D., Issautier, K., James, A.W., Janitzek, N., Janvier, M., Jeffrey, N., Jenkins, J., Khotyaintsev, Y., Klein, K.L., Kontar, E.P., Kontogiannis, I., Krafft, C., Krasnoselskikh, V., Kretzschmar, M., Labrosse, N., Lagg, A., Landini, F., Lavraud, B., Leon, I., Lepri, S.T., Lewis, G.R., Liewer, P., Linker, J., Livi, S., Long, D.M., Louarn, P., Malandraki, O., Maloney, S., Martinez-Pillet, V., Martinovic, M., Masson, A., Matthews, S., Matteini, L., Meyer-Vernet, N., Moraitis, K., Morton, R.J., Musset, S., Nicolaou, G., Nindos, A., O'Brien, H., Orozco Suarez, D., Owens, M., Pancrazzi, M., Papaioannou, A., Parenti, S., Pariat, E., Patsourakos, S., Perrone, D., Peter, H., Pinto, R.F., Plainaki, C., Plettemeier, D., Plunkett, S.P., Raines, J.M., Raouafi, N., Reid, H., Retino, A., Rezeau, L., Rochus, P., Rodriguez, L., Rodriguez-Garcia, L., Roth, M., Rouillard, A.P., Sahraoui, F., Sasso, C., Schou, J., Schühle, U., Sorriso-Valvo, L., Soucek, J., Spadaro, D., Stangalini, M., Stansby, D., Steller, M., Strugarek, A., Štverák, Š., Susino, R., Telloni, D., Terasa, C., Teriaca, L., Toledo-Redondo, S., del Toro Iniesta, J.C., Tsiropoula, G., Tsounis, A., Tziotziou, K., Valentini, F.,

Vaivads, A., Vecchio, A., Velli, M., Verbeeck, C., Verdini, A., Verscharen, D., Vilmer, N., Vourlidas, A., Wicks, R., Wimmer-Schweingruber, R.F., Wiegelmann, T., Young, P.R., Zhukov, A.N., 2020. The solar orbiter science activity plan. translating solar and heliospheric physics questions into action. *Astron. Astrophys.* 642, A3. doi:10.1051/0004-6361/202038445, arXiv:2009.10772.

Zurbuchen, T.H., Richardson, I.G., 2006. In-situ solar wind and magnetic field signatures of interplanetary coronal mass ejections. Springer New York, New York, NY. pp. 31–43. URL: https://doi.org/10.1007/978-0-387-45088-9_3, doi:10.1007/978-0-387-45088-9_3.

Zweben, S.J., Boedo, J.A., Grulke, O., Hidalgo, C., LaBombard, B., Maqueda, R.J., Scarin, P., Terry, J.L., 2007. Edge turbulence measurements in toroidal fusion devices. Plasma Physics and Controlled Fusion 49, S1–S23. URL: https://doi.org/10.1088/0741-3335/49/7/s01, doi:10.1088/0741-3335/49/7/s01.